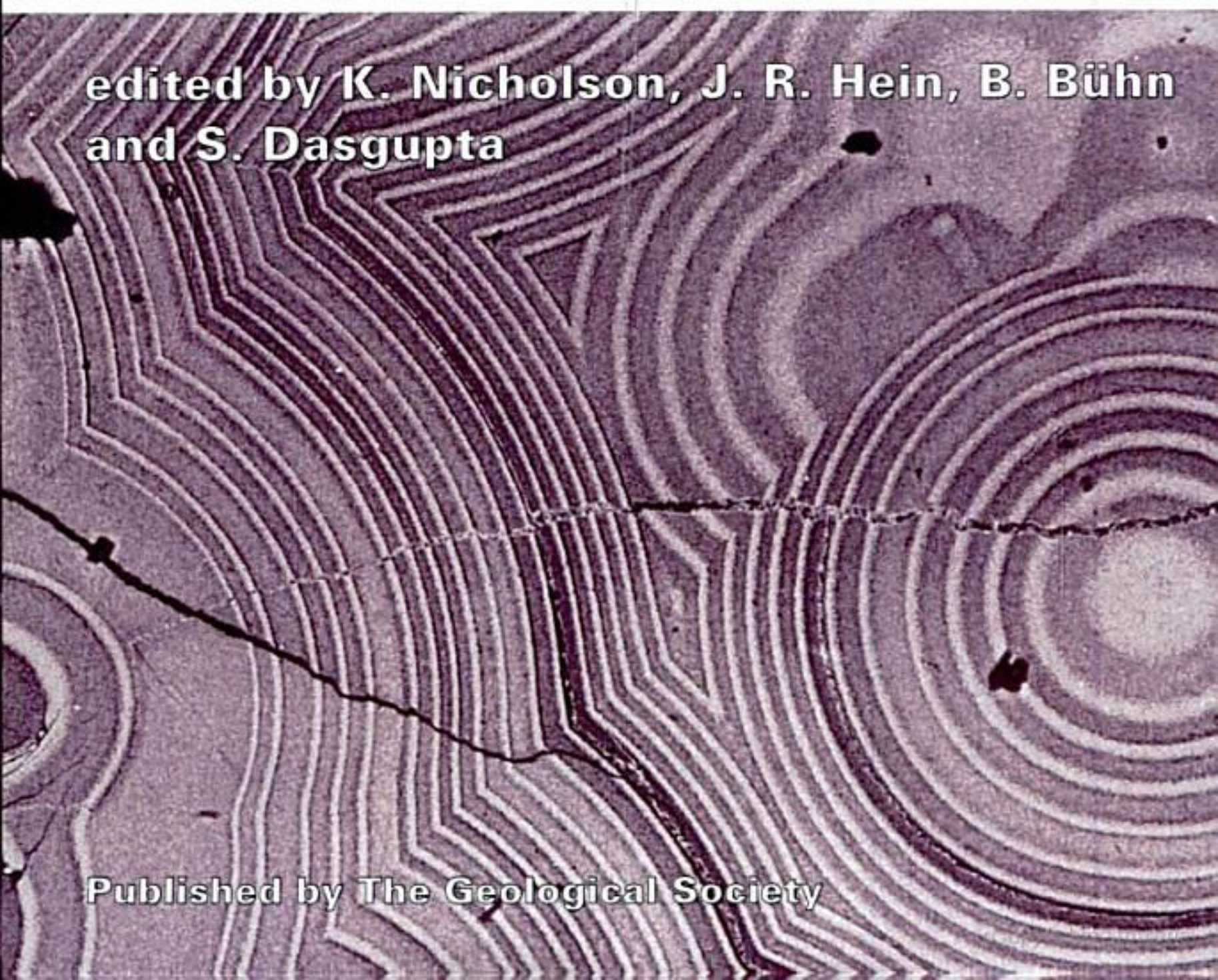


Manganese Mineralization: Geochemistry and Mineralogy of Terrestrial and Marine Deposits

**Geological Society
Special Publication
No. 119**

edited by **K. Nicholson, J. R. Hein, B. Bühn
and S. Dasgupta**

Published by The Geological Society



**Manganese Mineralization:
Geochemistry and Mineralogy of
Terrestrial and Marine Deposits**

Geological Society Special Publications
Series Editor A. J. FLEET

GEOLOGICAL SOCIETY SPECIAL PUBLICATION NO. 119

Manganese Mineralization:
Geochemistry and Mineralogy of
Terrestrial and Marine Deposits

EDITED BY

KEITH NICHOLSON

The Robert Gordon University, Aberdeen, UK

JAMES R. HEIN

United States Geological Survey

BERNHARD BÜHN

Justus-Liebig Universität, Giessen, Germany

and

SOMNATH DASGUPTA

Jadavpur University, India

1997

Published by

The Geological Society

London

THE GEOLOGICAL SOCIETY

The Society was founded in 1807 as The Geological Society of London and is the oldest geological society in the world. It received its Royal Charter in 1825 for the purpose of 'investigating the mineral structure of the Earth'. The Society is Britain's national society for geology with a membership of around 7500. It has countrywide coverage and approximately 1000 members reside overseas. The Society is responsible for all aspects of the geological sciences including professional matters. The Society has its own publishing house, which produces the Society's international journals, books and maps, and which acts as the European distributor for publications of the American Association of Petroleum Geologists, SEPM and the Geological Society of America.

Fellowship is open to those holding a recognized honours degree in geology or cognate subject and who have at least two years' relevant postgraduate experience, or who have not less than six years' relevant experience in geology or a cognate subject. A Fellow who has not less than five years' relevant postgraduate experience in the practice of geology may apply for validation and, subject to approval, may be able to use the designatory letters C Geol (Chartered Geologist).

Further information about the Society is available from the Membership Manager, The Geological Society, Burlington House, Piccadilly, London W1V 0JU, UK. The Society is a Registered Charity, No. 210161.

Published by The Geological Society from:
The Geological Society Publishing House

Unit 7, Brassmill Enterprise Centre
Brassmill Lane
Bath BA1 3JN
UK

(Orders: Tel. 01225 445046
Fax 01225 442836)

First published 1997

The publishers make no representation, express or implied, with regard to the accuracy of the information contained in this book and cannot accept any legal responsibility for any errors or omissions that may be made.

© The Geological Society 1997. All rights reserved. No reproduction, copy or transmission of this publication may be made without written permission. No paragraph of this publication may be reproduced, copied or transmitted save with the provisions of the Copyright Licensing Agency, 90 Tottenham Court Road, London W1P 9HE. Users registered with the Copyright Clearance Center, 27 Congress Street, Salem, MA 01970, USA: the item-fee code for this publication is 0305-8719/97/\$10.00.

British Library Cataloguing in Publication Data

A catalogue record for this book is available from the British Library.

ISBN 1-897799-74-8

Typeset by Aarontype Ltd, Unit 47, Easton Business Centre, Felix Road, Bristol BS5 0HE, UK

Printed by The Alden Press, Osney Mead, Oxford, UK.

Distributors

USA

AAPG Bookstore
PO Box 979
Tulsa
OK 74101-0979
USA

(Orders: Tel. (918) 584-2555
Fax (918) 560-2652)

Australia

Australian Mineral Foundation
63 Conyngham Street
Glenside
South Australia 5065
Australia

(Orders: Tel. (08) 379-0444
Fax (08) 379-4634)

India

Affiliated East-West Press PVT Ltd
G-1/16 Ansari Road
New Delhi 110 002
India

(Orders: Tel. (11) 327-9113
Fax (11) 326-0538)

Japan

Kanda Book Trading Co.
Tanikawa Building
3-2 Kanda Surugadai
Chiyoda-Ku
Tokyo 101
Japan

(Orders: Tel. (03) 3255-3497
Fax (03) 3255-3495)

Contents

Introduction

- NICHOLSON, K., HEIN, J. R., BÜHN, B. & DASGUPTA, S. Precambrian to Modern manganese mineralization: changes in ore type and depositional environment 1

Review

- ROY, S. Genetic diversity of manganese deposition in the terrestrial geological record 5

Precambrian deposits

- GLASBY, G. P. Fractionation of manganese from iron in Archaean and Proterozoic sedimentary ores 29
- KULIK, D. A. & KORZHNEV, M. N. Lithological and geochemical evidence of Fe and Mn pathways during deposition of lower Proterozoic Banded Iron Formation in the Krivoy Rog Basin (Ukraine) 43
- BÜHN, B. & STANISTREET, I. G. Insight into the enigma of Neoproterozoic manganese and iron formations from the perspective of supercontinental break-up and glaciation 81
- MANIKYAMBA, C. & NAQVI, S. M. Mineralogy and geochemistry of Archaean greenstone belt-hosted Mn formations and deposits of the Dharwar Craton: redox potential of proto-oceans 91
- MUKHOPADHYAY, J., CHAUDHURI, A. K. & CHANDA, S. K. Deep-water manganese deposits in the middle to late Proterozoic Penganga Group of the Pranhita–Godavari valley, South India 105
- NICHOLSON, K., NAYAK, V. K. & NANDA, J. K. Manganese ores of the Ghoriajhor – Monmunda area, Sundergarh District, Orissa, India: geochemical evidence for a mixed Mn source 117

Cenozoic deposits

- HEIN, J. R., KOSCHINSKY, A., HALBACH, P., MANHEIM, F. T., BAU, M., KANG, J. K. & LUBICK, N. Iron and manganese oxide mineralization in the Pacific 123
- CRONAN, D. S. Some controls on the geochemical variability of manganese nodules with particular reference to the tropical South Pacific 139
- VON STACKELBERG, U. Growth history of manganese nodules and crusts of the Peru Basin 153
- USUI, A. & SOMEYA, M. Distribution and composition of marine hydrogenetic and hydrothermal manganese deposits in the northwest Pacific 177
- NATH, B. N., PLÜGER, W. L. & ROELANDTS, I. Geochemical constraints on the hydrothermal origin of ferromanganese encrustations from the Rodriguez Triple Junction, Indian Ocean 199
- GLASBY, G. P., EMELYANOV, E. M., ZHAMOIDA, V. A., BATURIN, G. N., LEIPE, T., BAHLO, R. & BONACKER, P. Environments of formation of ferromanganese concretions in the Baltic Sea: a critical review 213
- REY, J., SOMOZA, L., MARTÍNEZ-FRÍAS, J., BENITO, R. & MARTÍN-ALFAGEME, S. Deception Island (Antarctica): a new target for exploration of Fe–Mn mineralization? 239
- CRESPO, A. & LUNAR, R. Terrestrial hot-spring Co-rich Mn mineralization in the Pliocene–Quaternary Calatrava Region (central Spain) 253

MICHAILIDIS, K. M., NICHOLSON, K., NIMFOPOULOUS, M. K. & PATRICK, R. A. D. An EPMA and SEM study of the Mn-oxide mineralization of Kato Nevrokopi, Macedonia, northern Greece: controls on formation of the Mn ⁴⁺ oxides	265
MIURA, H. & HARIYA, Y. Recent manganese oxide deposits in Hokkaido, Japan	281
Geochemistry and mineralogy	
GRAMM-OSIPOV, L. M. Formation of solid phases of manganese in oxygenated aquatic environments	301
NICHOLSON, K. & ELEY, M. Geochemistry of manganese oxides: metal adsorption in freshwater and marine environments	309
DASGUPTA, S. <i>P-T-X</i> relationships during metamorphism of manganese-rich sediments: current status and future studies	327
NIMFOPOULOUS, M. K., MICHAILIDIS, K. & CHRISTOFIDES, G. Zincian rancieite from the Kato Nevrokopi manganese deposits, Macedonia, northern Greece	339
GAMBLIN, S. D. & URCH, D. S. The determination of the valency of manganese in mineralogical and environmental samples by X-ray emission spectroscopy	349
Index	357

Precambrian to modern manganese mineralization: changes in ore type and depositional environment

KEITH NICHOLSON¹, JAMES R. HEIN²,
BERNHARD BÜHN³ & SOMNATH DASGUPTA⁴

¹ *Environmental Geochemistry Research Group, School of Applied Sciences,
The Robert Gordon University, Aberdeen AB25 1HG, UK*

² *US Geological Survey, MS 999, 345 Middlefield Road, Menlo Park, CA 94025, USA*

³ *Institut für Geowissenschaften und Lithosphärenforschung, Justus-Liebig Universität,
Senckenbergstrasse 3, D-35390 Giessen, Germany*

⁴ *Department of Geological Sciences, Jadavpur University, Calcutta 700032, India*

Manganese mineralization is diverse in occurrence, origin, mineralogy and geochemistry. These variations reflect differences in the processes of formation and depositional environments, which in turn are a response to changes in the land-ocean-atmosphere system over geological time. As such, manganese deposits can act as markers of major events in the dynamic evolution of the Earth's surface. Modern manganese accumulations provide insights into key factors controlling manganese deposition that cannot readily be determined from examination of ancient ores. A knowledge of oceanic currents, ocean chemistry or small-scale variations in physicochemical patterns of recent basins, for example, may extend our understanding of depositional processes in the past. Equally, the study of Precambrian deposits not only elucidates ancient mechanisms of manganese metallogenesis, but also helps to unravel the impact of comprehensive environmental changes on metal deposition on a scale not realized in younger geological times.

The papers collected in this volume provide insights into this changing nature of manganese mineralization from Precambrian sedimentary ores to crusts and nodules on the Cenozoic sea bed. The volume is introduced by **Supriya Roy** with a review of the range of terrestrial manganese deposits and their relative abundance through geological time.

Precambrian deposits

The manner in which manganese mineralization reflects changes in planetary environmental chemistry that was noted above and mentioned by Roy is further developed by papers in this section. **Glasby** illustrates the concomitant changes in iron-manganese aqueous geochemistry and fractionation with the evolution of

seawater chemistry. Low concentrations of sulphate ions in the early oceans prevented deposition of iron as a sulphide with a consequent reduction in iron-manganese fractionation in contrast to Phanerozoic deposits where fractionation can be significant. As a consequence, Precambrian banded iron formations commonly show high levels of manganese. This observation is taken further by **Kulik & Korzhnev** who developed a model for Ukrainian BIF deposition in which the manganese content is an indicator of the proportion of the original iron that precipitated as a carbonate.

Returning to the chemical evolution of the environment, **Bühn & Stanistreet** show that periods of manganese formation development are related to continental rifting periods. Precambrian glacial episodes may be causally related to such tectonic events, increasing ocean salinity and enhancing metal solubility to promote marine manganese and iron accumulation. The importance of seawater chemistry as a depositional control on manganese ores is further discussed by **Manikyamba & Naqvi** in considering deposits of the Dharwar Craton, India, which they suggest show evidence of enhanced biological activity in the local proto-ocean.

The palaeodepositional environment of Proterozoic sedimentary manganese ores is commonly cited as a shelf or basin margin setting. However, **Mukhopadhyay et al.**, by applying facies analysis to carbonaceous host sediments of the Pengana Group manganese deposits were able to recognize a deep-water, base-of-slope depositional setting which adds a previously unknown depositional regime for Precambrian manganese formations.

The sources of manganese in Precambrian deposits have been discussed by both Roy and Glasby, who recognize the greater importance of a hydrothermal contribution of manganese into early oceans relative to modern environments.

Lateral transport of hydrothermal manganese permitted it to be a principal source for the manganiferous shelf sediments common in the Proterozoic. *Nicholson et al.* used geochemical evidence to suggest a mixed manganese source for deposits in Orissa, India. There, episodic hydrothermal-source manganese precipitation is characterized by arsenic enrichments. These deposits are intermixed with arsenic-poor ores, with manganese contributed by a second, non-hydrothermal source.

Cenozoic deposits

Younger manganese deposits show a wide diversity of genetic types, from nodules, crusts and stratabound layers in ocean basins, to deposits precipitated from terrestrial and marine hydrothermal fluids. The papers in this section reflect this diversity in reviewing and describing representative deposits.

Hein et al. review the depositional processes, setting, morphology and chemistry of manganese-iron oxide mineralization in the Pacific Ocean. These include examples of oxides formed by hydrogenetic precipitation from ambient seawater, deposition from hydrothermal fluids and sediment pore waters, and replacement deposits. They also discuss the chemical mechanisms related to oxide formation. Biogeochemical controls on oxide chemistry are considered by *Cronan*. He highlights the importance of organic matter and therefore biological activity as a factor in manganese deposition in the South Pacific. As bioproductivity increases northwards towards the equator, there is a concomitant increase in the amount of manganese and trace metals that reach the sea bed, a trend reflected in the nickel and copper enrichments in manganese nodules. The importance of high biological activity to nodule development is discussed in relation to the Peru Basin by *von Stackelberg*. Like *Cronan*, he emphasizes the correlation between nodule abundance, growth rate and the CCD, the latter of which is controlled by bioproductivity. Large nodules show increased diagenetic accumulations as they sink in soft sediment to the redox boundary. Movement of the nodules by organisms between diagenetic and hydrogenetic growth regimes produces layering in the nodule. Variations in nodule abundance and chemistry with geological setting are recognised in the northwest Pacific Ocean by *Usui & Someya*. They produced a database of deposits in the area, through which they identify nodule-setting associations. Nodules and crusts on Cretaceous

seamounts, for example, are enriched in cobalt relative to other deposits.

Hydrothermal iron-manganese crusts from the Indian Ocean described by *Nath et al.* show depositional periods where a hydrogenetic input is dominant. The composition of the crusts reflect an episodic hydrothermal discharge and manganese contribution to the crusts – a modern analogue to the depositional process proposed by *Nicholson et al.* for a Precambrian ore.

As manganese ores can reflect changes in the natural chemical evolution of the environment, so they may also record zones of metal pollution. *Glasby et al.* describe the distribution, morphology and chemistry of rapidly growing concretions from the Baltic Sea and show how these are influenced by anthropogenic metal inputs, raising their potential as a sampling medium in environmental monitoring.

Hydrothermal fluids from both marine and terrestrial geothermal systems can deposit manganese minerals in sub-surface vein systems and stratabound layers as well as surface discharge precipitates. Both modern and ancient examples of these types of mineralization are described in the following papers. In the Antarctic, *Rey et al.* identified an area of redundant hot springs and fumaroles. Enrichments in the marine sediments of Deception Island show the area as an exploration target for iron-manganese mineralization. *Crespo & Lunar* describe a sequence in Spain where terrestrial hot-spring manganese mineralization grades into distal sedimentary, stratabound ores. These Cenozoic deposits are related to failed-rift volcanism and show high cobalt enrichments. Cenozoic manganese mineralization in Greece is described by *Michailidis et al.* who elucidate the controls on the formation of an oxide mineral assemblage formed by the weathering of vein carbonates and sulphide minerals. Modern manganese-depositing terrestrial hot-springs are rare. Those in Hokkaido, Japan are described by *Miura & Hariya*, who recognise a biogenic influence in some of the oxides deposited by these geothermal systems. Geochemical enrichments in the oxides are related to the manganese minerals present, and high arsenic values in some of the deposits are notable.

Geochemistry and mineralogy

Any investigation into the genesis of manganese mineralization needs to consider the geochemistry and mineralogy of the deposit. Experimental and modelling approaches to manganese geochemistry and mineralogy can further aid

our understanding of the formational and depositional processes involved and thereby our interpretation of deposit metallogenesis.

Gramm-Osipov examines the chemical thermodynamics of manganese oxide deposition in aqueous environments, with emphasis on seawater. He suggests that formation of the oxides is a two-stage process commencing with an oxyhydroxide compound that is subsequently transformed into more complex oxides. The processes behind the development of the distinctive genetic geochemical signatures of many deposits is investigated by **Nicholson & Eley**, who model and compare the adsorption of trace metals onto manganese oxides in simulated freshwater and seawater environments. They show that relative metal enrichments are less in seawater deposits due to multi-ion competition, and for the level of enrichments commonly observed in deep-sea nodules to be achieved, the active surface layer of the oxides must be replenished by regular oxide precipitation.

Metamorphosed sedimentary ores represent a major deposit type, but by their nature are demanding to model. Dasgupta critically reviews the mineralogical and geochemical changes that occur on metamorphism of manganiferous sedimentary rocks, and evaluates experimental data and the use of petrogenic grids. He additionally suggests areas for future research.

An unusually zinc-rich rancieite from Greece is described by **Nimfopoulous *et al.*** The mineral is formed in the later stages of the weathering profile of a carbonate-sulphide hydrothermal vein deposit. A novel, rapid method for the determination of manganese oxidation state in oxide minerals has been developed by **Gamblin & Urch**. They use variations in the form of the $K\beta$ X-ray emission spectrum related to the manganese oxidation state that can be easily recognized.

Overall the collection of papers in this volume illustrates the breadth of study necessary to understand the formation of manganese deposits – ores that provide markers to changes in

palaeo-environmental conditions and which may find future applications in environmental monitoring and technology.

This volume is the outcome of three IGCP 318 (Genesis and correlation of marine polymetallic oxides) meetings in Germany, the UK and India. The IGCP 318 session in Germany was held in Freiberg in conjunction with the seventy-second Annual Meeting of the German Mineralogical Association. The field workshop in India was to the Madhya Pradesh–Maharashtra manganese ore belt in central India. The UK meeting was part of a Lecture Series of The Geological Society of London that commemorates L. L. Fermor – an outstanding manganese researcher from the early part of this century. IGCP 318 ended in 1995 after a five-year tenure. This book is a fitting conclusion to the diversity and interdisciplinary nature of the IGCP 318.

As the work of L. L. Fermor was commemorated so, as this century draws to a close, we should also like to honour the contributions to the understanding of manganese mineralization made by D. A. Crerar, Roger Burns and J. Hem, their guidance and insights will be deeply missed.

The editors express their gratitude to the following reviewers:

I. Abs-Wurmbach	Alec Livingstone
W. Altermann	J. Gutzmer
J. Behrmann	Randolph A. Koski
Clive Boulter	P. A. Kukla
Barrie Bolton	D. A. Kulik
Nick J. Beukes	K. Langer
William F. Cannon	Frank T. Manheim
Se-Won Chang	J. Barry Maynard
N. Cook	A. Mookherjee
C. Cowan	S. Mitra
David Cronan	Keith Nicholson
Somnath Dasgupta	E. G. Nisbet
Eric H. De Carlo	S. Roy
Eric Force	I. G. Stanistreet
Neil Fortey	B. Stribrny
Y. Hariya	T. Will
James R. Hein	E. Woermann

Genetic diversity of manganese deposition in the terrestrial geological record

SUPRIYA ROY

Department of Geological Sciences, Jadavpur University, Calcutta – 700 032, India

Abstract: Terrestrial manganese deposits formed by hydrothermal, sedimentary and supergene processes. Ancient analogues of modern oceanic hydrothermal deposits formed in spreading centre and subduction-related settings and those deposited from terrestrial hot springs are discussed. Sedimentary Mn oxide deposits formed in shallow water at the margins of stratified oceans above the redoxcline during sea-level changes. Mn carbonate deposits probably formed by diagenesis through Mn oxyhydroxide reduction coupled with organic matter oxidation. Climatic variation, and basin water stratification, responsible for Mn concentration, were manifestations of atmospheric CO₂ content prompted by tectonism. Supergene manganese enrichment in continental weathering profiles was mainly dictated by climate, topography and drainage systems.

Manganese deposits of diverse genetic types occur in the terrestrial geological record (Roy 1981). These were produced by direct hydrothermal activity, sedimentary processes, and continental weathering. Although the processes may be interrelated, each involves distinct mechanisms that place the deposits into specific genetic types. Some of these processes are best understood in present-day depositional sites. The ancient environments were determined by the intensity and style of tectonism, volcanism and hydrothermal activity, the composition of the atmosphere and the hydrosphere, and the development of the biosphere, which all varied with time. It is my intention to unfold the total panorama of the environmental evolution during different time envelopes that produced a variety of manganese deposits in the past. Only major deposits and those providing distinctive evidence of their environment of deposition will be considered here.

Hydrothermal manganese deposits

Hydrothermal concentration of manganese as generally small deposits is fairly common in the geological record particularly during the Phanerozoic eon. These deposits are often stratabound, but may also occur as irregular bodies and epithermal veins in a large variety of host rocks. In many places, these ancient stratabound orebodies display characteristic tectonic, rock-association, mineralogical and chemical signatures that permit their correlation to deposits that are now being generated hydrothermally in the marine realm at or near spreading centres, mid-plate seamounts, and subduction-related island-arc settings. Emission of hydrothermal

solution in shallow continental basins (e.g. lakes) has also produced stratabound manganese deposits (Nicholson 1990). Vein-type hydrothermal deposits are hosted mainly in volcanics of wide-ranging compositions as well as in a variety of sedimentary rocks of different ages.

A number of deposits from active plate margins such as those of the northern Apennine assemblage (Bonatti *et al.* 1976), Pindos and Othris zones (Robertson & Varnavas 1993), and the Olympic Peninsula deposit (Park 1946) demonstrate their derivation from mid-ocean ridge settings (Table 1) with the volcanic rocks showing only MORB-type chemistry. Similar settings for hydrothermal manganese deposits have been reported from the Austrian Alps, Ethiopia and Japan.

Subduction-related stratabound and vein-type hydrothermal manganese deposits have been assigned different palaeotectonic settings such as fore-arc terraces, small inter-arc basins, shallow marginal basins and trenches adjacent to continental plate margins, and back-arc basins. The deposits are mostly hosted in sedimentary rocks (radiolarian chert, volcanoclastic rocks and hemipelagic rocks) overlying island-arc type basalts, andesite, dacite, and rhyolite. Different models have been expounded to explain the occurrences of these deposits in the given settings such as upward Mn-bearing fluid expulsion (at temperatures $\leq 100^\circ\text{C}$) by compaction and dewatering of subducting sediments in oceanic island-arcs (for discussions see Glasby 1988), and subduction of a mid-ocean ridge at a continental margin. However, determining the precise palaeotectonic setting of an ancient hydrothermal manganese deposit is a difficult task and a holistic assessment of all

Table 1. *Hydrothermal manganese deposits of mid-oceanic ridge type*

	Northern Apennine, Ophiolitic Complex, Italy	Pindos Geotectonic, Zone, Greece,	Othris, Greece,	Olympic Peninsula, USA
Age & geological sequence (bottom to top),	Late Jurassic; peridotite-gabbro-MOR basalt, radiolarian chert	Jurassic-Early Cretaceous; MOR basalt-metalliferous mudstone-radiolarian chert-red shale	Early Triassic to Cretaceous; late ultramafics-basalt/dolerite dykes-MOR basalt-chert and shale	Eocene; MOR basalt-pelagic limestone-argillite
Position of Mn and Mn-Fe-rich rocks	Mn-rich deposit at the base of Late Jurassic chert close to basalt-chert contact	Mn-rich deposit within radiolarites at the top of the sequence	Lenoid/stratified Mn deposit in chert-shale	Mn-rich lenses at the limestone-basalt contact
Mn-rich rock chemistry	Mn/Fe max. 768; low content of Ni, Co Cu, Zn; U/Th 1; total REE low; negative Ce anomaly	Mn/Fe 39 to 1086; very low Cu, Ni content	Mn/Fe 19 to 244; very low Cu, Ni, Co content	-
Other features	Fe-Cu-Zn sulphide deposits within basalt; low- to medium-grade seafloor hydrothermal metamorphism	Massive sulphide deposits in pillow basalts	Cu-rich pyrite as dykes and veins in mafic rock underlying chert-Mn horizon; Mn is either distal to hydrothermal discharge or related to off axis low temperature hydrothermal activity	Weak seafloor metamorphism
Modern analogues	TAG hydrothermal field, MAR 26° N	-	TAG area on MAR 26° N	-
References	Bonatti <i>et al.</i> (1976)	Robertson & Varnavas (1993)	Robertson & Varnavas (1993)	Park (1946)

geological and geochemical features is necessary. For example, the deposits of Manga Chrome, Smith Prospect (Sierra Nevada), Buckeye, Blue Jay, South Thomas (Franciscan Assemblage; Table 2) and that of Bald Knob, Carolina (Late Proterozoic; Flohr 1992) are geochemically similar but were formed in different tectonic environments and sometimes even by different processes. The mineral assemblages of these manganese deposits are also non-specific with respect to their palaeotectonic setting.

The chemistry of the ancient island-arc type-manganese deposits generally indicates their hydrothermal derivation (Table 2), although a dual imprint of hydrothermal and hydrogenous processes in the composition of manganese

crusts from similar present-day environments has been documented (Hein *et al.* 1988). The original geological setting of these ancient deposits is determined by the character and dominance of the volcanic and associated sedimentary rocks. Island-arc tholeiite, calc-alkaline basalt, andesite, dacite, and rhyolite are characteristic of a subduction-related setting including marginal basins and trenches and back-arc settings. The presence of volcanoclastic sediments, greywacke, biological detritus and radiolarites characterizes the subduction-related environments.

The Franciscan assemblage, California, demonstrates all attributes of a subduction-related setting. The question, however, is whether these

manganese deposits were produced in that setting or their presence there is merely incidental. Crerar *et al.* (1982) suggested that the manganese deposits at Blue Jay and South Thomas were created at a mid-ocean ridge setting similar to the present Galapagos Mounds situation and then transported to the present location. They did not, however, rule out a back-arc setting for these deposits. Huebner & Flohr (1990), on the other hand, suggested that the formation of these same deposits took place in marginal trenches of converging plate boundaries. Despite the controversy on the original site of formation of these deposits, the hydrothermal source for them and their present position in the subduction-related setting are valid. That various processes could operate in that tectonic setting is clearly shown by the Buckeye deposit. This deposit, while associated with a number of hydrothermal deposits of the Franciscan assemblage, has been shown to have formed by anoxic/suboxic diagenesis from a continental-margin sediment source rather than from hydrothermal solution (Hein & Koski 1987; Huebner & Flohr 1990; Huebner *et al.* 1992). Clearly much more work is required on such a complex assemblage before a well-integrated picture is obtained.

Much controversy exists over the original tectonic setting of the Troodos Massif, Cyprus and the Semail Nappe, Oman. Their generation was attributed to oceanic spreading centres analogous to the setting in different sectors (12° to 14°S and 21°N) of the East Pacific Rise today (Table 3; Fleet & Robertson 1980; Robertson & Boyle 1983). By contrast, smaller extensional regimes at supra-subduction zones were inferred as their locale of formation (Table 3; Pearce *et al.* 1984). Such controversies notwithstanding, manganese deposition is not affected because hydrothermal processes can operate in tectonic settings of both types. Hajash & Chandler (1981) conducted experiments reacting seawater with basalt, rhyolite and andesite at temperatures between 200 and 500°C, water/rock mass ratios between 5 and 50 and 1 kbar pressure and showed that similar ore-forming solutions were produced, a finding consistent with observations in natural situations.

Ancient hydrothermal manganese deposits also occur in continental settings as stratabound layers and veins in rocks of different varieties and ages. The stratabound San Francisco deposit, Mexico, overlies a lacustrine formation in a Tertiary continental-volcanic province. The ores (braunite, pyrolusite) interfinger with travertine and are spatially contiguous with iron deposits. Zantop (1978) concluded that a

continental hot spring deposited iron and manganese in the oxygenated lacustrine basin. A thick travertine apron overlies the Pleistocene stratabound hydrothermal manganese deposit at Golconda, Nevada, while in the Burmister deposit, Arizona (Late Pliocene) travertine is interlayered with Mn oxides (Hewett *et al.* 1963, cited by Roy 1981). Similar interlayering of Mn oxide with travertine has been produced by the currently active Akan hot spring, Hokkaido, Japan (Hariya 1980).

Hydrothermal vein deposits rich in manganese minerals derived from terrestrial hot springs are common. Rarely economic, these vein deposits may or may not be genetically or temporally linked to their host rocks. Thus, many of them are hosted in igneous rocks (varying from basalt to rhyolite) which might possibly supply the ore solutions. O'Reilly (1992) inferred that the vein-type New Ross manganese deposit, Canada, occurring in granite, was formed from a hydrothermal fluid 'exsolved' during final crystallization of the host rock. Other vein deposits occur in both clastic and chemical sedimentary rocks where the hydrothermal solution, derived from an external source, circulated through fractures in the host rocks.

The veins show diverse manganese mineralogy. Low-temperature veins consist of pyrolusite, cryptomelane, psilomelane, hollandite and todorokite, whereas others, formed from relatively higher temperature solutions, exhibit braunite, bixbyite, hausmannite, huebnerite and/or Mn silicates (rhodonite, bustamite, tephroite), Mn carbonate and Mn sulphide (alabandite). Barite, fluorite, calcite and quartz are characteristic accessory minerals (for details see Roy 1981, table 38). In many cases, the Mn-rich veins show spatial and temporal relations with hydrothermal base metal sulphides and gold-silver mineralization (for summary see Roy 1981).

Sedimentary manganese deposits

Sedimentary manganese deposits easily outclass the other types in respect of size and spatial and temporal distributions. These are hosted in sequences consisting of a variety of rock types, mostly sedimentary, rarely volcanic rocks, many of which provide useful information on tectonic setting and geochemical environment. Some of these rocks share a common genetic heritage with these deposits. Sedimentary manganese deposits evolve through a sequence of stages promoting supply of the metal from a source or

Table 2. Hydrothermal manganese deposits in subduction-related tectonic setting

	Palaeotectonic setting	Age	Volcanic rock-type	Associated sedimentary rocks	Position of Mn-ores	Chemical composition of Mn-ores	Other features/remarks
Toqumea, Tonga island (Hein <i>et al.</i> 1990)	(= Tonga Ridge, fore-arc terrace)	Early Miocene	Unknown	Volcaniclastic sediments	Veins, lenses, volcaniclastic rocks	Max. Mn/Fe 2596, max. Cu 202, Co 257, Ni 63, Ba 8420 (ppm)	—
Eua, Tonga Island (Hein <i>et al.</i> 1990)	(= Tonga Ridge, fore-arc terrace)	Mid-Eocene–Early Oligocene	Unknown	Limestone, weathered volcaniclastic sandstone	Stratiform layer in limestone; enrichment in volcaniclastic sandstone	Mn/Fe max. 448; max. Cu 440, Co 4240, Ni 775, Ba 12500 (ppm)	—
Franciscan Assemblage							
Blue Jay, South Thomas (Crerar <i>et al.</i> 1982; Huebner & Flohr 1990)	Marginal basin	Late Jurassic–Early Cretaceous	Alkaline basalt	Radiolarian chert and minor shale	As lenses interbedded with chert	Hydrothermal field in Fe–Mn–(Ni + Cu + Co) × 10 diagram; very low U and Th values, pronounced negative Ce anomaly	MOR setting also possible; may be similar to the Galapagos Mound deposits

Buckeye (Hein and Koski 1987; Huebner & Flohr 1990; Huebner <i>et al.</i> 1992)	Subduction-related trench at continental plate margins*	Late Jurassic-Early Cretaceous	None	Chert-shale overlying greywacke	Chert hosted	Mn/Fe 80; Cu, Co low, some enrichment in Ni, Zn; very low U and Th values	Metamorphosed to blueschist facies
Manga Chrome and Smith Prospect, Sierra Nevada, USA (Flohr & Huebner 1992)	Back-arc basin	Mid-Triassic-Early Jurassic	Island-arc tholeiite and calc-alkaline basalts (as clast)	Chert with volcanic clasts, argillites	As lenses enclosed in radiolarian chert	Plots in hydrothermal field; very low U and Th values	Metamorphosed to prehnite-actinolite facies (325°C, 2 kbar)
Florida Group Buena Vista, Solomon Island (Taylor 1976)	Island arc	Late Cretaceous-Miocene	Island arc tholeiite, andesite	Ochres, sinters, ironstone of Hanesavo Beds	Lenses of Mn oxide overlie ironstone and goethite-nontromite ochres	Mn/Fe 2.5 to 45; Cu, Co, Zn very low	Massive Cu-sulphide in mafic volcanics
Neogene Green Tuff belt, Japan (Moritani 1976; Hariya & Tatsumi 1981)	Subduction-related shallow marginal basin	Miocene	Andesite, dacite, rhyolite	Chert, argillite	Beds, lenses and veins in cherts	Unknown	Sometimes occur in outer zones of Kuroko base metal deposits (Ex. Manoka deposit)
Viti Levu, Fiji (Colley & Walsh 1987)	Small inter-arc basin	Late Oligocene-Mid-Miocene	Basalt transitional between arc-type and MORB	Hemipelagic Al-rich sediments; Fe-rich chalcodony; red clay; nontromitic clay	Within hemipelagic sediments associated with Fe-rich chalcodony and red clay	Plots in hydrothermal field in Fe-Mn-(Ni+Cu+Co) × 10 diagram	Enriched in both eruptive and erosional products of adjacent arcs

* This deposit is included here as integral part of the Franciscan hydrothermal assemblage, but the Mn-flux in the Buckeye deposits was probably derived by sub-oxic sediment diagenesis

Table 3. *Hydrothermal manganese deposits of Troodos Massif and Semail Nappe*

	Troodos Massif, Cyprus	Semail Nappe, Oman
Palaeotectonic Setting	Oceanic crust formed by sea floor spreading of mid-oceanic ridge type (Robertson & Boyle 1983; Varga & Moores 1985); supra-subduction spreading zone type (Pearce <i>et al.</i> 1984; Moores <i>et al.</i> 1984)	Oceanic crust formed by sea-floor spreading of mid-ocean ridge type (Fleet & Robertson 1980; Robertson & Boyle 1983); formed in a spreading centre in a marginal ocean in supra-subduction zone (Pearce <i>et al.</i> 1984)
Age and geological sequence (bottom to top)	Late Cretaceous to Early Tertiary Harzburgite, gabbro, sheeted dykes, lower pillow lava, upper pillow lava, pelagic chalk, radiolarite	Early Cretaceous Harzburgite-gabbro-sheeted dykes-trondhjemite-high level gabbro, lower lava, upper lava, metalliferous and/or pelagic sediments, exotic melange
Volcanic rock type,	Lower pillow lavas largely basaltic andesites (also subordinate dacite and keratophyre); upper pillow lavas mostly olivine basalts (also limburgite and picrite)	Lower lavas and pillow basalts (MORB type) with gradation to underlying sheeted dykes; upper lavas are basic, intermediate to acidic having island-arc affinities
Position of Mn/Fe-Mn-rich rocks	Mn halo around Fe-Cu-sulphides at the contact of lower lava and upper lava	Fe mounds with Mn within lowermost part of upper lava; Fe-Mn umbers within upper lava and overlie pillowed and brecciated upper lava
Fe-Mn-rich rock geochemistry	Basal umber: Fe ₂ O ₃ 62.2%, MnO 2.0%, Ba 756 ppm, Cu 3 ppm, Ni 336 ppm Higher dark umber: Fe ₂ O ₃ 42.9%, MnO 18.5%, Ba 1190 ppm, Cu 1400 ppm, Ni 190 ppm Negative Ce anomaly	Fe-rich mound: Fe ₂ O ₃ 9.5%, MnO 1.2%, Ba 13 ppm, Cu 15 ppm, Ni 17 ppm Black umber mound: Fe ₂ O ₃ 15.8%, MnO 26.2%, Ba 80 ppm, Cu 1361 ppm, Ni 160 ppm Supra lava umber: Fe ₂ O ₃ 26.3%, MnO 7.3%, Ba 216 ppm, Cu 527 ppm, Ni 303 ppm Negative Ce anomaly
Other features/indications	Fe-Cu sulphides present at the contact of lower and upper pillow lavas	Hydrothermal base metal sulphides present in lower lavas showing Mn halo
Modern analogues	EPR 12°-14°S (Robertson & Boyle 1983); FAMOUS and AMAR areas on MAR (Varga & Moores 1985)	EPR 21°N hydrothermal field (Robertson & Boyle 1983)

multiple sources, transport to a basin, and direct deposition or concentration aided by early diagenesis. Optimum efficiency at these stages in the past has been determined by the compositional evolution of the atmosphere and the hydrosphere. In contrast with modern large-scale deep-sea deposition, the geological settings of most ancient manganese deposits indicate formation in shallow-water basin-margin regimes. Direct bacterial oxidation-reduction of manganese, reported to occur in modern deposits and laboratory culture, has not been considered because its signature in ancient deposits is still ambiguous.

Evolution of the atmosphere and hydrosphere

The composition of the atmosphere and hydrosphere were initially controlled by mantle degassing followed progressively by photosynthesis and organic carbon burial. On the primitive Earth, a calculated solar luminosity lower by about 30% was compensated by high concentrations of CO₂ (produced by tectonically mediated rapid degassing) in the atmosphere, which increased the surface temperature and prevented global freezing (Kasting 1987). CH₄ and NH₃ were present perhaps only in trace

amounts in the early atmosphere as these are destroyed by photochemical reactions. The primitive atmosphere, therefore, was probably dominated by CO₂ (+CO) followed by N₂ with traces of H₂ reduced sulphur gases (Kasting 1993). Oxygen was present only in very low concentration (Cloud 1972, 1980 cited by Holland 1984; Kasting 1993). With time, photosynthetically produced oxygen and its increased relative proportion due to organic carbon burial gradually overwhelmed the volcanic flux of reduced gases. Kasting *et al.* (1993) speculated a more reduced state of the upper mantle in the primitive Earth and a progressive oxidation with time. They suggested that the evolution of mantle redox conditions and the state of oxidation of the atmosphere are closely inter-linked.

Atmosphere and hydrosphere oxygenation exerted a primary control on deposition of sedimentary ore deposits such as those of manganese and iron. Kasting (1987) proposed

a three-stage box model which was subsequently refined to indicate progressive increase in pO₂ in the Precambrian atmosphere-ocean system (Kasting 1992, 1993). A modified version of this model is given in Table 4.

Atmosphere and hydrosphere were thus modified at different times in terms of relative CO₂ versus O₂ concentrations and temperature, which influenced the geochemically controlled exogenic processes. Tectonic activity, differing in intensity and perhaps in style, was the driving force for the modifications of atmosphere-hydrosphere composition (Berner *et al.* 1983; Des Marais *et al.* 1992). Biological activity, particularly photosynthesis, had also an important role to play, but to be optimally effective a favourable tectonic domain was necessary. Initially produced photosynthetic oxygen was largely consumed by acidic volcanic gases and Fe²⁺ sinks. Conversely, tectonically induced organic carbon burial and/or decrease in volcanic/hydrothermal activity

Table 4. Anoxic-oxic evolution of the atmosphere and hydrosphere during the Precambrian (modified after Kasting 1987)

Stage	I	II	III	IV
Time envelope	c. 3.8 to between 2.4 and 2.0 Ga*	Between 2.4 and 2.0–1.9 Ga*	c. 1.9–0.9 Ga	c. 0.9–0.6 Ga
Atmosphere	Reducing; pO ₂ c. 10 ⁻¹⁴ PAL max.†	Oxidizing; pO ₂ ≈ 0.03 PAL max.†	Oxidizing; pO ₂ ≈ 0.002 PAL min.†	Oxidizing
Hydrosphere (surface)	Reducing with oxygen oases: pO ₂ ≈ 0.08 PAL max.†	Oxidizing	Oxidizing	Oxidizing
Hydrosphere (deep)	Reducing	Reducing	Oxidizing	Intermittently oxidizing and reducing
Sediment isotopic characteristics	δ ¹³ C ≈ 0‰ δ ³⁴ S -4 to +4‰	Increased δ ³⁴ S values	–	δ ³⁴ S -10 to +20‰‡; unusually low ⁸⁷ Sr/ ⁸⁶ Sr in carbonates of 800–600 Ma§; strongly negative δ ¹³ C between 850–670 Ma and 610–590 Ma , otherwise positive values

* Transition of Stages I and II at 2.4 Ga fixed based on data on detrital uraninite and pyrite and a restricted range of δ³⁴S values (Walker & Brimblecombe 1985; Lambert & Donnelly 1991). The time of transition may be shifted to c. 2.0 Ga if red beds are proved to have formed first at about 2.0 Ga.

† Kasting (1992, 1993)

‡ Lambert & Donnelly (1991)

§ Veizer *et al.* (1983)

|| Knoll *et al.* (1986).

could gradually lead to the concentration of oxygen in the atmosphere. Orogenic events in the Late Proterozoic produced continental clastic detritus that were weathered by draw-down of atmospheric CO₂ leading to decreased temperature and initiation of glaciation. By contrast, increase in tectonic activity and volcanic/hydrothermal input of CO₂ led to greenhouse conditions and deglaciation.

During the Archaean, the atmosphere was strongly depleted in oxygen (Table 4). A very low sulphate concentration in the hydrosphere with insignificant fractionation of sulphur isotopes have been proposed (Walker & Brimblecombe 1985; Grotzinger & Kasting 1993); the $\delta^{34}\text{S}$ values for sedimentary rocks of Archaean age fall in a narrow range (Lambert & Donnelly 1991) and $\delta^{13}\text{C}$ values are close to 0‰.

A considerable increase in the concentration of seawater sulphate occurred in the Early Proterozoic (2.5–2.3 Ga) and its range of $\delta^{34}\text{S}$ values increased. Enhanced levels of photosynthesis in the Early Proterozoic, coupled with a gradual decline in production of oxygen-sinks such as Fe²⁺, produced oxygen that could oxidize reduced sulphur species and also augment oxygen buildup of the atmosphere (Lambert & Donnelly 1991). The available $\delta^{13}\text{C}$ values in marine carbonates deposited throughout the Early and Mid-Proterozoic times stayed close to 0‰. (Schidlowski *et al.* 1983 cited by Lambert & Donnelly 1991). Carbonate carbon of Late Proterozoic age (*c.* 900–550 Ma), however, shows variable positive $\delta^{13}\text{C}$ values (indicating burial of organic carbon) interspersed with short-lived stints of negative values (800–670 Ma and 610–590 Ma; Knoll *et al.* 1986; Derry *et al.* 1992) correlated to glacial events. The higher ratios of ⁸⁷Sr/⁸⁶Sr in carbonates precipitated from seawater is correlated with greater continental erosion and supply, whereas this ratio is lower during times of strong hydrothermal activity. The mantle-like Nd isotope values of early Precambrian iron-formations, decreasing to much lower values with time, indicate that Nd inputs to the ocean gradually shifted from hydrothermal to continental source (Derry & Jacobsen 1990).

Stratified oceans were initiated during the prevailing high atmospheric CO₂ conditions during the Archaean with oxygenated surface water at basin margins (oxygen oases; related to shallow-water colonies of photosynthetic organisms?) and anoxic deep water (Table 4). With increase in p_{O_2} in the atmosphere by Early Proterozoic time, the entire surface waters became oxygenated while the deep-water zone remained reducing. Records of sea-level changes

(transgression–regression cycles) during that period are common (Beukes 1983; Gauthier-Lafaye & Weber 1989; Hein & Bolton 1993). Sea-level changes were caused evidently by increase in seafloor generation and enhancement of greenhouse gases in the atmosphere through tectonically induced volcanism and hydrothermal activity. Stratification of basin water was lost by further increase in atmospheric p_{O_2} by around 1.9 Ga (Table 4).

In the Late Proterozoic, however, the scenario changed again (Table 4). The break-up of the Mid-Proterozoic supercontinent (Lambert & Donnelly 1991) probably led to massive draw-down of atmosphere CO₂ (due to increased silicate weathering) and organic carbon burial (indicated by positive excursions of $\delta^{13}\text{C}$). This decreased the surface temperature to such an extent that global glacial events took place. At least four glacial events (Knoll *et al.* 1986) occurred during 850–590 Ma, intervened by stratified basins, transgressions and ocean anoxic events (OAE) during interglacial periods. Strong negative $\delta^{13}\text{C}$ excursions coincided with the Sturtian (850–670 Ma) and the Varangian (610–590 Ma) glacial events (Knoll *et al.* 1986). Seafloor hydrothermal activity is inferred to have been accentuated during the continental breakup as indicated by the unusually low ⁸⁷Sr/⁸⁶Sr ratio in 800–600 Ma carbonates (Veizer *et al.* 1983).

During the Late Proterozoic and Early Phanerozoic, the atmosphere and the entire hydrosphere were highly oxygenated approaching present p_{O_2} values. However, during that time evidence of short and fairly long-time changes in atmosphere and hydrosphere compositions have been indicated by a highly variable record of $\delta^{13}\text{C}$ values. Volcanism and other geological and biological processes, produced a greenhouse environment and rise of surface temperature many times (Fig. 1; Berner 1991). Such greenhouse-induced global warming took place at different times in the Early Palaeozoic and Mesozoic (Jenkyns 1980; Berner 1991). By contrast, cold climate prevailed during the Late Palaeozoic and the Late Cenozoic as indicated by the carbon cycle (Berner 1991), a conclusion that is in agreement with other independent estimates. During warm intervals and a positive $\delta^{13}\text{C}$ excursion, the oceans were again stratified and sea-level changes (transgression–regression cycles) attended by ocean anoxic events were operative. Transgression and upwelling were linked during regional deepening of the shelf areas (Jenkyns 1980) and organic matter was supplied from both the flooded continental area and the plankton blooms.

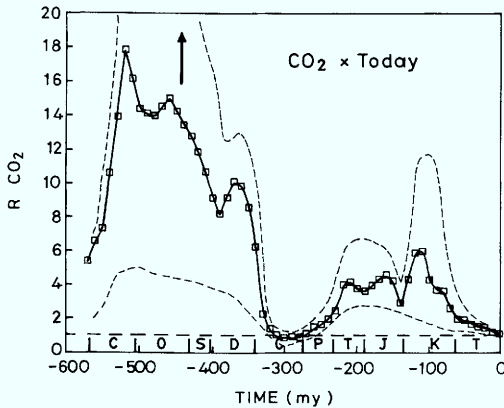


Fig. 1. Best estimate, or standard reference, curve of R_{CO_2} versus time. The arrow denotes that early Palaeozoic R_{CO_2} values may be higher. The dashed lines represent a rough estimate of error. (Berner, R. A. 1991. *American Journal of Science*, 291, 371. Reprinted by permission of American Journal of Science.)

Stratified basins: manganese concentration and deposition

The Black Sea, a classic example of a stratified basin, serves as a model for metal concentration in the H_2S -producing anoxic water column overlain by oxygenated water. Dissolved Mn^{2+} accumulates in the anoxic water and migrates by vertical advection-diffusion to the redox interface (Spencer & Brewer 1971); it reaches maximum concentration (*c.* 500 ppb) close to the interface. Above the redoxcline, Mn oxyhydroxide particulates form by oxidation of Mn^{2+} which sink back to the anoxic water and are dissolved. Similar stratified water columns develop in certain fjords (Saanich Inlet, Jacobs & Emerson 1982; Cariaco Trench, De Baar *et al.* 1988; Framvaren fjord, Jacobs *et al.* 1985) where Mn^{2+} behaves in the same manner. Only where the redoxcline impinges on the continental shelf of the Black Sea are Mn oxyhydroxides precipitated and retained (Sevast'yanov & Volkov 1966 cited in Roy 1981).

The euxinic deeper waters of the Black Sea have often been held responsible for supporting organic-rich black shale deposition. However, Calvert (1990) determined that the sediments accumulating now under anoxic conditions are poor in organic matter while Holocene sapropel (with 20 wt% organic carbon) underlying the surface sediments were deposited when the bottom waters were oxic. Therefore, the production of black shale was not dependent on water

column anoxia but rather on high organic productivity in oxygenated water (Pedersen & Calvert 1990 cited by Calvert & Pedersen 1993). Anoxic waters are not prerequisites for black shale deposition, rather black shale formation consumes oxygen from overlying waters and turns them anoxic.

Marine transgression during warm climate was causally related to stratification of the ocean when deep circulation was suppressed and oxygen solubility decreased. During transgression, the inundated continental areas supplied substantial organic debris which, together with the primary productivity in the surface water, transferred a large amount of organic matter to the bottom of the stratified epicontinental and ocean basins (Jenkyns 1980; Hallam 1987). The organic matter was bacterially degraded which further decreased oxygen content in the sediments and the bottom water and produced black shales on burial. High rates of deposition and burial of organic carbon, signalled by positive excursions of $\delta^{13}C$, have been inferred to have taken place during ocean anoxic events (OAE) causing global accumulation of black shales, for example during Early Toarcian, Late Cenomanian and Early Turonian times (Schlanger *et al.* 1987). Black shales are genetically related to Mn-rich carbonate deposits.

Source and transport of manganese

The precise determination of any particular source for manganese in ancient deposits is complex. Hydrothermal and terrestrial weathering processes serve as primary sources for manganese in the depositional basins, but in specific deposits the contribution of any particular source over another is difficult to assess. The few studies on REE patterns of ancient manganese deposits (Bau & Dulski 1993) indicate the source of manganese, but more such studies are needed for a clear picture. In the modern oceans it is now established that both near-field and far-field dispersal of manganese from the mid-ocean ridge hydrothermal fields takes place through buoyant plumes caught up by ocean currents (Klinkhammer & Hudson 1986). Thus, hydrothermally introduced manganese may be transported thousands of kilometres from the original site. However, the estimates made for hydrothermal component of the manganese budget in today's seawater vary widely. During the Archaean and Early Proterozoic, a more vigorous hydrothermal activity has been suggested (Holland 1984) with the associated anoxic deep-ocean as a repository of

hydrothermal manganese that was carried in solution. The magnitude of hydrothermal production of manganese probably decreased with time.

On the other hand, supply of manganese from terrestrial sources cannot be neglected. Surficial weathering processes are particularly active in humid tropical climates. Organic acids, produced by decomposing vegetation since the early Phanerozoic (Nicholson 1992), can leach manganese at different rates under various climatic conditions (Creerar *et al.* discussions and fig. 6a, b & c). The released manganese is carried by ground and surface waters to the lakes and the oceans. While transport of manganese to present-day northern hemisphere high-latitude lakes is fostered by acidic soil and ground water, in lower latitudes controls on river flux are more complicated.

The average concentration of dissolved manganese in river water is only a few parts per billion and its transport in ionic solution in an oxygenated environment for a long distance is difficult. Nevertheless, manganese can be transported as particulates or colloids and its gross riverine discharge to the oceans is considerable (Sapozhnikov 1970). Trefry & Presley (1982) showed that manganese transported to the ocean from coastal areas is mainly in particulate form. By contrast, Laxen *et al.* (1984) concluded that a major part of the $<0.015 \mu\text{m}$ Mn size-fraction is present as Mn^{2+} species soluble in river water in addition to a significant Mn-fraction occurring as colloids. They argued that particulate and soluble Mn-fractions were decoupled under the dynamic conditions in most rivers. The Kalix river, Sweden, is discharging into the Gulf of Bothnia both dissolved and particulate manganese and the dissolved/particulate ratio varies seasonally (Pontér *et al.* 1992).

The coastal zone has a big role to play in the geochemical cycle of manganese during transport. Deeper water in estuaries has increased salinity and alkalinity relative to surface waters. The mixing of river water and seawater in coastal zones may lead to flocculation of dissolved manganese carried by river water which may generate coastal Mn oxide deposits (Sundby *et al.* 1981; Frakes & Bolton 1992). However, in the coastal environments, river discharge as well as plankton blooms can enrich the sediments in organic matter. Bacterial decomposition may consume sufficient oxygen to turn the sediments suboxic or anoxic. Manganese oxide particulates buried in such sediments are thereby reduced and the released Mn^{2+} dissolved in pore water may be recycled to enrich overlying water for export out of the

coastal zone to the oceans (Sundby *et al.* 1981; Trefry & Presley 1982). If, however, the Mn^{2+} and dissolved bicarbonate concentration in the pore water reaches a level that exceeds the solubility product of a carbonate phase, Mn-bearing carbonates should be produced (Calvert & Pedersen 1993) and fixed within the reducing sediments thereby blocking the Mn^{2+} supply to the overlying water.

Manganese deposits: the Archaean inauguration

No manganese ore deposits are known to have formed during the first 800 million years of Earth history. This paucity of manganese deposits reflects the deficiency of oxygen in the atmosphere and hydrosphere (Table 4). By contrast, a banded iron formation (BIF), showing very low Mn-contents, occurs in the oldest known geological sequence (Isua Supracrustals, Greenland: 3.8 Ga) and continued to form throughout the Archaean. Preferential deposition of iron may have been facilitated by its lower solubility with respect to manganese, its faster rate of oxidation by limited photosynthetically derived oxygen and/or by photochemical oxidation of Fe^{2+} by solar UV radiation in the absence of the ozone screen (Cairns-Smith 1978; Braterman *et al.* 1983, 1984, all cited by Anbar & Holland 1992). Experiments conducted by Anbar & Holland (1992) showed that photochemical oxidation of Mn^{2+} is also possible, but the rate is much slower than it is for Fe^{2+} ; where both Mn and Fe are present in solution the rate of Mn^{2+} oxidation is decreased further.

Manganese deposits first started to form in Late Archaean time probably corresponding to the development of oxygen oases in the otherwise reducing hydrosphere (Table 4). Only a few deposits were formed during that time and these were spatially limited (Table 5). The deposits in Rio das Velhas Supergroup (Brazil) and Chitradurga Group (India) are restricted to the upper sedimentary rocks in greenstone belts. Manganese carbonate formed originally in carbon-rich pelitic sediments in geosynclinal setting of the Rio das Velhas Supergroup (Dorr *et al.* 1956). These deposits were metamorphosed producing Mn silicate-carbonate rocks. On the other hand, deposits of the Chitradurga group formed in the marginal shallow-water part of a basin as indicated by the associated sedimentary rocks including stromatolitic limestones (Baral 1986). The Mn oxide ores were metamorphosed to low grade.

Table 5. *Manganese deposits of Archaean age*

Age	Geological sequence	Deposits	Geological setting and features	References
c. 2.6 Ga	Chitradurga Group	Chitradurga–Tumkur, Kumsi–Hornhalli, Karnataka, India	Shallow-margin area of geosyncline; Mn oxide ore interstratified with chert & phyllite; spatially close to stromatolites	Roy (1981)
>2.6 Ga	Eastern Ghats Sequence	Kodur, Garividi, Garbham, Andhra, Pradesh, India	Shallow-water shelf (?); Mn oxide ore & Mn silicate-carbonate rocks present at different levels enclosed in calc-silicate & pelitic granulite	Roy (1981), Dasgupta <i>et al.</i> (1993)
>2.7 Ga	Rio das Velhas Supergroup	Morro do Mina, Minas Gerais, Brazil	Geosyncline; Mn silicate-carbonate rock enclosed in graphitic phyllite; mica-schist & amphibolite present	Dorr <i>et al.</i> (1956)
c. 3.0 Ga	Iron Ore Group	Joda, Kalimati, Gurda, Phagua, Mahulsukha, Orissa, India	Cratonic shelf; Mn oxide ore interstratified with shale; volcanic rocks present but not in direct contact	Roy (1981)

The Eastern Ghats sequence, India, metamorphosed to granulite facies, corresponds to Archaean high-grade terranes. Manganese oxide ores are hosted in pelitic and calc-silicate granulites (Roy 1981) while Mn silicate-carbonate rocks occur in calc-silicate granulites and garnetiferous quartzites (Dasgupta *et al.* 1993). The corresponding protoliths of the Mn oxide ores and the Mn silicate-carbonate rocks are inferred to be Mn oxide/hydroxide and Mn carbonate which had formed at different stratigraphic levels of the sequence. Signatures of the original geological setting of the Eastern Ghats sequence have almost totally been obliterated by multiple stages of deformation and metamorphism. Nevertheless, the deduced pre-metamorphic lithological sequence indicates deposition on a shallow-water shelf. The Iron Ore Group sequence, India, only incipiently metamorphosed and with orthoquartzite at the base was deposited in shallow water on a stable shelf. It neither corresponds to greenstone belts nor to high-grade terranes and is, thus, atypical of the common Archaean settings. The manganese orebodies (pyrolusite, manganite, cryptomelane, braunite) are interbedded with shale and are superficially modified by weathering.

For all these Archaean deposits, there is no evidence of *direct* volcanic/hydrothermal input of manganese. Volcanic rocks occasionally

present, are separated from the orebodies by intervening rocks that show Mn content not exceeding the crustal value. Thus, it is inferred that the source of manganese was seawater. The Archaean hydrosphere was largely reducing (Table 4) permitting buildup of dissolved manganese (possibly from a hydrothermal source) which by upwelling at basin-margin oxygen oases, was oxidized and precipitated on the cratonic shelves. The formation of Mn oxides is explained without much complication, but the mode of origin of the Mn carbonates has not been deciphered (although the restriction of Mn carbonate to carbon-rich rocks in Rio das Velhas Supergroup is noteworthy), because they have been overprinted by high-grade metamorphism.

Manganese deposits: the Proterozoic development

Large-scale deposition of manganese started from the Early Proterozoic. This was possible due to oxygenation of the atmosphere and stabilization of the stratified ocean system (Stage II; Table 4). At that time dissolved Mn²⁺ was concentrated in anoxic deep water and the source was hydrothermal or terrigenous.

Middle Proterozoic (*c.* 1.9–0.9 Ga; Stage III, Table 4) sections are practically barren of manganese deposits, except for very few small occurrences developed locally. This decline in manganese deposition can be attributed to the total oxygenation of the hydrosphere that prevented the buildup of dissolved manganese. The renaissance of manganese deposition in the Late Proterozoic (Stage IV, Table 4) was a response to a number of glacial–interglacial episodes and return of stratified oceans and oxygen minimum zones.

The Kalahari manganese field, Republic of South Africa, with a potential resource of 13 600 million metric tons of ore with Mn contents between 20 and 48% is the largest among all known land-based deposits (Table 6). This deposit occurs in three different layers interstratified with BIF of the Hotazel Formation (*c.* 2.24 Ga; Stage II, Table 4) of the Late Archaean to Early Proterozoic Transvaal Supergroup (*c.* 2.64–1.9 Ga; Beukes *et al.* 1993). The cyclic Mn ore layers are mainly composed of braunite–kutnohorite assemblage (Mamatwan-type; Beukes 1983; Kleyenstüber 1984). Signatures of trace and rare earth elements indicate that manganese was supplied by deep anoxic waters of a stratified ocean with a small

hydrothermal component (Beukes 1989). The $\delta^{13}\text{C}$ values of carbonates (kutnohorite, Mn-calcite) in the ores range between –12 and –16‰ indicating that part of the carbon is derived from organic carbon oxidation (Beukes 1993). The sedimentary manganese ores of Mamatwan-type (braunite–kutnohorite), in the western extension, have been modified by later hydrothermal alteration to an assemblage of braunite II, bixbyite, hausmannite, and a host of hydrous and anhydrous Mn silicates (Wessels-type; Kleyenstüber 1984).

In the Koegas Subgroup (Ghap Group, Transvaal Supergroup), Mn oxide orebodies (psilomelane, pyrolusite, jacobsonite, hausmannite, hematite) are interbedded with the Rooinekke iron formation. This iron formation, and by extension the manganese ore beds, were deposited following a major transgression (Beukes 1993). Anoxic deep seawater could be a plausible source of the metals in these deposits.

The geological setting of the Birimian Supergroup greenstone belt in the West African craton (Ghana, Ivory Coast, Burkina Faso, Mali, Eastern Liberia, Guinea) is unique among the Early Proterozoic sequences hosting manganese deposits (Table 6). More or less evenly spaced parallel belts of isoclinally folded volcanic rocks (mainly

Table 6. Manganese deposits of Early Proterozoic age

Age	Geological sequence	Deposits	Geological setting and features	References
<i>c.</i> 2.0 Ga	Sausar Group	Mansar, Chikla, Tirodi, India	Cratonic shelf; limestone–shale–orthoquartzite; no volcanic rock; Mn oxide ore beds in shale (Mansar Fm) and limestone (Lohangi Fm) metamorphosed to greenschist and amphibolite facies	Roy (1966, 1981)
<i>c.</i> 2.1 Ga	Francevillian Series	Okouma and Bangombé Plateaus, Gabon	Cratonic shelf; Mn carbonate interbedded with black shale, dolomite and sandstone; no volcanic rock	Gauthier–Lafaye & Weber (1989); Hein & Bolton (1993)
<i>c.</i> 2.3 to 2.0 Ga	Birimian Supergroup	Nsuta, Ghana; Mokta, Ivory Coast; Tambao, Burkina Faso	Greenstone belt formed in intracontinental rift; Mn carbonate in black shale in transition zone between volcanic & sedimentary rocks	Dorr (1968); Leube <i>et al.</i> (1990)
<i>c.</i> 2.64 to 1.9 Ga	Hotazel Fm (<i>c.</i> 2.24 Ga) Postmasburg Group, Transvaal Supergroup	Mamatwan, Wessels, South Africa	Cratonic shelf; Mn oxide & Mn carbonate ore interbedded with BIF	Beukes (1983); Kleyenstüber (1984)

basalts with MORB chemistry: age *c.* 2.3–2.2 Ga; Taylor *et al.* 1992) are closely related in space with sedimentary units (chemical sedimentary rocks, volcanoclastic rocks, argillites, turbidity-current-related wackstones) that show overlapping (*c.* 2.3–2.0 Ga) ages (Leube *et al.* 1990; Taylor *et al.* 1992). An intracontinental rift setting has been suggested for this greenstone belt (Leube *et al.* 1990). A chemical sedimentary facies composed of chert and Ca–Fe–Mg carbonate is associated with black shale ($\delta^{13}\text{C}$ –18.3 to –26.7‰; Leube *et al.* 1990) that hosts rhodochrosite beds (Dorr 1968). This lithofacies occurs in transitional zones between the volcanic belts and the sedimentary units. Birimian Supergroup rocks underwent only low-grade metamorphism. Economic manganese deposits occur as supergene enrichment products in weathered zones. The ultimate source of manganese is difficult to decipher. It may only be guessed that hydrothermal activity during intracontinental rifting could supply manganese that, through recycling, was deposited as sediments.

The Early Proterozoic Moanda deposit in the Francevillian Series (*c.* 2.1 Ga; Bros *et al.* 1992), Gabon, is the largest known black-shale-hosted Mn carbonate deposit (Table 6). Rhodochrosite beds are interstratified with black shale, dolomite, and sandstone in a sequence (FBI unit) that is underlain by sandstone-conglomerate (FA unit) of the epicontinental Francevillian Series (Weber 1973 cited by Leclerc & Weber 1980; Gauthier-Lafaye & Weber 1989). The FA unit consists of fluvial clastic rocks that are overlain by a deltaic and marine sequence. The black shales in the FB 1 unit, formed during marine transgression (Gauthier-Lafaye & Weber 1989), contain an average 7% (locally >20%) total organic carbon (Hein & Bolton 1993). The $\delta^{13}\text{C}$ values of the organic matter ranges between –25 and –38‰. (Gauthier-Lafaye & Weber 1989) while for rhodochrosite $\delta^{13}\text{C}$ is –16‰ (Hein & Bolton 1993). The Mn carbonate-rich horizons consist of Mn-rich dolomite, Ca-rhodochrosite, and minor but persistent pyrite. Hein & Bolton (1993) concluded that pyrite and rhodochrosite were formed by sulphate reduction coupled with organic matter oxidation during early diagenesis. From the REE characteristics of the ore samples they also concluded that the primary manganese mineralization took place from a reducing seawater source in an epicontinental basin during a transgression–regression cycle. Hein & Bolton (1993) aptly correlated this deposit with the first stage of large-scale burial of organic carbon and rapid increase in atmospheric oxygen (Stage II; Table 4). The economic ore zone consisting of

Mn oxide was produced by oxidation of Mn carbonates during weathering.

The Proterozoic (*c.* 2.0 Ga) Sausar Group, India, including the manganese deposits (Table 6), have been complexly deformed and metamorphosed to grades ranging from low greenschist facies to upper amphibolite facies. This sequence consists of metamorphosed equivalents of a limestone–shale–orthoquartzite assemblage (Roy 1966, 1981) indicating a shelf environment. The presence of dolomite at the top (Bichua Fm) indicates further shallowing of the basin. Interbanded Mn oxide orebodies (braunite, bixbyite, hollandite, jacobsonite, hausmannite) and Mn silicate–oxide rocks are interstratified with metapelites and orthoquartzites (Mansar Fm) and less commonly occur as conformable lenses in carbonate rocks of the older Lohangi Fm (Roy 1966, 1981). The protoliths of these Mn-rich rocks were Mn oxide/hydroxide sediments admixed with variable amounts of Fe, Si, and Al (Roy 1966, 1981; Dasgupta *et al.* 1990 and references therein). The Mn silicate–carbonate rocks, derived from Mn carbonate progenitor with admixed impurities, also occur as isolated pockets in the Mn oxide ore horizon of the Mansar Fm. The Mn oxide deposits are inferred to have formed on the continental shelf during a sea-level highstand, when detrital supply was minimal. Deposition above the redox interface produced Mn oxides even on the carbonate substrate (Lohangi Fm). Mn carbonate sediments in the Mansar Fm were diagenetically derived from Mn oxides by reaction with calcareous partings in isolated pools where an evaporative condition developed.

Sedimentary manganese deposits (cryptomelane, minor braunite), associated with BIF, occur in four stratigraphic horizons in the glaciogenic Late Proterozoic Santa Cruz Formation of the Jacadigo Group (900–600 Ma; Walde 1981 cited by Urban *et al.* 1992) at Urucum, Brazil (Table 7). Urban *et al.* (1992) suggested deposition of the orebodies in a narrow fjord-like basin. During glaciation, the underlying stagnant seawater was cut off from oxygen supply and was rendered anoxic by organic matter decomposition. Manganese and iron were thus mobilized from particulates and clastic grains to be concentrated in the dissolved state (compare situations in modern seasonally ice-covered lakes; Pontér *et al.* 1992 and references therein). Lateral transport of Mn^{2+} and Fe^{2+} ions to ice-free parts of the fjord or gradual regression of ice-cap promoted oxygenation and precipitation, first of iron and then of manganese dictated by their rates of oxidation and solubility difference. Climate-controlled

repeated transgression–regression of the ice-cap explains the rhythmic intercalation of the manganese ore horizons and the BIF as well as the coarse clastic zones between them. The source of the metals was seawater fed by continental run off.

The Late Proterozoic Damara Sequence, Namibia (Table 7) consists mainly of shelf facies sedimentary rocks, diamictites, and volcanic–sedimentary successions (Breitkopf 1988). The glaciogenic sequence of the Chuos Formation (750–650 Ma; Miller 1983a in Breitkopf 1988) of the Damara Sequence at Otjosondou consists of (bottom to top) lower quartzite, lower Mn horizon, BIF, upper Mn horizon, and upper quartzite (Bühn *et al.* 1992). These rocks have been metamorphosed to upper amphibolite facies. Protoliths identified for the Mn-rich rocks are almost pure and massive Mn–Fe oxides, interlayered Mn oxides and terrigenous sedimentary rocks and Mn–Fe enriched mudstones. Bühn *et al.* (1992) concluded that the Chuos Formation represents a transgressive–regressive sequence and they related transgression both to the opening of the proto-South Atlantic and the Khomas Sea and interglacial sea-level change. They inferred that the lower and the upper manganese ore horizons formed in transgressive

and regressive stages respectively. The interglacial transgression facilitated the formation of almost pure Mn–Fe oxides as the supply of terrigenous detritus was interrupted. Bühn *et al.* (1992) invoked a hydrothermal source for manganese derived from basin-centred volcanism as an alternative to the continental supply; they considered that transport of dissolved manganese in the Late Proterozoic oxidizing environment was not possible. But manganese is still supplied to the oceans by rivers in the present-day oxidizing environment. Moreover, Bau & Dulski (1993) determined a positive Ce anomaly from these ores and concluded their derivation from a continental source.

Late Proterozoic glaciation was most widespread in China. Three episodes are recorded of which the second, Nantuo ice age (*c.* 720–680 Ma; Fan *et al.* 1992), was most prominent. In the Datangpo black shale sequence, correlated with an interglacial interval of the Nantuo ice age, several Mn carbonate beds, interstratified with black shale, occur at Xiangtan, Minle, Datangpo, Guchen, Tangganshan, and other areas (Fan *et al.* 1992; Table 7). In most deposits, tillites have been recognized at the base and top of the black shale sequence. No iron formation has been recorded. Fan *et al.*

Table 7. Manganese deposits of Late Proterozoic age

Age	Geological sequence	Deposits	Geological setting and features	References
900–600 Ma	Santa Cruz Fm, Jacadigo Group	Urucum, Brazil	Glaciogenic sequence; four Mn oxide beds mostly intercalated with BIF; glaciomarine dropstones common in the sequence	Urban <i>et al.</i> (1992)
<i>c.</i> 750–650 Ma	Chuos Fm, Damara Sequence	Otjosondou, Namibia	Interglacial transgressive–regressive sequence; BIF sandwiched between Mn oxide horizons; metamorphosed to upper amphibolite facies	Bühn <i>et al.</i> (1992)
<i>c.</i> 720–680 Ma	Datangpo Sequence, Nantuo ice age	Xiangtan, Minle, Datangpo, Tangganshan, China	Interglacial transgressive sequence; Mn carbonate hosted in black shale underlain and overlain by tillite; no BIF	Fan <i>et al.</i> (1992)
<i>c.</i> 800 Ma	Penganga Group	Tamsi, Guda, Kanpa, India	Transgressive sequence; no evidence of glaciation; Mn oxide ore interbedded with chert enclosed in limestone; no BIF in the sequence	Chaudhuri <i>et al.</i> (1989); Roy <i>et al.</i> (1990)

(1992) inferred that the Mn carbonate deposits were formed in shallow estuarine basins during interglacial transgression aided by biochemical (algal) mediation.

Manganese deposits occur in the Late Proterozoic sedimentary sequence of the Penganga Group (Table 7), developed in Godavari Valley, a major continental rift area in India. Chaudhuri *et al.* (1989) first assigned a Group status to the Penganga sequence and established the following stratigraphy (bottom to top): basal arkosic sandstone on granitic basement, shale-sandstone intercalation, limestone, glauconitic sandstone, and shale. Volcanic rocks are absent and the sequence was not metamorphosed. The finely laminated thick limestone sequence has been inferred to have developed during a transgressive phase. The Mn oxide ores, interstratified with chert, are enclosed in the limestone section. Ores partly retained the primary minerals (todorokite and birnessite) that were in places converted to manganite, braunite, and bixbyite during late diagenesis (Roy *et al.* 1990). This partial conversion clearly shows that both braunite and bixbyite with extremely low iron contents can form during late diagenesis. The ores have been assigned a sedimentary origin with a seawater source. In spite of a Late Proterozoic age, the Penganga sequence does not show any evidence of glaciation.

Manganese deposits: the Phanerozoic finale

During the Phanerozoic, biodiversity increased and CO₂ content of the atmosphere fluctuated considerably (Fig. 1). This variation of CO₂ content was caused by changes in rates of sedimentary burial of organic matter, weathering of silicates and carbonate rocks on the continents and the release of CO₂ by volcanic and metamorphic processes (Berner 1991). Short and long-term interludes of warm climate corresponded with higher inputs of greenhouse gases to the atmosphere. Consequently, the oceans became intermittently stratified in conjunction with changes in sea level.

The development of sedimentary manganese deposits during the Phanerozoic has been more or less temporally coeval with stratified oceans, events of transgression and ocean anoxia (Cannon & Force 1983; Frakes & Bolton 1984, 1992; Force & Cannon 1988). During periods of greenhouse warming, dissolved manganese was concentrated in the deep anoxic part of the stratified basins. Cannon & Force (1983) and Force & Cannon (1988) visualized precipitation of Mn oxide/hydroxide at the feather edge of

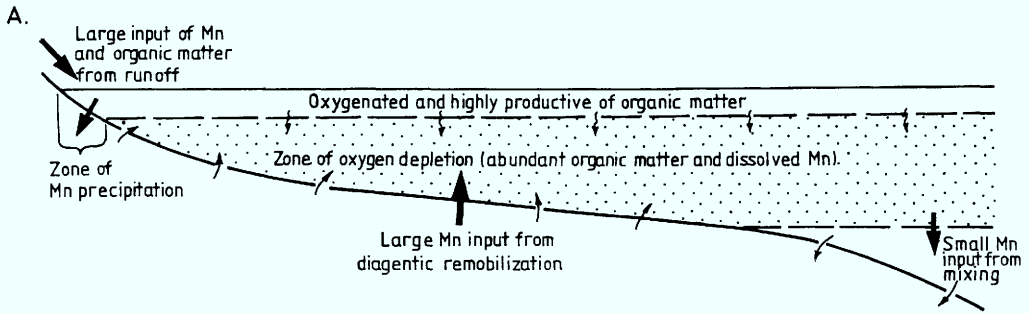
transgressive wedges on the continental shelf whereas Frakes & Bolton (1984) modelled manganese deposition mainly during marine regression at the Groote Eylandt deposit, Australia (Fig. 2). The veil effect (floculent fallout from river water) in the coastal areas by change in salinity and the shoreward bottom transport of manganese particulates by tidal lag (broom effect) have been considered as important parameters for generation of Mn oxide deposits (Fig. 2). Manganese carbonate deposition has also been correlated with transgression and ocean anoxic events, in dysaerobic and anoxic environments (Force & Cannon 1988; Jenkyns *et al.* 1991).

The Middle Ordovician Taojiang deposit, China, is the only well-documented economic concentration of manganese of early Palaeozoic age. Manganese carbonate ore beds occur in a sequence of black shale, Fe-Mn-bearing limestone, and calcareous claystone (Table 8). The ore-bearing horizon marks the transitional stage between peak transgression and the initiation of regression (Fan *et al.* 1992). The Mn carbonate ore (rhodochrosite, kutnohorite, Mn-calcite) shows a wide range of negative $\delta^{13}\text{C}$ values (-5.8 to -17.8‰, Okita & Shanks 1992; -9 to -22‰, Fan *et al.* 1992). Okita & Shanks (1992) concluded that particulate MnO₂ was originally precipitated and coupled oxidation of organic matter and reduction of MnO₂ produced diagenetic Mn carbonates with negative $\delta^{13}\text{C}$ values.

During the early Toarcian ocean anoxic event in Europe, Mn carbonate beds, in association with black shale, formed in rifted basins in continental margins in Austria, Germany, Hungary, Italy and Switzerland (Jenkyns *et al.* 1991). These widely scattered Mn carbonate beds are coeval (*tenuicostatum* to early *falciferum* Zones) and were formed just prior to black shale deposition. The deposits are also similar in character. The best-studied and economically viable deposit at Úrkút, Hungary is representative of these stratiform Mn carbonate occurrences.

The Mn carbonate deposits at Úrkút, Hungary, occurs in a marine sequence composed of bioclastic limestone, radiolarian clay marlstone and black shale (Table 8). The monomineralic rhodochrosite ore beds occur at two stratigraphic intervals within radiolarian clay marlstone just below black shales. Polgári *et al.* (1991) contended that euxinic conditions existed when sedimentation of marlstone took place. The ore beds lack pyrite, and show paucity of flora and fauna. The $\delta^{13}\text{C}$ values for rhodochrosite (average -14.5‰) show a negative linear correlation with Mn-content and a negative

TRANSGRESSION



REGRESSION

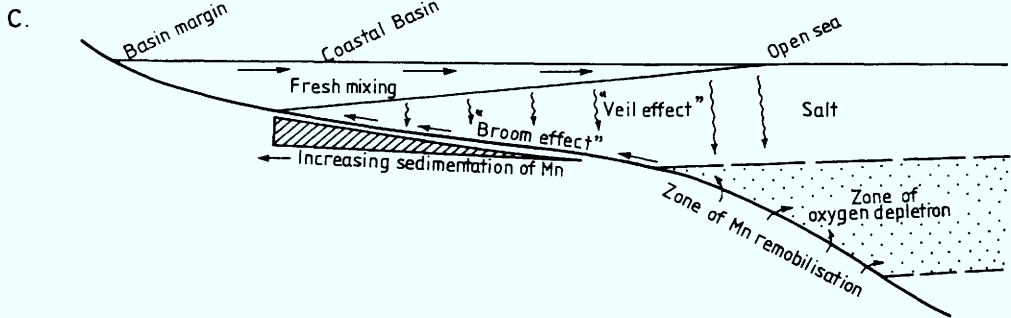
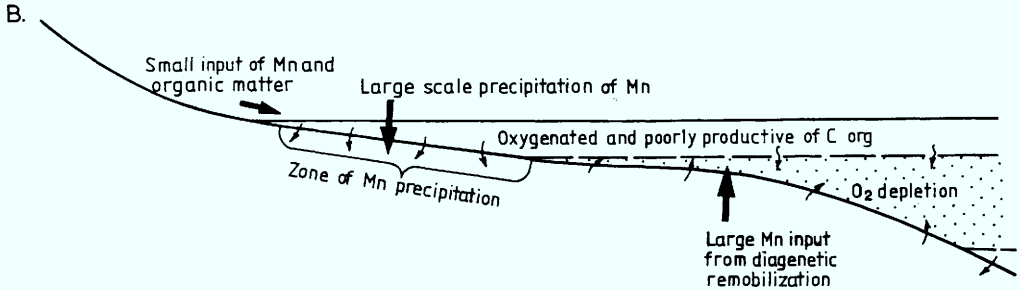


Fig. 2. (a) Relationships during marine transgression, showing narrow zone of Mn accumulation and concentration of dissolved Mn in water column. (b) Relationship during marine regression with abundant diagenetic remobilization and wide zone of final Mn precipitation. (c) Manganese sedimentation in coastal zone of intracratonic basin, showing veil effect (floculent fallout) from saline mixing and broom effect (bottom transport and concentration) from tidal activity. (Reproduced from Frakes & Bolton 1984).

exponential correlation with total organic carbon (TOC) indicating that rhodochrosite formed by early diagenesis involving organic matter oxidation. Polgári *et al.* (1991) concluded that dissolved manganese of unknown source accumulated in anoxic seawater and precursor Mn oxyhydroxides formed on the continental shelf above the redoxline. Reduction of this Mn oxyhydroxide was coupled with organic matter oxidation producing Mn carbonates. Additionally, Mn reduction and coupled oxidation of FeS (originally produced by seawater sulphate

reduction) might have taken place, inhibiting pyrite formation (cf. Aller & Rude 1988).

The giant stratiform rhodochrosite deposit at Molango, Hidalgo State, Mexico, is the only major manganese deposit in North America. The ore horizon occurs in the Chipoco facies (Table 8) at the base of the Taman Fm (marine limestone and shale; Kimmeridgian), and is in contact with the underlying Santiago Fm (calcareous and pyrite-rich black shale; Late Callovian to Late Oxfordian). A shallowing water depth from the lower Santiago Fm

Table 8. *Manganese deposits of Phanerozoic age*

Age	Geological sequence	Deposits	Geological setting and features	References
Early Oligocene	Early Kharkovian	Nikopol, Ukraine	Shallow-marine sandstone–glaucinitic claystone; facies change from Mn oxide to Mn carbonate ore	Varentsov & Rakhmanov (1980)
	Early Kharkovian	Chiatura, Georgia	Same as above	Bolton & Frakes (1985)
Late Cretaceous	–	Imini-Tasdremt, Morocco	Mn oxide beds interstratified with dolomite sandwiched between non marine sequences	Force <i>et al.</i> (1986)
Middle Cretaceous	Mullaman beds	Groote Eylandt, Australia	Mn oxide ores overlying glauconitic calcareous siltstone with Mn carbonate and pyrite resting on Precambrian sandstone	Frakes & Bolton (1984)
Late Jurassic	Taman Fm, Chipoco facies	Molango, Mexico	Rhodochrosite beds in marine limestone–shale sequence overlying black shale of Santiago Fm	Okita (1992)
Early Jurassic	–	Úrkút, Hungary	Rhodochrosite beds in radiolarian clay marlstone underlying black shale	Polgári <i>et al.</i> (1991)
Middle Ordovician	Modaoxi Fm	Taojiang, China	Mn carbonate beds occur in a sequence of black shale, limestone and calcareous shale	Fan <i>et al.</i> (1992)

to the Chipoco facies is indicated and Okita (1992) suggested that the manganese deposits formed 'either at the culmination of regression or the onset of transgression'. In the basal part of the Chipoco facies ('A-Bed'), pyritiferous Mn carbonate occurs which is overlain by the high-grade ore zone consisting of fine laminations of rhodochrosite alternating with silty shale. In the lower half of this ore zone, pyrite is rare, but magnetite and maghemite are present in silty layers. The ore zone peters out in the middle Chipoco interval. The lowermost part of the Chipoco facies is devoid of marine fauna, indicating dysaerobic to anaerobic conditions during sedimentation; the older Santiago Fm was deposited in an euxinic environment (Okita 1992).

Several features such as very low pyrite content, presence of Fe oxides, presence of rhodochrosite as the exclusive Mn phase, and the upsection evolution from dysaerobic to more oxidizing conditions provide the keys to the

formation of the Mn carbonate ore zone. Aller & Rude (1988) predicted that Mn oxide (taken as MnO₂) could be an important agent for oxidizing both sulphur and organic carbon. The rhodochrosite from the Molango deposit shows negative $\delta^{13}\text{C}$ values (average -13‰) and an antithetic correlation between $\delta^{13}\text{C}$ values and Mn content (Okita *et al.* 1988 cited by Okita 1992). Therefore, manganese reduction corresponded to organic matter oxidation and rhodochrosite and the Fe oxides were early diagenetic products. Cannon & Force (1983) suggested a stratified ocean model for the Molango deposit. However, Okita (1992) favoured river transport of manganese to the depositional basin considering the restricted spatial and temporal nature of the deposit against its enormous Mn metal reserve.

At Groote Eylandt, Australia, a large shallow-water stratiform manganese deposit occurs in the intra-cratonic Carpentaria basin. The orebody occurs in the Mullaman Beds (Late Albian to

Early Cenomanian) that uncomfortably overlies Middle Proterozoic sandstone (Table 8; Frakes & Bolton 1984). The deposit, composed mainly of Mn oxide pisoliths and oololiths, extends for about 22 km with a maximum thickness of 9 m (average 3 m). Immediately below this ore zone, a pyritiferous and glauconite-bearing calcareous siltstone is present, which also contains rhodochrosite and Mn calcite. The most interesting and critical feature recognized in the ore zone is the presence of both normal- and inverse-graded units of Mn oxide pisoliths and oololiths. Frakes & Bolton (1984) interpreted that the pisoliths and oololiths are of primary accretionary origin developed in a shallow-water marine environment. They also inferred that manganese, from a terrestrial source, was concentrated in the dissolved state in transgression-induced oxygen-deficient basin water during the Late Albian. The normal-graded ore units were possibly formed during peak transgression and the inverse-graded units were developed during marine regression (Fig. 2).

The Cenomanian–Turonian sedimentary Mn oxide deposits of Imini–Tasdremt belt, Morocco, are hosted in dolomite (Table 8). Stratiform orebodies are restricted to three levels in the dolomite horizon, two near the base and the third near the top. Pyrolusite, hollandite, coronadite and janggunitite constitute the ore. Force *et al.* (1986) observed that the ore-bearing dolomite horizon has been totally modified by diagenesis. In the Imini area a fossiliferous carbonate unit occurs. A marine, probably an inner shelf, depositional environment is indicated by the faunal assemblage. A rapid marine transgression recorded in this marginal sequence was largely responsible for supplying dissolved manganese from anoxic part of a stratified ocean to the Imini–Tasdremt area (Force *et al.* 1986; Thein 1990). A mixing zone of saline and fresh water is thought to have played a key role in the diagenetic modification of host carbonates (dolomitization) as well as the manganese deposits (oxidation of Mn carbonates). Alternatively, primary precipitation of manganese may have taken place in shifting mixing zones where anoxic seawater mixed with ground water delivered dissolved manganese to zones of fresh oxygenated ground water where precipitation of oxides occurred (Force *et al.* 1986). Following this mixing-zone model, Thein (1990) inferred that the anoxic zone of the stratified basin was supplied with manganese from continental weathering and that mixing occurred during sea-level highstand.

Very large deposits of unmetamorphosed Mn oxide and carbonate ores of Early Oligocene age

occur at Chiatura (Georgia), and Nikopol and Bol'shoi Tokmak (Ukraine) in shallow-marine intracratonic setting. The ore-bearing sequence at Chiatura uncomfortably overlies either the crystalline basement or Late Cretaceous limestone resting on the basement (Table 8). The ore-bearing Oligocene sequence at Nikopol and Bol'shoi Tokmak overlies basement rocks of the Ukrainian shield (Table 8). Features common to these deposits include, (a) a large number of ore-beds and lenses interstratified with or enclosed in orthoquartzite and glauconitic claystone, (b) nodular (oolitic and pisolitic) structure of the ores, and (c) a basinward facies change from oxides to carbonates. Such a zonal arrangement of manganese oxide, oxide plus carbonate, and carbonate at the Chiatura deposit was attributed to Eh variation from shallow to deep water during deposition (Betekhtin 1937 cited by Roy 1981). On the basis of aerobic faunal record in the manganese carbonate zone, this interpretation was rejected and later diagenetic change of Mn oxide to Mn carbonate was suggested (Strakhov & Shterenberg 1966; Strakhov *et al.* 1970; Danilov 1974 all cited by Roy 1981). Sapozhnikov (1970) proposed that dissolved Mn-rich anoxic water from this basin, on upwelling, supplied manganese to a near-shore environment to be deposited through oxidation in shallow-water.

Bolton & Frakes (1985) suggested that the Chiatura deposit formed during a transgressive–regressive cycle in a restricted arm of the Paratethys. They established that the Mn oxide and Mn carbonate oololiths and pisololiths formed by accretion in a shallow-marine low-energy setting, in contradiction to a diagenetic origin proposed by earlier workers. Bolton & Frakes (1985) identified both normal- and inverse-graded bedding in Mn oxide oololiths and pisololiths. They proposed that during transgression, manganese supplied by terrestrial weathering was concentrated in the dissolved state in oxygen-depleted seawater. The Mn carbonates formed in deeper offshore areas where reducing conditions prevailed while in shallow near-shore oxygenated regions Mn oxides were deposited. Following the Groote Eylandt model, Bolton & Frakes (1985) proposed that normally graded units were deposited in a late transgressive period and the inverse grading was formed by a combination of basin shallowing, increasing energy levels and greater oxygenation during the regressive phase.

Hein & Bolton (1992) presented carbon and oxygen isotope data from the Mn carbonate ores of Nikopol. $\delta^{13}\text{C}$ values vary between -9% and -16.5% . PDB (mean -11.9%) and $\delta^{18}\text{O}_{\text{SMOW}}$

values show a range of +26.7‰ to +30.8‰ (mean +29.6‰). These data indicate that carbon was almost equally derived from seawater bicarbonate and organic carbon degradation at a relatively low temperature. Hein & Bolton (1992) inferred that Mn oxyhydroxide probably formed initially and Mn carbonates were early diagenetically derived through the coupled reaction of organic matter oxidation and Mn reduction.

In summary, all important Phanerozoic manganese deposits were formed during transgression–regression cycles triggered by greenhouse conditions followed by oxygenation. However, all such cycles did not necessarily produce manganese deposits as, for example, during the early Palaeozoic. Most manganese deposition took place in intracratonic and rifted continental-margin basins and the source of manganese was inferred to be terrestrial weathering rather than oceanic hydrothermal effluent. Coastal processes have exerted important controls on the geochemical cycle of manganese (veil and broom effect) and these in concert with sea-level changes formed concentrated manganese deposits. Manganese carbonate deposits probably always formed during early diagenesis. Carbon isotope studies on Mn carbonates from the deposits at Taojiang, Urkút, Molango and Nikopol showed that Mn oxyhydroxide was initially precipitated and was reduced coupled with organic matter oxidation leading to formation of Mn carbonate. Conversely, the manganese oxide deposits of Imini–Tasdremt area were probably produced by conversion of originally formed Mn carbonate to oxide in a ground water–seawater mixing zone. The apparent lack of temporal as opposed to spatial contiguity of most important sedimentary manganese deposits through geological history has been rightly pointed out by Frakes & Bolton (1992) as enigmatic and only a satisfactory resolution of this issue will indicate how many genetic models need to be evoked to explain the origin of these deposits.

Supergene manganese deposits in the weathered zone

Concentrations of manganese in zones of terrestrial weathering are common and can yield commercial deposits. Climate and the initial Mn content in the source rock are crucial determinants in this process of manganese ore formation. For example, in arid to semi-arid conditions only thin and sporadic layers of Mn oxides (desert varnish) are formed by local

surficial migration and no commercial deposit is recorded. In temperate and subarctic climatic zones in higher latitudes of the northern hemisphere, humate-rich podzolic soil permits high mobility for manganese released by acidity and high-rate organic decay during weathering. As a result, manganese is neither retained as residual concentration nor allowed to reprecipitate within the weathered zone; it is entirely exported to the sedimentary cycle in lakes and bogs. Humid tropical climate with abundant rainfall and vegetation, in concert with suitable topography (e.g. plateaus), drainage system, and parent rock composition, can produce a manganese deposit within the zone of weathering (Crerar *et al.* 1972, fig. 6a, b, & c). The role of organic acids (humic acid, fluvic acid; formed by decay of vegetation) in chemical weathering of rocks and the release of manganese dissolved in acidic ground water has been emphasized by Crerar *et al.* (1972) and Nicholson (1992).

The leaching of manganese and iron may take place together or one in preference to the other. Selective leaching of manganese with respect to iron can occur by enzymatic microbial reduction. In the Al–Fe–Mn triad, the solubility of manganese is maximum (as is its mobility) and hence, during downward movement of iron and manganese in solution, a change in Eh–pH may lead to precipitation of iron in preference to manganese and an effective separation between the two may take place. Where the weathered profile attains sufficient thickness, the upper zone is depleted in manganese which travels deeper and is reprecipitated in the lower zone (Roy 1981 and references cited therein). Pracejus *et al.* (1988) invoked electrochemical reactions between Fe^{2+} (dissolved in ground water or adsorbed on kaolinite) and Mn^{4+} in the zone of weathering at Groote Eylandt deposit, Australia. According to their model, by these reactions Mn^{4+} in the oxide minerals was reduced and dissolved with consequent deposition of Fe^{3+} phases (goethite, hematite) and clay minerals. On transportation, dissolved Mn^{2+} cemented pisolitic and oolitic primary sedimentary ore, or formed mangcrete (Pracejus *et al.* 1988).

The sedimentary Mn oxide ore deposits of the Iron Ore Group (Bihar and Orissa) and the Dharwar Supergroup (Karnataka and Goa), India, show considerable chemical reworking in the weathered zone (Roy 1981). In many deposits, aluminium and iron (laterite) are characteristically concentrated in the upper zone and manganese in the lower zone of the weathered profile. In the Sausar Group, a large supergene deposit extending for about 1.5 km and of a thickness exceeding 130 m occurs at Dongri Buzurg. The

deposit was formed by oxidation of pre-existing metamorphosed Mn oxide (with Mn^{2+} and Mn^{3+}) and Mn silicate rocks (Roy 1981).

The rocks most amenable to supergene concentration of manganese in the weathering zone are Mn-rich carbonates followed closely by Mn silicate-carbonates. Mn oxides are either formed in situ by oxidation of the carbonates or through dissolution, limited vertical and lateral migration, and reprecipitation. Most sedimentary Mn carbonate deposits discussed in the earlier section, particularly those located in humid tropical climates, yielded supergene cappings of Mn oxide/hydroxide ores that often form large deposits. The best known deposits of this type occur in Brazil (Serra do Navio, Amapa; Morro da Mina, Minas Gerais; Azul, Para), Gabon (Moanda), Ghana, Ivory Coast, Burkina Faso, Eastern Liberia, and Mexico (Molango); smaller deposits occur at Urkút, Hungary, Philipsburg and Butte, USA, and Janggun mine, South Korea (for detailed discussion see Roy 1981). The ages of weathering in these deposits are poorly known, but it is suggested that supergene enrichment took place chiefly during the Cenozoic.

The only evidence of Proterozoic weathering producing commercial Mn oxide ores at the cost of manganiferous carbonates comes from deposits formed in palaeo-sinkholes in dolomites of the Campbellrand Subgroup (Ghap Group; Transvaal Supergroup) in South Africa. Development of these sinkholes and supergene enrichment of manganiferous dolomites to Mn oxides are attributed to weathering that took place preceding the deposition of the overlying Proterozoic Gamagara Formation of the Olifantshoek Group (Grobelaar & Beukes 1986). Such Mn oxide deposits are well-developed in Bishop, Glosam, and Lohatla mine areas and are composed dominantly of bixbyite and braunite, which might have formed by diagenesis (cf. Roy *et al.* 1990) of supergene Mn^{4+} -rich oxides after burial and superimposition of the Gamagara Formation. A later weathering cycle, probably during the Cenozoic, produced psilomelane and pyrolusite (Grobelaar & Beukes 1986).

The help and suggestions by S. Dasgupta, P. Sengupta and A. Mookherjee during preparation of the text are gratefully acknowledged. Sincere thanks are due to J. R. Hein who substantially improved the manuscript during review. An anonymous reviewer also contributed towards streamlining the manuscript. I am grateful to R. A. Berner and L. A. Frakes for their kind permission to reproduce figures from their papers. The work was done under IGCP Project 318: Genesis and Correlation of Marine Polymetallic oxides.

References

- ALLER, R. C. & RUDE, P. D. 1988. Complete oxidation of solid phase sulfides by manganese and bacteria in anoxic marine sediments. *Geochimica et Cosmochimica Acta*, **52**, 751–765.
- ANBAR, A. D. & HOLLAND, H. D. 1992. The photochemistry of manganese and the origin of banded iron formation. *Geochimica et Cosmochimica Acta*, **56**, 2595–2603.
- BARAL, M. C. 1986. Archean stromatolite from Dodguni belt of Karnataka craton, India. *Journal of the Geological Society of India*, **25**, 328–333.
- BAU, M. & DULSKI, P. 1993. Distribution of rare-earth elements in Precambrian sedimentary Fe-, Mn-, and P-deposits. *16th International Colloquium of Africa Geology, Extended Abstracts*, 27–28.
- BERNER, R. A. 1991. A model for atmospheric CO_2 over Phanerozoic time. *American Journal of Science*, **291**, 339–376.
- , LASAGA, A. C. & GARRELS, R. M. 1983. The carbonate-silicate geochemical cycle and its effect on atmospheric carbon dioxide over the past 100 million years. *American Journal of Science*, **283**, 641–683.
- BEUKES, N. J. 1983. Palaeoenvironmental setting of iron-formation in the depositional basin of the Transvaal Supergroup, South Africa. In: TRENDALL, A. F. & MORRIS, R. C. (eds) *Iron-formation: Facts and Problems*. Elsevier, Amsterdam, 139–209.
- 1989. Sedimentological and geochemical relationships between carbonate, iron-formation and manganese deposits in the early Proterozoic Transvaal Supergroup, Griqualand West, South Africa. *28th International Geological Congress, Washington DC, Abstracts*, **1**, 143.
- 1993. A review of manganese deposits associated with the early Proterozoic Transvaal Supergroup in Northern Cape Province, South Africa. *16th International Colloquium of Africa Geology, Extended Abstracts*, 37–38.
- , GUTZMER, J. & KLEYENSTÜBER, A. S. E. 1993. *Excursion Guide to Iron and Manganese Deposits of the Transvaal Supergroup, Griqualand West*. IGCP Project 318, South Africa Field Workshop, September 1993.
- BOLTON, B. R. & FRAKES, L. A. 1985. Geology and genesis of manganese oolites, Chiatura, Georgia, U.S.S.R. *Geological Society of America Bulletin*, **96**, 1398–1406.
- BONATTI, E., ZERBI, M., KAY, R. & RYDELL, H. S. 1976. Metalliferous deposits from the Apennine ophiolites: Mesozoic equivalents of modern deposits from oceanic spreading centre. *Geological Society of America Bulletin*, **87**, 83–94.
- BREITKOPF, J. H. 1988. Iron formation related to mafic volcanism and ensialic rifting in the southern margin zone of the Damara orogen, Namibia. *Precambrian Research*, **38**, 111–130.
- BROS, R., STILLE, P., GAUTHIER-LAFAYE, F. & WEBER, F. 1992. Sm–Nd isotopic dating of Proterozoic clay material: an example from the Francevillian sedimentary series, Gabon. *Earth and Planetary Science Letters*, **113**, 207–218.

- BÜHN, B., STANISTREET, I. G. & OKRUSCH, M. 1992. Late Proterozoic outer shelf manganese and iron deposits at Otjosondou (Namibia) related to the Damaran oceanic opening. *Economic Geology*, **87**, 1393–1411.
- CALVERT, S. E. 1990. Geochemistry and origin of the Holocene sapropel in the Black Sea. In: ITTEKKOT, V., KEMPE, S., MICHAELS, W & SPITZY, A. (eds) *Facts of Modern Biogeochemistry*. Springer, Berlin, 326–352.
- & PEDERSEN, T. F. 1993. Geochemistry of Recent oxic and anoxic marine sediments: implications for the geological record. *Marine Geology*, **113**, 67–88.
- CANNON, W. F. & FORCE, E. R. 1983. Potential for high-grade shallow-marine manganese deposits in North America. In: SHANKS, W. C. III, (ed.) *Cameron Volume on Unconventional Mineral Deposits*, Society of Mining Engineers, American Institute of Mining, Metallurgical and Petroleum Engineers, New York, 175–189.
- CHAUDHURI, A. K., DASGUPTA, S., BANDOPADHYAY, G., SARKAR, S., BANDOPADHYAY, P. C. & GOPALAN, K. 1989. Stratigraphy of the Penganga Group around Adilabad, Andhra Pradesh. *Journal of the Geological Society of India*, **34**, 291–302.
- COLLEY, H. & WALSH, J. N. 1987. Genesis of Fe-Mn deposits of southwest Viti Levu, Fiji. *Transactions Institution of Mining and Metallurgy, Section B, Applied Earth Sciences*, **96**, 201–212.
- CRERAR, D. A., CORMICK, R. K. & BARNES, H. L. 1972. Organic controls on the sedimentary geochemistry of manganese, *Acta Mineralogica-Petrographica*, **20**, 217–226.
- , NAMSON, J., CHYI, M. S., WILLIAMS, L. & FEIGENSON, M. D. 1982. Manganiferous cherts of the Franciscan assemblage: I. General geology, ancient and modern analogues, and implications for hydrothermal convection at oceanic spreading centers. *Economic Geology*, **77**, 519–540.
- DASGUPTA, S., BANERJEE, H., FUKUOKA, M., BHATTACHARYA, P. K. & ROY, S. 1990. Petrogenesis of metamorphosed manganese deposits and the nature of the precursor sediments. *Ore Geology Reviews*, **5**, 359–384.
- , HARIYA, Y. & MIURA, H. 1993. Compositional limits of manganese carbonates and silicates in granulite facies metamorphosed deposits of Garbham, Eastern Ghats, India. *Resource Geology Special Issue*, **17**, 43–49.
- DE BARR, H. J. W., GERMAN, C. R., ELDERFIELD, H. & VAN GAANS, P. 1988. Rare earth element distribution in anoxic waters of the Cariaco Trench. *Geochimica et Cosmochimica Acta*, **52**, 1203–1219.
- DERRY, L. A. & JACOBSEN, S. B. 1990. The chemical evolution of Precambrian seawater: evidence from REES in banded iron formations. *Geochimica et Cosmochimica Acta*, **54**, 2965–2977.
- , KAUFMAN, A. J. & JACOBSEN, S. B. 1992. Sedimentary cycling and environmental change in the Late Proterozoic: evidence from stable and radiogenic isotopes. *Geochimica et Cosmochimica Acta*, **56**, 1317–1329.
- DES MARAIS, D. J., STRAUSS, H., SUMMONS, R. E. & HAYES, J. M. 1992. Carbon isotope evidence for the stepwise oxidation of the Proterozoic environment. *Nature*, **359**, 605–609.
- DORR, J. V. N. 1968. Primary manganese ores. *Proceedings, 23rd Congress, Sociedade Brasileira do Geologia*, 1–12.
- , COELHO, I. S. & HOREN, A. 1956. The manganese deposits of Minas Gerais, Brazil. *22nd International Geological Congress, Symposium on Manganese*, **3**, 279–346.
- FAN, D., LIU, T. & YE, J. 1992. The process of formation of manganese carbonate deposits hosted in black shale series. *Economic Geology*, **87**, 1419–1429.
- FLEET, A. J. & ROBERTSON, A. H. F. 1980. Ocean-ridge metalliferous and pelagic sediments of the Semail Nappe, Oman. *Journal of the Geological Society, London*, **137**, 403–422.
- FLOHR, M. J. K. 1992. Geochemistry and origin of the Bald Knob manganese deposit, North Carolina. *Economic Geology*, **87**, 2023–2040.
- & HUEBNER, J. S. 1992. Mineralogy and geochemistry of two metamorphosed sedimentary manganese deposits, Sierra Nevada, California. *Lithos*, **28**, 57–85.
- FORCE, E. R. & CANNON, W. F. 1988. Depositional model for shallow-marine manganese deposits around black shale basins. *Economic Geology*, **83**, 93–117.
- , BACK, W., SPIKER, E. C. & KNAUTH, L. P. 1986. A ground-water mixing model for the origin of the Imini manganese deposit (Cretaceous) of Morocco. *Economic Geology*, **81**, 65–79.
- FRAKES, L. A. & BOLTON, B. R. 1984. Origin of manganese giants: sea level change and anoxic-oxic history. *Geology*, **12**, 83–86.
- & — 1992. Effects of ocean chemistry, sea level and climate on the formation of primary sedimentary manganese ore deposits. *Economic Geology*, **87**, 1207–1217.
- GAUTHIER-LAFAYE, F. & WEBER, F. 1989. The Francevillian (Lower Proterozoic) uranium ore deposits of Gabon. *Economic Geology*, **84**, 2267–2285.
- GLASBY, G. P. 1988. Hydrothermal manganese deposits in island arcs and related to subduction processes: a possible model for genesis. *Ore Geology Reviews*, **4**, 145–153.
- GROBBELAAR, W. S. & BEUKES, N. J. 1986. The Bishop and Glosam manganese mines and the Beeshoek Iron ore mine of the Postamasburg area. In: ANHAEUSSER, C. R. & MASKES, S. (eds) *Mineral Deposits of Southern Africa*. Geological Society of South Africa, Johannesburg, 957–961.
- GROTZINGER, J. P. & KASTING, J. F. 1993. New constraints on Precambrian Ocean composition. *Journal of Geology*, **101**, 235–243.
- HAJASH, A. & CHANDLER, G. W. 1981. An experimental investigation of high-temperature interactions between seawater and rhyolite, andesite, basalt and peridotite. *Contributions to Mineralogy and Petrology*, **78**, 240–254.

- HALLAM, A. 1987. Mesozoic marine organic-rich shales. In: BROOKS, J. & FLEET, A. J. (eds) *Marine Petroleum Source Rocks*. Geological Society, London, Special Publications, **26**, 251–261.
- HARIYA, Y. 1980. On the geochemistry and formation of manganese dioxide deposits. In: VARENTSOV, I. M. & GRASSELLY, G. (eds) *Geology and Geochemistry of Manganese*, **1**, E. Schweizerbart'sche Verlagsbuchhandlung, Stuttgart, 353–365.
- & TATSUMI, M. 1981. Hydrogen isotopic composition of MnO(OH) minerals from manganese oxide and massive sulfide (Kuroko) deposits of Japan. *Contributions to Mineralogy and Petrology*, **77**, 256–261.
- HEIN, J. R. & BOLTON, B. R. 1992. Stable isotope composition of Nikopol and Chiatura manganese ores, U.S.S.R.: implications for genesis of large sedimentary manganese deposits. *29th International Geological Congress, Kyoto, Abstracts*, **1**, 209.
- & — 1993. Composition and origin of the Moanda manganese deposit, Gabon. *16th International Colloquium on Africa Geology, Extended Abstracts*, 1150–1152.
- & KOSKI, R. A. 1987. Bacterially mediated diagenetic origin for chert-hosted manganese deposits in the Franciscan Complex, California Coast Range. *Geology*, **15**, 722–726.
- , GEIN, L. M. & MORRISON, S. 1988. Submarine ferromanganese mineralization in active volcanic arc systems. *Pacific Congress on Marine Science & Technology, PACON 88, Proceedings*, Honolulu, Hawaii, 83–88.
- , SCHULZ, M. S. & KING, J. K. 1990. Insular and submarine ferromanganese mineralization of the Tonga-Lau Region. *Marine Mining*, **9**, 305–354.
- HOLLAND, H. D. 1984. *The Chemical Evolution of the Atmosphere and Oceans*. Princeton University Press, Princeton, NJ.
- HUEBNER, J. S. & FLOHR, M. J. K. 1990. *Micro-banded Manganese Formations: Protoliths in the Franciscan Complex, California*. US Geological Survey Professional Paper **1502**.
- , — & GROSSMAN, J. N. 1992. Chemical fluxes and origin of a manganese carbonate-oxide-silicate deposit in bedded chert. *Chemical Geology*, **100**, 93–118.
- JACOBS, L. & EMERSON, S. 1982. Trace metal solubility in an anoxic fjord. *Earth and Planetary Science Letters*, **60**, 237–252.
- , — & SKEI, J. 1985. Partitioning and transport of metals across the O₂/H₂S interface in a permanently anoxic basin: Framvaren Fjord, Norway. *Geochimica et Cosmochimica Acta*, **49**, 1433–1444.
- JENKYN, H. C. 1980. Cretaceous anoxic events: from continents to oceans. *Journal of the Geological Society, London*, **137**, 171–188.
- , GECZY, B. & MARSHALL, J. D. 1991. Jurassic manganese carbonates of central Europe and the early Toarcian anoxic event. *Journal of Geology*, **99**, 137–149.
- KASTING, J. F. 1987. Theoretical constraints on oxygen and carbon dioxide concentrations in the Precambrian atmosphere. *Precambrian Research*, **34**, pp. 205–29.
- 1992. Models relating to Proterozoic atmosphere and ocean chemistry. In: SCHOPF, J. W. & KLEIN, C. (eds) *The Proterozoic Biosphere*. Cambridge University Press, New York, 1185–1187.
- 1993. Earth's early atmosphere. *Science*, **259**, 920–926.
- , EGGLE, D. W. & RAEBURN, S. P. 1993. Mantle redox evolution and the oxidation state of the Archean atmosphere. *Journal of Geology*, **101**, 245–257.
- KLEYENSTÜBER, A. S. E. 1984. The mineralogy of the manganese-bearing Hotazel Formation of the Proterozoic Transvaal sequence in Griqualand West, South Africa. *Transactions Geological Society of South Africa*, **87**, 257–272.
- KLINKHAMMER, G. P. & HUDSON, A. 1986. Dispersal patterns for hydrothermal plumes in the South Pacific using manganese as a tracer. *Earth and Planetary Science Letters*, **79**, 241–249.
- KNOLL, A. H., HAYES, J. M., KAUFMAN, A. J., SWETT, K. & LAMBERT, I. B. 1986. Secular variation in carbon isotope ratios from upper Proterozoic successions of Svalbard and East Greenland. *Nature*, **321**, 832–838.
- LAMBERT, I. B. & DONNELLY, T. H. 1991. Atmospheric oxygen levels in the Precambrian: a review of isotopic and geological evidence. *Paleogeography, Paleoclimatology, Paleoecology (Global Planetary Change Section)*, **97**, 83–91.
- LAXEN, D. P. H., DAVISON, W. & WOOF, C. 1984. Manganese chemistry in rivers and streams. *Geochimica et Cosmochimica Acta*, **48**, 2107–2111.
- LECLERC, J. & WEBER, F. 1980. Geology and genesis of the Moanda manganese deposits, Republic of Gabon. In: VARENTSOV, I. M. & GRASSELLY, G. (eds) *Geology and Geochemistry of Manganese*, **2**, E. Schweizerbart'sche Verlagsbuchhandlung, Stuttgart, 89–109.
- LEUBE, A., HIRDES, W., MAUER, R. & KESSE, G. O. 1990. The early Proterozoic Birimian Supergroup of Ghana and some aspects of its associated gold mineralization. *Precambrian Research*, **46**, 139–165.
- MOORES, E. M., ROBINSON, P. T., MALPAS, J. & XENOPHONOTOS, C. 1984. Model for the origin of the Troodos Massif, Cyprus, and other mid-east ophiolites. *Geology*, **12**, 500–503.
- MORITANI, T. 1976. Tertiary manganese mineralisation in Japan. In: GLASBY, G. P. & KATZ, H. R. (eds) *CCOP/SOPAC Technical Bulletin*, **2**, 80–82.
- NICHOLSON, K. 1990. Stratiform manganese mineralisation near Inverness, Scotland: A Devonian sublacustrine hot-spring deposit? *Mineralium Deposita*, **25**, 126–131.
- 1992. Genetic types of manganese oxide deposits in Scotland: Indicators of paleo-ocean spreading rate and a Devonian geochemical mobility boundary. *Economic Geology*, **87**, 1301–1309.
- OKITA, P. M. 1992. Manganese carbonate mineralization in the Molango District, Mexico. *Economic Geology*, **87**, 1345–1366.
- & SHANKS III, W. C. 1992. Origin of stratiform sediment-hosted manganese carbonate ore deposits: examples from Molango, Mexico and Taojiang, China. *Chemical Geology*, **99**, 139–164.

- O'REILLY, G. A. 1992. Petrographic and geochemical evidence for a hypogene origin of granite-hosted, vein-type Mn mineralization at the New Ross Mn deposits, Lunenburg County, Nova Scotia, Canada. *Economic Geology*, **87**, 1275–1300.
- PARK, C. F. 1946. The spilite and manganese problems of the Olympic Peninsula, Washington. *American Journal of Science*, **244**, 305–323.
- PEARCE, J. A., LIPPARD, S. J. & ROBERTS, S. 1984. Characteristics and tectonic significance of supra-subduction zone ophiolites. In: KOKELAAR, B. P. & HOWELLS, M. F. (eds) *Marginal Basin Geology*. Geological Society, London, Special Publications, **16**, 77–94.
- POLGÁRI, M., OKITA, P. M. & HEIN, J. R. 1991. Stable isotope evidence for the origin of the Urkút manganese ore deposit, Hungary. *Journal of Sedimentary Petrology*, **61**, 384–393.
- PONTÉR, C., INGRI, J. & BOSTRÖM, K. 1992. Geochemistry of manganese in the Kalix river, northern Sweden. *Geochimica et Cosmochimica Acta*, **56**, 1485–1494.
- PRACEJUS, B., BOLTON, B. R. & FRAKES, L. A. 1988. Nature and development of supergene manganese deposits, Groote Eylandt, Northern Territory, Australia. *Ore Geology Reviews*, **4**, 71–98.
- ROBERTSON, A. H. F. & BOYLE, J. F. 1983. Tectonic setting and origin of metalliferous sediments in the Mesozoic Tethys Ocean. In: RONA, P. A., BOSTRÖM, K., LAUBIER, L. & SMITH, K. L. JR. (eds) *Hydrothermal Processes of Seafloor Spreading Centres*. Plenum, New York, 595–663.
- & VARNAVAS, S. P. 1993. The origin of hydrothermal metalliferous sediments associated with the early Mesozoic Othris and Pindos ophiolites, mainland Greece. *Sedimentary Geology*, **83**, 87–113.
- ROY, S. 1966. *Syngenetic Manganese Formations of India*. Jadavpur University Press, Calcutta.
- 1981. *Manganese Deposits*. Academic Press, London.
- , BANDOPADHYAY, P. C., PERSEIL, E. A. & FUKUOKA, M. 1990. Late diagenetic changes in manganese ores of the upper Proterozoic Penganga Group, India. *Ore Geology Reviews*, **5**, 341–357.
- SAPOZHNIKOV, D. G. 1970. Geological conditions for the formation of manganese deposits of the Soviet Union. In: SAPOZHNIKOV, D. G. (ed.) *Manganese Deposits of Soviet Union*, Israel Program for Scientific Translations, 9–33.
- SCHLANGER, S. O., ARTHUR, M. A., JENKYN, H. C. & SCHOLLE, P. A. 1987. The Cenomanian-Turonian oceanic anoxic event. I. Stratigraphy and distribution of organic carbon-rich beds and the marine $\delta^{13}\text{C}$ excursion. In: BROOKS, J. & FLEET, A. J. (eds) *Marine Petroleum Source Rocks*. Geological Society London, Special Publications, **26**, 373–402.
- SPENCER, D. W. & BREWER, P. G. 1971. Vertical advection-diffusions and redox potentials as controls on the distribution of manganese and other trace metals dissolved in the waters of the Black Sea. *Journal of Geophysical Research*, **76**, 5877–5892.
- SUNDBY, B., SILVERBERG, N. & CHESSELET, R. 1981. Pathways of manganese in an open estuarine system. *Geochimica et Cosmochimica Acta*, **45**, 293–307.
- TAYLOR, G. R. 1976. Styles of mineralisation in the Solomon islands – a review. In: GLASBY, G. P. & KATZ, H. R. (eds) *CCOP/SOPAC Technical Bulletin*, **2**, 83–91.
- TAYLOR, P. N., MOORBATH, S., LEUBE, A. & HIRDES, W. 1992. Early Precambrian crustal evolution in the Birimian of Ghana: constraints from geochronology and isotope geochemistry. *Precambrian Research*, **56**, 97–111.
- THEIN, J. 1990. Paleogeography and geochemistry of the “Cenomano-Turonian” formations in the manganese district of Imini (Morocco) and their relation to ore deposition. *Ore Geology Reviews*, **5**, 257–291.
- TREFRY, J. H. & PRESLEY, B. J. 1982. Manganese fluxes from Mississippi delta sediments. *Geochimica et Cosmochimica Acta*, **46**, 1715–1726.
- URBAN, H., STRIBRNY, B. & LIPPOLT, H. J. 1992. Iron and manganese deposits of the Urucum district, Mato Grosso do sul, Brazil. *Economic Geology*, **87**, 1375–1392.
- VARENTSOV, I. M. & RAKHMANOV, V. P. 1980. Manganese deposits of the USSR (A Review). In: VARENTSOV, I. M. & GRASSELLY, G. (eds) *Geology and Geochemistry of Manganese*, **2**. E. Schweizerbart'sche Verlagsbuchhandlung, Stuttgart, 320–391.
- VARGA, R. J. & MOORES, E. M. 1985. Spreading structures of the Troodos ophiolite, Cyprus. *Geology*, **13**, 846–850.
- VEIZER, J., COMPSTON, W., CLAUER, N. & SCHIDLowski, M. 1983. $^{87}\text{Sr}/^{86}\text{Sr}$ in late Proterozoic carbonates: evidence for a “mantle event” at 900 Ma ago. *Geochimica et Cosmochimica Acta*, **47**, 295–302.
- WALKER, J. C. G. & BRIMBLECOMBE, P. 1985. Iron and sulfur in pre-biologic ocean. *Precambrian Research*, **28**, 205–222.
- ZANTOP, H. 1978. Geologic setting and genesis of iron oxides and manganese oxides in the San Francisco manganese deposit, Jalisco, Mexico. *Economic Geology*, **73**, 1137–1149.

Fractionation of manganese from iron in Archaean and Proterozoic sedimentary ores

G. P. GLASBY

*Department of Earth Sciences, University of Sheffield,
Sheffield S3 7HP, UK*

Abstract: The fractionation of manganese from iron through geological time has previously not been well understood. Iron deposits were considered to be abundant in the Precambrian and have declined in the Phanerozoic whereas manganese deposits appeared to show the opposite trend.

It is now seen that the Proterozoic banded iron formations contain about 200 times the amount of manganese in land-based manganese deposits and an order of magnitude more manganese than in deep-sea manganese nodules. The great abundance of manganese in these banded iron formation appears to resolve this problem.

In the Archaean and Proterozoic oceans, hydrothermal activity played a much more important role than at present due to the higher geothermal gradients. Upwelling of hydrothermally-derived iron, silica and manganese from anaerobic oceanic basins to more oxygenated shallow platform areas may have provided the unique conditions required for the formation of the Proterozoic banded iron formations which constitute the largest mineable reserve of any metal. An important factor in the formation of these deposits was the low sulphate ion content of the ocean waters. This ensured that the iron did not precipitate dominantly as pyrite under the reducing conditions then prevalent in the ocean waters. Manganese and iron could therefore display similar aqueous geochemistries. The reason for the separation of manganese from iron to form giant manganese deposits such as the Kalahari manganese deposit remains uncertain but variable redox conditions resulting from transgression and increasing atmospheric oxygen content or the influence of extensive hydrothermal activity may have been involved. Nonetheless, the similarity in the geochemistries of manganese and iron in the Palaeoproterozoic contrasts with the situation encountered in Phanerozoic manganese deposits in which iron became immobile in adjacent anoxic basins as pyrite thus ensuring the fractionation of manganese from iron. Oxidation of the ferrous ion could have taken place as a result of photosynthesis or of inorganic photochemical reactions. The formation of oxygen by these processes could have been the rate-determining step in the formation of the banded iron formations. It is possible that blooming by blue-green algae played a key role in the oxidation of the ferrous iron in the seawater. The seasonability of this blooming would then have resulted in the characteristic iron-rich and iron-poor microlaminae of these deposits.

In his excellent review of manganese metallogenesis, Roy (1988) has noted that the metallogenic development of iron and manganese follow opposite trends in respect to time. Iron deposits abound in the Precambrian and decline in the Phanerozoic whereas manganese deposits are scarce in the Archaean, moderately developed in the Proterozoic and are extensive in the late Phanerozoic. According to Roy (1988), such fractionation of iron and manganese in nature has not been explained so far and is considered to be a puzzle awaiting a suitable solution.

In fact, the above assertion may not be strictly true. Figure 1 shows the distribution of land-based manganese and iron deposits through geological time based on the data of Laznicka (1985) and Veizer *et al.* (1989). It is seen that the amounts of land-based manganese and iron

deposits are both at a maximum in the Proterozoic. However, only the manganese deposits display a second maximum in the Cenozoic (Laznicka 1992). This distribution would be markedly altered for manganese if oceanic deposits (manganese nodules) were included. In this case, the Cenozoic manganese deposits would dominate (Glasby 1988). In each case, terrestrial deposits are principally of chemical-sedimentary origin (making up 85% of manganese deposits and 74% of iron deposits, Veizer *et al.* 1989, or 96% of the manganese, Laznicka 1992).

Meyer (1981, 1985) has pointed out that the lower Proterozoic stratiform iron deposits are one of the sharpest and most significant geochemical anomalies in earth's history and that the locus of iron fixation has moved landward through geological time from the deep sea in

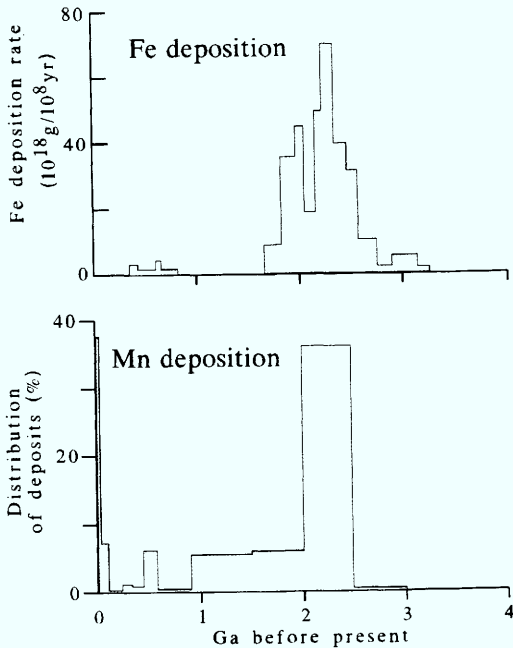


Fig. 1. Distribution of land-based manganese and iron deposits through geological time. Fe data from Isley (1995); Mn data from Veizer *et al.* (1989).

Archaean greenstone belts to shallow continental shelves during the formation of the Proterozoic banded iron formations and epicontinental seas in the Palaeozoic and Mesozoic (Young & Taylor 1989). At present, bog ores form on the land surface.

Roy (1988) considered the paucity of manganese deposits in the Archaean to be the result of two possible causes: (a) the volcanic/hydrothermal exhalations were too deficient in manganese to produce economic ore bodies or (b) the deposition of manganese was inhibited by the anoxic or oxygen-poor environment (Roy 1976, 1981; Windley 1977).

In this paper, it is hoped to consider the nature and origin of the Proterozoic banded iron formations with a view to establishing the nature of the fractionation of iron and manganese in the Proterozoic.

Proterozoic volcanic and hydrothermal exhalations

With regard to volcanic/hydrothermal activity in the Archaean and Proterozoic, it should be borne in mind that the heat production of the earth is thought to have been several times greater in the

early Precambrian than at present (Windley 1977, 1979; Bickle 1978; Sleep & Windley 1982; Abbott 1984; Abbott & Hoffman 1984; Abbott & Menke 1990; Isley 1995). The only effective means of dissipating the higher heat production was accelerated tectonic activity. The rate of plate production 2800 Ma ago has been estimated to have been about $18 \text{ km}^3 \text{ a}^{-1}$ compared with $3 \text{ km}^3 \text{ a}^{-1}$ at present. Hoffman & Ranalli (1988) have calculated that the generation rate of oceanic crust in the Archaean would have been about $130\text{--}195 \text{ km}^3 \text{ a}^{-1}$ compared to about $18 \text{ km}^3 \text{ a}^{-1}$ at present. In addition, geothermal gradients would have been higher in the Archaean ($>60^\circ\text{C km}^{-1}$) than at present ($<30^\circ\text{C km}^{-1}$) (Fryer *et al.* 1979). For comparison, the heat loss caused by oceanic hydrothermal circulation at present is about $4 \times 10^{19} \text{ cal a}^{-1}$ (or about 20% of the total heat loss of the earth) (Wolery & Sleep 1976; Sclater *et al.* 1981; Rona 1984; Rosenberg *et al.* 1988; Lupton *et al.* 1989). It is this heat transfer which promotes the hydrothermal mineralization associated with present-day oceanic spreading centres, back arc basins and hot spot volcanoes. Fyfe *et al.* (1978) have noted that the present oceans are largely fed by rivers with perhaps a 10% contribution from submarine hydrothermal systems (Rona 1988). In earlier times, ocean chemistry would tend to have been dominated by hydrothermal systems (Corliss *et al.* 1981; Appel 1983; Jacobsen & Pimentel-Klose 1988; Kump & Holland 1992; Siever 1992; Bühn & Stanistreet this volume).

To put these figures into perspective, Fyfe (1978) has shown that, for each 10 km^3 of basalt produced, the total heat input over 100 Ma would be of the order of $2 \times 10^{20} \text{ J}$ or enough to heat $5 \times 10^{17} \text{ g}$ of seawater to 100°C . We are therefore led to the conclusion that hydrothermalism was much more significant in the Archaean than at present (Burke & Kidd 1978; Veizer 1983; Worsley *et al.* 1985).

Fyfe (1978) has also calculated that cooling the MacGregor granitic batholith in Zimbabwe would have released enough energy to heat 10^{21} g of seawater to 100°C . Assuming that this fluid contained 100 ppm of iron, discharge of the iron into the oceans would have resulted in a deposit of about 10^{11} tonnes. Some authors have suggested that nearly all igneous activity in the Archaean was submarine (Fyfe 1977; Walker 1982), although this view is not universally accepted.

In addition, Fryer *et al.* (1979) have presented evidence that hydrothermal fluids were reducing in the Archaean* with iron dominantly in the divalent state. Rare earth analyses of

Precambrian iron formations indicate that europium was anomalously enriched in seawater as the divalent ion prior to 1900 Ma (Fryer 1977) (cf. Appel 1983; Fryer 1983; Barrett *et al.* 1988; Buhn & Stanistreet, this volume; Bau & Dulski in press). In the Archaean oceans, metals such as Cu, Hg, Pb, Zn, Mn, Fe and As could have been present in concentrations as high as in modern Red Sea deeps (Fyfe 1977; see also Cameron & Garrels 1980; MacGeehan & MacLean 1980; Belevtsev *et al.* 1983; Ewers 1983; Eriksson 1995). Fryer (1977) has also asserted that, in the Palaeoproterozoic, manganese was concentrated in the iron carbonate, iron silicate and iron sulphide phases of the banded iron formations and in limestones in the divalent state (Veizer 1978, 1983; Holland 1984). Arrhenius (1986) and Kuma *et al.* (1989) have suggested that rust minerals of hydrothermal origin might have been the precursor for the iron minerals which occur in banded iron formations (Murad & Johnston 1987).

The evidence therefore suggests that, in the Archaean and Palaeoproterozoic, hydrothermalism was much more significant than at present and that conditions were reducing so that iron, manganese and europium were dominantly in the divalent state. In such circumstances, it seems unlikely that manganese was absent from hydrothermal fluids as indicated by Roy (1988), and indeed concentrations would probably have been much higher than at present. For comparison, the manganese and iron contents of modern submarine hydrothermal fluids are in the ranges 0.7–1.5 mmol kg⁻¹ and 0.7–2.4 mmol kg⁻¹ respectively with a Fe/Mn ratio between 0.9 and 2.9 (Von Damm *et al.* 1985; Hudson *et al.* 1986; Klinkhammer & Hudson 1986). This compares with a Fe/Mn ratio in basalts of 50–60 and in modern metalliferous sediments of about 3.5.

In fact, few reliable data exist on the flux of elements into the modern oceans. For manganese, it would appear that the hydrothermal inputs dominate over riverine and atmospheric inputs (Wolery & Sleep 1976; Collier & Edmond 1984; Glasby 1988; German & Angel 1995). For iron, the data are much poorer but estimates for the riverine, atmospheric and hydrothermal inputs are <2.6, <14.2, 4.0–2.1 × 10⁶ t a⁻¹ respectively (Collier & Edmond 1984). Accepting these rather crude figures, it is seen that

atmospheric and hydrothermal inputs of iron dominate over riverine inputs in the modern ocean. Obviously, in the Proterozoic when hydrothermalism was more important, hydrothermal inputs of iron would increase substantially relative to the other inputs. Worsley & Nance (1989) have estimated that the amount of ferrous iron exiting oceanic ridges would have been at least 20 times greater than at present. In addition, Simonson (1985) has argued that a continental source for the iron can be dismissed because surface waters were sufficiently oxidizing to have ruled out transport of significant quantities of ferrous iron.

Manganese in banded iron formations

By way of background, Meyer (1981, 1985, 1988), Veizer *et al.* (1989) and Laznicka (1992) have reviewed ore-forming processes throughout geological time. For iron, the earliest formed major ore deposits were the Archaean massive sulphides (Franklin *et al.* 1981), although the Isua iron formation in Greenland has been dated at 3760 Ma (Shimizu *et al.* 1990). These deposits were followed by the Proterozoic banded iron formations which were quantitatively much more important. Present evidence suggests three periods of peak deposition of iron-rich sediments: mid-Archaean (3400–2900 Ma), Palaeoproterozoic (2500–1900 Ma) and Neoproterozoic (750–500 Ma). The deposits of Palaeoproterozoic age far outweigh those of all other ages accounting for 90% or more of the estimated total of 10¹⁵ tonnes of originally deposited iron formation (James & Trendall 1982; James 1983). Holland (1984, fig. 8.22) has plotted the occurrence of the banded iron formations through geological time and shown that the maximum tonnages were formed between 2500 and 2000 Ma with much smaller tonnages between 3500 and 3000 Ma, 2000 and 1500 Ma and 1000 and 500 Ma (Isley 1995, fig. 1). Rona (1988) noted that the Archaean is characterized by the lowest frequency of occurrence of massive sulphide deposits, although this may reflect problems of preservation of the ores.

We shall now consider the banded iron formations (BIF) (James & Sims 1973; Holland 1984; Cloud 1988). These deposits were formed between 2500 and 1900 Ma and represent the largest mineable reserves of any metal. They total about 6 × 10¹⁴ t and contain about 30% Fe and about 0.22% Mn (Bayley & James 1973; Beukes 1973; James & Trendall 1982; see also Trendall 1968; Davy 1983; Holland 1984; Braterman & Cairns-Smith 1987). These figures

* For comparison, the inferred characteristics of hydrothermal fluids from 13°N on the East Pacific Rise are $f_{O_2} = 10^{-35}$ atm., $f_{S_2} = 10^{-10}$ atm., $T = 35^\circ\text{C}$ and $\text{pH} = 3\text{--}4$ (Auclair *et al.* 1987).

correspond to 1.8×10^{14} t of Fe and 1.3×10^{12} t of Mn with a Fe/Mn ratio of about 140. Laznicka (1992) has estimated that the 70% of the land-based manganese occurs in banded iron formations.

To put these figures in perspective, the total land-based manganese deposits formed throughout geological time contain about 6.4×10^9 t of manganese, land-based manganese deposits formed in the Archaean and Proterozoic about 5.2×10^9 t of manganese and deep-sea manganese nodules about 10^{11} t of manganese (Glasby 1988; see also Veizer *et al.* 1989). The amount of manganese in the banded iron formations is therefore about 200 times the amount of manganese in land-based manganese deposits, about 250 times that in Archaean and Proterozoic manganese deposits and an order of magnitude greater than in deep-sea manganese nodules. Of course, these calculations are very approximate because the mean concentration of manganese quoted above for the banded iron formations is based on very few analyses of selected samples which cannot be considered representative. Furthermore, the areas and volumes of the banded iron formations discussed here represent only patches of a sedimentary formation which originally must have been much more extensive (e.g. James & Trendall 1982; Holland 1984; Schissel & Aro 1992). Similarly, the total quantity of manganese in deep-sea manganese nodules and sediments must have decreased as a result of subduction of oceanic crust. Rates of recycling of these deposits have been calculated by Veizer & Jansen (1979, 1985). Nonetheless, these figures do emphasize the enormous amount of manganese in the banded iron formations particularly compared to that in manganese ores from the same time period.

In fact, deep-sea manganese nodules are thought to contain 10^{11} tonnes of manganese formed over 12 Ma. Assuming that the banded iron formations formed over 600 Ma, it can be seen that the rate of deposition of iron in the banded iron formations is about $3 \times 10^5 \text{ t a}^{-1}$ which is about an order of magnitude higher than the rate of deposition of manganese in manganese nodules ($8 \times 10^3 \text{ t a}^{-1}$). However, the figure for the banded iron formations is an average and may be a gross underestimate for the reason given earlier. Braterman & Cairns-Smith (1987), for instance, have estimated that the deposition rate of iron in the Hamersley Basin was about $2.25 \times 10^7 \text{ t a}^{-1}$ (Holland 1984). By contrast, Isley (1995) has calculated the maximum deposition rate of iron in the Proterozoic to have been $7 \times 10^4 \text{ t a}^{-1}$. On the other

hand, the accumulation rate of the iron oxides in the banded iron formations can be calculated to be about $0.1\text{--}0.6 \text{ mm a}^{-1}$ if the microlaminae of banded iron formations are assumed to be annual (Cairns-Smith 1978; Braterman *et al.* 1983; Ewers 1983; Braterman & Cairns-Smith 1987; Klein & Beukes 1989; Kulik & Pokaljuk 1990). This gives an overall deposition rate about 10^5 times higher than that of manganese in deep-sea manganese nodules which are characterized by extremely low rates of deposition (Glasby 1988). These figures show that banded iron formations formed relatively rapidly for a chemical sedimentary deposit. However, Holland (1984) calculated that the deposition rate of iron at this time period was probably within a factor of two or three of the present-day input of sedimentary iron into the oceans and considered the banded iron formations to be analogous to the major sedimentary manganese deposits formed during the Phanerozoic.

Origin of banded iron formations

The origin of banded iron formations has been discussed by many authors (e.g. Govett 1966; Cloud 1973, 1988; Garrels *et al.* 1973; Drever 1974; Eichler 1976; Hargraves 1976; Windley 1977; Ewers 1980; McLennan 1980; Badham 1981; Gole & Klein 1981; Meyer 1981; James & Trendall 1982; Mel'nik 1982; Neelson 1982; Gross, 1983; Kimberley 1983; Loughheed 1983; Towe 1983; Trendall & Morris 1983; Walker *et al.* 1983; Holland 1984; Simonson 1985; Walker & Brimblecombe 1985; François 1987; Garrels 1987; Morris 1987, 1993; Rossignol-Strick 1987; Young 1988; Gregory *et al.* 1989; Kimberley 1989; Lambert 1989; Holland & Beukes 1990; Kulik & Pokaljuk 1990; Anbar & Holland 1992; Castro 1994; De Ronde *et al.* 1994; Krupp *et al.* 1994; Horstmann & Hälbig 1995; Isley 1995) and it is not the intention to repeat the ideas presented there. Nonetheless, it appears that the formation of these deposits resulted from the cumulative storage of ferrous iron from both anoxic weathering and volcanism in once extensive anaerobic marine basins (Cloud 1988). Upwelling of iron-rich waters to sources of oxygen in shallower basins or continental shelves would have favoured the oxidation and precipitation of iron as hematite (Fe_2O_3) and magnetite (Fe_3O_4) (or more probably colloidal iron oxyhydroxide particles, Ahn & Buseck 1990). In fact, the banded iron formations became a major sink for accumulated oxygen at this time and this helped control

the atmospheric oxygen content. The deposits appear to have formed at times of maximum transgression (Goode *et al.* 1983) which may have been related to glacial events (Young 1988, 1989; see also Cloud 1988; Bühn *et al.* 1992; Roy 1992; Klein & Beukes 1993; Melez-hik & Fallik 1994). This problem has been discussed in detail by Bühn & Stanistreet (this volume).

It has already been noted that the hydrothermal input of iron into the Proterozoic ocean was almost certainly much greater than its input into the modern oceans ($4.0\text{--}12.1 \times 10^6 \text{ t a}^{-1}$). This figure compares with the estimated deposition rate of iron in the banded iron formations in excess of $0.3 \times 10^6 \text{ t a}^{-1}$. There now appears to be strong evidence for a hydrothermal source for iron in the banded iron formations (Appel 1983; Gross 1983; Simonson 1985; Holm 1987 a; Jacobsen & Pimentel-Klose 1988; Kimberley 1989, 1994; Klein & Beukes 1989, 1993; Beukes *et al.* 1990; Morris 1993; Castro 1994; De Ronde *et al.* 1994; Gnaneshwar Rao & Naqvi 1995; Isley 1995; Manikyamba & Naqvi 1995; Bühn & Stanistreet this volume). Detailed studies of rare earth element (REE) distributions in banded iron formations also support a dominantly hydrothermal origin for the REE (Jacobsen & Pimentel-Klose 1988; Beukes & Klein 1990; Derry & Jacobsen 1990; Shimizu *et al.* 1990; Danielson *et al.* 1992; Alibert & McCulloch 1993; Bau 1993, 1994; Bau & Möller 1993; Bühn & Stanistreet this volume; Bau & Dulski 1996; Bau *et al.* 1996). In particular, Danielson *et al.* (1992) and Bau & Möller (1993) have argued that the disappearance of the Eu anomaly in these deposits towards the Proterozoic marks the change from mainly high-temperature to dominantly low-temperature hydrothermal alteration, although not all authors agree with this assessment (Erel & Stolper 1993). Thermodynamic calculations also suggest that the solution depositing banded iron formations must have been much richer in iron than was likely for Proterozoic seawater (Woods & Garrels 1992). A hydrothermal source of iron would help satisfy this requirement. However, Holland (1984) rejected the idea of a hydrothermal input of iron on the grounds that this source would have been too small.

The silica concentration in the oceans would also have been much higher than today (Ewers 1983). Siever (1977) has argued that chemical weathering of rocks would have delivered a much higher flux of silica into the oceans than at present whereas Simonson (1985) preferred a hydrothermal origin for the silica (Corliss *et al.* 1981; Belevtsev *et al.* 1983; Siever 1992). The

silica concentration in seawater would not have been limited by biological uptake as at present (Ewers 1983) and silica would have precipitated inorganically. Ewers (1983) has shown that there would have been ample silica in the seawater to supply the silica content of the banded iron formations. Holm (1987a) considered that iron precipitated from hot hydrothermal solutions during the deposition of banded iron formations whereas silica deposited from cool hydrothermal solutions.

Mass balance calculations have been presented by Holland (1984), Braterman & Cairns-Smith (1987) and Garrels (1987). Holland (1984) estimated that $30 \times 10^6 \text{ t a}^{-1}$ of iron could have been upwelled from suboxic bottom waters to the Hamersley Basin, Australia, in the Proterozoic and that this could account for the deposition of the Hamersley iron formation. A similar upwelling hypothesis was presented by Drever (1974). Garrels (1987), on the other hand, calculated that, for a $50 \text{ km} \times 50 \text{ km}$ basin, an influx of iron in streamwater of $0.6 \times 10^6 \text{ t a}^{-1}$ was required. Evaporation of these waters would then have led to the deposition of the banded iron formations. It is probable that these iron deposits were quite localized in extent (e.g., over areas of the order of 10^5 km^2).

Photochemical reactions may also have played an important role in precipitating the iron oxides (Cairns-Smith 1978; Braterman *et al.* 1983; Arrhenius 1987; Braterman & Cairns-Smith 1987; Castro 1994). In fact, the oxidation of ferrous ion could have taken place by two different mechanisms, as a result of photosynthesis or by inorganic photochemical oxidation (Cloud 1980; Ewers 1980, 1983; Belevtsev *et al.* 1983; Walker *et al.* 1983). The relative importance of these two mechanisms may have changed with time, the photochemical process being more important in the older deposits such as the Isua formation and the photosynthetic process more important in the Proterozoic deposits. The photosynthetic supply of oxygen could have been the limiting factor in the deposition of the Proterozoic iron formations and this could have been the rate determining factor in the deposition of these deposits (Worsley *et al.* 1986). Increased production of oxygen could then have been responsible for the much higher production of Palaeoproterozoic banded iron formations compared to their Archaean counterparts (James 1983). Photochemical experiments have shown that photo-oxidation of Mn^{2+} ions is inhibited in the presence of ferrous ions but that the Mn/Fe ratio of the resultant precipitates is about 1:50 which is of the same order as those observed in

banded iron formations (Anbar & Holland 1992). These experiments are consistent with a photochemical origin for the banded iron formations as proposed above. Recent work has also shown the possible photochemical oxidation of ferrous iron by CO₂ in the presence of anoxygenic phototrophic bacteria (Widdel *et al.* 1993; Ehrenreich & Widdel 1994).

One of the unanswered questions about banded iron formations is the origin of the banding (Morris 1993; Kulik & Korzhnev this volume). The microbands are generally considered to be annual varves (Ewers 1980; Holland 1984). Cloud (1980) thought that these microbands might reflect some relationship to a local and episodic biological source of oxygen. If oxidation of ferrous iron by photosynthetically derived oxygen was indeed the rate-determining step for the deposition of the banded iron formations as stated above, then a seasonality either of upwelling of iron-rich waters or of blooms of blue-green algae may have accounted for the microbanding (Belevtsev *et al.* 1983; Beukes 1983). It is possible that the total rate of photosynthesis at this time was limited by the environmental conditions in near-shore areas where blue-green algae flourished (Holland 1984). Descriptions of stromatolites in ancient deposits have been given by Awramik (1977), Hofmann & Schopf (1983), Krumbein (1983), Walter (1983) and Walter & Hofmann (1983) (Schidlowski 1988; Han & Runnegar 1992). Cloud (1988) has described microbiota in stromatolites of the Gunflint iron formation and suggested that these blue green algae may have played a direct role in the oxidation of ferrous iron (Lundgren & Dean 1979; Cloud 1980, 1983*a, b*; Crerar *et al.* 1980; Nealson 1982, 1983; Walker 1984; Holm 1987*a, b*, 1988, 1989; Mann *et al.* 1987; Castro 1994; Brown *et al.* 1995). Similar biota have been observed in modern deep-sea hydrothermal vents (Juniper & Fouquet 1988). Such a situation could have led to the formation of iron-rich and iron-poor bands. Biological factors may therefore have played a crucial role in the formation of the banded iron formations.

The role of transgression in the formation of banded iron formations has been emphasized (Klein & Beukes 1989, 1993; Roy 1992; Schissel & Aro 1992; Manikyamba & Naqvi 1995). On this model, ferrous iron and silica were enriched in ocean bottom waters mainly from hydrothermal sources during regression and deposition of iron carbonate phases took place during transgression. This model implies an anoxic deep ocean so that iron can be transported long distances as the ferrous ion (Kasting 1993). A

similar model has also been invoked to account for the origin of Palaeoproterozoic manganese deposits in South Africa, India and Gabon (Bühn *et al.* 1992; Roy 1992; Hein & Bolton 1993; Bühn & Stanistreet this volume). Diagenetic processes may also have played a role in segregating the primary iron oxide and silica phases once formed (Siever 1992; Kulik & Korzhnev this volume).

It is therefore probable that a combination of various influences (hydrothermalism, upwelling of suboxic ocean waters onto shallow platforms, transgression, evaporation and photosynthetic production of oxygen) have played a role in the deposition of the banded iron formations. Hargraves (1976), for instance, has suggested that the primordial sea could have accumulated iron and silica from hydrothermal sources for a period of about 1000 Ma. At about 2300 Ma, the sea shoaled in many areas to form shallow platforms (Eriksson 1995). This may have created the situation where iron minerals and silica could precipitate in the more oxygenated environment (Schissel & Aro 1992). In fact, this combination of circumstances proved to be the most favourable for iron formation in geological history.

Separation of manganese from iron

A question then arises about the fractionation of manganese from iron. Meyer (1981) has noted that the natural separation of manganese and iron was far more effective at the higher atmospheric oxygen levels of the Phanerozoic than in the Precambrian, even in the late Proterozoic, but considered the mechanism of this separation elusive.

In fact, Lepp (1963) has shown that the average Mn/Fe ratio of Precambrian iron formations (0.025) is very close to the crustal average (0.022) whereas the ratio for the Phanerozoic iron formations is substantially lower (0.009) (Lepp & Goldich 1964; Lepp 1968). This suggested that there was little or no separation of Mn from Fe in Precambrian iron formations. This difference in Mn/Fe ratios was considered to be a consequence of the lower atmospheric oxygen content during the formation of the Precambrian iron formations. It should be noted, however, that the average Mn/Fe ratio for Precambrian banded iron formations obtained in this study is 0.007 (about three times lower than the ratio in basalts). The reason for this difference is the higher Mn concentrations used by Lepp (1963) in his calculation (Lepp & Goldich 1964). If the value obtained here is correct, it indicates that some

fractionation of Fe relative to Mn did take place during the formation of the Precambrian iron formations.

Nonetheless, huge Palaeoproterozoic manganese deposits such as the Kalahari manganese deposit are known. This deposit contains about 2.7×10^9 t of Mn (Beukes 1994; Gutzmer & Beukes 1995) or 4.2×10^9 t of Mn equivalent to 23.4% of global land-based manganese deposits (Laznicka 1992). It is interbedded with the Hotazel iron formation and has an age between 2300 and ?2100 Ma (Beukes 1983; Schissel & Aro 1992) or post 2200 Ma (Cornell & Schütte 1995). Many Precambrian manganese ores are associated with banded iron formations and frequently occur at the margins of a central iron deposit (Crerar *et al.* 1980). An important question is why there should be this association of manganese and iron deposits. Bühn *et al.* (1992) and Bühn & Stanistreet (this volume) have attempted to answer this question for the Neoproterozoic manganese and iron formations. They suggested that separation of Mn from Fe could take place in a shallow basinal environment during a transgressive sequence as a result of redox processes. For the Kalahari manganese deposit, it has been suggested that each manganese bed corresponds with a peak marine transgression (Beukes 1983; Roy 1992; Schissel & Aro 1992). In addition, there is an upward increase in the abundance of manganese in the Transvaal iron formations which was thought to reflect increasing atmospheric oxygen contents with time (Beukes 1983; Holland & Beukes 1990). However, recent studies have challenged this notion and suggested that this deposit was formed as a result of hydrothermal exhalations as shown, for example, by the extensive hydrothermal alteration of the underlying Ongeluk lavas (Cornell & Schütte 1995, 1996). The northwestern part of the Kalahari manganese field is already known to contain hydrothermally reconstituted high-grade manganese ores (Miyano & Beukes 1987; Grobelaar *et al.* 1995; Gutzmer & Beukes 1995). Bau & Dulski (1996) have also presented evidence based on rare earth element analysis of a hydrothermal origin for the Transvaal iron formations. Clearly, these differences need to be resolved. In addition, the formation of this deposit corresponds to a global $\delta^{13}\text{C}_{\text{carb}}$ anomaly at 2200–2000 Ma which coincides with a number of major geological events (Melezhik & Fallick 1994). Whether the formation of the Kalahari manganese deposit is related to these events is a matter for conjecture.

Drever (1974) has proposed a detailed model for the Proterozoic banded iron formations in

which the entire ocean below the thermocline would have been anaerobic ($\text{O}_2 \approx 10^{-70}$ PAL) and the surface waters more oxidizing (Logan *et al.* 1995). In such circumstances, iron would have been present in seawater as the ferrous ion (Ewers 1980, 1983; Walker *et al.* 1983) and it was deduced that the supply of iron to the oceans was much greater than the supply of sulphate. All the sulphur in the deep waters of the ocean would then have been precipitated as pyrite and the content of the remaining ferrous ion in these waters would have been controlled by the solubility of siderite (*c.* 10 ppm, Crerar *et al.* 1980; Walker & Brimblecombe 1985; or 3 ppm, Holland 1984). When the deep-water upwelled, the dissolved ferrous iron would have been oxidized to goethite. A similar situation where the ocean was stagnant and stratified was also encountered in the late Precambrian and late Permian (Hoffman *et al.* 1990). This again has implications for iron and manganese deposition.

Cameron (1982, 1983) has concluded that the sulphate concentration of the Proterozoic oceans was low and its isotopic ratio was consistent with a submarine exhalative origin (Bottomley *et al.* 1992; Grotzinger & Kasting 1993), although not all authors agree (Holland 1984). Stability field diagrams also indicate low sulphate concentrations in the Proterozoic ocean (Garrels & Perry 1974). According to Walker & Brimblecombe (1985), the sulphate concentration of the Proterozoic ocean would have been about 3% of the present value. Isotopic evidence suggests that biological reduction of sulphate took place in the Archean under anaerobic conditions from a restricted reservoir at low sulphate concentrations (Goodwin *et al.* 1976; Thode & Goodwin 1983). Photosynthesis would have been less than 1% of the present-day rate during the Proterozoic so that reduction of sulphate ion to sulphide by organic matter in the oceans would have been relatively minor (Holland 1984). Assuming a hydrothermal origin for the banded iron formations, associated black smoker deposits would be expected (Cornell & Schütte 1995; Isley 1995; Vearncombe *et al.* 1995). The low sulphate content of seawater at this time would account for the low abundance of such sulphides.

The above situation contrasts with the Phanerozoic manganese deposits where dissolved manganese is enriched in anoxic basins but iron is precipitated in shales. Manganese oxides are then precipitated in shallow oxic zones following transgression (Glasby 1988; Roy 1992). In addition, iron in present-day hydrothermal fluids is precipitated immediately by oxidation as the fluids mix with seawater whereas in the

Palaeoproterozoic much of the iron would have remained in solution as ferrous iron (Drever *et al.* 1988). Phanerozoic ironstones are also thought to be related to transgressions (Van Houten & Arthur 1989).

The availability of sulphate ions with the resulting ability to precipitate iron as pyrite under reducing conditions is therefore seen as crucial to the fractionation of manganese from iron. In the Proterozoic, both manganese and iron were mobile because iron was present in solution as ferrous iron and could not be trapped in large quantities in the sediment as pyrite. This circumstance meant that manganese and iron displayed similar aqueous geochemistries and this led to the occurrence of manganese in the Proterozoic iron formations. In the Phanerozoic, on the other hand, iron became immobile because it was trapped as pyrite. Giant shallow-water manganese deposits therefore formed.

A similar explanation has been used to distinguish modern lake and shallow marine manganese nodules (Callender & Bowser 1976). Sulphate concentrations are very low in lake waters so that nearly all the iron in solution is available for oxide deposition. This situation contrasts with that in shallow marine environments where iron can be trapped in the sediments as pyrite. Mn/Fe ratios are therefore much higher in shallow marine nodules than in lake nodules.

A question remains as to what the oxygen content of the atmosphere would have been during the deposition of the banded iron formations (Walker 1977; Kasting & Walker 1981; Cloud 1983*b*, 1988; Holland 1984; Wayne 1985; Des Marais *et al.* 1992; Eriksson & Cheney 1992; Han & Runnegar 1992; Kasting 1993; Krupp *et al.* 1994). Holland (1984) deduced that it would have been about 0.02 of the present atmospheric level (PAL) whereas Cloud (1983) suggested somewhat less than 0.01 PAL. From the preceding discussion, it would appear that abundant iron and manganese was likely to be present at the time of deposition of the banded iron formations as a result of hydrothermal emanations. Stability field diagrams indicate that iron would have been precipitated preferentially to manganese in such poorly oxygenated environments and that manganese would tend to be deposited dominantly in the divalent state (Garrels & Christ 1965; Garrels & Perry 1974; Klein & Bricker 1977). However, it is possible that the oxygen content of the atmosphere increased during the period of deposition of these iron formations. In the Transvaal Supergroup, for example, the amount of manganese in

the iron formation increases upwards in the deposit (Beukes 1983) and evidence has been presented that the oxygen content increased from about 0.01 to about 0.15 PAL between 2200 and 1900 Ma (Holland & Beukes 1990). Krupp *et al.* (1994), on the other hand, calculated that photosynthetic oxygen production rates began to exceed oxygen consumption rates between 2350 and 2100 Ma. Nonetheless, the banded iron formations contain enormous amounts of manganese and clearly played a major role in the global history of manganese deposition.

Summary

Based on these ideas, it would seem that the previously described hydrothermal activity that characterized the Archaean and Proterozoic could have led to substantially enhanced contents of ferrous iron and silica in the oceans which would have served as the source for these elements in the banded iron formations. The banded iron formations therefore represent the deposition of the accumulated ferrous iron and silica introduced into the previously anaerobic oceans by hydrothermal activity. Deposition of these formations acted as a sink for any oxygen that may possibly have been generated and thereby acted as a control on the atmospheric oxygen content. The low sulphate concentrations of the Archaean and Proterozoic oceans also played a role in enabling these deposits to form. Red beds, representing an atmosphere of prevalent oxygen, did not appear until about 2000 Ma ago, i.e. after the banded iron formations had been largely deposited (see, however, Cloud 1980; Kasting & Walker 1981; Clemmey & Badham 1982).

It therefore appears that the Proterozoic banded iron formations may hold the key to the problems posed by Roy (1988) in that manganese is present in these deposits on a scale very much larger than previously envisaged. As such, they were of great significance in determining the fate of manganese in the Earth's early history.

I thank G. Arrhenius (Scripps Institution of Oceanography), B. Bühn (University of Giessen), E. R. Force (US Geological Survey), R. E. Krupp (German Geological Survey) and D. A. Kulik (Ukrainian Academy of Sciences) for their helpful comments on this manuscript. B. Bühn (University of Giessen) and P. Laznicka (University of Manitoba) are thanked for their assistance in compiling Fig. 1.

References

- ABBOTT, D. H. 1984. Archean plate tectonics revisited 2. Paleo-sea level changes, continental area, oceanic heat loss and the area-age distribution of the ocean basins. *Tectonics*, **3**, 709–722.
- & HOFFMAN, S. E. 1984. Archean plate tectonics revisited 1. Heat flow, spreading rate, and the age of subducting oceanic lithosphere and their effects on the origin and evolution of continents. *Tectonics*, **3**, 429–448.
- & MENKE, W. 1990. Length of the global plate boundary at 2.4 Ga. *Geology*, **18**, 58–61.
- AHN, J. H. & BUSECK, P. R. 1990. Hematite nanospheres of possible colloidal origin from a Precambrian banded iron formation. *Science*, **250**, 111–113.
- ALIBERT, C. & MCCULLOCH, M. T. 1993. Rare earth element and neodymium isotopic compositions of the banded iron-formations and associated shales from Hamersley, western Australia. *Geochimica et Cosmochimica Acta*, **57**, 187–204.
- ANBAR, A. D. & HOLLAND, H. D. 1992. The photochemistry of manganese and the origin of banded iron formations. *Geochimica et Cosmochimica Acta*, **56**, 2595–2603.
- APPEL, P. W. U. 1983. Rare earth elements in the early Archean Isua-iron-formation, West Greenland. *Precambrian Research*, **20**, 243–258.
- ARRHENIUS, G. 1986. Dysoxic environments as models for primordial mineralization. In: CAIRNS-SMITH, A. G. & HARTMAN, H. (eds) *Clay Minerals and the Origin of Life*. Cambridge University Press, Cambridge, 97–104.
- 1987. The first 800 million years: Environmental models for early Earth. *Earth, Moon, and Planets*, **37**, 187–199.
- AUCLAIR, G., FOUQUET, Y. & BOHN, M. 1987. Distribution of selenium in high-temperature hydrothermal sulphide deposits at 13° North, East Pacific Rise. *Canadian Mineralogist*, **25**, 577–587.
- AWRAMIK, S. M. 1977. Paleobiology of stromatolites. In: PONNAMPERUMA, C. (ed.) *Chemical Evolution of the Early Precambrian*. Academic Press, NY, 111–131.
- BADHAM, J. P. N. 1981. The origin of ore deposits in sedimentary rocks. In: TARLING, D. H. (ed.) *Economic Geology and Geotectonics*. Blackwell, Oxford, 149–191.
- BARRETT, T. J., FRALICK, P. W. & JARVIS, I. 1988. Rare-earth-element geochemistry of some Archean iron formations north of Lake Superior, Ontario. *Canadian Journal of Earth Science*, **25**, 570–580.
- BAU, M. 1993. Effects of syn- and post-depositional processes on the rare-earth element distribution in Precambrian iron-formations. *European Journal of Mineralogy*, **5**, 257–267.
- 1994. Comment on 'Modeling of rare-earth element partitioning between particles and solution in aquatic environments' by Y. EREL & E. M. STOLPER. *Geochimica et Cosmochimica Acta*, **58**, 4521–4523.
- & DULSKI, P. 1996. Distribution of yttrium and rare-earth elements in the Penge and Kuruman iron-formations, Transvaal Supergroup, South Africa. *Precambrian Research*, **78**.
- & MÖLLER, P. 1993. Rare earth element systematics of the chemically precipitated component in Early Precambrian iron formations and the evolution of the terrestrial atmosphere-hydrosphere-lithosphere system. *Geochimica et Cosmochimica Acta*, **57**, 2239–2249.
- , HÖHNDORF, A., DULSKI, P. & BEUKES, N. J. 1996. Sources of rare-earth elements and iron in palaeoproterozoic iron-formations from the Transvaal Supergroup, South Africa: Evidence from neodymium isotopes. *Journal of Geology*.
- BAYLEY, R. W. & JAMES, H. L. 1973. Precambrian iron-formations of the United States. *Economic Geology*, **68**, 934–959.
- BELEVTSSEV, Ya. N., BELEVTSSEV, R. Ya. & SIROSHAN, R. I. 1983. The Krivoy Rog Basin. In: TRENDALL, A. F. & MORRIS, R. C. (eds) *Iron-Formation Facts and Problems*. Elsevier, Amsterdam, 211–251.
- BEUKES, N. J. 1973. Precambrian iron-formations of Southern Africa. *Economic Geology*, **68**, 960–1004.
- 1983. Palaeoenvironmental setting of iron-formations in the depositional basin of the Transvaal Supergroup, South Africa. In: TRENDALL, A. F. & MORRIS, R. C. (eds) *Iron-Formation Facts and Problems*. Elsevier, Amsterdam, 131–209.
- 1994. Giant Early Proterozoic manganese and iron deposits of the Transvaal Supergroup, Northern Cape Province, South Africa (Abstract). *European Journal of Mineralogy*, **6** Beiheft 1, 324.
- & KLEIN, C. 1990. Geochemistry and sedimentology of a facies transition from microbanded to granular iron-formation in the early Proterozoic Transvaal Supergroup, South Africa. *Precambrian Research*, **47**, 99–139.
- , KAUFMAN, A. J. & HAYES, J. M. 1990. Carbonate petrography, kerogen distribution, and carbon and oxygen isotope variations in an Early Proterozoic transition from limestone to iron-formation deposition, Transvaal Supergroup, South Africa. *Economic Geology*, **85**, 663–690.
- BICKLE, M. J. 1978. Heat loss from the earth: A constraint on Archean tectonics from the relation between geothermal gradients and the rate of plate production. *Earth and Planetary Science Letters*, **40**, 301–315.
- BOTTOMLEY, D. J., VEIZER, J., NIELSEN, H. & MOCZYDLOWSKA, M. 1992. Isotopic composition of disseminated sulfur in Precambrian sedimentary rocks. *Geochimica et Cosmochimica Acta*, **56**, 3311–3322.
- BRATERMAN, P. S. & CAIRNS-SMITH, A. G. 1987. Photoprecipitation and the banded iron-formations—some quantitative aspects. *Origins of Life*, **17**, 221–226.
- & SLOPER, R. W. 1983. Photo-oxidation of hydrated Fe²⁺ significance for banded iron formations. *Nature*, **303**, 163–164.

- BROWN, D. A., GROSS, G. A. & SAWICKI, J. A. 1995. A review of the microbial geochemistry of banded iron-formations. *Canadian Mineralogist*, **32**, 1321–1333.
- BÜHN, B. & STANISTREET, I. G. 1997. Insight into the enigma of Neoproterozoic manganese and iron formations from the perspective of supercontinental breakup and glaciation. *This volume*.
- , — & OKRUSCH, M. 1992. Late Proterozoic outer shelf manganese and iron deposits at Otjondou (Namibia) related to the Damaran oceanic opening. *Economic Geology*, **87**, 1393–1411.
- BURKE, K. & KIDD, W. S. F. 1978. Were Archean continental geothermal gradients much steeper than those of today? *Nature*, **272**, 240–241.
- CAIRNS-SMITH, A. G. 1978. Precambrian solution photochemistry, inverse segregation and banded iron formations. *Nature*, **276**, 807–808.
- CALLENDER, E. & BOWSER, C. J. 1976. Freshwater ferromanganese deposits. In: WOLF, K. H. (ed.) *Handbook of Strata-Bound and Stratiform Ore Deposits*, **7**. Elsevier Amsterdam, 341–394.
- CAMERON, E. M. 1982. Sulphate and sulphate reduction in early Precambrian oceans. *Nature*, **296**, 145–148.
- 1983. Genesis of Proterozoic iron-formation: Sulphur isotopic evidence. *Geochimica et Cosmochimica Acta*, **47**, 1069–1074.
- & GARRELS, R. M. 1980. Geochemical compositions of some Precambrian shales from the Canadian Shield. *Chemical Geology*, **28**, 181–197.
- CASTRO, L. O. 1994. Genesis of banded iron-formations. *Economic Geology*, **89**, 1384–1397.
- CLEMMY, H. & BADHAM, N. 1982. Oxygen in the Precambrian atmosphere: An evaluation of the geological evidence. *Geology*, **10**, 141–146.
- CLOUD, P. 1973. Paleocological significance of the banded iron-formation. *Economic Geology*, **68**, 1135–1143.
- 1980. Early biogeochemical systems. In: TRUDINGER, P. A., WALTER, M. R. & RALPH, B. J. (eds) *Biogeochemistry of Ancient and Modern Environments*. Australian Academy of Science, Canberra, 7–27.
- 1983a. Banded iron-formation – a gradualist's dilemma. In: TRENDALL, A. F. & MORRIS, R. C. (eds) *Iron-Formation Facts and Problems*. Elsevier, Amsterdam, 491–512.
- 1983b. Aspects of Proterozoic biogeology. In: MEDARIS, L. G. JR. ET AL. (eds). *Proterozoic Geology: Selected papers from an International Proterozoic Symposium*. Geological Society of America Memoirs, **161**, 245–251.
- 1988. *Oasis in Space Earth History from the Beginning*. W. W. Norton & Co., NY.
- COLLIER, R. & EDMOND, J. 1984. The trace element geochemistry of marine biogenic particulate matter. *Progress in Oceanography*, **13**, 113–199.
- CORLISS, J. B., BAROSS, J. A. & HOFFMAN, S. E. 1981. An hypothesis concerning the relationship between submarine hot springs and the origin of life on Earth. *Oceanologia Acta*, No. SP, 59–69.
- CORNELL, D. H. & SCHÜTTE, S. S. 1995. A volcanic-exhalative origin for the world's largest (Kalahari) manganese field. *Mineralium Deposita*, **30**, 146–151.
- & — 1996. Reply to the discussion by N. Beukes and J. Gutzmer. *Mineralium Deposita*, **31**, 246–247.
- CRERAR, D. A., FISCHER, A. G. & PLAZA, C. L. 1980. Metallogenium and biogenic deposition of manganese from Precambrian to Recent time. In: VARENTSOV, I. M. & GRASSELLY, Gy. (eds) *Geology and Geochemistry of Manganese*, **3**. Hungarian Academy of Sciences, Budapest, 285–303.
- DANIELSON, A., MÖLLER, P. & DULSKI, P. 1992. The europium anomalies in banded iron formations and the thermal history of the oceanic crust. *Chemical Geology*, **97**, 89–100.
- DAVY, R. 1983. A contribution to the chemical composition of Precambrian iron-formations. In: TRENDALL, A. F. & MORRIS, R. C. (eds) *Iron-Formation Facts and Problems*. Elsevier, Amsterdam, 325–343.
- DERRY, L. A. & JACOBSEN, S. B. 1990. The chemical evolution of Precambrian seawater: Evidence from REE's in banded iron formations. *Geochimica et Cosmochimica Acta*, **54**, 2965–2977.
- DE RONDE, C. E. J., DE WIT, M. J. & SPOONER, E. T. C. 1994. Early Archean (>3.2 Ga) Fe-oxide-rich, hydrothermal discharge vents in the Barberton greenstone belt, South Africa. *Geological Society of America Bulletin*, **106**, 86–104.
- DES MARAIS, D. J., STRAUSS, H., SUMMONS, R. E. & HAYES, J. M. 1992. Carbon isotope evidence for the stepwise oxidation of the Proterozoic environment. *Nature*, **359**, 605–609.
- DREVER, J. I. 1974. Geochemical model for the origin of Precambrian banded iron formations. *Geological Society of America Bulletin*, **85**, 1099–1106.
- , LI, Y.-H. & MAYNARD, J. B. 1988. Geochemical cycles: The continental crust and the oceans. In: GREGOR, C. B., GARRELS, R. M., MACKENZIE, F. T. & MAYNARD, J. B. (eds) *Chemical Cycles in the Evolution of the Earth*. John Wiley & Sons, NY, 17–53.
- EHRENREICH, A. & WIDDEL, F. 1994. Anaerobic oxidation of ferrous iron by purple bacteria, a new type of phototrophic metabolism. *Applied and Environmental Microbiology*, **60**, 4517–4526.
- EICHLER, J. 1976. Origin of the Precambrian banded iron-formations. In: WOLF, K. H. (ed.) *Handbook of Strata-Bound and Stratiform Ore Deposits*, **7**. Elsevier, Amsterdam, 157–201.
- EREL, Y. & STOLPER, E. M. 1993. Modeling of rare-earth element partitioning between particles and solution in aquatic environments. *Geochimica et Cosmochimica Acta*, **57**, 513–518.
- ERIKSSON, K. A. 1995. Crustal growth, surface processes, and atmospheric evolution on the early Earth. In: COWARD, M. P. & RIES, A. C. (eds) *Early Precambrian Processes*. Geological Society, London, Special Publications, **95**, 11–25.
- ERIKSSON, P. G. & CHENEY, E. S. 1992. Evidence for the transition to an oxygen-rich atmosphere during the evolution of red beds in the lower Proterozoic sequences of southern Africa. *Precambrian Research*, **54**, 257–269.

- EWERS, W. E. 1980. Chemical conditions for the precipitation of banded iron formations. In: TRUDINGER, P. A., WALKER, M. R. & RALPH, B. J. (eds) *Biogeochemistry of Ancient and Modern Environments*. Australian Academy of Science, Canberra, 83–92.
- 1983. Chemical factors in the deposition and diagenesis of banded iron-formation. In: TRENDALL, A. F. & MORRIS, R. C. (eds) *Iron-Formation Facts and Problems*. Elsevier, Amsterdam, 491–512.
- FRANÇOIS, L. M. 1987. Reducing power of ferrous iron in the Archean Ocean, 2. Role of FeOH^+ photooxidation. *Paleoceanography*, **2**, 395–408.
- FRANKLIN, J. M., LYDON, J. W. & SANGSTER, D. F. 1981. Volcanic-associated massive sulfide deposits. *Economic Geology 75th Anniversary Volume*, 485–627.
- FRYER, B. J. 1977. Rare earth evidence in iron-formations for changing Precambrian oxidation states. *Geochimica et Cosmochimica Acta*, **41**, 361–367.
- 1983. Rare earth elements in iron-formation. In: TRENDALL, A. F. & MORRIS, R. C. (eds) *Iron-Formation Facts and Problems*. Elsevier, Amsterdam, 345–358.
- , FYFE, W. S. & KERRICH, R. 1979. Archean volcanogenic oceans. *Chemical Geology*, **24**, 25–33.
- FYFE, W. S. 1977. Effects on biological evolution of changes in ocean chemistry. *Nature*, **267**, 510.
- 1978. The evolution of the earth's crust: Modern plate tectonics to ancient hot spot tectonics. *Chemical Geology*, **23**, 89–114.
- , PRICE, N. J. & THOMPSON, A. B. 1978. *Fluids in the Earth's Crust*. Elsevier, Amsterdam.
- GARRELS, R. M. 1987. A model for the deposition of the microbanded Precambrian iron formations. *American Journal of Science*, **287**, 81–106.
- & CHRIST, C. L. 1965. *Solutions, Minerals, and Equilibria*. Harper and Row, NY, 450pp.
- & PERRY, E. A. 1974. Cycling of carbon, sulfur, and oxygen through geologic time. In: GOLDBERG, E. D. (ed.) *The Sea*, **5**. John Wiley, NY, 303–336.
- , — & MACKENZIE, F. T. 1973. Genesis of Precambrian iron-formations and the development of atmospheric oxygen. *Economic Geology*, **68**, 1173–1179.
- GERMAN, C. R. & ANGEL, M. V. 1995. Hydrothermal fluxes of metals to the oceans: a comparison with anthropogenic discharge. In: PARSON, L. M., WALKER, C. L. & DIXON, D. R. (eds) *Hydrothermal Vents and Processes*. Geological Society, London, Special Publications, **87**, 365–372.
- GLASBY, G. P. 1988. Manganese deposition through geological time: Dominance of the Post-Eocene deep-sea environment. *Ore Geology Reviews*, **4**, 135–144.
- GNANESHWAR RAO, T. & NAQVI, S. M. 1995. Geochemistry, depositional environment and tectonic setting of the BIF's of the Late Archean Chitradurga Schist Belt, India. *Chemical Geology*, **121**, 217–243.
- GOLE, M. J. & KLEIN, C. 1981. Banded iron-formations through much of geological time. *Journal of Geology*, **89**, 169–183.
- GOODE, A. D. T., HALL, W. D. M. & BUNTING, J. A. 1983. The Nabberu Basin of Western Australia. In: TRENDALL, A. F. & MORRIS, R. C. (eds) *Iron-Formation Facts and Problems*. Elsevier, Amsterdam, 295–323.
- GOODWIN, A. M., MONSTER, J. & THODE, H. G. 1976. Carbon and sulfur isotope abundances in Archean iron-formations and early Precambrian Life. *Economic Geology*, **71**, 870–891.
- GOVETT, G. J. S. 1966. Origin of banded iron formations. *Geological Society of America Bulletin*, **77**, 1199–1197.
- GREGORY, R. T., CRISS, R. E. & TAYLOR, H. P. 1989. Oxygen isotope exchange kinetics of mineral pairs in closed and open systems: Applications to problems of hydrothermal alterations of igneous rocks and Precambrian iron formations. *Chemical Geology*, **75**, 1–42.
- GROBBELAAR, W. S., BURGER, M. A., PRETORIUS, A. I., MARAIS, W. & VAN NIEKIERK, I. J. M. 1995. Stratigraphic and structural setting of the Griqualand West and Olifantshoek Sequences at Black Rock, Beeshoek and Rooinekke Mines, Griqualand West, South Africa. *Mineralium Deposita*, **30**, 152–161.
- GROSS, G. A. 1983. Tectonic systems and the deposition of iron-formation. *Precambrian Research*, **20**, 171–187.
- GROTZINGER, J. P. & KASTING, J. F. 1993. New constraints on Precambrian ocean composition. *Journal of Geology*, **101**, 235–243.
- GUTZMER, J. & BEUKES, N. J. 1995. Fault-controlled metasomatic alteration of Early Proterozoic sedimentary manganese ores in the Kalahari manganese field, South Africa. *Economic Geology*, **90**, 823–844.
- HAN, T.-M. & RUNNEGAR, B. 1992. Megascopic eukaryotic algae from the 2.1-billion-year-old Negaunee Iron-Formation, Michigan. *Science*, **257**, 232–235.
- HARGRAVES, R. B. 1976. Precambrian geologic history. *Science*, **193**, 363–371.
- HEIN, J. R. & BOLTON, B. R. 1993. Composition and origin of the Moanda manganese deposit, Gabron. In: *16th Colloquium on African Geology 14–16th September, 1993 Mbabane, Swaziland Extended Abstracts Volume I*, 150–152.
- HOFFMAN, A., GRUSZCZYNSKI, M. & MALKOWSKI, K. 1990. Oceanic delta-13-carbon values as indicators of atmospheric oxygen depletion. *Modern Geology*, **14**, 211–221.
- HOFFMAN, P. F. & RANALLI, G. 1988. Archean ocean flake tectonics. *Geophysical Research Letters*, **15**, 1077–1080.
- HOFMANN, H. J. & SCHOPF, J. W. 1983. Early Proterozoic microfossils. In: SCHOPF, J. W. (ed.) *Earth's Earliest Biosphere Its Origin and Evolution*. Princeton University Press, Princeton, NJ, 321–360.
- HOLLAND, H. D. 1984. *The Chemical Evolution of the Atmosphere and Oceans*. Princeton University Press, Princeton, NJ.

- & BEUKES, N. J. 1990. A paleoweathering profile from Griqualand West, South Africa: Evidence for a dramatic rise in atmospheric oxygen between 2.2 and 1.9 BYBP. *American Journal of Science*, **290-A**, 1–34.
- HOLM, N. G. 1987a. Possible biological origin of banded-iron formations from hydrothermal solutions. *Origins of life*, **17**, 229–250.
- 1987b. Biogenic influences on the geochemistry of certain ferruginous sediments of hydrothermal origin. *Chemical Geology*, **63**, 45–57.
- 1988. Carbon isotope distribution in organic matter and siderite of a modern metalliferous hydrothermal sediment and possible implications for gold associated with banded iron formation. *Marine Geology*, **84**, 201–207.
- 1989. The $^{13}\text{C}/^{12}\text{C}$ ratios of siderite and organic matter of a modern metalliferous hydrothermal sediment and their implications for banded iron formations. *Chemical Geology*, **77**, 41–45.
- HORSTMANN, U. E. & HÄLBICH, I. W. 1995. Chemical composition of banded iron-formations of the Griqualand West Sequence, Northern Cape Province, South Africa, in comparison with other Precambrian iron formations. *Precambrian Research*, **72**, 109–145.
- HUDSON, A., BENDER, M. L. & GRAHAM, D. W. 1986. Iron enrichments in hydrothermal plumes over the East Pacific Rise. *Earth and Planetary Science Letters*, **79**, 250–254.
- ISLEY, A. E. 1995. Hydrothermal plumes and the delivery of iron to banded iron formation. *Journal of Geology*, **103**, 169–185.
- JACOBSEN, S. B. & PIMENTAL-KLOSE, M. R. 1988. A Nd isotopic study of the Hamesley and Michipicoten banded iron formations: the source of REE and Fe in Archean oceans. *Earth and Planetary Science Letters*, **87**, 29–44.
- JAMES, H. L. 1983. Distribution of banded iron-formation in space and time. In: TRENDALL, A. F. & MORRIS, R. C. (eds) *Iron-Formation Facts and Problems*. Elsevier, Amsterdam, 471–490.
- JAMES, H. L. & SIMS, P. K. 1973. Precambrian iron-formations of the world. *Economic Geology*, **68**, 913–914.
- & TRENDALL, A. F. 1982. Banded iron formations: Distribution in time and paleoenvironmental significance. In: HOLLAND, H. D. & SCHIDLowski, M. (eds) *Mineral Deposits and the Evolution of the Biosphere*. Springer-Verlag, Berlin 199–217.
- JUNIPER, S. K. & FOUQUET, Y. 1988. Filamentous iron-silica deposits from modern and ancient hydrothermal sites. *Canadian Mineralogist*, **26**, 859–869.
- KASTING, J. F. 1993. Earth's early atmosphere. *Science*, **259**, 920–926.
- & WALKER, J. C. G. 1981. Limits on oxygen concentrations in the prebiological atmosphere and the rate of abiotic fixation of nitrogen. *Journal of Geophysical Research*, **86**, 1147–1158.
- KIMBERLEY, M. M. 1983. Constraints on genetic modelling of Proterozoic iron formations. In: MEDARIS, L. G. JR. ET AL. (eds). *Proterozoic Geology: Selected papers from an International Proterozoic Symposium*. Geological Society of America Memoirs, **161**, 227–235.
- 1989. Exhalative origin of iron formations. *Ore Geology Reviews*, **5**, 13–145.
- 1994. Debate about ironstone: has solute supply been surficial weathering, hydrothermal convection, or exhalation of deep fluids? *Terra Nova*, **6**, 116–132.
- KLEIN, C. & BEUKES, N. J. 1989. Geochemistry and sedimentology of a facies transition from limestone to iron-formation deposition in the Early Proterozoic Transvaal Supergroup, South Africa. *Economic Geology*, **84**, 1733–1774.
- & — 1993. Sedimentology and geochemistry of the glaciogenic Late Proterozoic Rapitan iron-formation in Canada. *Economic Geology*, **88**, 542–565.
- & BRICKER, O. P. 1977. Some aspects of the sedimentary and diagenetic environment of Proterozoic banded iron-formation. *Economic Geology*, **72**, 1457–1470.
- KLINKHAMMER, G. & HUDSON, A. 1986. Dispersal patterns for hydrothermal plumes in the South Pacific using manganese as a tracer. *Earth and Planetary Science Letters*, **79**, 241–249.
- KRUMBEIN, W. C. 1983. Stromatolites – the challenge of a term in space and time. *Precambrian Research*, **20**, 493–531.
- KRUPP, R. E., OBERTHÜR, T. & HIRDES, W. 1994. The Early Precambrian atmosphere and hydrosphere: Thermodynamic constraints from mineral deposits. *Economic Geology*, **89**, 1591–1598.
- KULIK, D. A. & KORZHNEV, M. N. 1997. Lithological and geochemical evidence of Fe and Mn pathways during deposition of Lower Proterozoic banded iron formation in the Krivoy Rog basin (Ukraine). *This volume*.
- & POKALJUK, V. V. 1990. A matter balance in sedimentary cycle of iron accumulation in Krivoy Rog basin. *Lithology and Ore Deposits*, **2**, 36–49 [in Russian].
- KUMA, K., PAPLAWSKY, W., GEDULIN, B. & ARRHENIUS, G. 1989. Mixed-valence hydroxides and bio-organic host minerals. *Origins of Life*, **19**, 573–602.
- KUMP, L. R. & HOLLAND, H. D. 1992. Iron in Precambrian rocks: Implications for the global oxygen budget of the ancient Earth. *Geochimica et Cosmochimica Acta*, **56**, 3217–3223.
- LAMBERT, I. B. 1989. Precambrian sedimentary sequences and their mineral and energy resources. In: PRICE, R. A. (ed.) *Origin and Evolution of Sedimentary Basins and their Energy and Mineral Resources*. American Geophysical Union Geophysical Monographs, **48**, 169–173.
- LAZNICKA, P. 1985. Strata-related deposits: classified by metals, lithologic associations, and some quantitative relationships. In: WOLF, K. H. (ed.) *Handbook of Strata-Bound and Stratiform Ore Deposits*, **12**, Elsevier, Amsterdam, 1–107.
- 1992. Manganese deposits in the global lithogenic system: Quantitative approach. *Ore Geology Reviews*, **7**, 279–356.

- LEPP, H. 1963. The relation of iron and manganese in sedimentary iron formations. *Economic Geology*, **58**, 515–526.
- 1968. The distribution of manganese in the Animikian iron formations of Minnesota. *Economic Geology*, **63**, 61–75.
- & GOLDICH, S. S. 1964. Origin of Precambrian iron formations. *Economic Geology*, **59**, 1025–1060.
- LOGAN, G. A., HAYES, J. M., HIESHIMA, G. B. & SUMMONS, R. E. 1995. Terminal Proterozoic reorganization of biogeochemical cycles. *Nature*, **376**, 53–56.
- LOUGHEED, M. S. 1983. Origin of Precambrian banded iron-formations in the Lake Superior region. *Geological Society of America Bulletin*, **94**, 325–340.
- LUNDGREN, D. G. & DEAN, W. 1979. Biogeochemistry of iron. In: TRUDINGER, P. A. & SWAINE, D. J. (eds) *Biogeochemical Cycling of Mineral-forming Elements*. Elsevier, Amsterdam, 211–251.
- LUPTON, J. E., BAKER, E. T. & MASSOTH, G. J. 1989. Variable $^3\text{He}/\text{heat}$ ratios in submarine hydrothermal systems: evidence from two plumes over the Juan de Fuca Ridge. *Nature*, **337**, 161–164.
- MACGEEHAN, P. J. & MACLEAN, W. H. 1980. An Archean sub-seafloor geothermal system, 'calc-alkali' trends, and massive sulphide genesis. *Nature*, **286**, 767–771.
- MCLENNAN, S. M. 1980. Timing and relationships among Precambrian crustal and atmospheric evolution and banded iron-formations. In: TRUDINGER, P. A., WALKER, M. R. & RALPH, B. J. (eds) *Biogeochemistry of Ancient and Modern Environments*. Australian Academy of Science, Canberra, 73–82.
- MANKYAMBA, C. & NAQVI, S. M. 1995. Geochemistry of Fe-Mn formations of the Archean Sandur schist belt, India – mixing of clastic and chemical processes at a shallow shelf. *Precambrian Research*, **72**, 69–95.
- MANN, H., TAZAKI, K., FYFE, W. S., BEVERIDGE, T. J. & HUMPHREY, R. 1987. Cellular lepidocrocite precipitation and heavy metal sorption in *Euglena* Sp. (unicellular alga): implications for biomineralization. *Chemical Geology*, **63**, 39–43.
- MELEZHUK, V. A. & FALICK, A. E. 1994. A worldwide 2.2–2.0 Ga-old positive $\delta^{13}\text{C}_{\text{carb}}$ anomaly as a phenomenon in relation to the Earth's major palaeoenvironmental changes. *Mineralogical Magazine*, **58A**, 593–594.
- MEL'NIK, Y. P. 1982. *Precambrian Banded Iron-Formations Physicochemical Conditions of Formation*. Elsevier, Amsterdam.
- MEYER, C. 1981. Ore-forming processes in geologic history. *Economic Geology 75th Anniversary Volume*, 6–41.
- 1985. Ore metals through geologic history. *Science*, **227**, 1421–1428.
- 1988. Ore deposits as guides to geologic history of the earth. *Annual Review of Earth and Planetary Sciences*, **16**, 147–171.
- MIYANO, T. & BEUKES, N. J. 1987. Physicochemical environments for the formation of quartz-free manganese oxide ores from the Early Proterozoic Hotazel Formation, Kalahari Manganese Field, South Africa. *Economic Geology*, **82**, 706–718.
- MORRIS, R. C. 1987. Iron ores derived by enrichment of banded iron-formation. In: HEIN, J. R. (ed.) *Siliceous Sedimentary Rock-Hosted Ores and Petroleum*. Van Nostrand Reinhold Company, NY, 231–267.
- 1993. Genetic modelling for banded iron-formation of the Hamersley Group, Pilbara Craton, Western Australia. *Precambrian Research*, **60**, 243–286.
- MURAD, E. & JOHNSTON, J. H. 1987. Iron oxides and hydroxides. In: LONG, G. J. (ed.) *Mössbauer Spectroscopy Applied to Inorganic Chemistry*. Plenum Publishing Corp., NY, 507–582.
- NEALSON, K. H. 1982. Microbiological oxidation and reduction of iron. In: HOLLAND, H. D. & SCHIDLÓWSKI, M. (eds) *Mineral Deposits and the Evolution of the Biosphere*. Springer-Verlag, Berlin, 51–66.
- 1983. The microbial iron cycle. In: KRUMBEIN, W. E. (ed.) *Microbial Geochemistry*. Blackwell, Oxford, 159–190.
- RONA, P. A. 1984. Hydrothermal mineralization at seafloor spreading centers. *Earth-Science Reviews*, **20**, 1–104.
- 1988. Hydrothermal mineralization at oceanic ridges. *Canadian Mineralogist*, **26**, 431–65.
- ROSENBERG, N. D., LUPTON, J. E., KADKO, D., COLLIER, R., LILLEY, M. D. & PAK, H. 1988. Estimation of heat and chemical fluxes from a seafloor hydrothermal vent field using radon measurements. *Nature*, **334**, 604–607.
- ROSSIGNOL-STRIK, M. 1987. Rainy periods and bottom water stagnation initiating brine accumulation and metal concentrations 2. Precambrian gold-uranium ore beds and banded iron formations. *Paleoceanography*, **2**, 379–394.
- ROY, S. 1976. Ancient manganese deposits. In: WOLF, K. H. (ed.) *Handbook of Strata-Bound and Stratiform Ore Deposits*, 7. Elsevier, Amsterdam, 395–476.
- 1981. *Manganese Deposits*. Academic Press, London.
- 1988. Manganese metallogenesis: A review. *Ore Geology Reviews*, **4**, 155–170.
- 1992. Environments and processes of manganese deposition. *Economic Geology*, **87**, 1218–1236.
- SCHIDLÓWSKI, M. 1988. A 3,800 million-year isotopic record of life from carbon in sedimentary rocks. *Nature*, **333**, 313–318.
- SCHISSEL, D. & ARO, P. 1992. The major early Proterozoic sedimentary iron and manganese deposits and their tectonic setting. *Economic Geology*, **87**, 1367–1374.
- SLATER, J. G., PARSONS, B. & JAUPART, C. 1981. Oceans and continents: Similarities and differences in the mechanisms of heat loss. *Journal of Geophysical Research*, **86**, 11 535–11 552.
- SHIMIZU, H., UMEMOTO, N., MASUDA, A. & APPEL, P. W. U. 1990. Sources of iron-formations in the Archean Isua and Malene supracrustals, West Greenland: Evidence from La-Ce and Sm-Nd isotopic data and REE abundances. *Geochimica et Cosmochimica Acta*, **54**, 1147–1154.

- SIEVER, R. 1977. Early Precambrian weathering and sedimentation: An impressionistic view. In: PONNAMPERUMA, C. (ed.) *Chemical Evolution of the Early Precambrian*. Academic Press, NY, 13–23.
- 1992. The silica cycle in the Precambrian. *Geochimica et Cosmochimica Acta*, **56**, 3265–3272.
- SIMONSON, B. M. 1985. Sedimentological constraints on the origins of Precambrian iron-formations. *Geological Society of America Bulletin*, **96**, 244–252.
- SLEEP, N. H. & WINDLEY, B. F. 1982. Archean plate tectonics: Constraints and inferences. *Journal of Geology*, **90**, 363–379.
- THODE, H. G. & GOODWIN, A. M. 1983. Further sulfur and carbon isotope studies of late Archean iron-formations of the Canadian Shield and the rise of sulfate reducing bacteria. *Precambrian Research*, **20**, 337–356.
- TOWE, K. M. 1983. Precambrian atmospheric oxygen and banded iron formations: delayed ocean model. *Precambrian Research*, **20**, 161–170.
- TRENDALL, A. F. 1968. Three great basins of Precambrian banded iron formation deposition: A systematic comparison. *Geological Society of America Bulletin*, **79**, 1527–1544.
- & MORRIS, R. C. (eds.) 1983. *Iron-Formation Facts and Problems*. Elsevier, Amsterdam.
- VAN HOUTEN, F. B. & ARTHUR, M. A. 1989. Temporal patterns among Phanerozoic oolitic ironstones and oceanic anoxia. In: YOUNG, T. P. & TAYLOR, W. E. G. (eds) *Phanerozoic Ironstones*. Geological Society, London, Special Publications, **46**, 33–49.
- VEARNCOMBE, S., BARLEY, M. E., GROVES, D. I., MCNAUGHTON, N. J., MIKUCKI, E. J. & VEARNCOMBE, J. R. 1995. 3.26 Ga black smoker-type mineralization in the Strelley Belt, Pilbara Craton, Western Australia. *Journal of the Geological Society, London*, **152**, 587–590.
- VEIZER, J. 1978. Secular variations in the composition of sedimentary carbonate rocks, II. Fe, Mn, Ca, Mg, Si and minor constituents. *Precambrian Research*, **6**, 381–413.
- 1983. Geologic evolution of the Archean-Early Proterozoic Earth. In: SCHOPF, J. W. (ed.) *Earth's Earliest Biosphere Origin and Evolution*. Princeton University Press, Princeton, NJ, 240–259.
- & JANSEN, S. L. 1979. Basement and sedimentary recycling and continental evolution. *Journal of Geology*, **87**, 341–370.
- & — 1985. Basement and sedimentary recycling-2: Time dimension to global tectonics. *Journal of Geology*, **93**, 625–643.
- , LAZNICKA, P. & JANSEN, S. L. 1989. Mineralization through geologic time: Recycling perspective. *American Journal of Science*, **289**, 484–524.
- VON DAMM, K. L., EDMOND, J. M., GRANT, B., MEASURES, C. I., WALDEN, B. & WEISS, R. F. 1985. Chemistry of submarine hydrothermal solutions at 21°N, East Pacific Rise. *Geochimica et Cosmochimica Acta*, **49**, 2197–2220.
- WALKER, J. C. G. 1977. *Evolution of the Atmosphere*. Macmillan, NY.
- 1982. Climatic factors on the Archean Earth. *Palaeogeography, Palaeoclimatology, Palaeoecology*, **40**, 1–11.
- 1984. Suboxic diagenesis in banded iron formations. *Nature*, **309**, 340–342.
- & BRIMBLECOMBE, P. 1985. Iron and sulfur in the pre-biologic ocean. *Precambrian Research*, **28**, 205–222.
- , KLEIN, C., SCHIDLowski, M., SCHOPF, J. W., STEVENSON, D. J. & WALTER, M. R. 1983. Environmental evolution of the Archean-Early Proterozoic earth. In: SCHOPF, J. W. (ed.) *Earth's Earliest Biosphere Its Origin and Evolution*. Princeton University Press, Princeton, NJ, 260–290.
- WALTER, M. R. 1983. Archean stromatolites: Evidence of the Earth's earliest benthos. In: SCHOPF, J. W. (ed.) *Earth's Earliest Biosphere Its Origin and Evolution*. Princeton University Press, Princeton, NJ, 187–213.
- & HOFMANN, H. J. 1983. The palaeontology and palaeoecology of Precambrian iron-formations. In: TRENDALL, A. F. & MORRIS, R. C. (eds) *Iron-Formation Facts and Problems*. Elsevier, Amsterdam, 373–400.
- WAYNE, R. P. 1985. *Chemistry of Atmospheres an Introduction to the Chemistry of the Atmospheres of Earth, the Planets, and their Satellites*. Clarendon Press, Oxford.
- WIDDEL, F., SCHNELL, S., HEISING, S., EHRENREICH, A., ASSMUS, B. & SCHINK, B. 1993. Ferrous iron oxidation by anoxygenic phototrophic bacteria. *Nature*, **362**, 834–836.
- WINDLEY, B. F. 1977. *The Evolving Continents*. John Wiley & Sons, London.
- 1979. Tectonic evolution of continents in the Precambrian. *Episodes*, **4**, 12–16.
- WOLERY, T. J. & SLEEP, N. H. 1976. Hydrothermal circulation and geochemical flux at mid-ocean ridges. *Journal of Geology*, **84**, 249–275.
- WOODS, T. I. & GARRELS, R. M. 1992. Calculated aqueous-solution-solid-solution relations in the low-temperature system CaO–MgO–FeO–CO₂–H₂O. *Geochimica et Cosmochimica Acta*, **56**, 3031–3043.
- WORSLEY, T. R. & NANCE, D. R. 1989. Carbon redox and climate control through Earth history: a speculative reconstruction. *Global and Planetary Change*, **1**, 259–282.
- , MOODY, J. B. & NANCE, R. D. 1985. Proterozoic to Recent tectonic tuning of biogeochemical cycles. In: SUNDQUIST, E. T. & BROECKER, W. S. (eds) *Carbon Cycle and Atmospheric CO₂: Natural Variations Archean to Present*. American Geophysical Union Geophysical Monographs, **32**, 561–572.
- , NANCE, R. D. & MOODY, J. B. 1986. Tectonic cycles and the history of the earth's biogeochemical and paleoceanographic record. *Paleoceanography*, **1**, 233–263.
- YOUNG, G. M. 1988. Proterozoic plate tectonics, glaciation and iron-formations. *Sedimentary Geology*, **58**, 127–144.
- 1989. Glaciation and tectonics. *Episodes*, **12**, 117.
- YOUNG, T. P. & TAYLOR, W. E. G. (eds) 1989. *Phanerozoic Ironstones*. Geological Society, London, Special Publications, **46**.

Lithological and geochemical evidence of Fe and Mn pathways during deposition of Lower Proterozoic banded iron formation in the Krivoy Rog Basin (Ukraine)

DMITRI A. KULIK^{1,2} & MICHAEL N. KORZHNEV¹

¹ *Institute of Geochemistry, Mineralogy and Ore Formation*

² *Metallogeny Department, National Academy of Sciences of the Ukraine,
34 Palladin Prospect, 252680 Kiev, Ukraine*

Abstract: Data on stratigraphy, chemical and mineral composition of siliciclastic and ferruginous rocks of greenschist to epidote-amphibolite metamorphic grade, multi-order cyclicity and banding, isotopic composition of sulphur and carbon and other features of the Krivoy Rog Supergroup metasedimentary rocks are summarized. They provide an insight into the primary sources and the nature of siliciclastic and chemogenic components of banded iron formation (BIF), as well as on pathways of Fe, Mn and Si in the Krivoy Rog palaeobasin at the time of BIF accumulation. Skelevat and Saxagan iron-ore Groups were deposited in a single cyclic transgressive–regressive sequence, probably in a trough-like land-locked basin with complex bottom topography defined by syn-sedimentary faults inherited from the earlier rift structures. Variations in sea level, humidity of climate, continental run-off, oceanic water inflows etc. many times provoked the rapid facies changes ranging from sedimentation of land-derived siliciclastics to deposition of nearly pure chemogenic sediments of the oxide facies BIF in the deeper parts of the basin. Up to seven pairs of schist (*s*-) and BIF (*f*-) horizons were deposited in the Saxagan Group. Lateral variations of their thicknesses, distribution of free carbon in the rocks and other data indicate that only parts of the basin at a given time were optimal for chemical sedimentation; major part of dissolved Fe, Si and Mn was supplied by constant or event inflow of suboxic ocean water.

The Mn content in the Krivoy Rog Supergroup BIFs could serve as an indicator of the fraction of total Fe that precipitated chemically as carbonate. The main part of Fe precipitation in form of Fe(III) hydroxide particles, possibly coated with amorphous silica, is due to a number of oxidation mechanisms operating in the photic surface water layer. On the basis of physicochemical considerations, it is concluded that the Mn CO₃ content in siderite (*c.* 2 mol %) contained in the BIF rocks reflects a uniform dissolved Mn concentration (*c.* 1 ppm) in the ocean and basin waters. Sedimentation of the typical association of Mg–Fe carbonates and silicates of the carbonate–silicate facies BIF could occur in the near-bottom water only in the case of strong enrichment in dissolved Fe(II) (up to 100–200 ppm) relative to the ocean water (1–10 ppm), which required a stratified brackish-water basin with an estuarine-type circulation. No enrichment in dissolved Mn(II) was possible until p_{O_2} in the atmosphere raised high enough for precipitation of particulate Mn oxide in the photic zone and its dissolution in the suboxic near-bottom waters.

Palaeoproterozoic basins of banded iron formation (BIF henceforth) contain about 80% of the world's economic iron resources (James & Trendall 1982). The BIFs of the Krivoy Rog basin, located in the southern part of the East European platform, have been studied over the last 100 years because of mining of high-grade iron ores and taconites. Compared to other basins like Hamersley or Transvaal, they have experienced higher-grade tectonometamorphism up to epidote-amphibolite facies (Belevtsev *et al.* 1983). For this reason, evidence of BIF deposition in the basin has been obscured. However, data on the stratigraphy, bulk and mineral composition, multi-order cyclicity, banding, and other lithological features of the Krivoy Rog BIF provide an insight into the primary sources and the nature of siliciclastic and

chemogenic components of BIF, as well as pathways of Fe, Si, Mn, and some trace elements in the Palaeoproterozoic basins. It seems that the Mn content in the BIF rocks of the Krivoy Rog Supergroup could serve as an indicator of dissolved Mn²⁺ levels in Palaeoproterozoic ocean, as well as of the amount of chemically precipitated Fe-carbonate under the influence of specific gently reducing conditions near the sediment–water interface.

The Krivoy Rog basin comprises the western part of the Middle Dnieper granite–greenstone terrain (MDGGT) of the Ukrainian shield (Fig. 1). The name traditionally refers only to the Krivoy Rog structure proper, a narrow synclinorium extending N–S up to 75 km, composed of metamorphic rocks of the Krivoy Rog Supergroup ('series' in the Russian stratigraphic

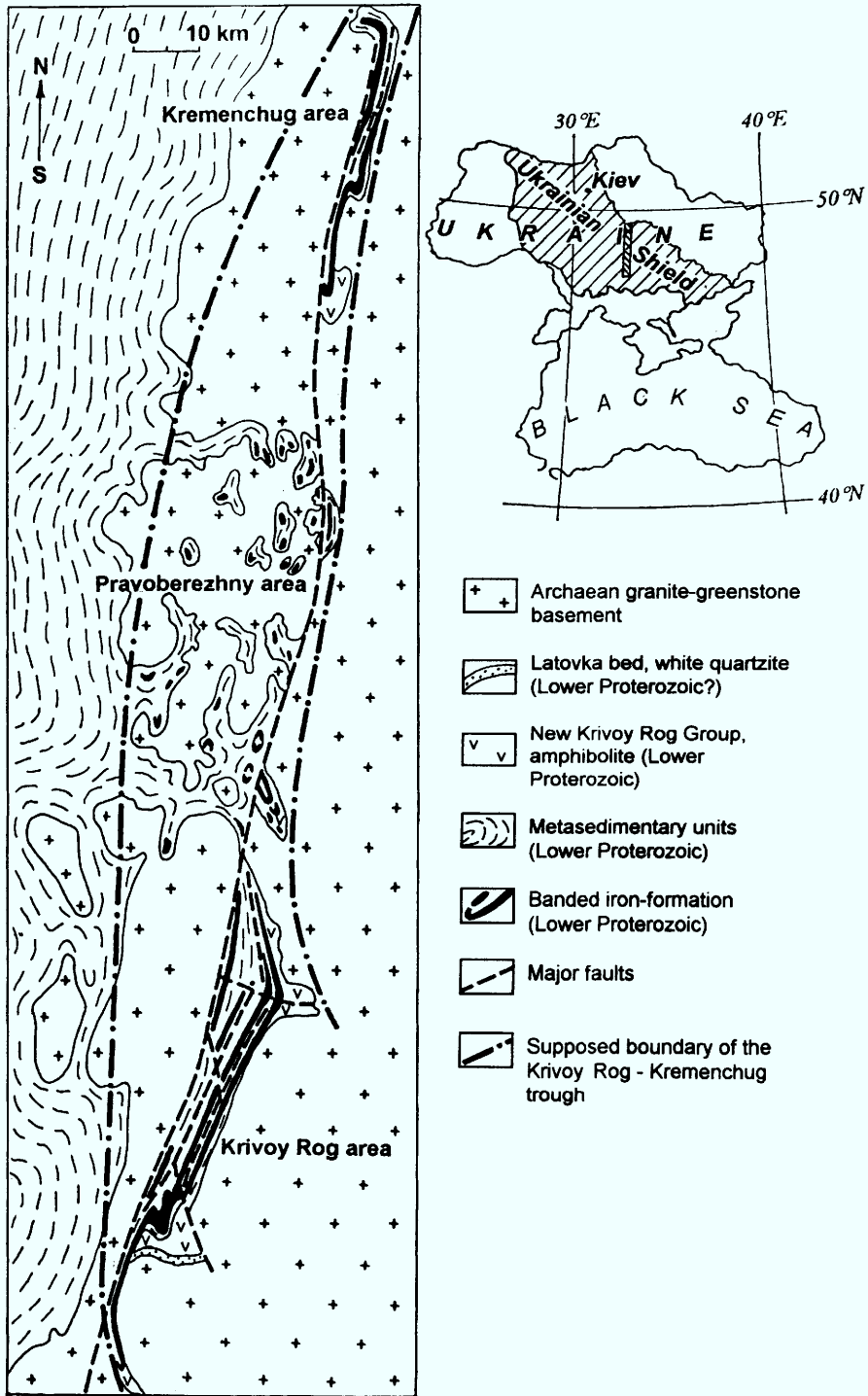


Fig. 1. Geological sketch of the Krivoy Rog-Kremenchug region of the Ukrainian Shield.

nomenclature is taken here as analogous to 'supergroup' in the terminology outside Russia and Ukraine). These rocks occur also northward in a number of small structures along the Krivoy Rog–Kremenchug deep-seated fault as far as the Kremenchug synclinorium on the north slope of the Ukrainian shield. Highly metamorphosed BIF within the Inghoul–Inghoulets Supergroup (regarded as lateral equivalent of the Krivoy Rog Supergroup) is distributed to the west of that fault zone in the Pravoberezhny area. All the occurrences of palaeoproterozoic BIF on the west flank of MDGGT therefore can be considered as relicts of a single Krivoy Rog palaeobasin of BIF accumulation.

Geological background

Notwithstanding the long history of mining and geoscientific studies within the basin, many questions remain controversial because of its very complicated geological structure. Detailed descriptions of the stratigraphy and tectonic setting have been published elsewhere (Belevtsev *et al.* 1983; Shcherbak *et al.* 1988; Plotnikov 1994; and references therein).

The Krivoy Rog and Kremenchug structures are considered here as the southern and northern fragments of the Krivoy Rog–Kremenchug trough (see Fig. 1). The axial part of the trough with BIF sequences appears to be eroded or buried under NE thrust blocks of granite–greenstone basement during later tectonics.

Major Krivoy Rog and Kremenchug faults divide the outcrop area into several zones with differing thicknesses and lithologies of the stratigraphic units. It is believed (e.g. Plotnikov 1994) that those faults inherit the ancient synsedimentary faults that divided the basin into parts with different depositional regimes. The faults appear to have developed as elements of a single deep-seated Krivoy Rog fault system. During subsequent tectonic stages, they also governed the distribution of plicative structures and metamorphic facies (cf. Belevtsev *et al.* 1989).

The Precambrian terrain of the Middle Dnieper region (MDGGT) is stratigraphically subdivided into three supergroups (Fig. 2) according to isochronic U–Pb ages measured from zircons of intrusive granites, metavolcanics and clastic metasediments by Shcherbak *et al.* (1989). The age of the Krivoy Rog Supergroup is limited by 2700 Ma (the minimum for zircons from siliciclastics of the Skelevat group) and 2080 Ma (zircons from granites cutting metamorphic rocks of the Krivoy Rog supergroup). This time span of about 700 Ma for the BIF

deposition cannot be made more precise because of the absence of definite metavolcanics within the Skelevat, Saxagan and Gdantsev Groups. However, the Upper Archaean BIF of the Belozherka Supergroup have been dated much better from the underlying and overlying acid metavolcanics (see Fig. 2).

The Krivoy Rog Supergroup, according to Belevtsev & Belevtsev (1981) and Belevtsev *et al.* 1983, can be divided into five groups ('suites' in Russian literature) (see Fig. 2): (1) *New Krivoy Rog Group* (metatholeiite and metaandesite–basalt overlying the Latovka white quartzite and metasandstone beds); (2) *Skelevat Group* (metaconglomerate–metasandstone, phyllitic schist, talc schist units); (3) *Saxagan Group* (up top seven pairs of alternated BIF (*f*-) and ferruginous schist (*s*-) members, numbered consecutively, e.g. *1f*, *2s*, *5f*, *6s*); (4) *Gdantsev Group* (lithoclastic breccia of BIF, metasandstone, (carbonaceous) schist, dolomite marble units), up to 800 m thick; (5) *Gleevat Group* (mainly metaconglomerate and metasandstone beds), up to 2.5 km thick.

There are major unconformities between all groups except the Skelevat and Saxagan Groups, which display a gradational contact (Fig. 2). Metamorphosed palaeosols (weathering crusts) are supposed to exist on the Archaean granite–greenstone basement and also between the New Krivoy Rog Group and the Skelevat Group (Kulish *et al.* 1987). Rocks of the Inghoul–Inghoulets Supergroup occur in the Pravoberezhny region and on the western limb of the Krivoy Rog structure. Its units can be correlated with those of the Krivoy Rog Supergroup as their lateral equivalents of lesser thickness.

In the Krivoy Rog and Kremenchug areas, the Skelevat Group rocks are widespread, though highly variable in thickness. In the Krivoy Rog structure for example the unit changes in thickness from tens of metres in the central part of the synclinorium up to 300 m thick in the Main syncline. From base upwards, the group is composed of arkose–quartzite, phyllitic and carbonate–talc schist units. The lowermost one is an intercalation of arkose and quartz metasandstone with lenses of metaconglomerate; the middle one comprises quartz–sericite phyllitic schist often enriched in biotite, and contains graphite and pyrite; the uppermost one consists of talc–actinolite and carbonate–chlorite–talc schist, rarely interbedded with talcose phyllite, metasandstone and metaconglomerate lenses. These rocks grade upwards into phyllitic schists of the *Is* member of the Saxagan (iron-ore) Group.

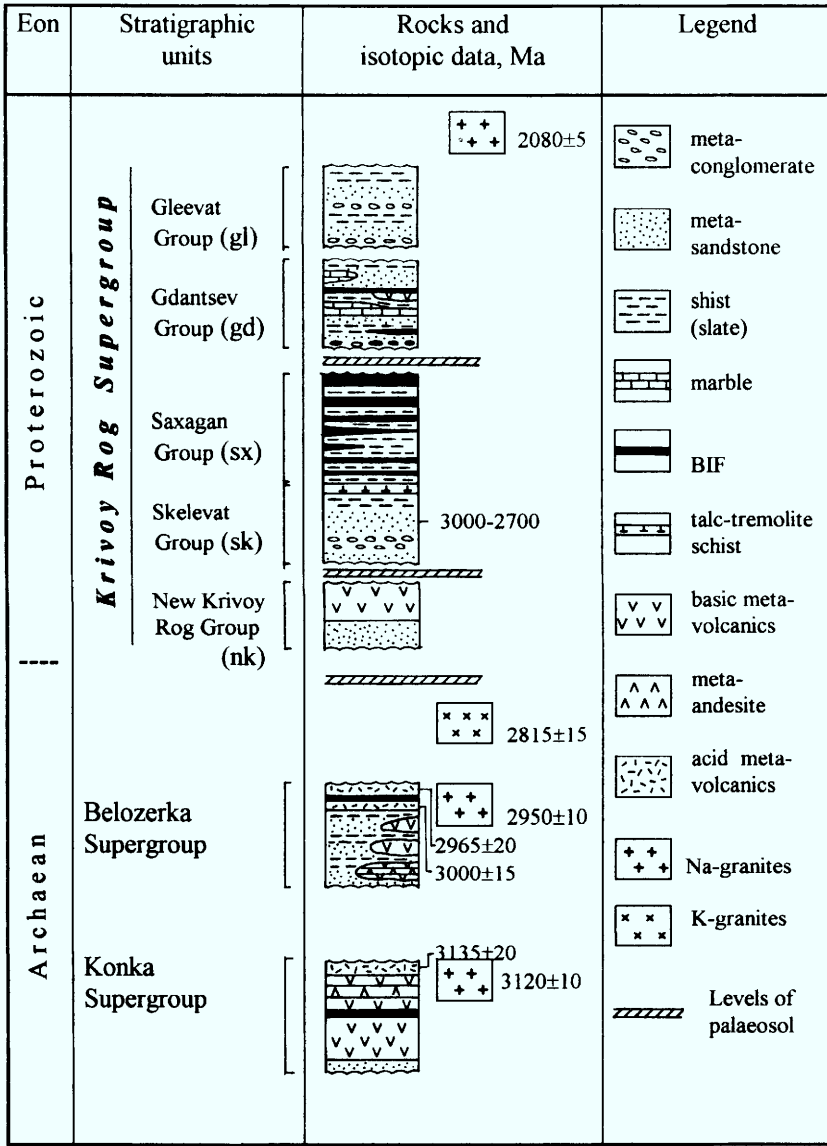


Fig. 2. General stratigraphic subdivision of the Precambrian terrain in the Middle Dnieper Area of the Ukrainian Shield. U-Pb isochron data on zircons (syngenetic for granites and acid metavolcanics and clastogenic from the coarse-grained metasediments) are from (Shcherbak *et al.* 1989).

Saxagan (iron-ore) Group

The Saxagan Group (300 to 1400 m thick) is a sequence of up to seven pairs of *ferruginous schist (s)* members and *ferruginous quartzite (f)* members numbered consecutively from base upwards (*1s, 1f, 2s, 2f* etc.; see Fig. 3). This subdivision has been made by Ya. N. Belevtsev mainly on petrographical grounds (see Belevtsev

et al. 1983), and does not correspond completely to the distinction of BIF and shale members, e.g., in the Hamersley Group (Morris 1993). Here we use the terms *schist* and *quartzite* because they are consistent to the metamorphic grade (upper greenstone to epidote-amphibolite facies; see Belevtsev R. *et al.* 1989) of the Krivoy Rog Supergroup rocks. Ferruginous quartzite (*f*) members are definitely the metamorphic

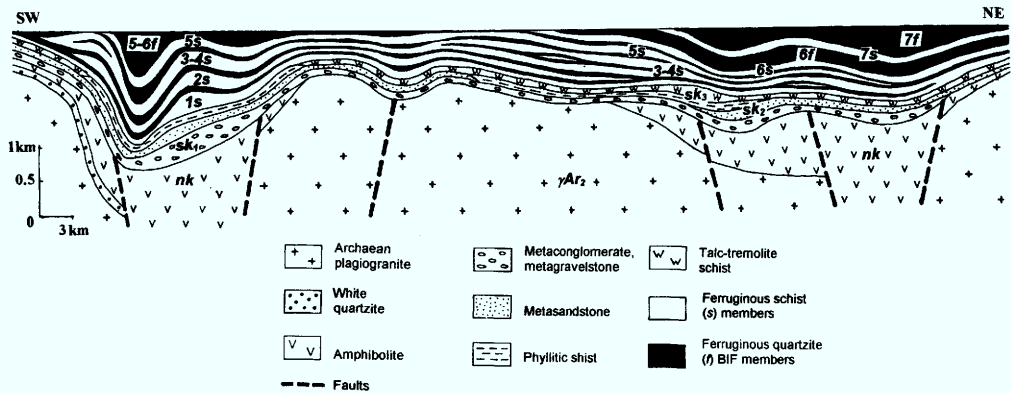


Fig. 3. Reconstructed thickness variations of BIF (*f*) and schist (*s*) members of the Saxagan Group along strike of the Krivoi Rog structure. See Fig. 2 for symbols of stratigraphic units. Subdivisions of Skelevat Group: *sk*₁, lower (metaconglomerate–metasandstone) unit; *sk*₂, middle (phyllitic schist) unit; *sk*₃, upper (carbonate–tremolite–talc schist, phyllitic schist) unit. 1*s*, 1*f*–7*f*, symbols of members of the Saxagan Group.

analogues of the oxide to carbonate facies mesobanded cherty BIF of other basins. Alternation of chlorite (garnet–biotite) schist interbands with magnetite–siderite (cumingtonite) and quartzite mesobands occurs in transitions between the *f*- and *s*-members; these parts could be taken as analogues to the silicate facies BIF (after James 1954). Pyritic graphite–biotite black schists are developed inconspicuously within 3–4*s* and 5*s* members as thin lenses between the quartz–sericite (phyllitic) schist beds. These pyrite-bearing black schists can be related to the sulphide facies BIF, though being of very limited occurrence for the Saxagan Group both in the Krivoi Rog and Kremenchug areas.

The gradual transition from the metamorphosed siliciclastics of the Skelevat Group through quartz–sericite schist, biotite schist (1*s*), silicate facies BIF, carbonate facies BIF, to oxide facies BIF (1*f*) demonstrates the transgressive facies profile typical for the Krivoi Rog basin. Repetition of this profile for other pairs of *s*- and *f*-members in the Saxagan Group, especially pronounced in the 2*f*, 4*f* and 5*f* members, represents the higher-order sedimentary cyclicity (Kulik 1991). The fact that 'oxide facies' hematite and magnetite sub-members thin-out first with a decrease of total thickness of the *f*-member with concomitant increase of thickness of adjacent *s*-members, leads to the implication that the oxide BIF facies were deposited in the deepest parts of the basin, incorporating the least amount of siliciclastic component (Belevtsev *et al.* 1983).

It seems difficult to reconstruct the exact facies patterns of BIF deposition in the Krivoi

Rog–Kremenchug trough, because only faulted fragments of the primary strata have been preserved and these have undergone subsequent deformation and metamorphism including local metasomatic alteration. In addition, very few continuous outcrops are available, most of them are open-cast mines. Comparing many available drillhole sections of Skelevat and Saxagan Groups from different parts of the Krivoi Rog structure, however, it is possible to reconstruct how the thickness of *f*- and *s*-members vary along strike of the Krivoi Rog trough (Fig. 3). There is no place where all seven pairs of *f*- and *s*-members occur in the same stratigraphic column. In the southwestern part, 5*f* is the uppermost member of the Saxagan Group, while the 3*f* is often missing. In the central (axial) part of the trough, the 3*f* member is always present, but towards its northeast edge it disappears again. In the northeast part of the trough, 6*f* and 7*f* members of the Saxagan Group become predominant in thickness, while the thickness of the lower part is strongly reduced at the cost of 4*f*, 3*f*, 2*f*, 4*s* and 2*s* members. These facts indicate that the maximum accumulation of the chemogenic BIF-material moved from the southwest to the northeast of the trough. Another interesting feature is that the thickness of the Saxagan Group increases from the central part of the basin towards its southern and northern ends, where the metavolcanics of the New Krivoi Rog suite are widespread. It seems from Fig. 3 that fault zones dividing the granite–greenstone basement into blocks have been active during deposition of the New Krivoi Rog, Skelevat and Saxagan Groups.

Siliciclastic metasediments

Gradual transitions exist between the schist (*s*) and ferruginous quartzite (*f*) members of the Saxagan Group in the Krivoy Rog basin. This transition is manifested in the decrease of thickness of individual phyllitic (quartz-sericite) schist and ferruginous (chlorite or garnet-biotite) schist interbands and their total volume fraction in the rock, accompanied by an increase in fraction of magnetite-, siderite- or hematite-rich bands. Even in the extreme BIF oxide facies (magnetite-hematite jaspilites), some rare and thin aluminosilicate-bearing interbands still exist. On the other hand, all schist units are enriched in iron relative to 'normal' shales. Hence, chemical and mineral composition of clastic metasediments of the Skelevat and Saxagan Groups could provide important information about the runoff area composition and tectonic regime during BIF accumulation.

Clastic component distribution

In the present context, pebbles from metaconglomerate beds of arkose-quartzite member of the Skelevat Group are most informative. Vein quartz, quartzite, quartz metasandstone, phyllitic schist, altered amphibolite, plagiogranite, and sporadic ferruginous quartzite were encountered as pebbles. Some amphibolite pebbles have relicts of amygdaloidal textures petrographically identical to those of metatholeiitic amphibolite of the underlying New Krivoy Rog Group. Such pebbles are most abundant in the lower part of the arkose-quartzite member near the unconformity, comprising up to 60–70% of the total number of pebbles. Most quartzite and metasandstone pebbles were probably derived from the same palaeosol developed on the Archaean granites as those in white (sericite) quartzites of the Latovka unit underlying the New Krivoy Rog Group (Kulish *et al.* 1987). This conclusion is also supported by distribution studies of clastogenic zircons (Shcherbak *et al.* 1989). Variations in metasandstone clastic material composition suggest that also plagiogranites and alkali granites were among granitoids of the runoff area. Some varieties of clastogenic zircons display isotopic ages of about 2700–2800 Ma, corresponding to the approximate time of alkali granite intrusions in the MDGGT (Shcherbak *et al.* 1989).

The main clastic minerals in schist members and interbands in ferruginous quartzites, preserved during metamorphism, are zircon and

quartz. Schists of the Saxagan Group occasionally display a blastosporamitic texture with rare rounded clastic quartz grains up to 1 mm in size. Because of metamorphism, no relict textures (like volcanic shards) can be distinguished.

It is very difficult to identify clastic quartz in BIF rocks, where it was initially mixed with chemically precipitated 'chert' and then lost its rounded grain shapes due to tectonometamorphic recrystallization. However, detrital quartz grains do exist in BIF as it is evidenced from studies of quartz thermoluminescence and decrepitation of fluid inclusions (Ramires & Troshchenko 1992). Though the common decrepitation temperature of inclusions in quartz from BIF rocks corresponds to that of greenschist metamorphism (300 to 500°C), some quartz grains show higher temperatures (750, 810, 920°C). Higher temperature peaks (320–360°C) usually related to Ti^{3+} centres in quartz of igneous rocks were also found on the thermoluminescence curves. Both facts can be explained only by admixture of clastic quartz derived from weathering of the Archaean magmatic rocks (mainly granites). It is difficult, however, to estimate the fraction of clastic quartz in the BIF from these data; it seems that this fraction does not exceed 10–20%, as can also be deduced from the Ti and Zr contents in the BIF rocks.

Studies conducted by Troshchenko & Ivanchenko (1982) on clastic zircons from rocks of the Saxagan Group included their morphological identification as zircons from different granitoids from the areas adjacent to the Krivoy Rog basin. The authors concluded that input of clastic material into the basin at Skelevat-Saxagan time took place from both eastern and western terranes. At early Skelevat time, clastics derived from the east predominated, but during the middle Saxagan time it changed to a mostly westerly derivation area. These conclusions are consistent with a well-documented shift of chemical BIF sedimentation maximum from the west to the east side of the Krivoy Rog-Kremenchug trough by the end of Saxagan time, as it is recorded by the thickness distribution of the 6*f* and 7*f* members.

Major and trace element distribution

Data on the distribution of major and trace element in clastic metasediments of the Krivoy Rog Supergroup can be found in many Russian publications. However, they are often scarce, outdated or of unsatisfactory quality. For that reason, the original samples collected by the

authors were analysed in laboratories of the Institute of Geochemistry, Mineralogy and Ore Formation of National Academy of Sciences (Kiev, Ukraine). Contents of major elements oxides were determined by routine wet chemical analysis, concentrations of trace elements by X-ray fluorescence (Mo, Cu, Zn, Ga, Pb, Rb, Sr, Y, Zr, Nb, Ba) or quantitative flame spectrometry analysis (Ni, Co, V, Cr, Sc, Li, Ce). These data (113 samples) have been processed statistically by means of the *R*- and *Q*-methods of

principal component analysis (Davis 1986), using the standard software for IBM/370 mainframes. These multivariate statistical methods permit to split a correlation matrix of the array of chemical data into three or four independent factors, i.e. persistent associations of intercorrelated variables. By considering the factor loadings obtained from the *R*-method, the factors usually can be related to geochemical processes governing the composition of the samples. From results of the *Q*-method one can assess to what

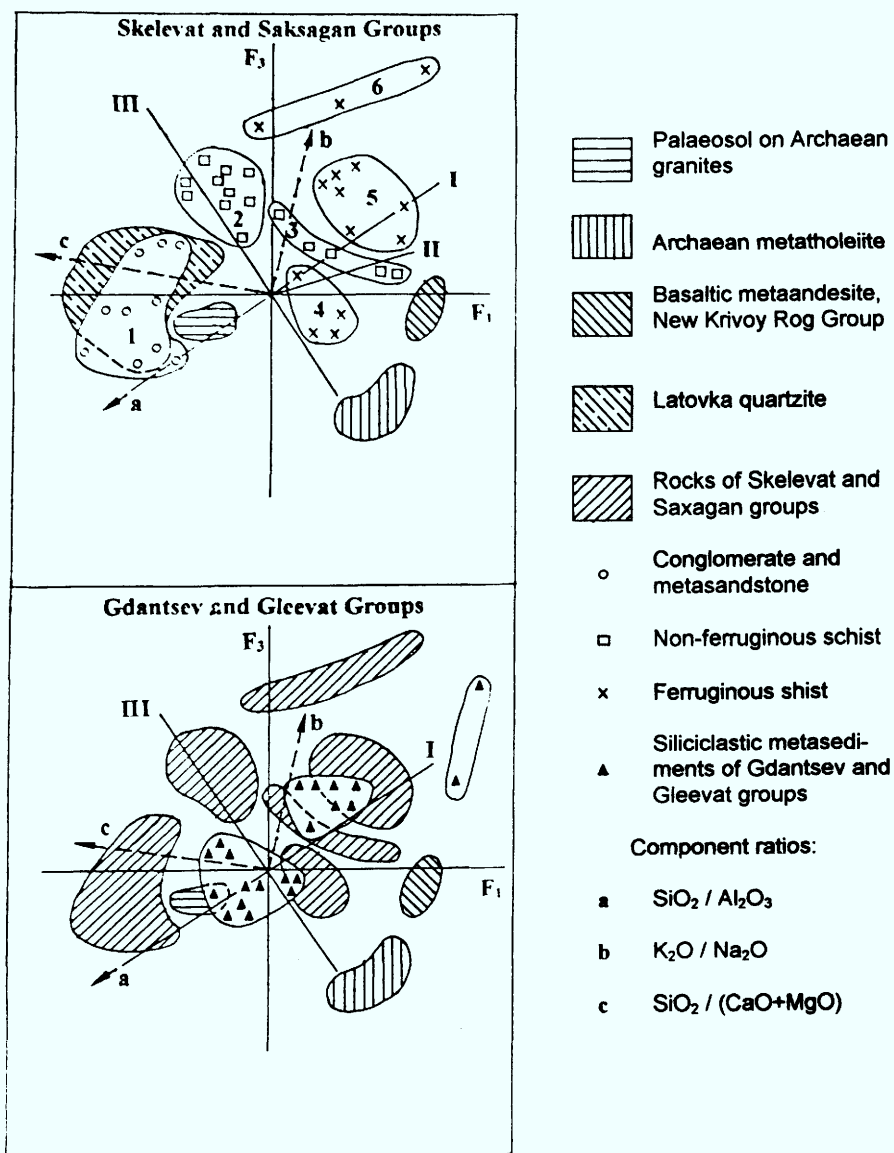


Fig. 4. *Q*-mode principal component diagrams showing trends in chemical composition of Krivoy Rog Supergroup non-ferruginous rocks (see also Table 2 for the group averages).

extent the composition of each sample can be explained in terms of the factors, and how the total set of samples is clustered into representative groups. The following four major factors can be recognized after processing of 113 original chemical analyses of the Krivoy Rog Series rocks:

- (1) TiO₂, FeO, MnO, CaO, P₂O₅, V, Zn, -SiO₂, -Mo, 24% of total sample variance;
- (2) FeO, Fe₂O₃, CO₂, -Al₂O₃, -TiO₂, -Zr, -Sc, -Co, -V, 21% of total sample variance;
- (3) K₂O, Rb, Li, Cs, -CaO, -Na₂O, 16% of total sample variance;
- (4) Ni, Co, Cr, 11% of total sample variance.

On these grounds, samples in the dataset were split into 19 groups as shown on the factor diagrams (Fig. 4); averages within those groups are presented in Table 1. Some comparisons of the composition of Krivoy Rog Supergroup metasediments to the unmetamorphosed sedimentary and pyroclastic rocks are given in Table 2.

Rare earth element (REE) distribution

Much attention is paid to the geochemistry of the rare earth elements (REE) in the BIF and associated rocks of Precambrian basins (e.g., Fryer 1983; Bau & Möller 1993). The data on REE distribution in the Krivoy Rog Supergroup are still scarce; analyses obtained by Tugarinov *et al.* (1973) still remain the only reliable dataset. The representative determinations from their tables have been replotted here into the chondrite-normalized REE spectra (Fig. 5).

The diagrams display three remarkable features: (1) most of the substantially metasedimentary rocks show a negative Eu anomaly; (2) the extreme chemogenic oxide facies BIF rocks (jaspilites) display a positive Eu anomaly; (3) some schists of the Saxagan Group reveal a negative Ce anomaly, while some jaspilites show a positive Ce-anomaly. However, the intermediate spectra reflecting mixtures of the siliciclastic and chemogenic BIF components are most common, in tune with the above data on chemical composition and distribution of clastic minerals in ferruginous rocks.

Chemogenic metasediments

It is believed that ferruginous quartzites in the Krivoy Rog basin, like their less metamorphosed

counterparts (cherty microbanded BIF of other Palaeoproterozoic basins) are products of chemical precipitation of dissolved iron and silica with variable additions of siliciclastic or volcanoclastic material. Hence, some details of this process could be understood from studies of cyclicity, multi-order banding and mineral and chemical composition of BIF rocks. Possible local impacts of post-sedimentary transformation, metamorphic recrystallization, tectonic deformation and metasomatic alterations should be eliminated. Physico-chemical data, models and considerations provide useful boundary conditions for these secondary processes, as well as for mechanisms and palaeoenvironments of BIF chemical precipitation and diagenesis (cf. Mel'nik 1982, 1986; Ewers 1983; Holland 1984; Drozdovskaya 1990; Anbar & Holland 1992).

Multi-order cyclicity and banding of ferruginous rocks

Several scales of cyclicity are distinguished in the sections of the Saxagan Group (Fig. 6). The alternation of ferruginous quartzite (*f*-) and ferruginous schist (*s*-) members is consistent with the lateral change in thickness and composition of the *f*- and *s*-members (see Fig. 3). In the areas where the *f*-member reaches maximum thickness, it usually can be subdivided into several submembers or lithofacies. In a complete (unweathered) profile, a microbanded hematite-magnetite BIF (jaspilite) sub-member always occurs in the middle. Vertically and laterally, it grades into a mesobanded magnetite quartzite, then a siderite-magnetite quartzite, then a chlorite-(garnet-biotite)-magnetite-siderite mesobanded rock ('schist-quartzite'), and finally into the ferruginous schist submembers of the adjacent *s*-members.

When thickness of the *f*-member decreases, it is the hematite-magnetite lithofacies that always thins out first, allowing the upper- and lower magnetite lithofacies to condense into one. Next to it, the middle magnetite sub-member thins out, and so on, resulting in the complete extinction of the *f*-member and condensation of the two *s*-members of increased thickness into one.

Different lithofacies also occur within the *s*-members. The ferruginous schist usually grades into the phyllitic (quartz-sericite) schist, with more or less thick beds of the black pyritic carbonaceous schist, chlorite-chloritoid schist, clean quartzite or even thin (1-4 m) meta-sandstone-metagravelstone lenses or beds (in the 2s member of the Saxagan Group of the

Table 1. Chemical composition of principal groups of siliciclastic metasediments and some metavolcanics from the Krivoy Rog Supergroup and Archaean granite-greenstone basement

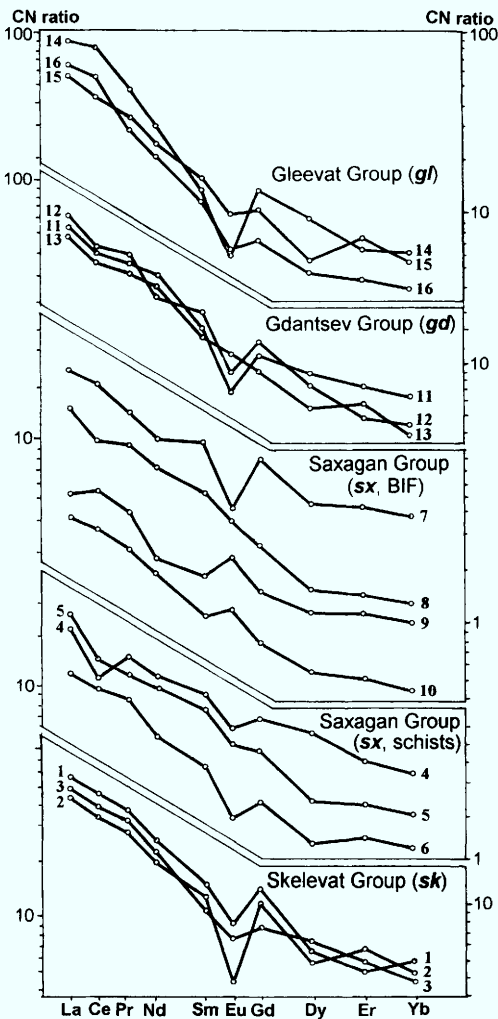
	1	2	3	4	5	6	7	8	9	10	11	12	13	14	15	16	17	18	19
<i>Major elements (wt%)</i>																			
SiO ₂	49.52	71.97	82.51	50.96	56.70	66.97	86.88	61.12	56.00	32.06	33.84	40.28	60.10	68.57	55.85	26.30	81.45	67.29	58.09
TiO ₂	0.80	0.31	0.18	0.76	0.92	0.55	0.15	0.63	0.66	0.35	0.36	0.48	0.21	0.38	0.58	0.13	0.18	0.38	0.49
Al ₂ O ₃	11.99	14.60	9.16	14.97	13.64	16.33	5.69	20.15	17.08	10.80	8.60	13.81	3.03	10.48	14.06	1.60	5.60	11.11	16.64
Fe ₂ O ₃	2.28	0.55	0.26	1.91	1.90	0.35	0.54	1.82	1.86	11.21	13.01	12.65	10.71	0.91	2.86	4.20	1.20	2.14	2.34
FeO	10.04	2.48	2.28	8.34	8.54	2.87	2.48	4.13	7.73	25.79	24.24	17.72	16.30	4.07	9.52	2.08	4.34	6.68	7.40
MnO	0.17	0.05	0.03	0.16	0.13	0.09	0.02	0.03	0.05	0.09	0.16	0.06	0.06	0.04	0.26	0.14	0.05	0.10	0.16
MgO	11.44	1.09	0.98	7.54	5.08	1.99	0.53	1.83	5.80	6.70	6.73	3.37	2.22	5.14	3.37	14.15	1.76	3.22	4.80
CaO	8.89	1.34	0.54	9.94	5.52	3.20	0.43	0.24	0.28	0.60	0.29	0.48	0.35	2.06	2.13	19.32	2.13	3.16	2.70
Na ₂ O	1.80	3.68	0.36	3.08	3.70	1.98	0.14	0.20	0.21	0.17	0.35	0.18	0.23	2.98	0.23	0.15	0.65	1.68	1.40
K ₂ O	0.17	2.25	2.00	0.28	1.20	3.07	1.71	5.95	4.44	0.44	0.44	5.74	0.80	0.83	3.79	0.48	0.83	2.07	3.40
S	0.09	0.04	0.06	0.04	0.03	0.05	0.18	0.18	0.37	0.08	0.34	0.07	0.14	0.02	0.48	2.74	0.02	0.05	0.21
P ₂ O ₅	0.12	0.08	0.05	0.07	0.11	0.10	0.04	0.05	0.04	0.16	0.11	0.11	0.10	0.12	0.22	0.12	0.07	0.12	0.14
CO ₂	0.79	0.30	0.25	0.30	0.70	0.63	0.57	0.82	0.70	7.38	7.15	2.38	3.64	1.93	3.23	21.96	0.54	0.99	0.61
LOI	1.85	1.16	1.35	1.59	1.80	1.77	0.79	2.86	4.60	4.46	2.38	2.68	2.39	1.34	2.67	7.56	1.31	1.13	1.88
Total	99.95	99.90	100.01	99.94	99.97	99.95	100.05	100.02	99.92	100.06	100.16	100.01	100.28	100.16	100.28	100.93	100.13	100.12	100.26
N	8	11	19	4	7	2	10	10	5	4	7	3	1	1	5	1	2	11	2
<i>Trace elements (ppm)</i>																			
Ni	210	24	28	150	53	95	140	125	975	15	26	13	10	60	75	20	45	80	150
Co	35	<2	2	20	30	25	18	72	50	<2	<2	<2	<2	10	11	<2	2	7	10
V	225	36	26	175	412	140	54	111	225	30	36	47	100	80	137	20	40	72	150
Cr	460	18	18	125	50	170	96	212	1625	50	60	90	30	150	125	200	40	127	250
Mo	<1	4	4	2	3	3	6	6	2	<1	<1	1	<1	4	2	2	4	3	3
Cu	39	34	26	28	31	60	21	25	31	41	86	63	15	5	42	25	25	20	25
Zn	63	35	20	50	73	12	23	31	70	39	31	100	15	20	145	30	20	48	87
Ga	11	19	14	14	30	10	Tr	19	10	7	30	13	5	10	26	10	7	22	35
Pb	14	7	8	7	16	45	21	20	55	15	12	13	5	15	26	<5	28	20	20
Rb	11	69	70	Tr	40	70	54	184	140	26	154	210	80	75	100	15	25	89	150
Sr	140	78	10	180	170	65	14	27	8	7	11	15	15	195	57	65	55	156	57
Y	21	6	6	24	29	10	6	16	8	34	16	17	10	10	37	10	7	14	12
Zr	70	140	82	92	151	120	120	154	65	57	66	83	45	175	232	60	87	170	117
Nb	5	3	2	3	4	4	6	12	7	2	5	4	6	10	45	<2	4	8	10
Sc	32	4	3	35	37	25	9	26	35	4	4	6	3	8	12	<2	3	8	15
Li	17	18	8	13	47	60	6	20	42	25	79	105	10	40	32	30	11	45	90
Cs	<1	1	<1	<1	2	1	<1	2	3	4	41	33	5	2	5	<1	5	<1	12
Ba	170	145	35	75	610	1750	150	330	250	120	690	670	15	200	250	800	240	515	700
N	8	11	19	4	7	2	10	10	5	4	7	3	1	1	5	1	2	11	2

Rock varieties (by numbers): Archaean granite-greenstone basement: 1, mafic metavolcanics; 2, metapaleosol on Archaean granites. New Krivoy Rog Group: 3, Latovka quartzites (redeposited paleosol on Archaean granites); 4, metatholeite; 5, meta-andesite-basalt; 6, meta-sandstone. Skelavat and Sasagan Groups: 7, conglomerate matrix and metasandstone; 8, non-ferruginous schists; 9, phyllitic schist (1/ member), 10-13, ferruginous shists. Gidantsev Group: 14, lithoclastic BIF; 15, metasandstone; 16, black schist (1.03% Cong); 17, dolomitic marble. Gleevat Group: 18, conglomerate matrix; 19, metasandstone.
 N = number of samples averaged within the group; LOI, loss on ignition + H₂O.

Table 2. Comparison of contents of some major components in metasedimentary rocks of the Skelevat and Saxagan Groups and some unmetamorphosed sedimentary and pyroclastic rocks (wt%)

Component	1	2	3	4	5	6	7	8	9	10	11	12	13
SiO ₂	86.2	61.1	56.0	32.1	33.9	40.3	95.4	77.1	44.5	58.3	50.9	48.7	53.6
TiO ₂	0.1	0.6	0.7	0.3	0.4	0.5	0.2	0.3	1.5	0.3	1.1	2.0	1.0
Al ₂ O ₃	5.5	20.1	17.1	10.8	8.5	13.8	1.1	8.7	37.8	18.7	22.8	14.1	19.6
Fe _{total}	2.6	4.4	7.3	27.4	28.0	22.6	0.4	1.6	1.2	3.4	6.2	7.0	4.0
MnO	0.02	0.03	0.05	0.09	0.16	0.06	—	0.2	—	—	0.02	—	—
MgO	0.5	1.8	5.8	6.6	6.8	3.4	0.1	0.5	0.3	4.6	1.9	6.4	3.3
Na ₂ O	0.1	0.2	0.2	0.2	0.3	0.1	0.1	1.5	0.4	2.2	0.5	6.2	3.5
K ₂ O	1.7	5.9	4.4	0.4	2.4	5.7	0.2	2.8	0.6	1.0	4.9	1.6	3.6

1–6, Metasediments of the Skelevat and Saxagan Groups (see also Fig. 4): 1, metagavelstone and metasandstone, 2,3, non-ferruginous schists, 4–6, ferruginous schists. Metasandstone: 7, quartz, 8, arkose. Clays: 9, kaoline; 10, montmorillonite; 11, illite. Tuffs: 12, basaltic; 13, andesitic (Voytkovich *et al.* 1990).



Kremenchug area). Some *s*-members may completely thin out, like the 6s member in the Southern Syncline of the Krivoy Rog basin (see Fig. 3).

Within each BIF lithofacies 20–100 cm thick 'cyclothem' can be distinguished, defined by the change of proportions of Fe oxides, Fe carbonates and ferrous aluminosilicate minerals. These minerals and quartz are not evenly distributed; instead, they comprise distinct mesobands 1–200 mm thick (see Fig. 6), marked from their neighbours by their internal mineralogical and textural features. Some mesobands display more or less preserved microbanding (in the terminology of Trendall 1972), or 0.1–5 mm thick 'aftvarves' as suggested by Morris (1993). Fine although non-persistent lamination of sub-millimetre scale defined by clouds of micron-size hematite grains is present in thick (2–7 mm) quartz-rich microbands of some red-chert-like quartz mesobands.

Fig. 5. Typical chondrite-normalized REE spectra for whole-rock analyses of metasediments from the Krivoy Rog Supergroup (plotted from the data of Tugarinov *et al.* (1973); REE concentrations in chondrite from Taylor & McLennan 1985). Skelevat Group (*sk*): 1,2, metasandstones; 3, phyllitic schist. Saxagan Group (*sx*): 4, quartz-sericite-chlorite schist (5s member); 5, biotite-chlorite schist (1s member); 6, quartz-chlorite schist (1s member); 7, chlorite-magnetite banded quartzite (5f member); 8,10, amphibole-magnetite quartzites; 9, amphibole-magnetite jaspilite; Gdantsev Group (*gd*): 11, graphite-carbonate-biotite schist; 12, feldspar-quartz metasandstone; 13, quartz-biotite schist. Gleevat Group (*gl*): 14, biotite-quartz metasandstone; 15, quartz-biotite schist; 16, carbonate-biotite metasandstone.

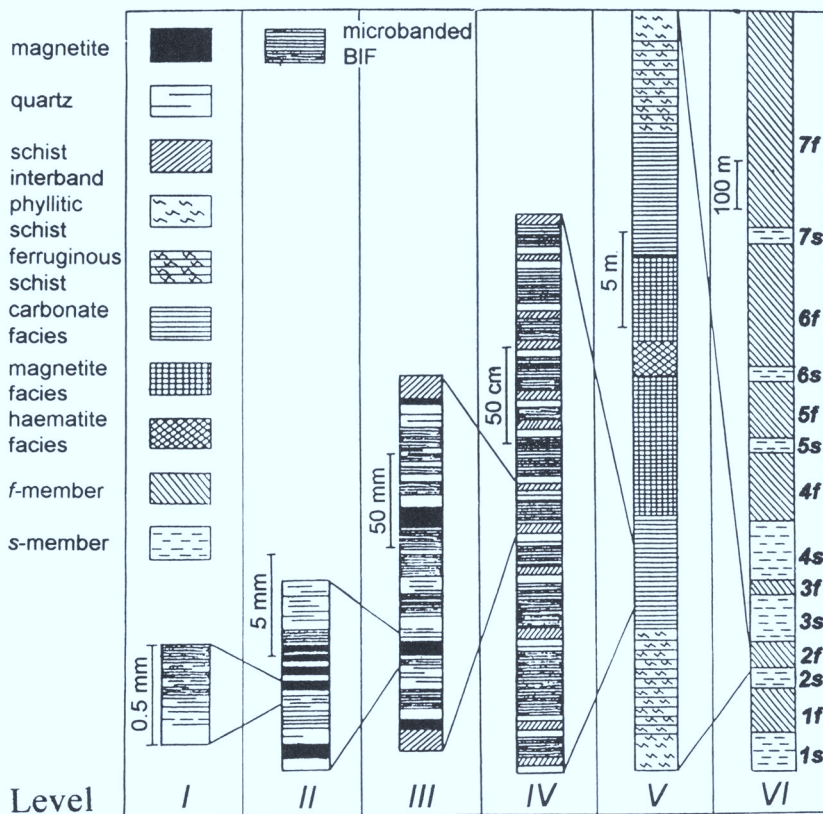


Fig. 6. Scales and levels of banding (I-III) and cyclicity (IV-VI) in the Saxagan Group. Modified from Kulik (1991).

Mesobanding. Mesobanding, the most prominent structural feature of BIF rocks, has been regarded for a long time as a sort of record bearing important information about the dynamic environment of BIF sedimentation. It is readily measurable from the diamond drilling cores. Looking for the factors and forces controlling the supply and precipitation of chemical and siliciclastic components, sequences of thicknesses of mesobands can be processed statistically in order to detect some periodicity or stochasticity that could be related to hydrological time series, astronomic cycles and others.

In order to achieve this, about 80 000 mesobands covering 30-90% of the total thickness of *f*-units were visually measured on diamond-drilling cores from unweathered BIF rocks (Kulik 1986). Samples were documented using a streak-print technique (cf. Morris & Ewers 1978), studied petrographically, and some bands were analyzed for major elements.

A petrographical classification of mesobands based on variations in mineral composition and

internal textures would result in an enormous number of types, because it depends on the metamorphic grade, which ranges from lower greenschist to amphibolite facies in the Krivoy Rog basin. Other complications involve the local alkaline metasomatic alterations, weathering and boudinage. The measurement, coding and statistical processing of mesobanding required a simple operational classification, which would not depend much on the above complicating factors and lithofacies changes and would permit visual identification of mesoband types.

Keeping this in mind, we classified the mesobands according to the prevalence of main chemical and mineral components into four principal types: *F* (mainly hematite/magnetite/siderite), *Q* (mainly quartz), *M* (microbanded mixed quartz-hematite/magnetite/siderite) and *S* ('schist', mainly aluminosilicate interbands). Mesobands of intermediate texture and composition, would then be coded with a combination of these letters, e.g., *MS* (microbanded mixed ferruginous-aluminosilicate). These mesoband

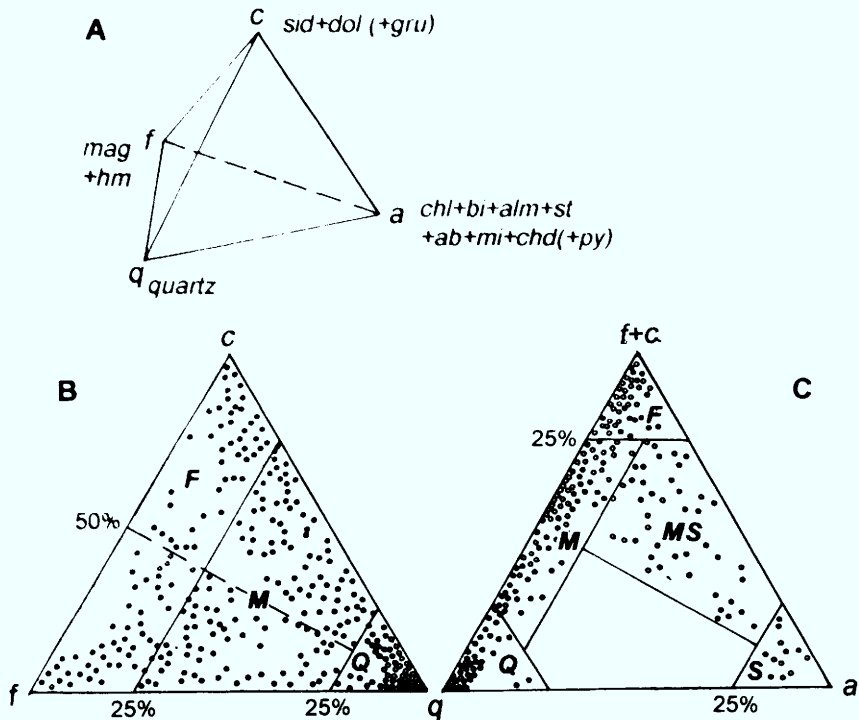


Fig. 7. Classification of micro- and mesobands by their mineral composition (for greenschist facies metamorphic grade, unweathered rocks). A, Baricentric tetrahedron; B, C, plots of mineral composition (vol.%) of 314 actual mesobands from BIFs of the Saxagan Group with fields of principal mesoband types. Measured with a grid counting method from thin sections under the microscope in transmitted and reflected light. Abbreviations of mineral names: *ab*, albite; *alm*, almandine; *bi*, biotite; *chl*, chlorite (thuringite, ripidolite, clinocllore); *chd*, chloritoid; *cum*, cummingtonite; *dol*, dolomite, ankerite; *gru*, grunerite; *hm*, hematite; *mag*, magnetite; *mi*, microcline; *py*, pyrite, pyrrhotite; *qu*, quartz; *sid*, siderite, sideroplesite; *st*, stilpnomelane.

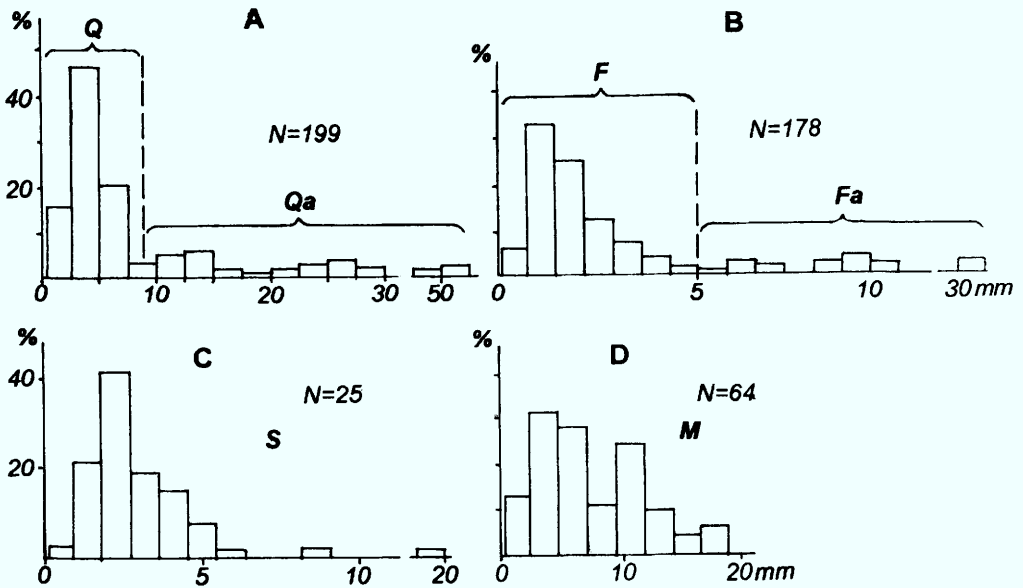


Fig. 8. Typical distributions of mesoband thickness for the principal mesoband types. A, Quartz mesobands from 7f member; B, magnetite mesobands from 4f member; C, mixed hematite-magnetite-quartz mesobands from 4f member; D, biotite interbands from 5f member. *N* = number of mesobands in a recorded sequence.

types are easily identifiable on clean surfaces of diamond drilling cores, and with difficulties in the rock specimen.

The mineral composition of BIF mesobands can be represented as a baricentric tetrahedron with *f*, *c*, *q* and *a* vertices representing the typical mineral assemblages of BIF lithofacies (Fig. 7a). Cumingtonite is taken together with sideropilesite because it is a typical metamorphic mineral forming in carbonate-rich bands at elevated temperatures and higher H₂O content in the fluid (cf. Mel'nik 1982; Klein 1983). It is clear from Fig. 7b & c that a continuum exists between compositions of *Q*, *F* and *M* bands, *F*, *M* and *S* bands, but not between *Q* and *S* bands. This feature is important for the interpretation of silica pathways in the palaeobasin.

Statistical processing of c. 200 records of 200–600 mesobands each has demonstrated (Kulik 1986, 1991) that thicknesses of *Q*, *F* and *S* mesobands in the *f*-members vary between 0.5 and 50 mm, while that of *M* (or *MS*) mesobands varies from 5 mm to 40 cm and more. Thicknesses of *Q* and *F* mesobands typically show a bimodal or left-skewed distribution (Fig. 8a & b). Thin (0.5–5 mm) *cyclic* mesobands comprise the majority (modal peak on the histogram), while a few thicker *anomalous* bands (7–70 mm) from the wide low peaks or long tails on the right side of the distribution curves. The *anomalous* mesobands also strongly differ in their inner texture and composition from the cyclic thin *Q* and *F* mesobands. On this basis, two additional types of *Qa* and *Fa* mesobands were recognized with thicknesses in the range 10–100 mm. Thicknesses of *S* interbands often show normal distributions, while *M* mesobands are closer to the polymodal or uniform distribution (Fig. 8c & d).

Plots of average thickness and volume fraction of mesobands across lithofacies profiles of the *f*-members (Kulik 1986, 1991) show that the proportions of mesoband types in the rock vary according to the BIF facies change (Fig. 9). Thicknesses of *Q*, *S* and (carbonate) *M* mesobands are maximal at the transition between the *f*- and *s*-members. A striking feature of nearly all records from all *f*-members is the constant mean thickness of the magnetite *F* mesobands (about 3–4 mm) while thicknesses of other mesoband types vary significantly across facies profiles and along strike. Together with polyhedral textural patterns of magnetite in the *F* mesobands, this may lead to important implications on its origin (see below).

On the above basis, the mesobanding can be divided into three rhythmical components (Kulik 1991); *cyclic contrast* (intermitting *Q*

and *F* mesobands), *cyclic uniform* (microbanded *M*, *FM* or *MS* mesobands), and *event asymmetric* (*Qa-S-Fa*, *Qa-Fa-S-Fa*, *Qa-Fa-S*, *S-Fa*, *Qa-Fa*, *S-Qa* rhythms). It has been found that up to 90% of event asymmetric rhythms are built around the *S* interbands. In about 80% of cases, a thick anomalous *Qa* band underlies the *S* interband, and the *Fa* band overlies it with 65–70% probability. Where *S* interbands are frequent (carbonate and silicate BIF facies), the event asymmetric rhythms seem to interfere and the pattern of mesobanding becomes quite irregular (Fig. 10). However, the asymmetry of such rhythms in the oxide facies BIF rocks is so persistent in the Krivoy Rog basin that it was possible to restore the stratigraphically correct sequence of completely mixed pieces of drilling core, using the asymmetric rhythms in order to find the top of each 20–40 cm long piece.

Microbanding. Microbanding is most distinct in some magnetite–hematite–quartz *M* mesobands, where it resembles annual varying. Each microband consists of iron-rich and quartz-rich laminae of similar thickness of 0.05–0.2 mm. In *Q*, *F* and *MS* mesobands, the internal layering also is often detectable; some of them reveal 6–14 residual microbands. Fe-rich microlayers, as a rule, are three to five times thicker in *F* bands, and three to ten times thinner in *Q* bands relative to quartz-rich laminae. The mineral composition of micro-mesobands depends on the BIF facies and metamorphic grade, according to the diagram of Klein (1983). The higher the metamorphic grade (and degree of recrystallization), the poorer is the preservation of microbands, until they become invisible in the BIF rocks of amphibolite facies (Pravoberezhny area).

It is problematic to assess the lateral continuity of microbanding because of widespread multi-order folding and lateral facies changes in the Saxagan Group rocks. A two- to three-times increase in thickness of mesobands in the core of a fold relative to its limbs (Fig. 11) is quite typical for the Krivoy Rog BIF. It is related to plastic flow of the BIF rocks during progressive metamorphic stages under tectonic stress (cf. Pirogov *et al.* 1989). *S* interbands present in the fold cores may be cut or distorted by sliding along them in the fold wings (Fig. 11a). Often, microbands may be visible only in the fold cores, while totally hidden in the *F* mesobands in the fold limbs (Fig. 11b); typical is a lateral transition of *M* to *F* mesobands at the expense of redistribution of SiO₂. An implication of these facts is that the mean thickness of *Q* and *M* mesobands depends on the position of a

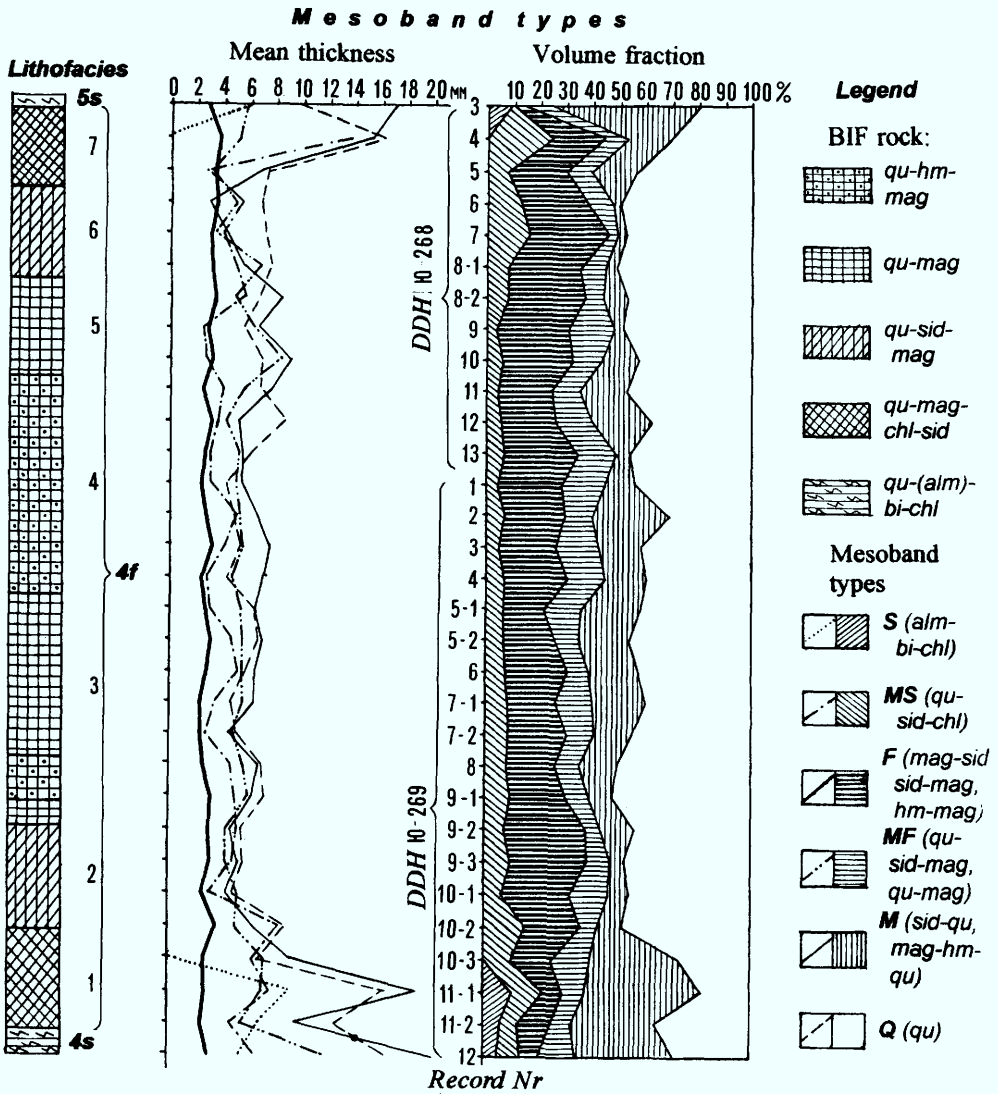


Fig. 9. Variations of mean mesoband thickness and volume fraction of mesobands in a lithofacies profile of the 4f member (Skelevat Magnetite deposit). Abbreviations of mineral names are the same as on Fig. 7.

recorded section relative to larger-scale folds. Hence, this parameter is not correlative in the Krivoy Rog basin (Kulik 1991), unlike that in the Hamersley basin (cf. Trendall & Blockley 1970; Morris 1993).

Since it is very difficult to determine the chemical composition of a single microlayer or microband, we used the petrographically measured mineral composition of the microbanded mesobands in order to estimate the quantities of iron m_{Fe} and silica m_{SiO_2} per unit area of a microband, using the approach of Trendall &

Blockley (1970). The following formula was used for calculations (Kulik 1986):

$$m_i = \frac{H}{n} \sum_j^L C_j \rho_j a_{ij} = h^* \rho^* w_i,$$

where i is an index of a chemical component in question, m_i is mean mass of the chemical component per unit area of mesoband, j indexes a rock-forming mineral ($j = 1, \dots, L$), H is thickness of a mesoband, n is number of microbands visible within a mesoband, h^* stands for the

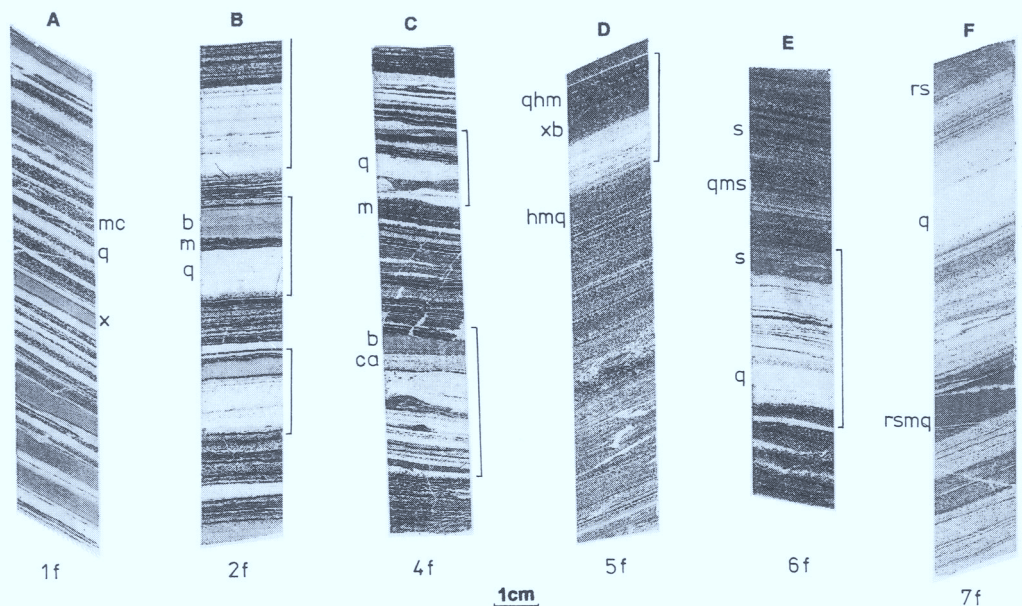


Fig. 10. Typical textural patterns of the micro- and mesobanded rocks from the *f*-members of the Saxagan Group. Photograph of streak-prints prepared according to Morris & Ewers (1978). Samples: A, mesobanded magnetite-chlorite-siderite rock, 1*f* member; B, magnetite quartzite with biotite *S* interbands and *Qa* mesobands, 2*f* member; C, magnetite quartzite, 4*f* member; D, hematite-magnetite jaspilite, 5*f* member; E, stilpnomelane-magnetite quartzite, 6*f* member; F, riebeckite-stilpnomelane-magnetite-quartz rock, 7*f* member. Straight quotes mark the anomalous mesorhythms. Lower-case letters denote minerals: *h*, hematite; *m*, magnetite; *c*, carbonate; *q*, quartz; *x*, chlorite; *b*, biotite; *a*, albite; *r*, riebeckite; *s*, stilpnomelane.

mean thickness of microbands within a mesoband, C_j is volume content of a mineral in the mesoband, ρ_j is density of a mineral, ρ^* is mean density of a mesoband, a_{ij} is weight content of a chemical component in the mineral (Table 3), a_i is weight content of a chemical component in the mesoband. Relative uncertainty of such estimates is about 10–15%. Figure 12 represents plots for 130 mesobands from all varieties of ferruginous quartzites of the Skelevat Magnetite deposit (4*f* member). Note the wide variation in m_{Fe} values for *F* mesobands and in m_{SiO_2} values for *Q* mesobands, while moderate scatter exists between 4 and 70 mg cm^{-2} for both parameters in the microbanded *M* mesobands. This may have an important effect on the interpretation of deposition rates and post-sedimentary transformations of BIF.

Structures distorting the mesobands. Many structures of presumably sedimentary-diagenetic origin affect micro- and mesobanding in the BIF cores and outcrops (Fig. 13). Tectonometamorphic structures like multi-order folding (see Fig. 11; Kulik & Chernovsky 1996) are also common. Microfolding often occurs only within microbanded *M* mesobands while it is absent in

adjacent *Q* or *Qa* bands, especially in magnetite quartzites of the 2*f* member in the southern part of the Krivoy Rog basin. Typical boudinage of *Q* or *F* mesobands (or even series of bands) occurs mainly in the monoclinical northern and southern parts of the basin. Tectonometamorphic structures usually can be identified microscopically from recrystallization patterns of quartz, magnetite or carbonates. Metamorphic banding, or 'pseudo-lamination', cutting primary banding, is often found in thicker chlorite-biotite *S* bands in silicate facies BIF (Kulik 1986).

Podding and thinning-out of *Q* mesobands are very common for the Krivoy Rog BIF rocks of oxide and carbonate facies. They are especially well-preserved in the Kremenchug area deposits (Fig. 13). Many of them indicate the centimetre-scale mobility of silica at diagenetic to anchimetamorphic stages. *Q*-bands at different levels compensate each other to maintain the constant thickness of the package and continuity of *F* microbands. Intra-band breccias, slumping, stylolites and micronodules (probably early diagenetic) were also encountered. Those structures, unlike tectonometamorphic ones, show no recrystallization of quartz and ore minerals,

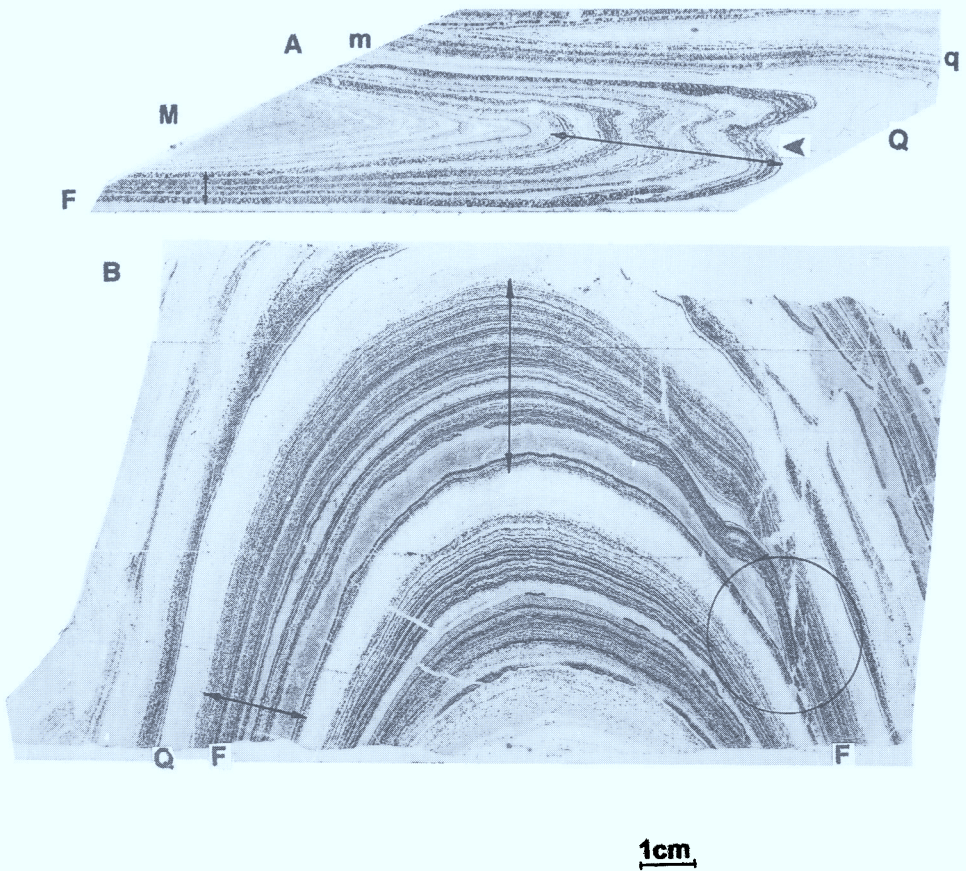


Fig. 11. Variations of thickness along strike in folded mesobands (photograph of streakprints). Samples: A, riebeckite-hematite-magnetite quartzite, 6f member, Saxagan district; B, chlorite-siderite-magnetite quartzite, 4f member (courtesy of B. A. Zankevich). Upper-case letters denote the mesoband types (see text). Pointer shows the microfolding and distinct microbanding in the core of a fold not visible on the limbs. Circle marks the area where sliding occurred along the *S* interband. See caption to Fig.10, for mineral symbols.

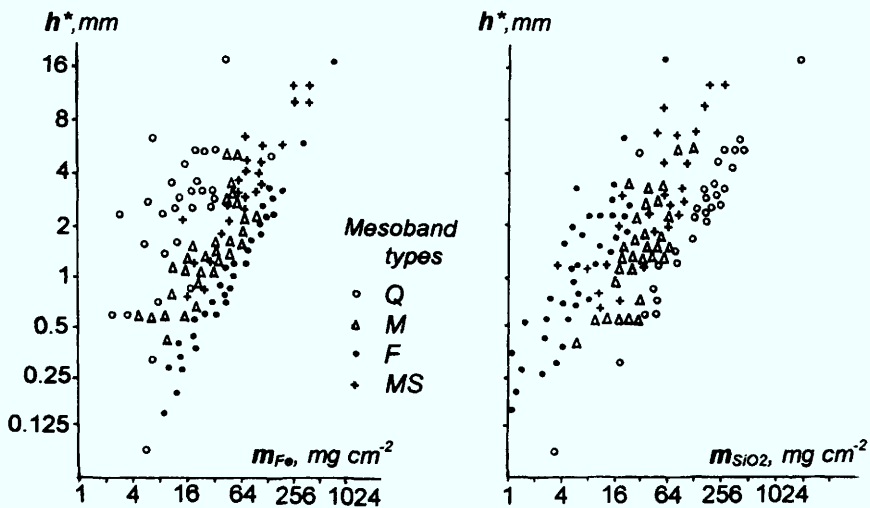


Fig. 12. Plots of mean microband thickness h^* versus the m_{Fe} and m_{SiO_2} parameters measured for 130 microbanded mesobands from ferruginous quartzites (4f member) from the Skelevat Magnetite deposit.

Table 3. Typical chemical compositions of the rock-forming minerals from ferruginous quartzites and schists of the Krivoy Rog basin

Mineral	Unit	SiO ₂	TiO ₂	Al ₂ O ₃	Fe ₂ O ₃	FeO	MnO	MgO	CaO	Na ₂ O	K ₂ O	CO ₂ + H ₂ O+ LOI	Total	Ref
Magnetite	1f	0.81	0.18	0.22	67.55	30.18	<0.01	0.51	0.06	-	-	-	99.51	20-5
Magnetite	2f	0.49	0.01	0.52	68.78	29.89	0.01	0.31	0.18	-	-	-	100.19	20-13
Magnetite	4f	0.63	0.11	0.29	68.12	30.04	<0.01	0.29	0.06	-	-	-	99.54	20-7
Magnetite	5f	0.86	0.04	0.22	68.26	30.32	0.01	0.23	0.06	-	-	-	100.00	20-4
Magnetite	6f	1.42	0.01	0.60	69.08	28.31	0.01	0.28	0.25	-	-	-	99.96	20-18
Hematite	1f	1.33*	0.45	0.41	95.97	0.58	<0.01	0.17	0.42	-	-	-	99.33	23-18
Hematite	4f	0.82*	0.04	0.66	96.46	1.14	<0.01	0.38	0.32	-	-	-	99.82	23-21
Quartz†	1f	99.73	-	-	-	0.2	0.0008	0.05	0.02	-	-	-	100.00	28-4
Quartz†	4f	99.77	-	-	-	0.2	0.0005	0.02	0.015	-	-	-	100.00	28-5
Quartz†	5s	99.90	-	-	-	0.08	0.0006	0.03	0.015	-	-	-	100.00	28-6
Siderite	4f	-	-	-	-	51.5	0.85	6.8	0.85	-	-	40.0	100.00	73-13
Siderite	4f	-	-	-	-	53.5	1.0	5.9	-	-	-	39.6	100.00	73-14
Siderite	5s	-	-	-	-	46.7	0.9	10.3	1.1	-	-	41.0	100.00	73-16
Dolomite	4f	<0.1	0.07	0.24	0.54	7.47	0.14	18.76	28.70	-	-	44.22	100.14	73-29
Dolomite	gd	2.74	0.02	0.31	0.55	-	0.12	18.47	32.42	-	-	44.91	99.54	73-31
Grunerite	2f	47.74	-	1.29	3.76	34.56	0.16	8.66	1.26	0.02	0.10	2.84	100.39	48-10
Grunerite	6s	50.61	0.21	0.99	2.78	37.92	0.23	5.89	0.39	0.09	0.09	1.24	100.44	48-20
Ripidolite	s	26.07	0.70	27.29	2.89	22.10	-	11.56	0.19	-	-	9.33	100.13	67-8
Thuringite	s	27.48	0.62	17.29	6.30	31.95	0.03	6.14	0.20	0.22	1.66	8.11	100.00	67-10
Thuringite?	f	31.14	0.57	18.28	5.13	27.70	0.01	5.77	0.09	0.34	4.26	6.65	99.94	67-11
Biotite,hydr	5f	42.12	0.45	15.37	7.57	16.23	0.08	6.66	0.34	0.05	3.68	7.84	100.39	59-81
Biotite?	s	35.94	1.30	17.81	3.54	17.82	0.03	10.37	0.23	0.20	7.70	4.51	99.45	59-77
Stilpnomelane	6f	37.42	0.24	6.28	10.70	17.52	0.12	13.46	0.98	0.05	7.72	4.86	99.35	64-5
Almandine	s	38.63	0.42	19.46	0.12	36.02	0.45	1.08	2.52	0.65	0.25	0.50	100.10	40-47
Almandine	s	40.69	0.07	18.32	0.95	33.29	0.70	1.61	1.26	0.85	0.40	1.68	99.82	40-50
Chloritoid	4f	25.24	0.16	39.00	1.47	24.43	0.01	2.42	0.25	0.18	0.10	6.92	100.18	66-2
Chloritoid	4s	33.09	0.46	34.32	1.33	22.12	0.03	2.21	0.23	0.11	0.18	5.85	99.93	66-4

Compiled from data of Lazarenko (1977), wet chemical analyses of monomineral samples, wt%.

LOI, loss on ignition.

References (Ref column) are in the form X-Y, where X is table no. and Y is column no. in Lazarenko (1977).

* Marked in the source table as 'insoluble residue'.

† Results of quantitative flame spectrometry analysis, recalculated to wt% of oxides, SiO₂ content calculated by difference from 100%.

? Uncertain identification of a mineral: thuringite is closer in composition to a hydrated biotite (next row); biotite has a composition similar to stilpnomelane.

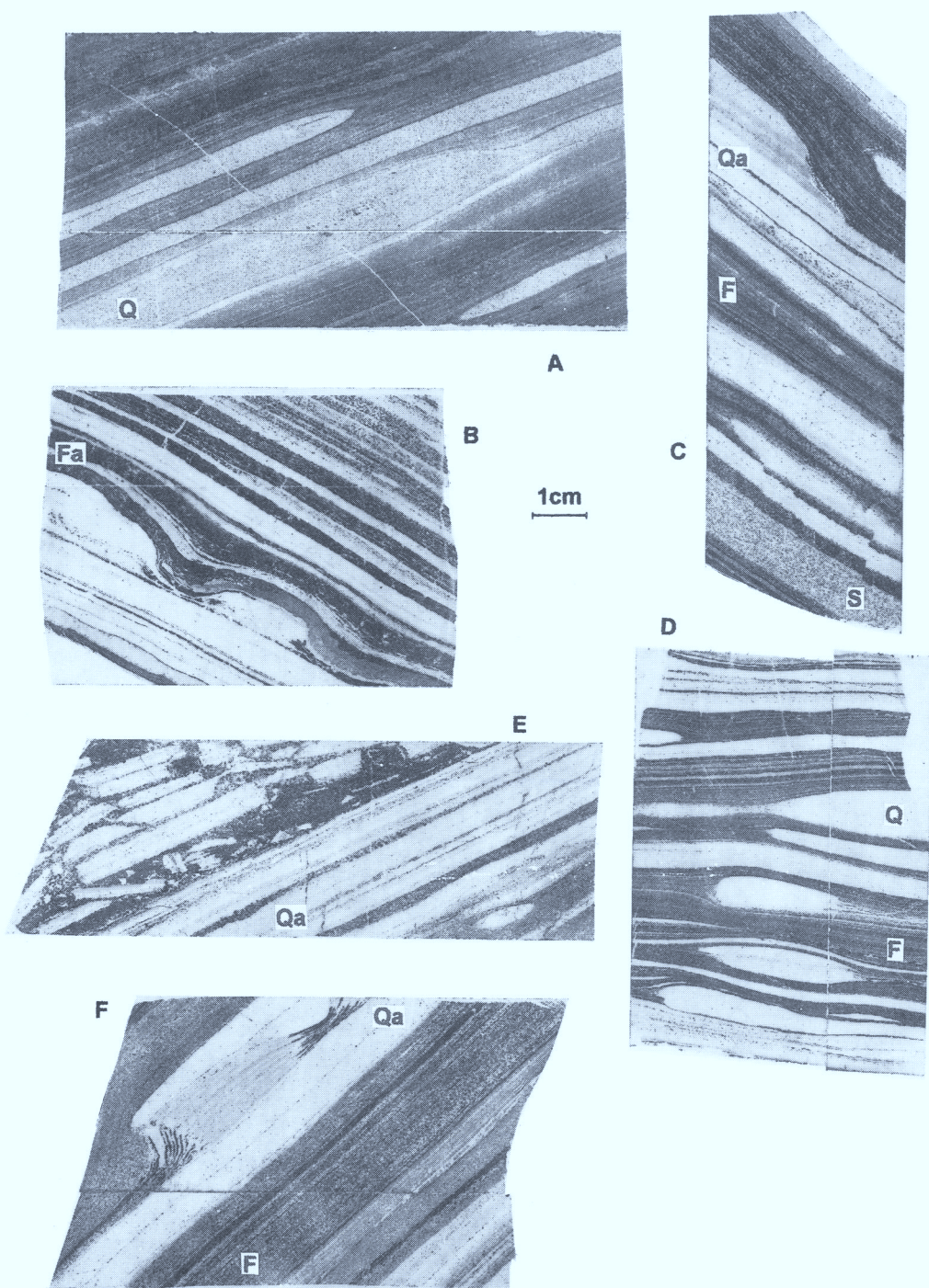


Fig. 13. Examples of sedimentary–diagenetic structures from the BIF rocks of the Saxagan Group (Kremenchug area). Photograph of streak-prints. Samples: A, compensated thin-outs of *Qa* mesobands in magnetite–riebeckite–ferriannite–grunerite–quartz rock; B, podding or slumping of *Qa* mesoband in siderite–magnetite quartzite; C, compensated thinnings of *Qa* mesobands, cummingtonite–magnetite quartzite; D, podding and thin-outs of *Q* mesobands in hematite–magnetite quartzite; E, intraband breccia of *Qa* mesobands in siderite–magnetite matrix; F, pocket-like structure in a red *Qa* mesoband with continuous Fe-rich microbands in magnetite–siderite quartzite. Letters denote the principal mesoband types.

although they indicate the early lithification of *Q* and *Qa* bands relative to *F* or *M* mesobands. Unlike in the Lake Superior BIF or Labrador Trough BIF (e.g. Klein 1983), no oolites, granules, desiccation cracks, wavy- and cross-bedding have been found in ferruginous rocks of the Krivoy Rog basin.

Mineral composition and mesoband textures

Mineralogical studies (Lazarenko 1977; Pirogov *et al.* 1989) point out that several generations of quartz, hematite, magnetite, Mg-Fe and Ca-Mg carbonates, Mg-Fe and Mg chlorites, biotite, stilpnomelane exist as main minerals of green-schist facies BIF in the Krivoy Rog basin; apatite, graphite, riebeckite, sericite, albite, aegirine, pyrite, pyrrhotite are often detected as trace minerals. Almandine, cummingtonite and actinolite are typical for higher-metamorphosed BIF in the southern and northern monoclinical parts of the basin as well as in the Kremenchug area. Metamorphic reactions in the BIF rocks have been extensively studied by Mel'nik (1982). Magnetite, pyrite, Fe(II) carbonates and silicates are replaced by dispersed iron oxides and clay minerals in weathered parts and in high-grade iron ores, while banding is usually well preserved there.

The least-metamorphosed *Qa*, *Q* and *M* bands reveal the typical granoblastic quartz aggregates with fine quartz-I grains (5–50 μm size) filled with the emulsoid hematite, chlorite, siderite and probably graphite (all grain sizes <5 μm). They underwent metamorphic recrystallization into mosaic textures with pure quartz-II grains (0.05–1 mm), euhedral magnetite, ankerite or sideroplesite (0.1–2 mm). The granoblastic textures of all *Q* and *Qa* mesobands do not permit to call them *chert* mesobands like in the very low-metamorphosed BIFs; instead, we have to use the petrographically correct terms *quartzite* for single bands and *ferruginous quartzite* for the BIF rock as a whole. The relict 'emulsoid' minerals are also found as poikilitic inclusions in albite grains from *S* interbands. Some magnetite *M* and *F* mesobands consist of magnetite microconcretions, polyhedral chains or stripes that apparently grew over the initial hematite microbands, similar to that described by Han (1978) and Morris (1993) in other BIFs. The subsequent metamorphic recrystallization transformed these overgrowths into a variety of coarse polyhedral magnetite, specularite and siderite aggregates. The average grain size in *F* mesobands is 0.1–1.0 mm while 0.002–0.01 mm in adjacent *Q* bands. Sparse magnetite porphyroblasts up to 5 mm in size are typical in *MS*

and *S* interbands in silicate facies BIF, especially in the *6s* member of the Saxagan Group.

Considerable work was carried out in determining the chemical composition of main minerals comprising the BIF rocks in the Krivoy Rog basin (Lazarenko 1977). In the context of this paper, the questions of interest are: how is Mn distributed between Mg-Fe minerals; which minerals are the hosts for Al, K and other elements of possible clastic origin. Table 3 summarizes the available data (though not always of high quality); their significance will be discussed later.

Chemical features of BIF rocks

The bulk chemical composition of the Krivoy Rog BIF (Table 4), similar to its counterparts in other palaeoproterozoic basins, is different from the composition of other sedimentary, metamorphic or magmatic rocks. Its main feature is a predominance of iron (formally >15% Fe) at quite low contents of Al, Ca, Ti, Na, K relative to 'normal shale' or average igneous rocks. The predominance of Mg over Ca, and K over Na is also characteristic (Mel'nik 1982, 1986). The rocks of the *f*- and *s*-members differ mainly in their Fe(III) and Al contents. Comparison of chemical features in the Krivoy Rog BIF is most informative in the lithofacies profile from phyllitic schist through ferruginous schist to silicate-, carbonate-, magnetite- and hematite-ferruginous quartzites. In such a profile, most components show an ordered distribution according to a decrease in siliclastic and an increase in primary chemogenic components (cf. Plaksenko 1966; Belevtsev *et al.* 1983).

Distribution of chemical components in the facies profile. A lithofacies profile through the *4f* member is a particularly good example for the ordered distribution of components. It was extensively studied in the Skelevat Magnetite deposit, where the *4f* member reaches its maximum thickness and is subdivided into seven sub-members numbered upwards (Shaposhnikov 1978). This sequence represents a complete lithofacies profile from garnet-chlorite-biotite schist with thick clean quartzite interbands (*4s* and *5s* members) to the hematite-magnetite quartzite (*4f* unit) in the middle of the *4f* member profile (Fig. 14). The regularities visible in this figure are basically the same for all BIF horizons in the Saxagan suite, though in the *5f* member the facies cycle is asymmetric with reduced thickness of the lower part. The *6f* and *7f* members each include up to five cycles

Table 4. Composition of principal varieties of BIF rocks of the Krivoy Rog and Kremenchug structures (compilation of data from Semenkenko 1978)

	SiO ₂	TiO ₂	Al ₂ O ₃	Fe ₂ O ₃	FeO	MnO	MgO	CaO	Na ₂ O	K ₂ O	S	P ₂ O ₅	CO ₂	LOI	Total	Unit	Ref
1	38.84	0.04	0.40	36.61	16.48	0.08	2.02	1.89	0.15	0.33	0.18	0.15	2.16	0.88	100.21	5f	5-3
2	37.95	0.06	0.31	36.55	15.80	0.05	1.80	1.30	0.10	0.09	0.04	0.21	3.58	3.26	101.10	4f	116-5
3	36.21	<0.01	0.48	41.06	18.54	0.05	2.05	0.68	0.28	<0.03	-	0.26	-	-	99.61	6f	105-4
4	36.72	0.07	0.70	30.42	18.50	0.09	3.04	0.90	0.14	0.12	0.06	0.21	6.61	1.19	98.77	4f	116-3
5	42.00	<0.01	1.10	21.90	19.50	0.15	3.75	1.90	0.07	0.17	0.19	0.16	9.00	0.29	100.18	2f	105-7
6	51.69	0.02	0.60	21.30	16.16	0.06	3.03	1.30	0.85	0.51	<0.01	0.11	4.10	0.62	100.35	6s	105-8
7	57.60	0.03	0.49	23.10	14.08	0.15	1.20	0.28	0.28	<0.03	0.17	0.09	2.32	1.12	100.91	6f	105-9
8	51.00	0.04	1.63	17.04	18.96	0.13	2.38	2.20	0.15	0.32	0.11	0.13	1.36	0.09	95.54	1f	105-11
9	36.00	0.25	4.60	18.54	19.20	0.08	2.17	0.60	0.28	0.10	-	0.40	7.52	8.61	98.35	6f	105-12
10	50.79	0.04	0.84	18.42	18.45	0.08	2.90	1.51	0.16	0.70	0.12	0.20	5.21	0.18	99.60	7f	105-13
11	51.65	-	1.48	19.95	13.18	0.14	4.18	1.74	-	0.36	0.38	-	4.05	2.15	99.26	6s	105-14
12	46.97	0.16	1.50	14.08	21.88	0.07	6.39	0.18	0.31	1.13	0.10	0.14	1.96	4.30	99.17	7s	105-15
13	55.07	-	2.45	15.16	13.14	0.08	4.14	1.31	0.27	0.63	-	0.27	3.90	2.20	98.61	7s	105-16
14	27.30	0.39	8.50	2.91	30.38	0.59	8.64	0.36	0.04	0.43	0.48	0.24	16.44	4.13	100.83	2f	105-17
15	63.96	0.39	0.71	8.82	19.97	0.02	3.11	0.46	0.26	0.16	0.09	0.09	0.44	1.65	100.13	6s	105-18
16	61.49	0.12	1.41	6.71	20.59	0.15	3.60	1.07	0.24	0.74	0.27	0.28	1.61	1.27	99.55	6s	105-19
17	41.08	0.03	0.62	36.53	15.53	0.14	1.98	1.47	0.03	0.35	0.07	0.18	2.03	0.69	100.73	27	67-1
18	43.89	0.08	1.83	26.04	17.62	0.14	2.76	1.77	0.08	0.41	0.18	0.19	2.60	1.52	99.11	36	67-2
19	50.42	0.07	1.34	17.34	19.29	0.12	4.79	1.75	0.07	0.34	0.12	0.08	3.01	1.05	99.79	27	67-6
20	50.34	0.12	1.86	8.65	23.17	0.12	4.42	3.90	0.05	0.30	0.12	0.12	5.42	1.14	99.73	8	67-5
21	49.13	0.19	6.94	5.14	27.25	0.16	2.61	0.79	0.14	0.62	0.13	0.10	3.02	3.33	99.55	7	67-3
22	51.13	0.05	8.21	6.12	23.52	0.17	4.24	1.77	<0.03	0.45	0.18	0.15	2.07	2.28	100.34	8	67-4

Krivoy Rog structure (samples): 1-7, (silicate)-(hematite)-magnetite quartzites; 8-13, magnetite-silicate-carbonate quartzites; 14-16, magnetite-carbonate silicate quartzites. Kremenchug structure (averages for lithologies, *N* of samples in the Unit column): 17, hematite-magnetite jaspilite; 18, magnetite quartzite; 19, carbonate-grunerite-magnetite quartzite; 20, magnetite-grunerite-carbonate quartzite; 21, quartz-chlorite ferruginous schist; 22, chlorite-carbonate ferruginous schist. LOI, loss on ignition, incl. H₂O.

References (Ref column) are in the form X-Y, where X is table no. and Y is column no. in Semenkenko (1978).

ranging from silicate to oxide (magnetite) facies. The corresponding sub-members are, however, laterally unstable and grade into each other at distances of 200–2000 m. The sections of *s*-members of the Saxagan Group cover either

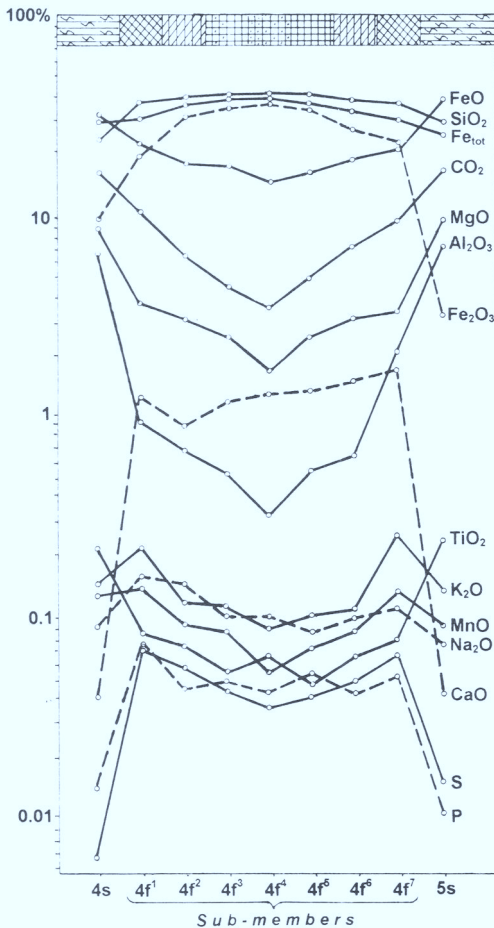


Fig. 14. Variation of chemical components in the cross section of 4f BIF member at Skelevat Magnetite deposit. Compiled from data of Shaposhnikov (1978). See legend to Fig. 9.

a complete facies profile (metasandstone–phyllitic schist–‘aspid’ schist–(garnet)–chlorite–biotite schist–interbedded quartzite + chlorite schist–silicate facies BIF) like in the 1s, 2s, 3–4s members, or only the last two parts of the profile as in the 6s and 7s members.

On the basis of statistical analysis of a vast array of geochemical data, Lizko (1979) has shown that the average contents of some main and trace elements in the ferruginous quartzites of *f*-members display a persistent change in the stratigraphic section of the Saxagan Group (Table 5). Notwithstanding the predominance of carbonate and silicate facies in 6f and 7f members, they show the least contents of Al, K, Mg, Mn, P, S compared to 1f and 2f members.

Distribution of Mn in BIF rocks and minerals. Little attention was paid to the Mn distribution in BIF of the Krivoy Rog basin; to date, no studies of the Mn geochemistry have been conducted in the region, probably because of the low content of Mn. Concentrations of Mn in the bulk unweathered ferruginous quartzites are typically highest in the chlorite–siderite varieties (0.1–0.4 wt%) and lowest in the hematite–magnetite jaspilites (0.01–0.04 wt%). This change in Mn content is weakly correlated with variations in CO₂ and MgO concentrations in the facies profile (Fig. 14).

Our chemical data for single *S*, *MS*, and *F* mesobands (Table 6) suggest that unlike Al, Ti and Zr, Mn is not enriched in chlorite–biotite or quartz–sericite schists or *S* interbands, but is closely bound to the significant content of Fe–Mg carbonate. This is supported also by the available data on Mn contents in rock-forming minerals of the BIF (see Table 3). Hematite, magnetite and quartz always contain very low amounts of Mn, which are less than 0.01%. Siderite and sideroplesite contain 0.2–2.6 mol% Mn, 0.1–1.8 mol% Ca and up to 15% Mg (see also Mel’nik 1986). Since 0.4% of Mn in the bulk rock roughly corresponds to 30% of sideroplesite containing 1.3% Mn, all three

Table 5. Variations of minor components in the unweathered ferruginous quartzites of *f*-members of the Saxagan Group in the Krivoy Rog area

BIF	Al ₂ O ₃	MgO	CaO	K ₂ O	Na ₂ O	Mn	P	S	Cu	Ni	Ti	Cr	Zn
1f	1.62	3.07	0.93	0.87	0.12	1500	840	870	10	10	100	4	30
2f	1.30	2.77	1.32	0.32	0.13	1800	780	680	20	5	60	Tr	30
4f	0.91	3.15	1.26	0.13	0.12	500	430	620	10	4	70	3	30
5f	0.83	1.55	0.74	0.15	0.23	270	320	530	13	10	24	3	30
6f	0.70	1.74	0.87	0.27	0.20	300	300	500	10	5	50	5	20
7f	0.48	1.22	0.61	0.30	0.12	300	180	570	13	6	90	Tr	20

Averages for members of the Saxagan Group, compiled from data of Lizko (1979).

Contents of Al₂O₃; MgO; CaO; K₂O; Na₂O are given in wt%, Mn; P; S; Cu; Ni; Ti; Cr; Zn, in ppm; Tr, trace concentrations.

Table 6. Chemical composition of single mesobands in comparison with whole-rock analyses and average composition of stratigraphic units in the Krivoy Rog BIF

Type, unit	SiO ₂	TiO ₂	Al ₂ O ₃	Fe ₂ O ₃	FeO	MnO	MgO	CaO	Na ₂ O	K ₂ O	P ₂ O ₅	CO ₂	H ₂ O+ LOI	S	Total	Ref
Qa	86.58	0.01	0.46	5.31	2.58	0.06	0.60	1.97	0.20	0.10	0.06	2.02	0.06	0.15	100.16	1
Fa	10.31	0.04	0.30	56.24	25.70	0.08	2.28	0.98	0.24	0.12	0.46	3.54	Tr	0.05	100.35	1
F	21.77	0.10	6.07	25.09	17.71	0.28	10.58	0.65	1.72	0.82	0.30	12.95	1.99	0.70	100.38	1
F	11.28	0.13	1.39	7.15	44.35	0.16	4.57	0.32	0.24	0.80	0.09	29.30	0.23	0.05	100.04	1
SF	43.00	0.11	2.33	12.20	25.00	0.11	3.10	0.65	0.24	2.32	0.09	8.96	1.45	0.03	100.22	1
S	38.06	0.47	15.86	2.85	27.20	0.04	5.03	0.55	0.20	1.10	0.11	2.74	5.96	0.03	100.20	1
S	41.98	0.74	16.91	6.98	16.70	0.07	6.00	Tr	0.32	3.08	0.09	3.78	3.83	0.01	100.43	1
2s	59.86	0.34	12.35	9.55	7.53	0.04	2.63	<0.1	*	2.77	0.14	†	4.74	0.1	100.05	2
4f ³	37.14	0.05	0.52	34.87	17.43	0.08	2.53	1.22	0.11	0.11	0.11	4.51	1.35	0.05	100.06	3
Sx	46.60	0.19	4.87	28.02	11.81	0.08	1.67	0.90	0.34	1.59	—	3.19	—	—	100.0	4

Content of C_{free}: Qa, 0.16%; SF, 0.64%.

Qa, red quartz mesoband with minor ankerite, graphite; magnetite BIF, 4f member, Skelevat Magnetite deposit; Fa, magnetite mesoband with minor quartz and siderite, magnetite BIF, 4f member, Skelevat Magnetite deposit; F, siderite-magnetite mesoband with biotite and albite, Skelevat Magnetite deposit; F, magnetite-siderite mesoband with minor biotite, carbonate BIF, 5f member, Saxagan district; SF, stilpnomelane-siderite interband, carbonate-silicate BIF, 7f member, Saxagan district; S, biotite-chlorite interband, silicate-carbonate BIF, 2f member, Saxagan district; S, biotite-chlorite interband, silicate-carbonate BIF, 5f member, Saxagan district; 2s, chlorite-quartz-biotite schist, 2s member, Saxagan district; 4f³, average for 4f³ submember, magnetite quartzite, Skelevat Magnetite deposit; Sx, average for the whole Saxagan Group.

Tr, trace.

* Alkalis are given as the sum of Na₂O and K₂O.

† CO₂ is included into loss on ignition.

References: (1) our data (Belevtsev *et al.* 1992); (2) Belevtsev & Belevtsev (1981); (3) Shaposhnikov (1978); (4) Plaksenko *et al.* (1988).

figures seem quite consistent for the rocks in question. Metamorphic minerals grunerite and almandine contain 0.1–1% Mn. Since the only diagenetic phase enriched in Mn is Mg-Fe-carbonate, this is an indirect evidence of formation of almandine and grunerite in reactions involving siderite. Mn content is lowest (0.01% or less) in the hematite/magnetite *F* and *M* mesobands (where Fe(III) hydroxide was the most probable initial precipitate); slightly higher Mn contents are due to the presence of Ca-Mg carbonate.

Variations of contents and isotopic composition of sulphur and carbon. Free carbon in the rocks of the Saxagan Group exists in the form of disordered graphite (the so-called 'graphitite', Lazarenko *et al.* 1977), either forming micro-layers or being disseminated in garnet-biotite schists or *S* interbands. The C_{Free} content varies between 0.01 and 0.7 wt%, with maximum concentrations in some *S* interbands in silicate facies and, very low contents in carbonate and oxide facies BIF (Mel'nik 1982, 1986). There is general opinion (based on isotope composition) that this carbon is of primary biogenic origin (hence denoted as C_{org}) (e.g. Schidlowski 1982). Sulphide is distributed in the lithofacies profile similarly to carbon, occurring mainly as fine-grained pyrite in black shales or *S* interbands, with bulk rock concentrations between 0.003

and 0.8%. In the southern and northern monoclinical parts of the Krivoy Rog basin where the rocks are metamorphosed to epidote-amphibolite grade, pyrite is replaced by well-crystallized pyrrhotite, distributed mainly in thin layers or veins. The oxide facies hematite-magnetite jaspilites are essentially free of both C_{org}, P and sulphides.

The sulphur isotope composition in pyrite shows the persistent change in the stratigraphic section of the Krivoy Rog Supergroup, being quite similar in the Krivoy Rog and the Kremenchug areas (Fig. 15). The δ³⁴S in sulphides from amphibolites of the New Krivoy Rog and from phyllitic and black schists of the Skelevat Group are close to the meteorite standard. In pyrites from the Saxagan Group rocks, δ³⁴S varies wider with up to -12.0‰ in magnetite quartzites. In pyrites from carbonaceous schists of the Gdantsev and Gleevat Groups, very scattered positive δ³⁴S (median value +17‰) have been detected (Savchenko 1991; Korzhnev & Fomin 1992).

Isotopically light carbon (PDB δ¹³C of -20 to -24‰) is measured in graphite, while intermediate values of δ¹³C of -10 to -13‰ are typically found in Mg-Fe carbonates from the BIF rocks. 'Normal marine' δ¹³C of -3 to +2‰ occurs in some Gdantsev Group carbonate rocks of the Krivoy Rog basin, while very light δ¹³C of -30 to -42‰ was measured in graphite

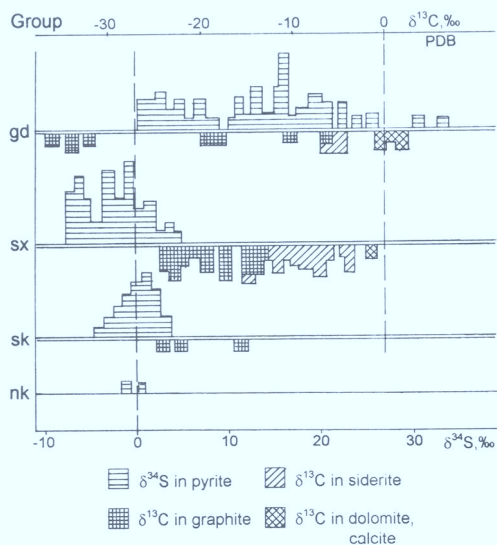


Fig. 15. Isotopic composition of sulphur from pyrite and carbon from graphite and carbonates from the metasedimentary rocks of the Krivoy Rog Supergroup (Krivoy Rog and Kremenchug areas). Replotted from data of Savchenko (1991). Stratigraphic symbols are the same as on Fig. 2.

from the adjacent carbonaceous schist (Fig. 15). This fits well to the data on other BIFs of same age (e.g. Baur *et al.* 1985; Perry & Ahmad 1981). An interpretation of these data in the context of depositional environment of BIF will be given below.

Inter-relations of siliciclastic and chemogenic components

Consideration of the above data suggests that the siliciclastic component is always present in variable quantities (from traces in hematite jaspilites to nearly 100% in phyllitic schists) throughout the BIF sequence of the Saxagan Group in the Krivoy Rog basin. Hence, the basic problem is how to discriminate the chemogenic and siliciclastic components in a given section or sample of the BIF rock. Because of the relatively high metamorphic grade this is not always possible; the geochemical evidence should be regarded as more preferable than petrographical ones in this case. The following facts could be taken as indications of a prevailing chemically precipitated component in the *F*, *M* and *Q* mesobands of ferruginous quartzites: (i) presence of microbanded (varved) distribution of quartz and iron minerals, resembling the evaporitic gypsum or carbonate sequences; (ii) chemical composition (major Fe, Si, O minor

Mg, Ca, C, Al, K, Na, Ti, Mn, P, S); (iii) much lower abundances of Al, Ti, Ca, K, Zr, S relative to *S*-interbands and schists from the adjacent *s*-members.

Evidence for the principally siliciclastic nature of phyllitic schists, ferruginous schists and aluminosilicate *S* interbands in ferruginous quartzites can be summarized as: (1) presence of clastic quartz grains in schists and small clastogenic zircons in all varieties of BIF rocks, and clear correlations between Al, Ti and K contents in the BIF mesobands (Fig. 16), suggesting variable but persistent presence of clastic components in all varieties of BIF rocks and mesobands; (2) gradual transitions from the oxide facies uniformly microbanded BIF units through the mesobanded oxide, carbonate, silicate BIF facies to the phyllitic or carbonaceous schist interbedded with clean quartzite, accompanied by the increasing contents of Al, Ti, K, Zr and other elements bound to aluminosilicate minerals or zircon.

Aluminosilicates in stratigraphic section of Saxagan Group. Notwithstanding the simple facies trend (see Fig. 14) elucidated from the composite or averaged whole-rock samples, the actual distribution pattern of aluminosilicate minerals at the centimetre to decimetre scale is very irregular and variable in the BIF rocks of the Saxagan Group, changing from *1f* to *7f* members (see Fig. 10). A striking feature of the BIF rocks of the Saxagan Group is that the bulk of aluminosilicate minerals occurs in the distinct

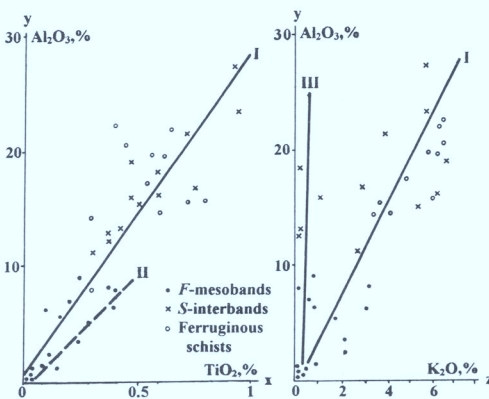


Fig. 16. Plots of Al_2O_3 versus TiO_2 and K_2O contents in *F* mesobands, *S* interbands and ferruginous schists (37 analyses total) from the Saxagan Group. Trend line I: samples from *1s*, *1f*, *2s*, *2f*, *4s*, *4f*, *5f* and *6s* members, correlation coefficient $r = 0.955$ (left graph) and $r = 0.53$ (right graph). Trend II: samples from *6f* and *7f* members; trend III: samples from *2f* member.

sporadic *S* interbands rather than in cyclically spaced microbands. *F*, *M* and *Q* mesobands in the *1f*, *2f*, *3f*, *4f*, *5f* and the lower part of *6f* members are nearly free of aluminosilicates. Only siderite-rich *M* (or *SM*) mesobands in the upper part of *6f* and in *7f* members contain a few percent of fine-grained annite, albite, stilpnomelane or biotite, though they are still concentrated in *S* interbands. Comparison of BIF banding between the Palaeoproterozoic Krivoy Rog basin and the Upper Archaean Byelozherka, Chertomyk and Kostomuksha deposits (Kulik 1991) demonstrates that *SM* or *MS* mesobands prevail in the latter, where biotite (or chlorite) forms the microlayers, either alone or together with siderite or magnetite comprising two- or three-component microbands.

In the BIF of the Saxagan Group (lower greenschist grade), four types of *S*-inter-bands can be distinguished by mineral paragenesis: (1) quartz–sericite, (pyrite)–graphite–quartz–biotite; (2) quartz–siderite–biotite–thuringite; (3) (albite)–(pyrite)–(magnetite)–chlorite–biotite–siderite; (4) (pyrite)–(graphite)–(stilpnomelane)–(riebeckite)–(albite)–(magnetite)–siderite–annite. The *S*-bands of type (1), grouped with thick *Qa*-bands ('clean quartzites'), are common in transition zones between *1s*, *2s*, *3s*, *4s* and *1f*, *2f*, *3f*, *4f* members, and throughout the *5s* and *7s* members. Some of type (1) *S* bands are under- and overlain by *S* bands of type (2), which are also widespread in the silicate- and carbonate ferruginous quartzites of *1f*, *2f*, *3f*, *4f* and *5f* members. Type (3) bands are typical for the carbonate–magnetite and magnetite quartzites in *2f* and *4f* members. In the *6f* and *7f* members they are replaced by type (4) *S* interbands. Since the four types of *S*-interbands can be readily distinguished macroscopically and petrographically, the described regularities are often used for the detailed stratigraphic correlations between the *f*- and *s*-members in different outcrops or drilling cores over the Krivoy Rog basin. Additional mineralogical and geochemical studies of *S* interbands and microbands are needed for a better understanding of the origin, conditions and depositional regime of the siliciclastic component in the BIF.

Discussion

Consideration of the above data on geological structure, composition and lithological features of the Krivoy Rog Supergroup metasediments suggests that the Skelevat and Saxagan Groups represent a single transgression–regression sequence. It started with the deposition of

alluvial fan conglomerates and gravelstones of the lower Skelevat Group, filling mainly the riftogenic deeps in the Archaean basement where tholeiites and basaltic andesites of the New Krivoy Rog Group had been already accumulated (Korzhnev & Pokalyuk 1993; see also Figs 1–3). Thereafter, sand, silt and mud were deposited in the entire basin, later transformed to metasandstones and phyllitic schists of the middle Skelevat Group. Some beds of these phyllites contain biotite, pyrite (with isotopically non-fractionated sulphur), and isotopically light graphite, indicating the restricted marine basin with terrigenous siliciclastic input, moderate bioproductivity and very weak sulphate reduction in sediments.

This sedimentation was interrupted by the deposition of a presumably ultrabasic volcanoclastic bed, now representing the carbonate–tremolite–talc schist unit of the upper Skelevat Group. This interpretation is supported by the fact that at the same stratigraphic level in the Inghoul–Inhoulets Supergroup, a meta-ultrabasic unit is present some 50–60 km NW off the northern part of the Krivoy Rog basin (Shcherbak *et al.* 1988), while in the SE part (eastwards of the Skelevat Magnetite deposit), the talc schists grade into phyllitic schist with thin lenses of metasandstones. The latter conformably grade into the typical quartz–sericite schist interbedded with thin bands of clean quartzite and ferruginous schist (the so-called *aspid schist*) of the *1s* member of the Saxagan Group, marking the beginning of BIF deposition.

Tectonic setting of the Krivoy Rog basin

In the Hamersley basin, the thicknesses of BIF and shale macrobands are very persistent, and even microbands can be traced for 150–300 km (Trendall 1972; Morris 1993). On the contrary, in the Krivoy Rog basin the *f*- and *s*-members often change in thickness at a short distance (see Fig. 3). Maximum thickness of the entire Saxagan Group occurs at the same localities where maximum thickness of underlying metabasites and metaconglomerates is recorded. This certainly indicates the active tectonic regime, suggesting that the deep-seated faults configuring the basin have also been active during BIF accumulation.

The following stages of tectonic development of the Krivoy Rog basin can be considered: (1) initiation of a rift at the margin of an Archaean plagiogranite–greenstone terrain traced by accumulation of the New Krivoy Rog mafic volcanics in a series of deeps; (2) renewal of the rift

fault systems and amalgamation of the deeps into a trough-like basin, where the transgressive sequences of the Skelevat and Saxagan suites were deposited; (3) beginning of orogenic movements of the granite–greenstone basement blocks with sedimentation of coarse-grained sediments of the Gdantsev and Gleevat suites. Before and after stage (1), two periods of tectonic uplift and stabilization marked by formation of palaeosols took place (Kulish *et al.* 1987; Kulik & Pokalyuk 1990).

The following facts support the above interpretation of the intracratonic trough-like Krivoy Rog palaeobasin: (i) narrow area of Lower Proterozoic BIF distribution extending S–N along the Krivoy Rog–Kremenchug fault over 200 km; (ii) presence of long-living syndimentary faults in the Krivoy Rog and Kremenchug structures (Plotnikov 1994), marked by rapid lateral facies changes of *s*- and *f*-members of the Saxagan Group, and the presence of slumping structures in ferruginous schists and interband microbreccias in ferruginous quartzites (see Fig. 12); (iii) reduction of stratigraphic profiles and thicknesses of the Saxagan Group in the easternmost and westernmost thrust fragments of the Krivoy Rog structure; (iv) input of the siliciclastic component from both western and eastern areas adjacent to the trough, as indicated by studies of zircons in the BIF (Troshchenko & Ivanchenko 1982); (v) enrichment of the Saxagan Group rocks with siliciclastics concentrated in the *s*-members and *S* interbands in the *f*-members.

Nature of the siliciclastic component in BIF

Lithologies and geochemical features of meta-siliciclastic sediments interbedded with BIF members of the Saxagan Group can be interpreted from the factor diagrams (see Fig. 4) and comparisons in Table 2. Factor (1) may reflect the mechanical separation of quartz from other clastics during transport and re-deposition, because the axis of this factor coincides with the $\text{SiO}_2/\text{Al}_2\text{O}_3$ ratio (Fig. 4). Factor (2), especially applied to the Saxagan Group schists, reflects a fraction of chemogenic iron precipitation imposed onto clastic sediments. The absence of SiO_2 from the signature of factor (2) suggests the alternative interpretation of the factor (1) as independent deposition of silica comprising the *Q* bands in ferruginous schists. Factor (3) can be related to the degree of chemical weathering of the granite–greenstone basement of the adjacent low-standing hinterlands supplying fine clastics probably carried by

sluggish rivers. Factor (4) may be related to the distal volcanoclastic input, though its direct lithological evidence was probably destroyed by metamorphism.

Occurrence of quartz metasandstones throughout the Krivoy Rog Supergroup adds evidence in favor of the intracratonic basin model. Phyllitic (quartz–sericite) schists common to the Skelevat and Saxagan Groups are very close in chemical composition to a mixture of quartz and hydromicaceous clays (see Table 2). Quartz–biotite schists differ from the former in having higher Fe and MgO contents, indicating a higher fraction of montmorillonite clays in the initial sediments. In this case, minor presence of fine mafic to andesitic volcanoclastics can not be excluded regarding the elevated Ni, Co, Cr contents. Thin beds of carbonaceous schists within *2s*, *3s*, *4s* members of the Saxagan Group may point to stagnation episodes triggered by increased bioactivity in the basin. The conditions of sedimentation of thin chlorite–chloritoid beds in the same members still remain enigmatic.

Chondrite-normalized REE patterns for schists (see Fig. 5) can add to the interpretation of the runoff area composition around the Krivoy Rog basin. Many patterns display a negative Eu-anomaly, which has been interpreted for the Lower Proterozoic clastic rocks by Taylor & McLennan (1985) as reflecting major changes in the Earth's crust composition by the end of the Archaean due to the large-scale intrusion of alkaline granites (exposed both to the east and west of the modern Krivoy Rog basin). This infers the presence of weathered products of such granites transported from the surrounding terranes as fine clastic load during BIF deposition.

Sources of Fe and Si and rates of their deposition

Lithological studies of cyclicity and banding in the Krivoy Rog BIF suggest that two quite different environments could have existed in the palaeobasin. One of them deposited the fine siliciclastic material of quartz–hydromicaceous composition, probably derived from weathering of the adjacent subdued hinterlands and being transported into the basin by sluggish rivers. Low to moderate bioproduction and virtually no chemical precipitation occurred in this extreme environment, as inferred from the phyllitic schists from the Skelevat Group and *1s*, *3s* and *4s* members of the Saxagan Group. Another environment produced the finely varved chemically precipitated sediments probably comprised

of Fe(III) hydroxides and silica with a small to negligible fraction of siliciclastics, C_{org} and carbonates; this extreme case is inferred for the magnetite–hematite jaspilites or *M* mesobands of the *4f* and *5f* members. Other lithofacies of the Saxagan Group can be interpreted assuming that these two depositional environments have been constantly competing at different time and space scales, trying to eliminate each other, overlapping when and where the silicate facies BIF has been accumulated.

If so, then we can try to assess the rate of chemical BIF deposition assuming that the microbanding in the magnetite–hematite *M* mesobands (i.e., extreme oxide BIF lithofacies) can be attributed to annual varving (Kulik 1991). This assumption has been verified earlier by Trendall (1972) on the basis of well-preserved microbanding in BIFs of the Hamersley basin (Western Australia). The h^* values (see Fig. 12) for *M* mesobands would correspond to a linear deposition rate (after compaction) of 0.4–4 mm a⁻¹ with a mean value of about 0.8 mm a⁻¹ or 800 m Ma⁻¹. Observations of mesoband thickness variations in folded rocks (and most of the Krivoy Rog BIF rocks are folded; see Fig. 11) and of lateral transitions between the *Q*, *M* and *F* bands (see Fig. 13) lead to the conclusion that most Fe-rich microlayers visible in the *M* and *F* bands are actually two, three or more condensed microbands. Therefore, only the minimum h^* values, and m_{Fe} values for microbanded *Q* mesobands can be regarded as reflecting the sedimentation rate (Kulik 1991). This correction gives a linear rate of 0.1–0.5 (mean 0.3) mm a⁻¹ (or 300 m Ma⁻¹), with a flux of Fe deposition of 4–40 cm⁻² a⁻¹ (median value 33 mg Fe cm⁻² a⁻¹ or 45 mg Fe₂O₃ cm⁻² a⁻¹). Trendall & Blockley (1970) obtained a value of 22.5 mg Fe cm⁻² a⁻¹, which is very close to our estimate. From the corresponding m_{SiO_2} values, the flux of SiO₂ to the sediment is estimated from Fig. 12 to be 10–70 mg cm⁻² a⁻¹, with a mean value of 60 mg cm⁻² a⁻¹. Obviously, these figures display large variance and their uncertainty should be taken as 0.5 orders of magnitude or more.

Nevertheless, the rate of 22.5 mg cm⁻² a⁻¹ (Trendall & Blockley 1970) or similar has been used by many authors (e.g. Drever 1974; Ewers 1983; Holland 1984; Kulik & Pokalyuk 1990; Morris 1993) in order to assess the dynamic aspects of Fe and Si supply to basins of BIF deposition. Other lithological approaches to estimate the BIF deposition rate produced figures ranging from about 87 m Ma⁻¹ (Trendall 1972) to 650 m Ma⁻¹ or more (Morris 1993) for the Hamersley Group (Western Australia). Klein & Beukes (1989) deduced a rate of

568 m Ma⁻¹ (1 m in 1760 years) for the deposition of siderite–chert microbands in the Kuruman BIF of the Transvaal basin (South Africa). All these numbers are in conflict with bulk deposition rates obtained from the U–Pb zircon ages. It follows from Fig. 2 that the Krivoy Rog Supergroup (about 4 km thick) has been accumulated in a time of about 700 Ma with a rate of 5–6 m Ma⁻¹. The figure almost certainly includes major breaks in sedimentation. Recently, precise instrumental determinations of zircon U–Pb ages were performed on tuff layers within the Hamersley Group (Arndt *et al.* 1991) and the Ghaap Group, Transvaal (Barton *et al.* 1994). Both authors reported the age of the Kuruman BIF (Transvaal) and the Dales Gorge member BIF (Hamersley) within 2500–2450 Ma and the bulk deposition rates for both sequences with about 3 m Ma⁻¹. The conflict between the lithological and isotope-age estimations still needs to be resolved. One explanation could be that the deposition rate of shales is much lower than for chemical BIF sediments due to the hiatuses in siliciclastic sedimentation.

Nevertheless, the deduced chemical sedimentation rates of 33 mg Fe cm⁻² a⁻¹ and 60 mg SiO₂ cm⁻² a⁻¹ provide a semi-quantitative basis for the considerations about the input dynamics of dissolved components into the realms of BIF deposition. Taking the area of the Krivoy Rog basin as 5000–10 000 km², this gives the annual inputs of dissolved Fe and Si as 10⁶–10⁵ tons per year. Since the content of siliciclastic component in the oxide and carbonate facies BIF comprises less than 10–15%, this means an average clastic load of *c.* 10¹¹–10¹⁰ t Ma⁻¹.

These figures seem to be quite compatible to the models of Fe and Si supply from the deep ocean water (Borchert 1952; Drever 1974; Holland 1984; Klein & Beukes 1989; Morris 1993), with a significant fraction of Fe being derived from hydrothermal systems of mid-ocean ridges, as it is suggested on the base of REE data (e.g. Derry & Jacobsen 1990). The alternative hypothesis is that dissolved Fe and Si were supplied by rivers draining weathering crusts of the adjacent granite–greenstone or volcanic terrains (e.g. Strakhov 1963; Belevtsev *et al.* 1983; Reimer 1987; Drozdovskaya 1990; Hälbich & Altermann 1991).

The role of dissolved Fe and Si entering the Krivoy Rog palaeobasin from a terrigenous source can be checked by balance calculations based upon the sedimentation rates (defined above), and on lithological–geochemical studies of metamorphosed palaeosols underlying the BIF in the Krivoy Rog basin (Kulik & Pokalyuk 1990). There, the palaeoweathering profiles have

been reconstructed with the quartz–montmorillonite–kaolinite (now quartz–chlorite–sericite) zone on top of mafic volcanics of the New Krivoy Rog Group, and the illite–kaolinite–quartz (now sericite–quartz) zone on top of Archaean plagiogranites. No significant iron sulphides were found in both profiles. Release of dissolved Si, Fe and Mn was calculated from the chemical compositions of the zones assuming no mobility of Al and Ti (their ratio remains constant in both profiles). It has been found (Kulik & Pokalyuk 1990) that 90% Fe (55.6 kg), 95% Mn (0.6 kg) and 25% Si (220.5 kg) could be leached from 1 m³ of plagiogranite; 30% Fe (75.7 kg), 25% Mn (0.9 kg) and 30% Si (201 kg) were leached from 1 m³ of basalt. If all this Fe was chemically deposited in the BIF then its release from siallitic weathering of the Middle Dnieper granite–greenstone terrain with an area of 150 000 km² and 100 m Ma⁻¹ mean denudation rate was quite sufficient to match the 10⁶ tons of mean annual Fe deposition in the Krivoy Rog basin proper.

The problem of this model is, however, that about three times more silica and 60–120 times more siliciclastic material than present in the Saxagan Group BIF would have to be deposited simultaneously in the palaeobasin, but no clean quartzites and schists of sufficient volume are known in the Krivoy Rog structure on this stratigraphic level. An implication is that only about 1% of the eroded siliciclastics and a few percent of Fe, Mn and Si leached from weathering crusts could be transported into the palaeobasin directly. The bulk of them entered the ocean far from the actual areas of BIF deposition, contributing to the global cycle of Fe and Si, and then, without the clastic load, reached the BIF sedimentation areas through indirect ways (Kulik & Pokalyuk 1990). An alternative explanation (Mel'nik 1982) suggests that dissolved Fe and Si derived from both terrigenous and hydrothermal sources accumulated in the anoxic ocean water during a long time in the Late Archaean until BIF was deposited under favourable conditions. However, as it was pointed out by Ewers (1983), in this case, at the beginning of BIF sedimentation, the concentrations of dissolved iron Fe(aq) and dissolved silicon Si(aq) in the ocean water would not have been less than 800–1000 ppm and 1300–2000 ppm, respectively. On the basis of physico-chemical considerations, such concentrations are not realistic (see below), and therefore the 'accumulation hypothesis' seems inconsistent with the chemical data.

Thus, we accept the model of BIF deposition in the upwelling areas (Borchert 1952; Drever

1974; Holland 1984; Klein & Beukes 1989; Morris 1993) or land-locked basins (see below), with constant or intermittent supply of Fe(aq) and Si(aq) by the inflow of deep suboxic ocean water. Both components could enter the ocean from various sources (hydrothermal influx, benthic release of Fe, continental runoff etc.). Areas of chemical and clastic sedimentation thus have been separated in space. This model does not require an oxygen-free atmosphere, since it postulates existence of the ocean-wide shallow-water chemocline. However, we will try to show that the Mn content in the BIF and its change with time seems to provide the upper limit to the oxidizing potential of Palaeoproterozoic surface water and atmosphere.

REE data (see Fig. 5) support the assumption about the combined hydrothermal and terrigenous input for the sedimentation of the oxide and carbonate facies of the Krivoy Rog BIF. Some ferruginous quartzites have low REE contents and display a positive Eu anomaly. The latter, according to Fryer (1983), may reflect a volcano-hydrothermal input, especially pronounced in Archaean BIFs. Negative Ce anomalies in schists of the Saxagan Group may witness the slightly oxidizing conditions in surface waters, leading to oxidation of Ce and its leaching from clay particulates. There are no such anomalies in the underlying schists of the Skelevat Group. The dissolved Ce could enter the basin of BIF sedimentation with continental runoff, which is reflected by positive Ce anomalies in some ferruginous quartzites. These, however, can be completely masked by mixing of chemogenic and siliciclastic material in the silicate facies BIF.

Pathways of Fe, Si and Mn in the Krivoy Rog palaeobasin

From the above considerations on the geological setting and the distribution of land-derived siliciclastics in the Skelevat and Saxagan Groups, we have come to the conclusion that the Krivoy Rog BIF was deposited in a land-locked, intracratonic basin at least 150–200 km long and 50–70 km wide and elongated in submeridional direction, and split into several sub-basins of varying (generally shallow) depth by synsedimentary faults inherited from the former rift framework. This basin with a significant runoff from adjacent terranes, at least periodically, was connected to the ocean via straits or sills from the SW side, as indicated by the decreasing thickness of all *s*-members and

the Skelevat Group in this direction (see Fig. 3). For the sake of better understanding of the palaeoenvironment in the basin, it is useful first to consider some modern counterparts.

Analogues of modern land-locked basins. Distribution of lithofacies, water chemistry and stratification in land-locked basins are controlled mainly by the hydrodynamic circulation, which in turn depends on the relations between evaporation, continental runoff and deep ocean water inflow (Grasshoff 1975). For instance, the Red and Mediterranean Seas are characterized by strong evaporation and weak runoff. No permanent stratification nor stagnant deep waters with elevated concentrations of Fe(aq) and Mn(aq) exist in such basins. Volcaniclastics or siliciclastics from the adjacent deserts are brought into the basin mainly via aeolic transport; carbonate (reef) facies are common in the nearshore environments. The Black Sea differs in the predominance of runoff over evaporation and, hence, in higher siliciclastic load and bioproductivity. The surface water layer is brackish and leaves the Black Sea as a surface current into the Bosphorus strait, while more saline Mediterranean water constantly enters the Black Sea via the bottom current. Due to salinity/density gradients, a permanent stratification exists, with very slow exchange between oxygenated surface water and stagnant deep sulphidic water bodies (through the chemocline at 150–180 m). This leads to the deposition of hemipelagic muds enriched in C_{org} and Fe sulphides. Mn(aq) is released from sediments, accumulating in the stagnant water body to concentrations of *c.* 0.2–0.3 ppm, while the Fe(aq) content (0.01 ppm) is limited by precipitation of amorphous FeS in the water column. Both Fe(aq) and Mn(aq) are oxidized to particulate (hydr)oxides at the chemocline, while sinking Mn particles become re-dissolved in the upper 60–90 m layer of stagnant water (Lewis & Landing 1991).

These three seas are not very suitable counterparts to the Krivoy Rog basin because they are floored by oceanic crust and seem also to be rather too large and deep. Perhaps, a better comparison would be the Baltic Sea. This is a shallow estuarine-type basin where the continental runoff largely exceeds evaporation, leading to permanent salinity stratification. The halocline is located at varying depths (10–70 m) between the surface brackish water (5–15‰ salinity) and the deep water (17–25‰ salinity) (cf. Grasshoff & Voipio 1981). In summer, a thermocline develops at 10–25 m depth that is completely destroyed during the turnover in

October–November. The bottom topography is very complex, with mean depths about 40–80 m, several sills, basins (50–70 m) and deeps (200–400 m). In those deeps, a stagnant near-bottom water with H_2S exists periodically, separated by the chemocline at 150–170 m depth. High bio-production is typical for the summer time, resulting in the deposition of C_{org} -rich terrigenous muds at 20 m depth and deeper in coastal areas and in the central Baltic Sea (e.g., Bornholm basin). In the Gotland and Landsort deeps microbanded Holocenic muds below the chemocline contain up to 8% C_{org} , 30% Carhodochrosite, some amorphous siderite, Fe monosulphide (FeS) or greigite (Fe_3S_4) (cf. Suess 1979; Emelyanov 1981, 1986). Because of strong benthic release due to microbial oxidation of buried C_{org} , high concentrations of Fe(aq) up to 0.2–2.0 ppm and Mn(aq) up to 0.7–4.0 ppm exist in the stagnant near-bottom waters, either in the deeps (e.g. Dyrssen & Kremling 1990) or (seasonally) in coastal areas (e.g. Balzer 1982). Near the chemocline, the upper layer of particulate matter is enriched in Mn and Ba, while the lower layer (a few to tens metres downward) is enriched in Fe (Boström *et al.* 1988). This chemogenic particulate matter is transported by currents to other areas of the Baltic proper. The abundant Fe–Mn crusts are locally fast growing near the sediment–water interface (SWI) in coastal areas at 20–25 m water depth in SW Baltic (Suess & Djafari 1977; Heuser 1988) or in sediments of the Gulf of Bothnia (e.g., Boström *et al.* 1982). Hence, there are two sedimentary ore microfacies forming at present in the Baltic Sea basin: (i) the shallow-water Fe–Mn-oxide accumulations and (ii) the Mn-carbonate-rich microbanded muds of the stagnant Gotland and Landsort deeps.

The striking features of the sedimentary environment in the Baltic Sea are (i) complex bottom topography and current patterns; (ii) very limited spasmodic water exchange with the North Sea through the Danish Straits less than 20 m deep. In these straits, the surface and bottom currents like those in the Bosphorus Strait cannot exist simultaneously. Instead, the outflow of brackish surface water from the Baltic Sea takes place in 2–10 year periods, interrupted by the powerful short-time inflows of saline North Sea water during winter storms (Grasshoff & Voipio 1981). Such event inflows form the near-bottom currents that spread during several months throughout the entire basin and completely destroy the stagnant water bodies in the Gotland and other deeps. These major geochemical perturbations are thought to play the key role in the geochemical

cycling of Fe and Mn leading to deposition of the sedimentary ore microfacies (Emelyanov 1986).

Palaeoenvironmental model for the Krivoy Rog basin. As follows from the above review, the intracontinental basins located in the moderate humid climatic zone, such as the Baltic Sea, display permanent stratification which can lead to strong accumulation of dissolved Fe and Mn by benthic release in stagnant deeps even at present high levels of bioproduction and atmospheric oxygen. Variations in bottom topography, currents, sea level, climate humidity, input of the oceanic water etc. can lead to steep facies changes or even periods of clastic sedimentation or erosion over the entire basin. Hence, only parts of the basin at a given time may be appropriate for chemical sedimentation. Projecting these circumstances to the palaeoenvironment of BIF deposition, we can expect the cyclic vertical and lateral lithofacies changes with a predominance of the silicate-carbonate facies BIF, which is indeed typical for the Krivoy Rog basin. Such a comparison also involves the assumptions that oxygen partial pressure p_{O_2} in the air did not exceed 0.02 PAL (present atmospheric level), p_{CO_2} was much higher (0.01–0.1 bar), and bioproduction in the photic zone of the oceans and mixed-water basins was much lower than today. These factors in turn caused the predominance of suboxic marine sediments and deep waters (Holland 1984; Walker 1984). Finally, concentration and pathways of Si in Precambrian oceans would be totally different than at present because of the absence of silica-secreting organisms (Siever 1992). Keeping this in mind and taking for

granted that biogeochemical interactions governing the cycles of Fe and Mn in Palaeoproterozoic were essentially the same as today, we can imagine the palaeoenvironment of BIF deposition in the Krivoy Rog basin as depicted in Fig. 17. The summary of possible pathways of Fe, Mn, Si and C_{org} in the locality of BIF sedimentation is presented in Fig. 18. These pathways and processes will be discussed in the following sections.

It is instructive to compare the palaeoenvironmental model suggested here for the Krivoy Rog basin with published models for the contemporaneous Hamersley basin, Western Australia (see Morris 1993). The key conclusion from such a comparison is that although geochemically and petrographically similar, the Saxagan and Hamersley BIF sequences were deposited in tectonically and topographically very different basins. The iron formations in the Hamersley basin were deposited on a large, flat, rather stable pericratonic platform, probably isolated from land by straits precluding input of siliciclastics (Morris & Horwitz 1983; Morris 1993). At low sea level or absence of upwelling, the carbonate facies were first deposited on the platform, indicating evaporitic conditions and absence of significant concentrations of Fe and Mn in surface waters. Very persistent and correlatable BIF units without lateral facies transitions accumulated during long periods of time due to stable upwelling currents at low bioproduction in the photic zone, interrupted only by distal pyroclastic input. On the contrary, the Krivoy Rog BIF was formed in a tectonically labile trough-like land-locked basin with different depths and rapid lateral facies transitions. Close intercalation of BIF with schist beds

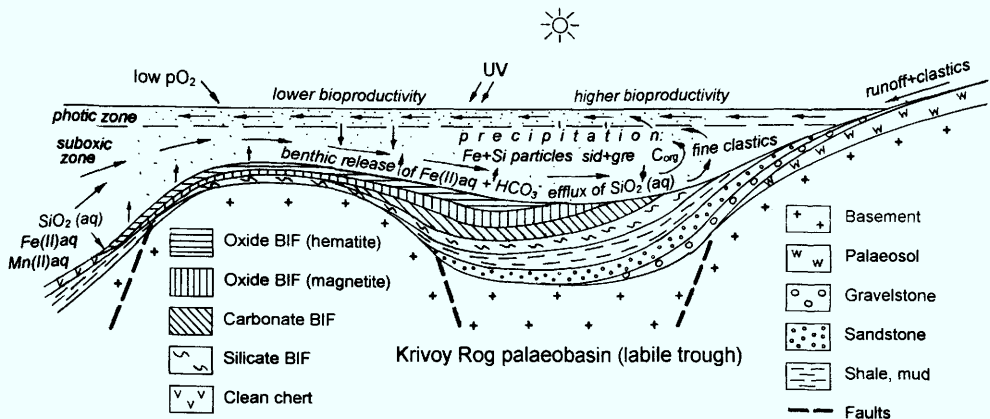


Fig. 17. Model environment of Palaeoproterozoic BIF deposition in the land-locked Krivoy Rog-type basin. Distribution of sedimentary facies is shown for transgressive hemicycle.

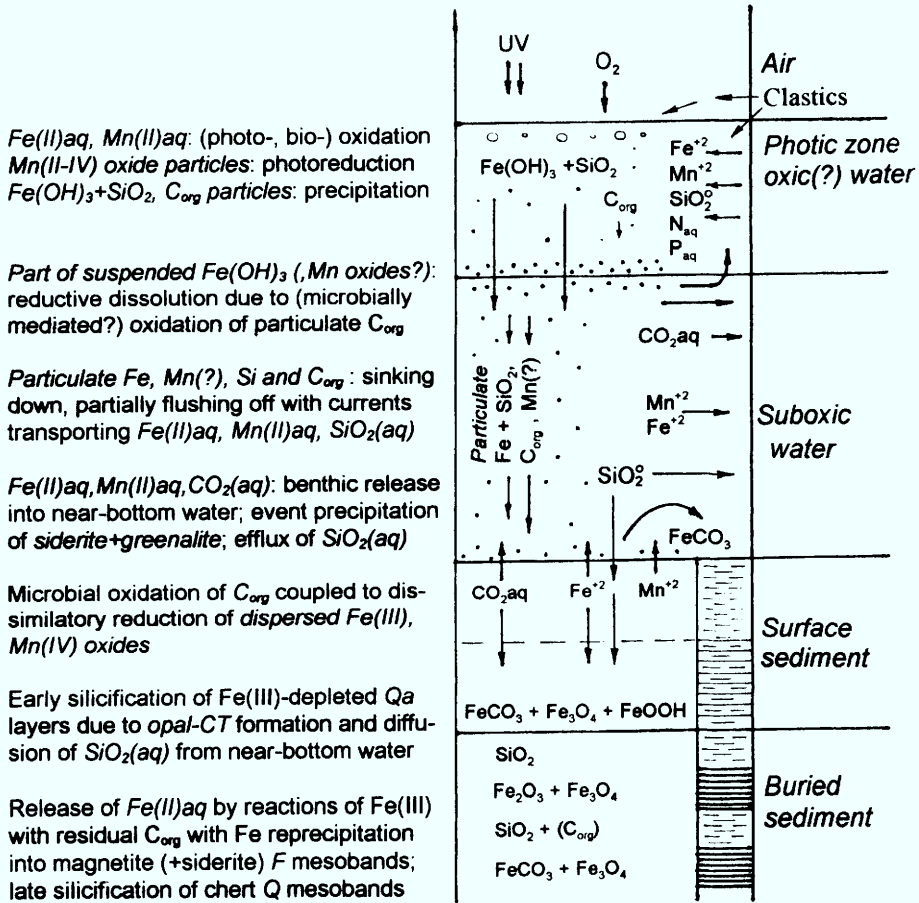


Fig. 18. Tentative pathways for Fe, Mn, Si and C_{org} in the water-sediment column of BIF deposition in the Krivoy Rog palaeobasin.

and interbands indicates active and variable hydrodynamics in the basin of moderate to shallow depth, probably caused by variations in riverine input, sea level and irregular ocean water inflows.

Mechanisms of Fe, Si and Mn precipitation and dissolution. Figure 18 summarizes the geochemical processes that could have occurred in the water-sediment column of the BIF depositional area, based on their possible modern counterparts in stratified lakes and seas (e.g., Burdige 1993).

It is assumed that in Palaeoproterozoic time, a delicate balance has been maintained between slow oxygen flux into the deep ocean water and low organic productivity in a thin photic (mildly oxic) layer. Under such conditions, dissolved Fe(II) and Mn(II) (mainly in the form of Fe²⁺ and Mn²⁺ ions) accumulated in the suboxic deep

ocean water to concentrations of about 1 ppm, analogous to the pore water Fe and Mn concentrations in the modern suboxic deep-sea sediments (Holland 1984). The ocean water most probably was enriched in dissolved SiO₂ to concentrations of c. 60 ppm, established by sorption equilibrium with clay particles or zeolites (Siever 1992). Since pCO₂ in the atmosphere was likely to be much higher than today, pH of the surface water would be lower (6.0–6.5 against 7.5–8.3).

During BIF deposition, Fe(aq) and Mn(aq) entered the basin from the suboxic ocean water reservoir at concentrations of about 1–5 ppm. In the surface water, Fe(aq) could be oxidized to particulate Fe(III) hydroxide by several processes either at suboxic or mildly oxic conditions. These may have been photo-oxidation, photosynthesis or contact with the atmospheric O₂, considered in detail by Anbar & Holland

(1992 and references therein). The rate and role of each process should have been controlled by p_{O_2} and p_{CO_2} in the atmosphere. The lifetime of Fe oxyhydroxide in the water column today is highly subject to microbial oxidation kinetics (Nealson & Myers 1992; Stumm 1992), although the slower rate of dissolution allows Fe(III) particles to penetrate the water column in coastal or shelf areas (10–200 m depth). Flocculation of fresh Fe(III) hydroxide in the water oversaturated with respect to quartz most probably caused the surface precipitation of dispersed silica onto Fe(III) hydroxide (Harder & Flehmig 1970). If so, the particles coated with a layer of amorphous silica crystallites could reach the bottom very effectively together with minor particles of C_{org} . Silica coating probably restricted the longer contact of Fe-oxyhydroxide surface with seawater, and thus prevented it from sorption of minor components like P, Ba, Mn, As, Zn, Cu, Ni, Co, providing the low contents of these elements in BIFs. On the contrary, these elements were effectively adsorbed and concentrated in Fe–Mn ores and nodules deposited in the Phanerozoic and modern marine environments like the Baltic Sea (e.g. Boström *et al.* 1982).

In association with fine siliciclastic muds, the precipitation of silica as opal-CT could take place directly from the porewater in sediments due to the efflux from the silica-rich near-bottom water (Siever 1992), leading to the formation of the early diagenetic chert bands and pods. Since such bands in the Krivoy Rog basin are always associated with ferruginous schist but not with quartz-sericite schist (assumed to be derived mainly from a terrigenous source), this would imply that the bulk of Fe(aq) and Si(aq) were transported into the basin with inflowing ocean water.

Similarly, Mn(aq) at initial concentrations *c.* 1–3 ppm could be oxidized to particulate Mn_3O_4 or MnOOH by atmospheric or photosynthetic oxygen in the photic zone. The rate of photochemical Mn^{+2} oxidation ($0.1 \text{ mg cm}^{-2} \text{ a}^{-1}$) was estimated to be 1000 times slower than that of Fe(aq); hence photo-reduction of particulate Mn could be much more significant in the ancient surface ocean water (Anbar & Holland 1990). Mn-oxide particles not coated with SiO_2 most probably quickly redissolved microbially just entering the suboxic water layer, similar to the stratified Baltic or Black Sea columns today (see Boström *et al.* 1988; Lewis & Landing 1991). If so, then behaviour of Mn would be different from that of Fe in the stratified suboxic water column of BIF deposition. While particulate Fe(III) could

effectively reach the sediment due to silica coatings and (possibly) slow dissolution kinetics, Mn-oxide particles (if any) quickly completely re-dissolved in the water column. As in the modern basins, significant part of Fe and Mn particles forming in the photic zone or near the redoxcline could also be flushed off with horizontal currents.

The rarity of sulphides in the BIF rocks, their weakly isotopically fractionated sulphur and the isotopic composition of carbon in graphite and carbonates suggest that suboxic type diagenesis prevailed in the fresh BIF sediment, resulting in the benthic release of dissolved Fe(II) and carbon dioxide at the cost of microbial C_{org} oxidation in the surface sediment coupled with dissimilatory reduction of Fe(III) hydroxide (Walker 1984) (and of terrigenous particles of Mn oxide). This, in turn, requires low (bio)productivity in the surface water layer, since at high production and high burial rates of C_{org} , abundant iron sulphides would accumulate in the marine sediment with strong sulphate reduction, causing low Fe(aq) concentrations in the pore- and near-bottom water, e.g., like in the Black Sea (Lewis & Landing 1991). Dissolved CO_2 formed by oxidation of organic matter would have $\delta^{13}\text{C} \approx -20\%$. Release of this CO_2 together with Fe(aq) to the near-bottom water and their mixing with the 'normal marine' dissolved CO_2 ($\delta^{13}\text{C} = 0\%$) would create the local near-bottom environment where precipitation of Mg–Fe carbonate with intermediate $\delta^{13}\text{C} \approx -10\%$ became possible (Walker 1984). In the presence of fine terrigenous clay particles or volcanic ash at elevated concentration of dissolved Fe and SiO_2 (60 ppm), Fe(II) silicates would easily form (e.g. Harder 1978), transformed by metamorphism into stilpnomelane or thuringite phases which are so typical for the Krivoy Rog BIF. The opal-CT formation at early diagenetic stages in the layers of the Fe(III) hydroxide–silica precipitate would certainly decrease the Si(aq) concentration in the pore-water, triggering the diffusion of Si(aq) from the near-bottom water. At favourable conditions, this process could result in the early silicification of some varve sequences, leading to the formation of thick *Qa* mesobands. Rapid event deposition of Mg–Fe carbonate or silicate from Fe(aq) that accumulated in the near-bottom water, could be triggered by the clastic suspension fall-out and followed by the early diagenetic silicification of Fe-depleted layers in the sediment. This is an attractive, though rather speculative, explanation for the close association of *Qa* mesobands and *S* interbands in the event asymmetric rhythms (Kulik 1991).

The outcome of the previous discussion is that in the stratified closed basin of BIF deposition, a sort of 'geochemical trap' for iron would have been effective in order to ensure the deposition of carbonate facies BIF. Figure 17 shows an inflow of suboxic ocean water with 2 ppm Fe(aq), 3 ppm Mn(aq) and 60 ppm SiO₂(aq) into the basin. This solution is generally carried within the near-bottom currents over the basin until mixing with brackish surface water occurs mainly in coastal mixing zones. Thereafter, the water is carried with surface currents back towards straits. In the photic zone with low to moderate bioproduction, Fe(III) precipitates and sinks down with C_{org} and SiO₂ as described earlier; some minor part of these particles is flushed off with currents. As oceanic suboxic water inflow proceeds, Fe(II)aq is released into the near-bottom water from the suboxic sediments due to C_{org} oxidation. The higher the Fe(aq) content in the near-bottom water, the more Fe(III) is subsequently precipitated in the photic zone, precipitating into the suboxic sediment and increasing the benthic release of Fe(aq). This positive feedback can be limited either by precipitation of Mg-Fe carbonates and silicates in the near-bottom waters or in mixing zones, or by a cessation of the ocean water inflow. In the latter case, the Fe content in the sediment would gradually decrease or could be hindered by increased siliciclastic deposition. The described dynamics of Fe cycling in the BIF palaeobasin resembles that inferred by Emelyanov (1986) for the deposition of Mn-rich sapropelic muds in the Gotland and Landsort deeps of the Baltic Sea. The difference consists mainly in the overall oxidation state of the ocean and atmosphere, and in the silica cycling. Clearly, the seasonal, annual or long-term perturbations of climatic and hydrodynamic factors in the basin with variations of sea level and basin topography should create a great variety of rhythmic patterns of varving and mesobanding as in the case of the Krivoy Rog BIF.

Physico-chemical constraints on Fe and Mn cycles. As follows from the previous considerations, and the chemical data of Tables 2, 3 and 4, the only way of Mn precipitation in the Krivoy Rog palaeobasin could be in the form of Mn-Mg-Fe carbonate. Iron carbonates in the carbonate facies BIF always contain 12–20% MgCO₃ and 0.2–6% MnCO₃ end-members (Klein 1983; Mel'nik 1986). It is known (Essene 1983) that a continuous range of solid solutions exists between FeCO₃ and MnCO₃, and between FeCO₃ and MgCO₃ end-members

both in metamorphic and hypergenic carbonates. Though a miscibility gap appears to exist between MnCO₃ and MgCO₃, Fe carbonates containing less than 20% MgCO₃ can be taken as ideal solutions at any mole fraction of MnCO₃. At low Fe(aq) and high Mn(aq) concentrations in sediment pore water, dispersed rhodochrosite of up to 40% CaCO₃ (Suess 1979) may also form. Therefore, the mole fractions of Mg and Mn end-members in chemogenic siderites would reflect the activity ratios of Mg⁺² and Mn⁺² to Fe⁺² in the water solution.

Mel'nik (1982, 1986) considered phase relations in the system 'aqueous solution + dispersed siderite, greenalite, hydromagnetite and Fe sulphides' assuming a *p*CO₂ of 0.1 bar. It follows from his Eh–pH diagrams, that formation of the siderite–greenalite association in seawater would be possible only in a very narrow range of pH (6.0–6.5) and Eh (–0.1–0.0 V), i.e. at suboxic conditions; the equilibrium concentration of Fe⁺² in this system must be 100–200 ppm (Mel'nik 1986, fig. 24). Concentration of SiO₂(aq) controlled by Fe(II) silicates certainly would be less than the solubility of amorphous silica (100 ppm), but higher than the solubility of quartz (10 ppm). At higher contents of dissolved Si, precipitation of Fe(II) silicate is favoured relative to magnetite; for that reason, direct precipitation of magnetite in BIF sediments is hardly probable.

In equilibrium with an aqueous electrolyte and assuming equal activity coefficients for Fe⁺², Mg⁺² and Mn⁺², the distribution coefficients for Mg in siderite *D*_{Mg} and for Mn in siderite *D*_{Mn} are simply related to the solubility products of siderite *K*_{Fe} (10^{–10.46}, calculated from data of Mel'nik (1986)), magnesite *K*_{Mg} (10^{–8.15}, calculated from data of Mel'nik (1986)) and rhodochrosite *K*_{Mn} (10^{–10.9}, from Garrels *et al.* 1960), their respective mole fractions in solid solution *n*_{Fe}, *n*_{Mg}, *n*_{Mn}, and the total molalities of Fe, Mg and Mn in aqueous solution {Fe⁺²}, {Mg⁺²}, {Mn⁺²} (e.g., Morel & Hering 1993, p. 559):

$$D_{\text{Mg}} = \frac{n_{\text{Mg}}}{n_{\text{Fe}}} \cdot \frac{\{\text{Fe}^{+2}\}}{\{\text{Mg}^{+2}\}} \approx \frac{K_{\text{Fe}}}{K_{\text{Mg}}};$$

$$D_{\text{Mn}} = \frac{n_{\text{Mn}}}{n_{\text{Fe}}} \cdot \frac{\{\text{Fe}^{+2}\}}{\{\text{Mn}^{+2}\}} \approx \frac{K_{\text{Fe}}}{K_{\text{Mn}}}.$$

Let us consider the typical siderite from the Krivoy Rog basin containing 86 mol% FeCO₃ (*n*_{Fe} = 0.86), 12 mol% MgCO₃ (*n*_{Mn} = 0.12) and 2 mol% MnCO₃ (*n*_{Mn} = 0.02). Given the total Fe(aq) concentration in the ancient suboxic

seawater $\{\text{Fe}^{+2}\} = 0.002$ molal (*c.* 112 ppm), we can calculate from the above equations that the Mg(aq) concentration in solution will be 0.057 molal (1385 ppm) and Mn(aq) = 0.000016 molal (or 0.85 ppm). Since concentration of Mg(aq) in normative seawater is 0.05315 molal (1290 ppm) (e.g., Grasshoff 1975; Kulik & Harff 1993), these approximate figures are in excellent agreement (within the uncertainty of solubility products) with the assumption that the major-ion composition of Palaeoproterozoic seawater was similar to the present (Holland 1984). Comparison of the Fe(aq) concentration (100–200 ppm) needed to precipitate siderite and greenalite with that assumed for the deep ocean water (1–10 ppm, see above) implies that cycling of Fe in a stratified Krivoy Rog palaeobasin increased the Fe concentration at least 10–20 times, leaving the concentration of Mn(aq) unchanged at the level about 1 ppm which would be the same as in the deep ocean.

Significance of Mn concentrations in BIF rocks. It is well known that the solubility of Mn sulphides is higher than that of rhodochrosite MnCO_3 (e.g., Balzer, 1982). Carbonate therefore is the only form of Mn precipitate in reducing marine or lacustrine waters. From the data of Table 3, it follows that this is true also for the Krivoy Rog BIF. Extremely low contents of Mn in hematite and magnetite (<0.01%) and the complete absence of Mn oxide minerals suggest that there was no burial of MnO even if it could precipitate as oxide particles in the photic zone. Hence, the amount of MnO in the bulk BIF rock or in a mesoband w_{MnO} would define the initial content of chemogenic Mg–Fe carbonate w_{carb} in the BIF sediment, and a fraction of iron precipitated into this carbonate $X(\text{Fe}_{\text{carb}}) = w_{\text{carb}}c_{\text{FeO}}/w_{\text{FeO}}$, where c_{FeO} is the FeO content in carbonate (*c.* 50 wt%). This must hold also for highly metamorphosed BIF rocks where siderite is destroyed by decarbonatization reactions; in this case, Mn is partitioned into grunerite or almandine. Since the Mn content in siderites c_{MnO} is usually 1 wt% (see Table 3), we can use the following relation: $w_{\text{carb}} = 100w_{\text{MnO}} \cdot \text{Application of this formula to the data from Tables 5 and 6 easily shows that the initial carbonate content } w_{\text{carb}} \text{ varied from less than 1\% in the oxide facies BIF, chlorite } S \text{ interbands, } Qa \text{ and magnetite } Fa \text{ mesobands to 20–22\% in silicate–carbonate facies BIF or carbonate } F \text{ mesobands carrying 40–60\% of total Fe.}$

As follows from the composition of siderites in the Krivoy Rog ferruginous quartzites, the Mn(aq) concentration in the Krivoy Rog palaeobasin was about 1 ppm, the same as postulated

by Holland (1984) for the suboxic ocean water. Carbonate compositions of 6% MnCO_3 or more (Klein 1983) from younger BIF of the Labrador Trough would require a higher Mn(aq) concentration of 6–10 ppm and slightly lower Fe(aq) concentrations in the near-bottom or mixed zone waters. This can be attributed either to a higher background level of dissolved Mn in the ocean at about 2100 Ma ago, or to a higher oxidation potential in the photic zone, when the oxidative Mn precipitation into particulate oxide became possible, and some particles could already penetrate the redoxcline and enrich the suboxic water body. The raise of p_{O_2} in the atmosphere would shift this dynamic ratio (Mn dissolved in suboxic water/Mn oxidized into particles in the photic zone) to higher concentrations of Mn(aq), until solubility of dispersed rhodochrosite (60–80 ppm) is achieved in the near-bottom waters. From that time on, cycles of Fe and Mn both were working in full strength in the basin, producing sediments containing chert, Fe(III) oxide, Mg–Fe carbonate and Mn carbonate. This assemblage is indeed present, for instance, in the Fe–Mn carbonate lithofacies of the Hotazel banded Fe–Mn formation in South Africa (cf. Miyano & Beukes 1987).

As p_{O_2} increases in the atmosphere, the chemoclines for Mn and Fe would deepen. Since Mn(IV) oxides are reduced and dissolved at higher oxidative potential than Fe(III) oxides, it may happen that the entire basin water becomes oxic with respect to iron, stopping Fe cycling, while a thin near-bottom water layer still remains reducing with respect to Mn. In this extreme case, very intensive precipitation of particulate Mn oxides would be expected with some silica producing sediment compositions as inferred for the 'oxide facies' braunite beds of the Hotazel formation.

It is clear that the suggested palaeoenvironmental model is capable to explain most of the known regularities in the distribution of Fe and Mn both in BIFs and banded manganese formation. This model can be developed and quantified by means of physicochemical modelling using modern thermodynamic databases, algorithms for computation of complex geochemical equilibria, and kinetic and sorption data (D. A. Kulik, in prep.). The qualitative conclusion is that the very low Mn content in the Krivoy Rog BIF witnesses Mn concentrations in the ocean water at the time of its deposition. No Mn enrichment of waters was possible, either because p_{O_2} in the atmosphere was too low relative to the kinetics of dissolution of particulate Mn oxide, or the Mn oxides could not

precipitate at all in the presence of Fe(aq), which is the stronger acceptor for photosynthetic oxygen. The iron-manganese enrichment became possible at a later stage of terrestrial

evolution, when increased atmospheric p_{O_2} could ensure such rate of formation of particulate Mn oxide in the photic zone that it could reach the suboxic water body, thus providing either

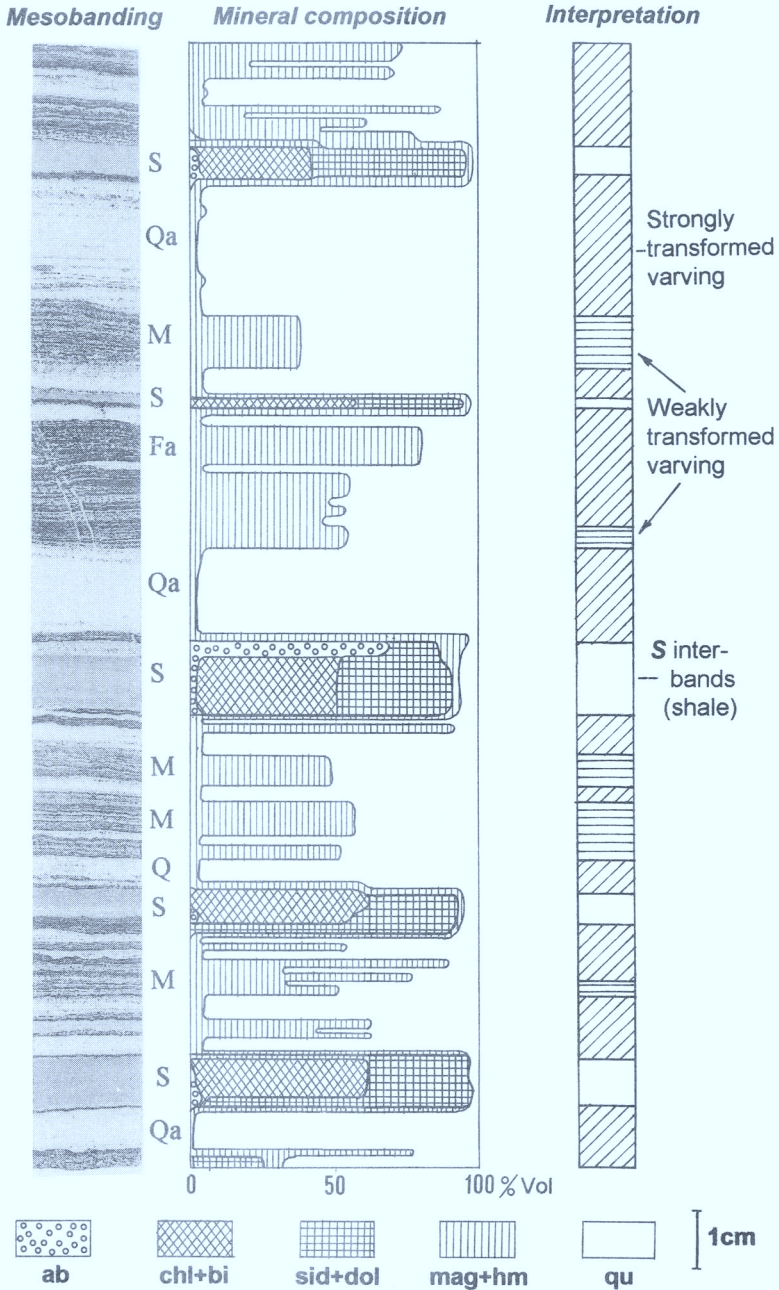


Fig. 19. Variation of mineral parageneses in a sequence of mesobands, determined microscopically from a series of thin and polished sections of a sample of mesobanded magnetite quartzite, 4f member, Skelevat Magnetite deposit. Photograph of streak-print; the column 'interpretation' shows the distribution of S-interbands and the inferred degree of post-sedimentary transformation.

Mn-Fe-carbonate, Mn-carbonate or Mn-oxide lithofacies in the Hotazel-type formation.

Post-sedimentary transformation of BIF. Figure 19 demonstrates variations in mineral composition of typical samples of magnetite quartzite. These variations are quite drastical especially between *Qa* and *Fa* bands, and can be explained only partially by the sedimentation processes. Intensive post-sedimentary transformation processes have been invoked by many workers beginning from the prominent work of Svital'skii *et al.* (1932) to explain the contrast mesobanding in BIFs (see also Trendall & Blockley 1970; Kulik 1991, 1993). These processes seem to be effective at the earliest stages of diagenesis and continued until metamorphism, leading to the formation of economically important polyhedral magnetite in ferruginous rocks of the oxide facies BIF.

The primary chemogenic BIF sediment most probably consisted of dispersed Fe(III) hydroxide, Mg-Fe(II) carbonate, Mg-Fe silicate, amorphous silica, and minor C_{org} (e.g. Mel'nik 1982; Klein 1983). Suboxic early diagenesis of BIF sediments was governed by the amount and distribution of those components between laminae. At least part of *Q* and many *Qa* mesobands could form by (microbially coupled) Fe(III) reduction- C_{org} oxidation, with reduction of Fe(III) to magnetite, siderite or greenalite in the deeper sediment layer, and diffusional release of Fe(aq) and isotopically light CO_2 into the near-bottom water, followed by early silicification of some microbands due to diffusional transport of dissolved silica from the near-bottom water (see Fig. 13). This early silicification is evidenced by the intraband breccias of *Q* mesobands cemented with carbonate-magnetite or carbonate and by podding or slumping filled by carbonate-silicate material (see Fig. 12).

At the second stage of transformation (anchi-metamorphic, at $T > 150^\circ C$ and $P > 1$ kbar), the diffusion-controlled redox redistribution of Fe(aq) could take place at millimeter scale across the microbanding. Oxidation of residual C_{org} within microbands of mainly quartz-hematite composition by reaction with hematite would release dissolved Fe(II) (and protons) into the pore fluid. Transported by diffusion or infiltration to the adjacent quartz-hematite bands without C_{org} , Fe^{2+} and hydrogen ions would reduce hematite to magnetite (Kulik 1993), resulting in the magnetite overgrowth on specularite needles or tablets oftenly described in the oxide facies BIF (see Han 1978; Kulik 1986; Morris 1993). Finally, thin *Q*

and *F* (magnetite) mesobands should form instead of the initial subtle varving (Kulik 1993), which could be preserved only in the mixed hematite-bearing *M* mesobands (Fig. 19), where C_{org} probably was too low. Thermal deconsolidation (Valeev & Evtekhov 1991), tectonic stress and crystallization force of growing magnetite grains would also have caused mobility of silica and transport of dissolved Fe and Si at the centimetre to decimetre scale. This explains late podding and thinning-outs of *Q* bands with continuous Fe-rich laminae (see Fig. 13), plastic flow of the rock during folding, and may be invoked to explain the genesis of the high-grade magnetite and martite iron ores (Kulik 1993).

This accomplishes our qualitative genetic model for the deposition of the Krivoy Rog BIF. This model is, of course, rather tentative and certainly needs much better justification in the future by geochemical and experimental studies. Nevertheless, it seems to explain consistently all the known facts discussed in this paper, thus providing a clear guideline for subsequent studies of Krivoy Rog-type BIFs and its comparison with counterparts on other continents.

The authors are grateful to N. J. Beukes, W. Altermann, B. Böhn and an anonymous reviewer. The manuscript benefited from their comments and helpful suggestions. Special thanks are due to the late Ya. N. Belevtsev who introduced both authors into geological studies of the Krivoy Rog basin, to G. P. Glasby for stimulating discussions on the geochemistry of manganese, and to I. N. Kulik for drafting and re-drawing the complicated figures.

References

- ANBAR, A. D. & HOLLAND, H. D. 1992. The photochemistry of manganese and the origin of banded iron-formations. *Geochimica et Cosmochimica Acta*, **56**, 2595-2603.
- ARNDT, N. T., NELSON, D. R. *et al.* 1991. The age of the Fortescue Group, Hamersley Basin, Western Australia, from ion microprobe zircon U-Pb results. *Australian Journal of Earth Sciences*, **38**, 261-281.
- BALZER, W. 1982. On the distribution of iron and manganese at the sediment-water interface: thermodynamic versus kinetic control. *Geochimica et Cosmochimica Acta*, **46**, 1153-1161.
- BARTON, E. S., ALTERMANN, W., WILLIAMS, I. S. & SMITH, C. B. 1994. U-Pb zircon age for a tuff in the Campbell Group, Griqualand West Sequence, South Africa: Implications for Early Proterozoic rock accumulation rates. *Geology*, **22**, 343-346.

- BAU, M. & MÖLLER, P. 1993. Rare earth element systematics of the chemically precipitated component in Early Precambrian iron formations and the evolution of the terrestrial atmosphere-hydrosphere-lithosphere system. *Geochimica et Cosmochimica Acta*, **57**, 2239–2249.
- BAUR, M. E., HAYES, J. M., STUDLEY, S. A. & WALTHER, M. R. 1985. Millimeter-scale variations of stable isotope abundances in carbonates from banded iron formations in the Hamersley Group of Western Australia. *Economic Geology*, **80**, 270–282.
- BELEVTSSEV, YA. N. & BELEVTSSEV, R. YA. 1981. *Geological structure and iron ores of the Krivorozhsky basin*. Naukova Dumka Publ., Kiev. **48**.
- BELEVTSSEV, R. YA., BELYAEV, O. YA. *et al.* 1989. [*Precambrian iron formations of the European part of the USSR: Metamorphism*]. Naukova Dumka, Kiev. **180** [in Russian].
- BELEVTSSEV, YA. N., BELEVTSSEV, R. YA. & SIROSHTAN, R. I. 1983. The Krivoy Rog basin. In: A. F. TRENDALL, A. F. & MORRIS, R. C. *Iron-formation: Facts and Problems*. Elsevier, Amsterdam, 211–251.
- BELEVTSSEV, YA. N., KULIK, D. A. *et al.* 1992. [*Precambrian banded iron-formation of the European part of the USSR. Iron accumulation in Precambrian*]. Naukova Dumka, Kiev, **228** [in Russian].
- BORCHERT, H. 1952. Die Bildungsbedingungen mariner Eisenerzlagerstätten. *Chemie der Erde*, **16**, 49–74.
- BOSTRÖM, K., INGRI, J. & PONTÉR, C. 1988. Origin of iron-manganese-rich suspended matter in the Landsort Deep, NW Baltic Sea. *Marine Chemistry*, **24**, 93–98.
- , WIBORG, L., & INGRI, J. 1982. Geochemistry and origin of ferromanganese concretions in the gulf of Bothnia. *Marine Geology*, **50**, 1–24.
- BURDIGE, D. J. 1993. The biogeochemistry of manganese and iron reduction in marine sediments. *Earth-Science Reviews*, **35**, 249–284.
- DAVIS, J. C. 1986. *Statistics and data analysis in geology*. 2nd ed., Wiley, New York.
- DERRY, L. A. & JACOBSEN, S. B. 1990. The chemical evolution of precambrian seawater: evidence from REEs in banded iron formations. *Geochimica et Cosmochimica Acta*, **54**, 2965–2977.
- DREVER, J. I. 1974. Geochemical model for the origin of Precambrian banded iron formations. *Geological Society of America Bulletin*, **85**, 1099–1106.
- DROZDOVSKAYA, A. A. 1990. [*Chemical evolution of the ocean and atmosphere in the geological history of the Earth*]. Naukova Dumka, Kiev. **208** [in Russian].
- DYRSSEN, D. & KREMLING, K. 1990. Increasing hydrogen sulfide concentration and trace metal behaviour in the anoxic Baltic waters. *Marine Chemistry*, **30**, 193–204.
- EMELYANOV, E. M. 1981. [Alumosilicate-carbonate-manganiferous lithologo-geochemical area of the Gotland and Landsort Deeps]. In: LISITSYN, A. P. & EMELYANOV, E. M. (eds). [*Sediment formation in the Baltic Sea*]. Nauka, Moscow, 136–180 [in Russian].
- 1986. Basins of the Baltic Sea – traps for elements. *Finnish Marine Research*, **253**, 79–96.
- EWERS, W. E. 1983. Chemical factors in the deposition and diagenesis of banded iron-formation. In: TRENDALL, A. F. & MORRIS, R. C. (eds), *Iron-formation: Facts and problems*. Elsevier, Amsterdam, 491–512.
- ESSENE, E. J. 1983. Solid solutions and solvi among metamorphic carbonates, with applications to geological thermobarometry. In: REEDER, R. J. (ed.) *Carbonates: Mineralogy and Chemistry*. Mineralogical Society of America Reviews in Mineralogy, **11**, 77–96.
- FRYER, B. J. 1983. Rare earth elements in iron-formation. In: TRENDALL, A. F. & MORRIS, R. C. (eds) *Iron-formation: Facts and problems*. Elsevier, Amsterdam, 345–358.
- GARRELS, R. M., THOMPSON, M. E. & SIEVER, R. 1960. Stability of some carbonates at 25°C and 1 atmosphere total pressure. *American Journal of Science*, **258**, 402–418.
- GRASSHOFF, K. 1975. The hydrochemistry of landlocked basins and fjords. In: RILEY, J. P. & SKIRROW, G. (eds) *Chemical oceanography*. 2nd ed. Academic Press, London, 455–597.
- & VOIPIO, A. 1981. 4. Chemical oceanography. In: VOIPIO, A. (ed.) *The Baltic Sea*. Elsevier Oceanography Series, **30**, 183–218.
- HÄLBICH, I. W. & ALTERMANN, W. 1991. The genesis of BIF in the Transvaal Supergroup, South Africa. In: PAGEL, M. & LEROY, J. L. (eds), *Source, transport and deposition of metals*. Balkema, Rotterdam, 287–290.
- HAN, TSU-MING 1978. Microstructures of magnetite as guides to its origin in some Precambrian iron-formation. *Fortschritte der Mineralogie*, **B56**, 105–142.
- HARDER, H. 1978. Synthesis of iron layer silicate minerals under natural conditions. *Clays and Clay Minerals*, **26**, 65–72.
- & FLEHMIG, W. 1970. Quarzsynthese bei tiefen Temperaturen. *Geochimica et Cosmochimica Acta*, **34**, 295–305.
- HEUSER, H. 1988. *Beobachtungen und Untersuchungen zur Genese von Flachwasser-Manganknollen in der Kieler Bucht (westl.Ostsee)*. Dr.Rer.Nat. Dissertation, Berichte Geologisch-Palaeontologisches Institut Kiel, **26**, 135pp.
- HOLLAND, H. D. 1984. *The chemical evolution of the atmosphere and oceans*. Princeton University Press, Princeton, NJ.
- JAMES, H. L. 1954. Sedimentary facies of iron-formation. *Economic Geology*, **49**, 235–293.
- & TRENDALL, A. F. 1982. Banded iron-formation: Distribution in time and paleoenvironmental significance. In: HOLLAND, H. D. & SHIDLOWSKI, M. (eds). *Mineral Deposits and the Evolution of the Biosphere*. Springer, New York 199–217.
- KLEIN, C. 1983. Diagenesis and metamorphism of Precambrian banded iron-formation. In: TRENDALL, A. F. & MORRIS, R. C. (eds) *Iron-formation: Facts and problems*. Elsevier, Amsterdam, 417–469.

- & BEUKES, N. J. 1989. Geochemistry and sedimentology of a facies transition from limestone to iron-formation deposition in the early Proterozoic Transvaal Supergroup, South Africa. *Economic Geology*, **84**, 1733–1774.
- KORZHNEV, M. N. & FOMIN, YU. A. 1992. [Evolution of conditions of accumulation of the Krivoy Rog series from the geochemical and isotopic data]. *Geological Journal (Kiev)*, **3**, 93–99 [in Russian].
- & POKALYUK, V. V. 1993. [Geochemical features of metabasites in the Krivoy Rog basin]. [*Transactions of the National Academy of Sciences of the Ukraine*], **1**, Kiev, 70–74 [in Russian].
- KULIK, D. A. 1986. [*Types and genesis of banded structures in banded iron formation of the Saksagan Group in Krivoy Rog basin (Ukrainian Shield)*]. Cand. Geol.-Min. Sci. Diss., Institute of Geochemistry and Physics of Minerals, Kiev [in Russian].
- 1991. [Rhythmic banding as reflection of conditions of sedimentation and diagenetic transformation of banded iron formation rocks]. In: KRAVCHENKO, V. M. & KULIK, D. A. (eds) [*Precambrian iron formations of the European part of the USSR. Genesis of iron ores*]. Naukova Dumka, Kiev, 22–42 [in Russian].
- 1993. [Dynamics of low-grade metamorphic ore formation in the Precambrian banded iron-formations]. In: BELEVTSYEV, YA. N. (ed.) [*Metallogeny of Precambrian and metamorphogenic ore formation*]. Naukova Dumka, Kiev, 175–183 [in Russian].
- & CHERNOVSKY, M. I. 1996. Fractal properties of multi-order folding as a tool for exploration of low-grade iron ores in the Krivoy Rog basin (Ukraine). *Geologische Rundschau*, **85**, 3–11.
- & HARFF, J. 1993. Physicochemical modeling of the Baltic Sea water-sediment column: I. Reference ion-association models of normative seawater and of Baltic Sea brackish waters at salinities 1–40‰, 1 bar total pressure and 0 to 30°C temperature (system Na–Mg–Ca–K–Sr–Li–Rb–Cl–S–C–Br–F–B–N–Si–P–H–O). *Meerwissenschaftliche Berichte Warnemünde*, **6**, 1–80.
- & POKALYUK, V. V. 1990. [Matter balance in the sedimentation cycling of the Krivoy Rog basin]. *Lithology and mineral deposits*, **2**, 36–49 [in Russian].
- KULISH, YE. A., POKALYUK, V. V. & RESHETNYAK, V. V. 1987. [Mineralogical and geochemical features of the Upper Archaean palaeosol in the Krivoy Rog basin]. *Transactions of the All-Union Mineralogical Society*, **116**, 564–573 [in Russian].
- LAZARENKO, E. K. (ed.) 1977. [*Mineralogy of the Krivoy Rog basin*]. Naukova Dumka, Kiev, **542** [in Russian].
- LEWIS, B. L. & LANDING, W. M. 1991. The biogeochemistry of manganese and iron in the Black Sea. *Deep-Sea Research*, **38**, Supplement 2, S773–S803.
- LIZKO, L. I. 1979. [Geochemical features of ferruginous quartzites of Krivoy Rog and their use in stratigraphic correlation]. In: SIDORENKO, A. V. (ed.) [*Precambrian iron formations*]. Nauka, Moscow, 97–149 [in Russian].
- MEL'NIK, YU. P. 1982. *Precambrian banded iron-formation: Physicochemical conditions of formation*. Elsevier, Amsterdam.
- 1986. [*Genesis of the Precambrian banded iron-formations*]. Naukova Dumka, Kiev, **236** [in Russian].
- MIYANO, T. & BEUKES, N. J. 1987. Physicochemical environments for the formation of quartz-free manganese oxide ores from the Early Proterozoic Hotazel Formation, Kalahari Manganese Field, South Africa. *Economic Geology*, **87**, 706–718.
- MOREL, F. M. M. & HERING, J. G. 1993. *Principles and applications of aquatic chemistry*. Wiley Interscience, New York.
- MORRIS, R. C. 1993. Genetic modelling for banded iron-formation of the Hamersley Group, Pilbara Craton, Western Australia. *Precambrian Research*, **60**, 243–286.
- & EWERS, W. E. 1978. A simple streak-print technique for mapping mineral distributions in ores and other rocks. *Economic Geology*, **73**, 562–566.
- & HORWITZ, R. C. 1983. The origin of the BIF-rich Hamersley Group of Western Australia – deposition on a platform. *Precambrian Research*, **21**, 273–298.
- NEALSON, K. N. & MYERS, C. R. 1992. Microbial reduction of manganese and iron: New approaches to carbon cycling. *Applied Environmental Microbiology*, **58**, 439–443.
- PERRY, E. C. JR. & AHMAD, S. N. 1981. Oxygen and carbon isotope geochemistry of the Krivoy Rog iron formation, Ukrainian SSR. *Lithos*, **14**, 83–92.
- PIROGOV, B. I., EVTEKHOV, V. D. et al. 1989. [*Precambrian iron formations of the European part of the USSR: Mineralogy*]. Naukova Dumka, Kiev, **168** [in Russian].
- PLAKSENKO, N. A. 1966. [*Principal regularities of iron-formation deposition in the Precambrian*]. Voronezh Univ. Publ., Voronezh, **264** [in Russian].
- , GOR'KOVETS, V. YA. et al. 1988. [*Precambrian iron formations of the European part of the USSR: Formation types*]. Naukova Dumka, Kiev, **188** [in Russian].
- PLOTNIKOV, A. V. 1994. [Tectonic structure and evolution of the Krivoy Rog ore basin as a deep-seated fault zone]. *Geotectonics*, **2**, Moscow, 33–48 [in Russian].
- RAMIRES, G. K. A. & TROSHCHENKO, V. N. 1992. [Palaeoreconstruction of the Saksagan suite metamorphic rocks in the South region of the Krivoy Rog basin]. *News of High school, Geology and Prospecting series*, **6**, Moscow, 47–52 [in Russian].
- REIMER, T. O. 1987. Weathering as a source of iron in iron-formations: The significance of aluminium-enriched paleosols from the Proterozoic of South Africa. In: APPEL, P. W. U. & LA BERGE, G. L. (eds) *Precambrian iron formations*. Theophrastus, Athens, 601–620.
- SAVCHENKO, L. T. 1991. [Regularities of variations in the isotope compositions of sulfur, carbon and oxygen in banded iron formations]. In: KRAVCHENKO, V. M. & KULIK, D. A. (eds) [*Precambrian iron formations of the European part of the USSR. Genesis of iron ores*]. Naukova Dumka, Kiev, 51–64 [in Russian].

- SCHIDLOWSKI, M. 1982. Content and isotopic composition of reduced carbon in sediments. In: HOLLAND, H. D. & SHIDLOWSKI, M. (eds) *Mineral Deposits and the Evolution of the Biosphere*. Springer, New York, 103–122.
- SEMENENKO, N. P. (ed.) 1978. [Iron formations of the Ukrainian Shield], 2. Naukova Dumka, Kiev [in Russian].
- SHAPOSHNIKOV, V. A. 1978. [The Skelevat Magnetite deposit]. In: SEMENENKO, N. P. (ed.) [Iron formations of the Ukrainian Shield], 2. Naukova Dumka, Kiev, 201–248 [in Russian].
- SHCHERBAK, N. P., BELEVTSSEV, YA. N. *et al.* 1988. [Precambrian iron-formations of the European part of the USSR. Stratigraphy]. Naukova Dumka, Kiev, 192 [in Russian].
- , ARTEMENKO, G. V. *et al.* 1989. [Geochronological scale of the Precambrian of the Ukrainian Shield]. Naukova Dumka, Kiev, 144 [in Russian].
- SIEVER, R. 1992. The silica cycle in the Precambrian. *Geochimica et Cosmochimica Acta*, 56, 3265–3272.
- STRAKHOV, N. M. 1963. [Types of lithogenesis and their evolution in the Earth history]. Gosgeoltekhizdat, Moscow [in Russian].
- STUMM, W. 1992. *Chemistry of the solid-water interface*. Wiley Interscience, New York.
- SUESS, E. 1979. Mineral phases formed in anoxic sediments by microbial decomposition of organic matter. *Geochimica et Cosmochimica Acta*, 43, 339–352.
- & DJAFARI, D. 1977. Trace metal distribution in Baltic Sea ferromanganese concretions: Inferences on accretion rates. *Earth and Planetary Science Letters*, 35, 49–54.
- SVITAL'SKII, N. I., POLOVINKINA, YU. I. *et al.* 1932. [The iron deposit of the Krivoy Rog]. Transactions of VGRO NKTP USSR, 253, Moscow-Leningrad [in Russian].
- TAYLOR, S. R. & MCLENNAN, S. M. 1985. *The continental crust: its composition and evolution*. Blackwell Scientific, Boston.
- TRENDALL, A. F. 1972. Revolution in Earth history. *Journal of the Geological Society of Australia*, 19, 287–311.
- & BLOCKLEY, J. G. 1970. *The iron formations of the Precambrian Hamersley Group, Western Australia; with special reference to the associated crocidolite*. Western Australia Geological Survey Bulletin, 119.
- TROSHCHENKO, V. N. & IVANCHENKO, V. V. 1982. [Zircon as an indicator of clastic material in the Krivoy Rog series metasediments.] In: BELEVTSSEV, YA. N. (ed.), [Problems of metamorphogenic ore formation in the Precambrian]. Nauchnaya Kniga, Kiev, 77–79 [in Russian].
- TUGARINOV, A. I., BALASHOV, YU. N. & GAVRILOVA, P. K. 1973. [Distribution of the rare earth elements in the Palaeoproterozoic Krivoy Rog Supergroup]. *Geokhimiya* 1, 28–34 [in Russian].
- VALEEV, O. K. & EVTEKHOV, V. D. 1991. [Thermal deconsolidation of the Precambrian ferruginous-siliceous rocks and its role in the processes of ore formation]. *News of High School, ser. Geology and Prospecting*, 9, 58–66 [in Russian].
- VOYTKEVICH, G. V., KOKIN, A. V. *et al.* 1990. [Handbook of Geochemistry]. Nedra, Moscow [in Russian].
- WALKER, J. C. G. 1984. Suboxic diagenesis in banded iron formations. *Nature*, 309, 340–342.

Insight into the enigma of Neoproterozoic manganese and iron formations from the perspective of supercontinental break-up and glaciation

BERNHARD BÜHN¹ & IAN G. STANISTREET²

¹*Institut für Geowissenschaften, Justus-Liebig-Universität, Senckenbergstrasse 3, D-35390 Giessen, Germany*

²*Department of Earth Sciences, University of Liverpool, PO Box 147, Liverpool L69 3BX, UK; and Postgraduate College for Geoscientific Research in Africa, University of Würzburg, Germany*

Abstract: The genesis of manganese and iron formations (MnF and IF) is a closely related process during the Proterozoic, in which oceanic crustal venting provided metal-rich solutions to be deposited on adjacent continental shelves. Their deposition in condensed marine sequences occurred when continental break-up initiated a major transgression and provided favourable conditions for precipitation of chemical sediments from seawater. The Neoproterozoic Rodinian supercontinental break-up shows the relationship between this tectonic process, climate, and MnF/IF genesis. Metallogenesis followed particular rift–drift transitions during supercontinental break-up. MnFs/IFs are often associated with glaciomarine sedimentary rocks. Higher O₂/CO₂ during continental rifting would, through inducing glacial conditions and withdrawing seawater, increase ocean salinity and thereby allow both deposition of glaciomarine sediments and precipitation of evaporites. Salinities would have been particularly enhanced in the restricted oceanic basins provided by early supercontinental rifting, where atmospheric evaporation would also have played a part. Accumulation of Mn and Fe in the Neoproterozoic may be directly related to a probably glacially derived increased ocean salinity that promoted accumulation and storage of Mn and Fe in ocean water through increased Mn, Fe, and Ba(?) solubility. Very similar processes may have been effective in Palaeoproterozoic times, although then a higher amount of Fe and Mn discharge and different ocean chemistry would have superseded the effect of ocean salinity. Chemical Mn and Fe precipitates related to supercontinental break-up in the Proterozoic as well as the Phanerozoic indicate a similar relationship between tectonics and ore accumulation. The resultant close time and space relationship between potent oceanic source and suitable continental-shelf depositional settings optimised accumulation and preservation of ancient Mn–Fe deposits. This scenario is at variance from present-day environments where source and suitable precipitation areas of long-term preservation potential are mostly widely separated in space.

Manganese depositing scenarios seem to have occurred during specific intervals throughout geological history. Among these, manganese and iron formations (MnFs, IFs) of Neoproterozoic age hold a particularly important place in Mn and Fe metallogenesis. This is because they developed during only a short time interval distinctly separated from the giant Palaeoproterozoic Mn and Fe deposits of this kind (Klein & Beukes 1992; Schissel & Aro 1992), and represent the last manifestation of coupled MnFs and IFs on a regional scale before the IF decline in the Phanerozoic. An enigma is that, on the one hand, Neoproterozoic MnFs and IFs are associated with glaciogenic rocks and, on the other, with evaporites and carbonates. Another aspect of the formations are the contrasts in palaeogeographic data that have led to debates on the possibility of low-latitude glaciations and

ultimately to a reinterpretation of their depositional palaeo-latitudes (see Meert & Van der Voo 1994). Despite these particular Neoproterozoic scenarios and differing atmospheric/hydrospheric conditions relative to the Palaeoproterozoic, there are nevertheless distinct similarities in the lithostratigraphic sections and palaeotectonic settings of MnF/IF-bearing sequences in general, and there appears to be no reason to invoke grossly differing mechanisms, sources and conditions of sedimentation.

In recent years numerous contributions have elucidated continental plate configurations and dynamics for the Neoproterozoic on palaeomagnetic and geological grounds (Bond *et al.* 1984; Hoffman 1991; Murphy & Nance 1991; Dalziel 1992; Young 1992; Powell *et al.* 1993; Meert & Van der Voo 1994; Torsvik *et al.* 1995). Another group of authors has focused on the evolution of

the atmosphere–hydrosphere system (e.g. Knoll *et al.* 1986; Brasier 1992; Des Marais *et al.* 1992; Derry *et al.* 1992; Kump & Holland 1992; Veizer 1992; Des Marais 1994) and to some extent addressed tectonic or climatic issues. Modes of Proterozoic metallogenesis of MnFs and IFs have been envisaged in several models (Roy 1988; Kimberley 1989, 1994; Bühn *et al.* 1992, 1993; Klein & Beukes 1993; Isley 1995). Only a few have included a consideration of tectonic or climatic controls (Young 1988, 1989, 1995*a, b*), although Proterozoic IF and MnF lithologies reflect several specific environmental conditions that must have occurred both at the source and depositional site. The causative circumstances reflected by the production of shelf-edge MnFs and IFs shed light on tectonics and climatic conditions during their precipitation, especially when glacial deposits are associated. It is the intention here to combine knowledge of MnF and IF depositional regimes with that of palaeo-reconstructions and climatic settings with special regard to the Neoproterozoic.

Genetic relationship between Precambrian IFs and MnFs

The decline of IFs during the Phanerozoic has no comparable equivalent in manganese metallogenesis, and numerous Mn deposits of post-Precambrian time are encountered (see Roy 1988). These deposits are not associated with IFs, and models for their genesis have been put forward e.g. by Force & Cannon (1988) and Frakes & Bolton (1984) taking into account Mesozoic and Cenozoic palaeoenvironments. Most Palaeo- and Neoproterozoic MnFs occurrences are associated with IFs (one exception being Neoproterozoic MnFs in India, although they are hosted in part by Fe-rich carbonates; see also Mukhopadhyay *et al.* this volume) and consequently it is of concern as to what extent IF and MnF metallogenesis are coupled processes during the Precambrian. Kimberley (1989) assumed the same oceanic crustal source for both Fe and Mn, but favoured a differential dissolution process rather than that of differential precipitation because of the lack of a lateral Fe/Mn variation in MnFs and IFs. Hence he proposed selective leaching and separation of the metals already at the source. This implies that MnFs and IFs would precipitate from different solutions and that the separation mechanisms operate already during the alteration process.

Proterozoic manganese formations, however, do display a Mn/Fe variation both along strike

and stratigraphically. Visser (1954) reported a gradational transition from manganese ores into manganese banded ironstones from the Palaeoproterozoic manganese fields in South Africa. Schissel & Aro (1992) described lateral interfingering of manganese with iron formations. Also, Martin (1965) noted a lateral gradation of manganese ores into manganeseiferous hematite–magnetite rocks from the Neoproterozoic Damara Belt in Namibia. Examples of vertical gradation are widespread (Nel *et al.* 1986; Beukes 1983; Bau & Bühn unpubl. data). Gradation between MnFs and IFs indicates a direct genetic connection, with the conditions that are responsible for metal separation operating predominantly at the depositional site and not in the source area. A pre-disposition in the oceanic alteration zones or during transport cannot be ruled out, but it is suggested that Fe and Mn are leached together in one process and precipitate from essentially the same solutions. Although most Proterozoic MnFs are directly associated with IFs, the opposite is often not true. This has been explained by the higher oxidizing conditions required for the precipitation of manganese relative to iron, which are not always met at the depositional site, and/or by the inhibition of Mn^{2+} photo-oxidation in the presence of iron (Anbar & Holland 1992). Even if a differential dissolution process can be inferred, both precipitates originate from the same hydrothermal source area and form overall by the same depositional mechanism. This intimate but not exclusive connection between MnFs and IFs shows that their genetic aspects have to be treated together and that the issues they raise need to be solved in a joint approach.

Source of the metals

There are at least three specific requirements that have to be met to explain the accumulation of MnFs and IFs in the Proterozoic: (i) the production of dissolved Fe and Mn; (ii) the accumulation and storage process (with or without transport) of the solutions in appreciable quantities; and (iii) a mechanism for their selective precipitation. It is now commonly accepted that the metals derive from the alteration of oceanic crust through venting fluids (see e.g. Kimberley 1989). Fe and Mn could, if necessary, be effectively separated at the vents from base metals and sulphide (Bühn *et al.* 1992).

The lack of a normalized Eu anomaly in most Neoproterozoic IFs is characteristic in contrast with the strongly positive Eu anomalies of

Palaeoproterozoic IFs (Derry & Jacobson 1990). The latter are attributed to high-temperature alteration of oceanic crust which would reduce Eu to the divalent state and produce a positive Eu anomaly in the solution (Bau & Möller 1993). Low-temperature solutions, on the other hand, would not be able to reduce Eu^{3+} , and Bau & Möller (1993) attributed decreasing $(\text{Eu}/\text{Sm})_{\text{cn}}$ during the Precambrian to the increasing predominance of low-temperature alteration of oceanic crust. If one accepts that mantle temperatures and oceanic crustal alteration processes in the Neoproterozoic are broadly comparable to contemporary conditions, then, low-temperature alteration would indeed be the prominent mechanism because high-temperature ($>200^\circ\text{C}$) alteration is extremely localized in modern oceanic crust (Rona 1984). Low-temperature alteration processes preferentially leach Fe and Mn, and would have been the dominant alteration mechanism over large areas adjoining the rift axes of oceanic spreading ridges, whereas high-temperature alteration would have been very restricted both in space and time (e.g. Rona 1984). The dominance of low-temperature hydrothermal fluids as a Mn and Fe source could also explain the lack of a Eu anomaly in Neoproterozoic IFs. There is no obvious reason for a higher dilution of Neoproterozoic Fe/Mn solutions relative to Palaeoproterozoic solutions as put forward by Klein & Beukes (1993) to explain the lack of this Eu anomaly (certainly not when a severe glaciation extracts large volumes of ocean water), and the low-temperature alteration model would provide a more consistent explanation.

Relatively low temperatures of leaching fluids have an impact not only on the REE distribution but also on the total amount of Fe and Mn leached. Hydrothermal fluids at 425°C are able to dissolve 100 times more Fe than at 350°C (Seyfried & Janecky 1985). In present-day environments, metals like Fe and Mn disperse from vents and plumes into the oceans to an overwhelming extent (Feely *et al.* 1994), whereas base metals precipitate directly from the plumes. The temperature-dependence of Fe leaching and higher Fe fluxes in the Archaean and Palaeoproterozoic (see Kump & Holland 1992) is reflected also by the fact that Neoproterozoic IFs and MnFs are much smaller in size and tonnage than higher-temperature-derived Palaeoproterozoic accumulations. Given these considerations, the mere presence of Neoproterozoic MnFs and IFs after a long absence from the sedimentary record since the Palaeoproterozoic requires explanation. Mechanisms are required in the Neoproterozoic to produce,

store, and accumulate solutions in spite of a much less effective source in terms of total amount of venting.

Geotectonic setting of Proterozoic MnFs and IFs

The relationship between exhalative activity and rifting episodes is crucial in understanding MnF and IF metallogenesis. The Neoproterozoic was a time of supercontinental rifting and reorganization of continents (e.g. Murphy & Nance 1991). Iron formations developed in rift-related palaeoenvironments both in the Palaeoproterozoic (Schissel & Aro 1992; Morey 1983) and Neoproterozoic (Bühn *et al.* 1992, 1993), and most of these IFs are related to continental break-up sequences (Kimberley 1989; Roberts & Gale 1978; Bühn *et al.* 1992). There is strong evidence that during the entire Proterozoic continental break-up, associated transgressive events, and MnF/IF genesis were closely related in space and time. This relationship also holds for younger manganese accumulations e.g. the Jurassic of the Gulf of Mexico, where MnF genesis is correlated with early rifting and production of oceanic crust (Salvador 1987).

The large supercontinent envisaged for the Neoproterozoic (Rodinia) is thought to have assembled by the latest at 1100–1000 Ma (Powell *et al.* 1993; Gurnis & Torsvik 1994; Des Marais 1994). Break-up of this supercontinent is divided into two rifting episodes (Powell *et al.* 1993; Meert & van der Voo 1994). Supercontinental break-up takes place because large continents store heat in the mantle that leads to strong upwelling and will elevate and extend the plate until failure and break-up ensues (Worsley *et al.* 1984; Gurnis 1988). Models predict a major transgression when continents subside after break-up. From the average horizontal stress, Gurnis (1988) derived an approximate maximum difference in elevation between peak updoming and peak subsidence of about 3 km, although extensional effects within the supercontinent may limit this effect. Nevertheless the considerable degree of uplift and thermal cooling that followed must have major influence on erosion rates and sea level.

Iron formations of the Neoproterozoic and also the Palaeoproterozoic (Klein & Beukes 1989) comprise part of transgressive sequences, and the same holds for the rarer associated manganese formations that are coeval with peak transgression (e.g. Schissel & Aro 1992; Bühn *et al.* 1992). The deposition of IFs in the Neoproterozoic Rapitan Group, previously correlated with maximum glaciation and regression

(Young 1976), has been reinterpreted by Klein & Beukes (1993) to represent maximum ice retreat and transgression leading to IF deposition. In contrast with the interpretation of Klein & Beukes (1993) that MnF/IF deposition is a direct result of inter-glacial sea-level rise, we consider the major transgression represented by these chemical sediments to be triggered by thermal subsidence of the continental margins after an extensional rifting and break-up episode.

Transgressive near-shore sandstone deposits of Neoproterozoic age overlying basement lithologies initially reflect this major transgression and are overlain by chemical IF and/or MnF precipitates in India (Bandopadhyay 1988), Namibia (Bühn *et al.* 1992), and Brazil (Urban *et al.* 1992). The same relationship holds for Palaeoproterozoic IFs in North America (Simonson 1985), and the South African Transvaal Supergroup MnFs and IFs are laterally correlated with nearshore arenites towards the interior of the Kapvaal craton (N. J. Beukes pers. comm.). We believe that this reflects the major transgression developed during continental break-up, which flooded the continental shelves and led to highly mature, reworked sandstone deposits near shore, and to pelagic conditions on the middle- to outer-shelf. An unconformity and related conglomerates may be developed at the base of the transgressive sequence which can be interpreted as the break-up unconformity. The vertical lithological change over a small stratigraphic interval in the order of tens of centimetres (Ojakangas 1983; Bühn *et al.* 1992) from mature clastic rocks to chemical precipitates with little terrigenous input proposes a very rapid transgression, which might be expected during the break-up of continental lithosphere as modelled by Gurnis (1988). Metallogenesis in the Neoproterozoic Damara rocks occurred at the rift–drift transition when continental margins subsequently thermally subsided, lithospheric extensional stress was released through the development of oceanic rift systems and the associated transgression inundated adjacent shelf areas. By this means the source of Mn and Fe exhalation developed immediately adjacent to pelagic conditions on top of long-lived continental lithosphere. These are ideal conditions to receive and preserve the resulting MnF and IF accumulations for long periods of Earth history.

Global tectonics and climate

Many Neoproterozoic IFs and MnFs are associated with glaciomarine sediments. On the

other hand, the glaciogenic diamictites are in places interbedded with evaporites. Evaporite minerals were found in the Canadian Rapitan iron formation (Young 1976), a seeming contradiction with the occurrence of associated glaciogenic sediments. Previous palaeomagnetic data and plate tectonic reconstructions (see Hoffman 1991; Brasier 1992; Dalziel 1992) supported the low to intermediate palaeolatitudes of glacial sediments, evaporites and IFs/MnFs. An attempt to resolve these contradictions has been the interpretation of the so-called tillites as impact (e.g. Oberbeck *et al.* 1993) or as mass-flow deposits (Schermerhorn 1974, 1983). The generally accepted view was that of an extensive glaciation in which floating ice sheets extended to equatorial latitudes (e.g. Klein & Beukes 1993) of a 'snowball earth' (Kirschvink 1992). This model was questioned recently by Meert & Van der Voo (1994) on the basis of new palaeopositions of the continents. They concluded that all Neoproterozoic glaciomarine sediments were deposited at latitudes $\geq 25^\circ$. Nevertheless, it is clear that Neoproterozoic glaciations existed and were associated with an appreciable accumulation of Fe and Mn on passive margin continental shelves.

Meert & Van der Voo (1994) also noted a synchronicity of glaciation and passive margin evolution. The connection between MnF/IF accumulation (on passive margins) and glaciation indicates that a genetic relation exists between both of these and global tectonic configurations. The connection of climatic changes on Earth with tectonic processes as a function of atmospheric CO_2 was stressed by Young (1989), who related rifting-induced high-standing continents with cold periods, although this did not apply during the break-up of Pangaea. Carbon isotopes verified this connection, and a stepwise oxidation of the Proterozoic palaeoenvironment with peaks in O_2/CO_2 concomitant with major rifting processes in the Palaeo- and Neoproterozoic, respectively, was envisaged by Des Marais *et al.* (1992). Higher O_2/CO_2 would have had an impact on climate resulting in glacial conditions (see e.g. Broecker 1982). Schermerhorn (1983) proposed that the Neoproterozoic glaciation is due to an atmospheric CO_2 depletion. Rifting and continental break-up of the Neoproterozoic supercontinent, which increased the atmospheric O_2/CO_2 ratio, may therefore have been the direct cause of a prominent glaciation. Discussion on this possible genetic relation is still going on (see Powell 1995 and Young 1995b). It is nevertheless significant in this respect that glaciogenic deposits may closely relate to continental break-up

although the relative timing is different. Break-up episodes of Laurentia were reported as following the deposition of glaciogenic sediments (Powell *et al.* 1993; Meert & Van der Voo 1994), whereas the glaciogenic facies in the Namibian Neoproterozoic are interpreted to have followed immediately continental break-up between the Kalahari and Congo cratons (Stanistreet *et al.* 1991).

Although an anoxic atmosphere, as stated by Kimberley (1989), is not a sufficient or at least not the only cause for IF (and MnF) genesis, the favourable conditions for MnF and IF accumulation during the Palaeoproterozoic are no longer valid for the Neoproterozoic. The oxidation of hydrosphere and atmosphere proceeded during the Proterozoic and mantle temperatures decreased, so that both submarine leaching of metals and their accumulation in the hydrosphere were no longer as effective as they had been in the early Precambrian. This is supported by the simple fact that Neoproterozoic IFs and MnFs are far less prominent in size than their Palaeoproterozoic counterparts. The question then arises whether there is a direct link between IF/MnF genesis and glaciation in the Neoproterozoic, which could substitute for those favourable conditions generally pertaining to the Palaeoproterozoic and provide additional parameters relevant for MnF and IF genesis. Des Marais *et al.* (1992) envisaged that the earliest known glaciations coincide with the Palaeoproterozoic era, but indication for earlier glacially derived diamictites is given from the Archaean Pongola Sequence in southern Africa (Von Brunn & Gold 1993). The clast population in the ferruginous matrix there also comprises iron formation, chert and quartzite, and the sequence from an arenaceous to a diamictite assemblage may be related to rifting of the basin (Von Brunn & Gold 1993). Although the connection between MnFs/IFs and glaciation is most obvious in the Neoproterozoic, diamictites are for example intercalated in the Palaeoproterozoic Transvaal Supergroup between the Griquatown and Kuruman iron formations, and the Hotazel MnFs (Beukes 1986). Glacial deposits and related IFs/MnFs are therefore encountered both in the Palaeo- and the Neoproterozoic (and the late Archaean?), although this facies association is more common in the latter when the glaciations were probably more severe and extensive. In this respect Klein & Beukes (1993) argued for a stagnant ocean model during Neoproterozoic glaciation that allowed reducing conditions to develop for accumulation of Fe and Mn in the water column. This model therefore invokes the

occurrence of IFs and MnFs in the Neoproterozoic as due to a prominent, possibly global glaciation that allowed for the build-up of metal-rich solutions in highly stagnant, reducing oceans.

Kimberley (1989) expressed the view that IFs generally precipitate from saline waters, keeping in mind that the solubility of Fe increases with increasing salinity. There is indeed widespread evidence of high salinity of waters that produced several IFs and MnFs (e.g. Young 1976). The presence of riebeckite in South African Palaeoproterozoic IFs (Beukes 1986) may even be interpreted as being due to previous evaporite minerals. In this respect, Kimberley (1989) argued for the role of dissolution of evaporites in rifted basins (e.g. Red Sea Basin, Rona 1988), which could contribute to a higher Fe solubility. Having established that MnF/IF deposition followed rift-drift transitions, this view makes sense in that IFs and MnFs always overlie continental rift sequences that initially developed in restricted Red Sea-type basins in which evaporites could have developed. However, such rift evaporites are not always recorded in Earth history. Young (1976) pointed out that evaporites (salts, carbonates etc.) could precipitate during glaciation, because salinity increase 'may be effected equally by freezing or evaporation of water'. This very important statement can explain the co-existence of evaporites and glaciomarine sediments and, in addition, could enhance the solubility of Fe by increased salinity (e.g. Kwak *et al.* 1986) during glaciation. Broecker (1982) calculated a quite remarkable salinity increase of seawater of $3.5 \pm 1\%$ over today's value during glaciation. This situation would further promote a density-stratified sea favourable for the accumulation and storage of metals. The salinity increase may well have been localized but could have played a prominent role in the build-up of metal-rich solutions. Salinities would have been even further enhanced in restricted newly opening oceanic basins due to localized evaporative effects. In this regard it is significant that Neoproterozoic MnF deposits in Namibia developed at the blind end of a restricted newly forming oceanic gulf that was undergoing severe glaciation (Stanistreet *et al.* 1991; Bühn & Stanistreet 1992/93). The Neoproterozoic glaciation, through withdrawal of large quantities of water, could therefore provide specific conditions for enhanced Fe and Mn solubility, so that there apparently exists a direct connection between Neoproterozoic supercontinental rifting, glaciation, and the late pulse of Fe and Mn accumulation (Fig. 1). Glaciation may therefore be a direct cause for MnF/IF

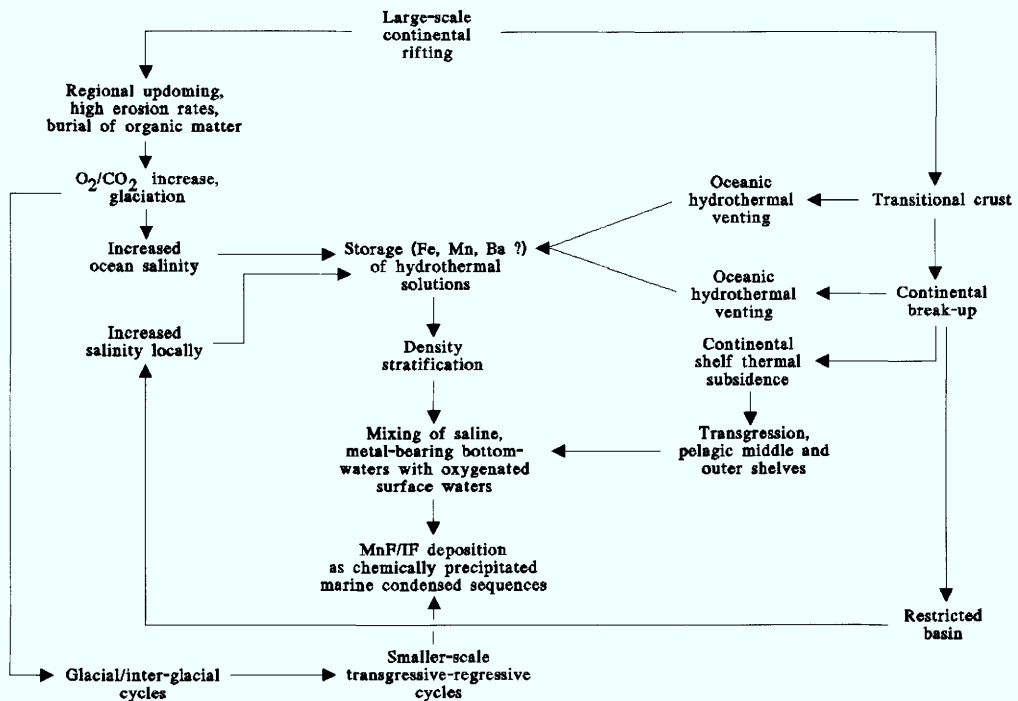


Fig. 1. Relationship between supercontinental break-up, climatic changes, oceanic crustal evolution, and deposition of manganese and iron formations. This scheme specifically applies to Neoproterozoic MnFs and IFs, but may be largely applicable to the Palaeoproterozoic.

accumulation in the Neoproterozoic, whereas in the Palaeoproterozoic it may simply have enhanced its formation during a time of other overwhelmingly favourable conditions, which together allowed accumulation of giant Mn and Fe ore deposits.

Depositional sequences

Several models propose glaciogenic transgressive/regressive cycles for Fe and Mn deposition in Neoproterozoic IFs (Bühn *et al.* 1992, 1993; Urban *et al.* 1992; Klein & Beukes 1993). The latter authors proposed stagnant oceans during glaciation for the build-up of Fe-rich solutions and downwelling of O₂-rich waters in interglacial periods to deposit Fe by oxidation. Reducing conditions to accumulate Fe during widespread glaciation would have contributed to the accumulation of Fe and Mn in stratified basins, but the salinity is thought to play the important role for the build-up of the metal-rich solutions. The salinity increase may have been due to glaciation and withdrawal of large quantities of water during the Neoproterozoic (see Young 1976). Glacial/interglacial episodes

may then account for smaller-scale sedimentary cycles and episodic deposition of different IF and MnF ore varieties (Bühn *et al.* 1993), during which ice retreat and transgression then have led to interglacial deposition of pure MnF and IF facies. However, we believe that the primary, large-scale transgression that was capable of providing middle- to outer-shelf pelagic conditions suitable for chemical precipitates was due to tectonic effects, namely break-up of a supercontinent and thermal subsidence of the adjacent shelf areas. The reduced amount of seawater and resulting salinity increase promoting the build-up of metal-rich solutions would therefore not be counterbalanced by a break-up-related transgression, since the latter would not represent an eustatic sea-level rise but is linked to relative thermal subsidence not affecting the total amount of seawater.

Palaeoenvironmental reconstructions suggest that manganese deposits occur closer to the shoreline than the associated IFs, and that Mn precipitation was due to increased mixing of bottom waters with oxygenated surface waters. Samples collected along the gradual transition from IF into MnF in Neoproterozoic deposits of Namibia yielded continuously changing rare

Table 1. Element variations in Proterozoic iron and manganese formations

	IF			MnF
	MnO	Fe ₂ O ₃	Ba (ppm)	Ba
<i>Neoproterozoic</i>				(wt%)
E. Damara (Namibia) ¹	0.01	5–20	160–4600	1.2–7.9
W. Damara (Namibia) ²	c. 0.15	35–65	50–135	
Urucum (Brazil)	0.01–0.05	c. 95	40–130	0.2–4.0
Rapitan Group (Canada) ³	0.01–0.09	34–50	20–330	
Penganga beds (India)				–0.5
<i>Palaeoproterozoic</i>				(ppm)
Lake Superior type (Canada) ⁴	0.6	40	160	
Biwabik IF (USA) ⁵	0.7	41		
Transvaal Supergroup (S-Africa) ⁶	0.2–0.4	30–70	c. 20	50–250 ⁷
Sausar Group (India)				1000–8000

¹ Böhn *et al.* 1992; ² Bretkopf 1988; ³ Klein & Beukes 1993; ⁴ Gross & McLeod 1980; ⁵ Lepp 1966; ⁶ Beukes & Klein 1990; ⁷ J. Gutzmer pers. comm.

earth element patterns along the profiles, which support this regional distribution with IFs deposited on the outer shelf (Bau & Böhn unpubl. data). Oxide facies MnFs commonly display a higher clastic component in the form of disseminated or laminated silts and clays than iron formations, reflecting the nearer-shore setting of MnFs where the pelagic and hemipelagic middle-shelf realm receives more fine-grained, distal sediment from the continent. Metamorphism would transfer these mixed chemical/clastic rocks into gonditic ore varieties (Dasgupta *et al.* 1990; Böhn *et al.* 1995).

The geochemical affinity of Ba and Mn as reflected by the high Ba contents (as e.g. barite, kryptomelane) is a common feature of many manganese formations (Table 1), but poses problems as to the regional distribution of MnFs and IFs on an oxidized continental shelf. If Fe- and Mn-rich solutions encounter the shelf by a transgressive event and/or upwelling currents, Ba should precipitate readily at moderately oxidising conditions where IFs form. However, barite is not associated with IFs worldwide in such high quantities as with manganese formations. If Ba precipitated from the same solution as Fe and Mn (originating from hydrothermal vents of the open sea), there must have been a mechanism to prevent Ba precipitation together with Fe and to allow transport of Ba and Mn towards highly oxidizing environments. An increased salinity may enhance Ba solution as chloride, but the presence of sulphate should immediately precipitate barite. It is not convincing to argue for grossly different sulphur activities or sulphur species predominance in waters across the continental shelf. Another explanation could

be the presence of organic material to produce highly resistant organo-complexes that can drastically increase the solubility of the cations. Experiments of Desai & Ganguly (1980) showed the stability of Mn, Ba, Fe and Zn complexes (among others), depending on the type of chemical bonds and the type of organic matter. It was recently pointed out by Shock & Koretsky (1995) that metal-organic complexes are likely candidates for an efficient transport of metals in any geological environment. Therefore, the role of organic matter may be significant in transport processes of Ba (and also Fe, Mn?) towards highly oxidising depositional sites.

Discussion and conclusions

There is striking similarity in the driving forces of Precambrian IF and MnF metallogenesis with those of younger periods, that is the break-up of Pangea, during which condensed marine sequences also reflect thermal subsidence of continental shelves. Garzanti (1993) described Himalayan ironstones that postdate domal uplift and increased clastic supply, and mark subsequent thermal subsidence and transgression related to episodes of Gondwana continental break-up during the Permian and Early Cretaceous. Enhanced production of oceanic crust would tend to induce a 'greenhouse' climate and level-out previously increased O₂/CO₂ ratios. It is most remarkable that Mn metallogenesis also reaches a further peak during the Cretaceous and Jurassic. The Lower Cretaceous in Australia bears the huge Groote Eylandt shallow-marine manganese deposits; the

Jurassic of Morocco (Bou Arfa), Mexico (Molango), and Hungary (Urkut) hosts minable manganese accumulations. However, in contrast with the Proterozoic, the intimate association of stratiform manganese and iron accumulations is missing in the Phanerozoic. It is possible that the absence of glaciomarine conditions at such a late stage in Pangean supercontinental break-up was one major factor in this dissimilarity with its Neoproterozoic Rodinia counterpart.

The intimate association of supercontinental break-up and MnF-IF precipitation in the geological past proposes an answer to the question as to why present-day Mn deposits differ so markedly from ancient shelf-type deposits. Present-day oceanic exhalative Mn is produced from sites above relatively cooled mantle at flanks of spreading ridges within large oceanic basins. These sites are in the main distant from potential shelf depositional areas. Mn is therefore deposited on oceanic crust with low long-term preservation potential. In contrast, the accumulation of Mn in ancient shelf settings described here occurred during specific phases of supercontinental break-up, when factors all conspired to promote the genesis and preservation of Mn deposits. The setting brought together exhalatives released from sites flanking spreading centres above relatively hot sub-supercontinental mantle, immediately adjacent to suitable shelf settings that acted as Mn repositories. In addition, these settings on continental lithosphere had long-term preservation potential geologically.

In this sense, genetic aspects of Proterozoic MnFs and IFs are significant for palaeogeographic reconstructions in the way that they reflect specific environments for both the source and the depositional regimes. IFs and MnFs can mark pulses in the break-up of supercontinents when adjacent continental shelves are drowned and provide pelagic shelf areas for the deposition of oceanic venting fluids. This relationship holds for Neoproterozoic, Palaeoproterozoic(?) and Cretaceous/Jurassic Mn and Fe accumulations. Climatic indicators especially developed in the Neoproterozoic elucidate the impact of continental break-up and climate, and the latter seems to promote accumulation and storage of metals in basin waters through an increase in ocean salinity. We believe that supercontinental break-up and related climatic changes are most important in Proterozoic MnF/IF genesis (especially for the Neoproterozoic) and that, vice versa, the development of stratiform, shelf-based MnFs and IFs might be used as tracers for detecting earlier periods of supercontinental break-up.

We would like to thank P. Richter and M. Grünhäuser for XRF data, F. Zereini for donation of samples, and are grateful for suggestions made by two reviewers. Funding and support by the Geological Survey of Namibia and the Deutsche Forschungsgemeinschaft are gratefully acknowledged. The e-mail address of B. Bühn is bernhard.buehn@geo.uni-giessen.de.

References

- ANBAR, A. D. & HOLLAND, H. D. 1992. The photochemistry of manganese and the origin of banded iron formations. *Geochimica et Cosmochimica Acta*, **56**, 2595–2603.
- BANDOPADHYAY, P. C. 1988. Syndepositional and postdepositional features of the manganese ore deposits of the Proterozoic Penganga Group, Adilabad district, Andhra Pradesh, India. *Mineralium Deposita*, **23**, 115–122.
- BAU, M. & MÖLLER, P. 1993. Rare earth element systematics of the chemically precipitated component in early Precambrian iron-formations and the evolution of the terrestrial atmosphere-hydro-sphere-lithosphere system. *Geochimica et Cosmochimica Acta*, **57**, 2239–2249.
- BEUKES, N. J. 1983. Paleoenvironmental setting of iron-formations in the depositional basin of the Transvaal Supergroup, South Africa. *In: TRENDALL, A. F. & MORRIS, R. C. (eds) Iron-formations: Facts and problems*. Elsevier, Amsterdam, 131–210.
- 1986. The Transvaal Sequence in Griqualand West. *In: ANHAEUSSER, C. R. & MASKE, S. (eds) Mineral deposits of Southern Africa*. Geological Society of South Africa, 819–828.
- & KLEIN, C. 1990. Geochemistry and sedimentology of a facies transition – from microbanded to granular iron-formation – in the early Proterozoic Transvaal Supergroup, South Africa. *Precambrian Research*, **47**, 99–139.
- BOND, G. C., NICKERSON, P. A. & KOMINZ, M. A. 1984. Breakup of a supercontinent between 625 Ma and 555 Ma: New evidence and implications for continental histories. *Earth and Planetary Science Letters*, **70**, 325–345.
- BRASIER, M. D. 1992. Global ocean-atmosphere change across the Precambrian-Cambrian transition. *Geological Magazine*, **129**, 161–168.
- BREITKOPF, J. H. 1988. Iron formations related to mafic volcanism and ensialic rifting in the Southern Margin Zone of the Damara Orogen, Namibia. *Precambrian Research*, **38**, 111–130.
- BROECKER, W. S. 1982. Ocean chemistry during glacial time. *Geochimica et Cosmochimica Acta*, **46**, 1689–1705.
- BÜHN, B. & STANISTREET, I. G. 1992/93. A correlation of structural patterns and lithostratigraphy at Otjosondu with the Damara Sequence in the southern Central Zone, Namibia. *Communications of the Geological Survey Namibia*, **8**, 15–21.
- , — & OKRUSCH, M. 1992. Late Proterozoic outer shelf manganese and iron deposits at Otjosondu (Namibia) related to the Damaran oceanic opening. *Economic Geology*, **87**, 1393–1411.

- , — & — 1993. Preservation of sedimentary features in Late Proterozoic manganese and iron formations (Namibia) through Upper Amphibolite facies metamorphism: Protoliths, paleoenvironments and ore genesis. *Resource Geology Special Issue*, **17**, 12–26.
- , OKRUSCH, M., WOERMANN, E., LEHNERT, K. & HOERNES, S. 1995. Metamorphic evolution of Neoproterozoic manganese formations and their country rocks at Otjosondu, Namibia. *Journal of Petrology*, **36**, 463–496.
- DALZIEL, I. W. D. 1992. On the organization of American plates in the Neoproterozoic and the breakout of Laurentia. *Geological Society of America Today*, **2**, 237–241.
- DASGUPTA, S., BANERJEE, H., FUKUOKA, M., BHATTACHARYA, P. K. & ROY, S. 1990. Petrogenesis of metamorphosed manganese deposits and the nature of the precursor sediments. *Ore Geology Reviews*, **5**, 359–384.
- DERRY, L. A. & JACOBSEN, S. B. 1990. The chemical evolution of Precambrian seawater: Evidence from REEs in banded iron formations. *Geochimica et Cosmochimica Acta*, **54**, 2965–2977.
- , KAUFMAN, A. J. & JACOBSEN, S. B. 1992. Sedimentary cycling and environmental change in the Late Proterozoic: Evidence from stable and radiogenic isotopes. *Geochimica et Cosmochimica Acta*, **56**, 1317–1329.
- DESAI, M. V. M. & GANGULY, A. K. 1980. Organometallic interactions of manganese and other heavy metals in the marine environment. In: VARENSOV, I. M. & GRASSELY, GY. (eds) *Geology and geochemistry of manganese*, Akademiai Kiado, Budapest, 389–410.
- DES MARAIS, D. J. 1994. Tectonic control of the crustal organic carbon reservoir during the Precambrian. *Chemical Geology*, **114**, 303–314.
- , STRAUSS, H., SUMMONS, R. E. & HAYES, J. M. 1992. Carbon isotope evidence for the step-wise oxidation of the Proterozoic environment. *Nature*, **359**, 605–609.
- FEELY, R. A., MAASOTH, G. J., TREFRY, J. H., BAKER, E. T., PAULSON, A. J. & LEBON, G. T. 1994. Composition and sedimentation of hydrothermal plume particles from North Cleft segment, Juan de Fuca Ridge. *Journal of Geophysical Research*, **99**, B3, 4985–5006.
- FORCE, E. R. & CANNON, W. F. 1988. Depositional model for shallow-marine manganese deposits around black shale basins. *Economic Geology*, **83**, 93–117.
- FRAKES, L. A. & BOLTON, B. R. 1984. Origin of manganese giants: Sea level change and anoxic-oxic history. *Geology*, **12**, 83–86.
- GARZANTI, E. 1993. Himalayan ironstones, “superplumes”, and the breakup of Gondwana. *Geology*, **21**, 105–108.
- GROSS, G. A. & MCLEOD, C. R. 1980. A preliminary assessment of the chemical composition of iron formation in Canada. *Canadian Mineralogist*, **181**, 223–229.
- GURNIS, M. 1988. Large-scale mantle convection and the aggregation and dispersal of supercontinents. *Nature*, **332**, 695–699.
- & TORSVIK, T. H. 1994. Rapid drift of large continents during the late Precambrian and Paleozoic: Paleomagnetic constraints and dynamic models. *Geology*, **22**, 1023–1026.
- HOFFMAN, P. F. 1991. Did the breakout of Laurentia turn Gondwanaland inside-out? *Science*, **252**, 1409–1412.
- ISLEY, A. E. 1995. Hydrothermal plumes and the delivery of iron to banded iron formation. *Journal of Geology*, **103**, 169–185.
- KIMBERLEY, M. M. 1989. Exhalative origins of iron formations. *Ore Geology Reviews*, **5**, 13–145.
- 1994. Debate about ironstones: has solute supply been surficial weathering, hydrothermal convection, or exhalation of deep fluids? *Terra Nova*, **6**, 116–132.
- KIRSCHVINK, J. L. 1992. Late Proterozoic low-latitude global glaciation: The snowball Earth. In: SCHOPF, J. W. & KLEIN, C. (eds) *The Proterozoic biosphere: A multidisciplinary study*. Cambridge University Press, Cambridge, 51–53.
- KLEIN, C. & BEUKES, N. J. 1989. Geochemistry and sedimentology of a facies transition from limestone to iron-formation deposition in the early Proterozoic Transvaal Supergroup, South Africa. *Economic Geology*, **84**, 1733–1774.
- & — 1992. Time distribution, stratigraphy and sedimentological setting, and geochemistry of Precambrian iron-formations. In: SCHOPF, J. W. & KLEIN, C. (eds) *The Proterozoic biosphere: A multidisciplinary study*. Cambridge University Press, Cambridge, 139–146.
- & — 1993. Sedimentology and geochemistry of the glaciogenic Late Proterozoic Rapitan iron-formation in Canada. *Economic Geology*, **88**, 542–565.
- KNOLL, A. H., HAYES, J. M., KAUFMAN, A. J., SWETT, K. & LAMBERT, I. B. 1986. Secular variations in carbon isotope ratios from Upper Proterozoic successions of Svalbard and East Greenland. *Nature*, **321**, 832–838.
- KUMP, L. R. & HOLLAND, H. D. 1992. Iron in Precambrian rocks: Implications for the global oxygen budget of the ancient Earth. *Geochimica et Cosmochimica Acta*, **56**, 3217–3223.
- KWAK, T. A. P., BROWN, W. M., ABEYSINGHE, P. B. & TEONG HING TAN 1986. Fe solubilities in very saline hydrothermal fluids: Their relation to zoning in some ore deposits. *Economic Geology*, **81**, 447–465.
- LEPP, H. 1966. Chemical composition of the Biwabik Iron Formation, Minnesota. *Economic Geology*, **61**, 243–250.
- MARTIN, H. 1965. *The Precambrian geology of South-west Africa and Namaqualand*. Precambrian Research Unit, University of Cape Town.
- MEERT, J. G. & VAN DER VOO, R. 1994. The Neoproterozoic (1000–540 Ma) glacial intervals: No more snowball earth? *Earth and Planetary Science Letters*, **123**, 1–13.

- MOREY, G. B. 1983. Animikie basin, Lake Superior region, U.S.A. In: TRENDALL, A. F. & MORRIS, R. C. (eds) *Iron-formations: Facts and problems*. Elsevier, Amsterdam, 13–67.
- MUKHOPADHYAY, J., CHAUDHURI, A. K. & CHANDA, S. K. 1997. Deep-water manganese deposits in the middle to late Proterozoic Penganga Group of the Pranhita–Godavari valley, South India. *This volume*.
- MURPHY, J. B. & NANCE, R. D. 1991. Supercontinent model for the contrasting character of Late Proterozoic orogenic belts. *Geology*, **19**, 469–472.
- NEL, C. J., BEUKES, N. J., & DE VILLIERS, J. P. R. 1986. The Mamatwan manganese mine of the Kalahari manganese field. In: ANHAEUSSER, C. R. & MASKE, S. (eds) *Mineral deposits of Southern Africa*. Geological Society of South Africa, 963–978.
- OBERBECK, V. R., MARSHALL, J. R. & AGGARWAL, H. 1993. Impacts, tillites and the breakup of Gondwanaland. *Journal of Geology*, **101**, 1–19.
- OJAKANGAS, R. W. 1983. Tidal deposits in the Early Proterozoic basins of the Lake Superior region – The Palms and the Pokegama Formations: Evidence for subtidal shelf deposition of Superior-type banded iron-formation. In: MEDARIS, L. G. (ed.) *Early Proterozoic Geology of the Great Lake Region*. Geological Society of America Memoirs, **160**, 49–66.
- POWELL, C. M. A. 1995. Comment on: “Are Neoproterozoic glacial deposits preserved on the margins of Laurentia related to the fragmentation of two supercontinents?” by G. M. YOUNG. *Geology*, **23**, 1053–1054.
- , LI, Z. X., MCELHINNY, M. W., MEERT, J. G. & PARK, J. K. 1993. Paleomagnetic constraints on timing of the Neoproterozoic breakup of Rodinia and the Cambrian formation of Gondwana. *Geology*, **21**, 889–892.
- ROBERTS, D. & GALE, G. H. 1978. The Caledonian–Appalachian Iapetus Ocean. In: TARLING, D. H. (ed.) *Evolution of the Earth's crust*. Academic Press, London, 255–342.
- RONA, P. A. 1984. Hydrothermal mineralization at seafloor spreading centers. *Earth-Science Reviews*, **20**, 1–104.
- 1988. Hydrothermal mineralization at oceanic ridges. *Canadian Mineralogist*, **26**, 431–465.
- ROY, S. 1988. Manganese metallogenesis: A review. *Ore Geology Reviews*, **4**, 155–170.
- SALVADOR, A. 1987. Late Triassic–Jurassic paleogeography and origin of the Gulf of Mexico basin. *American Association of Petroleum Geologists Bulletin*, **71**, 419–451.
- SCHERMERHORN, L. J. G. 1974. Late Precambrian mixites: Glacial or non-glacial? *American Journal of Science*, **274**, 673–824.
- 1983. Late Proterozoic glaciation in the light of CO₂ depletion in the atmosphere. In: MEDARIS, L. G., BYERS, C. W., MICKELSON, D. M. & SHANKS, W. C. (eds) *Proterozoic Geology*. Geological Society of America Memoirs, **161**, 309–315.
- SCHISSEL, D. & ARO, P. 1992. The major Early Proterozoic sedimentary iron and manganese deposits and their tectonic setting. *Economic Geology*, **87**, 1367–1374.
- SEYFRIED, W. E. JR & JANECKY, D. R. 1985. Heavy metal and sulfur transport during subcritical and supercritical hydrothermal alteration of basalt: influence of fluid pressures and basalt composition and crystallinity. *Geochimica et Cosmochimica Acta*, **49**, 2545–2560.
- SHOCK, E. L. & KORETSKY, C. M. 1995. Metal-organic complexes in geochemical processes: Estimation of standard partial molal thermodynamic properties of aqueous complexes between metal cations and monovalent organic acid ligands at high pressures and temperatures. *Geochimica et Cosmochimica Acta*, **59**, 1497–1532.
- SIMONSON, B. M. 1985. Sedimentological constraints on the origins of Precambrian iron-formations. *Geological Society of America Bulletin*, **96**, 244–252.
- STANISTREET, I. G., KUKLA, P. A. & HENRY, G. 1991. Sedimentary and basinal responses to a Late Precambrian Wilson Cycle: the Damara Orogen and Nama Foreland. *Journal of African Earth Sciences*, **13**, 141–156.
- TORSVIK, T. H., LOHMANN, K. C. & STURT, B. A. 1995. Vendian glaciations and their relation to the dispersal of Rodinia: Paleomagnetic constraints. *Geology*, **23**, 727–730.
- URBAN, H., STRIBRNY, B. & LIPPOLT, H. J. 1992. Iron and manganese deposits of the Urucum District, Mato Grosso do Sol, Brazil. *Economic Geology*, **87**, 1375–1392.
- VEIZER, J. 1992. Life and the rock cycle. *Nature*, **359**, 587–588.
- VISSER, D. J. L. 1954. Deposits of manganese ore on Rooinekke and neighbouring farms, District Hay. *Transactions of the Geological Society South Africa*, **57**, 61–75.
- VON BRUNN, V. & GOLD, D. J. C. 1993. Diamictite in the Archaean Pongola Sequence of southern Africa. *Journal of African Earth Sciences*, **16**, 367–374.
- WORSLEY, T. R., NANCE, D. & MOODY, J. B. 1984. Global tectonics and eustasy for the past 2 billion years. *Marine Geology*, **58**, 373–400.
- YOUNG, G. M. 1976. Iron-formation and glaciogenic rocks of the Rapitan Group, Northwest Territories, Canada. *Precambrian Research*, **3**, 137–158.
- 1988. Proterozoic plate tectonics, glaciation and iron-formations. *Sedimentary Geology*, **58**, 127–144.
- 1989. Glaciation and tectonics. *Episodes*, **12**, 117.
- 1992. Late Proterozoic stratigraphy and the Canada–Australia connection. *Geology*, **20**, 215–218.
- 1995a. Are Neoproterozoic glacial deposits preserved on the margins of Laurentia related to the fragmentation of two supercontinents? *Geology*, **23**, 153–156.
- 1995b. Are Neoproterozoic glacial deposits preserved on the margins of Laurentia related to the fragmentation of two supercontinents? Reply. *Geology*, **23**, 1054–1055.

Mineralogy and geochemistry of Archaean greenstone belt-hosted Mn formations and deposits of the Dharwar Craton: redox potential of proto-oceans

C. MANIKYAMBA & S. M. NAQVI

National Geophysical Research Institute, Hyderabad – 500 007, India

Abstract: Late Archaean greenstone belts of the Dharwar supergroup are uniquely characterized by a marker horizon that consists of Fe + Mn formations, carbonates (\pm stromatolites), and phyllites (\pm organic matter). Microfossils are found in cherts associated with stromatolites and banded Fe–Mn carbonate. Manganese-bearing arenites–argillites–carbonates have a varied mineralogy that is reflected by variations in chemical composition. Trace elements characteristic of felsic and volcanic rocks such as Zr, Hf, Rb, Sr, U, Th, Ni, Cr, Co, V, and Sc are low or high depending on the amount and type of clastic debris deposited with the chemical precipitates. REE also are influenced by the clastic fluvial and hydrothermal fluxes. Banded Fe + Mn carbonate–chert rocks (BMF) contain lower amounts of REE compared to samples containing ripidolite, which have higher Al_2O_3 , Σ REE, Zr and Hf contents. Both positive and negative Eu, La and Ce anomalies are observed which reflect variable mixing of hydrothermal solutions with ambient ocean water and divergent clastic material. The data indicate that FeO, MnO and SiO_2 were added to the Archaean proto-ocean by hydrothermal solutes produced along a spreading ridge axis. The redox potential of these proto-oceans was very low near the ridge axis, but increased towards the shelf, due to higher organic productivity and photosynthesis reflected by the presence of stromatolites, organic matter, and microbiota. Precipitation of stable Mn oxides at the margin of the greenstone belts is probably the consequence of the high redox potential.

Studies of oceanic manganese nodules and Phanerozoic Mn deposits have clearly demonstrated that Mn transport and deposition are dependent on the redox potential of the oceans (Hem 1972; Elderfield *et al.* 1981; Roy 1981; Frakes & Bolton 1984, 1992; Bolton & Frakes 1985; Klinkhammer *et al.* 1986; Force & Cannon 1988; Glasby 1988; Okita *et al.* 1988; Bolton *et al.* 1990; Sugisaki *et al.* 1991; Nicholson 1992; Hein & Bolton 1993). This conceptual framework of Mn precipitation can be extended to Proterozoic sequences also (Schissel & Aro 1992; Buhn *et al.* 1992). Proterozoic deposits of the Kalahari, Transvaal basin, South Africa is one of the manganese giants and is associated with stromatolites and organic matter (Litherland & Malan 1973; Beukes 1983; Frakes & Bolton 1984). However, in Archaean greenstone sequences Mn precipitation is extremely rare (Roy 1981; Manikyamba & Naqvi 1995). Only late Archaean greenstone belts of the Dharwar craton, Singhbhum craton and the Michipicoten belt of Superior province, Canada contain significant Mn deposits (Goodwin *et al.* 1985; Manikyamba & Naqvi 1995). Therefore, these Archaean Mn formations and Mn deposits present a rare opportunity for understanding the biogeochemical processes that prevailed in the Archaean proto-oceans and the antiquity of photosynthesis. These rocks are very useful for

qualitative assessment of the O_2 content of the early hydrosphere and atmosphere. In view of the above, the Mn formations of the Dharwar craton have been studied in detail. Deposits studied are confined to a specific lithotectonic and stratigraphic horizon found at the western margin of the Shimoga, Chitradurga, and Sandur schist belts (Fig. 1). A brief summary of the mineralogical, geochemical and palaeobiological work carried out on rocks from the Sandur schist belt is given below.

Geology of the Dharwar craton with special reference to the Sandur schist belt

The Dharwar craton is primarily made up of gneisses and greenstone belts that formed from 3.5 to 2.5 Ga (Naqvi & Rogers 1987). The greenstone belts are generally divided into the older Sargur group and younger Dharwar supergroup which were punctuated by a vast crust-forming event at 3.0 Ga ago. The Dharwar supergroup rests on the Peninsular gneisses with a profound unconformity represented by a quartz pebble conglomerate; this supergroup has been divided into the Bababudan and Chitradurga groups (Swami Nath & Ramakrishnan 1981). The specific horizon dividing these groups is uncertain. The stratigraphy and

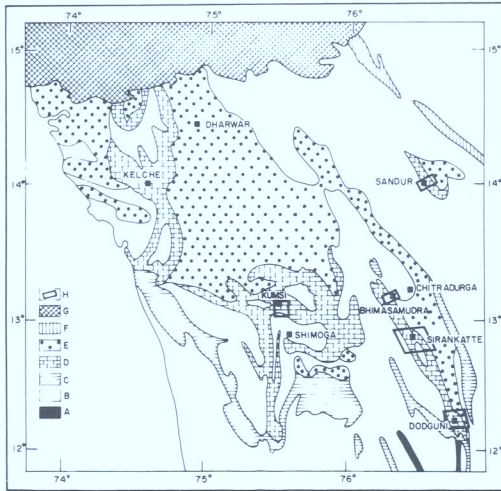


Fig. 1. Map of Karnataka showing distribution of Mn-bearing strata in Late Archaean greenstone belts. A, Older schist belts. B, Tonalite-trondhjemite gneiss and unclassified granitoids. C, Greenstone belts formed on a shallow water shelf made up of mainly volcanics, argillite, quartzite and BIFs. D, Parts of younger greenstone belts consisting of Fe-Mn formations with quartzite, carbonate (\pm stromatolites), carbonaceous phyllite, and argillite deposited on a shallow water shelf with high organic productivity and redox potential. E, Part of the younger greenstone belts developed in deeper water and consisting of volcanic rock, graywacke, argillite, and BIFs (oxide, carbonate and sulfide facies). F, Unclassified greenstone belts (Deccan Traps) and Proterozoic sedimentary basins. G, Younger cover of volcanic rocks (Deccan Traps) and Proterozoic sedimentary basins. H, Areas studied in detail.

structure of the craton is highly debated. Recent summaries have presented the entire spectrum regarding this debate (Radhakrishna & Naqvi 1986; Naqvi & Rogers 1987). Mn formations are found only along the western margin of the Shimoga, Chitradurga and Sandur schist belts (Fig. 1), and many workers believe that this Mn bearing horizon marks the boundary between the Bababudan and Chitradurga groups (Chadwick *et al.* 1981). This horizon is invariably associated with current-bedded quartzites, stromatolitic carbonates, and carbonaceous phyllites. The upper part of this marker horizon shows a transition from quartzite to banded iron formation in the Sandur, Chitradurga and Shimoga schist belts (Manikyamba & Naqvi 1995). All these characteristics of this very important horizon are exemplified at the western margin of the Sandur schist belt.

The Sandur schist belt is situated in the eastern part of the Dharwar craton (Fig. 2)

and consists of four major formations: Yeswanthanagar, Deogiri, Donimalai and Nandihalli formations (Table 1; Roy & Biswas 1979, 1983). The Yeswanthanagar formation rests on 3.0 Ga old gneisses (Taylor *et al.* 1984) and is mainly made up of mafic and ultramafic rocks interbedded with fuchsite quartzite and current-bedded quartzite (Table 1). The Yeswanthanagar formation also contains layers of Mg-rich metasedimentary rocks. This formation is followed by the Deogiri formation which begins with a conglomerate of unknown origin followed by current-bedded quartzite. Some layers of the quartzite are ripple marked on which growth of stromatolitic carbonates took place (Fig. 3a). These stromatolites and carbonates are interlayered with argillite that together compose several repetitive layers; these rocks all contain Mn concentrations above the crustal average. Mn-rich layers are rhythmically interbedded with shales and show primary sedimentary bedding planes (Fig. 3b). The thickness of the sedimentary layers varies from a few millimetres to about a metre. Some shale layers have very low Mn contents whereas others have MnO concentrations ranging up to 60% or more. Sedimentary layers have been folded and refolded. Supergene processes generated high-grade Mn ores consisting of several secondary minerals, such as cryptomelane. Manganese-bearing strata are confined to the Deogiri formation (Fig. 1).

The Donimalai formation is mainly made up of several types of volcanic rocks and a sequence of interbedded BIFs (Fig. 3c), shale, chert and carbonaceous schist. The entire spectrum of BIFs, namely oxide, carbonate, silicate and sulphide facies, are present in the Donimalai formation (Manikyamba 1992; Manikyamba *et al.* 1993). The Donimalai formation is considered by Roy & Biswas (1983) as stratigraphically younger than the Deogiri formation, whereas, Mukhopadhyay & Matin (1993), and Manikyamba & Naqvi (1995) demonstrated that these two sequences are time equivalent and were deposited in a continuous watermass of contrasting physiochemical characteristics. The Deogiri and Donimalai sequences are followed by the Nandihalli formation, which consist of active plate-margin turbidites and volcanic rocks.

Compositions of volcanic rocks of the Yeswanthanagar, Deogiri, Donimalai and Nandihalli formations are distinct from each other and depend on their tectonic setting, defined by associated sedimentary rocks. The volcanics of the Yeswanthanagar formation are predominantly made up of ultramafic rocks whereas

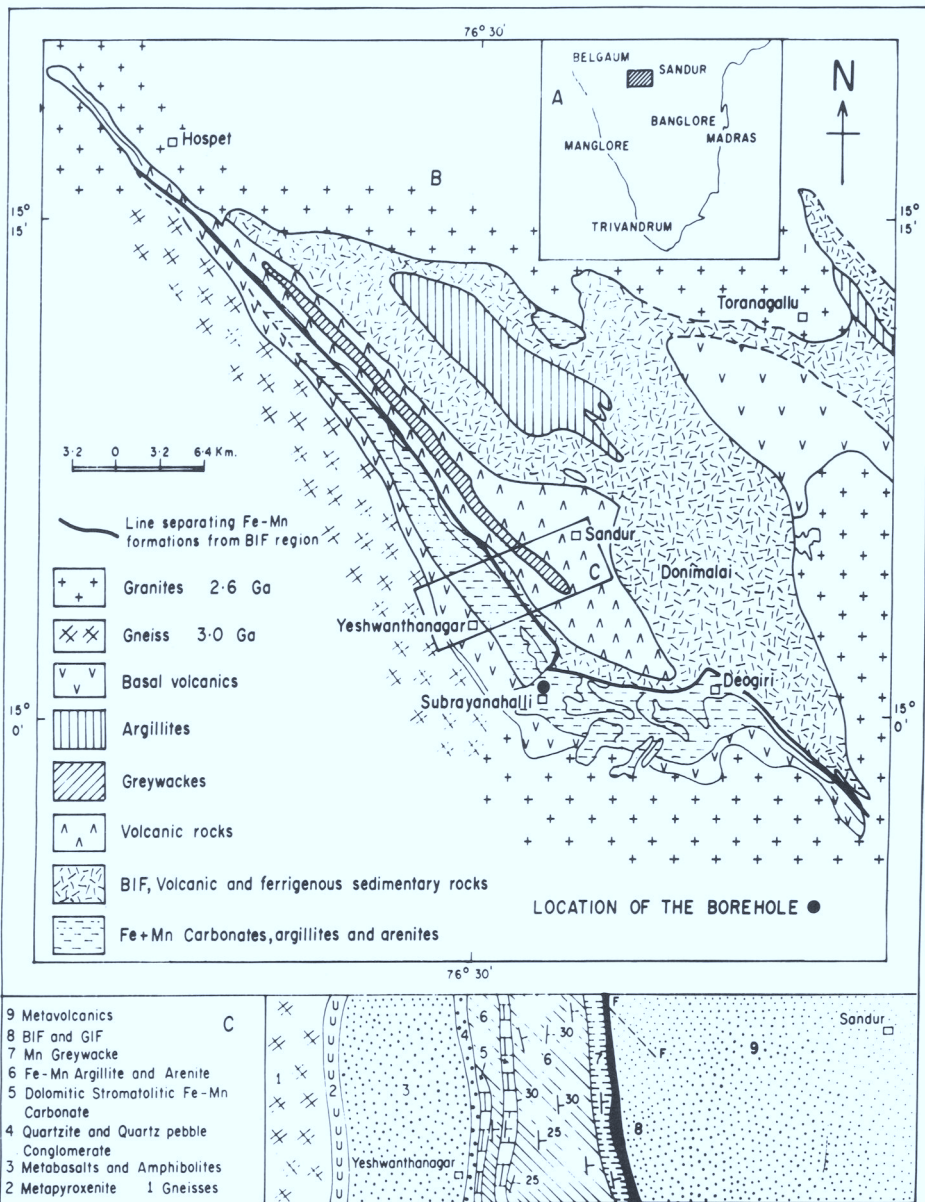


Fig. 2. Simplified geological map (after Roy & Biswas 1983) of Sandur schist belt. (a) Location of Sandur belt in the Dharwar craton. (b) General geology of Sandur belt; note the line separating Fe-Mn formations from BIF rich region. Location of the bore hole is given as bold filled circle. (c) Geological map of the area shown in (b) where detailed sampling of the Fe + Mn formations was carried out. GIF, granular iron formation.

those of the Deogiri and Donimalai formations are mainly high-Mg basalt and tholeiitic basalt. Metavolcanic rocks of the Nandihalli formation are either tholeiites or intermediate and acid rocks (Manikyamba & Naqvi 1999). The Deogiri and Donimalai formations have several beds of carbonate and chert that

contain stromatolites and either confirmed and/or suspected microbiota. The closure of the basin under compressional tectonics was accompanied by intrusion of K-rich granite dated at 2.6 Ga. Recent Sm-Nd radiometric dating of geologically equivalent volcanic rock from the Chitradurga schist belt yielded an age of

Table 1 *Stratigraphic succession of the Sandur schist belt*

Roy & Biswas (1983)	Present paper		
Intrusive granites Closepet granite (Torangallu granite)	Tensional Stage (Basin Margin)		Compressional stage (active plate margin)
<i>Nandihalli Formation</i> Greywacke and Argillite Acid volcanics Metabasalt–Metagabbro	Shallow shelf (West) Fe–Mn rich	Deep shelf (East) BIF rich	Intrusive granites (2.6 Ga)
<i>Donimalai Formation</i> Banded ferruginous chert iron ore (BIF) Acid volcanics Argillite/andalusite schist Pyroclastic breccia Volcanic agglomerate Conglomerate Metabasalt Fuchsite quartzite			Greywackes and argillite Acid volcanics Metabasalt
<i>Deogiri Formation</i> Manganiferous greywacke Quartzite and arenite Metabasalt Dolomitic limestone	<i>Deogiri Formation</i> Fe–Mn greywacke Fe–Mn argillite Fe–Mn carbonate Fe–Mn argillite Stromatolitic- Fe–Mn-bearing carbonate	<i>Donimalai Formation</i> BIF Shale (iron ores) BIF Shale Basalt Pyroclastics Conglomerate Metabasalt BIF–GIF–PIF	
<i>Yehwanthanagar Formation</i> Metapyroxenite Quartzite Metabasalt and amphibolite	Fe–Mn-bearing quartzite Metapyroxenite Quartzite Metabasalt		
Peninsular gneiss	Peninsular gneiss 3.0 Ga		

GIF, granular iron formation; PIF, peloidal iron formation.

2722 ± 54 Ma (unpublished data of the Geochronology Group, NGRI Report, 1992–93). The belt has been intensely deformed producing extremely tight first generation isoclinal folds, second generation coaxial isoclinal folds and third generation open folds (Roy & Biswas 1983; Mukhopadhyay & Matin 1993). The metamorphism varies from lower greenschist facies to lower amphibolite facies. However, the western margin has been subjected to very high stress and directional pressure.

Mineralogy

The Mn formations have a complex mineralogy as a consequence of their genesis from the mixing of clastic and chemical sedimentary

processes (Manikyamba & Naqvi 1995). The arenites are made up of quartz, micas, chlorites and Mn oxides. Mn oxides are both primary and secondary and the distinction between the two cannot be made by ordinary microscopic studies. However, in the ore beds, minerals are predominantly cryptomelane, psilomelane, pyrolusite, and braunite along with hematite, whereas, in the proto-ore, below the zone of secondary enrichment, primary Mn minerals are Mn siderite and pyrolusite. Rhythmic microbands of chert and Mn siderite contain interstitial Mn oxides (Fig. 4a), in addition to Mn oxide concentration at the boundary between chert and carbonate layers (Fig. 4a). The Mn siderite may have formed by reaction between Mn–Fe oxides and CO₂ released from degradation of organic matter. The *in situ* growth of

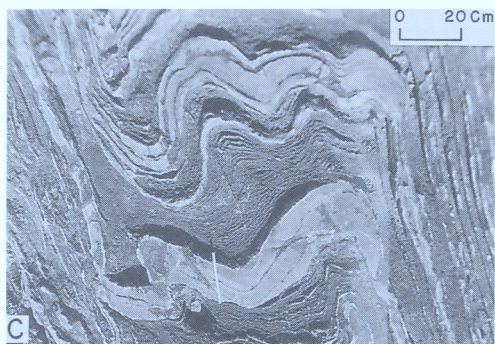
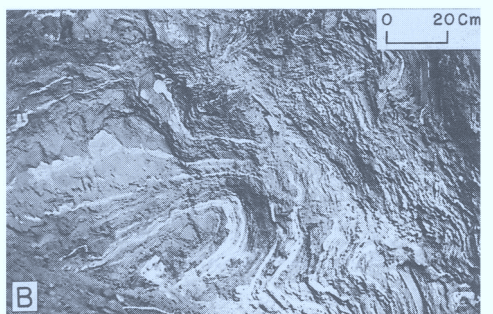
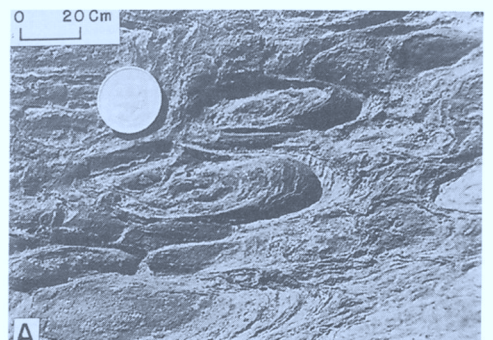


Fig. 3. (a) Field photograph of stromatolites in manganese carbonate of Deogiri formation. (b) Folded bedding planes in Mn formation. White layers are rich in clay minerals, while dark layers are rich in manganese. (c) Rhythmic bedding in BIF. Note the presence of thick and thin layers.

Mn-siderite rhombohedra in the borehole samples supports this inference (Fig. 4b). Most probably both primary and diagenetic Mn siderite are present in these rocks. The composition of the carbonates from the borehole samples varies from Mn siderite to siderite along with kutnahorite and ferroan dolomite (Table 2; Fig. 5). Ripidolite is a very common mineral associated with Mn siderite, Mn oxides, and quartz. The stromatolitic carbonates consist

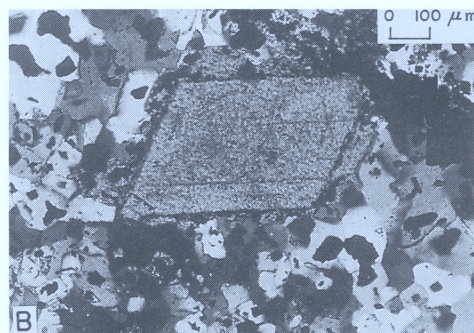
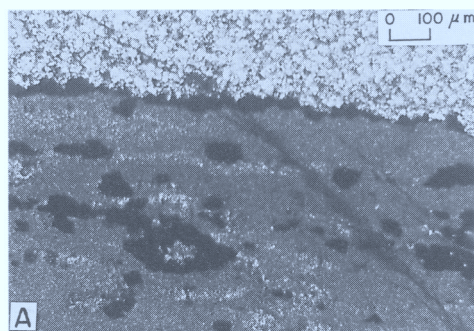


Fig. 4. (a) Photomicrograph of banded Mn-siderite chert. Note the presence of Fe-Mn oxides at boundary. (b) Mn-siderite rhombohedra in chert; Rhomb is surrounded by Fe-Mn oxides.

of dolomite, siderite, Mn siderite, ripidolite, quartz and organic carbon that is recrystallized to graphite. Interstitial specks of carbon are found between septa of stromatolites. Argillaceous layers are made up of variable amounts of quartz, ripidolite, Mg chlorite, plagioclase, mica and Fe-Mn oxides.

Palaeobiology

The most outstanding feature of the Sandur schist belt is evidence for primitive life forms. Stromatolites (Fig. 3a) that contain organic matter are found in the Mn formation. These stromatolites themselves do not contain microfilaments, but the $\delta^{13}\text{C}$ of graphite and carbonate samples (four) from them yielded values of -26% and -1.6% respectively. The graphite value substantiates that it is of organic origin. Because the stromatolites of the North Pole Pilbara rocks (Australia) are now considered as probably abiogenic (Lowe 1994), the stromatolites of Sandur are among a few Archaean biogenic stromatolites of the world. In addition

Table 2. Chemical composition of the minerals constituting Fe–Mn formation of the Sandur schist belt

Element	Microcrystalline quartz			Ripidolite			Kutnahorite		
	Range		Mean (3)	Range		Mean (7)	Range		Mean (4)
SiO ₂	92.5	99.6	95.8	22.7	29.9	24.2	0.06	0.07	0.18
TiO ₂	bd	bd	bd	0.07	1.32	0.28	0.01	0.04	0.03
Al ₂ O ₃	bd	0.23	bd	20.4	24.9	21.8	bd	bd	bd
FeO ^T	0.41	0.46	0.44	26.2	35.3	33.4	5.6	7.5	6.4
MnO	0.04	0.08	0.06	1.23	2.31	1.56	15.3	19.4	17.4
MgO	bd	0.03	bd	7.03	7.63	7.21	6.72	7.93	7.05
CaO	0.03	0.05	0.04	0.09	1.87	0.54	27.3	28.8	28
Na ₂ O	bd	bd	bd	0.11	2.24	0.64	0.05	bd	0.05
K ₂ O	0.03	0.06	0.05	0.14	0.66	0.25	0.03	0.06	0.04
Cr ₂ O ₃	bd	bd	bd	0.01	0.10	0.06	0.03	0.13	0.07
Ni	0.02	0.07	0.04	0.03	0.07	0.05	0.05	0.09	0.07

Element	Mn-siderite			Siderite			Hematite		
	Range		Mean (48)	Range		Mean (25)	Range		Mean (35)
SiO ₂	0.01	24.11	0.83	0.01	1.17	0.38	0.04	2.06	0.71
TiO ₂	0.01	0.08	0.02	0.01	0.06	0.04	0.01	0.10	0.04
Al ₂ O ₃	0.01	0.64	0.25	0.01	0.73	0.23	0.01	7.35	1.26
FeO ^T	21.8	38.5	29.3	43.2	69.2	57.3	76.0	99.3	86.3
MnO	14.6	34.3	22.4	0.03	1.70	0.69	0.01	1.14	0.24
MgO	0.59	3.22	1.67	0.04	7.86	3.36	0.01	0.25	0.08
CaO	1.84	4.26	2.47	0.01	1.08	0.28	0.02	0.21	0.06
Na ₂ O	0.02	3.59	0.30	0.01	1.58	0.79	0.02	1.52	0.23
K ₂ O	0.01	1.48	0.12	0.02	0.61	0.14	0.03	0.44	0.09
Cr ₂ O ₃	0.01	0.18	0.06	0.01	0.08	0.03	0.01	0.79	0.12
Ni	0.01	0.13	0.03	0.01	0.13	0.04	0.01	0.15	0.05

bd, below detection limit. Compositions are estimated by electron probe micro analyser. Ripidolite composition was determined in Fe + Mn banded carbonates.

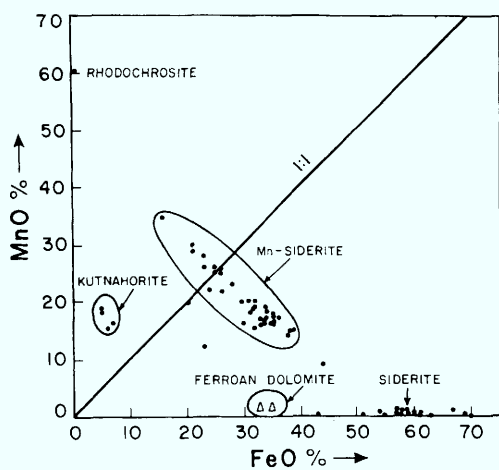


Fig. 5. Distribution of Fe and Mn in different carbonates.

to the stromatolites, a chert band in the Donimalai formation contains microfossils of cyanobacteria (Fig. 6a; Naqvi *et al.* 1987; Venkatachala *et al.* 1989, 1990). Also, several bands of chert and ferruginous chert contain permineralized filamentous structures that cut across chert grains (Fig. 6b). The width of these filamentous structures is not more than 10 μm . At several places the filaments are filled by hematite and at other places they are filled by quartz (Fig. 6b). A cell wall is visible in many filaments, but organic matter is found only in a few. Lenses 0.5–10 m thick in the suspected microfossil-bearing chert are composed of carbonaceous phyllites with a mean bulk $\delta^{13}\text{C}$ value of -26% (mean of four samples) (Manikyamba 1992; Naqvi *et al.* 1987). The filling of the microfilaments by iron and Mn oxides is commonly observed in the form of microlayering made up of a chain of single grains of

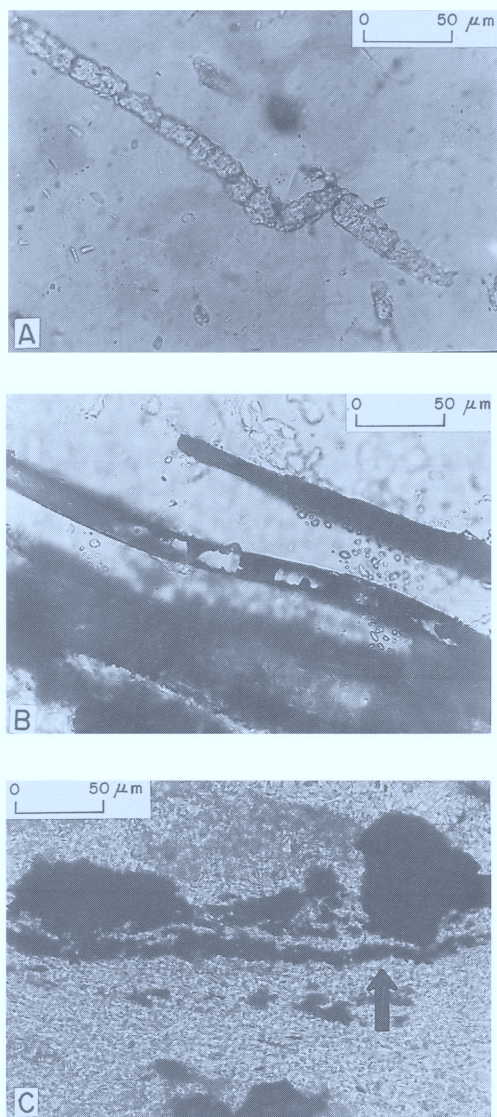


Fig. 6. (a) Microfossil of cyanobacteria in chert. (b) Microfilaments (suspected microfossil) in ferruginous chert. (c) Filamentous structure shown by the arrangement of single grain of hematite in BIF.

hematite or Mn oxide (Fig. 6c). Since iron and Mn oxides can oxidize organic matter, this may explain the absence of organic matter in the filamentous structure and therefore the uncertainty about their biogenesis. This process has significantly influenced filament preservation. Furthermore, subsequent metamorphism has complicated the identification of these structures as undoubted microfossils. However, the $\delta^{13}\text{C}$ (-26% value of one sample) of the graphite

reported for a sample containing microstructures clearly demonstrates that organic productivity and photosynthesis were occurring during the late Archaean. The *in situ* growth of Mn siderite (Fig. 4a and b) and siderite in chert bands with sporadic Fe–Mn oxides indicates that the reaction between Fe–Mn oxides and organic matter took place during diagenesis. Mn-siderite rhombs are surrounded by Fe–Mn oxides (Fig. 4b). A few rhombohedra were separated and their composite $\delta^{13}\text{C}$ is -1.6% . This value indicates that organic matter may have been autocatabolically consumed by the Fe–Mn oxides to produce Fe–Mn carbonates. The average $\delta^{13}\text{C}$ value of marine carbonate is about 0% PDB. It becomes negative if organic matter is altered and provides CO_2 for the carbonates. Therefore -1.6% $\delta^{13}\text{C}$ value for the Archaean carbonate, the time when biogenic processes were very juvenile, indicates the incorporation of minor amounts of CO_2 derived from organic matter. Similarly, the $\delta^{13}\text{C}$ of the Archaean ocean water may only be inferred from the $\delta^{13}\text{C}$ values of the carbonates of that time and thus this value indicates only the possible incorporation of organic matter-derived CO_2 . If organic matter-derived CO_2 was not incorporated, this value would be expected to be somewhat positive (see Schidlowski 1985, 1990). Fe–Mn oxyhydroxides were more abundant than organic matter and thus some remained as Fe–Mn oxides. The presence of microspheroids that consist of rims of iron oxide and centers of silica (Manikyamba 1992) may also be considered as evidence of involvement of biogeochemical processes in the precipitation of iron and Mn oxides in this belt. These microspheroids are considered to be coccoids and according to LaBerge (1986) are somewhat similar to *Eosphera tyleri*. However, Ahn & Buseck (1990) suggested that only microspheroids of less than $10\ \mu\text{m}$ size and having a siderite core may be considered of biogenic origin. We find that the microspherules from our samples are made up of single grains of iron minerals arranged in rings in cross section within a chert matrix and may be remnants of a primitive bacteria (Manikyamba 1992).

Geochemistry

The complexity of the mineralogy of Fe–Mn formations and the processes involved in their genesis are reflected in their major, trace, and rare earth element compositions. Selected analyses are given in Table 3. Since significant but variable contributions have been made by three

different processes, namely chemical, terrigenous, and volcanoclastic sedimentation, the bulk compositions show large variations. The linear relationship between Fe and Mn (Fig. 5)

for siderites disappears when the bulk compositions of arenites, argillites, and carbonates are considered (Fig. 7a). This scatter is a result of variable contributions of fine-grained

Table 3. Chemical composition of selected samples of Fe + Mn formation and banded iron formation

	4C	11A	12C	GRM11	CM52	CM121	CM133	CM134	CM73	MM15*
wt%										
SiO ₂	30.5	49.9	12.7	41	59.6	40.1	63.3	64.9	52.5	77.5
TiO ₂	0.11	0.11	0.21	0.70	0.46	0.52	0.18	0.31	0.21	BDL
Al ₂ O ₃	0.13	0.13	0.48	8.67	13.87	5.48	Tr	0.16	3.07	0.05
Fe ₂ O ₃	2.11	3.26	25.26	24.38	2.46	35.09	25.31	15.46	2.15	17.72
FeO	12.4	11.6	21.2	12.8	Tr	Tr	Tr	Tr	Tr	na
MnO	22	17.4	16.2	3.2	3.2	10.34	6.32	8.04	5.22	0.35
MgO	2.67	1.12	2.10	3.71	0.01	0.01	0.01	0.31	0.03	1.00
CaO	9.49	1.48	5.04	2.08	0.86	0.01	0.01	0.28	19.15	0.05
Na ₂ O	0.02	0.14	0.11	0.07	0.26	0.51	0.01	0.48	0.38	0.10
K ₂ O	0.06	0.14	0.28	1.02	8.68	6.41	0.35	0.10	1.56	0.002
LOI	20.87	15.60	17.58	3.50	10.20	3.10	3.12	8.70	16.70	0.01
Total	100.37	100.88	101.08	101.11	99.55	101.53	98.58	98.74	100.93	96.73
ppm										
Sc	0.41	0.77	12.56	3.27	9.80	7.34	4.33	2.99	7.19	0.56
V	25.8	29.5	766.4	78.4	65.9	153.0	175.5	153.2	67.8	0.9
Cr	23.5	42.6	163.5	103.8	191.8	201.5	41.1	35.3	72.5	2.3
Co	3.4	16.3	33.2	16.2	21.3	45.7	57.01	38.3	32.3	57.8
Ni	6.3	30.08	165	33.9	16.5	70.7	28.03	16.9	14.8	9.0
Cu	5.4	50.4	59.3	6	9.7	45.9	11.5	36.8	8.6	3.3
Zn	14.9	25.4	99.6	71.5	30.4	90.8	30.6	28.6	18.7	17.1
Ga	na	na	na	na	15.7	15.1	10.5	15.7	17.1	na
Rb	1.5	2	10.3	18.6	122.5	10.2	12.2	0.4	44.4	0.2
Sr	18	4.8	33.1	8.9	56.3	64.7	85.04	33.3	99.97	0.01
Y	3.6	2.9	3.4	5	58.7	14.3	1.2	1.5	33.5	0.3
Zr	2.3	3.7	10.8	106.1	903.0	88.6	5.02	3.9	164.4	0.3
Nb	0.1	0.2	0.4	1.9	27.4	3.8	0.7	0.3	5.4	0.1
Ba	Tr	Tr	Tr	245.4	369.0	27.2	35.3	Tr	56.2	8.4
Hf	0.02	0.04	Tr	5.01	13.43	1.21	0.11	Tr	1.02	0.02
Ta	Tr	Tr	Tr	1.03	1.51	0.18	0.09	0.05	0.13	na
U	Tr	Tr	0.01	1.93	3.08	1.24	0.28	0.02	0.63	na
Th	Tr	0.02	Tr	9.83	14.02	2.15	0.06	0.01	1.83	na
La	1.62	1.78	33.86	31.46	883.80	10.64	0.13	4.56	28.07	15.53
Ce	2.73	5.10	0.73	39.27	22.24	12.84	0.80	1.88	18.57	0.13
Pr	0.29	0.47	0.15	3.39	2.53	2.11	0.08	0.17	1.79	0.02
Nd	1.15	2.07	0.63	11.59	10.69	7.29	0.27	0.62	8.13	0.10
Sm	0.21	0.48	0.10	2.32	3.27	1.27	0.07	0.09	2.03	0.04
Eu	0.07	0.14	0.05	0.53	0.83	0.32	0.09	0.02	0.50	0.02
Gd	0.28	0.52	0.15	2.40	3.68	1.74	0.06	1.08	2.22	0.05
Tb	0.04	0.06	0.02	0.33	0.75	0.28	0.01	0.15	0.34	0.03
Dy	0.24	0.30	0.14	1.80	6.10	1.88	0.01	0.09	2.04	0.08
Ho	0.04	0.07	0.02	0.46	1.54	0.37	0.01	0.19	0.42	0.02
Er	0.03	0.23	0.06	1.58	5.74	1.12	0.05	0.07	1.20	0.09
Tm	0.01	0.02	0.01	0.24	0.81	0.15	0.01	0.09	0.15	0.02
Yb	0.07	0.11	0.04	1.71	6.13	1.01	0.08	0.07	0.95	0.11
Lu	0.01	0.01	0.01	0.40	0.98	0.14	0.01	0.01	0.10	0.01
ΣREE	6.79	57.89	35.97	97.48	949.09	41.16	1.68	9.09	59.09	16.25
LREE	6.00	56.43	35.47	88.03	922.53	34.15	1.35	7.32	58.59	15.82
HREE	0.72	1.32	0.45	8.92	25.73	6.69	0.24	1.75	7.42	0.41

*MM15, BIF; 4C, 11A, 12C, and GRM11 are banded Fe + Mn carbonates; CM52, 121, 133, 133 and 134 are Fe + Mn arenites and argillites; CM73 is a stromatolitic carbonate. na, not analysed. Tr, trace.

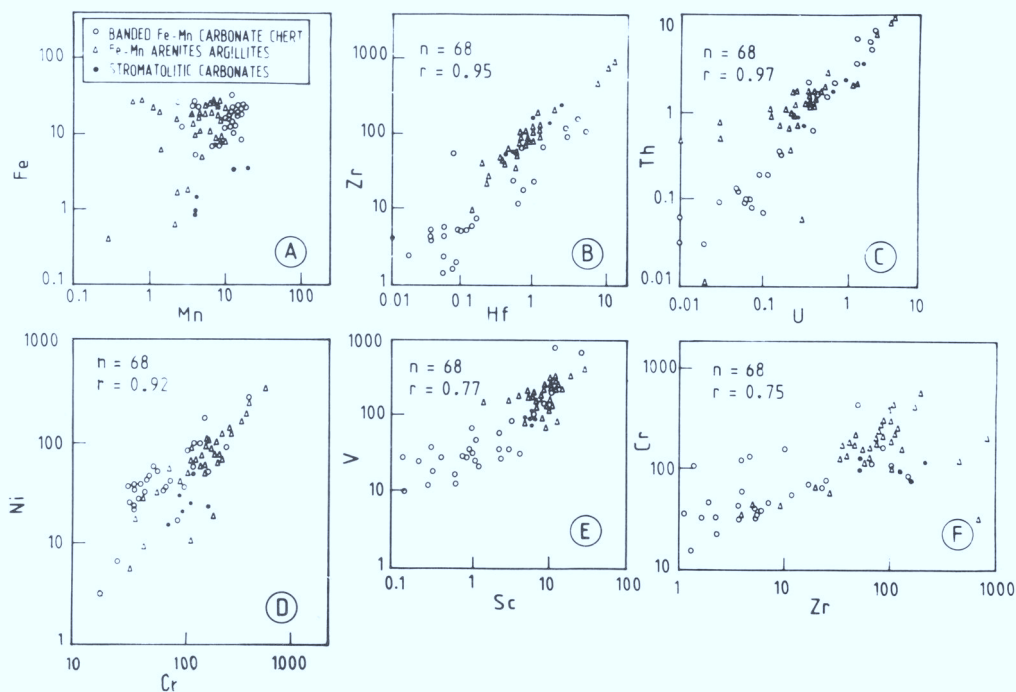


Fig. 7. (a) Scatter of Fe and Mn in whole rock samples of Fe-Mn formations. (b) Distribution of Zr and Hf in the Fe-Mn formation. (c) Distribution of U and Th in the Fe-Mn formation. (d) Distribution of Ni and Cr in Fe-Mn formation. (e) Distribution of Sc and V in the Fe-Mn formation. (f) Distribution of Zr and Cr in the Fe-Mn formation.

argillaceous debris. Although ore formation was mainly due to supergene enrichment, the original variability of the Fe and Mn contents of the proto-ore probably contributed to the grade of the Mn ores. The primary composition of the proto-ore was high in Mn, enhancing its economical potential. All other major element components show large variations (Manikyamba 1992; Manikyamba & Naqvi 1995). Since different sedimentary processes interacted, SiO_2 dilution did not vary linearly with other major element constituents of these rocks (Manikyamba & Naqvi 1995).

Major element compositional variation is clearly reflected in trace elements also. Zr and Hf, probably the best indicators of terrigenous contribution, increase simultaneously from Fe-Mn carbonate to Fe-Mn argillites (Fig. 7b). The beds that are rich in ripidolite and other diagenetic and metamorphic aluminosilicates have higher concentrations of Zr and Hf. Similarly, Th and U concentrations show strong positive correlation (Fig. 7c). The high concentrations of both U and Th can be explained only if a significant terrigenous

sedimentary component has been deposited along with the chemical precipitates.

The volcanoclastic component of these polygenetic sediments is reflected by their Ni, Cr, V and Sc concentrations. Ni and Cr concentrations also show a strong positive correlation (Fig. 7d). The concentrations of Cr and Ni reach up to 630 ppm and 338 ppm, respectively, strongly suggesting that basic and ultrabasic volcanoclastic debris have also been deposited in the basin along with chemical precipitates and felsic debris. This high Cr- and Ni-containing debris could have come from a continental source or from the basin itself. The Yeshwantanagar formation that underlies these rocks consists mainly of ultramafic rocks containing about 40% MgO, 1800–2000 ppm Cr and 1000–1200 ppm Ni (unpublished data of the authors). Mafic rocks are also abundant in this formation. This formation probably provided the mafic and ultramafic debris to the younger sequence. This inference is strongly substantiated by V and Sc contents (Fig. 7e) which also increase simultaneously from carbonates to argillites. Furthermore, the simultaneous increase of Cr and Zr

(Fig. 7f) indicates that argillaceous layers have a variable contribution from both felsic and mafic sources.

One of the major contributions during the last few years for understanding the genesis of iron formations has been made through the study of REE distribution patterns in these rocks and their possible derivation from hydrothermal emanations at oceanic spreading centers (Fryer 1977*a, b*; Dymek & Klein 1988; Klein & Beukes 1989; Beukes *et al.* 1990). Comparison between REE data of hydrothermal solutions from vent sites on the EPR and MAR have shown that the Fe, Mn, and Si contents of BIF and BMF may have been provided by similar hydrothermal activity during Archaean times (Dymek & Klein 1988; Naqvi *et al.* 1989; Manikyamba *et al.* 1993; Bau & Moller 1993; Alibert & McCollough 1993; Manikyamba & Naqvi 1995). REE patterns of representative samples of Mn-bearing carbonates, arenites, and argillites are shown in Fig. 8a and b. Many samples of banded siderite-chert formation show a strong La anomaly (Fig. 8a). This La enrichment by hydrothermal solutions is clearly evident in samples of low Σ REE, but it has been superimposed by the La content of the terrigenous material (Fig. 8a). Due to the deposition of terrigenous material, several samples show medium to high enrichment in Σ REE with negative Eu anomalies. Some of these samples show a distinct positive Ce anomaly (Fig. 8b) indicating that oxidation of Ce^{3+} to Ce^{4+} took place in the basin and the Ce^{4+} was adsorbed by the argillaceous layers. Rocks from the BIF found to the east of the Mn-bearing horizon (Table 3) have a distinct positive Eu anomaly and depleted Σ REE (Fig. 8a). However, in the Fe-Mn formations the Eu anomaly has been influenced by terrigenous input as some of the argillite samples exhibit negative Ce and Eu anomalies with HREE enriched over LREE. Such samples have higher Th and Zr contents and thus exhibit a stronger terrigenous signature. Similarly, stromatolitic carbonates show La enrichment, but a negative Eu anomaly (Fig. 8a), possibly reflecting the oxidation of MOR hydrothermal solutions at the basin margin.

The REE contents and patterns of the Mesozoic cherts are distinct from those of the Archaean cherts, which closely resemble those of cherty BIFs (Manikyamba *et al.* 1993; Khan & Naqvi 1995; Arora *et al.* 1995). Because Mesozoic cherts originated as biogenic deposits and there is yet no positive evidence of the existence of Si-secreting bacteria during the Archaean, the Si content of Archaean BIFs and Fe-Mn formations is considered to be provided by hydrothermal activity at MOR and precipitated

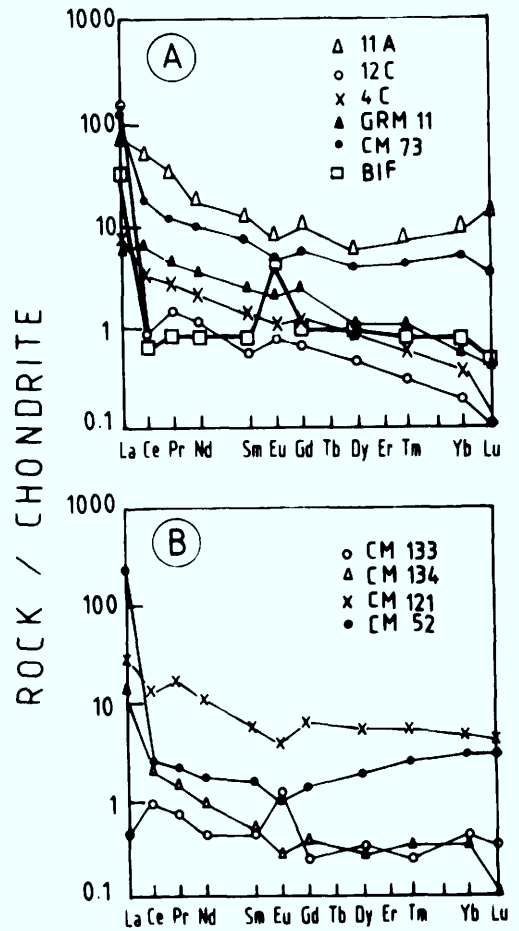


Fig. 8. (a) REE pattern of the selected samples of Fe-Mn banded carbonates. 11A, 12C, 4C and GRM11 are Fe-Mn banded carbonates. BIF, banded iron formation; CM73, stromatolitic carbonate. (b) REE patterns of selected samples of arenite, and argillite. CM133, 134, 121 and 52 are Fe + Mn-bearing arenites and argillites.

inorganically. This inference is strongly supported by the Si anomalies that occur around spreading center vents (Campbell *et al.* 1988). It has been inferred that due to higher exit temperatures, large quantities of dissolved Si was brought to the proto-oceans (Gnaneshwar Rao & Naqvi 1995; Manikyamba & Naqvi 1995).

Redox potential of Archaean proto-oceans

One of the major debates in Archaean geology is the nature of the primitive atmosphere (Kasting 1987). Many contemporary workers believe that

the primitive atmosphere was anoxic and that very little dissolved O₂ was available in early Archaean proto-oceans (Cloud 1973; Walker *et al.* 1983; Walker 1987; Kasting 1987; Morris 1993). However, this hypothesis is not uniformly accepted and it has been proposed that considerable amounts of O₂ were present in the primitive atmosphere (Towe 1983, 1990; Dymek & Klein 1988). The photoelectric ultra-violet and radiolytic dissociation of water to produce oxygen have been proposed by a few workers (Mel'nik 1982; Draganic *et al.* 1991). Klein & Beukes (1989) and Beukes *et al.* (1990), based on carbon isotopic data for rocks from the Transvaal basin, have decoupled the organic productivity and the precipitation of banded iron formation. However, the invariable association of manganese formations, carbonaceous phyl-lites, stromatolites, microbiota, and banded iron formations from the late Archaean greenstone belts of Sandur, Chitradurga and Shimoga schist belts (Venkatachala *et al.* 1989) indicate that photosynthetic activity may have played a very important role in precipitation of iron and manganese as stable oxides. It is fairly clear that in the Phanerozoic the higher redox potential of ocean waters resulted in the precipitation of Mn oxides (Frakes & Bolton 1984, 1992). Mn nodules of the present-day ocean floors also precipitated when sufficient O₂ was available to oxidize dissolved Mn. For Proterozoic basins, there is also very close association between stromatolites, organic matter and Mn deposition (Litherland & Malan 1973; Beukes 1983). It is only in the Archaean that little precipitation of Mn has taken place (Roy 1981) which is most probably related to the low level of O₂ fugacity (Manikyamba & Naqvi 1995). It is only in a few greenstone belts that Mn has been deposited (Roy 1981; Goodwin *et al.* 1985; Manikyamba & Naqvi 1995). The iron and manganese fractionation based on the redox potential or O₂ fugacity has long been recognized (Krauskopf 1957). Therefore, abundant stable Mn oxides in late Archaean greenstone belts is itself evidence that the dissolved O₂ in the proto-oceans, at least along the margins, was high enough to allow for precipitation of stable Mn oxides. It cannot be a simple coincidence that along with these Fe-Mn formation horizons, stromatolitic carbonates, carbonaceous phyl-lites, and microbiota-bearing cherts are found. The $\delta^{13}\text{C}$ values of the graphite (-26%) are strong evidence that the carbon present in these belts is cooked kerogen. Furthermore, in the geological record prior to 2.9-2.7 Ga, no thick horizons of BIFs, Mn strata, carbonaceous phyl-lites, stromatolites

or microbiota are found. In addition, deposition of BIFs almost stopped, except in a few places, after the appearance of red beds around 2.1-1.9 Ga. Therefore, the Mn formations of the greenstone belts of Karnataka are an important indication that the late Archaean proto-ocean of this region had advanced biogenic developments.

We express our gratitude to H. K. Gupta, Director, NGRI for his keen interest, support, and permission for publication of this work, which has been funded by DST and CSIR. R. Natarajan, V. Balaram, P. K. Govil, and T. Gnaneshwar Rao provided the analyses and helped in various ways in writing this paper. We are extremely grateful to the two anonymous reviewers who have critically reviewed the earlier manuscript and improved it considerably. N. Rajan is thanked for her help in word processing.

References

- AHN, J. H. & BUSECK, P. R. 1990. Haematite nanospheres of possible colloidal origin from a Precambrian banded iron formation. *Science*, **250**, 111-113.
- ALIBERT, C. & MCCULLOCH, M. T. 1993. Rare earth element and neodymium isotope composition of the banded iron formation and associated shales from Hamersley, Western Australia. *Geochimica et Cosmochimica Acta*, **57**, 187-204.
- ARORA, M., GOVIL, P. K., CHARAN, S. N., UDAY RAJ, B., BALARAM, V., MANIKYAMBA, C., CHATTERJEE, A. K. & NAQVI, S. M. 1995. Geochemistry, economic importance and origin of late Archaean BIFs: An example from the Bababudan schist belt, Karnataka Nucleus, India. *Economic Geology*, in press.
- BAU, M. & MOLLER, P. 1993. Rare earth element systematics of the chemically precipitated component in Early Precambrian iron formations and the evolution of the terrestrial atmosphere-hydrosphere-lithosphere system. *Geochimica et Cosmochimica Acta*, **57**, 2239-2249.
- BEUKES, N. J. 1983. Palaeoenvironmental setting of iron formations in the depositional basin of the Transvaal Supergroup, South Africa. *In*: TRENDALL, A. F. & MORRIS, R. C. (eds) *Iron Formations: Facts and Problems*. Elsevier, Amsterdam, 131-209.
- , KLEIN, C., KAUFMAN, A. J. & HAYES, J. M. 1990. Carbonate petrography, kerogen distribution and carbon and oxygen isotope variations in an early Proterozoic transition from limestone to iron formation deposition, Transvaal Supergroup, South Africa. *Economic Geology*, **85**, 633-690.
- BOLTON, B. R. & FRAKES, L. A. 1985. Geology and genesis of manganese oolite, Chiatre, Georgia, USSR. *Geological Society of American Bulletin*, **96**, 87-102.

- , EXON, N. F. & OSTWALT, J. 1990. Thick ferromanganese deposits from the Dampier Ridge and the Lorde Howe Rise off eastern Australia. *B.M.R. Journal of Australian Geology and Geophysics*, **11**, 421–427.
- BUHN, B., ION, C. S. & OKRUCH, M. 1992. Late Proterozoic outer shelf manganese and iron deposits of Otzonzondu (Nambia) related to the Damaran oceanic opening. *Economic Geology*, **87**, 1375–1393.
- CAMPBELL, A. C., BOWERS, T. S., MEASURES, C. I., FALKNER, K. K., KHADEM, M. & EDMOND, J. M. 1988. A time search of vent fluid compositions from 21°N East Pacific Rise (1979–1981, 1985). *Journal of Geophysical Research*, **93**, 4537–4549.
- CHADWICK, B., RAMAKRISHNAN, M. & VISWANATHA, M. N. 1981. The stratigraphy and structure of the Chitradurga region: An illustration of cover-basement interaction in the late Archaean evolution of the Karnataka Craton, Southern India. *Precambrian Research*, **16**, 31–54.
- CLOUD, P. E. 1973. Palaeobiological significance of the banded iron formation. *Economic Geology*, **68**, 1135–1143.
- DRAGANIC, I. G., BIERQBASSE, E., DRAGANIC, Z. D. & SEHESTED, K. 1991. Decomposition of ocean waters by potassium – 40 radiation 3800 Ma ago as a source of oxygen and oxidizing species. *Precambrian Research*, **52**, 337–345.
- DYMEK, R. F. & KLEIN, C. 1988. Chemistry, petrology and origin of banded iron formation lithologies from the 3800 Ma Isua supracrustal belt, West Greenland. *Precambrian Research*, **39**, 247–302.
- ELDERFIELD, M., HAWKESWORTH, C. H., GREAVES, M. J. & CALVERT, S. E. 1981. Rare earth element geochemistry of oceanic ferromanganese nodules and associated sediments. *Geochimica et Cosmochimica Acta*, **45**, 513–528.
- FORCE, E. R. & CANNON, W. F. 1988. Depositional model for shallow-marine manganese deposits around black shale basins. *Economic Geology*, **83**, 93–117.
- FRAKES, L. A. & BOLTON, B. R. 1984. Origin of manganese giants: sea-level change and anoxic-oxic history. *Geology*, **12**, 83–86.
- & — 1992. Effects of ocean chemistry, sea level and climate on the formation of primary sedimentary manganese ore deposits. *Economic Geology*, **87**, 1207–1217.
- FRYER, B. J. 1977a. Rare earth evidence in iron formation for changing Precambrian Oxidation states. *Geochimica et Cosmochimica Acta*, **41**, 361–367.
- 1977b. Trace element geochemistry of the Soko-man Iron Formation. *Canadian Journal of Earth Sciences*, **14**, 1598–1610.
- GLASBY, G. P. 1988. Manganese deposition through geological time—dominance of the post-Eocene deep-sea environment. *Ore Geology*, **4**, 135–144.
- GNANESHWAR RAO, T. & NAQVI, S. M. 1995. Geochemistry, depositional environment and tectonic setting of the Late Archaean Chitradurga schist belt, India. *Chemical Geology*, **121**, 217–247.
- GOODWIN, A. M., THODE, H. G., GHAN, C. L. & KARKHANSIS, S. N. 1985. Chemostratigraphy and origin of the late Archaean siderite-pyrite rich Helen Iron Formation, Michipicoten belt. *Canadian Journal of Earth Sciences*, **22**, 72–84.
- HEIN, J. R. & BOLTON, B. R. 1993. Composition and origin of the Moanda Manganese Deposit, Gabon. *16th International Colloquium on African Geology, Extended Abstracts*, 150–152.
- HEM, J. D. 1972. Chemical factors that influence the availability of iron and manganese in aqueous system. *Geological Society of American Bulletin*, **83**, 443–450.
- KASTING, J. F. 1987. Theoretical constraints on oxygen and carbon dioxide concentrations in the Precambrian atmosphere. *Precambrian Research*, **34**, 205–229.
- KHAN, R. M. K. & NAQVI, S. M. 1996. Geochemistry of banded iron formations from Kushtagi schist belt, Dharwar craton, India. *Mineralium Deposita*, **31**, 123–133.
- KLEIN, C. & BEUKES, N. J. 1989. Geochemistry and sedimentology of a facies transition from limestone to iron-formation deposition in the early Proterozoic Transvaal Supergroup, South Africa. *Economic Geology*, **84**, 1733–1774.
- KLINKHAMMER, G., ELDERFIELD, H., GREAVES, M., RONA, P. & NELSEN, T. 1986. Manganese geochemistry near high temperature vents in the Mid-Atlantic Ridge rift valley. *Earth and Planetary Science Letters*, **80**, 230–240.
- KRAUSKOPF, K. B. 1957. Separation of manganese from iron in sedimentary processes. *Geochimica et Cosmochimica Acta*, **12**, 61–84.
- LABERGE, G. L. 1986. A model for the biological precipitation of Precambrian iron formation (Abstract). In: ASHWAL, L. D. (ed.) *Workshop on Early Crustal Genesis: The World's Oldest Rocks*. LPI Technical Report, **86-04**. Lunar and Planetary Institute, Houston, 71–75.
- LITHERLAND, M. & MALAN, S. P. 1973. Manganiferous stromatolites from the Precambrian of Botswana. *Journal of the Geological Society, London*, **129**, 543–544.
- LOWE, D. R. 1994. Abiological origin of described stromatolites older than 3.2 Ga. *Geology*, **22**, 387–390.
- MANIKYAMBA, C. 1992. *Geochemistry of Iron and Manganese Formations of Sandur Schist Belt, Dharwar Craton, India*. PhD thesis, Osmania Univ., Hyderabad, India.
- & NAQVI, S. M. 1994. Geochemical manifestations of higher Archaean geothermal regime in greenstone belt, an example from Sandur schist belt, India. Abst. 30th Annual Convention of Indian Geophysical Union, Hyderabad, p. 141–142.
- & — 1995. Geochemistry of Fe-Mn formations of the Sandur schist belt, India – mixing of clastic and chemical processes at a shallow shelf. *Precambrian Research*, **72**, 69–95.
- , BALARAM, V. & NAQVI, S. M. 1993. Geochemical signatures of polygenetic origin of a banded iron formation (BIF) of the Archaean Sandur greenstone belt (schist belt) Karnataka Nucleus, India. *Precambrian Research*, **61**, 137–164.

- MEL'NIK, Y. P. 1982. *Precambrian banded iron formation. Physico-chemical condition of formation.* Elsevier.
- MORRIS, R. C. 1993. Genetic modelling for banded iron-formation of the Hamersley Croup, Pilbara Craton, Western Australia. *Precambrian Research*, **60**, 243–286.
- MUKHOPADHYAY, D. & MATIN, A. 1993. The structural anatomy of the Sandur schist belt – a greenstone belt in the Dharwar craton of South India. *Journal of Structural Geology*, **15**, 309–322.
- NAQVI, S. M. & ROGERS, J. J. W. 1987. *Precambrian Geology of India. Oxford Monographs on Geology and Geophysics*, **6**, Oxford University Press, Oxford.
- , VENKATACHALA, B. S., MANOJ SHUKLA, KUMAR, B., NATARAJAN, R. & MUKUND SHARMA 1987. Silicified cyanobacteria from the cherts of Archaean Sandur schist belt, Karnataka, India. *Journal Geological Society of India*, **29**, 535–539.
- , SRINIVASAN, R., UDAY RAI, B., SHUKLA, M., VENKATACHALA, B. S. & SHARMA, M. 1989. Archaean stromatolites and microbiota from Dharwar schist belts, India. (Abs) *28th International Geological Congress, Washington, USA*, **2**, 494.
- NICHOLSON, K. 1992. Genetic types of manganese oxide deposits in Scotland. Indicators of paleo-ocean-spreading rate and a Devonian geochemical mobility boundary. *Economic Geology*, **87**, 1301–1335.
- OKITA, P. M., MAYNARD, J. B., SPIKER, E. C. & FORCE, E. R. 1988. Isotopic evidence for organic matter oxidation by manganese reduction in the formation of stratiform manganese carbonate ore. *Geochimica et Cosmochimica Acta*, **52**, 2679–2685.
- RADHAKRISHNA, B. P. & NAQVI, S. M. 1986. Precambrian continental crust of India and its evolution. *Journal of Geology*, **94**, 145–166.
- ROY, S. 1981. *Manganese Deposits.* Academic Press, London.
- & BISWAS, S. K. 1979. Metamorphic history of the Sandur schist belt, Karnataka. *Journal Geological Society of India*, **20**, 179–187.
- & — 1983. Stratigraphy and structure of Sandur schist belt, Karnataka. *Journal Geological Society of India*, **24**, 19–28.
- SCHIDLowski, M. 1985. Early life and mineral resources. *Nature*, **21**, 11–17.
- 1990. Early evolution of life and economic mineral and hydrocarbon resources. In: NAQVI, S. M. (ed.) *Precambrian Continental Crust and its Economic Resources.* Elsevier, Netherlands, 669.
- SCHISSEL, D. & ARO, P. 1992. The major early Proterozoic sedimentary iron and manganese deposits and their tectonic setting. *Economic Geology*, **87**, 1367–1374.
- SUGISAKI, R., SUGITANI, K. & ADOCHI, N. 1991. Manganese carbonate bands as an indicator of hemipelagic sedimentary environments. *Journal of Geology*, **99**, 23–40.
- SWAMI NATH, J. & RAMAKRISHNAN, M. 1981. *Early Precambria supracrustals of Southern Karnataka.* Geological Society of India, Memoirs, **112**.
- TAYLOR, P. N., MOORBATH, S., CHADWICK, B., RAMAKRISHNAN, M. VISWANATHA, M. N. 1984. Petrology, chemistry and isotopic ages of Peninsular Gneiss, Dharwar acid volcanic rocks and the Chitradurga Granite with special reference to the late Archaean evolution of the Karnataka craton, Southern India. *Precambrian Research*, **23**, 349–375.
- TOWE, K. M. 1983. Precambrian atmospheric oxygen and banded iron formations: A delayed ocean model. *Precambrian Research*, **20**, 161–170.
- 1990. Aerobic respiration in the Archaean? *Nature*, **348**, 54–56.
- VENKATACHALA, B. S., NAQVI, S. M., CHADHA, M. S. & 13 OTHERS, 1989. Paleobiology and Geochemistry of the Precambrian stromatolites and associated sedimentary rocks from the Dharwar craton: constraints on Archaean biogenic processes. *Himalayan Geology*, **13**, 1–20.
- , SHUKLA, M., SHARMA, M., NAQVI, S. M., SRINIVASAN, R. & UDAY RAJ, B. 1990. Archaean microbiota from the Donimalai formation, Dharwar supergroup, India. *Precambrian Research*, **47**, 27–34.
- WALKER, J. C. G. 1987. Was the Archaean biosphere upside down? *Nature*, **329**, 710–712.
- , KLEIN, C., SCHIDLowski, M., SCHOPF, J. W., STEVENSON, D. J. & WALTER, M. R. 1983. Environmental evolution of the Archaean-Early Proterozoic Earth. In: SHOPF, J. W. (ed.) *Earth's Earliest Biosphere – Its Origin and Evolution.* Princeton Univ. Press, Princeton, NJ, 260–290.

Deep-water manganese deposits in the mid- to late Proterozoic Penganga Group of the Pranhita–Godavari Valley, South India

JOYDIP MUKHOPADHYAY¹, ASRU K. CHAUDHURI² & S. K. CHANDA³

¹ *Department of Geology, Durgapur Govt. College, Durgapur-713214, India*

² *Geological Studies Unit, Indian Statistical Institute, 203 Barrackpore Trunk Road, Calcutta-700 035, India*

³ *Department of Geological Sciences, Jadavpur University, Calcutta-700 032, India*

Abstract: Facies analysis of the unmetamorphosed sediments enclosing the stratiform manganese oxide deposits of the mid- to late Proterozoic Penganga Group identifies the base of slope of a distally steepened deep-water ramp as their site of accumulation. The interpretation is based on their close association with a variety of mass flow deposits ranging from limestone conglomerates to calcarenites and deep-water, plane-bedded micritic limestone devoid of current- or wave-generated structures as well as detritus coarser than fine silt. These deposits occur within a major transgressive succession. The base of slope origin of stratiform manganese deposits is uncommon in the rock record and their origin is to be constrained against the background of base of slope depositional setting.

Sedimentary manganese ores are known to accumulate in highly variable depositional milieu from lacustrine to oceanic settings (Roy 1981, 1988). They are found in both shallow- and deep-water settings at present, whereas shelf-related depositional regime appears to represent the most favoured site of manganese deposition in the rock record (Beukes 1983; Cannon & Force 1983; Frakes & Bolton 1984; Bolton & Frakes 1985; Force & Cannon 1988). Occurrences in shallow depositional settings is well in accord with the oxygenating conditions required for deposition of manganese minerals in their high valency state. In contrast, the dearth of land-based deep-water manganese deposit remains an enigma in sedimentary manganese metallogenesis (Roy 1988) when their common occurrence in modern oceanic basins is considered.

In recent years Böhn *et al.* (1992, 1993) suggested an outer shelf origin of manganese deposits associated with metamorphosed Damara Sequence of Namibia based mainly on lithofacies and tectonic setting. Beukes (1989), of course, suggested that the manganese in the Transvaal Supergroup was derived from deep marine setting with a small hydrothermal component deduced on the basis of geochemical considerations.

The unmetamorphosed middle to late Proterozoic manganese oxide deposits (Roy *et al.* 1990) of the Penganga Group provides a unique opportunity for detailed facies analysis of the enclosing sediments. These manganese deposits are hosted within deep-water micritic limestones (Roy 1988; Chaudhuri *et al.* 1989; Roy *et al.*

1990). In this paper we propose to constrain the depositional setting of manganese deposits through facies analysis of the host carbonates.

Geologic setting

The Proterozoic of the Pranhita–Godavari Valley

The Penganga Group constitutes a part of the middle to late Proterozoic Godavari Supergroup (Chaudhuri & Howard 1985; Chaudhuri & Chanda 1991) of the Pranhita–Godavari Valley basin in South India. The basin (Pranhita–Godavari Valley basin), commonly cited as a major Proterozoic continental rift basin (Naqvi & Rogers 1987), served as a repository of sedimentary sequences formed in a variable spectrum of environments ranging from continental to deep marine. The Supergroup has been subdivided into several groups on the basis of genetically related lithologic assemblages. The age relationship between different groups is still uncertain. However, the lower and middle parts of the Supergroup comprise carbonate-dominated assemblages, both shallow and deep marine whereas the upper part is represented by continental siliciclastics (Chaudhuri & Chanda 1991). The Penganga Group, occupying the northwestern part of the outcrop belt (Fig. 1), is dominated by a deep water limestone–shale assemblage with a subordinate basal unit of shallow marine siliciclastics. Until now it is not known to have any depositional contact with other carbonate-dominated groups, but it

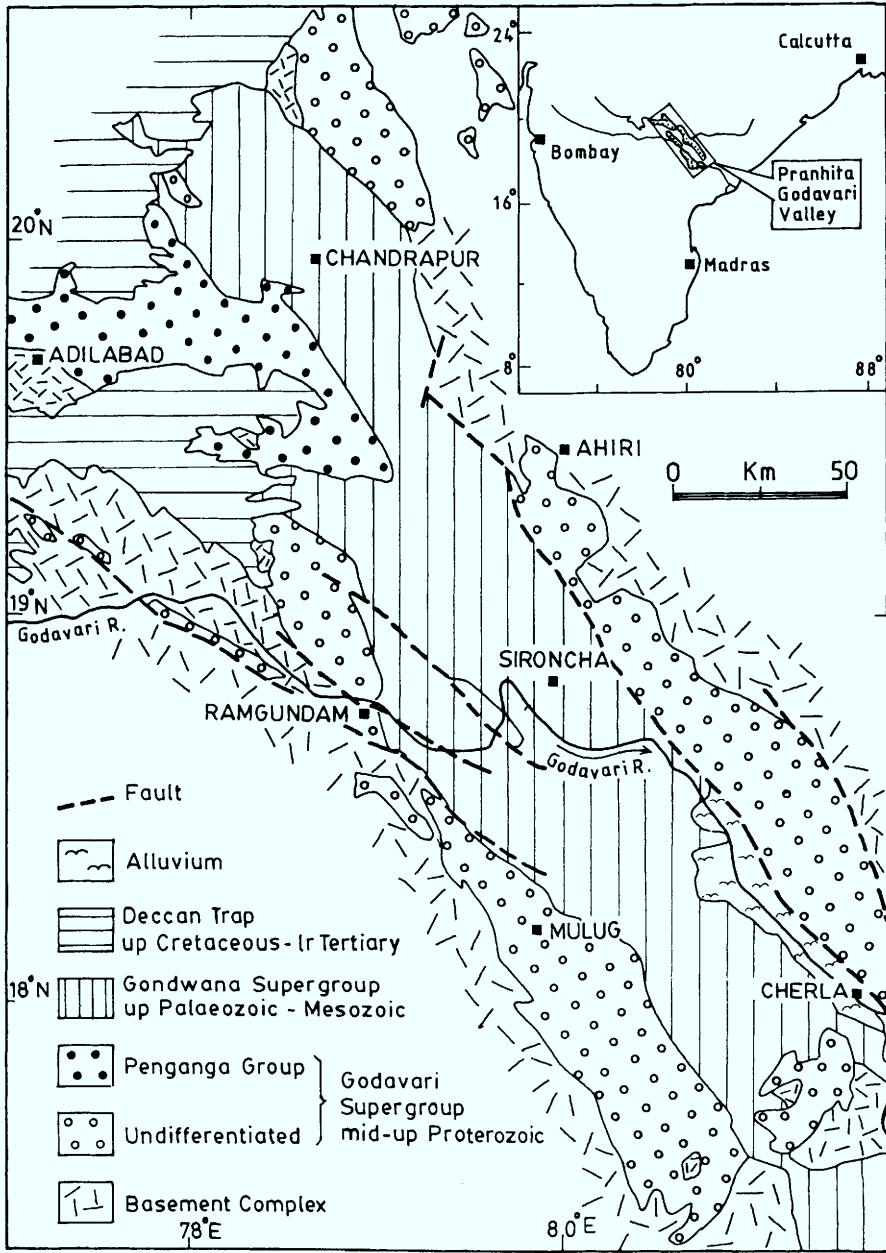


Fig. 1. Geological map of the Pranhita-Godavari Valley showing distribution of different subdivisions of the Godavari Supergroup.

unconformably underlies the continental siliciclastics.

Felsic volcanics and pyroclastics have been lately reported from the deep as well as the shallow-water sediments in some groups of the Godavari Supergroup (Chaudhuri & Chanda

1991). No evidence of volcanic activity has so far been detected in the Penganga sediments around Adilabad, but has been reported from a succession in the central part of the Pranhita-Godavari Valley, which may be homotaxial to the Penganga succession.

The Penganga Group

The Penganga Group around Adilabad (Fig. 2) unconformably overlies a granitic/gneissic basement, and is divided into three formations, which in the ascending order are the Pranhita Sandstone, the Chanda Limestone and the Sat Nala Shale (Chaudhuri *et al.* 1989). The Pranhita Sandstone is a cross-bedded, subarkosic sandstone of shallow shelf origin. It passes upward to the Chanda Limestone which consists essentially of plane-bedded micritic limestones with thin marl intercalations. The limestone is punctuated by lime-clast conglomerates of mass flow origin and turbidites at various stratigraphic levels. Current-/wave-generated structures or detritus coarser than fine silt is conspicuously absent except for in a few turbidite beds. Shallow-water calcareous constituents like ooids and stromatolites are also absent.

The Chanda Limestone can be subdivided into a number of stratigraphically controlled, colour-defined units (Fig. 3a). The basal unit is brown, which successively changes upward to pink, steel grey, black, steel grey and lastly to brown at the top, before grading into the brown

Sat Nala Shale. The same order of superposition of the colour-defined units has been noted everywhere in the relatively shoreward part of the basin. Towards the interior, however, the lower brown, the pink and part of the lower steel grey limestone grade into a highly siliceous grey limestone (Fig. 3a & b). The succession in the interior part of the basin is characterized by abundant intraformational mass flow deposits, whereas these are only locally developed in the shoreward part. In both cases, however, the mass flow deposits are invariably interbedded with micritic limestone. Almost all the limestone intervals contain early diagenetic pyrite nodules, and the highest concentration of the pyrite has been recorded in the siliceous grey interval.

Manganese deposits of the Penganga Group

The manganese ore deposits are confined entirely to the siliceous grey limestone, and occur as thin, persistent stratiform bodies enclosed within the limestone with sharp upper and lower contacts. The ore-bearing intervals occur at least in two different stratigraphic levels, and the thicker horizon has an average

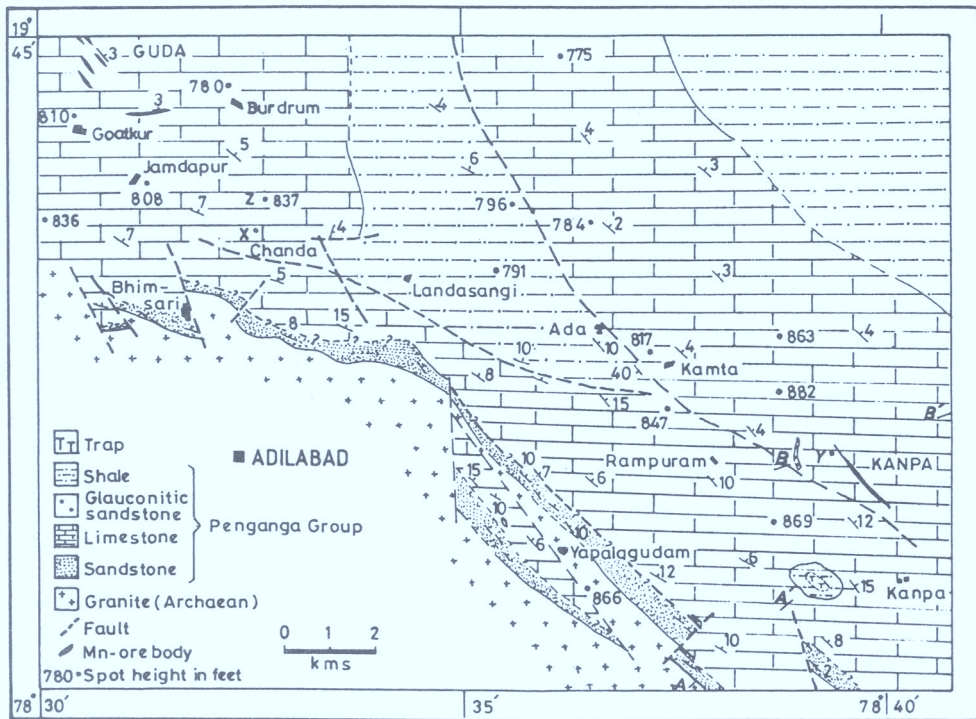


Fig. 2. Geological map of the Penganga Group around Adilabad, Andhra Pradesh, India (modified after Chaudhuri *et al.* 1989).

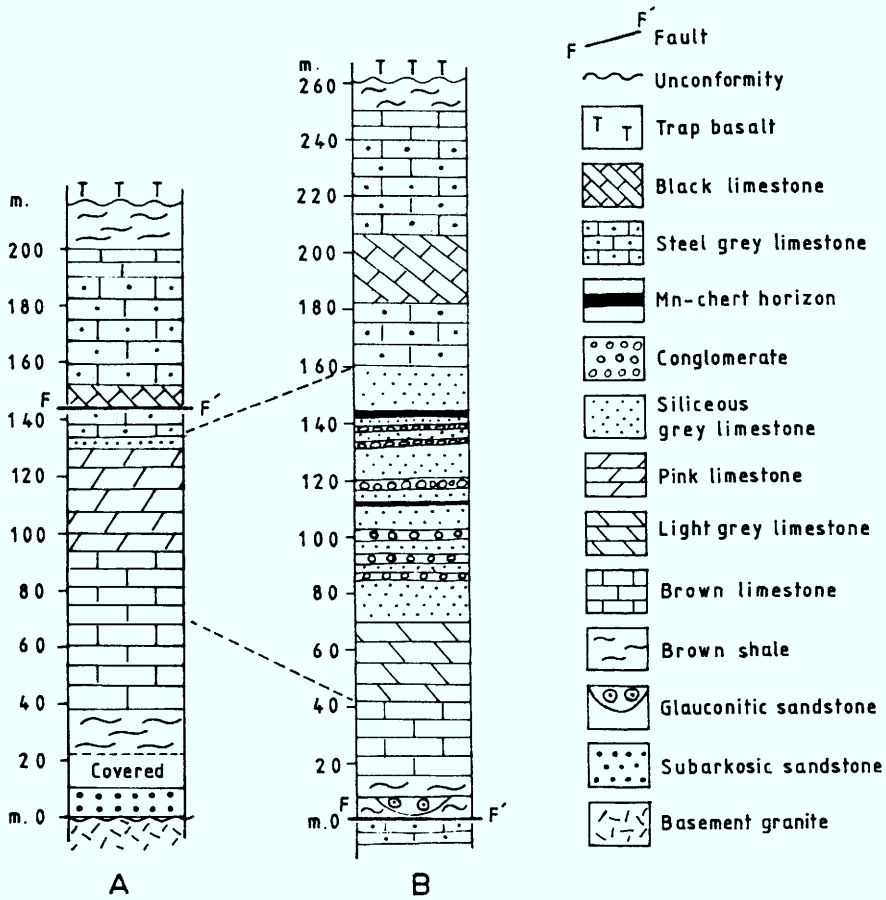


Fig. 3. Stratigraphic sections showing colour-defined intervals of the Chanda Limestone. (a) along AA and (b) along BB in Fig. 2.

total thickness of 70 cm. The ore-bearing horizons (Fig. 4) comprise thin beds and laminae of manganese oxide ores, ranging in thickness from 1 mm to approximately 5 cm, interstratified with



Fig. 4. Manganese oxide ore beds interstratified with bedded chert.

comparably thick beds of chert-jasper and/or limestone.

Todorokite and birnessite are the major manganese oxide minerals with subordinate amounts of manganite, braunite, bixbyite, Psilomelane, pyrolusite and cryptomelane (see Roy *et al.* 1990 for details). Roy *et al.* (1990) interpreted the todorokite and birnessite as the pristine primary sedimentary minerals, which were subsequently diagenetically converted to other phases.

Siliceous grey limestones and their facies types

The siliceous grey limestone, the exclusive host of the manganese ore bodies, is a light bluish to light greenish micritic limestone containing about 20% silica. The rock is extremely homogeneous, both mineralogically and texturally

throughout its outcrop, covering about 400 km² in the study area. The silica was identified as quartz in XRD analysis. It also occurs in the micrite size range and is very uniformly dispersed throughout the body of the limestone. The compositional homogeneity of the micritic beds is interrupted by beds slightly enriched in silica and clayey insoluble residues or by millimetres-thick pressure-solution seams. The siliceous limestone includes a large number of autoclastic mass flow deposits ranging from coarse debris flow conglomerates to calcarenites and possible calcisiltites. Precompactional authigenic pyrite is a common constituent of the limestone. It occurs as nodules varying in size from <1 cm to 10 cm and is found to be fairly uniformly distributed throughout the beds. Barite occurs locally as small nodules.

Facies types

Bedded micritic limestone facies. This is the most abundant of all the facies types and is characterised by five types of bedding style, labelled (a) to (e), described below. All the bed types are laterally very persistent, and may be traced for several tens to hundreds of metres, depending on exposure conditions.

Type a: thick, massive beds without any internal lamination (Fig. 5). The bed thickness normally ranges between 10 and 30 cm.

Type b: thick, massive beds with poorly developed, laterally impersistent, plane to wavy internal laminae (Fig. 6a).

Type c: thin, alternate silica-rich and silica-poor plane beds varying in thickness from 2 to 5 cm. The individual beds do not show any internal lamination.

Type d: plane to slightly undulatory thin laminae, ranging in thickness from 2 to 5 mm,



Fig. 5. Thick massive even beds of micritic, siliceous grey limestone (Type a). Note insoluble residue-rich partings or thin beds (Type c) in between thick beds.

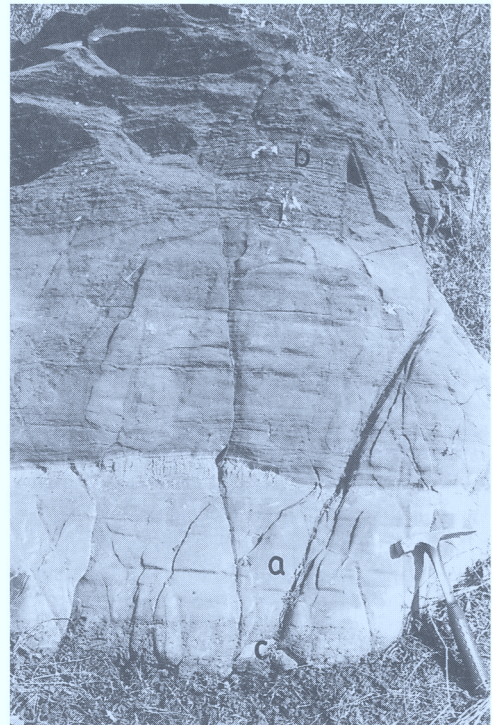


Fig. 6. Thick bed (a) of micritic siliceous limestone with poorly developed plane to wavy lamination (Type b) grades upward into thin plane-laminated (b) micritic limestone (Type d). Calcarenite bed (c) at the base.

closely associated with normally graded conglomerates, calcarenites and massive beds of type b (Fig. 6b).

Type e: thin beds, about 5 cm thick, with internal climbing ripple lamination (Fig. 7) characterized by well preserved stoss side and

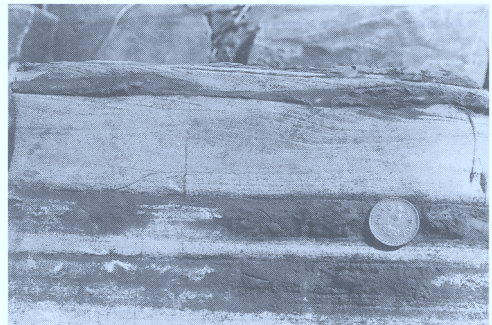


Fig. 7. Climbing ripple lamination within micritic siliceous grey limestone (Type e). Note low angle of climb.

low angle of climb (similar to type B of Jopling & Walker 1968).

Interpretation. The extremely homogeneous plane beds and laminae in micritic limestones without any shallow-water components closely resemble hemipelagic to pelagic slope carbonates. Lime-mudstones and calcisiltites with variable amounts of silt to clay-size insoluble residues are typical of ancient carbonate slope deposits (Wilson 1969; Cook & Enos 1977; Flügel 1982; Cook & Mullins 1983). In modern environments, fine-grained, undisturbed pelagic carbonate oozes normally are volumetrically most important on upper gullied part of the slope, rather than in the areas where they are diluted by sediment gravity flow deposits (Mullins & Neumann 1979). Thin, plane and climbing ripple lamination in the siliceous limestone strongly suggest emplacement by turbidity currents (Walker 1967; Mullins & Neumann 1979).

Lime-clast conglomerate facies. The lime-clast conglomerates comprise boulder to pebble size, platy, autoclastic lime-clasts set within lime-mud matrix. Clasts of bedded chert-jasper and interstratified chert and manganese occur in a few bodies. The conglomerate beds, in general, are laterally extensive sheets to tabular bodies with sharp lower and upper bounding surfaces. The lower bounding surfaces in several bodies are erosional whereas in the majority of the beds, they are non-erosive and planar. Thickness of the beds varies between 15 cm and 3.5 m. Individual beds may be clast-supported (Fig. 8), matrix-supported or are matrix-supported in the upper and clast-supported in the lower part. The matrix content, in general, is quite high, and may range up to about 25% by volume. In a majority of the conglomerate bodies, the clasts are highly disorganized (Figs 8 & 9) although these are



Fig. 9. Clast-supported, inversely graded conglomerate.

oriented parallel to sub-parallel to the bounding surfaces in a few bodies. Most commonly, individual beds are either ungraded or normally graded (Fig. 10). About 15 cm thick inversely graded beds (Fig. 9) and thicker inverse to normally graded beds have been observed locally.

Interpretation. Complete absence of extrabasinal clasts or of clasts derived from shallow-water carbonates strongly suggests that the conglomerates were derived intrabasinally and originated within the slope environments. Poorly sorted, clast-supported to mud-supported fabrics, often with floating clasts in inverse, inverse to normally graded as well as ungraded massive beds strongly suggest that the conglomerates were emplaced by debris flows (Hampton 1975; Walker 1975; Middleton & Hampton 1976; Lowe 1982). The normally graded conglomerates with pebble to coarse sand-grade clasts and a few floating outsize clasts (Fig. 10) could be a product of cohesive turbulent debris flow or high, density turbidity flows (Lowe 1982). Inversely graded beds with appreciable amount of muddy matrix (Fig. 9)



Fig. 8. Clast-supported, ungraded lime-clast conglomerate of debris flow origin. Note boulder-size, disorganized clasts.



Fig. 10. Clast-supported, normally graded pebbly conglomerate. Note floating outsize clasts and plane laminations developed at the top.

are identified as deposits of modified grain flows which would require a high gradient of 9–14° to maintain its mobility (Lowe 1976). The debris flow comprising only of pelagic carbonates further suggests that the flows originated by remolding of submarine slides (Cook 1979*a, b*). Tabular bed morphology without any appreciable basal erosion suggests that majority of beds were emplaced on the lower slope (Cook & Mullins 1983) and a few could also extend onto the adjacent basin floor (Crevello & Schlager 1980).

Calcarenite facies. The calcarenites occur as thin sheets (Fig. 11) interbedded with the micritic limestones and consist exclusively of small sand-size clasts of siliceous micritic limestone within a matrix of same composition. The sheets normally range in thickness from 5 to 15 cm, but may vary between 1 and 25 cm. The calcarenite sheets typically have sharp lower bounding surfaces, and are often gradationally overlain by plane-laminated (bed type d) or thick-bedded micrites with poorly developed internal lamination (bed type b). The coarsest of the calcarenites are pebbly and matrix-rich, and may be ungraded or normally graded. Relatively thinner beds are poor in matrix, and show well-developed normal grading.

Interpretation. The lithological similarity between the clast and the matrix in the calcarenites with those of the conglomerates strongly suggests that the calcarenites represent the finer grained products of the slides that generated the conglomerates. Massive, indistinctly graded to ungraded, matrix-rich calcarenites with or without muddy capping are likely to be a product of muddy turbidity flows (Ghibaudo 1992; Mullins & Cook 1986). Thin, normally graded calcarenites with plane-laminated micrite at the top (Fig. 11) represent

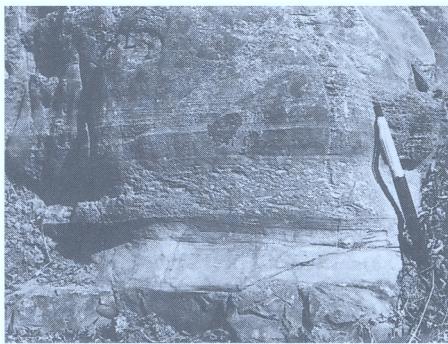


Fig. 11. Normally graded calcarenite capped by thin plane laminae.

top-truncated Bouma sequences T_A to T_{AB} (see Cook & Mullins 1983). Although turbidites may be deposited at different parts of the slope, the top-truncated turbidites are commonly found in the lower slope environments (Cook & Mullins 1983).

Facies sequences and associations

The gravity flow deposits do not show any organization that resemble submarine fan sequences. Rather, they are more randomly distributed with two end member types, the thin-bedded turbidites and thick-bedded debris flow conglomerates. Random association of coarse and fine mass flow deposits militates against a point source canyon-fan depositional system. The sheet-like geometry of the mass flow units with slightly erosional to non-erosional bases indicates that the debris were emplaced by sheet flows. The sequence resembles the slope apron deposits, that are characteristic of carbonate platform sequences world wide (Cook *et al.* 1972; Schlager & Chermak 1979; Crevello & Schlager 1980; Mullins *et al.* 1984; Mullins & Cook 1986).

Despite the fact that debris flow conglomerates occur randomly in deep-water carbonate slope environments, and that huge debris flows are capable of travelling down the slope into the distal basin plain (Crevello & Schlager 1980), the study of a number of sections led to the identification of three preferred facies sequences (*sensu* Walker & Mutty 1973) that can be interpreted in terms of a carbonate slope apron model (Mullins & Cook 1986).

Sequence 1. The sequence (Fig. 12) is characterised by thick conglomerates interbedded with thick-bedded micritic limestones. The conglomerates characteristically show erosional lower bounding surfaces and are normally highly muddy often with matrix-supported clasts ranging up to boulder size. Most of the conglomerates are ungraded or normally graded near the top. Inversely graded conglomerates, though rare, are typical of this sequence. Only thin units (about 7 cm) of interstratified bedded chert and manganese ore may occur in this sequence.

Sequence 2. The sequence (Fig. 12) is dominated by conglomerates and calcarenites interbedded with different types of beds of the micritic limestone, namely types a and e. The conglomerates are extensive parallel-sided sheets without any evidence of erosion at their base. They are normally clast-supported and usually ungraded. Conglomerates normally grading

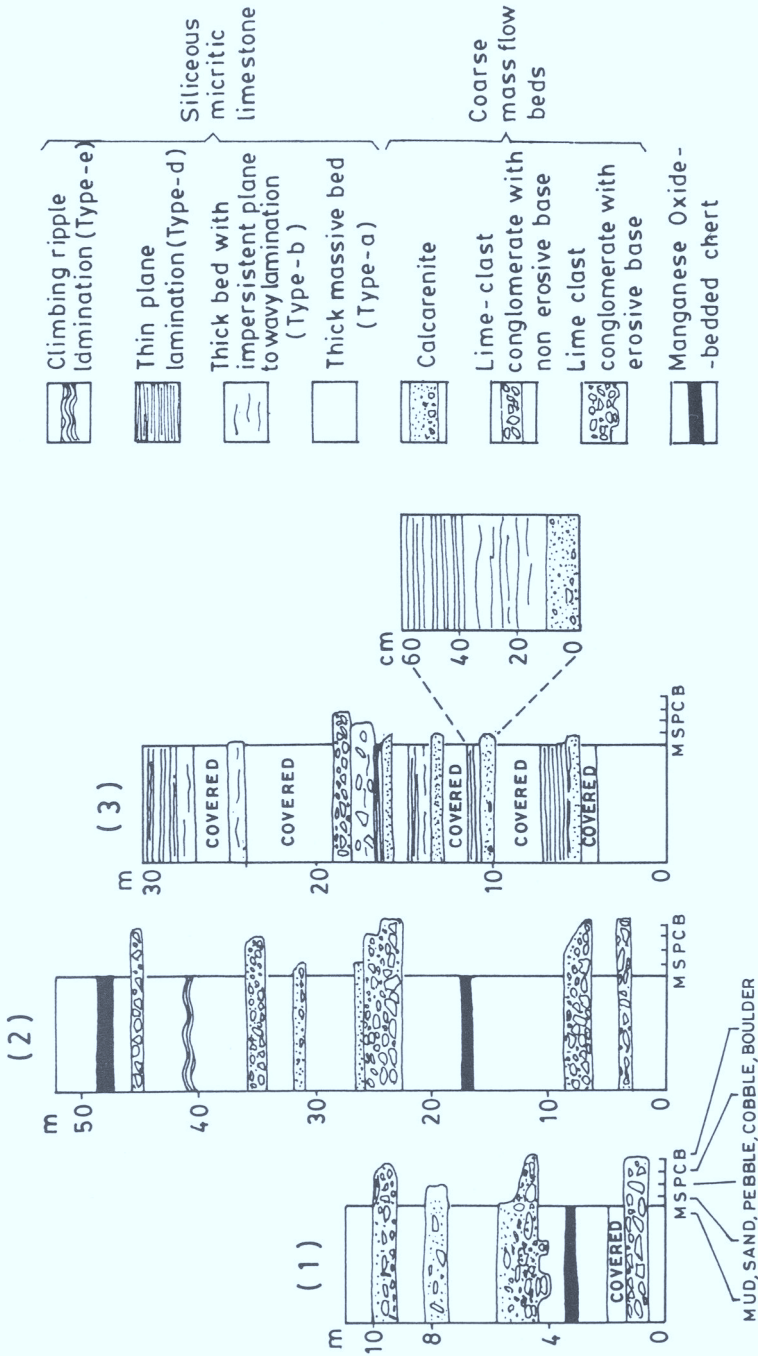


Fig. 12. Lithologies showing facies sequences: (a) Sheet-like lime-clast conglomerates with erosive base alternating with thick, massive micritic siliceous limestone. (Location X in Fig. 2). (b) Succession dominated by lime-clast conglomerate with non-erosive planar base. Conglomerates alternate with thick-bedded, massive micritic limestone and a few beds of calcarenite and climbing ripple lamination. (Location Y in Fig. 2). (c) Succession dominated by graded calcarenite and micritic limestone with thin lamination as well as thick beds with faint lamination. Lime-clast conglomerate beds are rare. (Location Z in Fig. 2).

upwards into micrites are, however, quite common. Clasts are generally smaller than those in the conglomerates of sequence 1. Calcarenites occur quite frequently, and are mostly top-truncated Bouma sequences, namely, T_A and T_{AB} . The manganese bearing horizons are almost exclusive to this sequence.

Sequence 3. The sequence (Fig. 12) is dominated by calcarenites and different types of micritic limestones. Coarse, chaotic conglomerates are rare. Thin sheets of normally graded or ungraded calcarenites interbedded with thick micritic beds with a poorly developed internal lamination or with units of very well developed thin plane laminae (types b and d) are typical of this sequence.

Facies association and depositional environment of the Penganga manganese

Monotonous, persistent plane-bedding and absence of any wave- or current-generated structures in the micritic limestones suggest a setting below storm wave base. Absence of any coarse clastics other than intraformational mass flow deposits is also consistent with this interpretation. Overall similarity of colour-defined intervals of the Chanda Limestone in terms of composition, structure and organisation suggests that all the intervals were deposited within a narrow bathymetric range and the succession evolved within a deep-water ramp setting. The

relative abundance of mass flow deposits in the inner part, in comparison with shoreward part of the basin, suggests distal steepening of a gently sloping, deep carbonate platform. Interestingly, the siliceous grey limestone, the exclusive host of the manganese ore beds, is restricted to the slope developed at the distally steepened end of the platform.

Variations in the nature of the lower bounding surfaces of the slope-related conglomerates in the siliceous grey limestone, the clast size, the matrix content and the nature of the clast contacts, as well as the frequency of turbidites as opposed to debris flow beds collectively suggest that the facies sequences represent well-defined facies associations, and can be assigned to specific depositional environments. An overall off-slope fining trend with increasing abundance of calcarenite and calcisiltite characterize many carbonate slope environments (Cook & Mullins 1983; see also McIlreath & James 1978).

The basal erosional surfaces common to the conglomerates of sequence 1 suggest deposition within the cannibalistic zone of the slope. Turbidites and coarse debris flow conglomerates with broad shallow channelization are typical of the inner apron of the base of a slope setting (Mullins & Cook 1986). In contrast with sequence 1 sequence 3 is dominated by fine calcarenites and thin, plane-laminated micrites representing the more distal environments. They closely resemble the base of the slope to basin plain palaeoenvironment. Sequence 2 is

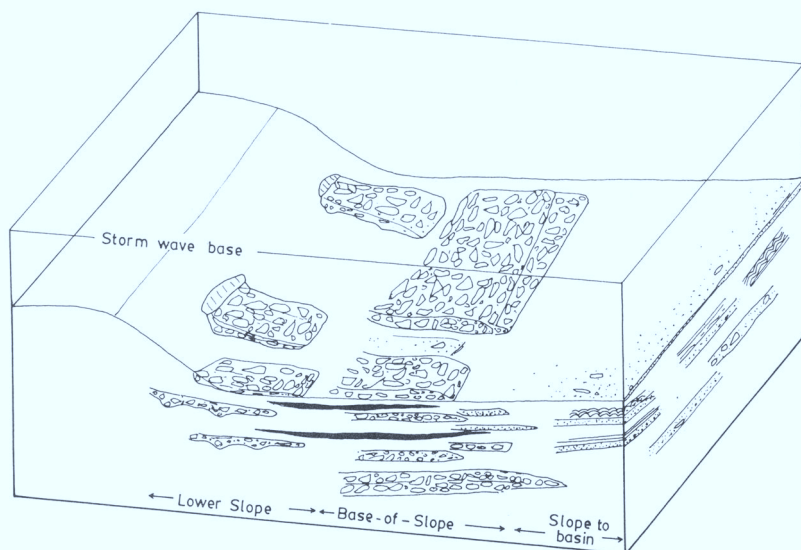


Fig. 13. Schematic model of palaeoenvironmental setting for manganese mineralization. Mn-ore horizons are restricted within lower slope to base of slope setting.

dominated by clast-supported conglomerates without any basal erosion conforming to the outer apron palaeoenvironment (cf. Mullins & Cook 1986), located intermediate between the inner apron and the zone of slope to basin transition. In all measured sections limestone conglomerates are intercalated with hemipelagic to pelagic micritic limestones. The manganese ore beds interstratified with bedded chert occur in the hemipelagic to pelagic intervals of mainly outer apron and only rarely in the inner apron environments of the base of slope setting (Fig. 13).

Discussion on the constraints of the origin of Penganga manganese ores

The Penganga deposits stand apart from most other known manganese deposits in terms of their mode of occurrence and depositional setting. Neoproterozoic manganese deposits are often associated with banded iron formations. Precambrian interlayered chert–manganese oxide deposits, on the other hand, are uncommon. Besides the occurrence around Adilabad (India), chert–manganese deposits are known from the little studied Archaean Chitradurga Group of South India (Roy 1981). Roy *et al.* (1990) proposed that Penganga manganese oxide deposits are of sedimentary origin and, based on Chaudhuri *et al.* (1989), concluded that the manganese formed below wave base. Analysis of trace and rare earth elements led Beukes (1989) to suggest that the manganese deposits in the Proterozoic Transvaal Supergroup were derived from deep marine water with a small hydrothermal component, without specifying the bathymetry of the site of accumulation. Bühn *et al.* (1992) interpreted that the manganese deposits in the Neoproterozoic Damara Sequence of Namibia formed under pelagic conditions in the outer shelf environments and related the development of shelf pelagic condition to a major transgressive event. The geological setting of the Penganga manganese deposit in broad terms is not far from that of the Namibian manganese deposits. However, the Penganga deposit is associated with the base of a slope of a distally steepened, deep carbonate platform, whereas the Namibian deposit formed in a siliciclastic, outer shelf environment. Again, unlike the Damara deposit, the Penganga deposit is free from any association with iron formation.

Sedimentary manganese deposits in shelf settings have often been linked with oceanic upwelling during transgressive–regressive cycles within an overall transgressive phase (Cannon & Force 1983; Frakes & Bolton 1984; Bolton &

Frakes 1985; Force & Cannon 1988). Deep-water manganese deposits of the Damara Sequence have also been related to transgressive phase with attendant upwelling (Bühn *et al.* 1992, 1993). The carbonates overlying shallow-water siliciclastics in the Penganga succession indeed indicate a major transgression. Applicability of the hypothesis of upwelling or any inference on the origin for the Penganga manganese deposit, however, must take into consideration their base of slope depositional setting and lack of association with iron formation.

The present work is a part of a research programme on the Proterozoic of the Pranhita–Godavari Valley initiated and funded by the Indian Statistical Institute, Calcutta. The facies analysis of the carbonate rocks forms a part of the PhD programme of J.M. We were greatly benefited from our discussions with S. Roy and N. J. Beukes. We acknowledge the encouragement received from S. Dasgupta for writing this paper. D. K. Saha prepared the typescript and A. K. Das drafted the diagrams. J. M. and S. K. C. acknowledge funding from the UGC and the Jadavpur University respectively.

References

- BEUKES, N. J. 1983. Paleoenvironmental setting of iron-formations in the depositional basin of the Transvaal Supergroup, South Africa. In: TRENDALE, A. F. & MORRIS, R. C. (eds) *Iron-formations: Facts and Problems*. Amsterdam, Elsevier, 139–209.
- 1989. Sedimentological and geochemical relationships between carbonate, iron-formation and manganese deposits in the Early Proterozoic Transvaal Supergroup, Griqualand West, South Africa. *Abstract volume, 28th International Geological Congress, Washington, DC, USA*, 143.
- BOLTON, B. R. & FRAKES, L. A. 1985. Geology and genesis of manganese oolite, Chiatura, Georgia, USSR. *Geological Society of America Bulletin*, **96**, 1398–1406.
- BÜHN, B., STANISTREET, I. G. & OKRUSCH, M. 1992. Late Proterozoic outer shelf manganese and iron deposits at Otjosondu (Namibia) related to the Damara Oceanic opening. *Economic Geology*, **87**, 1393–1411.
- , — & — 1993. Preservation of sedimentary features in Late Proterozoic manganese and iron-formations (Namibia) through upper amphibolite facies metamorphism: protoliths, paleoenvironment and ore genesis. *Resource Geology, Special Issue*, **17**, 12–26.
- CANNON, W. F. & FORCE, E. R. 1983. Potential for high-grade shallow marine manganese deposits in North America. In: SHANKS, W. C. (ed.) *Unconventional mineral deposits*. New York, American Institute of Mining Metallurgy and Petroleum Engineers, 175–190.

- CHAUDHURI, A. & CHANDA, S. K. 1991. The Proterozoic Basin of the Pranhita-Godavari Valley: An overview. In: TANDON, S. K., PANT, C. C. & CASSHYAP, S. M. (eds) *Sedimentary Basins of India*. Gyanodaya Prakashani, Nainital, 13-29.
- & HOWARD, J. D. 1985. Ramagundam Sandstone: Middle Proterozoic shoal bar sequence. *Journal of Sedimentary Petrology*, **55**, 392-397.
- , DASGUPTA, S., BANDYOPADHYAY, G., SARKAR, S., BANDYOPADHYAY, P. C. & GOPALAN, K. 1989. Stratigraphy of the Penganga Group around Adilabad, Andhra Pradesh. *Journal of Geological Society of India*, **34**, 291-302.
- COOK, H. E. 1979a. Ancient continental slope sequences and their value in understanding modern slope development. In: DOYLE, L. S. & PILKEY, O. H. (eds) *Geology of continental slopes*. Society of Economic Paleontologists and Mineralogists, Special Publications, **27**, 287-305.
- 1979b. Generation of debris flows and turbidity current flows from submarine slides. *American Association of Petroleum Geologists Bulletin*, **63**, 435.
- & ENOS, P. 1977. *Deep-water carbonate environments*. Society of Economic Paleontologists and Mineralogists, Special Publication, **25**.
- & MULLINS, H. T. 1983. Basin margin environment. In: SCHOLLE, P. A., BEBOUT, D. G. & MOORE, C. H. (eds) *Carbonate depositional environments*. American Association of Petroleum Geologists Memoir, **33**, 540-616.
- , McDAVID, P. N., MOUNTJOY, E. W. & PRAY, L. C. 1972. Allochthonous carbonate debris flows at Devonian bank ('reef') margins. Alberta, Canada. *Bulletin of the Canadian Petroleum Geologists*, **20**, 439-497.
- CREVELLO, P. D. & SCHLAGER, W. 1980. Carbonate debris sheets and turbidites, Euxoma Sound, Bahamas. *Journal of Sedimentary Petrology*, **50**, 1121-1147.
- FORCE, E. R. & CANNON, W. F. 1988. Depositional model of shallow marine manganese deposits around black shale basins. *Economic Geology*, **83**, 93-117.
- FLÜGEL, E. 1982. *Microfacies analysis of limestones*. Springer Verlag, Berlin, 633pp.
- FRAKES, L. A. & BOLTON, B. R. 1984. Origin of manganese giants: sea level changes and anoxic history. *Geology*, **12**, 83-86.
- GHI BAUDO, G. 1992. Subaqueous sediment gravity flow deposits: practical criteria for their field description and classification. *Sedimentology*, **39**, 423-454.
- HAMPTON, M. A. 1975. Competence of fine-grained debris flows. *Journal of Sedimentary Petrology*, **45**, 834-844.
- JOPLING, A. V. & WALKER, R. G. 1968. Morphology and origin of ripple-drift cross lamination, with examples from the Pleistocene of Massachusetts. *Journal of Sedimentary Petrology*, **38**, 971-989.
- LOWE, D. R. 1976. Grain flow and grain flow deposits. *Journal of Sedimentary Petrology*, **46**, 188-199.
- 1982. Sediment gravity flows II: Depositional models with special reference to deposits of high density turbidity currents. *Journal of Sedimentary Petrology*, **52**, 279-298.
- MCILREATH, I. A. & James, N. P. 1978. Facies models-13. Carbonate slopes. *Geoscience Canada*, **5**, 189-199.
- MIDDLETON, G. V. & HAMPTON, M. A. 1976. Subaqueous sediment transport and deposition by sediment gravity flows. In: STANLEY, D. J. & SWIFT, D. J. P. (eds) *Marine sediment transport and environmental management*. New York, John Wiley and Sons, 197-218.
- MULLINS, H. T. & Cook, H. E. 1986. Carbonate apron models: alternatives to the submarine fan model for paleoenvironmental analysis and hydrocarbon exploration. *Sedimentary Geology*, **48**, 37-79.
- & NEUMANN, A. C. 1979. Deep-carbonate bank margin structure and sedimentation in the Northern Bahamas. In: DOYLE, L. S. & PILKEY, O. H. (eds) *Geology of continental slopes*. Society of Economic Paleontologists and Mineralogists, Special Publication, **27**, 165-192.
- , HEATH, K. C., BAREN, H. M. & NEWTON, C. R. 1984. Anatomy of modern open ocean carbonate slope: Northern Little Bahama Bank. *Sedimentology*, **31**, 141-168.
- NAQVI, S. M. & ROGERS, J. J. W. 1987. *Precambrian Geology Formations of India*. Oxford University Press, Oxford.
- ROY, S. 1981. *Manganese Deposits*. Academic Press, London, 458pp.
- 1988. Manganese metallogenesis: A review. *Ore Geology Reviews*, **4**, 155-170.
- , BANDYOPADHYAY, P. C., PERSEIL, E. A. & FUKUOKA, M. 1990. Late diagenetic changes in manganese ores of the Upper Proterozoic Penganga Group, India. *Ore Geology Reviews*, **5**, 341-357.
- SCHLAGER, W. & CHERMAK, A. 1979. Sediment facies of platform-basin transition, Tongue of the Ocean, Bahamas. In: DOYLE, L. S. & PILKEY, O. H. (eds) *Geology of continental slopes*. Society of Economic Paleontologists and Mineralogists, Special Publications, **27**, 193-208.
- WALKER, R. G. 1967. Turbidite sedimentary structures and their relationship to proximal and distal depositional environments. *Journal of Sedimentary Petrology*, **37**, 25-43.
- 1975. Generalised facies models for resedimented conglomerates of turbidite association. *Geological Society of America Bulletin*, **86**, 737-748.
- & Mutti, E. 1973. Turbidite facies and facies associations. In: MIDDLETON, G. V. & BOUMA, A. H. (eds) *Turbidites and deep water sedimentation*. Anaheim, California. Society of Economic Paleontologists and Mineralogists, Pacific Section Short Course, 119-158.
- WILSON, J. L. 1969. Microfacies and sedimentary structures in "deeper water" lime-mudstone. In: FRIEDMAN, G. M. (ed.) *Depositional environments in carbonate rocks*. Society of Economic Paleontologists and Mineralogists, Special Publications, **14**, 4-19.

Manganese ores of the Ghoriajhor–Monmunda area, Sundergarh District, Orissa, India: geochemical evidence for a mixed Mn source

KEITH NICHOLSON,¹ V. K. NAYAK² & J. K. NANDA²

¹ *Environmental Geochemistry Research Group, School of Applied Sciences, The Robert Gordon University, Aberdeen AB1 1HG, UK*

² *Department of Applied Geology, Indian School of Mines, Dhanbad 826 004, India*

Abstract: The Proterozoic sedimentary manganese ores of the Gangpur Series, Orissa, India are of gonditic type and are variable in size, depth and grade of ore. The host sediments were deposited in a shallow shelf environment, as reflected in the variable clastic input into the sequence. Braunite and hollandite are the principal ore minerals, with bixbyite, rare jacobsonite and rare vredenburghite. Manganese minerals in the gondites are spessartine and rhodite, together with quartz and aluminosilicates. Supergene weathering and enrichment of the ore horizon and gondite produced secondary ores composed of cryptomelane and pyrolusite. The geochemistry of the deposits shows Mn/Fe \approx 4, low trace element concentrations and arsenic enrichments that exceed 3000 mg kg⁻¹. These are interpreted as indicating a mixed hydrogenetic–hydrothermal source for the manganese oxides of the original precursor (pre-metamorphism) sediments. Regional metamorphism to amphibolite grade transformed this variable oxide–clastic sequence into manganese ores, sharply interbedded with gondites.

The regional metamorphism of sediments enriched in manganese, and low in iron, was first subjected to detailed investigation by Fermor (1909) who studied the metasedimentary manganese deposits of India in a now classic work. It was he who suggested that the original sediments contained unusually high levels of manganese oxides, and he who introduced the term 'gondite' to rocks bearing a quartz–spessartine assemblage (Stanton 1972). Roy has made a similarly extensive study on the metamorphosed deposits of India and the behaviour of manganese oxide minerals on metamorphism under differing conditions (summarized in Roy 1981).

The gonditic-type manganese ores of the Ghoriajhor–Monmunda area were first described by Fermor (1911–12). He considered the manganese deposits of the Gangpur to be the eastern extension of the well-known manganese belt of the Sauser Group in Central India. Prasad Rao & Murty (1956) studied the manganese ore deposits of Orissa and Bihar, and corroborated with both Fermor (1911–12) and Krishnan (1937) in that the Gangpur ores are of gonditic nature. Mineralogical and paragenetic aspects of the ores of the Ghoriajhor–Monmunda area have also been studied by Deb & Majumdar (1963) and Chatterjee (1964).

This paper describes the gonditic ores of the Ghoriajhor–Monmunda area, Orissa, India and considers the possibilities for the source of the manganese in the original unmetamorphosed

precursor sediments, as defined by geochemical patterns derived from studies on modern oxide deposits.

Geological and structural setting

The host rocks for the ore sequence are Precambrian pelitic schists of the Gangpur Series, an easterly extension of the Sauser Belt (Fermor 1911–12; Roy 1981), in the Ghoriajhor Formation. The sediments were deposited at 1700–2000 Ma and metamorphosed to amphibolite facies at around 850 Ma. Krishnan (1937) suggested that the Gangpur metasediments are older than the Iron Ore Series, and forms a major anticline plunging eastward and overturned to the north. Dunn & Dey (1942), however, envisaged that the Gangpur metasediments represent a part of the Iron Ore Series. Banerjee (1967) and Kanungo & Mahalik (1967) developed structure and stratigraphic relationships in the area. However, a more recent study by Chaudhuri & Pal (1983) based on the tectonic history of the area, correlated the stratigraphy of the entire western Gangpur Group. This was re-evaluated by Sarangi (1983), who agreed with the findings of Chaudhuri & Pal (1983). In general, however, the overall structure of the Gangpur Series is debated and controversy persists on the age relations with the Iron Ore Series.

The manganese ores

The Proterozoic manganese ore deposits are distributed in a 64 km long belt in Sundergarh District, Orissa, India (Fig. 1). The area (22°0'–22°10' N, 84°5'–84°15' E) lies in the Survey of India Toposheet 73-B/4. The area is 50 km from Gangpur which is about 600 km SW of Calcutta.

The manganese ore deposits of the Ghoria-Monmunda area are of gonditic nature and associated with metasediments which belong to the Ghoriajhor Formation of the Gangpur Series (Fig. 2). The orebody is 3 km long and 20 m wide, and is interbedded with gondite and quartzite. It shows a conformable relationship with mica schist and phyllites, and in some areas with laterite.

There is one major and two minor ore horizons in the Ghoriajhor–Monmunda area. In general, the manganese orebodies are discontinuous, lensoid in shape and trend NE–SW. The ores are of gonditic type and are variable in size, depth and grade of ore. Deposits occur as irregular lenses and pockets, with the largest individual ore body being 200 m long, 10 m wide and mined to a depth of 30 m. The morphology of the ore is similarly variable with massive, banded and botryoidal or mamillated textures recorded.

The ores were discovered in 1907 and mining commenced that year with peak production in the period 1908–1910 when around 130 000 tons of ore were produced. The mine closed in 1933 and, apart from a brief opening of the mine in 1948, has remained closed since that time.

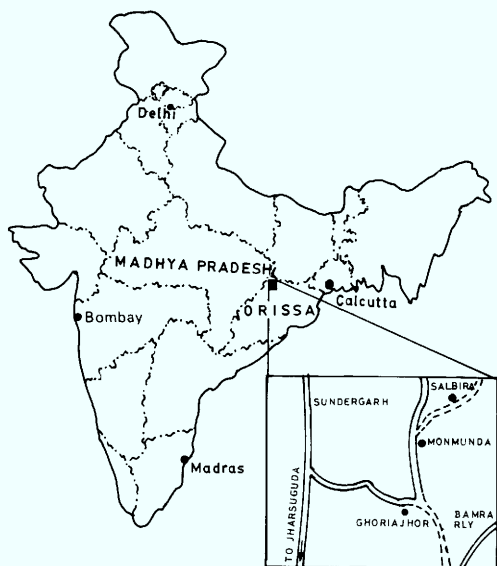


Fig. 1. Location of Sundergarh District, Orissa, India.

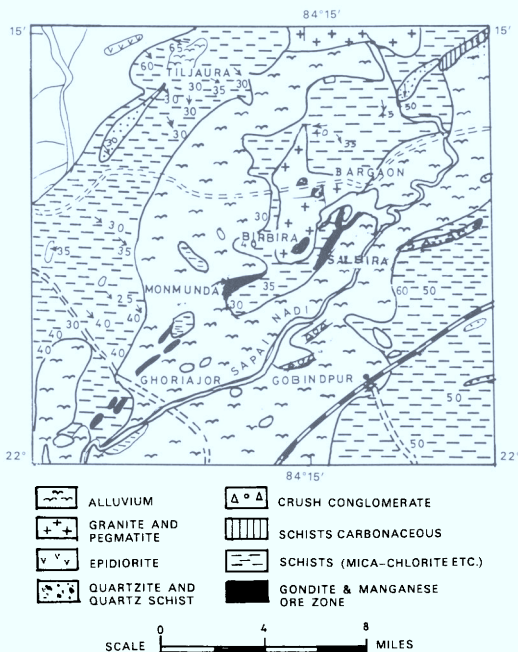


Fig. 2. Geological map and manganese deposits of Gangpur (after Krishnan 1937).

Mineralogy

The mineralogy of the ore was determined by X-ray powder diffraction and reflected light microscopy on polished sections. In the ore horizons, braunite and hollandite are the principal minerals with bixbyite and rare jacobsite and rare vredenburgite. Manganese minerals in the gondites are spessartine and rhodite, together with quartz and aluminosilicates. Supergene weathering and enrichment of the ore horizon and gondite produced cryptomelane and pyrolusite.

The paragenesis of the ore minerals is presented in Table 1. Early and late phases of braunite formation are recognized. The initial braunite is followed by hollandite and bixbyite formation. Late braunite with jacobsite and vredenburgite represent the final stages of the primary ore. Pyrolusite and cryptomelane are contemporaneous being formed following oxidation of the primary sequence.

Geochemistry

The chemical composition of representative samples of the primary ore sediments was determined by ICP-AES following a HF-HCl digestion. The results are presented in Table 2.

Table 1. *Paragenesis of ore minerals*

<i>Primary minerals</i>		
Braunite	—	—
Hollandite	—	
Bixbyite	—	
Jacobsite		—
Vredenburgite		—
<i>Secondary minerals</i>		
Pyrolusite		—
Cryptomelane		—

The low trace element content of the oxides is striking, as is the consistency of the Mn/Fe ratio. Only arsenic achieves significant concentrations and this is not found in all samples, copper and zinc do show some slight enrichments, but not to the levels that may be expected in marine deposits for example. The possible application of geochemical signatures defined on modern and unmetamorphosed sediments is discussed below.

Genetic model

Palaeoenvironmental reconstructions show that Proterozoic sedimentary manganese deposits are commonly deposited in a shelf-basin margin environment, in contrast to modern deep-ocean deposits (e.g. Dasgupta *et al.* 1992; Böhn & Stanistreet this volume, Glasby this volume). The host lithologies to the Orissa manganese ores were deposited in such an environment (Roy 1981; Dasgupta *et al.* 1990, 1992), and the

near-shore setting is reflected in the variable clastic input to the sediments. The original manganese oxides were deposited as a consequence of upwelling anoxic deep-ocean water entering into, and mixing with, the oxygenated, shallow water regime of the basin margin – a commonly invoked mechanism and one that has been suggested for the lateral Sansur sequence manganese ores (Dasgupta *et al.* 1992). Regional metamorphism to amphibolite grade transformed this variable oxide-clastic sequence into manganese ores, characterized by a braunite-hollandite assemblage, sharply interbedded with gondites. Subsequent weathering and supergene enrichment of this sequence produced the secondary oxide assemblage.

Manganese source in original sediments

It is recognized that the composition of the existing gondites and manganese ores reflect that of the original chemical-clastic sediments (e.g. Böhn & Stanistreet this volume; Dasgupta this volume). However, the source of the manganese that lead to the deposition of these initial oxides is more problematic.

It may be possible to use the geochemistry of the metamorphosed ores as a guide to the origin of the original manganese oxides. Such an approach is well established in non-metamorphosed ores (Nicholson 1992*a, b* and references therein) but the application of such diagnostic geochemical signatures to metamorphosed sediments would assume that this signature has been preserved in the meta-sediments. Roy (1981) and Dasgupta *et al.* (1990) have noted that the discrete contact boundaries between oxide and gondite sediments, and their respective mineral assemblages, is an indication that oxygen diffusion between layers was minimal or non-existent and different f_{O_2} conditions existed between the sediments which therefore behaved as independent chemical systems. Further, Dasgupta *et al.* (1992) noted that the effect of metamorphic recrystallization is limited to the redistribution

Table 2. *Geochemistry of manganese ores*

	x	Range
wt%		
Al	1.10	0.27–2.37
Ca	0.63	0.18–0.91
Mg	0.10	0.05–0.20
Fe	4.87	3.20–7.37
Mn	19.87	13.93–28.94
Na	0.23	0.19–0.29
K	0.37	0.19–0.47
P	<0.01	<0.01–0.14
Mn/Fe	4.14	3.93–4.35
ppm		
As	1131	49–3162
Co	102	63–149
Cu	222	49–404
Mo	<0.32	<0.32
Ni	64	11–96
Pb	30	18–44
V	<0.19	<0.19
Zn	168	73–302

of elements in co-existing phases. Under such circumstances it may not be unreasonable to assume that the bulk trace element signatures of the original sediments have been preserved despite recrystallization of the mineral assemblage. Developing this argument further, it is possible to make some deductions based upon established geochemical patterns (Nicholson 1992*a, b*).

The low concentrations of transition metals (Table 2) notably Co, Cu, Ni, Pb and Zn, indicate that these are not deep oceanic deposits. In any case, a coastal or shallow shelf sea setting is more common for deposits of this age, an interpretation that is consistent with the trace element signature and the stratigraphic interpretation for depositional environment of the host sediments (Roy 1981; Dasgupta *et al.* 1990, 1992).

The Mn/Fe ratio is remarkably constant at c. 4 (Table 2), indicating some degree of fractionation between the elements, but not as great as seen in Phanerozoic sedimentary deposits – a difference noted by Glasby (this volume). A lacustrine depositional environment can be excluded as such sediments typically show a Mn/Fe ratio < 1, and this would also not fit with the palaeoenvironmental reconstruction. Further, the ratio is higher than that typical of marine hydrogenetic deposits which tends to be around unity. At Mn/Fe = 4 the ratio is, however, within that displayed by sedex deposits ($0.1 < \text{Mn/Fe} < 10$). However, as Glasby (this volume) points out, differences in seawater chemistry in the proterozoic prevented a high level of Mn–Fe fractionation and the Mn/Fe ratio must therefore be interpreted with some caution.

Hydrothermal discharge into the proterozoic oceans was greater than in the Phanerozoic (Glasby this volume), and as such may have imparted a lasting geochemical signature into hydrogenetic manganese oxides depositing from seawater with a marked hydrothermal input. In this regard, the elevated arsenic content in several samples is interesting as this is diagnostic of a hydrothermal manganese input to the sediments (Cronan 1972; Nicholson 1992*a, b*). However, this enrichment is irregular as seen by the data range in Table 2 and the overlapping hydrogenetic–hydrothermal field in which the samples plot on Fig. 3. The irregular nature of the arsenic enrichment is indicative and characteristic of episodic discharges of hydrothermal fluid. Similar episodic arsenic discharges and precipitates have been recorded in terrestrial geothermal systems (Nicholson & Parker 1990; Parker & Nicholson 1990) and can therefore be

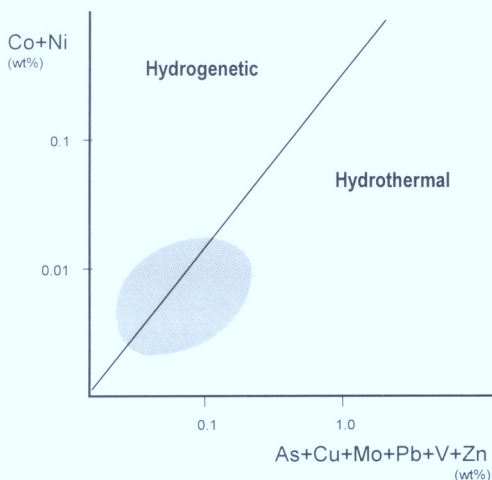


Fig. 3. Plot of manganese ore geochemistry on the hydrogenetic–hydrothermal diagnostic diagram of Nicholson (1992*a*).

used as a tracer of hydrothermal input (see also the arsenic concentrations reported from Japanese geothermal discharges by Miura & Hariya this volume). Since manganese oxide deposition clearly continued in the absence of hydrothermal input, this suggests a second source, such as ambient seawater, for the Mn in the original sediments. It may be argued that the arsenic enrichments could have been caused by an episodic mixing of terrestrial arsenic-rich and marine Mn-rich fluids in the depositional environment. This is an unlikely mechanism though, since if a terrestrial hydrothermal source were present, arsenic enrichments in Mn-poor, clastic sediments would similarly occur and these are not seen.

Conclusion

The Proterozoic sedimentary ores of the Ghorajhor–Monmunda area are similar to those found in the lateral Sauser Group, and in common with similar deposits world-wide were deposited in a near-shore shelf environment from the mixing of upwelling anoxic deep-ocean water with oxygenated near-surface seawater. The low trace element concentrations in the ores support such a depositional environment. Variable arsenic in the oxides is indicative of a significant, if episodic, hydrothermal contribution to the upwelling waters. However, additional Mn source(s) are implied by the continued deposition of oxides in the absence of this hydrothermal input. The application of

diagnostic geochemical signatures to metamorphosed deposits appears to yield reasonable results if applied with discretion. Differences between Precambrian and Phanerozoic seawater composition and consequent changes in Mn and Fe aqueous geochemistry and Mn-Fe fractionation, mean the Mn/Fe ratio is less diagnostic than in modern deposits.

References

- BANERJEE, P. K. 1967. *Revision of the stratigraphy, structure and metamorphic history of the Gangpur Series, Sundergarh District, Orissa*. Records of the Geological Survey of India, **95**, 327-346.
- BÜHN, B. & STANISTREET, I. G. 1997. Insight into the enigma of Neoproterozoic manganese and iron formations from the perspective of supercontinental break-up and glaciation. *This volume*.
- CHATTERJEE, P. B. 1964. *Geology of the eastern extremity of gondites and associated rock types in and around Ghoriajhor, Sundergarh District, Orissa*. MSc thesis, Jadavpur University, Calcutta.
- CHAUDHURI, A. K. & PAL, A. B. 1983. Structural history as an aid in Precambrian stratigraphic correlation - an example from the Gangpur Group in Eastern India. *Journal of the Geological Society of India*, **24**, 522-532.
- CRONAN, D. 1972. The Mid-Atlantic Ridge near 45°N, XVII: Al, As, Hg and Mn in ferruginous sediments from the Median Valley. *Canadian Journal of Earth Sciences*, **9**, 319-323.
- DASGUPT, S. 1997. *P-T-X relationships during metamorphism of manganese-rich sediments: current status and future studies*. *This volume*.
- , BANERJEE, H., FUKUOKA, M. BHATTACHARYA, P. K. & ROY, S. 1990. Petrogenesis of metamorphosed manganese deposits and the nature of the precursor sediments. *Ore Geology Reviews*, **5**, 359-384.
- , ROY, S. & FUKUOKA, M. 1992. Depositional models for manganese oxides and carbonate deposits of the Precambrian Sauser Group, India. *Economic Geology*, **87**, 1412-1418.
- DEB, S. & MAJUMDAR, P. 1963. Mineragraphic study of the manganese ores of Choriajhor, Sundergarh District, Orissa. *Proceedings of the Indian Science Congress 50th Session*, 261.
- DUNN, J. A. & DEY, A. K. 1942. Geology and petrology of Eastern Singhbhum and surrounding areas. *Memoirs of the Geological Survey of India*, **69**, 281-456.
- FERMOR, L. L. 1909. *The manganese deposits of India*. Memoirs of the Geological Survey of India, **37**.
- 1911-12. Notes on the manganese ores deposits of Gangpur State, Bengal, and on the distribution of the gondite series in India. *Records of the Geological Survey of India*, **41**, 12-21.
- GLASBY, G. P. 1997. Fractionation of manganese from iron in Archaean and Proterozoic sedimentary ores. *This volume*.
- KANUNGO, D. N. & MAHALIK, N. K. 1967. Structure and stratigraphic position of the Gangpur Series in the Archaean of Peninsular India. *Proceedings of the Upper Mantle Project, NGRI, Hyderabad*, 458-478.
- KRISHNAN, M. S. 1937. The geology of the Gangpur state, Eastern States. *Memoirs of the Geological Survey of India*, **71**, 14-84.
- MIURA, H. & HARIYA, Y. 1997. Recent manganese oxide deposits in Hokkaido, Japan. *This volume*.
- NICHOLSON, K. & PARKER, R. J. 1990. Geothermal sinter chemistry: Towards a diagnostic signature and a sinter geothermometer. In: HARVEY, C. C., BROWNE, P. R. L., FREESTONE, D. H. & SCOTT, G. L. (eds) *Proceedings of the 12th NZ Geothermal Workshop*. Auckland University Press, Auckland, 97-102.
- NICHOLSON, K. 1992a. Contrasting mineralogical-geochemical signatures of manganese oxides: guides to metallogenesis. *Economic Geology*, **87**, 1253-1264.
- 1992b. Genetic types of manganese oxide deposits in Scotland: Indicators of paleo-ocean spreading rate and a Devonian geochemical mobility boundary. *Economic Geology*, **87**, 1301-1309.
- PARKER, R. J. & NICHOLSON, K. 1990. Arsenic in geothermal sinters: Determination and implications for mineral exploration. In: HARVEY, C. C., BROWNE, P. R. L., FREESTONE, D. H. & SCOTT, G. L. (eds) *Proceedings of the 12th NZ Geothermal Workshop*. Auckland University Press, Auckland, 35-39.
- PRASAD RAO, G. H. S. V. & MURTY, Y. G. K. 1956. Manganese ore deposits of Orissa and Bihar, India. *20th International Geological Congress, Mexico, Symposium on Manganese*, **4**, 115-131.
- ROY, S. 1981. *Manganese deposits*. Academic Press.
- SARANGI, A. K. 1983. Stratigraphy of the Gangpur Group - A re-evaluation. *Geos, IIT, Kharagpur, India*, **9**, 29-36.
- STANTON, R. L. 1972. *Ore petrology*. McGraw-Hill.

Iron and manganese oxide mineralization in the Pacific

JAMES R. HEIN¹, ANDREA KOSCHINSKY², PETER HALBACH²,
FRANK T. MANHEIM³, MICHAEL BAU⁴, JUNG-KEUK KANG⁵
& NAOMI LUBICK¹

¹ *US Geological Survey, MS 999, 345 Middlefield Road, Menlo Park, CA 94025, USA*

² *Fachrichtung Rohstoff und Umweltgeologie, Freie Universität, Malteserstrasse 74–100,
Haus B, D-12249, Berlin, Germany*

³ *US Geological Survey, WHOI, Quissett Campus, Woods Hole, MA 02543, USA*

⁴ *PB 4.3 Lagerstättenbildung, GeoForschungsZentrum Potsdam, Telegrafenberg A-50,
D-14473, Potsdam, Germany*

⁵ *Korea Ocean Research and Development Institute, Ansan, PO Box 29,
Seoul, 425–600, Korea*

Abstract: Iron, manganese, and iron–manganese deposits occur in nearly all geomorphologic and tectonic environments in the ocean basins and form by one or more of four processes: (1) hydrogenetic precipitation from cold ambient seawater, (2) precipitation from hydrothermal fluids, (3) precipitation from sediment pore waters that have been modified from bottom water compositions by diagenetic reactions in the sediment column and (4) replacement of rocks and sediment. Iron and manganese deposits occur in five forms: nodules, crusts, cements, mounds and sediment-hosted stratabound layers. Seafloor oxides show a wide range of compositions from nearly pure iron to nearly pure manganese end members. Fe/Mn ratios vary from about 24 000 (up to 58% elemental Fe) for hydrothermal seamount ironstones to about 0.001 (up to 52% Mn) for hydrothermal stratabound manganese oxides from active volcanic arcs. Hydrogenetic Fe–Mn crusts that occur on most seamounts in the ocean basins have a mean Fe/Mn ratio of 0.7 for open-ocean seamount crusts and 1.2 for continental margin seamount crusts. Fe–Mn nodules of potential economic interest from the Clarion–Clipperton Zone have a mean Fe/Mn ratio of 0.3, whereas the mean ratio for nodules from elsewhere in the Pacific is about 0.7. Crusts are enriched in Co, Ni and Pt and nodules in Cu and Ni, and both have significant concentrations of Pb, Zn, Ba, Mo, V and other elements. In contrast, hydrothermal deposits commonly contain only minor trace metal contents, although there are many exceptions, for example, with Ni contents up to 0.66%, Cr to 1.2%, and Zn to 1.4%. Chondrite-normalized REE patterns generally show a positive Ce anomaly and abundant Σ REEs for hydrogenetic and mixed hydrogenetic–diagenetic deposits, whereas the Ce anomaly is negative for hydrothermal deposits and Σ REE contents are low. However, the Ce anomaly in crusts may vary from strongly positive in East Pacific crusts to slightly negative in West Pacific crusts, which may reflect the redox conditions of seawater. The concentration of elements in hydrogenetic Fe–Mn crusts depends on a wide variety of water column and crust surface characteristics, whereas concentration of elements in hydrothermal oxide deposits depends of the intensity of leaching, rock types leached, and precipitation of sulphides at depth in the hydrothermal system.

Classification and distribution

Iron and manganese oxide deposits forming in the ocean basins vary from nearly pure Fe oxide to nearly pure Mn oxide, with a complete range of iron and manganese concentrations between these two end members (Table 1). Iron deposits are enriched in iron over mean seawater contents by more than 50 million times and over mean lithosphere contents by an order of magnitude. Marine stratabound manganese deposits are enriched in manganese over seawater contents by more than 90 million times and over

lithosphere contents by two to three orders of magnitude. This paper discusses the formation of iron and manganese oxides that form discrete deposits in deep water (>800 m) and does not discuss lower-level concentrations found mixed with other sediment types, for example metalliferous sediments.

Iron and manganese deposits are ubiquitous in the ocean basins and occur in nearly all tectonic and geomorphological environments. These deposits form by four general processes (Table 2): (1) *hydrogenetic* precipitation from cold ambient seawater; (2) precipitation from

Table 1. Mean abundances of Fe and Mn in marine oxide deposits compared to their abundance in seawater and the Earth's crust

	% Mn	% Fe	Fe/Mn	Enrichment of Mn over		Enrichment of Fe over	
				Seawater	Lithosphere	Seawater	Lithosphere
Seawater	0.0000005	0.000001	2.0	—	—	—	—
Lithosphere	0.1	5.5	55	2.0×10^5	—	5.5×10^6	—
Fe–Mn Crusts	26	19	0.7	5.2×10^7	260	1.9×10^7	3.5
Stratabound Mn	47	1.8	0.04	9.4×10^7	470	1.8×10^6	—
Ironstones	0.01	51	5100	2.0×10^4	—	5.1×10^7	9.3

hydrothermal fluids that leached sediments and oceanic crust; (3) precipitation from sediment pore waters that were modified from bottom water compositions by diagenetic reactions in the sediment column; (4) replacement of rocks and sediment. Many marine deposits form by combinations of these four processes. These four processes produce five morphological types of Fe–Mn deposits: (1) nodules and micromodules; (2) crusts and pavements; (3) cements and fracture and vein infillings; (4) mounds and chimneys; (5) sediment-hosted stratabound layers and lenses (Table 2).

The five morphological types of iron and manganese deposits combined with the four processes of formation can be placed in the marine environments in which they are known to occur, as outlined in Table 2. Emboldened entries in Table 2 show six combinations that are common and widespread in the oceans. (1) abyssal plain Fe–Mn oxyhydroxide nodules form by a combination of hydrogenetic and diagenetic processes (Fig. 1; Heath 1981); (2) Fe–Mn oxyhydroxide crusts form by purely hydrogenetic precipitation on hard-rock substrates of midplate volcanic edifices (Fig. 2a; Halbach *et al.* 1982; Hein *et al.* 1987a); (3) Mn-oxide and Fe-oxide crusts form by predominantly hydrothermal precipitation at oceanic spreading axes and midplate volcanic edifices (Toth 1980; Puteanus *et al.* 1991; Stoffers *et al.* 1993); (4) Fe–Mn-oxyhydroxide crusts form by a combination of hydrogenetic and hydrothermal precipitation in active volcanic arcs and spreading centers (Fig. 2b; Hein *et al.* 1987b); (5) stratabound layers and lenses of Mn oxide (more rarely Fe oxide) precipitate from hydrothermal fluids that leached volcanic rocks and volcanoclastic sediments in active volcanic arc environments and midplate volcanic edifices (Fig. 3a; Hein *et al.* 1987b, 1994 1995); and (6) Manganiferous sandstone forms from hydrothermal fluids that circulate through active volcanic arcs and midplate volcanic edifices and cement volcanoclastic sands where Eh conditions are oxidizing (Fig. 3b;

Hein *et al.* 1987b, 1994 1995). Other apparently minor deposit types occur in various ways and in various places within the ocean basins (Table 2). These different types of ferromanganese deposits can be distinguished by their mineralogy, Fe/Mn ratios, trace metal contents, rare-earth element patterns, and growth rates.

Data set and methods

This report is based on samples collected from North Pacific seamounts by the US Geological Survey (Fig. 4). Samples from the eastern North Pacific were collected within the 200 mile Exclusive Economic Zone (EEZ) of the United States; those from the central Pacific are from the EEZ of Johnston Island (east-central Pacific) and the Marshall Islands (west-central Pacific); and those from the West Pacific are from the EEZ of the Federated States of Micronesia (FSM) and the Republic of Palau. Hydrothermal Mn samples were collected from the Yap Arc (FSM), the active volcanic arc in the Commonwealth of the Northern Mariana Islands, the rift zones adjacent to the islands of Hawaii and Maui, and the Valu Fa back-arc basin spreading axes and the Tonga volcanic arc in the South Pacific (Fig. 4). Hydrothermal ironstones are from the Johnston Island, Kingman–Palmyra Islands, and Marshall Islands EEZs. Fe–Mn nodule data are for the Clarion–Clipperton Fe–Mn Nodule Zone (Fig. 4) and from other Pacific abyssal plains as reported by Haynes *et al.* (1985).

Seamounts from which the deposits were collected vary greatly in size, but are commonly very large, comparable in size to mountain ranges that occur on the continents (Fig. 5). Most seamounts were sampled only a few times, or very rarely up to 12 times. Consequently, the distribution of Fe and Mn deposits and the geology of the seamounts are poorly known. In addition, only 10–15 of the tens of thousands of seamounts that occur in the Pacific have been mapped in detail using swath bathymetry and side-scan sonar.

Table 2. Form, processes of formation, and environment of marine ferromanganese oxide deposits

	Hydrogenetic	Hydrothermal	Diagenetic	Hydrogenetic and hydrothermal	Hydrogenetic and diagenetic	Replacement
Nodules	Abyssal plains, oceanic plateaus, seamounts ¹	Submerged calderas and fracture zones	Abyssal plains, oceanic plateaus	Submerged calderas	Abyssal plains, oceanic plateaus ¹	All areas (nodule nuclei)
Crusts	Midplate volcanic edifices ²	Active spreading axes, volcanic arcs, fracture zones, midplate edifices	—	Active volcanic arcs, spreading axes, off axis seamounts, fracture zones	Abyssal hills	Midplate edifices (crust substrate rock)
Sediment-hosted, stratabound layers and lenses	—	Active volcanic arcs, large midplate volcanic edifices, sediment-covered spreading-axes	Continental margins ³	—	—	Continental margins, volcanic arcs, midplate edifices
Cements	Midplate volcanic edifices ⁴	Active volcanic arcs, large midplate volcanic edifices ⁵	Midplate volcanic edifices ⁴	—	Midplate volcanic edifices ⁴	Volcanic arcs, midplate edifices
Mounds and chimneys	—	Back-arc basins, spreading centres, volcanic arcs	—	—	—	—

¹ Less common on ridge, continental slope and shelf.² Includes seamounts, guyots, ridges and plateaus.³ Fe and Mn carbonate lenses and concretions.⁴ Mostly fracture and vein fill, cement for volcanic breccia.⁵ Mostly cement for breccia, sandstone and siltstone.

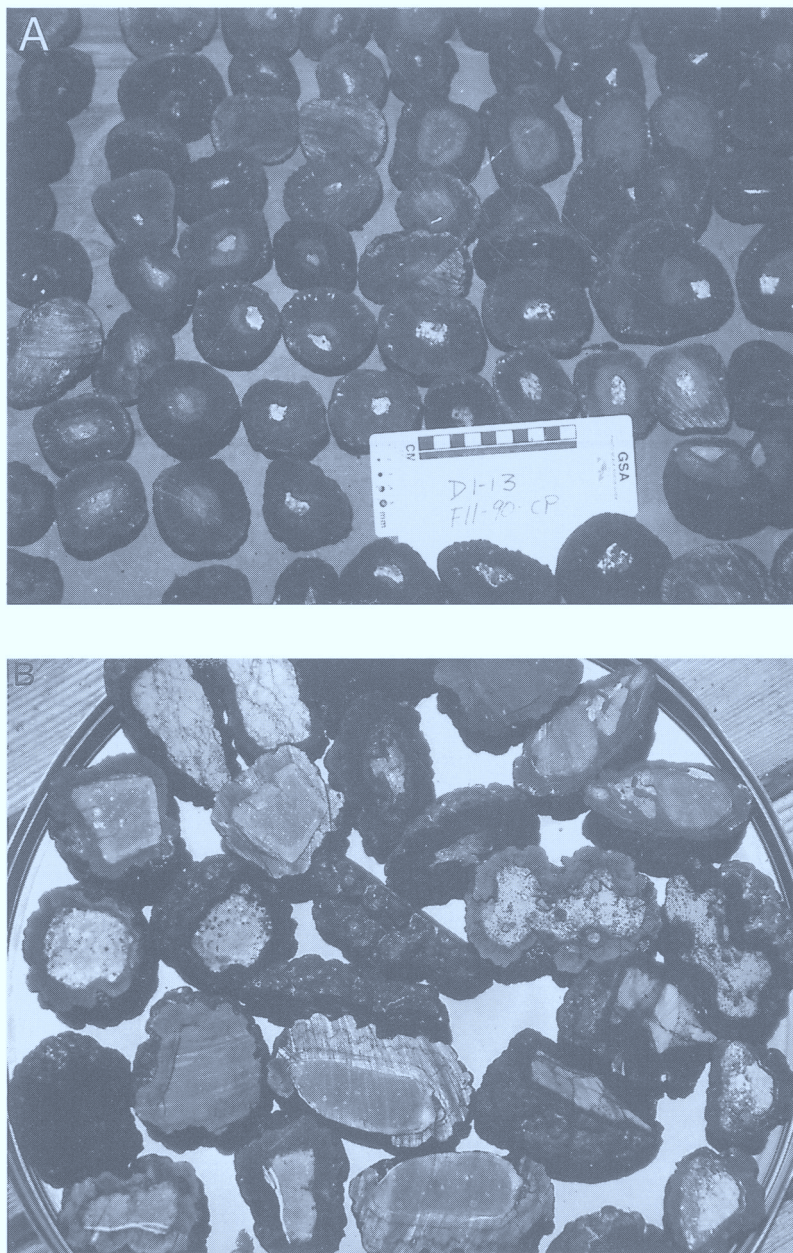


Fig. 1. (a) Photograph showing internal structure typical of abyssal Fe-Mn nodules with small nucleus and thick oxide layers; note that distinct growth layers are visible in some nodules; scale is in centimetres. (b) Typical 4–8 cm long seamount nodules showing a large rock nucleus and relatively thin oxide layers.

Details about the analytical techniques used can be found in Hein *et al.* 1992. Briefly, concentrations of most elements in Fe-Mn crusts were determined by inductively coupled plasma-atomic emission spectrometry (ICP-AES), except K, Zn and Pb, which were

determined by flame atomic-absorption spectroscopy, and As, Cr and Cd which were determined by graphite-furnace atomic absorption spectroscopy. Platinum group elements and rare earth elements were determined by ICP-MS.

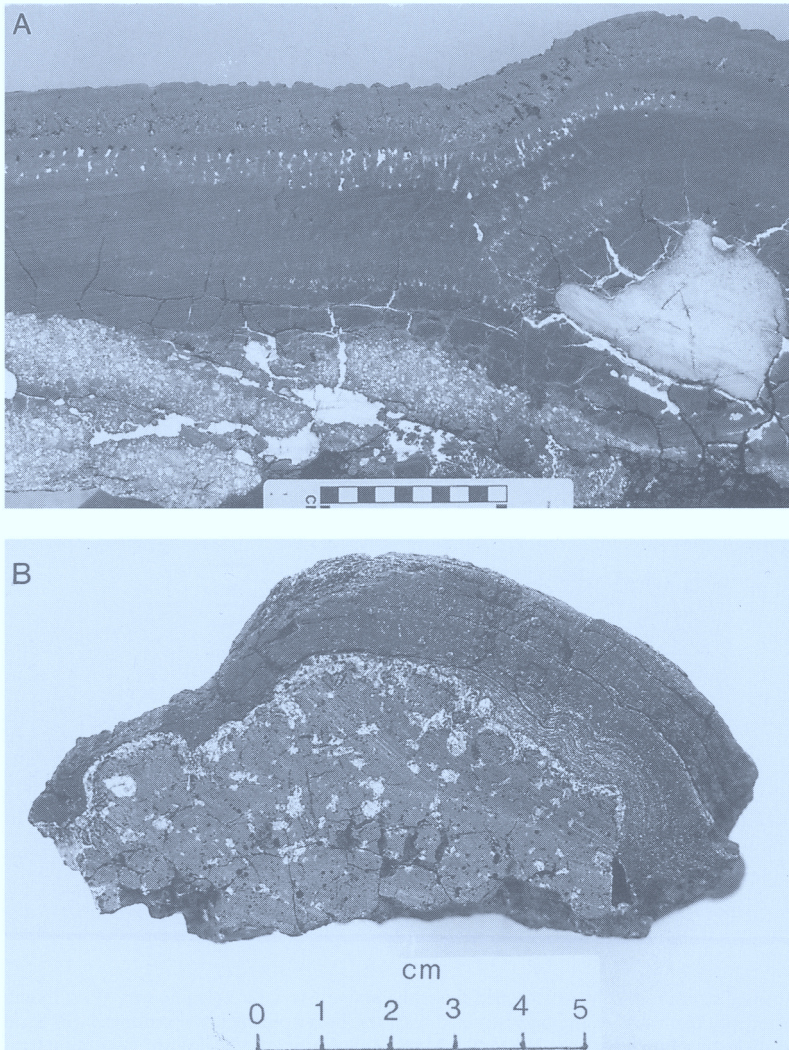


Fig. 2. (a) Photo of hydrogenetic Fe–Mn crust from Lomilik Seamount, Marshall Islands; this up to 18 cm thick crust grew on a phosphatized hyaloclastite substrate rock and contains fractures filled by carbonate fluorapatite; distinct growth layers can be seen; some of the very porous layers have pores filled with either carbonate sediment or CFA. (b) Mixed hydrothermal–hydrogenetic Fe–Mn crust from Gorda Ridge, Northeast Pacific. The crust shows distinct growth layers and Fe-rich laminae near the base; substrate rock is amygdaloidal basalt. Scales are in centimetres.

Composition

Mineralogy

The mineralogy of most deep-sea Fe–Mn deposits is relatively simple. Hydrogenetic crusts and nodules are composed of Fe-rich δ -MnO₂ (ferruginous vernadite; Bolton *et al.* 1988) and X-ray amorphous Mn-bearing FeOOH (Mn-feroxyhyte; Varentsov *et al.* 1991;

Table 3). These two phases are commonly epitaxially intergrown (Burns and Burns 1977); rarely, feroxyhyte crystallizes as goethite in the older parts of thick crusts. δ -MnO₂ has only two X-ray reflections, at 1.4 Å and 2.4 Å, which vary widely in sharpness as the result of crystallite size and manganese content. Minor amounts of quartz and feldspar are commonly present, and carbonate fluorapatite (CFA) impregnates the inner parts of most thick Fe–Mn crusts.

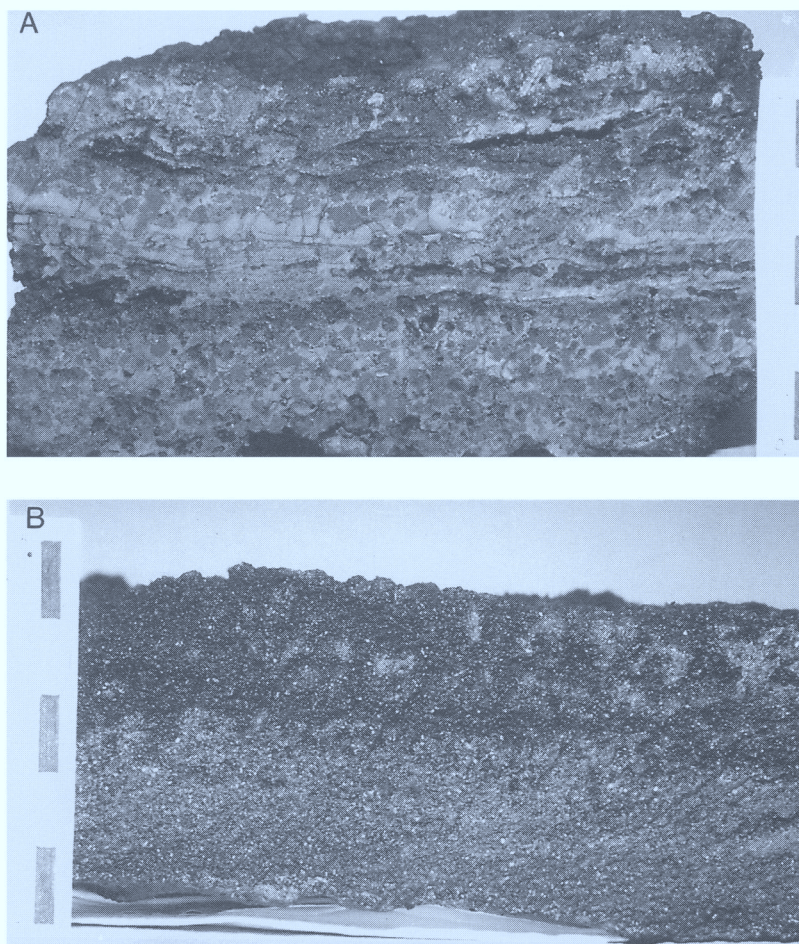


Fig. 3. (a) Photo of stratabound Mn-oxide bed from the active Mariana volcanic arc, West Pacific showing a submetallic luster; the top third of the bed is mixed with the host volcanoclastic sediment. (b) Stratabound Mn-cemented volcanoclastic sandstone from the active Mariana volcanic arc. Scales are in centimetres.

Diagenetic Fe–Mn nodules are composed of a 10 Å manganite, which we will refer to as todorokite and a 7 Å manganite, which we will refer to as birnessite. The terminology of these phases (includes busserite) remains controversial (Burns *et al.* 1983; Usui *et al.* 1989). Todorokite, with X-ray reflections at 1.4, 2.4, 3.3, 4.8 and 9.6 Å, can be of two varieties. One variety is stable and the other collapses to birnessite upon air drying (Fig. 6; Halbach *et al.* 1981; Usui *et al.* 1989; Schulz and Hein 1991). Birnessite has X-ray reflections at 1.4, 2.4, 3.5 and 7.1 Å. Many hydrothermal samples described in the literature as birnessite may have had an *in situ* todorokite mineralogy. Clastic grains and authigenic minerals such as zeolites and barite may also be present in nodules.

Hydrothermal manganese deposits are also composed of both types of todorokite, birnessite, and δ -MnO₂; pyrolusite forms the dominant manganese mineral in some Yap arc samples (Table 3; Hein *et al.* 1992). Hydrothermal ironstones are composed mostly of goethite, with variable amounts of CFA and minor to moderate amounts of clastic minerals.

Geochemistry

As mentioned previously, seafloor iron and manganese deposits show a wide range of compositions. Fe/Mn ratios vary from about 24 000 (up to 58% elemental Fe = 92% FeOOH) for hydrothermal seamount ironstones to about

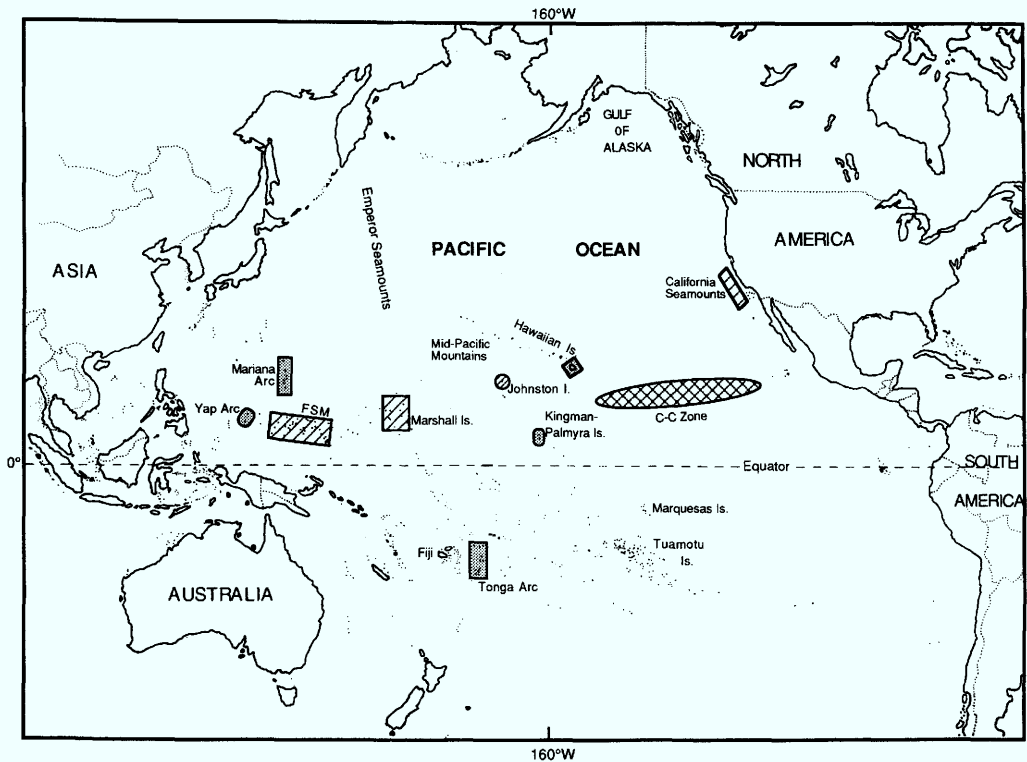


Fig. 4. Location of most deposits discussed in this study: ruled boxes are where hydrogenetic deposits were collected, although hydrothermal ironstones were also collected from the Marshall and Johnston Islands areas; shaded boxes are areas where hydrothermal deposits were collected; cross-ruled area is the Clarion-Clipperton Fe-Mn Nodule Zone; FSM is the Federated States of Micronesia. The California Seamounts area is designated as the East Pacific, Johnston Island as the east-central Pacific, Marshall Islands as the west-central Pacific, and FSM as the West Pacific.

0.001 (up to 52% Mn = 82% MnO₂) for hydrothermal stratabound Mn oxides from active volcanic arcs (Table 4 shows mean values; Schulz and Hein 1991; Hein *et al.* 1994 1995; Hein 1995, unpublished data). In contrast to the very high fractionation of iron and manganese in hydrothermal deposits, hydrogenetic Fe-Mn crusts show little fractionation, with a mean Fe/Mn ratio of 0.7 for open-ocean seamount crusts and 1.0–1.3 for continental margin seamount crusts (Table 4). Fe-Mn nodules of potential economic interest from the Clarion-Clipperton Zone (Fig. 4; C-C Zone) have a low mean Fe/Mn ratio of 0.3, whereas the mean ratio for nodules from elsewhere in the Pacific is about 0.7. C-C Zone nodules are the least enriched in iron among the different diagenetic and hydrogenetic deposit types.

Fe-Mn crusts and nodules have high contents of Co and Ni and Cu and Ni, respectively (these economically important elements are underlined in Table 4), and both deposit types have

significant concentrations of Zn, Ba, Mo, and V; in addition, Pt (to 2 ppm), Pb, Ce and Sr contents are especially high in crusts.

Important changes in the composition of Fe-Mn crusts with water depth and latitude have been studied in some detail (Aplin and Cronan 1985; Hein *et al.* 1987a; Halbach *et al.* 1989a; Hodgkinson and Cronan 1991; De Carlo and McMurtry 1992). These changes reflect differences in water column properties primarily determined by development of the oxygen minimum zone and proximity of the equatorial zone of high biological productivity. Fe-Mn crust compositions reflect these differences in redox potential of seawater. These same kinds of changes should be reflected in crusts from different longitudes because the oxygen contents of seawater at shallow and intermediate depths increase continuously from the East to West Pacific (Fig. 7; Deuser 1975; Kester 1975). The four enclosed areas in Fig. 7 represent the areas for the first four columns of data in Table 4

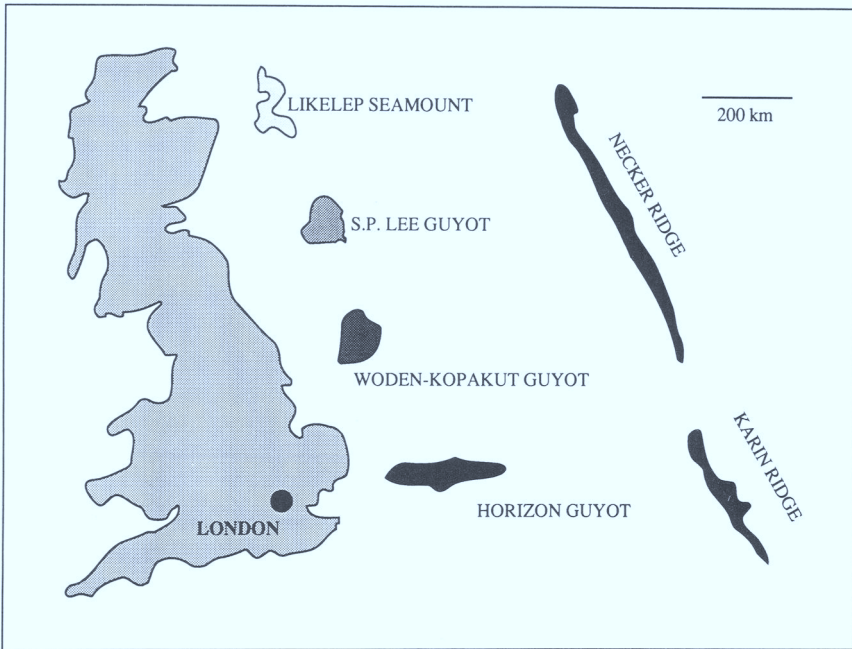


Fig. 5. Comparison of the size of typical central Pacific seamounts and ridges sampled for this study compared to the size of the UK. Necker Ridge is from the Hawaii EEZ, Karin Ridge and Horizon Guyot are from the Johnston Island EEZ, S.P. Lee Guyot is from the Kingman–Palmyra Islands EEZ, and Woden–Kopakut Guyot and Likelep Seamount are from the Marshall Islands EEZ.

superposed on oxygen content contours. The changes in Fe–Mn crust compositions across the North Pacific can be ascribed to three basic processes: (1) dilution by clastic input to the East Pacific crusts and by clastic plus hydrothermal input to West Pacific crusts; (2) increasing oxygen content from east to west, which affects

redox sensitive elements such as cerium; (3) increased input of elements indicative of high biological productivity in the East Pacific crusts. These differences in Fe–Mn crust compositions cannot be explained by differences in water depths among the different areas because the mean water depths from which samples were

Table 3. *Mineralogy of marine Fe–Mn deposits*

	Dominant	Commonly present	Less commonly present
Hydrogenetic Fe–Mn crusts and Nodules	δ -MnO ₂ (Fe-vernadite) Fe-oxyhydroxide (Mn-feroxyhyte)	CFA, quartz, feldspar	Goethite, todorokite, calcite
Diagenetic Fe–Mn nodules	Todorokite Birnessite Fe-oxyhydroxide	Quartz, feldspar, zeolites, CFA	Clay minerals, calcite, barite
Hydrothermal stratabound Mn	Todorokite Birnessite Rarely pyrolusite	δ -MnO ₂	Quartz, feldspar
Hydrothermal ironstone	Goethite	CFA	Quartz, feldspar, zeolites

CFA, Carbonate fluorapatite; many other minerals are rare.

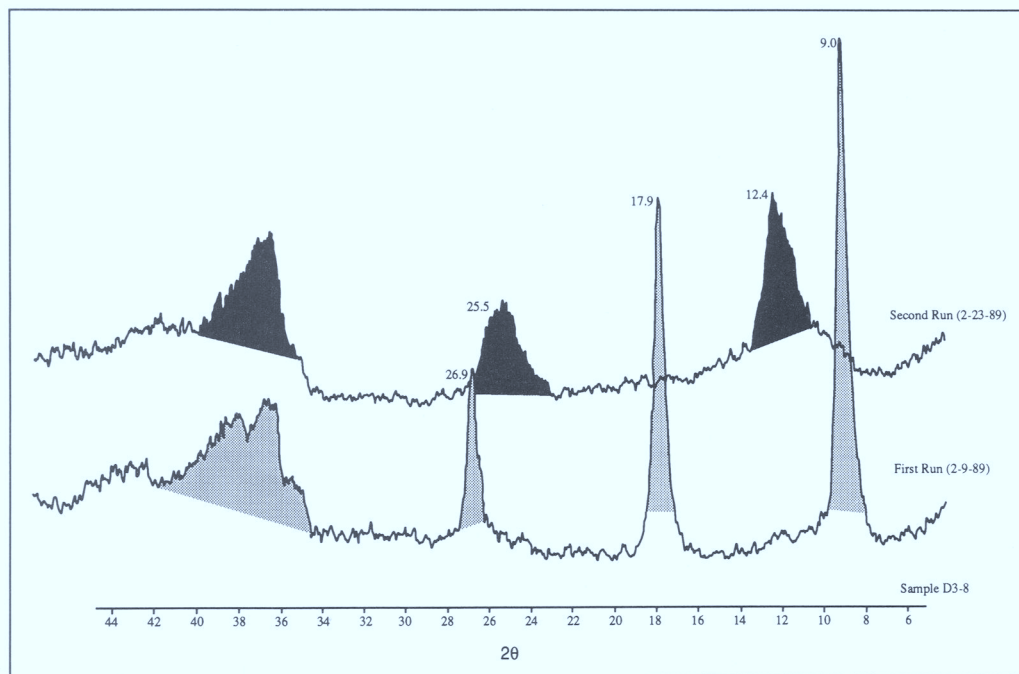


Fig. 6. X-ray diffractogram of hydrothermal todorokite that was kept in water after collection at sea and X-rayed immediately after removal from the water. The sample was then allowed to dry in air for two weeks and was X-rayed again. The 10 Å todorokite collapsed completely to 7 Å birnessite. Sample D3-8 is from the Mariana Arc.

collected are about the same. Crusts and nodules from the Southeast Pacific also have a hydrothermal input that varies with proximity to the numerous spreading centres in that area (Lyle 1981; Chen & Owen 1989).

The continental margin crusts have high Fe/Mn ratios relative to central Pacific crusts, which, combined with dilution affects, produces crusts with lower contents of manganophile elements such as Co, Ni, Zn, Mo, and Pb. Relatively high Si, Al, and Cr contents in continental margin crusts reflect the higher influx of aluminosilicate detritus. The relatively high Ca and P contents of central Pacific crusts reflect a diagenetic CFA component in those crusts. Twice as much Ba in East Pacific Fe-Mn crusts compared with crusts from other areas reflects very high rates of biological productivity. Uniformly increasing V in crusts from east to west in the North Pacific may reflect the higher Fe contents and greater hydrothermal input to west Pacific crusts, although the mean variation from east to west is only 110 ppm. Alternatively, because V is a redox sensitive element (Wehrli & Stumm 1989), its distribution may reflect the redox potential of seawater across the North Pacific. Mean As contents

vary only by 43 ppm among the areas studied. Elements that are concentrated in Fe-Mn crusts by oxidation reactions (Co, Ce and maybe Pt) might be expected to occur in higher concentrations in West Pacific crusts. However, the regional pattern is somewhat masked by local conditions where upwelling around seamounts mixes the various water layers. Regardless, the Ce anomaly does increase for crusts from the East Pacific through the west-central Pacific areas (Table 5). However, this increase in Ce relative to its neighbouring elements in the Periodic Table, which can be attributed to increased oxidation of Ce, is not reflected in the Ce abundances (Table 4) or the total REE abundances (Table 5). In contrast, Pt concentration increases markedly in crusts from the East Pacific through the west-central Pacific areas, then decreases in crusts collected around the West Pacific volcanic arcs. This dramatic increase in Pt contents may reflect its incorporation into the crusts through an oxidation reaction ($\text{Pt}^{2+} \rightarrow \text{Pt}^{4+}$) rather than through a reduction reaction ($\text{Pt}^{2+} \rightarrow \text{Pt}^0$; see Halbach *et al.* 1989b for a discussion of these two reactions). A better reflection of regional oceanographic characteristics would occur if only the

Table 4. Mean bulk composition of Fe-Mn deposits from the Pacific on a hygroscopic water-free basis

Fe/Mn wt %	Hydrogenetic Fe-Mn crusts				Pacific Fe-Mn nodules				Hydrothermal stratabound deposits					
	West Pacific n = 32	West-central Pacific n = 73	East-central Pacific n = 97	East Pacific n = 56	C-C Zone n = x†	Other Abyssal areas n = x†	Mariana Arc n = 26	Yap Arc n = 7	Tonga Arc n = 4	Valu Fa Ridge* n = 8	Hawaii rift zones n = 11	Ironstones, central Pacific n = 6		
	1.01	0.64	0.71	1.27	0.27	0.69	0.04	0.05	0.07	0.03	0.04	>2565		
Fe	21.8	17.0	19.2	21.5	6.9	12.7	1.7	2.2	2.7	1.3	1.9	51.3		
Mn	21.6	26.6	26.9	16.9	25.4	18.5	47.2	44.2	40.4	51.6	46.4	<0.02		
Si	5.8	3.0	4.6	11.4	7.6	8.8	2.3	3.2	5.1	0.90	2.2	1.3		
Na	1.9	1.9	2.0	1.9	2.8	2.1	2.0	1.9	3.4	4.3	2.8	0.17		
Al	1.4	0.71	0.88	2.1	2.9	3.0	0.72	1.1	2.5	0.24	1.0	0.62		
K	0.58	0.54	0.61	0.88	1.0	0.93	1.1	1.0	0.65	0.50	1.1	<0.13		
Mg	1.2	1.2	1.2	1.2	1.7	1.4	1.9	2.4	1.8	0.57	2.7	0.32		
Ca	2.9	6.4	3.4	1.9	1.7	1.8	1.8	1.5	2.3	1.7	2.0	2.5		
Ti	1.1	1.1	1.3	0.60	0.53	0.78	0.51	0.09	0.15	0.03	0.23	0.07		
P	0.51	1.8	0.66	0.42	0.10†	0.10†	0.07	0.07	0.05	0.02	0.04	1.9		
H ₂ O ⁺	10.3	8.2	9.3	10.4	7.5‡	7.5‡	8.8	9.0	9.2	8.7	8.3	10.3		
CO ₂	0.75	1.2	0.69	0.42	0.16‡	0.16‡	0.16	0.17	0.22	0.28	0.23	0.34		
ppm														
Ni	3851	5728	4926	3258	12 800	6300	330	4518	67	44	1585	238		
Cu	1014	1053	1187	756	10 200	4200	263	2632	72	112	83	<5		
Co	4427	7993	8110	3118	2 400	2400	96	450	30	40	326	<23		
Zn	757	870	773	694	1 400	900	2574	1621	104	95	390	328		
Ba	1695	2074	2033	4159	2 800	2000	1511	3089	507	1243	883	199		
Mo	445	562	532	382	450	360	663	324	394	1658	312	101		
Sr	1703	1853	1798	1397	700	700	561	851	332	452	520	691		
Ce	871	1137	1306	1167	530‡	530‡	23	36	20	12	20	24		
Y	207	268	228	176	133‡	133‡	17	37	23	12	14	23		
V	736	725	713	626	470	480	203	529	197	5	162	538		
Pb	1484	1809	1875	1373	450	820	70	88	58	53	30	12		
Cr	34	15	9.0	34	27	25	2.9	436	2.7	2.3	32	252		
Cd	2.7	4.1	3.5	3.2	12	11	20	44	6.1	0.83	28	1.2		
As	286	247	290	278	159‡	159‡	69	49	20	16	21	325		
Pt§ (ppb)	239	634	244	82	97‡	97‡	28	76	9	5	33	11		

C-C Zone means Clarion-Clipperton Nodule Zone.

* Valu Fa Ridge is a back-arc basin spreading centre in Lau Basin west of the Tonga Arc.

† Number of samples is different for each element (columns 5-6; after Haynes *et al.* 1985): n = 100-1000 for Si, Na, Al, K, Mg, Ca, Ti, Ba, Mo, Sr, V, Cr, Cd, As, P, Ce, Y;

n = 1000-2000 for Zn, Pb; n = 2000-2400 for Fe, Mn, Ni, Cu, Co.

‡ Means for the entire Pacific, contents not given by region as with other elements (Haynes *et al.* 1985).

§ Number of samples analysed for Pt is less than the number for other elements: for columns 1-12 respectively, n = 17, 20, 25, 15, 5, 8, 2, 1, 1, 2, 2.

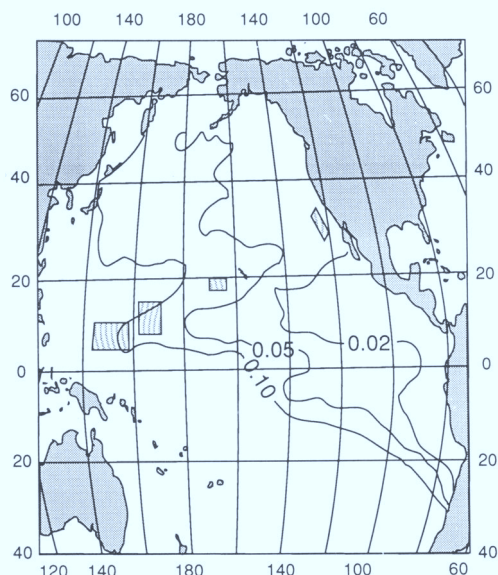


Fig. 7. Location of four Pacific areas where compositions of hydrogenetic Fe–Mn crusts were averaged (Table 4). The four areas are superposed on contours of oxygen content of seawater in ml l^{-1} , which reflects the higher rates of biological productivity in the eastern Pacific.

outer few millimeters of crusts are analysed and compared among the various areas, rather than comparing bulk crust compositions.

In contrast to hydrogenetic and diagenetic deposits, hydrothermal deposits generally contain much lower concentrations of minor metals, although we are learning about many exceptions, for example: Stratabound Mn oxides from Hawaii rift zones have contents of Ni up to 0.23% and Cr to 312 ppm; similar deposits from the Yap volcanic arc have Ni contents to 0.66%, Cu to 0.37%, Zn to 0.26%, Ba to 0.41%, and Cr to 0.17%; similar deposits from the active Mariana Arc have Zn contents to 1.4% and Mo to 0.14%; Mn-cemented sandstones from the Yap arc have Cr contents to 1.2% and Ni to 0.17% (see Table 4 for mean contents, where

Table 5. Changes in mean Pt contents and Ce^* of bulk hydrogenetic crusts across the Pacific (see Fig. 7)

Pacific Area	Ce^*	ΣREEs	Pt (ppb)
East	1.5	1717	82
East-central	1.7	1980	244
West-central	1.9	1560	634
West	1.1	1466	239

Ce^* , chondrite-normalized $2\text{Ce}/\text{La} + \text{Pr}$.

especially high values are underlined). High Zn, Mo, Cd, Ni, and Cr contents characterize hydrothermal manganese deposits, whereas very high Cr and high As, V and P contents characterize hydrothermal ironstones (Table 4). A high Li content of the Mn oxide deposits is apparently the best indicator of formation by marine hydrothermal processes in all tectonic environments (L. H. Chan and Hein 1995 unpublished data; Hodkinson *et al.* 1994). Hydrothermal Mn deposits from oceanic spreading axes have especially low trace metal contents (Toth 1980), as do some midplate hotspot deposits (Hodkinson *et al.* 1994).

Chondrite-normalized REE patterns generally show a positive Ce anomaly and abundant total REEs for hydrogenetic and mixed hydrogenetic-diagenetic deposits, whereas the Ce anomaly is negative for hydrothermal deposits and total REE contents are low (Fig. 8). However, the Ce anomaly in hydrogenetic crusts may vary from strongly positive in most east-central Pacific crusts to slightly negative in many West Pacific crusts, which may reflect the redox conditions of seawater. Although, crusts from all Pacific areas show highly variable Ce anomaly characteristics that probably reflect local redox conditions. In addition, the Ce anomaly of hydrothermal deposits ranges from strongly negative to no anomaly (Fig. 8), depending on the rate of precipitation and the amount of mixing with seawater.

Origins

The four mechanisms discussed previously for the formation of marine iron and manganese deposits are general and do not describe the chemical interactions that take place in the water column and at the surface of the deposits where precipitation of oxides occurs. In fact, the types of reactions that occur in the water column and at the precipitation surface are poorly known. The ultimate sources of Fe and Mn are river and hydrothermal inputs to the ocean. In seawater, elements may occur in their elemental form, or they may form inorganic and organic complexes, which in turn may form colloids that interact with each other and with other dissolved metals. Study of the colloidal chemistry of iron, manganese, and associated metals in seawater with respect to Fe–Mn crust formation is attracting much attention (e.g. Koeppenkastrop & De Carlo 1992; Koschinsky 1994; Koschinsky and Halbach 1995). Thermodynamic and surface- and colloidal-chemical considerations have shown

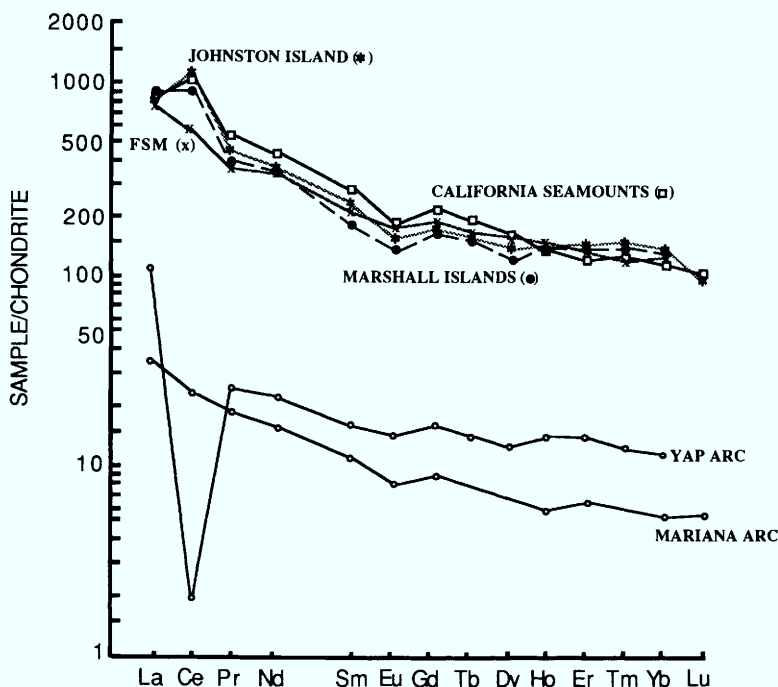
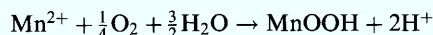
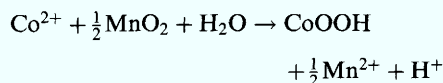


Fig. 8. Typical rare-earth element patterns (chondrite normalized) for hydrogenetic Fe-Mn crusts from the Marshall Islands, Johnston Island, FSM, and California Seamount areas, showing positive Ce (except for FSM area) and Gd anomalies. Hydrothermal stratabound Mn from the Mariana and Yap volcanic arcs show respectively no Ce anomaly and a large negative Ce anomaly, the latter indicating very rapid precipitation; these two patterns mark the range for hydrothermal stratabound Mn deposits from West Pacific arcs. Hydrogenetic deposits are much more enriched in REEs than are the hydrothermal deposits.

that most major and minor hydrogenetic elements that compose crusts and nodules occur in a variety of inorganic complexes in seawater (Fig. 9; Koschinsky 1994). The iron and manganese colloidal phases scavenge trace metals via adsorption, where hydrated cations (Co, Ni, Zn, etc.) are attracted to the negatively charged surface of manganese oxides and anions and large complexes with low charge-density (Pb, V, As, etc.) are attracted to the slightly positive charge of the iron hydroxide surfaces.

Mixed iron and manganese colloids precipitate onto hard-rock surfaces as poorly crystalline or X-ray amorphous oxyhydroxides. Trace elements are incorporated into the deposits either by co-precipitation, or by diffusion of the adsorbed ions into the manganese and iron oxyhydroxide mineral lattices. Cobalt is strongly enriched in hydrogenetic deposits because it is oxidized from Co^{2+} to the less soluble Co^{3+} at the crust surface, possibly through a disproportionation process as described by Hem (1978):



Lead may also be partly enriched in hydrogenetic deposits by a similar mechanism (Aplin & Cronan 1985), although recent sequential leaching studies suggest that much of the Pb may not be incorporated through oxidation (Koschinsky 1994). In contrast, Ti may be enriched in crusts as the result of precipitation from seawater as a separate colloidal phase (Koschinsky 1994).

The dominant controls on the concentration of elements in hydrogenetic deposits are the concentration of each element in seawater, its particle reactivity, and its residence time; the relative amount of major oxides (Fe/Mn) in the deposits, which is determined by their ratio in colloidal flocs suspended in seawater (Aplin & Cronan 1985); the colloid surface charge and

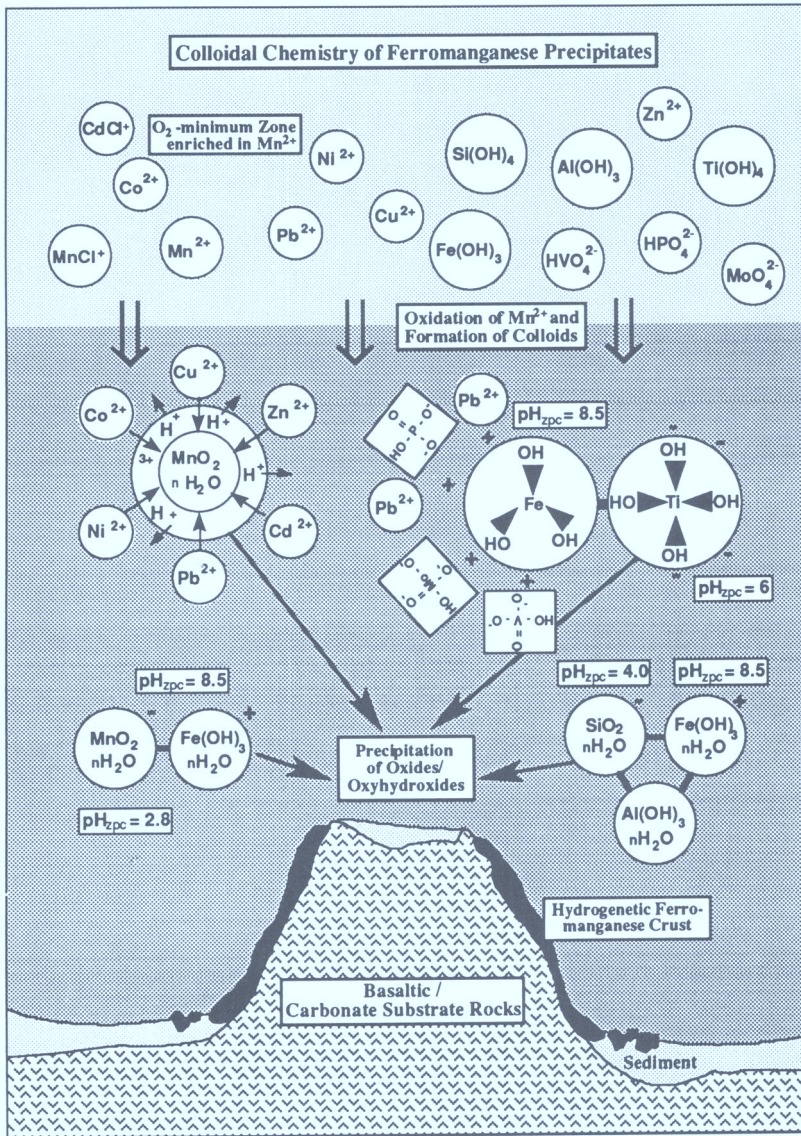


Fig. 9. Colloidal-chemical model for formation of hydrogenetic crusts showing formation of complexes and colloidal phases, adsorption of heavy metals, the pH of the zero point of charge (zpc), and precipitation of oxides on seamount hard-rock outcrops (from Koschinsky & Hallbach 1995).

Table 6. Growth rates of marine Fe-Mn deposits

	Growth rates (mm Ma ⁻¹)
Hydrogenetic crusts and nodules	0.5-15
Mixed	20-100
Stratabound	10 ³ -10 ⁵

Mixed refers to hydrogenetic plus diagenetic and hydrothermal plus hydrogenetic

types of complexing compounds, which will determine the amount of scavenging that takes place in the water column (Koschinsky 1994); the degree of oxidation of MnO_2 (O/Mn), which in turn depends on the oxygen content and pH of seawater (Gramm-Osipov *et al.* 1994); the amount of surface area available for accretion onto the deposits, which for crusts is extremely large, 250-380 m² g⁻¹ (Stashchuk *et al.* 1994);

and the amount of dilution by detrital and diagenetic phases. Elements that form carbonate complexes in seawater behave independently from those that form hydroxide complexes, indicating different modes of removal from seawater onto the Fe–Mn crusts (Bau *et al.* 1995). For example, Y and the REEs may be removed by formation of surface complexes, whereas Ti may be removed by precipitation as a hydroxide.

Very slow growth rates ($0.5\text{--}15\text{ mm Ma}^{-1}$) characterize hydrogenetic precipitation (Table 6), which promotes enrichment of minor elements through greater degrees of scavenging by the major oxides. Precipitation will be slower where the oxygen-minimum zone intersects the seafloor than it will be above and below that zone, because Mn is more soluble in low-oxygen seawater. However, the crust surface exposed at the seafloor may not always be a recent growth surface (Chabaux *et al.* 1995) because of either mechanical erosion or oxygen contents insufficient to permit oxidation of the major metals.

Hydrothermal deposits grow much more rapidly than hydrogenetic deposits (Table 6). The minor element contents of hydrothermal deposits depends on the amount of leaching of rocks and sediments by the hydrothermal fluids, the composition of the rocks and sediments being leached, the amount of mixing with seawater, the temperature of the fluids, precipitation of sulfides at depth, and the degree of fractionation of manganese and iron. The deposits will have low minor-metal contents if the fluids are discharged into the water column before the oxides are precipitated on the seafloor near the vent. This is characteristic of hydrothermal crusts on sediment-free spreading axes. The farther the fluids move away from the vents and mix with seawater, the more the precipitates will approach the composition of hydrogenetic crusts (Manheim & Lane-Bostwick 1988). Mixed hydrothermal-hydrogenetic deposits can be traced for many tens of kilometres away from vent sites (Weiss 1977; Hein *et al.* 1987b; Lavelle *et al.* 1992). Hydrothermal deposits may be enriched in minor metals if there was intense leaching of the host rocks, precipitation occurred below the seafloor, and sulfide precipitation at depth was minor. High contents of Ni and Cr indicate that ultramafic rocks were leached, whereas high contents of Cu, Zn or Pb indicate that sulfide precipitation at depth in the hydrothermal system was not significant enough to remove these elements from the mineralizing fluids. Leaching of mafic, intermediate, and silicic igneous rocks and sediments derived from those rocks will produce enrichments in other element, such as Mo (Hein *et al.* 1995, unpublished data).

Work completed in cooperation with IGCP project 318, Genesis and Correlation of Marine Polymetallic Oxides. The e-mail address of Hein is jhein@octopus.wr.usgs.gov.

References

- APLIN, A. C. & CRONAN, D. S. 1985. Ferromanganese oxide deposits from the central Pacific, I. Encrustations from the Line Islands Archipelago. *Geochimica et Cosmochimica Acta*, **49**, 427–436.
- BAU, M., KOSCHINSKY, A., DULSKI, P. & HEIN, J. R. 1996. Comparison of the partitioning behaviours of yttrium, rare earth elements, and titanium between hydrogenetic marine ferromanganese crusts and seawater. *Earth and Planetary Science Letters*, in press.
- BOLTON, B. R., EXON, N. F., OSTWALD, J. & KUDRASS, H. R. 1988. Geochemistry of ferromanganese crusts and nodules from the South Tasman Rise, southeast of Australia. *Marine Geology*, **84**, 53–80.
- BURNS, R. G. & BURNS, V. M. 1977. Mineralogy. In: GLASBY, G. P. (ed.) *Marine Manganese Deposits*. Elsevier, Amsterdam, 185–248.
- , — & STOCKMAN, H. W. 1983. A review of the todorokite-buserite problem: implications to the mineralogy of marine manganese nodules. *American Mineralogist*, **68**, 972–980.
- CHABAUX F., COHEN, A. S., O'NIIONS, R. K. & HEIN, J. R. 1995. ^{238}U – ^{234}U – ^{230}Th chronometry of Fe–Mn crusts: Growth processes and recovery of thorium isotopic ratios of seawater. *Geochimica et Cosmochimica Acta*, **59**, 633–638.
- CHEN, J. C. & OWEN, R. M. 1989. The hydrothermal component in ferromanganese nodules from the Southeast Pacific Ocean. *Geochimica et Cosmochimica Acta*, **53**, 1299–1305.
- DE CARLO, E. H. & MCMURTRY, G. M. 1992. Rare-earth element geochemistry of ferromanganese crusts from the Hawaiian Archipelago, central Pacific. *Chemical Geology*, **95**, 235–250.
- DEUSER, W. G. 1975. Reducing environments. In: RILEY, J. P. & SKIRROW, G. (eds) *Chemical Oceanography*, **3**. Academic Press, London, 1–37.
- GRAMM-OSIPOV, L. M., HEIN, J. R. & CHICHKIN, R. V. 1994. Manganese geochemistry in the Karin Ridge region: Preliminary physicochemical description. In: HEIN, J. R., BYCHKOV, A. S. & GIBBS, A. E. (eds) *Data and results from R. V. Aleksandr Vinogradov cruises 91-AV-19/1, North Pacific hydrochemistry transect; 91-AV-19/2, North equatorial Pacific Karin Ridge Fe–Mn crust studies; and 91-AV-19/4, Northwest Pacific and Bering Sea sediment geochemistry and paleoceanographic studies*. US Geological Survey Open File Report, **94-230**, 99–102.
- HALBACH, P., KRIETE, C., PRAUSE, B. & PUTEANUS, D. 1989b. Mechanisms to explain the platinum concentration in ferromanganese seamount crusts. *Chemical Geology*, **76**, 95–106.
- , —, MANHEIM, F. T. & OTTEN, P. 1982. Co-rich ferromanganese deposits in the marginal seamount regions of the central Pacific basin—results of the Midpac '81: *Erzmetall*, **35**, 447–453.

- , SATTLER, C.-D., TEICHMANN, F. & WAHSNER, M. 1989a. Cobalt-rich and platinum-bearing manganese crust deposits on seamounts: Nature, formation, and metal potential. *Marine Mining*, **8**, 23–39.
- , SCHERHAG, C., HEBISCH, U. & MARCHIG, V. 1981. Geochemical and mineralogical control of different genetic types of deep-sea nodules from the Pacific Ocean. *Mineralium Deposita*, **16**, 59–84.
- HAYNES, B. W., LAW, S. L., BARRON, D. C., KRAMER, G. W., MAEDA, R. & MAGYAR, M. J. 1985. *Pacific manganese nodules: Characterization and processing*. US Bureau of Mines Bulletin, **679**.
- HEATH, G. R. 1981. Ferromanganese nodules of the deep sea. *Economic Geology*, **75**, 736–765.
- HEIN, J. R., AHN, J.-H. *et al.* 1992. *Geology, geophysics, geochemistry, and deep-sea mineral deposits, Federated States of Micronesia: KORDI-USGS R.V. Farnella cruise F11-90-CP*. US Geological Survey Open File Reports, **92-218**.
- , FLEISHMAN, C. L., MORGENSON, L. A., BLOOMER, S. H. & STERN, R. J. 1987b. *Submarine ferromanganese deposits from the Mariana and Volcano volcanic arcs, West Pacific*. US Geological Survey Open File Reports, **87-281**.
- , GIBBS, A. E., CLAGUE, D. A. & TORRESAN, M. 1996. Hydrothermal mineralization along submarine rift zones, Hawaii. *Marine Georesources and Geotechnology*, **14**, 177–203.
- , MORGENSON, L. A., CLAGUE, D. A. & KOSKI, R. A. 1987a. Cobalt-rich ferromanganese crusts from the Exclusive Economic Zone of the United States and nodules from the oceanic Pacific. In: SCHOLL, D. W., GRANTZ, A. & VEDDER, J. G. (eds) *Geology and Resource Potential of the Continental Margin of Western North America and Adjacent Ocean Basins—Beaufort Sea to Baja California*. Circum-Pacific Council for Energy and Mineral Resources, Earth Science Series, Houston, Texas, **6**, 753–771.
- , YEH, H.-W., GUNN, S. H., GIBBS, A. E. & WANG, C.-H. 1994. Composition and origin of hydrothermal ironstones from central Pacific seamounts. *Geochimica et Cosmochimica Acta*, **58**, 179–189.
- HEM, J. D. 1978. Redox processes at surfaces of manganese oxide and their effects on aqueous metal ions. *Chemical Geology*, **21**, 199–218.
- HODKINSON, R. A. & CRONAN, D. S. 1991. Regional and depth variability in the composition of cobalt-rich ferromanganese crusts from the SOPAC area and adjacent parts of the central equatorial Pacific. *Marine Geology*, **98**, 437–447.
- , STOFFERS, P., SCHOLTEN, J., CRONAN, D. S., JESCHKE, G. & ROGERS, T. D. 1994. Geochemistry of hydrothermal manganese deposits from the Pitcairn Island hotspot, southeastern Pacific. *Geochimica et Cosmochimica Acta*, **58**, 5011–5029.
- KESTER, D. R. 1975. Dissolved gases other than CO₂. In: RILEY, J. P. & SKIRROW, G. (eds) *Chemical Oceanography*, **1**. Academic Press, London, 497–556.
- KOEPPEKASTROP, D. & DE CARLO, E. H. 1992. Sorption of rare-earth elements from seawater onto synthetic mineral particles: An experimental approach. *Chemical Geology*, **95**, 251–263.
- KOSCHINSKY, A. 1994. *Geochemische Krustenprofile und sequentielle Laugungsversuche an Manganerzkusten aus dem Zentralpazifik zur Klärung von Genese und Elementassoziationen*. Berliner Geowissenschaftliche Abhandlungen, Reihe A, Band **158**.
- & HALBACH, P. 1995. Sequential leaching of marine ferromanganese precipitates: Genetic implications. *Geochimica et Cosmochimica Acta*, **59**, 5113–5132.
- LAVELLE, J. W., COWEN, J. P. & MASSOTH, G. J. 1992. A model for the deposition of hydrothermal manganese near ridge crests. *Journal Geophysical Research*, **97**, 7413–7427.
- LYLE, M. 1981. Formation and growth of ferromanganese oxides on the Nazca plate. In: KULM, L. D., DYMOND, J., DASCH, E. J., HUSSONG, D. M. & RODERICK, R. (eds) *Nazca Plate: Crustal Formation and Andean Convergence*. Geological Society of America Memoirs, **154**, 269–294.
- MANHEIM, F. T. & LANE-BOSTWICK, C. M. 1988. Cobalt in ferromanganese crusts as a monitor of hydrothermal discharge on the Pacific sea floor. *Nature*, **335**, 59–62.
- PUTEANUS, D., GLASBY, G. P., STOFFERS, P. & KUNZENDORF, H. 1991. Hydrothermal iron-rich deposits form the Teahitia-Mehitia and Macdonald hot spot areas, southwest Pacific. *Marine Geology*, **98**, 389–409.
- SCHULZ, M. S. & HEIN, J. R. 1991. *Petrography and chemistry of hydrothermal manganese oxyhydroxides from the Mariana and Izu-Bonin volcanic arcs, West Pacific*. US Geological Survey Open File Reports, **91-557**.
- STASHCHUK, M. F., CHERVONETSHY, D. V., KAPLUN, E. V., CHICHKIN, R. V., AVRAMENKO, V. A., TISHCHENKO, P. YA. & GRAMM-OSIPOV, L. M. 1994. Adsorption properties of ferromanganese crusts and nodules. In: HEIN, J. R., BYCHKOV, A. S. & GIBBS, A. E. (eds) *Data and results from R. V. Aleksandr Vinogradov cruises 91-AV-19/1, North Pacific hydrochemistry transect; 91-AV-19/2, North equatorial Pacific Karin Ridge Fe-Mn crust studies; and 91-AV-19/4, Northwest Pacific and Bering Sea sediment geochemistry and paleoceanographic studies*. US Geological Survey Open File Reports, **94-230**, 93–98.
- STOFFERS, P., GLASBY, G. P., STÜBEN, D., RENNER, R. M., PIERRE, T. G., WEBB, J. & CARDILE, C. M. 1993. Comparative mineralogy and geochemistry of hydrothermal iron-rich crusts from the Pitcairn, Teahitia-Mehitia, and Macdonald hot spot areas of the S.W. Pacific. *Marine Georesources and Geotechnology*, **11**, 45–86.
- TOTH, J. R. 1980. Deposition of submarine crusts rich in manganese and iron. *Geological Society of America Bulletin*, **91**, 44–54.

- USUI, A., MELLIN, T. A., NOHARA, M. & YUASA, M. 1989. Structural stability of marine 10 Å manganates from the Ogasawara (Bonin) Arc: Implication for low-temperature hydrothermal activity. *Marine Geology* **86**, 41–56.
- VARENTSOV, I. M., DRITS, V. A., GORSHKOV, A. I., SIVTSOV, A. V. & SAKHAROV, B. A. 1991. Mn–Fe oxyhydroxide crusts from Krylov Seamount (eastern Atlantic): Mineralogy, geochemistry and genesis. *Marine Geology* **96**, 53–70.
- WEHRLI, B. & STUMM, W. 1989. Vanadyl in natural waters: Adsorption and hydrolysis promote oxygenation. *Geochimica et Cosmochimica Acta*, **53**, 69–77.
- WEISS, R. F. 1977. Hydrothermal manganese in the deep sea: scavenging residence time and Mn/³He relationship. *Earth and Planetary Science Letters*, **37**, 257–262.

Some controls on the geochemical variability of manganese nodules with particular reference to the tropical South Pacific

D. S. CRONAN

*Marine Mineral Resources Programme, Department of Geology, Imperial College,
London SW7 2BP, UK*

Abstract: Superimposed on traditional controls on manganese nodule compositional variability, such as metal source and nodule mineralogy, are additional controls related to biological productivity, water depth, the depth of the calcite compensation depth (CCD) and the nature of the associated sediments. Fluxes of Mn, Ni, and Cu to the nodules increase in equatorial regions of high biological productivity but high values of these metals in south equatorial Pacific nodules appear to occur only within about 200m of the CCD. This is thought to result from the concentration of labile organic matter there, the decay of which fuels the diagenetic reactions leading to Mn, Ni, and Cu enrichment in the nodules. However, this process appears to be at its most intense on the flanks of the South Pacific equatorial high productivity zone. Under the most highly productive waters, Mn, Ni, and Cu rich nodules do not occur at any depth nor are nodules abundant there. This is thought to be due to the presence of biogenic silica, the concentration of which is not depth dependent, as the main diluent of the labile organic material at depths near and below the CCD under the most highly productive waters.

Nodule variability

Nature of compositional variability

That manganese nodules exhibit considerable compositional variability has been known ever since the deposits were first described in detail by Murray & Renard (1891). However, it was not until the advent of sophisticated analytical techniques in the post-Second World War period that the compositional variability of most elements in manganese nodules could be quantified with precision. Cronan (1976) attempted to compile all the chemical data on manganese nodules then available into tables illustrating both the average composition of various groups of nodules and the average abundances of elements in them in relation to their average crustal abundances. The minimum and maximum contents of Fe, Mn, Co, Cu and Ni, two of the major and three of the more economically important metals, were found to vary considerably both within each ocean and from one ocean to another. Additionally, within the Pacific Ocean, elements like Si, Ti, Ga, K, Zr, Mo and Pb had been found to vary by more than a factor of 10 (Mero 1965); other elements such as Zn and V, and a host of rare metals, also show considerable variations in concentration. Most striking are enrichments of many elements in manganese nodules over their average crustal abundances. For example, Mn, Mo, Co and Tl are concentrated more than 100-fold relative to their average crustal abundance, Ni, Ag, Ir and

Pb from 50-fold to 100-fold, and V, Cu, Zn, Cd, Yb, W and Bi from 10 to 50-fold. However, these enrichments conceal considerable variations in the concentrations of many individual elements (Cronan 1976, table 28.2).

There are various ways of expressing the variability in the composition of manganese nodules. This has been done in terms of their regional variability throughout the oceans, their variability in relation to depth within the oceans, their variability in relation to different types of depositional environments, and their variability in relation to their mineralogy. Each of these will be briefly reviewed below.

The first person to draw attention to the regional compositional variability of manganese nodules in any detail was Mero (1965). He produced a map showing different compositional regions of the Pacific based on variations in the concentrations of Mn, Fe, Ni, Co and Cu. This showed that nodules from adjacent to continents, particularly in the eastern Pacific, were enriched in Fe or Mn (A or B regions), whereas nodules from pelagic areas of the Pacific far from land tended to be rich in either Ni and Cu (C regions), or in Co (D regions). These results were amplified by Cronan & Tooms (1969) and Cronan (1972) who, using a different data-set to that used by Mero, demonstrated similar regional compositional variations in nodules throughout the Pacific Ocean. Calvert (1978, pp. 54–56) combined both previous data sets and, together with new data, produced more comprehensive individual compositional maps

for Mn/Fe, Ni, Cu, and Co in nodules in the Pacific than had hitherto been available, confirming and refining the conclusions based on the earlier work. Using non-linear mapping, Howarth *et al.* (1977) attempted to express on one map the regional variability shown by most of these data.

Less work has been done on regional compositional variability of nodules in the Atlantic and Indian Oceans than on those in the Pacific, possibly because they have been thought to exhibit less economic potential than Pacific nodules. Nevertheless, some variability in composition of Indian Ocean and Atlantic Ocean nodules does occur, particularly in the Indian Ocean. Results of these studies have been summarized by Cronan (1975), Cronan & Moorby (1981), Frazer & Wilson (1979), Sudhakar (1989) and several others.

Variations in the composition of manganese nodules with depth were noted by Menard (1964) who showed that Co was generally enriched in deposits with decreasing depth. This was confirmed by the results of Mero (1965), Cronan & Tooms (1969), and others who showed that, in addition, Ni and Cu tended to increase in nodules with increasing depth, but that this increase was not linear (Fig. 1). Subsequently, Aplin & Cronan (1985), Halbach & Puteanus (1988) and references therein, and others, refined our knowledge of the effect of depth on the composition of marine ferromanganese oxide deposits in general, principally Co-rich crusts but also nodules, showing that

several other elements exhibit depth variations albeit not as great as for the elements mentioned above.

Another way of expressing the compositional variability of manganese nodules is in relation to their depositional environments. Price & Calvert (1970) and Cronan (1977), among others, grouped published nodule analyses into several depositional environments and made an attempt to differentiate nodule composition between the environments. Nodules from only four of the environments showed significant compositional differences. These are continental margins which tend to host deposits very rich in Mn, volcanically active ocean ridges which tend to host deposits richer in Fe than in Mn, seamounts which tend to host deposits rich in Co and showing many features in common with Co-rich manganese crusts (Hein *et al.* this volume), and lastly the abyssal sea floor which in some areas tends to host nodules rich in Ni and Cu. Most subsequent work on nodule compositional variability in relation to depositional environment has concentrated on elucidating and explaining the variability shown by deposits on the abyssal sea floor.

A fourth way of expressing the compositional variability of manganese nodules is in terms of their mineralogical variability (Buser & Grutter 1956; Cronan & Tooms 1969; Burns & Burns 1977; Cronan 1980; Takematsu *et al.* 1989 and others). Nodules containing δMnO_2 (vernadite) are more enriched in Fe and Co than nodules containing 10 Å manganite (todorokite/buserite), which are enriched in Mn, Ni, and Cu.

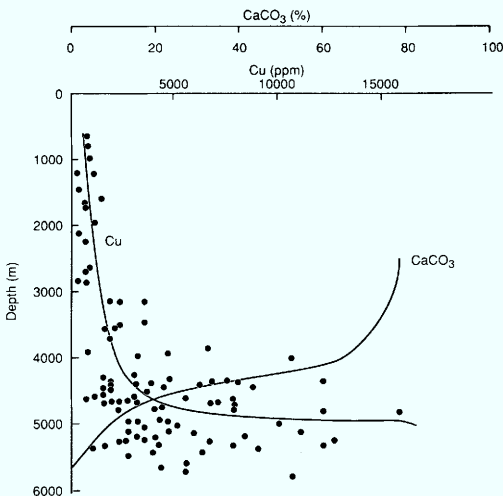


Fig. 1. Relationships of Cu content (solid circles) in Pacific nodules and CaCO_3 for Pacific sediments versus water depth (From Cronan 1980) (the behaviour of Ni with depth is similar to that of Cu).

Causes of compositional variability

Much of the variability in the composition of manganese nodules referred to above has, among other things, been reviewed in relation to sources of elements supplied to the deposits whose end member compositions tend to be different from each other (Cronan 1980; Takematsu *et al.* 1989 and others). A hydrogenous end member derived from ambient seawater supplies precipitates to nodules with an Mn/Fe ratio in the region of about 1 and with a significant trace element content. Diagenetic sources supply precipitates with an Mn/Fe ratio greater than 1; some diagenetic nodules are very enriched in Mn. Hydrothermal fluids supply precipitates either enriched in Fe or Mn which are generally depleted in trace metals. Halmyrolytic sources from low temperature volcanic rock alteration supply precipitates enriched in Fe relative to Mn and which are

low to moderate in trace element content. The location of individual nodules relative to any of these different sources has a considerable effect on their composition, and much of the compositional variability in nodules within the oceans can be related to which of the sources is dominant. However, even on the scale of a single nodule, metal sources can vary. This is best exemplified in nodules from the north-eastern equatorial Pacific that show a smooth upper hydrogenous surface deriving metals from seawater and a more bulbous diagenetic lower surface deriving metals from interstitial waters of the sediments. Ni, Cu and Mn are preferentially supplied to undersides of these nodules whereas Fe and Co are preferentially supplied to their upper surfaces. It has been clear, therefore, for some time that metal source, both on an ocean-wide scale and on the scale of a single nodule, can be of considerable importance in determining the compositional variability of manganese nodules.

The effects of water depth on nodule composition are somewhat complex. Depth variability in nodule composition has been variously ascribed to degree of oxidation of the depositional environment, the selective dissolution of carbonate material supplying metals to the nodules in variable amounts as the carbonates dissolve with depth, and to variations in the rate of accumulation of the sediments associated with nodules at different depths (Mero 1965; Pautot & Melguen 1979; Cronan 1980; Aplin & Cronan 1985 and others). For example, it might be concluded that the relationship between Cu enrichment in nodules and dissolution of calcium carbonate with increasing depth shown in Fig. 1 is a cause and effect one, with the increasing concentration of Cu in the nodules being supplied by that released on dissolution of the calcareous remains. However, this is unlikely to be the case. A more likely possibility is that the reduction in sedimentation rates associated with the dissolution of calcium carbonate near the CCD leads to increased concentrations of organic phases in the sediments (see p. 146) whose decay can promote reactions that diagenetically enrich Cu (and Ni) in the nodules (Cronan 1984, 1987). In support of this, Fig. 1 shows that the highest Cu contents are not in the deepest water nodules below the CCD in the Pacific, but in those located around 5000 m.

Additional research on the geochemistry of manganese nodules has exemplified how the degree of diagenetic activity in their host sediments can exert an important influence on their composition (Dymond *et al.* 1984; Aplin & Cronan 1985 and others). As summarized by

Takematsu *et al.* (1989) and Cronan *et al.* (1991a), nodules formed on oxic sediments underlain by reducing sediments tend to be very rich in diagenetically mobilized manganese (c. 30–40%); the Mn has been remobilized upwards from the reducing sediments and the resultant nodules tend to be poor in all other metals. They have Mn/Fe ratios up to about 30. Nodules formed under processes of oxic diagenesis without reducing sediments at depth receive metals remobilized by oxidation of organic matter in the near surface sediments. The metals released either accumulate on the buried undersides of nodules or on those completely buried in the uppermost sediments. Nodules formed under such conditions tend to be rich in Mn (25–30%), Ni (1–1.5%), and Cu (1–1.5%) and poor in Co (0.1–0.25%) and have Mn/Fe ratios of between 1 and 5.

Nodules formed by hydrogenous processes were initially thought to be entirely non-diagenetic and to have received all metals from ambient seawater or unenriched interstitial waters of seawater composition in a manner analogous to the formation of manganese encrustations on sediment free substrates. These nodules are poorer in Mn (15–20%), Ni (0.4–0.8%); and Cu (0.2–0.6%) and richer in Co (0.3–0.6%) than those formed under conditions of oxic diagenesis, and have lower Mn/Fe ratios. However, Aplin & Cronan (1985) showed that when resting on or in sediments even these nodules can contain some minor sediment-derived diagenetic component, and suggested that no nodules in such a situation can be considered to be entirely free of diagenetic influences.

Nodules in the tropical South Pacific

Regional setting

Nodules in the tropical South Pacific have been studied by a number of workers including Mero (1965), Cronan & Tooms (1969), Price & Calvert (1970), Piper & Williamson (1977), Usui (1984), Halbach *et al.* (1981), Cronan (1984, 1987), Cronan *et al.* (1991b, c), Cronan & Hodkinson (1994) and others; reviews on some of this work have been written by Exon (1983), Cronan (1984, 1987) and Glasby *et al.* (1986). The present review seeks to expand on these earlier ones.

The area of the South Pacific of interest here is between the equator and about 20° S, including parts of the Melanesian, West Central Pacific, East Central Pacific and Northeastern Pacific Basins, the North Penrhyn, South Penrhyn and Samoan Basins, and the Samoan and Aitutaki

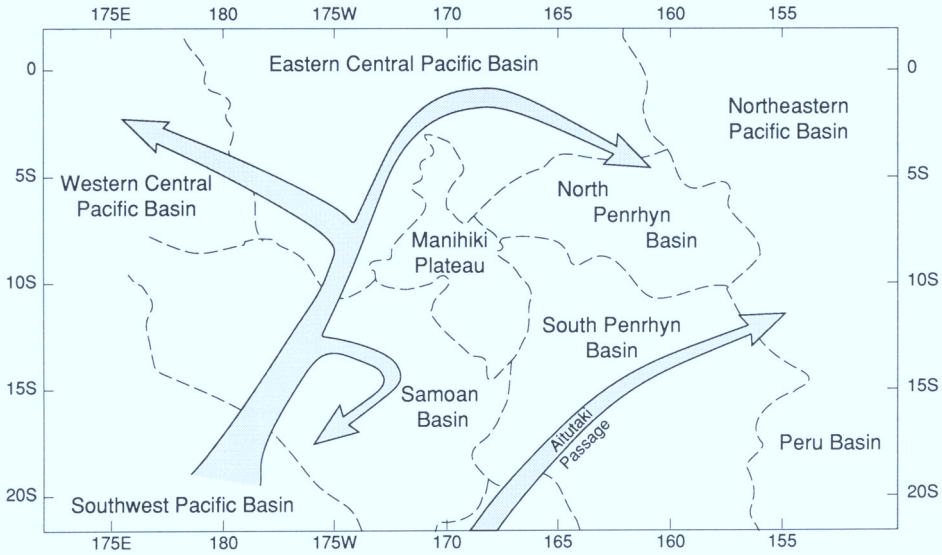


Fig. 2. Manganese nodule provinces in the equatorial South Pacific, with paths of the Antarctic Bottom Water (arrows). (From Cronan *et al.* 1989.)

Passages (Fig. 2). Shallower areas are floored with calcareous ooze, but below 5000 m the normal sediment is red clay (Exon 1983), except in parts of the equatorial region where it is siliceous ooze. The areas of the East and West Central Pacific Basins considered here have sediment types ranging from siliceous ooze in the north to calcareous clay in the south (Exon 1983). In the North Penrhyn Basin the sediment varies from calcareous ooze to calcareous clay. To the south, a slight rise separates this basin from the South Penrhyn Basin where clays are abundant. In the Samoan Basin the deep-water sediments are dominantly volcanogenic turbidites and ash deposits near the Samoan Islands and these have inhibited nodule growth. However, in the southeast part of the basin, silty clays of pelagic origin are common and nodules are present.

Productivity isolines of Berger *et al.* (1987) in the central Pacific (Fig. 3) show that highest biological productivity in the study area, nearly $60 \text{ g C m}^{-2} \text{ a}^{-1}$, occurs in the north and that it decreases towards the south reaching values less than $35 \text{ g C m}^{-2} \text{ a}^{-1}$. This agrees in general with older compilations of Pacific surface biological productivity such as that of Koblenz-Mishke *et al.* (1970) and Flemming (1957), although numerical differences between the different compilations exist.

The position of the CCD in the region has been estimated by Miller & Cronan (1994) from chemical analyses of sediments and smear slide data (Fig. 4). Close to the Equator it is very similar to more general estimates of its position in the equatorial South Pacific based only on smear slide data (Cronan *et al.* 1991*b, c*), but it differs somewhat to the south where data were not previously available.

Bottom currents carrying oxygen-rich Antarctic Bottom Water (AABW) cause dissolution, erosion, and redeposition of deep-water sediments in the central South Pacific, thus lowering sedimentation rates over wide areas and favouring the growth of manganese nodules (Pautot & Melgou 1979). Hydrocasts and current measurements (Lonsdale & Smith 1980) and examination of seismic profiles (e.g. Pautot & Melgou 1979) have defined the regional paths of the AABW (Fig. 2). It flows north through the Southwest Pacific Basin as a western boundary current. East of Samoa it bifurcates with the major stream flowing northward through the Samoan Passage allowing a body of the AABW to enter the North Penrhyn Basin, with the minor stream flowing northeastward into the South Penrhyn basin through the Aitutaki Passage. This passage has a depth range of 4900 m to around 5500 m. In general, Aitutaki Passage sediments consist of homogeneous dark-brown to dark-reddish pelagic clay (Glasby *et al.* 1983).

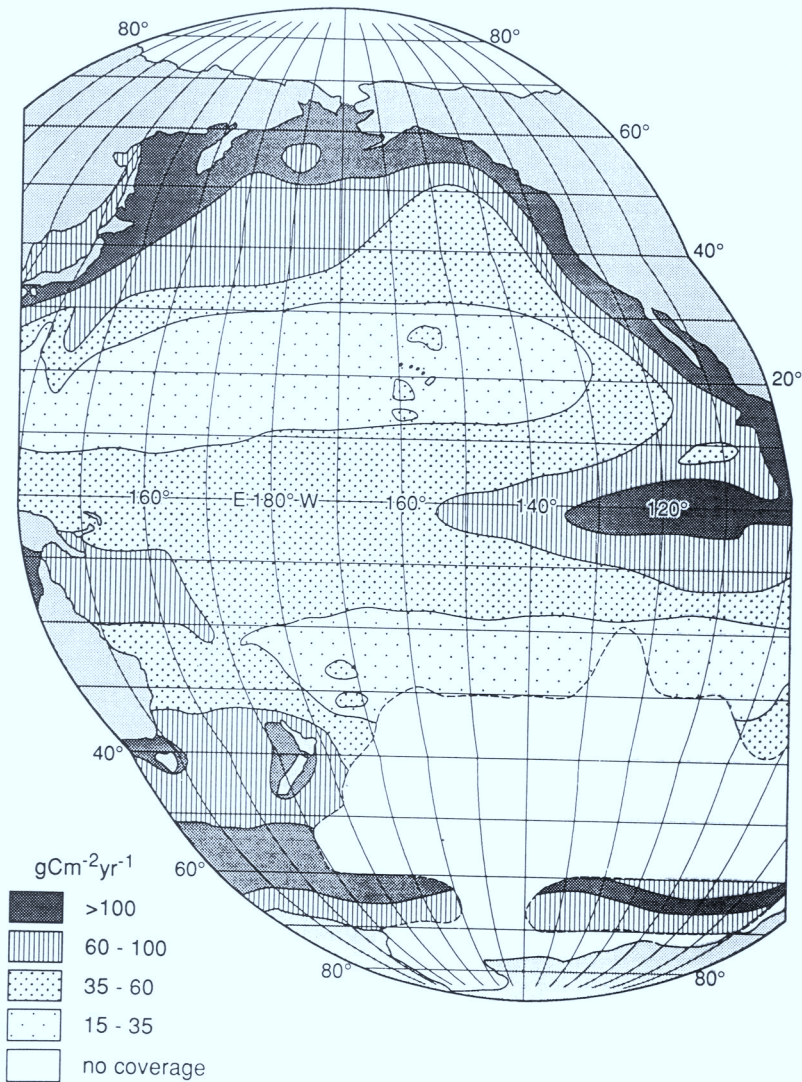


Fig. 3. Biological productivity in the Pacific Ocean in $\text{gC m}^{-2} \text{a}^{-1}$ (from Cronan & Hodkinson 1994 after Berger *et al.* 1987).

Variations in nodules with latitude

The generalized latitudinal relations of Mn, Ni + Cu and Co through the area are shown in Figs 5–7 based on the data of Halbach *et al.* (1980), Halbach *et al.* (1981), Glasby (1981), Exon (1983), Glasby *et al.* (1983), Usui (1984) and Aplin & Cronan (1985). The plots show an overall increase in maximum content of Mn and Ni + Cu towards the equator; the relationship for Co is more subtle. On detailed examination of the data, four major latitudinal zones can be distinguished in the tropical South Pacific.

(a) The equatorial region ($0\text{--}2^\circ \text{S}$) is a zone of low average metal content lying beneath the centre of highest biological productivity.

(b) A zone of very high Mn and Ni + Cu grades, extending from 2° to approximately 4°S , lies beneath the areas bordering the centre of the equatorial zone of high biological productivity.

(c) A zone of moderate Mn and Ni + Cu grades extends from 4°S to about 12°S , underlying the zone of decreasing productivity and is floored with calcareous or zeolitic clays.

(d) The most southerly of the zones, characterised by low Mn and Ni + Cu grades,

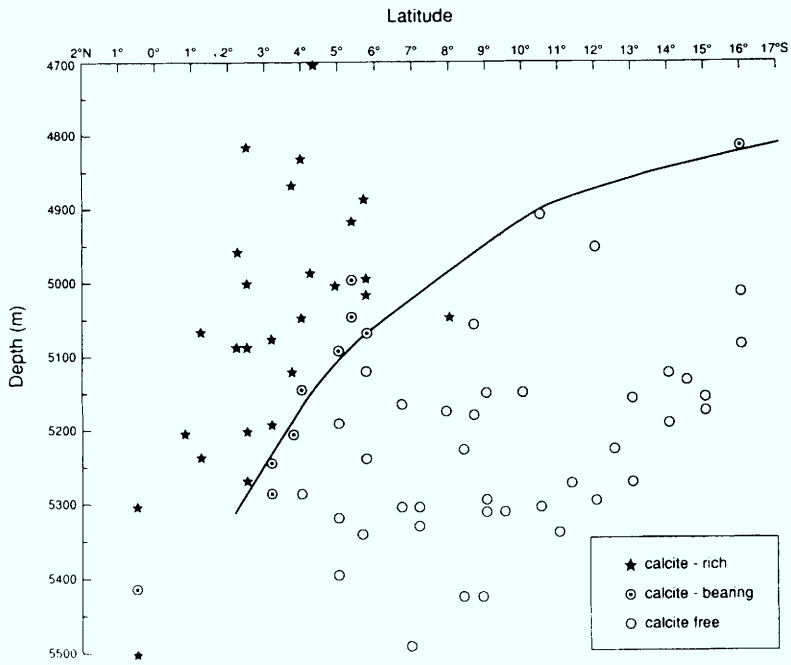


Fig. 4. Variability in depth of the CCD in the equatorial South Pacific (from Miller & Cronan 1994).

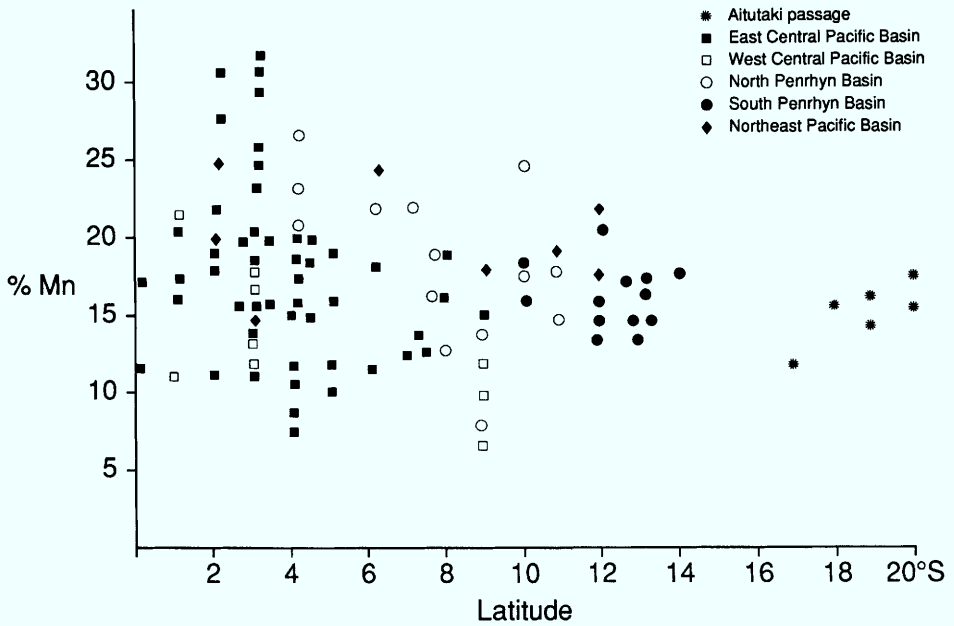


Fig. 5. Plot of nodule Mn content against latitude in the equatorial South Pacific (from Cronan *et al.* 1989).

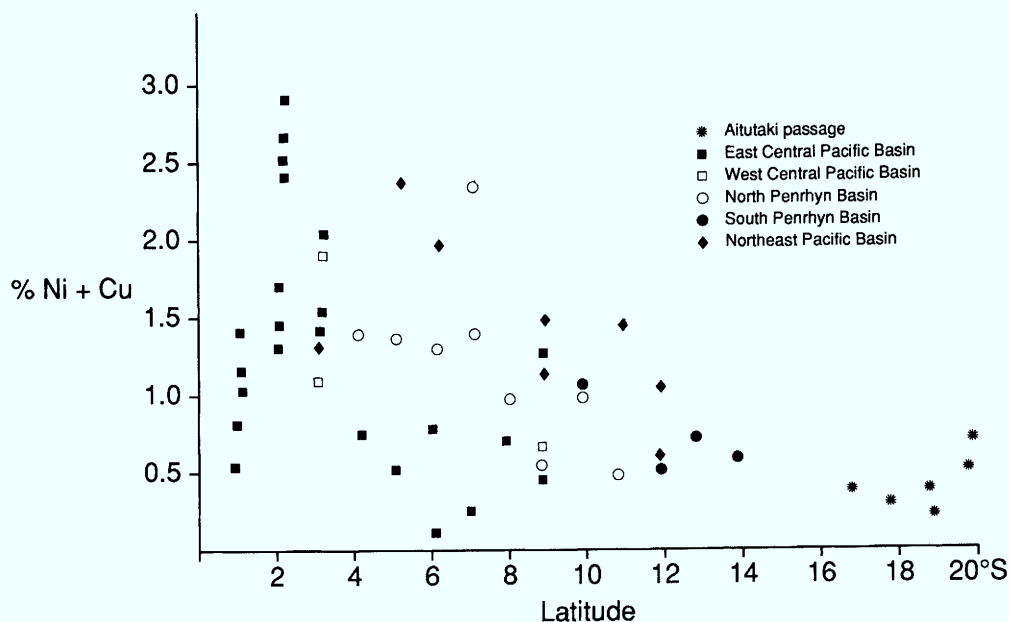


Fig. 6. Plot of nodule Ni + Cu content against latitude in the equatorial South Pacific (from Cronan *et al.* 1989).

extends from about 12°S to 20°S, with nodules occurring on calcareous or zeolitic clays. The highest Co contents are recorded in this zone.

The Aitutaki-Jarvis Transect

The recognition of the possible economic importance of manganese nodules in the Exclusive Economic Zones of some of the island nations of the tropical South Pacific (Cronan 1984) led to more detailed studies in some of them. As part of this work, the Aitutaki-Jarvis

Transect (AJT), was sampled (Fig. 8) (Cronan *et al.* 1987). This is located in the North and South Penrhyn Basins, immediately to the west of the Manihiki Plateau (Fig. 8). The seafloor is predominantly flat to gently undulating, containing small abyssal hills, and is mostly floored with pre-Quaternary zeolitic pelagic clays grading into siliceous and calcareous sediments in the north (Nakao & Mizuno 1982).

Mineralogy. Although both 10 Å manganite and δMnO_2 can co-exist in nodules (Roy *et al.* 1990 and references therein), nodules in which

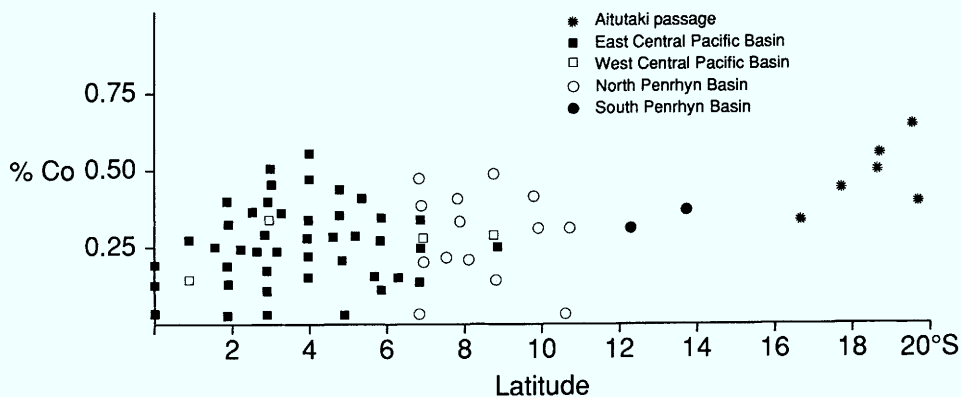


Fig. 7. Plot of nodule Co against latitude in the equatorial South Pacific (from Cronan *et al.* 1989).

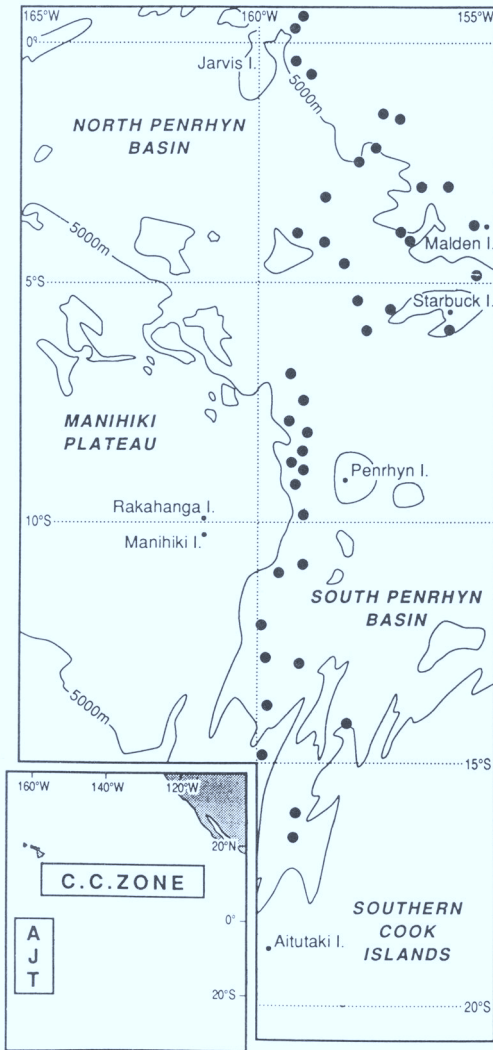


Fig. 8. Location of sample stations on the the Aitutaki-Jarvis Transect (AJT) in the equatorial South Pacific (from Cronan & Hodkinson 1994).

10 \AA manganite predominates have been found to occur most abundantly in areas where diagenetic cycling of metals through the uppermost sediments occurs. By contrast, δMnO_2 predominates in hydrogenous nodules that receive most of their metals from seawater or unenriched interstitial waters of the sediments.

According to Cronan & Hodkinson (1994), immediately adjacent to the equator ($0\text{--}2^\circ\text{S}$) on the AJT, in the region of highest biological productivity, nodules show either low 10 \AA manganite/ δMnO_2 ratios or a total absence of any 10 \AA manganite. This suggests that these

nodules are predominantly hydrogenous with little diagenetic influence on them. Between 2°S and 6°S , with limited exceptions, 10 \AA manganite/ δMnO_2 ratios are significantly higher and reach a maximum at around 5.5°S , whilst further south the ratios are again lower.

A plot of the 10 \AA manganite/ δMnO_2 ratio in the nodules with water depth along the AJT (Cronan & Hodkinson 1994), shows that the highest ratios occur in the depth range 5000 to 5300 m. This depth range corresponds well with the depth range of the CCD along the transect (Miller & Cronan 1994). In order to assess the relationship between the CCD and 10 \AA manganite content more closely, a plot of the 10 \AA manganite/ δMnO_2 ratio with vertical distance above and below the CCD is shown in Fig. 9. This indicates that maximum ratios occur within a depth range of 100 m above and below the CCD. Such a trend supports the concept of increased diagenetic influences on the nodules in the vicinity of the CCD.

The above trends can most likely be related to productivity and sedimentation rate variations in that 10 \AA manganite is well developed in nodules near the CCD under the flanks of the high productivity zone, where, as a result of calcite dissolution, labile organic material can become sufficiently concentrated in the sediments to lead to diagenetic manganese mineral forming reactions (Cronan & Hodkinson 1994). 10 \AA manganite is rare or absent in nodules where labile organic material is likely to be diluted, such as under the axis of the high productivity region near the equator, and in the south of the Transect where low productivity results in little organic carbon being supplied to the seafloor. In each of these situations, and at depths well above or below the CCD all along the Transect, there is likely to be insufficient organic carbon per unit volume of sediment to favour extensive diagenetic 10 \AA manganite formation in nodules and hydrogenous δMnO_2 predominates instead.

Organic carbon data on AJT sediments support the above conclusions. The sediments contain between 0.03 and 1.67% organic carbon (Miller 1992) and, as the AJT is remote from continental masses, most of this must result from biological production in the near surface ocean. Organic carbon shows a non-linear relation to water depth (Fig. 10), increasing to a maximum coincident with the CCD and decreasing below it (Fig. 11). Latitudinally, it peaks at between 5° and 7°S (Fig. 10), the latitudinal range of maximum 10 \AA manganite/ δMnO_2 ratios in the nodules (Cronan & Hodkinson 1994). These relationships are

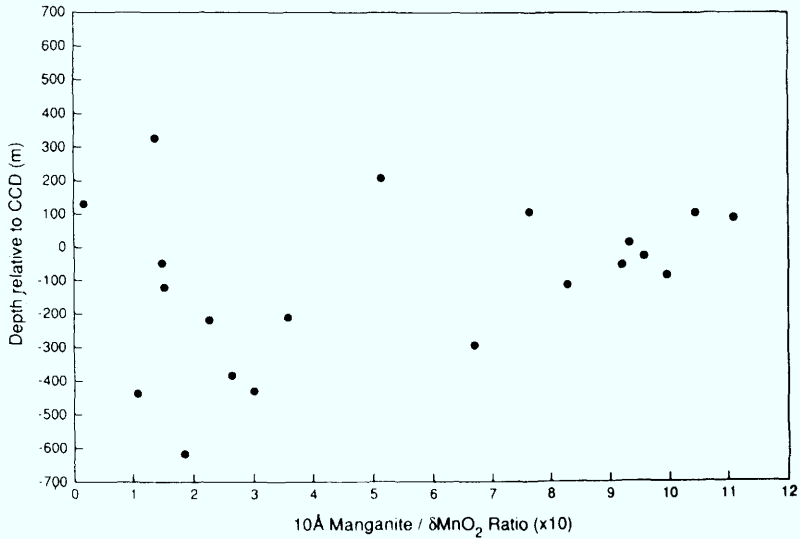


Fig. 9. Variability in the mineralogy of AJT nodules with distance from the CCD (from Cronan & Hodkinson 1994).

confirmed when the organic carbon contents of the sediments are recalculated carbonate-free (Miller & Cronan 1994).

Geochemistry. Comparison by Cronan & Hodkinson (1994) of bulk nodules data from the Transect with previously published Pacific-wide nodules data (Halbach & Puteanus 1988) shows that the transect nodules occupy the lower and middle parts of the Mn/Fe range for Pacific nodules. However, nodules from the north of the transect have the highest Mn/Fe ratios and

highest Ni and Cu concentrations (Fig. 12). This reflects the diagenetic influence outlined above on them.

Superimposed on general compositional relationships between the AJT nodules and water depth (Cronan *et al.* 1991*b*) are variations in nodule composition with position relative to the CCD. According to Cronan & Hodkinson (1994), in areas underlying high-productivity waters in the north of the transect, Mn, Ni, and Cu tend to exhibit maximum values in nodules near the CCD. These trends might at least be

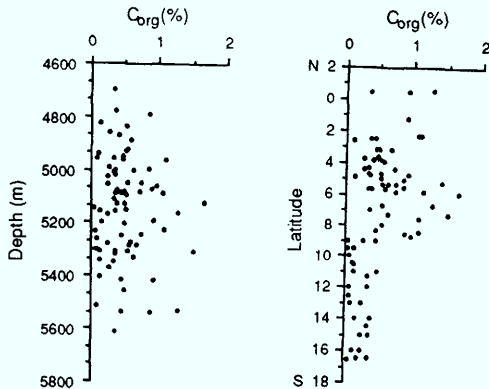


Fig. 10. Depth related and latitudinal variations of organic carbon in AJT sediments (Miller 1992).

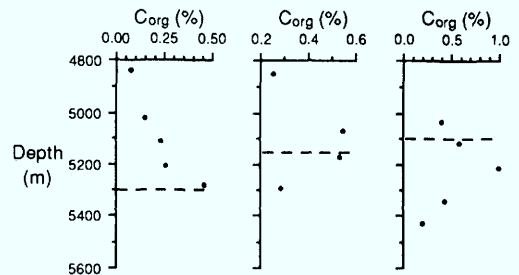


Fig. 11. Depth-related variations of organic carbon in surface sediments from AJT Station groups at 2.5° S, 4° S and 9° S. (The dashed lines represent the approximate depth of the CCD) (Miller 1992).

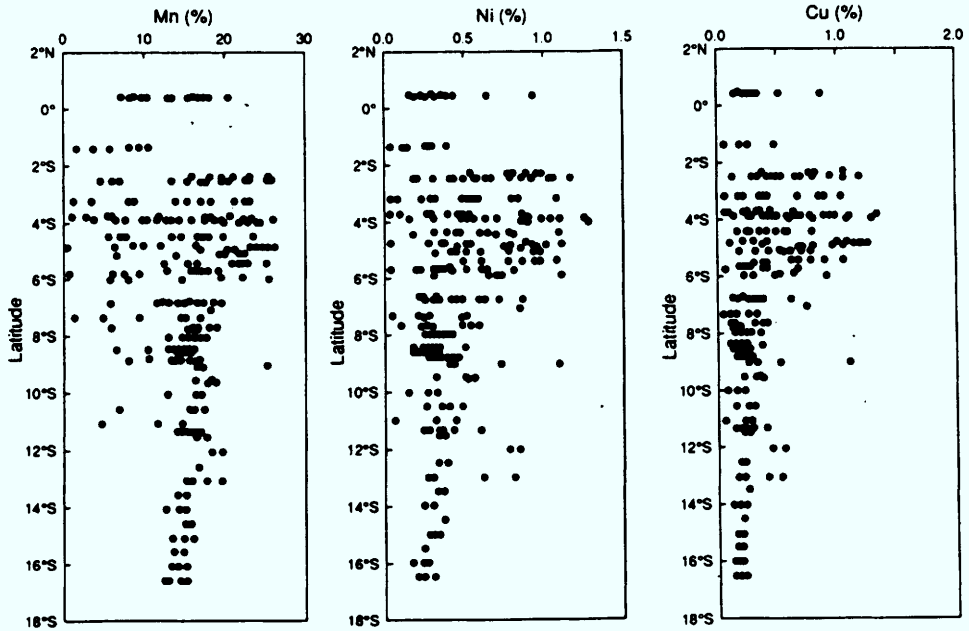


Fig. 12. Variability in the Mn, Ni and Cu contents of AJT nodules with latitude (from Cronan & Hodkinson 1994).

partly explained in terms of the hypothesis that above the CCD in the north of the transect, dilution of labile organic material by biogenic carbonate debris reduces its ability, on decay, to drive the diagenetic reactions leading to 10 Å manganite formation and Ni, Cu and Mn enrichment, whereas below the CCD a greater proportion of the organic phases decay in the water column thereby reducing their availability to the carbonate-free sediment and thus reducing their ability to promote diagenetic reactions in the nodules there also. The organic carbon data of Miller (1992) support this as organic carbon is clearly enriched in sediments from 5000–5300 m depth (Figs 10 & 11), the depth range of the CCD between 2° and 6° S (Fig. 4). In the south of the transect, there is probably insufficient organic matter supplied to the seafloor to promote diagenetic metal enrichments in nodules at any depth. Thus, it can be envisaged that under conditions of reduced carbonate sedimentation close to the CCD, the organic carbon content of the sediment increases to such an extent that its decay will drive the oxic diagenetic reactions leading to Mn, Ni, Cu and 10 Å manganite enrichment in the nodules. Non-diagenetically mediated elements in nodules such as Fe and Co, tend to behave the reverse of the diagenetically mediated Mn, Ni,

and Cu (Fig. 13). Under high-productivity waters, their contents decrease in the nodules towards the CCD and then increase again below it (Cronan & Hodkinson 1994). Fe and Co tend to be enriched in δMnO_2 -rich nodules that form

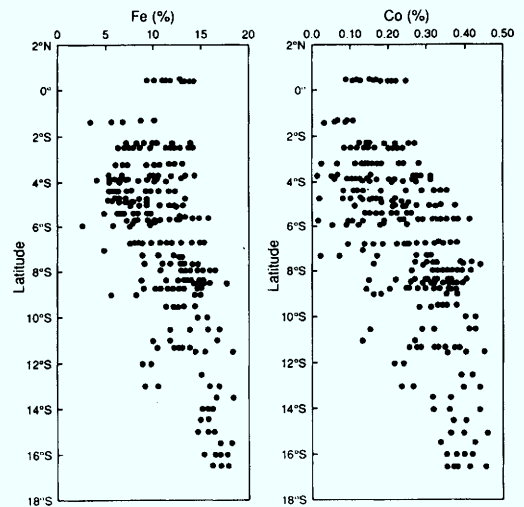


Fig. 13. Variability in the Fe and Co contents of AJT nodules with latitude (from Cronan & Hodkinson 1994).

preferentially away from the CCD and thus there may be a mineralogical influence on the behaviour of these elements just as 10 Å manganite exhibits an influence on the abundance of Mn, Ni and Cu.

Although, according to Cronan & Hodkinson (1994), overall maxima of Mn, Ni and Cu on the AJT occur in the latitudinal range in which the diagenetically formed 10 Å manganite predominates (2–6° S), examination of Figs 5–7 and Fig. 12 shows a very wide scatter of metal values within this latitudinal range, which diminishes both to the north and south. This high scatter of Mn, Ni and Cu contents may be explained by the varying composition of the nodules with distance from the CCD. Those of predominantly diagenetic origin near the CCD exhibit high Mn, Ni and Cu values for the reasons discussed above, whereas those of predominantly hydrogenous origin formed at the same latitude but away from the CCD exhibit lower values of these metals. Further north and south, the nodules are all predominantly hydrogenous and 10 Å manganite is rare or absent. Thus, Mn, Ni and Cu are, on average, lower there and the scatter in their values is reduced. It can therefore be concluded that the latitudinal variations in the Mn, Ni and Cu contents of tropical Central South Pacific nodules can be largely accounted for by a hydrogenous source of these metals throughout the area, superimposed on which is a diagenetic source in the north (2–6° S) at depths near the CCD, but not in the very north (0–2° S) where siliceous sedimentation prevails.

Under the zone of highest productivity, north of about 2° S, although organic carbon falls to the seafloor in abundance, at and below the CCD its concentration in the sediments is diluted by biosilica (radiolarian and diatom remains), probably to too low a level to drive reactions enriching Mn, Ni and Cu in nodules on its decay. Siliceous remains are the main sediment builders at depths at and below the CCD in areas of highest biological productivity. This fact is of critical importance in explaining why highest grade Mn, Ni, Cu and 10 Å manganite-rich nodules have not been found in the equatorial Pacific under areas of highest biological productivity (Cronan 1994). Admittedly, Ni and Cu rich nodules are found on siliceous sediments in the Clarion–Clipperton Zone region to the north, but this is on the northern margin of the high productivity zone and the rate of accumulation of the siliceous sediments is low. From this it can be concluded that where the rate of accumulation of biogenic silica is *high enough* to replace biogenic calcium carbonate as the major diluent of organic

carbon in the sediments, the organic carbon decay related reactions leading to Mn, Ni, Cu and 10 Å manganite enrichment in nodules at and below the CCD will be suppressed.

Summary

The detailed causes of variations in manganese nodules are still under investigation. Nevertheless, certain factors are clear that may have a worldwide applicability in predicting areas of potentially economic nodules. A major influence on the N–S variability in nodule mineralogy and composition in the tropical South Pacific is the northwards increasing biological productivity. This increases the amounts of Mn, Ni, Cu and organic carbon that reach the seafloor and enhances the diagenetic chemical reactions that take place there.

The significance of organic carbon in nodule formation is that its decay promotes the chemical reactions that lead to the formation of 10 Å manganite and the redistribution of Mn, Ni and Cu leading to their enrichment in the nodules under areas of high biological productivity. However, when the N–S variations in Mn, Ni and Cu are examined in detail, they are found to peak between 2° and 6° S and not in the area of highest productivity on the equator. Extremely high biological productivity appears to counteract 10 Å manganite, Mn, Ni and Cu enrichment in nodules. This is because the rate of accumulation of their associated sediments, which is strongly influenced by the calcium carbonate compensation depth and biogenic silica production, is too high.

In the central tropical South Pacific, the CCD varies from about 4800 m, at 16° S to about 5300 m at 2° S. Much of the seafloor in the north is above the latter depth and thus carbonate sediments predominate there. However, sedimentation rates are reduced in the vicinity of and below the CCD. When the mineralogy and composition of the nodules is related to their distance from the CCD, it is found that between about 2° and 6° S, 10 Å manganite and Mn, Ni and Cu tend to show maximum abundances within about 200 m above or below it.

These observations can be explained in terms of the behaviour of organic carbon with depth and sedimentation rate. Above the CCD, organic carbon is diluted by biogenic carbonate debris in a high sedimentation rate regime, reducing its ability to drive, through its decay, the chemical reactions leading to 10 Å manganite and Mn, Ni and Cu enrichment in the nodules. Below the CCD a greater proportion of the organic carbon

decays in the water column rather than being deposited, thereby reducing its supply to the underlying carbonate-free sediments and thus its availability to promote the 10 Å manganite and Mn, Ni and Cu enrichment in the nodules there too. At and near the CCD, reduced sedimentation rates enhance the organic carbon content of the sediments and maximise its influence on 10 Å manganite and Mn, Ni and Cu enrichment in the nodules. South of 6° S, as biological productivity falls off, there is probably insufficient organic carbon being supplied to the seafloor to lead to 10 Å manganite and Mn, Ni and Cu enrichment in the nodules at any depth. North of 2° S biogenic silica replaces pelagic clay as the main sediment builder at and below the CCD, and its high rate of accumulation effectively dilutes the concentration of labile organic material at all depths to levels below which its decay can promote the formation of diagenetic 10 Å manganite and Mn-, Ni- and Cu-rich nodules.

References

- APLIN, A. & CRONAN, D. S. 1985. Ferromanganese oxide deposits from the Central Pacific Ocean II – nodules and associated sediments. *Geochimica et Cosmochimica Acta*, **49**, 437–451.
- BERGER, W. H., FISCHER, K., LAI, C. & WU, G. 1987. *Ocean productivity and organic carbon flux*. Scripps Institution of Oceanography Reference Series, **87–30**.
- BURNS, R. G. & BURNS, V. M. 1977. Mineralogy of manganese nodules. In: GLASBY, G. P. (ed.) *Marine Manganese Deposits*. Elsevier, Amsterdam, 99–139.
- BUSER, W. & GRUTTER, A. 1956. Über die Natur der Manganknollen. *Schweizerische Mineralogische Petrographische Mitteilungen*, **36**, 49–62.
- CALVERT, S. E. 1978. Geochemistry of oceanic ferromanganese deposits. In: PATTON, A., DEACON, G., HUTCHINSON, K. & RANKEN, M. (eds) *Sea Floor Development: Moving into Deeper Water*. *Philosophical Transactions of the Royal Society London*, **A290**, 43–73.
- & PRICE, N. B. 1977. Geochemical variation in ferromanganese nodules and associated sediments from the Pacific Ocean. *Marine Chemistry*, **5**, 43–74.
- CRONAN, D. S. 1972. Regional geochemistry of ferromanganese nodules in the World Ocean. In: HORN, D.R. (ed.) *Ferromanganese deposits on the Ocean Floor*. Office of the IDOE, National Science Foundation, Washington, DC, 19–30.
- 1975. Manganese nodules and other ferromanganese oxide deposits from the Atlantic Ocean. *Journal of Geophysical Research*, **80**, 3831–3837.
- 1976. Manganese nodules and other ferromanganese oxide deposits. In: RILEY, J. P. & CHESTER (eds) *Chemical Oceanography*, **5**, Academic Press, London, 217–263.
- 1977. Deep sea manganese nodules: distribution and geochemistry. In: GLASBY, G. P. (ed.) *Marine Manganese Deposits*. Elsevier, Amsterdam, 11–44.
- 1980. *Underwater Minerals*. Academic Press, London.
- 1984. Criteria for the recognition of areas of potentially economic manganese nodules and encrustations in the CCOP/SOPAC region of the central and southwestern tropical Pacific. *South Pacific Marine Geological Notes*, **3**, 1–17.
- 1987. Controls on the nature and distribution of manganese nodules in the western equatorial Pacific Ocean. In: TELEKI, P. G., DOBSON, M. R., MOORE, J. R. & VON STACKELBERG, U. (eds) *Marine Minerals, Advances in Research and Resource Assessment*. D. Reidel, Dordrecht, 177–188.
- 1994. *Evaluation of marine minerals in EEZs*. Marine Research Review 6. The Marine Technology Directorate, London.
- & HODKINSON, R. A. 1994. Element supply to surface manganese nodules along the Aitutaki–Jarvis Transect, South Pacific. *Journal of the Geological Society, London*, **151**, 391–401.
- & MOORBY, S. A. 1981. Manganese nodules and other ferromanganese deposits from the Indian Ocean. *Journal of Geological Society, London*, **138**, 527–539.
- & TOOMS, J. S. 1969. The geochemistry of Mn nodules and associated pelagic deposits from the Pacific and Indian Oceans. *Deep Sea Research*, **16**, 335–359.
- , MEADOWS, P. & TIFFIN, D. 1987. *A study of manganese nodules, crusts and deep-sea sediments in the northern Cook Islands, Central Line Islands and adjacent high seas. Cruise report of the Crossgrain Expedition Leg 3*. Scripps Institute of Oceanography, Unpublished Cruise Report.
- , HODKINSON, R. A., MILLER, S. & HONG, L. 1989. *Manganese nodules and cobalt-rich crusts in the EEZ's of the Cook Islands, Kiribati and Tuvalu*. CCOP/SOPAC Technical Report **88**, Suva, Fiji.
- , GALACZ, A., MINDSZENTY, A., MOORBY, S. A. & POLGARI, M. 1991a. Tethyan ferromanganese oxide deposits from Jurassic rocks in Hungary. *Journal of the Geological Society, London*, **148**, 655–668.
- , HODKINSON, R. A. & MILLER, S. 1991b. Manganese nodules in the EEZ's of island countries in the southwestern equatorial Pacific. *Marine Geology*, **98**, 425–435.
- , —, — & HONG, L. 1991c. An evaluation of manganese nodules and cobalt-rich crusts in South Pacific Exclusive Economic Zones, I. Nodules and crusts in and adjacent to the EEZ of the Cook Islands (the Aitutaki–Jarvis Transect). *Marine Mining*, **109**, 1–28.
- DYMOND, J., LYLE, M., FINNEY, B., PIPER, D. Z., MURPHY, K., CONNARD, R. & PISIASIS, N. 1984. Ferromanganese nodules from MANOP sites H, S & R: Control of mineralogical and chemical composition by multiple accretionary processes. *Geochimica et Cosmochimica Acta*, **48**, 931–949.

- EXON, N. F. 1983. Manganese nodule deposits in the Central Pacific Ocean and their variation with latitude. *Marine Mining*, **4**, 79–107.
- FLEMMING, R. H. 1957. General features of the ocean. In: HEDGPATH, J. W. (ed.) *Treatise on Marine Ecology and Palaeoecology*. Geological Society of America Memoirs, **67**, 87–107.
- FRAZER, J. & WILSON, L. L. 1979. *Manganese nodule deposits in the Indian Ocean*. Scripps Institution of Oceanography Reference Series **79-18**.
- GLASBY, G.P. 1981. Manganese nodule studies in the SW Pacific. *South Pacific Marine Geological Notes*, **2**, 37–46.
- , THUSSEN, T., PLUGER, W. L., FRIEDRICH, G., MANGINI, A., STOFFERS, P., DOMINIK, J., FRENZEL, G., ANDREWS, J. E. & ROONWAL, G. S. 1983. *Manganese nodule distribution, mineralogy and geochemistry and relation to sediment type in the Aitutaki Passage, SW Pacific*. Hawaii Institute of Geophysics Reports, **HIG-83-1**.
- , EXON, N. F. & MEYLAN, M. A. 1986. Manganese nodules in the SW Pacific. In: CRONAN, D. S. (ed.) *Sedimentation and Mineral Deposits in the Southwest Pacific Ocean*. Academic Press, London, 237–262.
- HALBACH, P. & PUTEANUS, D. 1988. Geochemical trends of different genetic types of nodules and crusts. In: HALBACH, P., FRIEDRICH, G. & VON STACKELBERG, U. (eds) *The Manganese Nodule Belt of the Pacific*. Enke, Stuttgart, 61–69.
- , MARCHIG, V. & SCHERHAG, C. 1980. Regional variations in Mn, Ni, Cu and Co of ferromanganese nodules from a basin in the southeast Pacific. *Marine Geology*, **38**, M1–M9.
- , HEBISCH, V. & SCHERHAG, C. 1981. Geochemical variations of ferromanganese nodules and crusts from different provinces of the Pacific Ocean and their genetic control. *Chemical Geology*, **34**, 3–17.
- HEIN, J. R., KOSCHINSKY, A., HALBACH, P., MANHEIM, F. T., BAU, M., KANG, J. K. & LUBICK, N. 1997. Iron and manganese oxide mineralization in the Pacific. *This volume*.
- HOWARTH, R. J., CRONAN, D. S. & GLASBY, G. P. 1977. Non-linear mapping of regional geochemical variability of manganese nodules in the Pacific Ocean. *Transactions of the Institution of Mining and Metallurgy (Ser B)*, **86**, 87–90.
- KOBLENZ-MISHKE, O. I., VOLKOVINSKY, V. V. & KABANOVA, J. G. 1970. Plankton primary production in the World Ocean. In: WOOSTER, W. (ed.) *Scientific Exploration of the South Pacific*. National Academy of Science, Washington DC, 183–193.
- LONSDALE, P. & SMITH, S. M. 1980. "Lower insular rise hills" shaped by the bottom boundary current in the mid-Pacific. *Marine Geology*, **34**, M19–M25.
- MENARD, H. W. 1964. *The Marine Geology of the Pacific*. McGraw Hill, New York.
- MERO, J. L. 1965. *The Mineral Resources of the Sea*. Elsevier, Amsterdam.
- MILLER, S. 1992. *Geochemistry of pelagic sediments associated with manganese nodules in the Central Pacific*. PLD thesis, University of London.
- & CRONAN, D. S. 1994. Element supply to surface sediments and interrelationships with nodules along the Aitutaki–Jarvis Transect, South Pacific. *Journal of the Geological Society, London*, **151**, 403–412.
- MURRAY, J. W. & RENARD, A. F. 1891. *Deep Sea Deposits*. Reports of the Scientific Results of HMS Challenger 1873–76. HMSO, London.
- NAKAO, S. & MIZUNO, A. 1982. Regional sedimentologic data: the Central Pacific Wake–Tahiti Transect, GH 80-1 Cruise. In: *The Wake–Tahiti Transect in the Central Pacific*. Geological Survey of Japan, Cruise Reports, **18**, 95–123.
- PAUTOT, G. & MELGUEN, M. 1979. Influence of deep water circulation and seafloor morphology on the abundance and grade of central South Pacific manganese nodules. In: BISCHOFF, J. L. & PIPER, D. Z. (eds) *Marine geology and oceanography of the pacific manganese nodule province*. Plenum Press, New York, 621–649.
- PIPER, D. Z. & WILLIAMSON, M. E. 1977. Composition of Pacific Ocean ferromanganese nodules. *Marine Geology*, **23**, 285–303.
- PRICE, N. B. & CALVERT, S. E. 1970. Compositional variation in Pacific Ocean ferromanganese nodules and its relationship to sediment accumulation rates. *Marine Geology*, **9**, 145–171.
- ROY, S., DASGUPTA, S., MUKHOPADHYAY, S. & FUKUOKA, M. 1990. Atypical ferromanganese nodules from pelagic areas of the Central Indian Basin, equatorial Indian Ocean. *Marine Geology*, **92**, 269–284.
- SUDHAKAR, M. 1989. Ore grade manganese nodules from the Central Indian Basin. *Marine Mining*, **8**, 201–214.
- TAKEMATSU, N., SAYO, Y. & OKABE, S. 1989. Factors controlling the chemical composition of marine manganese nodules and crusts: a review and synthesis. *Marine Chemistry*, **26**, 41–56.
- USUI, A. 1984. Regional variation of manganese nodule facies on the Wake–Tahiti Transect: morphological, chemical and mineralogical study. *Marine Geology*, **54**, 27–51.

Growth history of manganese nodules and crusts of the Peru Basin

U. VON STACKELBERG

*Bundesanstalt für Geowissenschaften und Rohstoffe, Stilleweg 2,
30655 Hannover, Germany*

Abstract: In the nodule field of the Peru Basin, situated south of the zone of high bioproductivity, a relatively high flux of biogenic matter explains a distinct redox boundary at about 10 cm depth separating very soft oxic surface sediments from stiffer suboxic sediments. Maximum abundance (50 kg m^{-2}) of diagenetic nodules is found near the calcite compensation depth (CCD), currently at 4250 m. There, the accretion rate of nodules is much higher (100 mm Ma^{-1}) than on ridges (5 mm Ma^{-1}). Highest accretion rates are found at the bottom of large nodules that repeatedly sink to a level immediately above the redox boundary. There, distinct diagenetic growth conditions prevail and layers of dense laminated Mn oxide of very pure todorokite are formed. The layering of nodules is mainly the result of organisms moving nodules within the oxic surface sediment from diagenetic to hydrogenetic environments. The frequency of such movements is much higher than that of climatic changes. Two types of nodule burial occur in the Peru Basin. Large nodules are less easily moved by organisms and become buried. Consequently, buried nodules generally are larger than surface nodules. This type of burial predominates in basins. At ridges where smaller nodules prevail, burial is mainly controlled by statistical selection where some nodules are not moved up by organisms.

During RV *Sonne* cruise SO-04 in 1978, manganese nodules of unusual size were found in the Peru Basin (Fig. 1) (Thijssen *et al.* 1981). Due to the economic interest in manganese nodules at that time, another cruise with RV *Sonne* (SO-11) followed in 1979 that led to the discovery of a huge nodule field. Studies following this cruise resulted in concepts of sedimentation and nodule growth history in the Peru Basin (Halbach *et al.* 1980; Stoffers *et al.* 1984; Thijssen *et al.* 1985; Mangini *et al.* 1987). Highest nodule coverage was found in water depths between 4000 and 4200 m near the calcite compensation depth (CCD).

Large nodules with a maximum size of 24 cm accreted with rates up to 190 mm/Ma^{-1} in the outer part and 30 mm Ma^{-1} in the inner part based on U–Th isotopic dating (Reyss *et al.* 1982, 1985; Lemaitre *et al.* 1984; Lemaitre 1987). The high accretion rates of nodules are assumed to result from strong diagenetic remobilization of metals, mainly of Mn within the sediment. Therefore, compared to the Clarion–Clipperton Zone (CCZ) nodules, those of the Peru Basin are rich in Mn but poor in Fe, Cu, and Ni (Halbach *et al.* 1980; Marchig & Reyss 1984).

The thickness of Quaternary sediment is highly variable, probably as a consequence of erosional processes (Stoffers *et al.* 1982, 1984). The uppermost about 8 cm thick, very soft surface sediment, called the semi-liquid layer is assumed to play an important role in the growth and transport of the nodules (Halbach *et al.* 1981).

During RV *Sonne* cruise SO-61 in 1989, a long-term, large-scale disturbance–recolonization experiment (DISCOL) was carried out at the NE margin of the Peru Basin nodule field (Fig. 1) (Thiel & Schriever 1990). A plow harrow of 8 m width was towed across the seafloor of the DISCOL area in a spoke-like pattern and the impact on the benthic faunal communities was investigated.

During the RV *Sonne* cruise SO-79 (18 April–9 June 1992), we hydroacoustically surveyed two areas each $70 \times 55 \text{ km}$ in size in the central part of the nodule field immediately south of the highly productive surface waters of the eastern equatorial Pacific Ocean (Figs 2 and 3). We investigated the bathymetry, seismic character of sediments, and seafloor reflectivity using Hydro-sweep, Parasound, and Side-scan sonar, respectively. Furthermore, we carried out geological, geochemical, biological, and water chemical studies. This interdisciplinary work aimed to assess the potential impact of nodule mining on the deep-sea ecosystem of the Peru Basin.

In this paper the results of geological–geochemical studies of ferro-manganese nodules and crusts recovered during cruise SO-79 are presented.

Sampling and analytical techniques

During cruise SO-79, manganese nodules were collected at 82 locations and crusts at 12 locations (Figs 2 and 3). Samples were recovered using the following

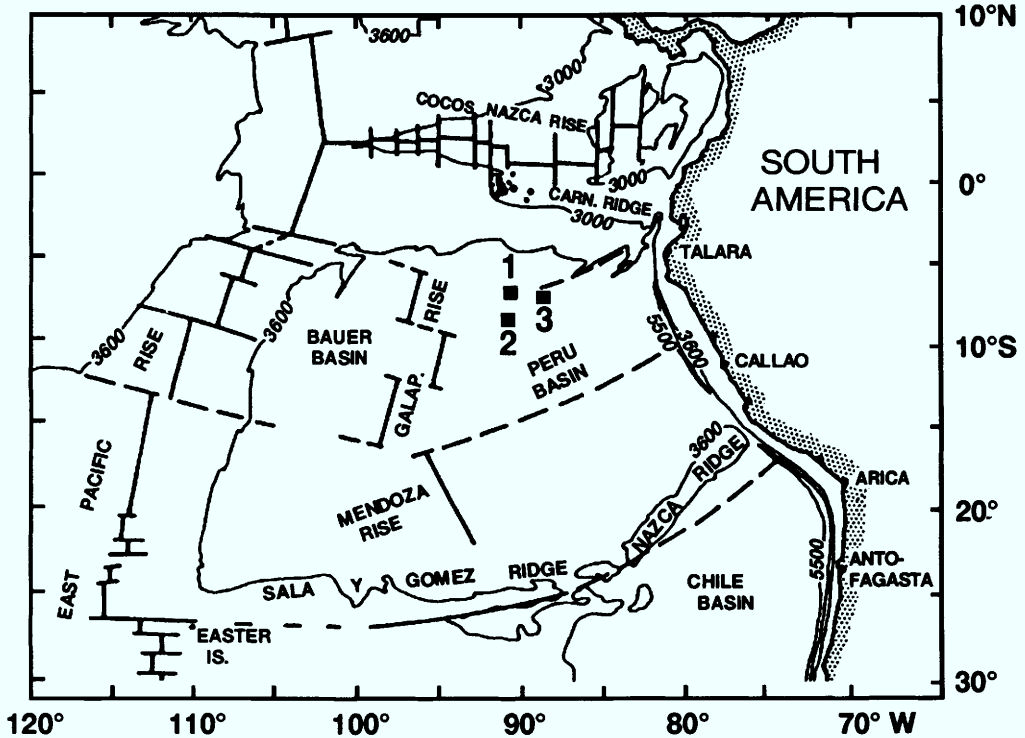


Fig. 1. Location of survey areas in the Peru Basin. 1 and 2 are survey areas A1 and A2 of RV *Sonne*, respectively cruise SO-79. 3 is DISCOL area.

tools: box grab sampler (KG), free-fall grab sampler (BG), TV-grab sampler (GA), dredge (KD), multi corer (MC), piston corer (KL), gravity corer (SL), long box corer (KA), free-fall corer (BL) and water sampler (WS).

The photosled (FS) was deployed 8 times with a recovery of 7212 colour photographs.

The upper surface of all nodules from box grabs that appeared to be in an undisturbed position was marked immediately after recovery. We also marked nodules from free-fall grabs if the bottom side was recognizable via adhering sediment.

All nodules were weighed dried. To convert the weight and number of nodules from box grabs with a surface recovery of $50 \times 50 \text{ cm} = 0.25 \text{ m}^2$ to data of abundance (kg m^{-2}), and number ($n \text{ m}^{-2}$), respectively, we used a conversion factor of 4.0. The conversion factor for free-fall grabs was 7.52.

A total of 2052 manganese nodules were characterized following a classification scheme of Moritani *et al.* (1977), Usui (1982), and von Stackelberg & Marchig (1987). A total of 365 nodules were impregnated with 'Caparol' (a dispersion paint binder) and cut vertically with respect to the position on the seafloor. The polished sections of both halves were studied under the microscope and the internal growth structure was described, outlined, and photographed. Individual layers of special interest for geochemical and

mineralogical analysis were sampled under the microscope with a needle drill.

The mineralogical composition of individual growth layers of nodules and crusts was determined by X-ray diffraction analysis. XRF and ICP-MS methods were used to analyse the chemical composition including REE concentrations. Because of high concentration of Ba in diagenetic nodules values for Eu were not plotted on REE diagrams.

Distribution on the seafloor

In study areas A1 and A2 we collected surface and buried ferro-manganese nodules at 82 locations (Figs 2 and 3). Nodules occur in basins, on seamounts and ridges in water depths between 3726 and 4404 m. Only on the upper part of the large seamount in A1 were no nodules found.

Manganese crusts were found on the large seamount of A1 at water depths between 1987 and 3954 m (12 KG, 21 KD, 22 KD, 35 SL, 65 GA, 68 SL). In A2 we recovered crusts from abyssal hills and ridges at water depths between 3621 and 4062 m (143 GA, 145 KD, 151 KG, 157 GA, 158 KD, 177 KD).

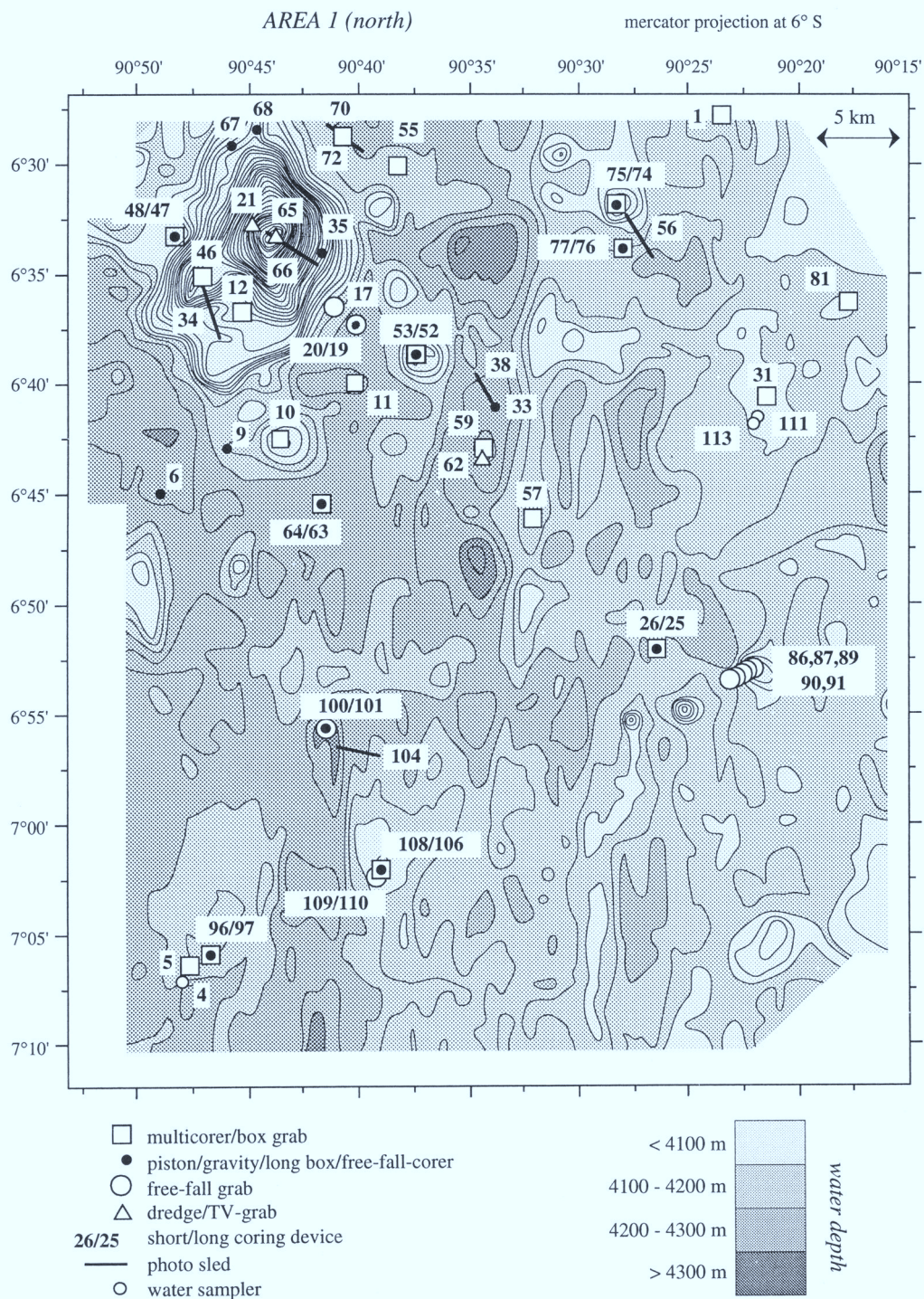


Fig. 2. Survey area A1. Bathymetry and location of sampling stations and photo sled tracks.

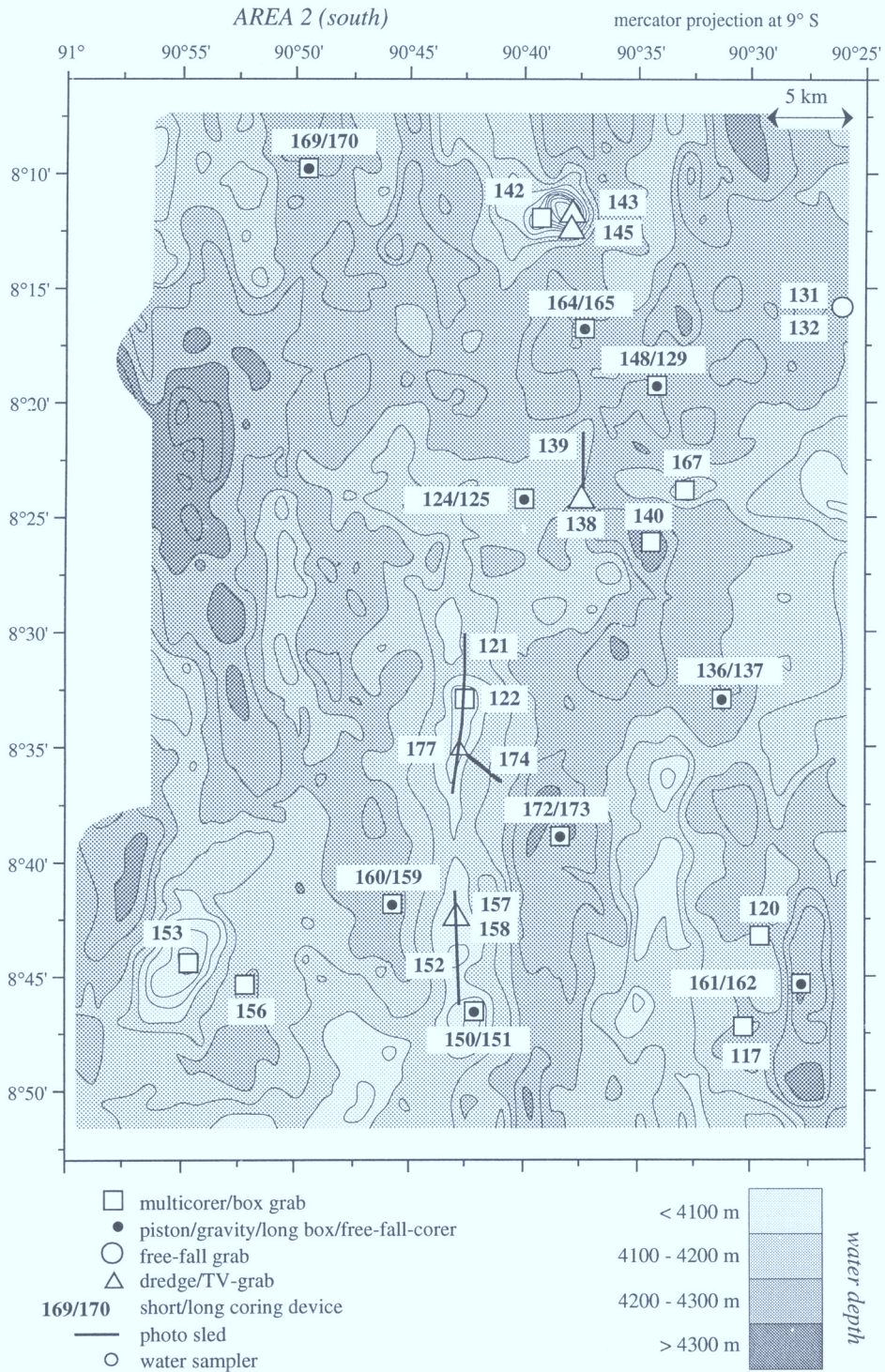


Fig. 3. Survey area A2. Bathymetry and location of sampling stations and photo sled tracks.

A side-scan sonar survey revealed the small-scale variability of Fe–Mn nodule coverage with elongated patches of low reflectivity that is most obvious on ridges and less pronounced in basins (Wiedicke *et al.* in press). The patchiness is assumed to reflect mainly variations in erosional

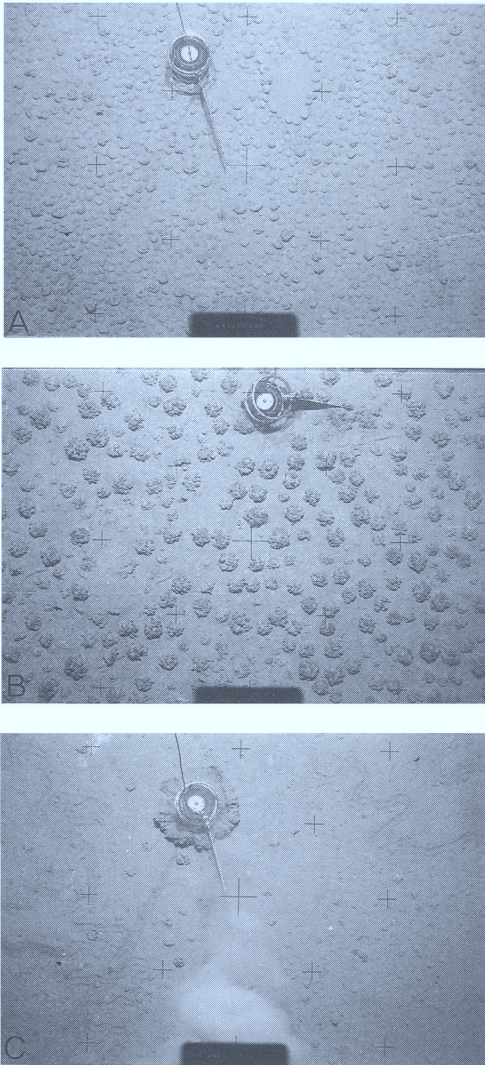


Fig. 4. (a) Dense coverage of relatively small nodules (<5 cm in diameter). Bioturbation has formed a ring of nodules. Outer ring of compass = 25 cm. 121 FS, water depth = 4060 m. (b) Less dense coverage of large nodules (about 10 cm in diameter). Traces of burrowing. 152 FS, water depth = 4055 m. (c) Sediment surface with few partly buried nodules and meandering plow marks and traces of biota. 121 FS, water depth = 4060 m.

Table 1. Number and abundance of manganese nodules from box grabs ($50 \times 50 \times 50$ cm)

Area	Number ($n\ m^{-2}$)	Abundance ($kg\ m^{-2}$)
A1	max. 392 (3961 m, seamount) av. 136	max. 50 (4257 m, basin) av. 23
A2	max. 684 (3995 m, seamount) av. 250	max. 36 (4326 m, basin) av. 18

bottom current activity. This is supported by the ground check of photosled tracks.

Colour photographs of the seafloor have indicated a great variability of nodule size and coverage. We observed areas of very dense coverage of relatively small nodules (<5 cm in diameter), areas of less dense coverage of larger nodules (5–21 cm) (Figs 4a and b), and areas free of nodules. Compared to the Clarion–Clipperton Zone (CCZ) we found a relatively large number of benthic organisms associated with meandering plow marks and burrows as well as rings and double rows of nodules (Fig. 4c).

The number of nodules per m^2 calculated from box grab recovery is greatest on the top of abyssal hills (Tables 1 and 2). This is true for both survey areas with A2 showing higher values than A1. The nodule abundance ($kg\ m^{-2}$), however, is higher in basins. The comparison of areas A1 and A2 shows maximum values for A1. Therefore, compared to A2, A1 is characterized in general by smaller numbers of nodules, but greater abundance and therefore greater average size.

Eighty-four nodules buried in the sediment deeper than 20 cm were found. Maximum depth was 10.21 m. 75% of the buried nodules occur in water depths deeper than 4200 m.

Nuclei

Nodule growth always starts at a hard nucleus. A total of 365 polished sections revealed 418 nuclei. This means that some nodules contain more than one nucleus. We distinguished the following types of nuclei: sediment (S), Mn-impregnated sediment (SI), organic remains (O), volcanic material, including palagonite (B), mineral grains (M), hydrothermal material (Y), and nodule fragments (N). We did not observe pumice nuclei which are frequent in the CCZ (von Stackelberg 1987).

The numerical distribution of nucleus types of a total of 418 nuclei is as follows: S=17, SI=89, O=15, B=46, M=12, Y=23, N=216. This indicates the distinct predomi-

nance of N-nuclei (52%) followed by S+SI-nuclei (25%).

Hydrothermal material (Y) includes Mn oxide with a submetallic luster, Fe oxyhydroxide, Fe

Table 2. Characteristics of nodule assemblages from box grabs (KG) and free-fall grabs (BG)

Area	Station	Water depth m	Number $n\ m^{-2}$	Abundance $kg\ m^{-2}$	Shape type + number	Nucleus type + number	Histogram type	
A1	59 KG	4339	104	7.60	IS 7, I 7	N 7, SI 1	A	
	63 KG	4257	40	49.60	ID 4, IE 3	N 2, O 1	A	
	25 KG	4170	48	17.20	IE 4, IS 3	N 3	A	
	97 KG	4148	64	44.20	I 6, ID 3	N 1	A	
	01 KG	4119	84	32.80	IS 8, IE 6	N 13	A	
	55 KG	4119	48	—	ID 5, IE 3	N 7, SI 2	A	
	81 KG	4067	144	13.40	IE 19, I 11	N 6	A/B	
	106 KG	4025	172	13.40	IE 28, E 6	N 3	A/B	
	10 KG	3961	392	19.20	IE 65, E 2 18	N 26, B 3	B	
	74 KG	3878	260	9.60	E 22, E 2 17	N 19, SI 14	B	
	12 KG	3698	0	—	—	—	—	
	46 KG	3485	0	—	—	—	—	
	101 BG	4313	165	6.76	IS 9, I 8	N 1	A	
	19 BG	4202	218	12.63	I 14, IS 8	S 1	A/B	
	91 BG	4143	489	16.90	IE 22, I 20	N 10, B 3	B	
	90 BG	4119	985	15.40	I 36, E 32	N 9, SI 7	B	
	17 BG	4099	241	11.28	E 11, I 9	S 5, B 1	B	
	89 BG	4051	601	12.05	C 2 39, I 12	SI 5, N 1	B	
	110 BG	4033	188	9.80	E 11, IE 6	SI 3	A/B	
	109 BG	4032	30	0.75	IE 3	—	—	
	87 BG	3961	45	1.50	E 3	SI 7, B 2	—	
	44 BG	3937	910	10.15	I 59, P 34	N 6, B 5	B	
	42 BG	3896	203	0.90	I 14, P 8	B 7, N 2	B	
	86 BG	3896	225	3.76	E 18, E 2 5	SI 6, N 5	A/B	
	40 BG	3833	135	1.50	I 9, P 3	B 5, N 3	A/B	
	A2	140 KG	4326	16	36.40	IE 2, ID 1, IS 1	N 1	A
		173 KG	4273	32	9.60	IS 6	N 1, S 1	A
		165 KG	4250	84	20.60	IE 6, D 4	N 2	A
		159 KG	4249	328	12.40	E 47, IE 19	N 4	B
		170 KG	4239	140	13.00	E 11, I 8	N 3, O 1	B
129 KG		4225	244	25.60	E 29, I 13	N 3	B	
117 KG		4218	288	7.60	E 31, I 17	N 6	B	
156 KG		4210	184	15.80	IE 20, E 18	N 5	B	
167 KG		4102	208	19.00	E 30, E 2 9	Y 24, N 4	A/B	
122 KG		4077	204	22.60	E 19, E 2 7	SI 4, N 2	A/B	
142 KG		3995	684	23.20	I 50, E 2 46	N 7, B 7	B	
151 KG		3953	0	—	—	—	—	
153 KG		3902	584	12.00	I 49, IE 37	SI 7, B 2	B	
132 BG		4220	90	26.69	E 3, IE 2	SI 2, N 1	A	
131 BG		4219	53	24.44	IE 4	—	—	

The nodule number ($n\ m^{-2}$) was calculated by conversion of nodule number from box grabs with a surface recovery of $0.25\ m^2$ and from free-fall grabs with a surface recovery of $0.133\ m^2$.

The number of nodules of different shape type and of nucleus type refers to the original recovery of box grabs and free-fall grabs, respectively. Only most frequent types of shapes and nuclei are shown.

Types of nodule shapes: S, spherical; D, discoidal; ID, irregularly discoidal; E, ellipsoidal; IE, irregularly ellipsoidal; E2, half-ellipsoidal; P, polylobate; C, cylindrical; C2, half-cylindrical; T, tabular, I, irregular.

Types of nuclei: N, nodule fragment; S, sediment; SI, Mn-impregnated sediment; O, organic remains; B, volcanic material; Y, hydrothermal material.

Types of histograms: A, basins; B, topographic highs; A/B, intermediate.

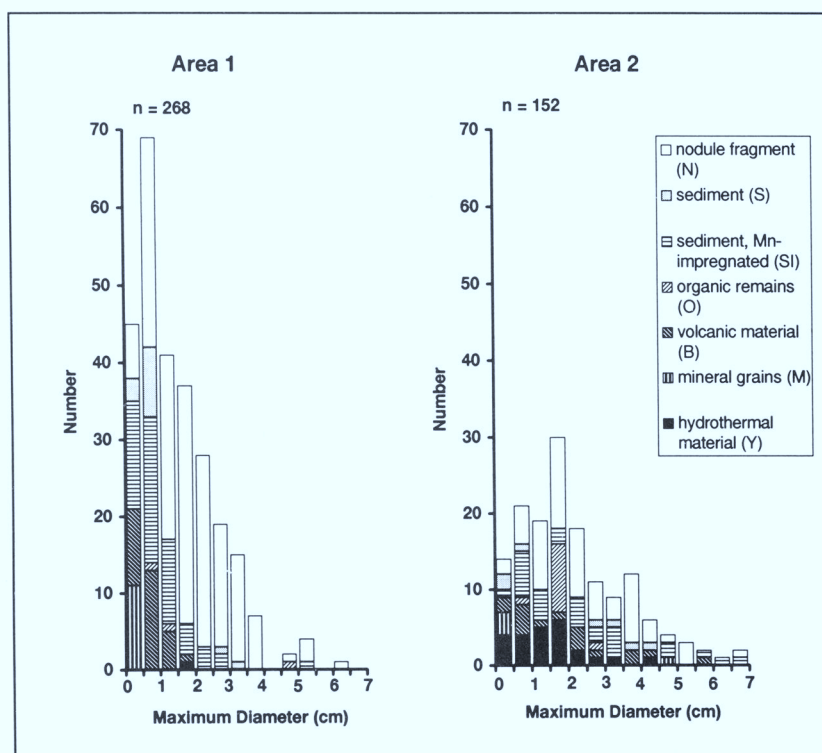


Fig. 5. Distribution of type and size of nuclei of nodules in areas A1 and A2.

silicate, goethite, chalcedony, and quartz (Marchig *et al.* in press).

The size of nuclei (maximum diameter) ranges from 1 mm to 7.0 cm with a maximum occurrence between 0.5 and 1.0 cm for A1 and between 1.5 and 2.0 cm for A2 (Fig. 5).

N, S and O-nuclei occur in both areas and each bathymetric domain with a predominance of N-nuclei in basins (Fig. 6). B, M, and Y-nuclei are mainly observed in shallower water on seamounts and ridges. A few B-nuclei may be found also in narrow basins (e.g. 160 KA, 162 MC), which indicates reworking. Y-nuclei occur mainly in area A2, only one specimen was found in area A1.

Surface features

Shape

The nodule shapes range from regular types such as spherical (S) and discoidal (D) to irregular types, such as irregular (I) and tabular (T) (Fig. 7). Ellipsoidal (E) nodules represent the most frequent type. A distinct number of irregularly

shaped nodules could be identified as halves of ellipsoidal nodules (E2), fragmented perpendicularly to the longest axis. Cylindrically shaped nodules (C) are due to Mn-encrustation of indurated burrow tubes. Repeatedly these tubes were fragmented lengthwise forming half-cylinders (C2). Shape types with a prefixed I (e.g. ID, IE) indicate a more or less distinct irregularity.

S and D-type nodules predominate in water depths >4200 m at least in area A1. E, EI, and I-type nodules are found in both areas and each bathymetric domain. E2, P, C, and T-type nodules mainly occur at or near topographic highs.

D and S-type nodules make up to 32% of the buried nodules, but only 12% of surface nodules (Figs 7 and 8).

Surface texture

The most conspicuous feature of the Peru Basin nodules is their cauliflower-shaped surface texture (cf), which is mainly observed on large nodules with a diameter >6 cm (Fig. 9a). The cusps with diameters between 0.5 and 6.5 cm

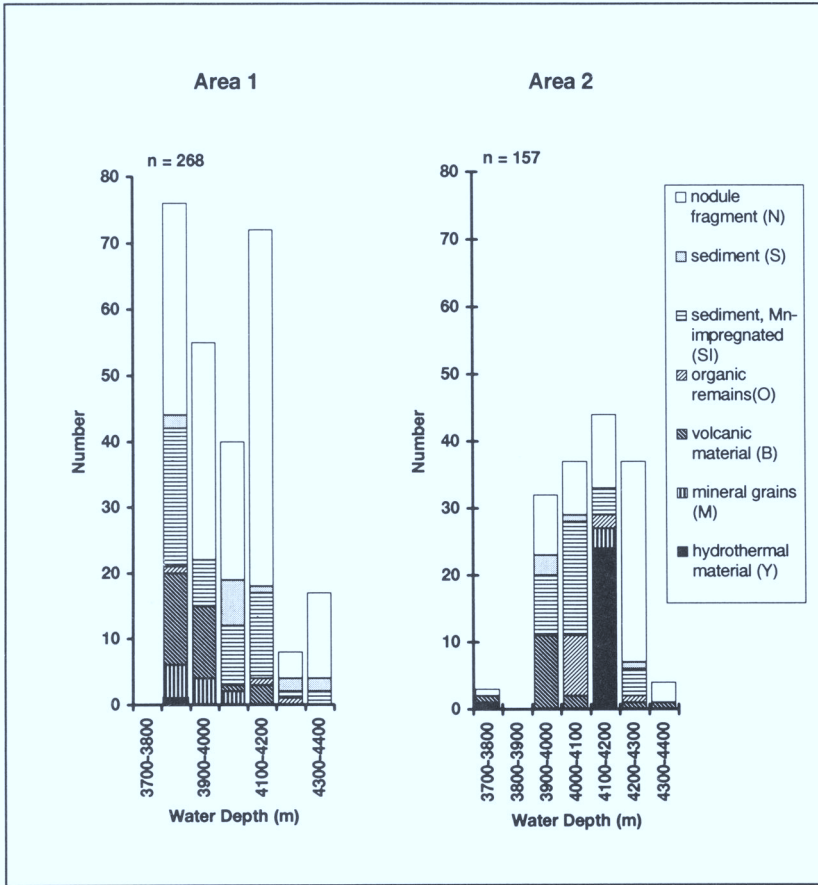


Fig. 6. Distribution of nodule nuclei type versus water depth in areas A1 and A2.

may have a rough or smooth surface. Most frequent is the rough surface texture of r-type (Table 3). In contrast to CCZ nodules, the bottom surface of Peru Basin nodules is frequently smooth. The number of nodules with a rough top and smooth bottom (r/s-type nodules) in area A1 is distinctly greater than in A2, especially if we assume that part of the nodules where the top was not distinguished (r+s-type) are of r/s-type. Nodules with a smooth top and rough bottom (s/r-type), however, predominate in A2. This indicates an approach to CCZ growth conditions in A2. The s-type nodules which are smooth all around mainly occur on or near seamounts or ridges of both areas.

Sessile organisms, mainly foraminifera, are attached to the surface of all nodules. Abundance and types of organisms are different on the top and bottom of the nodules.

Although the shape of nodules is identical for surface and buried nodules, the surface textures

are different. Buried nodules rarely show s-type, but predominantly r and r·s-type surface. Buried nodules are always brittle due to incipient dissolution. Dissolution apparently reduces the stability of the growth structures that finally may result in a soft black powder.

Internal growth structures

Similar to other nodules, Peru Basin nodules are characterized by layered growth. Not all types (a-g) that were described from the CCZ (von Stackelberg & Marchig 1987) were found in the Peru Basin, however, one distinct type (h) occurs. Altogether five different types of internal structure can be identified:

- 1 laminated to columnar = b;
- 2 dendritic = d;
- 3 massive, non-directional = e;
- 4 dense, pillar = f;
- 5 dense, laminated = h.

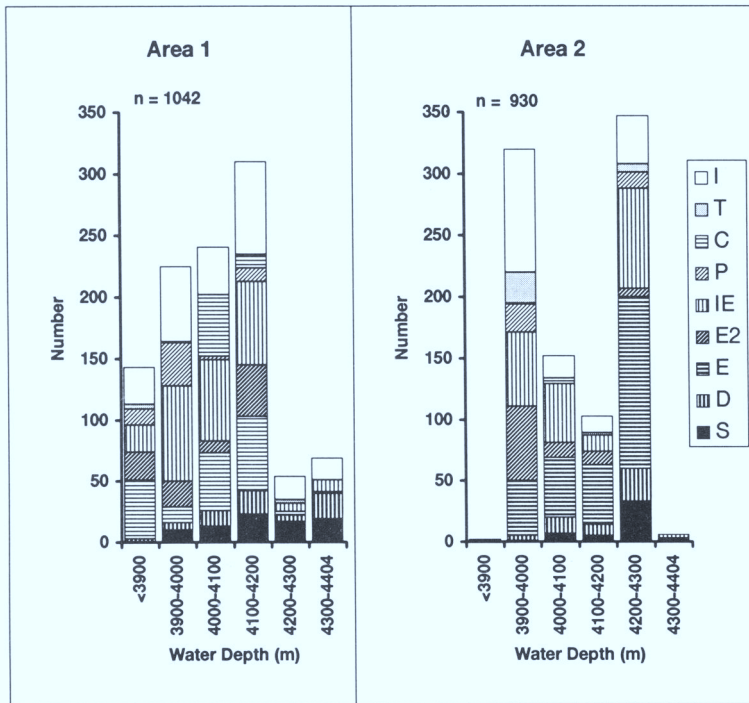


Fig. 7. Distribution of nodule shape versus water depth in areas A1 and A2. S, spherical; D, discoidal; E, ellipsoidal; E2, half ellipsoidal; IE, irregularly ellipsoidal; P, polylobate; C, cylindrical; T, tabular; I, irregular.

Dense dark-brown b-type structures are forming at the top of nodules and crusts and represent hydrogenetic growth within the near-bottom water. d-type growth occurs on the bottom of nodules where diagenetic production

of Mn oxide takes place within the sediment. A narrow sequence of b and d-layers normally characterizes small nodules and the inner part of large nodules. e-type growth containing many yellow sediment particles only

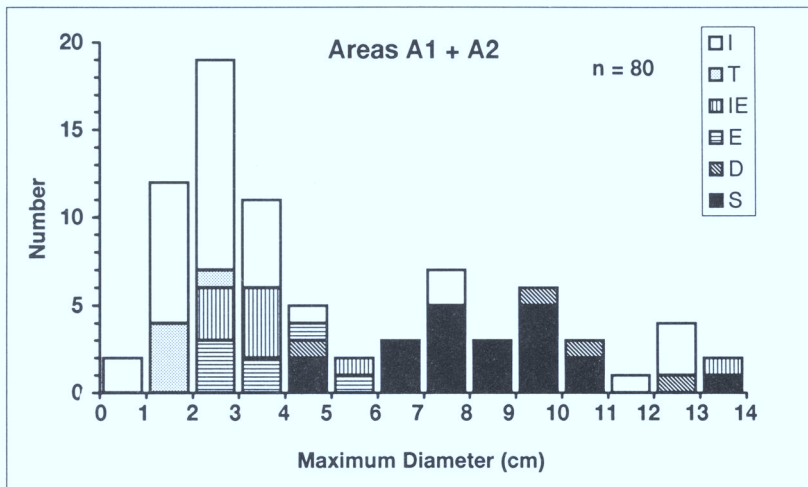


Fig. 8. Distribution of shape versus size of nodules buried >20 cm in areas A1 plus A2. For explanation of symbols see Fig. 7 caption.

occurs in crusts, which may form nuclei of nodules. f-type growth is only found in crusts and represents extremely pure hydrogenetic growth.

Pale-grey h-growth with submetallic luster alternates with grey d-type growth on the bottom side mainly of large nodules. h-layers predominantly occur in the outer part of nodules (Fig. 9b). The larger the nodule the thicker and more frequent are the h-layers, which are up to 8 mm thick. The transition from d to h-growth is gradational, while the transition from h to d-growth is sharp where d-growth starts with a thin layer of dark-grey laminated Mn oxide similar to b-growth. At the outer surface of nodules this sharp border is responsible for the smooth bottom surface of r/s-type nodules. The smooth s-type may cover up to 70% of the basal surface of the nodule. However, only a very restricted area at the lowermost part of some nodules is smooth. A lateral wedging of the h-layers is seen in nodule sections. In general, h-layers are thicker in area A1 than in area A2 nodules. h-layers are characterized by many inclusions of siliceous microfossils, such as diatoms and radiolarians (Fig. 10a and b). Mostly the siliceous skeletons were dissolved and only imprints and casts are preserved. Sometimes the siliceous material is replaced by Mn oxide. Dense, laminated h-growth is a distinct growth type of Peru Basin nodules, which had been described by Halbach *et al.* (1981) and Thijssen *et al.* (1981) and which may be compared to the 'massive zone' described by Sorem & Fewkes (1979) for nodules from other areas.

Nodules <7 cm in diameter show a more or less symmetric distribution of growth layers; larger ones, however, often reveal asymmetric growth (Fig. 9b). In A1, out of 15 nodules with a maximum diameter >9 cm, seven had grown asymmetrically and eight symmetrically. In A2 the ratio is 6/16 for asymmetrically to symmetrically grown nodules of the same size class. Seven of the 37 large nodules just mentioned are buried nodules. Six of the seven buried nodules show asymmetric growth.

Buried nodules reveal the same internal structures as surface nodules even if they are less compact. However, the d and h- structures even of the inner part of large buried nodules,

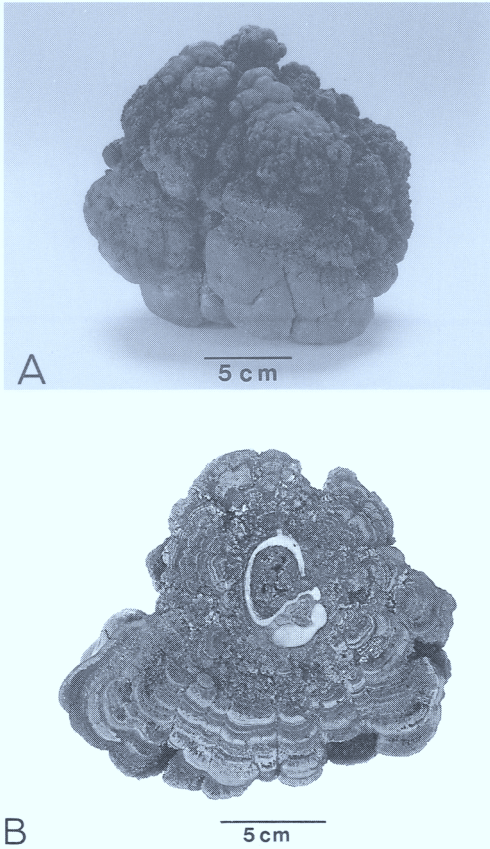


Fig. 9. (a) Large manganese nodule with cauliflower-shaped surface (cf) and smooth surface texture (s) on the bottom and rough surface texture (r) on top. 25 KG, water depth 4170 m. (b) Polished section of a large manganese nodule with a nucleus of a cetacean earstone and pale-grey dense laminated h-type growth layers in the outer part. Grey dendritic d-type growth predominates in the inner part. 63 KG, water depth 4257 m.

Table 3. Surface texture of manganese nodules (incl. buried nodules)

Area	Top/bottom				Both sides			Top not identified		Total no.
	r/s	s/r	r/r.s	r	r.s	s	r + r.s	r + s		
A1	40	26	6	732	72	154	4	41	1075	
A2	4	142	10	507	209	30	60	12	974	
A1 + A2	44	168	16	1239	281	184	64	53	2049	

r, rough; s, smooth; r.s, intermediate texture between rough and smooth.

are dark-brown, whereas they are grey to light-grey in surface nodules. Dissolution effects obliterated the submetallic luster of the h-layer.

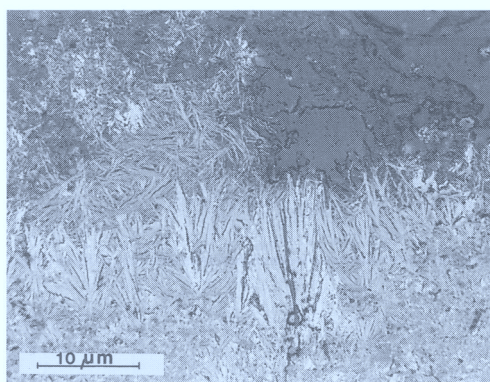
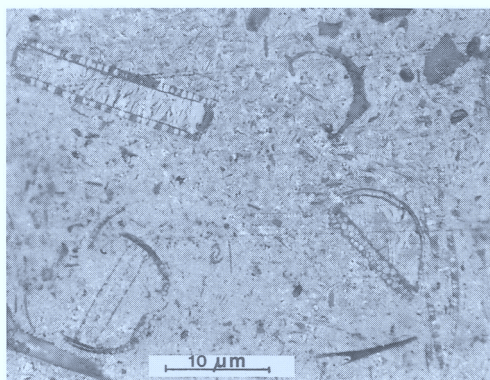
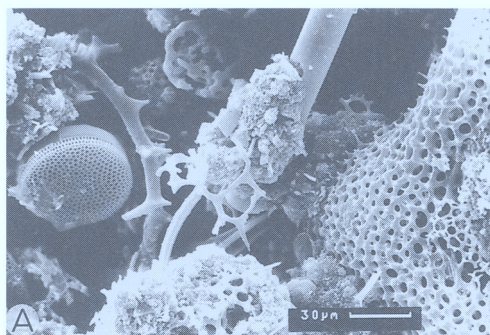


Fig. 10. (a) SEM photograph of the outer surface of a h-growth layer with inclusions of diatoms and radiolarians. 25 KG, water depth 4170 m. (b) Photograph of polished section of a h-type growth layer with inclusions of diatoms. The frustules are filled with coarse-grained Mn oxide. 62-KD, water depth 4320 m. (c) Photograph of polished section of a h-type growth layer with up to 15 μm long torokite crystals growing into pores of the Mn oxide. 62 KD, water depth 4320 m.

Size distribution

The Peru Basin is characterized by the occurrence of extremely large nodules with maximum diameters up to 21 cm. Nodules smaller than 1.5 cm are scarce. The histogram for all surface nodules in area A1 shows a distinct maximum at 3.5–4.0 cm and a indistinct rarity of nodules in the size class 7.0–7.5 cm (Fig. 11). In A2 the maximum is at 2.5–3.0 cm.

A total of 34 histograms were plotted for box core (KG) and free-fall grab (BG) samples (Table 2). We observed three types of histograms: Type A which is widely ranging in diameter and has a low number (n) of nodules occurs in wide basins (Fig. 12a). Type B which has a distinct maximum in diameter between 2 and 3 cm and a low number of nodules, is typical of slopes, tops of seamounts and ridges, and narrow basins (Fig. 12b). Type A/B is an intermediate type of pattern found on wide plateaus and ridges and on seamounts (Fig. 12c). There is a good correlation between histogram types and sea-floor morphology which does not strictly depend on bathymetry.

B and A/B-type histograms are characterized by the predominance of E, E2, IE, and I-shaped nodules and by the scarceness of S and D-nodules; S and D-nodules are typical of A-histograms.

The histogram for all buried nodules in areas A1 and A2 shows a maximum for the size class 2–3 cm and a minimum at 5–6 cm (Fig. 8). 36% of the buried nodules are >6 cm (max. diameter), while only 18% of the surface nodules exceed that size. In general, buried nodules are larger than surface nodules (Fig. 13). This has already been suggested by Stoffers *et al.* (1982) and Thijssen *et al.* (1985). In the size class >6 cm S and D-nodules prevail, while in the size class <6 cm I, E, and T-nodules predominate.

Chemical and mineralogical composition

A number of layers of different growth structures were prepared and analysed in order to study their chemical and mineralogical composition (Table 4). We made analyses for well-defined growth layers of b, d, e, f, and h-type and for a few layers of mixed growth type, in some samples from different depths within the nodule or crust. We prepared samples from 10-3, 10-4, and 52-1 nodule nuclei, and from 108-1 crust of manganese impregnated sediment in a sediment core at a depth of 485 cm. Manganese crusts 22-2, 143-8, 145-1 to 3, 177-1 to 2 were dredged from the seafloor surface and analysed.

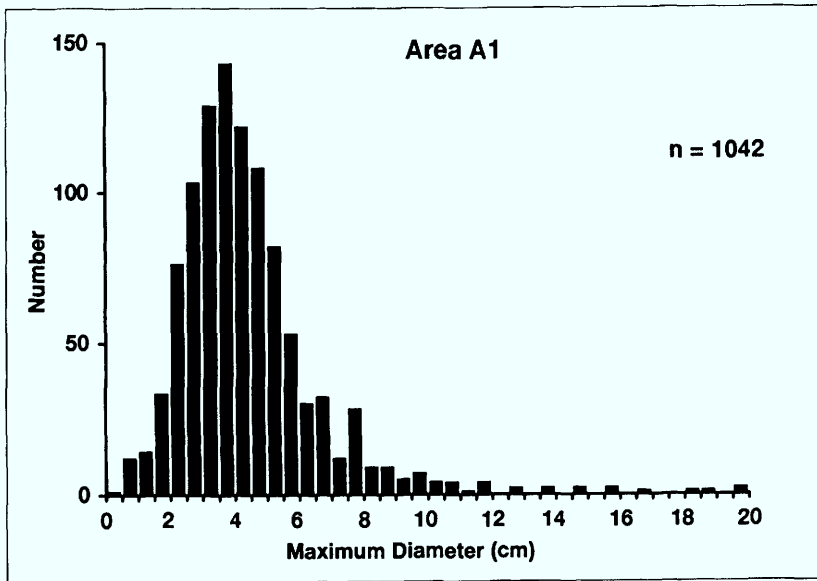


Fig. 11. Size distribution of surface nodules in area A1.

If we plot Ni + Cu versus Mn/Fe it is obvious that growth types of the same internal structure cluster within the diagram (Fig. 14).

The growth types h, d and d + h are characterized by the predominance of todorokite or birnessite with h-types being composed particularly of pure todorokite or birnessite. The crystals of those minerals grow perpendicularly to the growth layers or to the outer surface of cavities. Those crystals are extremely long (up to 15 μm) within diatom frustules, or within open cavities (Fig. 10b and c). Under the microscope with crossed nicols h-layers show a stronger birefringence than d-layers which normally start with a thin isotropic finely laminated dark-grey growth layer. $\delta\text{-MnO}_2$ is restricted to b- and e-growth types which appear more or less isotropic.

The REE distribution shows high values for hydrogenetic crusts and low values for diagenetic nodules (Fig. 15). The upper three diagenetic nodules in Fig. 15 are characterized by normal dendritic d-growth, the lower eight nodules show a particularly dense, laminated h-growth. For some samples the Mn/Fe ratio is shown in the diagram; it indicates a negative correlation between Mn/Fe and total REE contents.

If we compare the chemical and mineralogical composition of surface and buried nodules, we do not observe a clear trend. This might be expected because buried nodules in general are partly dissolved (Table 4). The ratio of

abundance of todorokite versus birnessite in surface nodules is 1.3, in buried nodules 3.0. This phenomenon was already observed by Nedjatpoor *et al.* (1985) in Peru Basin nodules, and was explained by expulsion of water from the todorokite during burial, which increases the stability of the todorokite lattice.

Growth rates

From radiochemical high-resolution profiles of ^{230}Th via alpha-spectrometry and thermal ionization spectrometry (TIMS), growth rates were calculated for two nodules in intervals of 0.4 mm and 3 mm, respectively (Bollhöfer *et al.* 1995). For the outer 4 mm of laminated to columnar b-growth of nodule 106 (max. diameter 7.5 cm; water depth 4025 m) a growth rate of about 5 mm Ma^{-1} was found. 25 mm of dendritic (d) and dense, laminated (h) growth in the outer part of nodule 63 (max. diameter 13 cm; 4257 m) revealed a growth rate of about 100 mm Ma^{-1} . Due to the concentration of siliceous microfossils the highest growth rates are assumed for h-type layers. The inner part of nodule 63, representing 33 mm to 50 mm from the surface, showed growth rates of about 40 mm Ma^{-1} . Similar results had been published by Finney *et al.* (1984) and Reyss *et al.* (1985).

J. Fenner (pers. comm. 1995) found imprints of 19 different species of diatoms in nodule 62 which shows internal growth structures similar

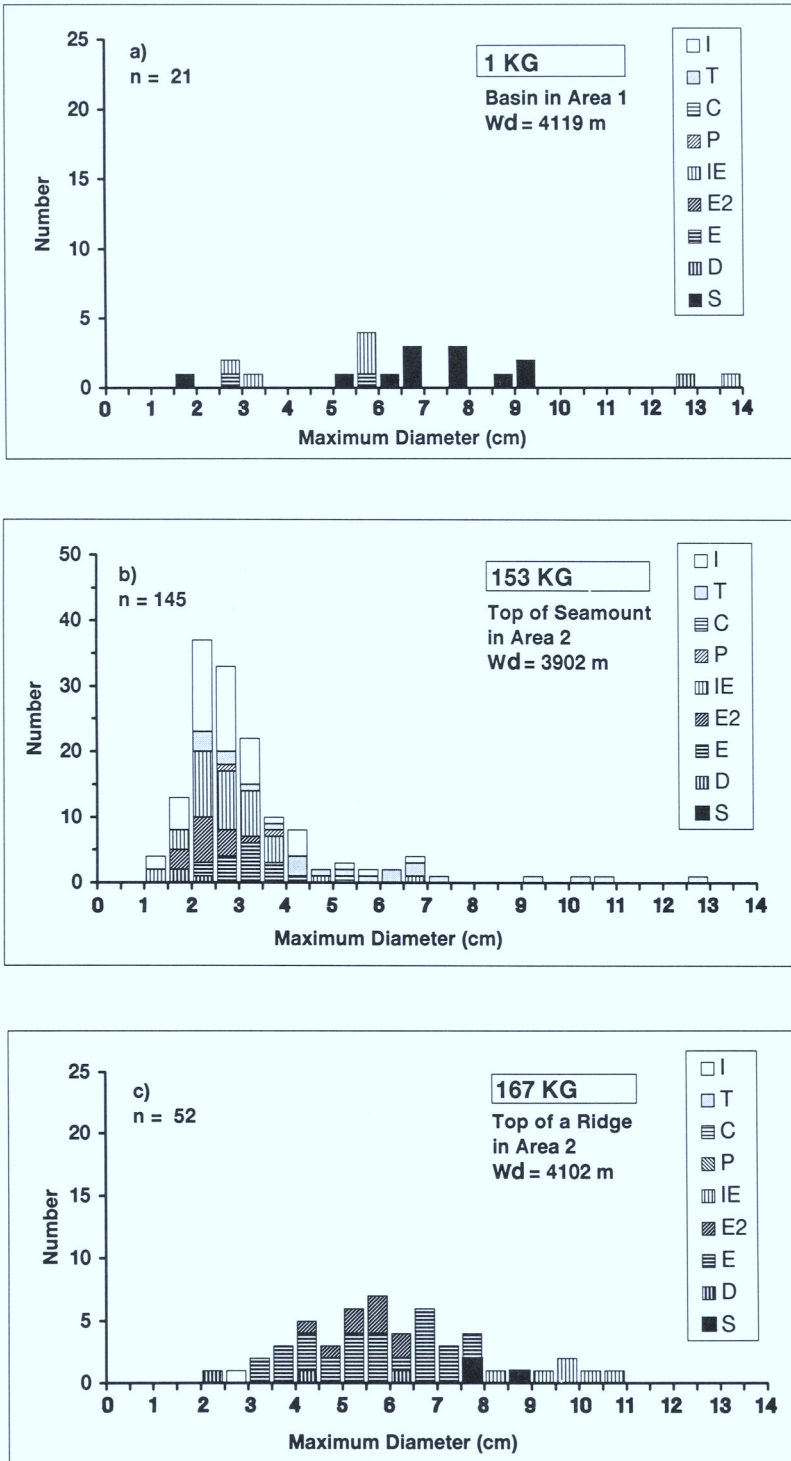


Fig. 12. Size distribution of surface nodules. (a) Type A from a basin in A1. (b) Type B from top of a seamount in A2. (c) Type A/B from top of a ridge in A2.

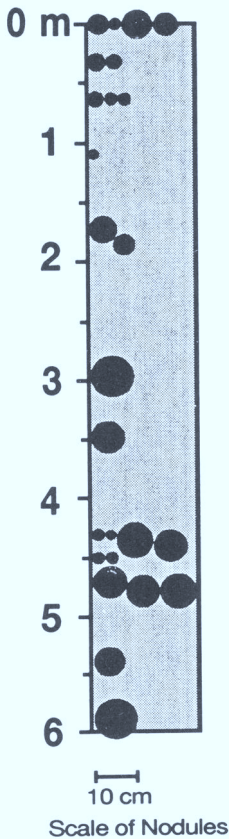


Fig. 13. Buried manganese nodules in Quaternary sediments of long box core 64 KA in A1, water depth is 4260 m. Scale of nodule size is 2.5 times larger than scale of core length.

to those of nodule 63. From the stratigraphic range of the diatoms a maximum age of 1.8 Ma for nodule 62 is assumed. This corresponds well with the age that can be estimated from the growth rates based on radiochemical measurements in nodule 63. Furthermore, buried nodules were found only in Quaternary sediments.

Discussion

Influence of sediments on nodule growth

If we want to understand the processes of nodule growth, we firstly must have a close look at the processes within the sediments on which the nodules rest.

Based on a detailed study of a large number of sediment cores (in total 37 with a recovery of 375 m sediment), we can draw a schematic

diagram of the sedimentation in the Peru Basin (Fig. 16) (Riech *et al.* in press; Weber *et al.* 1995). A dark-brown oxic surface layer of about 10 cm thickness is underlain by yellowish-brown to olive suboxic sediments. Due to the high supply of organic matter to the seafloor there is a strong diagenetic recycling during the Quaternary mainly of Mn. Mn oxide is dissolved and transported up in porewaters. Above the distinct redox boundary at about 10 cm below the seafloor, Mn oxide precipitates due to the increased content of oxygen dissolved in the pore water. Here, micro- and macro-nodules are formed. While the oxic surface sediment is very soft, the suboxic sediments are stiff.

The thickness of the oxic layer does not depend on the water depth of the sample location. On topographic highs, however, the redox boundary is assumed to be less distinct due to the winnowing of fine organic-rich material that is transported downslope into the basins.

Strong bioturbation characterizes the sediments of the Peru Basin. Burrowing is observed at the seafloor as well as in the sediment column. This process helps to keep nodules at the sediment surface.

The calcite compensation depth (CCD) is currently at 4250 m. Carbonate-poor sediments below the CCD show lower values of wet-density and shear-strength than carbonate-rich ones above the CCD (Halbach *et al.* 1994). Snoeckx & Rea (1994) and Riech *et al.* (in press) described a positive correlation between CaCO_3 and dry bulk density for sediments from the eastern equatorial Pacific Ocean and from the Peru Basin, respectively. The difference in stiffness of the sediments above and below the CCD in areas A1 and A2 will, among other factors, determine the type and intensity of bioturbation and the degree of immersion of nodules into the surface sediments which in turn must influence the nodule type. During the growth period of the nodules the depth of the CCD has changed several times (Weber *et al.* 1995). This must have influenced the growth character of nodules.

Maximum abundance of nodules for box grab samples was found near the CCD with 50 kg m^{-2} at 4257 m in area A1 and 36 kg m^{-2} at 4326 m in area A2 where growth rates are extremely high, nodules are large and diagenetic growth prevails (Tables 1 and 2). Along the Aitutaki-Jarvis transect in the central South Pacific, Cronan & Hodkinson (1994) observed a predominance of diagenetically grown nodules near the CCD. Due to the lack of sample locations deeper than 100 m below the CCD in areas A1 and A2 we

can only assume that nodule growth also is less diagenetic at levels more than 100 m below the CCD in the Peru Basin.

Supply of nuclei

The difference in frequency of occurrence of nuclei is due to the difference in availability of source material. N-nuclei which account for 52% of all nuclei were supplied by fragmentation of nodules. This fragmentation is due to shrinkage by ageing in hydrogenetically grown nodules from ridges with dense internal growth structures, or due to separation of growth cusps of diagenetically grown basin nodules. These cusps are only weakly connected to the nodule and easily may be detached by benthic organisms feeding on other organisms attached to the nodule surface or feeding on crevice fauna living in the sediment-filled interstices of the highly porous Mn oxide (Thiel *et al.* 1993). Therefore, N-nuclei of nodules in shallower water mostly show hydrogenetic b and e-growth types and nodules in deeper water show nuclei of diagenetic d and h-growth type. S and SI-nuclei which amount to 25% of all nuclei were supplied from indurated horizons found repeatedly in the sediment column (Riech *et al.* in press). B, M, and Y nuclei were supplied from outcropping volcanic rocks. The supply of the different types of nuclei distinctly determine the type of nodule assemblages. The increased supply of nuclei on topographic highs is the reason for the large number of nodules in B-type histograms while the low number in A-type histograms of basins is due to the highly reduced supply of nuclei, predominantly of nodule fragments (Fig. 12a and b).

Factors controlling shape and surface texture of nodules

The predominance of S- and D-type nodules in basins is due to increased accretion rates, which tend to form regularly-shaped nodules (Fig. 7). At shallower water depth, where the accretion rate is low, nodule shape is strongly determined by the shape of the nuclei. There, we observe an increased occurrence of E2 and P-nodules, because nodules with dense growth structures more easily break forming E2-nodules. In other words, nodules with a smooth surface show an increased tendency to form polylobate P-nodules due to the agglutination of sessile foraminifera growing in the area of contact between two sub-nodules (von Stackelberg

1984). Cylindrically shaped C-nodules grown around burrow tubes were only found on seamounts and ridges. These tubes probably were supplied from outcropping older indurated sediment horizons. The same may be true for most of the tabular T-nodules.

The cauliflower-shaped surface texture (cf) mainly of large nodules is the result of extremely high accretion rates (Fig. 9a). The bottom surface of cf-shaped nodules can be smooth, however, it is more frequently rough, which depends on the depth of immersion into the oxic surface sediments. The general predominance of a rough r-type surface in areas A1 and A2 indicates the predominance of diagenetic growth conditions. The occurrence of smooth s-type surface texture on the bottom of nodules, especially in area A1, is due to strong diagenetic growth conditions near the redox boundary.

Factors controlling nodule growth

Finney *et al.* (1984) and Dymond *et al.* (1984) assumed that for nodules from the Guatemala Basin, which are similar to nodules of the Peru Basin, accretionary processes were controlled by variations in (a) orientation, (b) degree of burial, (c) input of metal-bearing detritus, and (d) intensity of diagenetic reactions in the sediments underlying nodules. Factors a and b are determined by the disturbance of benthic organisms, and c and d by the non-steady-state flux of biogenic matter. We will discuss here the relevance of these assumptions to the growth history of nodules in the Peru Basin.

The growth rate of d- and h-layers determined by isotopic dating is extremely high: about 100 mm Ma^{-1} which is 20 times higher than that of b-growth layers. The incorporation of large siliceous skeletons into the h-layers also indicates rapid growth because at low accretion rates they would have dissolved (Fig. 10b and c). This rapid growth is assumed to occur immediately above the redox boundary while the slow growth of the b-layers takes place above the sediment surface within the sea water. The study of box grabs indicates that small nodules very rarely reach the level of rapid growth and are characterized by the predominance of slow b-growth. Large nodules repeatedly sink to the depth where d- and h-layers grow rapidly. Due to the strong difference in growth rates, d- and h-growth widely rules out the b-growth.

The great difference in growth rates for both small and large nodules is also the reason for the widely ranging diameter in A-type histograms from basins indicating two types of nodule

Table 4. Manganese nodules and crusts – Mineralogical and chemical composition of different growth structures

Sample	Growth structure	XRD	Burial depth (cm)	SiO ₂ (%)	TiO ₂ (%)	Al ₂ O ₃ (%)	Fe ₂ O ₃ (%)	MnO (%)	Mn/Fe	MgO (%)	CaO (%)	Na ₂ O (%)	F ₂ O (%)	LOI (%)	As (mg.kg ⁻¹)	Ba (mg.kg ⁻¹)	Ce (mg.kg ⁻¹)	Co (mg.kg ⁻¹)	Cu (mg.kg ⁻¹)	*La (mg.kg ⁻¹)	Mo (mg.kg ⁻¹)	Ni (mg.kg ⁻¹)	Sr (mg.kg ⁻¹)	Zn (mg.kg ⁻¹)	*Zr (mg.kg ⁻¹)
01-1	h	t	-	2.69	0.04	0.81	0.71	59.52	92.83	3.03	1.71	2.74	0.08	22.54	28	3390	55	122	1318	7	331	3036	471	582	18
01-2	h	b	-	2.78	0.03	0.57	0.59	56.71	106.44	1.48	1.87	4.07	0.07	21.29	20	1672	35	251	1969	6	286	2703	324	312	18
19-1	h	b	-	2.77	0.02	0.79	0.79	54.16	75.92	2.09	1.57	0.58	0.07	24.00	168	1139	91	51	1021	1	451	1369	325	257	1
59-1	h	t	-	3.37	0.04	0.98	0.87	56.47	71.88	3.43	1.24	1.97	0.10	23.16	16	5036	77	202	2033	19	209	6168	712	1117	27
59-3	h	b	-	3.35	0.04	0.93	0.76	53.66	78.19	2.04	1.54	4.06	0.07	22.00	14	1843	46	92	1389	1	419	2450	362	448	24
62-1	h	-	-	2.76	0.04	0.83	0.84	58.21	76.74	3.12	1.64	3.22	0.08	22.25	39	3227	44	50	1344	8	540	3053	447	765	29
62-3	h	b	-	3.95	0.05	0.85	0.76	51.08	74.43	1.81	1.69	3.24	0.07	23.09	29	1795	41	175	1258	9	326	2656	350	440	24
62-6	h	-	-	2.80	0.03	0.81	0.67	54.19	89.57	2.89	1.53	0.81	0.08	23.50	104	2200	142	34	1074	1	561	3505	372	774	1
63-2	h	b	-	4.47	0.00	0.96	0.87	53.25	67.78	2.27	1.46	0.66	0.07	23.80	32	1309	48	58	1161	1	585	1280	293	357	1
173-1	h	-	-	4.58	0.07	1.33	0.86	51.41	66.20	1.77	1.28	0.63	0.08	22.80	126	1545	141	47	1273	1	616	1016	229	294	1
Mean value				3.35	0.04	0.89	0.77	54.87	80.00	2.39	1.55	2.20	0.08	22.84	58	2316	72	108	1384	5	432	2724	389	535	14
10-1	d + b	b, t	-	6.67	0.32	1.92	8.54	36.21	4.70	2.03	2.07	0.69	0.37	26.40	250	856	233	209	4005	82	544	12454	542	1572	193
10-3	d	t	-	6.35	0.21	2.02	5.15	41.09	8.84	3.16	1.86	0.76	0.25	24.00	246	2096	229	133	6652	77	445	10803	493	2793	50
59-2	d	t	-	5.64	0.09	1.85	2.02	44.09	24.17	3.39	1.23	2.39	0.12	29.21	22	5165	74	671	5783	29	237	9954	550	1277	62
59-4	d	b, t	-	6.40	0.10	2.06	2.16	49.87	25.57	2.83	1.72	3.04	0.15	23.69	34	4048	73	145	4691	17	588	9404	453	1378	68
62-2	d	t, b	-	6.16	0.08	1.97	1.46	49.96	37.89	3.15	1.53	2.60	0.12	26.80	30	4008	60	96	3405	21	536	8401	422	1333	47
62-4	d	t	-	4.91	0.09	1.74	2.33	48.40	23.00	3.09	1.39	0.89	0.15	25.60	197	4047	209	97	4805	3	407	7502	441	1198	1
63-1	d + b	b	-	7.61	0.13	1.95	5.70	39.64	7.70	1.82	1.87	0.78	0.30	28.20	224	889	86	135	3675	1	647	9064	434	1683	72
106-1	d	b	-	6.73	0.21	2.10	5.61	40.71	8.04	2.08	1.93	0.65	0.30	24.20	235	946	187	131	5119	45	529	13067	422	1971	91
156-1	d + b	t	4	10.25	0.30	2.95	7.91	32.80	4.59	2.23	2.34	0.75	0.35	27.20	161	2249	230	362	6911	68	634	14077	577	1533	171
156-3	d	t	20	6.33	0.13	2.11	3.18	46.18	16.08	2.46	1.63	0.77	0.20	27.60	102	2798	169	258	5409	2	427	10281	405	1257	9
156-4	d	b	20	5.88	0.17	2.00	3.85	41.62	11.97	2.15	1.61	0.65	0.21	22.80	259	1799	205	166	4166	74	456	10068	383	1352	19
Mean value				6.63	0.17	2.06	4.36	42.78	15.69	2.58	1.74	1.27	0.23	25.97	160	2589	160	218	4966	38	495	10461	466	1577	71

10-2	b	d	-	8.22	0.39	1.48	13.49	30.04	2.47	1.67	2.53	0.60	0.43	27.60	252	1248	264	344	3386	109	584	10359	853	1160	293
22-2	b	d	-	5.65	1.16	0.55	21.26	23.74	1.24	1.51	2.66	1.23	0.72	37.00	224	1170	585	7127	253	192	380	3576	1200	495	409
106-2	b	t	-	8.77	0.27	2.49	9.84	32.99	3.71	2.25	2.44	0.69	0.36	26.00	150	1620	192	294	5913	54	635	12646	702	1630	259
143-8	b	t, d	-	9.62	0.52	2.47	14.25	29.66	2.30	2.59	2.21	1.69	0.34	30.50	119	1616	215	1298	5353	102	295	13400	830	877	487
145-1	f	d	-	6.63	0.70	0.76	22.68	22.95	1.12	1.37	2.56	1.18	0.73	35.10	254	1215	381	1520	1027	220	474	3450	1150	482	555
145-2	f	d	-	6.02	0.58	0.62	20.90	23.25	1.23	1.32	2.51	1.13	0.63	38.60	238	1337	286	1485	1160	204	503	3860	1121	460	453
145-3	b	d	-	7.95	0.58	1.06	26.04	20.43	0.87	1.39	2.56	1.27	0.68	35.80	250	1584	266	1347	1218	215	423	2636	1202	526	592
156-2	b+d	t	4	15.95	0.30	4.92	10.32	28.97	3.11	3.60	1.87	0.95	0.34	20.60	220	2745	225	664	10103	72	363	13128	515	911	327
177-1	b	t	-	13.19	0.35	4.03	10.25	28.88	3.12	2.86	2.43	0.91	0.36	24.20	116	2347	229	327	6415	79	371	12157	619	1093	263
Mean value				9.11	0.54	2.04	16.56	26.77	2.13	2.06	2.42	1.07	0.51	30.60	203	1654	294	1601	3870	139	448	8357	910	848	404
33-1	d+h	t	-	13.19	0.21	2.57	6.05	35.53	6.50	3.27	1.40	0.81	0.15	22.60	183	2786	220	1218	11562	6	120	12999	663	1430	100
33-2	d+h	t	118	9.81	0.18	2.53	4.03	42.04	11.55	3.21	1.25	1.01	0.16	22.20	138	4849	290	537	8246	43	146	8198	575	974	42
33-3	d+h	b	424	4.09	0.03	1.19	0.95	52.29	60.95	1.95	1.33	0.64	0.09	22.60	100	2070	91	38	2004	1	653	4982	253	932	1
52-1	d+h+b	t	-	9.18	0.26	2.51	9.69	35.03	4.00	2.30	2.39	0.68	0.33	24.60	212	1741	190	251	6332	68	550	12940	663	1699	260
53-1	d+h	t	616	12.57	0.21	2.81	6.82	35.92	5.83	3.77	1.40	0.90	0.19	22.20	156	3397	220	987	10832	32	74	8665	569	1117	141
62-5	d+h	b	-	4.64	0.04	1.42	1.23	49.36	44.44	1.53	1.23	0.54	0.12	24.80	122	1825	104	49	2104	3	627	4836	231	858	1
64-1	d+h	b	-	5.82	0.05	1.44	1.78	48.24	30.01	1.77	1.44	0.65	0.13	24.40	216	1937	78	68	2443	1	586	5710	289	1183	1
64-2	d+h	t	170	14.01	0.22	3.06	6.50	32.19	5.48	3.17	1.35	0.89	0.20	24.60	240	3787	210	1150	11890	26	87	12197	560	1309	113
64-3	d+h	t	540	8.04	0.06	1.27	3.24	46.27	15.81	3.43	1.01	1.01	0.14	23.40	243	6655	233	319	4708	25	160	4479	608	782	1
Mean value				9.04	0.14	2.09	4.48	41.87	20.51	2.71	1.42	0.79	0.17	23.49	179	3227	182	513	6680	23	334	8445	490	1143	73
10-4	e	d	-	12.64	0.28	2.32	25.75	20.69	0.89	1.86	2.01	0.72	0.51	26.20	154	2467	96	284	2253	120	333	3928	961	907	573
108-1	e	t	485	24.58	0.22	4.34	8.84	20.18	2.53	4.54	1.50	1.18	0.48	20.40	221	17849	318	438	5736	30	47	6101	962	753	68
177-2	e	d	-	10.16	0.46	1.88	24.47	23.65	1.07	1.88	2.40	0.59	0.60	25.40	419	2190	304	493	3217	204	546	4490	1133	679	629
Mean value				15.79	0.32	2.85	19.69	21.51	1.50	2.76	1.97	0.83	0.53	24.00	265	7502	239	405	3735	118	309	4840	1019	780	423

22-2, 108-1, 143-8, 145-1 to 3, 177-1 to 2 are crusts, 10-3 to 4, 52-1 are nuclei.

Growth structure: b, laminated to columnar; d, dendritic; e, massive, non-directional; f, dense, pillar; h, dense, laminated.

XRD: t, todorokite; b, birnessite; d, δ -MnO₂.

* 1 mg kg⁻¹, below detection limit.

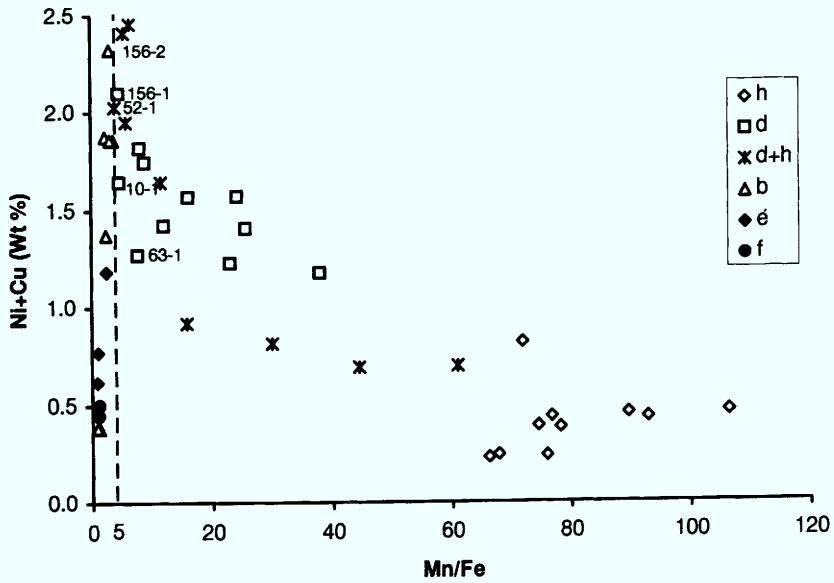


Fig. 14. Distribution of distinct growth layers within the diagram Ni + Cu versus Mn/Fe. Types of growth layers are: h, dense, laminated; d, dendritic; b, laminated to columnar; e, massive, non-directional; f, dense, pillar.

growth (Fig. 12). In shallower water, which is dominated by low growth-rate nodules, B-type histograms show a distinct maximum due to the uniform process of nodule growth. Generally, large nodules (e.g. 156-3 and 4) show d- and

h-type growth structures and high Mn/Fe ratios in the outer part indicating diagenetic growth. The inner part of large nodules (e.g. 59-4, 62-4), as well as the complete growth sequence of small nodules (e.g. 156-1 and 2), is characterized by

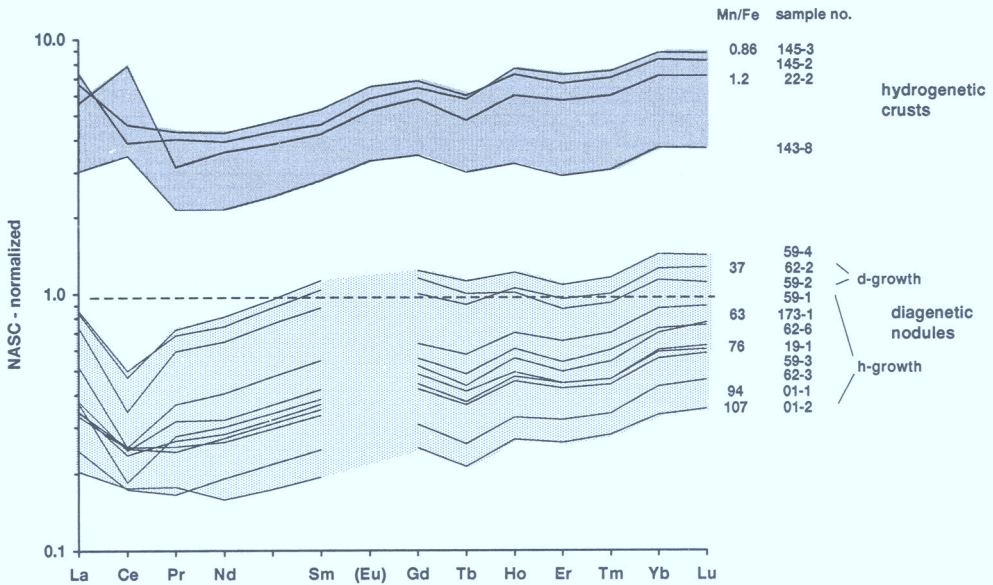


Fig. 15. Rare earth element distribution of distinct growth layers from hydrogenetic crusts and diagenetic nodules and Mn/Fe ratio for some of the samples. No data for EU content of diagenetic nodules.

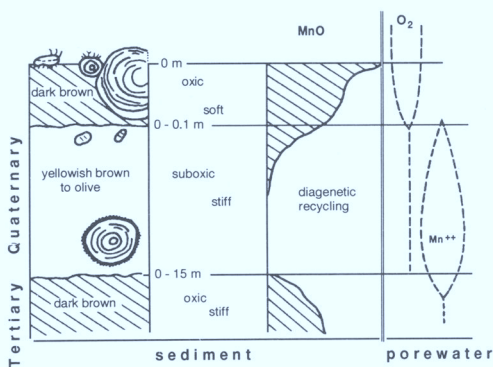


Fig. 16. Schematic diagram of sedimentation and nodule formation in the Peru Basin. Porewater composition is assumed.

b- and d-growth structures and low Mn/Fe ratios more typical of hydrogenetic growth. Growth at the top of nodules should be hydrogenetic with b-type structures and δ -MnO₂. This, however, was only observed for small nodules (10-2) on topographic highs. Larger nodules from basins (10-1, 63-1) reveal more diagenetic influence with a mixture of b- and d-growth. Todorokite and birnessite compose these nodules, whereas δ -MnO₂ is lacking, even at the nodule top. This conspicuous difference between large and small nodules is also true for the nodule assemblage of, for example, a single box grab. Therefore, predominance of either diagenetic or hydrogenetic growth mainly depends on nodule size, degree of burial, and accretion rate and not so much on a change of environment due to climatic variations.

h-growth layers are not observed in CCZ nodules, they were, however, described for nodules from the Panama Basin (Dymond *et al.* 1984; Finney *et al.* 1984). h-layers indicate specific environmental conditions.

In the Peru Basin small surface nodules normally do not contain h-layers. The larger the nodules the thicker and the more frequent are dense, laminated h-layers. Large nodules have a better chance to reach the level of the redox boundary within the sediment where apparently optimum diagenetic growth conditions occur. Here, at the boundary of oxic and suboxic sediments, normally, dendritic diagenetic d-growth should occur. Therefore, the occurrence of dense, laminated h-growth needs explanation. The redox boundary is responsible not only for the change in color and chemical composition but also for the abrupt shift from very soft to stiff sediments. Large nodules

sinking into the surface of the stiff sediments produce a mould. Due to the higher consolidation of the sediment this mould will not be destroyed by flowing movement of the sediment when the nodule is pushed upwards by burrowing organisms. Therefore, an open space is formed which immediately is filled with pore water and suspended sediment. Such a process combined with the sudden change between oxic and suboxic environment at that level may be the reason for the extremely rapid and undisturbed growth of more or less pure todorokite and birnessite. A similar kind of precipitation apparently occurs within diatom frustules and sediment cavities.

Following Usui *et al.* (1986) and Hein *et al.* (1990), hydrothermal crusts of densely laminated Mn oxide material are assumed to precipitate in an open space formed within the surface sediment isolated from seawater above the sediment-water interface. A similar process may be responsible for the diagenetic growth of h-growth layers in the Peru Basin. The similarity of both types of Mn oxide is indicated by the extreme purity of todorokite, by the high Mn/Fe ratio and low Ni + Cu content, and by the nearly identical REE concentration, except for Ce. Data for hydrothermal crusts recovered during cruise SO-79 will be presented by Marchig *et al.* (in press).

Factors controlling nodule composition

Maximum values of Ni + Cu correspond to Mn/Fe ratios of about 5 (Fig. 14). This culmination was called 'point of reversal' by Halbach *et al.* (1981) who investigated bulk samples of nodules. We, however, only analyzed distinct growth layers. To the left of that point of reversal we find mainly samples of b-, e- and f-growth type. Samples of b-, e- and f-growth layers with Ni + Cu contents below 1% are only composed of δ -MnO₂ which indicates a pure hydrogenetic growth. The samples of e- and b-growth type with higher Ni + Cu content contain δ -MnO₂ and increasingly todorokite and birnessite. This indicates enhanced diagenetic influence. Near Mn/Fe = 5 we find samples (10-1, 63-1, 156-1) of layers grown at the upper surface of nodules showing a transition between d and b-type. Sample 156-2 prepared from a layer underneath 156-1 contains a transitional growth type between b- and d-growth which explains the elevated content of Ni + Cu. Sample 52-1 was collected from a nodule fragment nucleus with a mixture of d-, h- and b-growth layers. The samples further to the right in the

diagram only contain d- and h-growth types and are increasingly diagenetic. d-growth types mostly have higher Ni + Cu concentrations than h-growth types. Samples with a mixture of d- and h-growth layers occupy an intermediate position. Pure h-layer have extremely high Mn/Fe ratios (max. 107) and very low Ni + Cu contents. Halbach *et al.* (1988) explained the decreasing content of Ni + Cu with increasing diagenetic influence by a lowering of Eh which results in higher contents of Mn²⁺ substituting for Ni and Cu in exchangeable Me²⁺ positions of the todorokite lattice.

Obviously, distinct growth layers cluster in the diagram and give much better information about environmental growth conditions than bulk samples. However, we must realize that even such growth layers are always composed of finer layers on a micron scale which represent different micro environments (Sorem & Fewkes 1979; Halbach *et al.* 1981; Thijssen *et al.* 1981; von Stackelberg & Marchig 1987).

Hydrogenetic ferromanganese oxides with a predominance of δ -MnO₂ show much higher REE concentration than the diagenetic oxides being composed mainly of todorokite or birnessite (Fig. 15) due to the long contact of the nodule top with sea water (Glasby 1973; Murphy & Dymond 1984). The h-type growth layers represent extreme diagenetic growth conditions and reveal the lowest REE concentration, which has been already described by Halbach & Puteanus (1988). The strong increase of the Mn/Fe ratio from 0.86 for a hydrogenetic crust to 107 for a diagenetic h-type growth layer of a nodule (Fig. 15) is paralleled by a general decrease of REE and is due to the predominance of δ -MnO₂ in the hydrogenetic samples and of todorokite and birnessite in the diagenetic samples. Within the diagenetic nodules, the Mn/Fe ratio increase positively correlates with the purity of todorokite and birnessite, which is assumed to indicate oxygen-deficient conditions (Halbach *et al.* 1981).

Biogenic movement of nodules ruling out variations of biogenic flux

From downcore records of organic carbon, Finney *et al.* (1988) calculated the depth of the former redox boundary in the Guatemala Basin. The depth of the redox boundary in the sediment oscillates from 5 to 25 cm over the past 400 ka with a periodicity of about 100 ka. These oscillations which are due to a non-steady-state flux of biogenic matter, may control the accretion of nodules. Such oscillations may also occur

in the Peru Basin. However, we have to consider carefully whether variations of the depth of the redox boundary or variations in the intensity of bioturbation are more decisive for the growth of Peru Basin nodules.

During a time interval of 100 ka which is assumed to represent one of the periodic oscillations of the redox boundary about 0.5 m of sediment accumulated (Weber *et al.* 1995) and a number of pushes by benthic organisms are needed to prevent burial of the nodule and to keep it near the sediment surface. Obviously, the frequency of pulses of benthic lifting is much higher than that of the oscillation of the depth of the redox boundary. We must assume that each pulse of lifting is documented in the fine layering of the nodules because within the upper 10 cm of sediment there is a very steep geochemical gradient. Additionally, however, the influence of redox variations may be superimposed on that of bioturbation-induced growth pattern.

Due to the oscillation of the position of the redox boundary we might expect variations in the accretion-type of nodules with a smooth transition from one type to the other. We observe, however, sequences with a development of growth types oriented in one direction and sharp boundaries between the extreme opposite types. h-growth is followed at a sharp boundary by d-growth which often starts with a thin layer of isotropic material similar to b-growth and d-growth turns into h-growth. Therefore, each sequence shows a development from slightly hydrogenetic to distinctly diagenetic growth conditions abruptly changing again to hydrogenetic growth conditions. This may indicate stepwise upward movements due to biogenic lifting.

Furthermore, variation in the consolidation of surface sediments due to the changing position of the CCD with time must have controlled the type and intensity of bioturbation and of nodule movement.

Lifting and burial of nodules

Nodules are turned over and rotated during the process of biogenic lifting, small nodules much more frequently than large ones. Some surface nodules have actually been turned over relatively recently; this is indicated by the fact that the smooth cauliflower-shaped surface that only develops on the bottom of nodules was located on the top, or by the occurrence of special sessile organisms found at the upper surface of nodules that only live on the bottom surface. Such selective turnover of nodules can be explained

only by bioturbation and not by bottom currents or seismicity.

Large nodules show an increased tendency for asymmetric growth, which is due to the reduced chance of being rotated by benthic organisms. The increased probability to become stuck in the stiff suboxic sediment caused a distinct number of such nodules to become buried. Therefore, buried nodules show a higher percentage of asymmetric growth than surface nodules.

Only large nodules with distinct asymmetric growth are suitable to study environmental changes. Smaller ones were rotated repeatedly and only a random mixture of environmental signals can be inferred. However, even the growth of large nodules with asymmetric accretion is controlled by two types of change in environment. The first is an active one and results from benthic lifting, the second is passive, and due to variations of biogenic flux.

The predominant occurrence of buried nodules in deeper water may partly be due to the fact that long box cores that are especially favourable for collecting buried nodules, were only used in deep water and not on slopes. However, in the Peru Basin the probability of nodule burial is in fact higher in deeper than in shallower water. This is explained by the growth rate, which may be 20 times higher in deep water (>4250 m) resulting in large, mainly regular-shaped (D- and S-type) nodules that are less favourable for being lifted and more easily become buried.

Although many surface nodules show a smooth s-texture bottom, s-texture is never observed on buried nodules. Apparently, a final dendritic overgrowth occurs before accretion terminated after burial and only r- or r·s-surface texture is found. Due to the reducing environment in deeper parts of the sediments, buried nodules are partly dissolved which changes the colour and stability of the growth layers.

Comparing the histograms of surface nodules with those of buried nodules we observe a distinct bimodal size distribution for buried nodules and a mainly single mode distribution for surface nodules (Figs 8 and 11). Buried nodules, compared to surface nodules, show a slight shift to the left of the maximum and minimum size distribution and a very high percentage (32%) of large nodules (>5 cm). The shift of the maximum indicates a favoured supply of nodules <3 cm. The concentration of large nodules is due to the accelerated process of burying large, fast-growing nodules.

Finney *et al.* (1984) observed a similar bimodal size distribution for buried nodules of

the Guatemala Basin. They suggested that nodules larger than 8 cm extend so deeply into the sediment that bioturbation can no longer move them up and that nodules smaller than 2 cm are not easily distinguished from the surrounding sediment by benthic organisms. According to McCave (1988), however, particles >2 mm of deep-sea sediments are pumped upwards by burrowing activity. The model of Heath (1979) that assumes that growth rate of nodules and the probability of their burial are independent of size, does not fit the data for Peru Basin nodules.

Large nodules preferably are buried in the Peru Basin, mainly because they get stuck in the stiff sediment below the redox boundary. However, we doubt that small nodules are concentrated amongst the buried nodules because they are not easily distinguished by benthic lifters. The size distribution of nuclei, especially in area A1 shows that the maximum number is found for maximum diameters <2 cm (Fig. 5). If those nuclei were not distinguished by benthic organisms, they would have been buried and not have formed the nuclei of nodules. It is assumed, however, that buried nodules are generally smaller than surface nodules, because they are representatives of an early growth stage of the nodule assemblage. Due to a statistical selection, a few nodules especially from the prevailing size class failed to be lifted. This model which was observed in the CCZ (von Stackelberg 1987) is true only for areas with low accretion rates. In the Peru Basin, however, there may be extreme differences between growth rates of nodules from basin and ridge positions. Therefore, in shallower water the model of statistical selection prevails, while in deeper water the model of immersion of large nodules predominates. This may explain the bimodality of collective histograms indicating two types of burial.

Conclusions

The two survey areas of the RV *Sonne* cruise SO-79 are situated at the southern margin of the zone of high bioproductivity of the eastern equatorial Pacific. Therefore, relatively strong bioturbation characterizes the seafloor and the sediment column.

Most of the manganese nodules of the Peru Basin occur at the seafloor surface within a soft, semi-liquid oxic sediment layer of about 10 cm thickness covering stiff suboxic sediments that contain a number of buried nodules. This distinct redox boundary is the result of a relatively high flux of organic carbon.

At present, the CCD is at 4250 m. Due to calcite dissolution sediments near the CCD have a lower shear-strength than those occurring above the lysocline. Near the CCD occurs a maximum abundance (50 kg m^{-2}) of nodules of distinct diagenetic growth character.

A large number of nodules (B-type) occur on topographic highs because of increased supply of nuclei. In basins small numbers of nuclei are supplied which results in only few nodules (A-type).

The accretion rates of the outer part of large nodules occurring mainly in basins are high (about 100 mm Ma^{-1}) while their inner part normally shows lower accretion rates (about 40 mm Ma^{-1}). Small nodules from basins are assumed to have similar low accretion rates as the center of large ones due to similar chemical and mineral compositions. Small nodules from topographic highs are characterized by very low accretion rates (about 5 mm Ma^{-1}). Variations in accretion rate depend on variations in chemical environment. There are strong differences in the chemical environment at the seafloor between ridge and basin areas. Strong differences in the chemical environment are also observed at each location within the oxic surface layer of the sediment column. Highest accretion rates are found immediately above the redox boundary where dense, laminated layers (h-type) of very pure todorokite grow diagenetically. Slow growth rates occur where nodules are in contact with the bottom water and hydrogenetic growth layers of columnar b-type are formed. Small nodules rarely reach the level of rapid growth near the redox boundary because they are easily rotated and moved upwards by benthic organisms. Large nodules may be rotated and lifted less easily. They repeatedly sink to the depth of rapid accretion and commonly show asymmetric growth. The variation in environment controls the accretion rate, the growth type and its composition, the nodule shape and surface texture, and the nodule size.

The predominance of rapid diagenetic growth especially at the lower surface of large nodules widely rules out the slow hydrogenetic growth occurring only at the upper surface. The type of nodule growth is mainly controlled by nodule size and depth of immersion which determine the accretion rate.

The apparently extremely rapid growth of dense, laminated h-type layers on the bottom of large nodules may be explained by the precipitation of Mn oxide in open space at the boundary of the stiff suboxic and soft oxic sediments. This open space is formed as a result of the upward displacement of nodules by burrowing organism.

Biogenic benthic displacement of nodules are much more frequent than climatic changes. Therefore, fine layering of nodules is mainly due to biogenic movement of nodules within the oxic surface sediment from one environment to another. Climatic variations control the general chemical environment and its signature is superimposed on these smaller-scale variations.

Compared to cores from the Clarion-Clipperton Zone, we found a relatively large number of buried nodules in Peru Basin cores. Due to the reducing environment in the suboxic sediments, buried nodules are partly dissolved. Large nodules, especially in basin sediment, have an increased probability to sink into the sediment, to become stuck in the stiff suboxic sediments, and finally to become buried. Therefore, buried nodules are generally larger than surface nodules.

This enhanced selection of large nodules to become stuck is the dominant type of burial in basins. On ridges where smaller nodules predominate, burial is controlled mainly by a statistical selection of nodules not to be moved up by organisms. This type of burial is typical of the Clarion-Clipperton Zone nodules.

The contributions of the following staff members of BGR are greatly appreciated: J. Fenner for microscopic determination of diatoms, H. Rask and H. Karmann for computerized data processing, line drawing and photographing nodules, H. Rösch for X-ray diffraction analysis, U. Siewers for XRF and ICP-MS analysis, S. Stäger for SEM photographs. Special thanks are due to H. Beiersdorf and U. von Rad for reviewing the manuscript. We acknowledge the financial support of the Bundesministerium für Forschung und Technologie.

References

- BOLLHÖFER, A., EISENHAUER, A., PECH, D., FRANK, N., MANGINI, A. & VON STACKELBERG, U. 1995. High resolution profiles of ^{238}U -, ^{234}U -, ^{232}Th - and ^{230}Th in Mn-nodule 63 KG from the Peru Basin via alpha- and high precision mass spectrometry (TIMS) (Abstract). *Statusseminar 'Marine Geowissenschaften' Bremen*, 82.
- CRONAN, D. S. & HODKINSON, R. A. 1994. Element supply to surface manganese nodules along the Aitutaki-Jarvis Transect, South Pacific. *Journal of the Geological Society, London*, **151**, 39–401.
- DYMOND, J., LYLE, M., FINNEY, B., PIPER, D. Z., MURPHY, K., CONRAD, R. & PISIAS, N. 1984. Ferromanganese nodules from the MANOP Sites H S, and R- Control of mineralogical and chemical composition by multiple accretionary processes. *Geochimica et Cosmochimica Acta*, **48**, 931–949.

- FINNEY, B., HEATH, G. R. & LYLE, M. 1984. Growth rates of manganese-rich nodules at MANOP Site H (Eastern North Pacific). *Geochimica et Cosmochimica Acta*, **48**, 911–919.
- , LYLE, M. W. & HEATH, G. R. 1988. Sedimentation at MANOP Site H (Eastern Equatorial Pacific) over the past 400,000 years: climatically induced redox variations and their effects on transition metal cycling. *Paleoceanography*, **3**, 169–189.
- GLASBY, G. P. 1973. Mechanisms of enrichment of the rarer elements in marine manganese nodules. *Marine Chemistry*, **1**, 105–125.
- HALBACH, P. & PUTEANUS, D. 1988. Geochemical trends of different genetic types of nodules and crusts. In: HALBACH, P., FRIEDRICH, G. & VON STACKELBERG, U. (eds). *The manganese nodule belt of the Pacific Ocean*. Ferdinand Enke, Stuttgart, 61–69.
- , MARCHIG, V. & SCHERHAG, C. 1980. Regional variations in Mn, Ni, Cu, and Co of ferromanganese nodules from a basin in the Southeast Pacific. *Marine Geology*, **38**, M1–M9.
- , SCHERHAG, C., HEBISCH, U. & MARCHIG, V. 1981. Geochemical and mineralogical control of different genetic types of deep-sea nodules from the Pacific ocean. *Mineral Deposita*, **16**, 59–84.
- , OEBIUS, H.-U., GRONENBERG, M. & GRUPE, B. 1994. *Boden-mechanische Eigenschaften von Tiefseesedimenten in Manganknollenfeldern als Funktion des sedimentpetrographischen Aufbaus, MEPA SED*. Endbericht, FU/VWS Berlin.
- HEATH, G. R. 1979. Burial rates, growth rates, and size distribution of deep-sea manganese nodules. *Science*, **205**, 903–904.
- HEIN, J. R., SCHULZ, M. S. & KANG, J.-K. 1990. Insular and submarine ferromanganese mineralization of the Tonga-Lau region. *Marine Mining*, **9**, 305–354.
- LEMAITRE, N. 1987. *Les nodules polymetalliques du bassin du Peru*. These, Université de Paris-Sud, Centre d'Orsay.
- , REYSS, J. L. & MARCHIG, V. 1984. Géologie marine. – Différences de composition chimique entre les faces opposées d'un nodule de manganèse orienté du Bassin du Pérou. *Comptes Rendus de l'Académie des Sciences, Paris*, **298**, Serie II, 407–410.
- MANGINI, A., STOFFERS, P. & BOTZ, R. 1987. Periodic events of bottom transport of Peru Basin sediment during the late Quaternary. *Marine Geology*, **76**, 325–329.
- MARCHIG, V. & REYSS, J. L. 1984. Diagenetic mobilisation of manganese in Peru Basin sediments. *Geochimica et Cosmochimica Acta*, **48**, 1349–1352.
- MARCHIG, V., VON STACKELBERG, U., WIEDICKE, M., DURN, G. & MILOVANOVIC, D. In press. Hydrothermal activity associated with off-axis volcanism in the Peru Basin. *Marine Geology*.
- MCCAVE, I. N. 1988. Biological pumping upwards of the coarse fraction of deep-sea sediments. *Journal of Sedimentary Petrology*, **58**, 148–158.
- MORITANI, T., MARUYAMA, S., NOHARA, M., MATSUMOTO, K., OGITSU, T. & MORIWAKI, H. 1977. Description, classification and distribution of manganese nodules. *Cruise report, Geological Survey of Japan*, **8**, 136–158.
- MURPHY, K. & DYMOND, J. 1984. Rare earth element fluxes and geochemical budget in the eastern equatorial Pacific. *Nature*, **307**, 444–447.
- NEDJATPOOR, M., STOFFERS, P. & GLASBY, G. P. 1985. Influence of ageing effects on manganese nodule mineralogy. *Neues Jahrbuch für Mineralogie, Mh*, **5**, 204–208.
- REYSS, J. L., LEMAITRE, N., KU, T. L., MARCHIG, V., SOUTHON, J. R., NELSON, D. E. & VOGEL, J. S. 1985. Growth of a manganese nodule from Peru Basin: A radiochemical anatomy. *Geochimica et Cosmochimica Acta*, **49**, 2401–2408.
- , MARCHIG, V. & KU, T. 1982. Rapid growth of a deep-sea manganese nodule: Effect of diagenetic source of manganese. *Nature*, **295**, 101–103.
- RIECH, V., WEBER, M. E., WIEDICKE, M., MARCHIG, V. & CEPEK, P. In press. A six Ma sedimentary record in the Peru Basin: Geochemical indications for a significant redox shift at the end of the Pliocene. *Marine Geology*.
- SNOECKX, H. & REA, D. K. 1994. Dry bulk density and CaCO₃ relationship in upper Quaternary sediments of the eastern equatorial Pacific. *Marine Geology*, **120**, 327–333.
- SOREM, R. K. & FEWKES, R. H. 1979. *Manganese nodules*. Plenum, New York, 1–723.
- STACKELBERG, U. VON 1984. Significance of benthic organisms for the growth and movement of manganese nodules, Equatorial North Pacific. *Geology and Marine Letters*, **4**, 37–42.
- 1987. Pumice and buried manganese nodules from the equatorial North Pacific Ocean. *Geologisches Jahrbuch*, **D87**, 229–285.
- & MARCHIG, V. 1987. Manganese nodules from the equatorial North Pacific Ocean. *Geologisches Jahrbuch*, **D87**, 123–227.
- STOFFERS, P., SIOULAS, A., GLASBY, G. P. & THIJSEN, T. 1982. Geochemical and sedimentological studies of a box core from the western sector of the Peru Basin. *Marine Geology*, **49**, 225–240.
- , —, —, SCHMITZ, W. & MANGINI, A. 1984. Sediments and micronodules in the northern and central Peru Basin. *Geologische Rundschau*, **73**, 1055–1080.
- THIEL, H. & SCHRIEVER, G. 1990. Deep Sea Mining, Environmental Impact and the DISCOL Project. *AMBIO*, **19**, 245–250.
- , —, BUSSAU, C. & BOROWSKI, C. 1993. Manganese nodule crevice fauna. *Deep Sea Research*, **40**, 419–423.
- THIJSEN, T., GLASBY, G. P., SCHMITZ-WIECHOWSKI, A., FRIEDRICH, G., KUNZENDORF, H., MUELLER, D. & RICHTER, H. 1981. Reconnaissance survey of manganese nodules from the northern sector of the Peru Basin. *Marine Mining*, **2**, 382–428.
- , —, FRIEDRICH, G., STOFFERS, P. & SIOULAS, A. 1985. Manganese nodules in the central Peru Basin. *Chemie der Erde*, **44**, 1–46.

- USUI, A. 1982. Variability of manganese nodule deposits: The Waikē to Tahiti transect. *Cruise report, Geological Survey of Japan*, **18**, 138–223.
- , YUASA, M., YOKOTA, S., NOHARA, M., NISHIMURA, A. & MURAKAMI, F. 1986. Submarine hydrothermal manganese deposits from the Ogasawara (Bonin) arc, off the Japan Island. *Marine Geology*, **73**, 311–322.
- WEBER, M. E., WIEDICKE, M., RIECH, V. & ERLKEUSER, H. 1995. Carbonate preservation history in the Peru Basin: Paleooceanographic implications. *Paleoceanography*, **10**(4), 775–780.
- WIEDICKE, M. & WEBER, M. E. In press. Small-scale variability of seafloor features in the northern Peru Basin. Results from acoustic survey methods. *Marine Geophysical Researches*.

Distribution and composition of marine hydrogenetic and hydrothermal manganese deposits in the northwest Pacific

AKIRA USUI¹ & MASAO SOMEYA²

¹ *Geological Survey of Japan, 1-1-3 Higashi, Tsukuba, Ibaraki, Japan 305*

² *Metal Mining Agency of Japan, Tokiwa Buklding, 1-24-14 Toranomon, Minato-ku, Tokyo, Japan 105*

Abstract: The distribution and composition of Mn deposits in the northwest Pacific (15–50° N and 120–160° E) are characterized using a Mn deposits database compiled from our original data, published and unpublished papers, published databases, and other international sources. The results demonstrate a close association with geological settings. Hydrogenetic nodules and crusts formed in areas of erosion or nondeposition on Cretaceous seamounts and plateaus of the Pacific plate, and to a lesser extent on seamounts of remnant arcs of Palaeogene to Neogene ages. The Cretaceous seamount deposits are most enriched in Co, and the plateaus less so, while both show moderate Ni enrichment. Nodules and crusts are rare in enclosed backarc basins, which have not been affected by deep water circulation. A slight early-diagenetic influence is observed in some Pacific basin nodules. By contrast, modern hydrothermal Mn deposits are broadly distributed on active submarine volcanoes and backarc rifts. These hydrothermal Mn deposits consist typically of pure Mn oxide containing negligible levels of metals except for Mg, Ba, K and Li. Similar fossil hydrothermal Mn deposits are observed in places on old basement or within deep cores as geological records of past hydrothermal activity.

Manganese deposits, typically forming nodules or crusts, are nearly ubiquitous on the sea floor and on topographic highs where the supply of terrigenous, volcanogenic and biogenic components is very low. Nodules and crusts have been found from the tropical climatic belt to the Antarctic regions in the world oceans (Manheim & Lane-Bostwick 1989; Hein *et al.* 1987; Usui *et al.* 1989). Similar fossil manganese deposits have been also found, albeit much less common, within DSDP/ODP sediment cores as old as the late Cretaceous (Glasby 1978; Usui & Ito 1994). In the northwest Pacific region little is known of the distribution and compositions of manganese deposits from the continental margin and adjacent deep sea areas. We have had an opportunity to summarize all available data on manganese deposits from this area and compile a manganese deposits database in cooperation with domestic and international colleagues.

Though few systematic research cruises on marine mineral resources have been conducted in the area, a significant amount of data on manganese deposits have been acquired by Japanese and other organizations over the past 20 years. The Geological Survey of Japan (GSJ) started basic research on mineral resources in 1970 and has conducted hydrothermal mineral investigations (1984–1989) and geological mapping (since 1974) in areas adjacent to the Japanese Islands. The Metal Mining Agency of Japan (MMAJ) started manganese crust

exploration in 1985 in the mid-Pacific Mountains area. Most of the presented data come from these two organizations.

In this report we present the overview of mode of occurrence, distribution and composition of manganese deposits in the northwest Pacific, and discuss their genetic relationships to topography and geological setting.

Sources of data

Our database includes four types of files: reference, location, description and analysis. The reference file includes published papers, reports, and books from international sources. We obtained unpublished data through the courtesy of colleagues from USA, Russia, Germany, China, France, Korea and Japan. We selected some data from the public databases of NOAA, Scripps Institution of Oceanography, US Geological Survey, IFREMER, and SEATAR. The total number of sample locations searched is greater than 14 000, locations of described manganese deposits is about 1100, and data sets of chemical analysis is about 2600 (Table 1). 44% of description data sets and 65% of chemical data sets originate from GSJ and MMAJ. The chemical data include new chemical analyses on 110 manganese samples from previously undescribed locations within the area from GSJ collections.

Table 1. *Source of data for this study*

	location	Description	Chemical	Bibliography
Japan	9113	660	2141	196
GSJ	7513	302	537	74
MMAJ	175	157	1122	4
TOKAI	74	86	215	24
ORI	393	75	121	37
MAR	49	19	0	15
JAM	170	9	0	11
Others	739	12	156	31
USA	3861	241	241	15
Russia/USSR	197	109	184	15
Germany	90	20	10	3
France	8	6	15	1
China	365	16	13	4
Korea	41	–	–	–
Total	13675	1052	2614	217

MMAJ, Metal Mining Agency of Japan; TOKAI, Tokai University; ORI, Ocean Research Institute, University of Tokyo; MAR, Maritime Agency of Japan; JAM, Japan Marine Science & Technology Center.

The number of sample locations is significant for simple statistical analyses and regional characterization, as they are spatially well distributed. Most samples were collected by dredging and sediment coring. Some TV/camera and submersible observations are also included. In the description file, location data, type, size and thickness of manganese deposits, bottom material, and nucleus/substrate are cited if available. The analysis file includes brief descriptions, type, mineral composition and concentrations of up to 55 elements.

Study area and field setting

The study area is bounded by 15–50° N and 120–160° E lines. The area includes a variety of geological environments; active island-arc-trench systems, remnant arcs, deep-sea basins, active and inactive backarc basins, oceanic seamounts and continental shelves (Fig. 1). The most prominent topographic features is the two active island-arc systems extending N–S to NE–SW. The Pacific basin is characterized generally by abyssal plains of 5000–6000 m water depths and scattered seamounts, guyots and plateaus. Marginal basins of 3000–5000 m water depths are associated with the volcanic arcs. Tectonically, the area is located within the boundaries of the Pacific plate, Eurasia plate, Philippine Sea plate and, probably, North American plate. The plates are principally bounded by active island arc-trench systems

(Kuril–Japan–Bonin–Mariana and Nankai–Nanseishoto arcs). Figure 1 shows a simplified tectonic features of the area.

The Pacific plate in this area includes the oldest oceanic crust formed during the Jurassic. The Pacific plate and Philippine Sea plates are moving towards and colliding with the Eurasia plate in a NE to ENE direction forming active volcano chains and trenches. Active backarc spreading is taking place in the Mariana trough, Okinawa trough, and Bonin backarc depressions located west of the submarine volcanic chains. There are some aseismic ridges on the the Philippine Sea plate. Abandoned Tertiary back-arc rifts form several large back-arc basins (Okhotsk, Japan, Shikoku, Parece Vela and, possibly, Philippine basins) in the marginal seas. Remnant arcs (Daito, Kyushu–Palau, Nishi–Shichito and West Mariana ridges) rest on the Philippine Sea plate and separate the basins. Palaeographic reconstructions (Seno & Maruyama 1984; Honza & Tamaki 1985; Tamaki 1985) indicate that the major marginal basins formed in the Palaeogene (Philippine basin) and the Neogene (other basins). The abyssal sea floor of the basins is filled mostly with terrigenous and volcanogenic sediments.

Occurrence and distribution of manganese deposits

Descriptive and compositional data of the deposits collected in the northwest Pacific by

numerous institutions during the past two decades enable us to characterize the regional distribution and to delineate relations with geological settings, although they are far from

sufficient to characterize small-scale variations or to estimate economic potential.

Earlier geochemical and mineralogical studies of marine manganese deposits have revealed

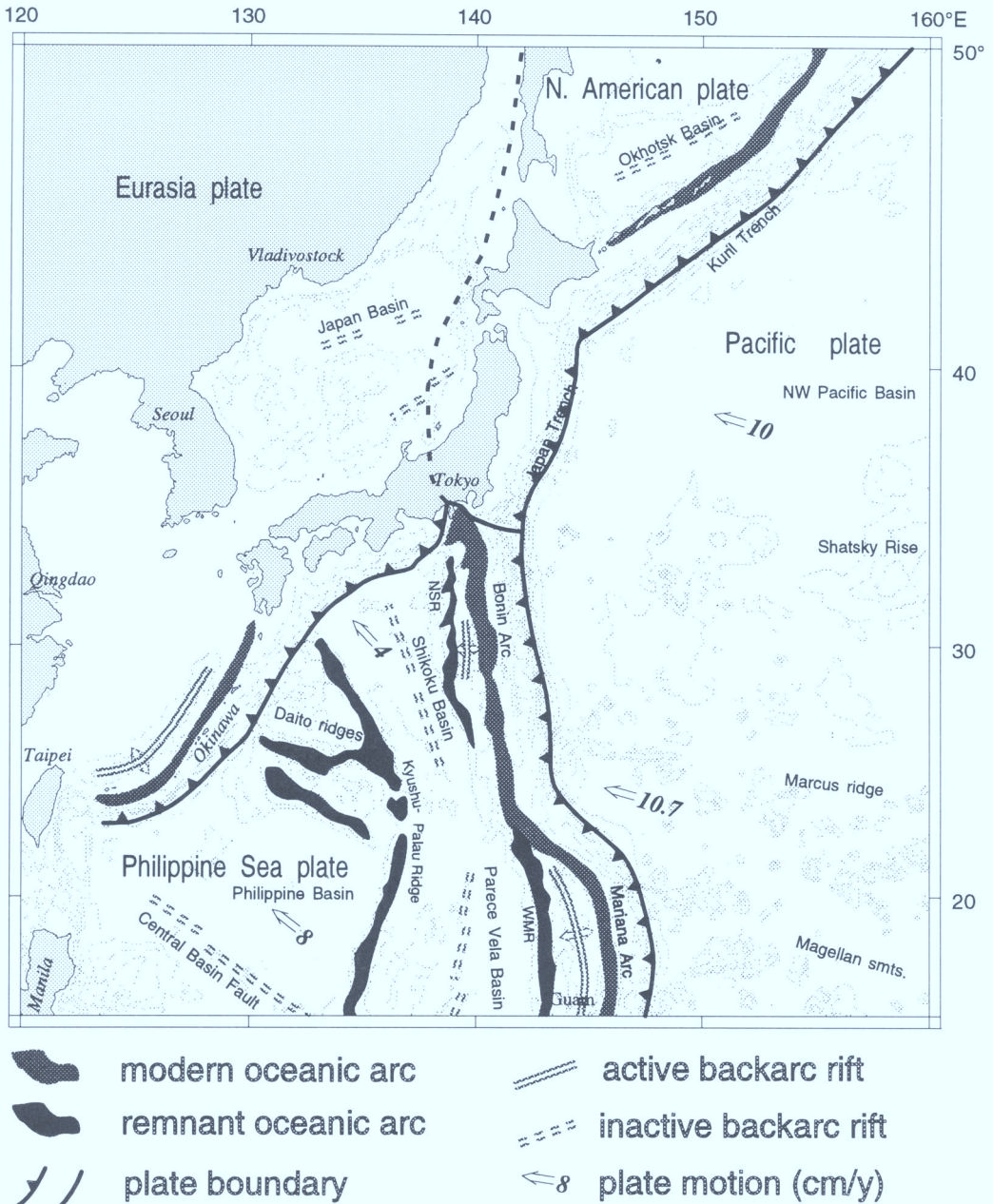


Fig. 1. Tectonic and topographic map of survey area. The tectonic map was modified from Seno & Maruyama (1984) and Drummond *et al.* (1985). The topographic contours at 1000 m intervals are based on digital data of the Hydrographic Office (1989). NSR, Nishi-Shichito ridge; WMR, West Mariana ridge. Thick broken line is the inferred boundary between the Eurasia and North American plates.

three typical origins; hydrogenetic, early-diagenetic, and hydrothermal (Halbach & Özkara 1979; Usui 1979; Usui *et al.* 1989). The origin of manganese deposits can be determined by mineral composition. Hydrogenetic manganese deposits usually form nodules, crusts, coatings of boulders and thin stains, which cover nuclei or substrates with less than 1 mm to more than 150 mm thick layers. The composition and size of nuclei and substrates are variable and include basalt, andesite, sandstone, phosphorite, granitic rocks, pumice, zeolitic rock, limestone, fossils, *etc.* (Hein *et al.* 1987; Usui *et al.* 1994). Thick crusts (more than 100 mm) have been recovered only from old Pacific seamounts and plateaus (mostly Cretaceous) at water depths shallower than 2500 m (Fig. 2). Moderately thick crusts and nodules occur on seamounts of the Tertiary remnant arcs. Only very thin coatings and stains of hydrogenetic manganese develop in the modern arc areas. No deposits are observed on continental shelves and slopes. The thicker hydrogenetic crusts and nodules occur in areas of older basement (Fig. 3).

The general distribution of hydrogenetic and hydrothermal deposits is shown in Fig. 4. On the

Pacific basin floor, nodules rarely occur despite the old age of the basement. Surficial manganese nodules on the sea bed at water depths below 5000 m are reported from only ten locations out of more than 200 locations investigated. Similarly, marginal basins formed by backarc rifting yield scarce nodules. The lack of nodule development on the deep sea floors is generally due to a relatively high terrigenous and volcanogenic supply during the Quaternary. In fact, we have found deeply buried nodules in five DSDP cores within this area, which indicates increased sedimentation rates since the Pliocene (Shipboard Scientific Party 1985). Another reason for the scarcity of nodules may be deficient circulation of oxygenated deep waters. As indicated by tectonic reconstruction, adjacent back-arc basins, especially Okhotsk, Japan and Shikoku basins, would have been isolated from northward deep-water circulation because of the shallow oceanic arcs (Kyushu-Palau and Bonin-Mariana) that existed since the Neogene.

Wide-spread hydrothermal manganese deposits are often found in the active submarine volcanoes and backarc rifts. For example, manganese deposits cover wide areas of the

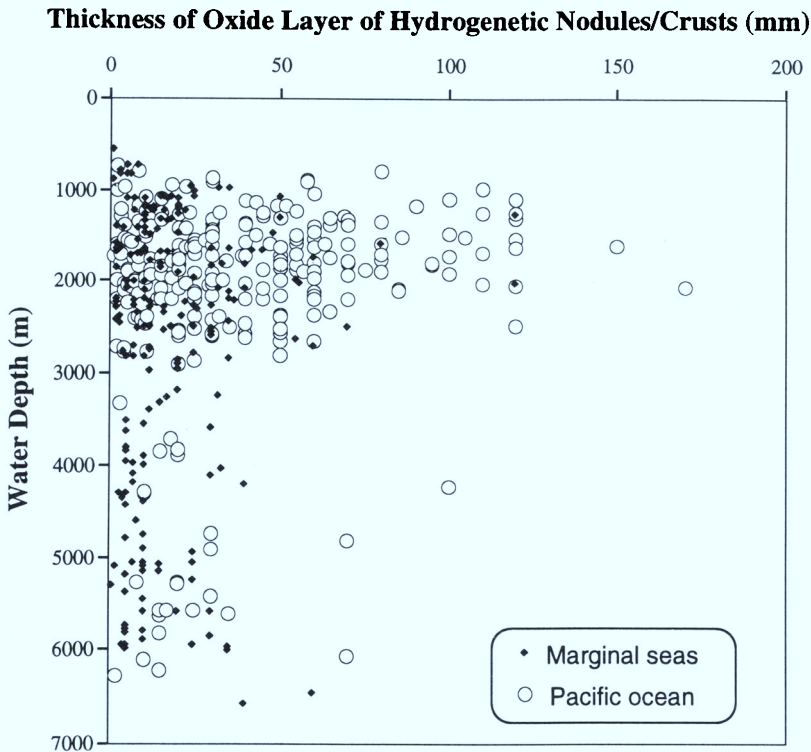


Fig. 2. Relationship between thickness of hydrogenetic deposits and water depth. Each thickness represents the maximum within samples from each station.

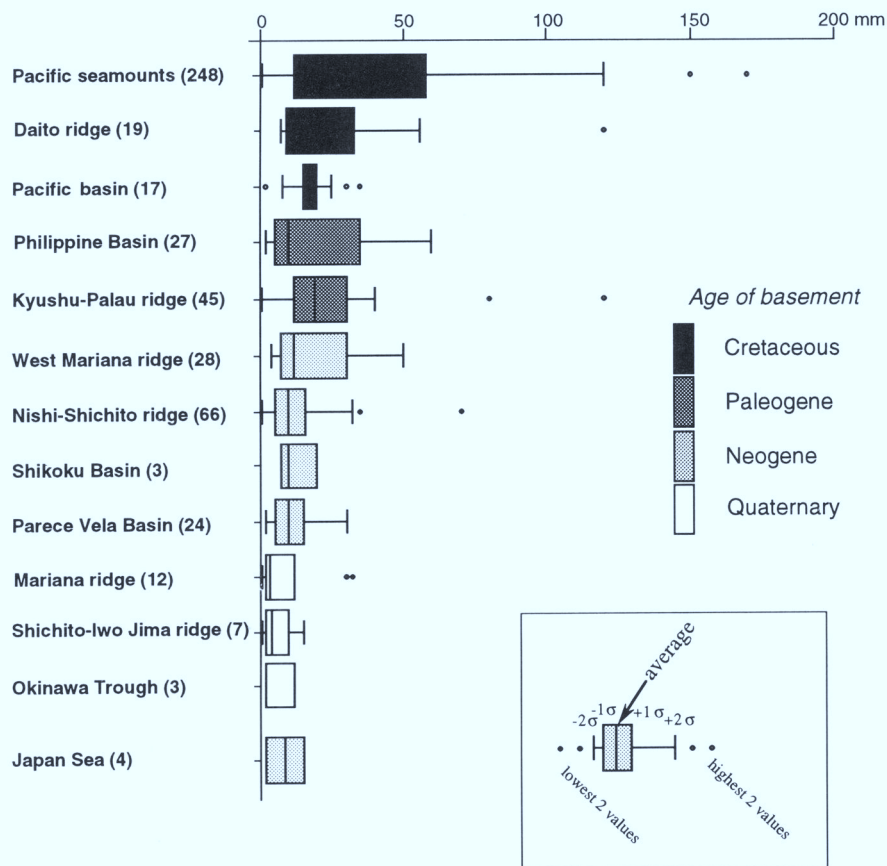


Fig. 3. Thickness of oxide layers of hydrogenetic nodules and crusts and the variation with province and basement age.

flank of Kaikata seamount on a scale of several kilometres in the Bonin arc (Usui & Nishimura 1992). Hein *et al.* (1987) also found nearly ubiquitous distribution of hydrothermal manganese deposits in the submarine volcanoes in the northern part of the Mariana arc. The manganese deposits are occasionally associated with hydrothermal iron oxide deposits. The growth rate of hydrothermal manganese deposits is probably three orders of magnitude or more higher than that of hydrogenetic deposits (Usui *et al.* 1989).

By contrast, fossil hydrothermal manganese deposits occur on inactive ridges (Tertiary remnant arcs) and topographic highs (Usui *et al.* 1986). The deposits are usually coated with younger hydrogenetic crusts and serve as nuclei for nodules. Such deposits record past hydrothermal activity at extinct submarine volcanoes and spreading centres. Such deposits have been recovered from Nishi-Shichito ridge, Kyushu-Palau ridge, Central Basin ridge in Philippine

Sea, Japan Sea and Shatsky rise. On the other hand, evidence of hydrothermal manganese mineralization is encountered in Oligocene to Pleistocene sediments of ODP drill cores from the Bonin forearc and back-arc basins (Usui 1992).

Compositional characteristics in relation to geological environments

Bulk mineralogy

The mineralogy of marine manganese deposits is important because it reflects the origin and partly determines chemical composition. Although the crystallographic description and mineral chemistry of marine manganese deposits are still controversial, they are principally categorized into three mineral series. The hydrogenetic mineral vernadite is a poorly crystalline iron and manganese oxide. The



Fig. 4. Occurrence of manganese deposits in relation to topography (contour: 1000 m interval). The plot shows occurrence of manganese deposits whose thickness exceed 1 mm.

early-diagenetic mineral buserite is a nearly stoichiometric sheet-structured manganate that can accommodate Cu and Ni as interlayer-stabilizing exchangeable cations. Todorokite is a typical hydrothermal mineral with structural tunnels commonly accommodating Mg and/or Ba. The latter two minerals are believed to be a structurally linked continuous series (Usui *et al.* 1989; Mellin & Lei 1993). The above mineral terms are common in the literature, although todorokite is the only formally approved mineral name (Burns *et al.* 1985).

According to mineralogical criteria, the mineral components of manganese deposits of the northwest Pacific are subdivided as follows.

- (1) Iron-rich vernadite. A commonly occurring hydrogenetic iron-manganese oxide (Mn/Fe is around 1 to 2). It is poorly crystallized (only two diffuse lines at 2.4 and 1.4 Å d-spacings) and has randomly-stacked sheets (Ostwald 1984) with a variety of minor metallic elements, but usually with enrichment in Co, Pb, and Ni.
- (2) Iron-poor vernadite. A peculiar iron-poor manganese oxide occurring as old substrates or

nuclei of younger crusts or nodules (iron-rich vernadite) only from Pacific seamounts in places. The XRD pattern is the same as above. Minor metallic elements and detrital minerals (Si and Al) are significantly lower than in iron-rich vernadite. In contrast Pt and P are often enriched.

(3) Cu–Ni-rich busserite. A typical high Cu and Ni sheet manganate accommodating these elements as interlayer cations (Arrhenius & Tsai 1981; Giovanoli 1985*a, b*; Golden *et al.* 1986). This phase is not common in the northwest Pacific deposits, whereas it is very common in high-grade manganese nodules in the central and eastern Pacific nodule provinces. The mineral is believed to form from dissolved manganese in interstitial waters during early diagenesis of reducing surface siliceous sediments. Diagnostic reflections are 9.8–9.6 Å and 4.9–4.8 Å d-spacings together with those of vernadite in common.

(4) Cu–Ni-poor busserite. An isomorphic variation of above busserite, but without divalent transition metals. Mg, Ca and Na may occupy the interlayer cation sites instead. This phase is occasionally observed in low-temperature hydrothermal vents. However, it can form during rapid supply of dissolved manganese from highly reduced sediments and subsequent oxidation by normal sea water. The mineral in some samples shows 7 Å and 3.5 Å reflections on dehydration in air at room temperature. This is the phase that is called birnessite in the literature.

(5) Todorokite. A tunnel-structure manganate typically of hydrothermal origin (Turner & Buseck 1981; Post & Bish 1988). Ba and Mg may be minor essential elements, but other metallic elements are generally negligible. XRD pattern is similar to Cu–Ni rich busserite but can be discriminated by thermal treatment (Usui *et al.* 1989).

Besides common occurrences of the above five types of manganese minerals, very rare occurrences of pyrolusite and rhodochrosite are reported. Pyrolusite (β -MnO₂) has been observed in association with fossil hydrothermal manganese deposits from shallow inactive seamounts in the Bonin ridge (Usui *et al.* 1986; Yuasa & Nishimura, unpublished). They may be of hydrothermal or subaerial weathering origin. Pyrolusite was reported also to occur in an active submarine volcano from the Yap arc just south of the study area (Hein *et al.* 1992). Rhodochrosite was described as a secondary mineral in organic-rich sediments at depths of 60–730 m below the sea floor in an ODP core from the Japan Basin (Matsumoto 1992).

Accessory minerals associated with oxide layers are mostly silicate minerals incorporated during growth; quartz, plagioclase, and clay minerals. Apatite and calcite are common in nodules and crusts from topographic highs.

Bulk chemistry

The bulk chemical composition of manganese deposits in the northwest Pacific varies widely; for example from less than 0.2–4000 for Mn/Fe ratio, and from a few ppm to 1.5 wt% Co. The great variability in the bulk composition of the manganese deposits is primarily determined by variable amounts of the mineral components of different origins listed above. Figures 5 and 6 illustrate well the separated modes of occurrences of hydrothermal versus hydrogenetic and diagenetic deposits. The concentrations of manganese and iron are also diluted by incorporated detrital particles, such as sediments and rock particles. The conventional ternary plot of minor metal elements to Mn and Fe again distinguishes well different deposit types (Fig. 7).

Hydrothermal manganese deposits show the most characteristic chemical composition; very high Mn/Fe ratio and very low concentrations of metallic elements, such as Cu, Ni, Co, Pb, Zn, V, Y, U, Th and REEs (Figs 5 & 8). The detrital components, as reflected by Si, Al, and Ti contents, are also generally low. By contrast, Mg and Ba, which may be essential to todorokite formation (Golden *et al.* 1986, 1987), are significantly high, and Li, Mo, Zn and Cd are occasionally high. These hydrothermal manganese deposits are commonly associated with modern active submarine volcanoes (Cronan *et al.* 1982; Hein *et al.* 1987; Uspenskaya *et al.* 1990; Usui *et al.* 1989; Iizasa *et al.* 1993). The most extensive distribution has been described to occur in the Bonin (Ogasawara) and Mariana volcanic arcs, and less frequently in the Kuril arc. Smaller modern hydrothermal manganese deposits were found in the backarc depression in the Okinawa Trough and Bonin backarc rifts. Similar deposits occur on inactive ridges and spreading centers as records of past low-temperature hydrothermal activity (Shterenberg *et al.* 1989, 1990; Usui *et al.* 1986). Fossil hydrothermal manganese deposits often serve as nuclei for hydrogenetic nodules and as substrates of hydrogenetic crusts on seamounts of remnant arcs (e.g. Nishi–Shichito ridge and Kyushu–Palau ridge, Usui *et al.* 1986). Fragments of the deposits were collected on seamounts in the Japan Sea, Philippine Sea, Shatsky Rise and in ODP drill cores (Usui 1992). The chemical and

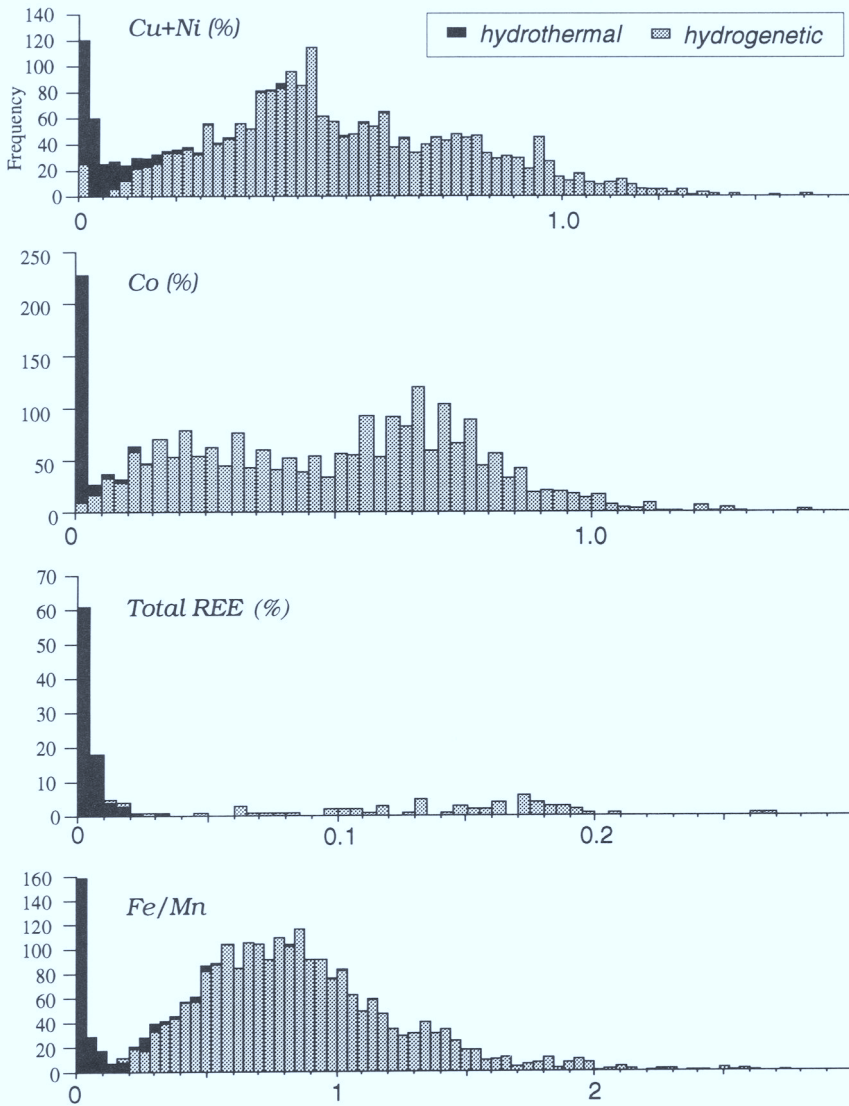


Fig. 5. Frequency diagrams of Cu, Ni, Co and REE for bulk samples and Fe/Mn ratio, showing bimodal distribution that reflects origin of deposits.

mineralogical characteristics are similar to those of modern deposits, but Ba is more abundant in fossil deposits. There is no other clear compositional difference between modern and fossil deposits.

Hydrogenetic nodules and crusts are widely distributed on topographic highs and/or on outcrops of old rocks. As inferred from slow rates of growth of hydrogenetic deposits, thicker oxide layers of nodules and crusts correlate with older substrate rocks (Fig. 3). The mean lowest growth rate may be about several mm per million years or less. Mineralogically, the crust

and nodules are composed chiefly of iron-rich vernadite regardless of place of formation. The most typical chemical characteristic is high Fe, in general, and high contents of the minor metals, such as Co, Ni, Pb, Y V and Pt. Among hydrogenetic deposits (nodules and crusts), there are some secondary minor differences associated with different geological and geophysical environments (Fig. 8); between basins and seamounts and between Pacific and marginal seas. High Co, Pt and Ni are associated only with Pacific seamount deposits. Pb is generally high in seamount deposits in the Pacific and marginal

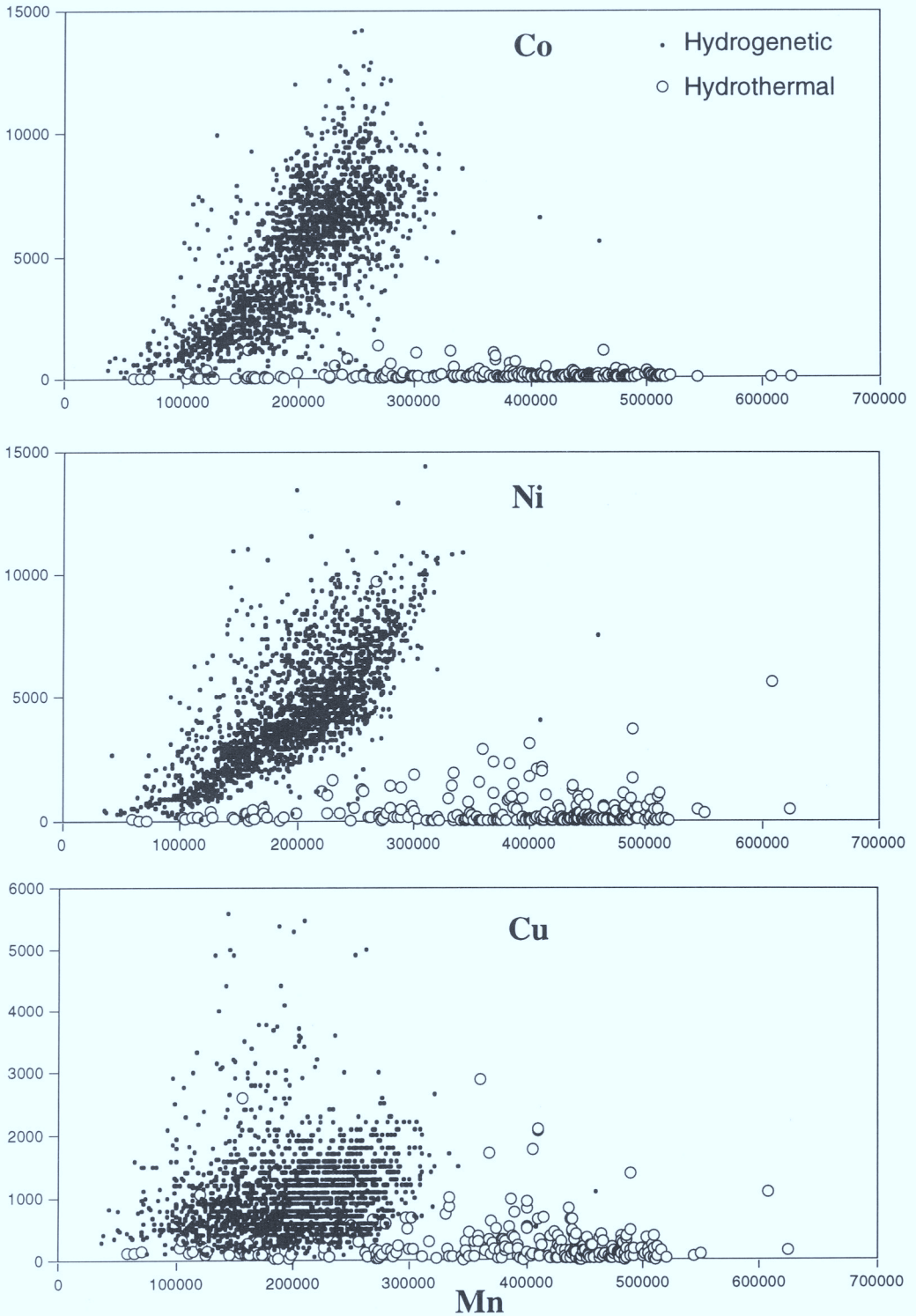


Fig. 6. Correlation plots of Co, Ni, and Cu versus Mn. Co and Ni show similar abundances and pattern, while Cu contents are significantly lower and scattered.

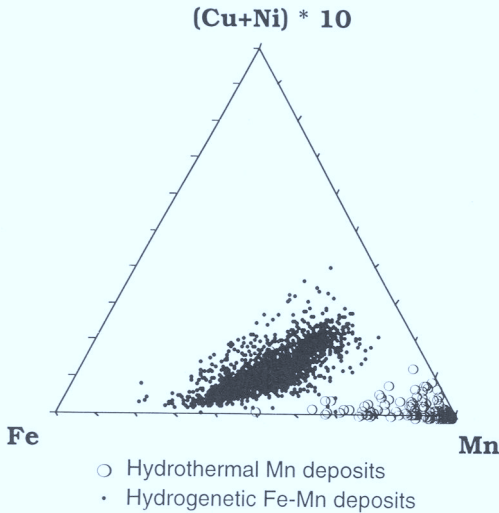


Fig. 7. Ternary diagram of (Cu + Ni)-Mn-Fe for manganese deposits from this area.

seas, whereas Cu displays the opposite behavior. Other elements (alkali, alkali earth and some other metals) show no significant differences with environments.

The evidence for early diagenetic influence on the composition of manganese deposits from surface sediments is not clear, except for slightly higher Cu in basin nodules of the Pacific and the marginal seas than those from seamounts. However, the averaged concentration of Cu of the basin nodules is 4 or 5 times lower than in those of high-grade nodule in the central-eastern Pacific basin. In fact, buserite is very rarely identified in basin nodules from the northwest Pacific.

Variations with water depth

The relationship between element concentrations and water depth has been reported by previous investigators especially in the central Pacific seamount areas (Halbach *et al.* 1986a; Aplin & Cronan 1985; De Carlo *et al.* 1987). Halbach *et al.* (1983), for instance, pointed out a decrease of Co and Ni within the 1000–4500 m water depth range. However, in some places, this apparent depth dependency can be explained simply by different origins of the deposits (McKelvey *et al.* 1983). Here the relationship of metal concentration to water depth is evaluated only for selected hydrogenetic nodule and crust deposits for 31 elements. Of these, Mn (or Mn/Fe), Co, Pt, Ca, P and, possibly, Ti, Ni, Pb and Zn, are enriched in deposits at water depths between 1000 and 2500 m relative to

deeper water deposits (Fig. 9). However, no clear systematic decrease of the contents of these elements with increasing water depth is observed. The range of high concentrations of Mn, Co, and Pt is consistent with the idea of redistribution of the metals through the oxygen minimum zone (Halbach 1986b), taking the subsidence of the seamounts into account. Deposits with high Mn/Fe ratios (2–10) are not associated with high Ni and Cu or with the diagenetic mineral buserite. This suggests that the enrichment of Ni is not caused by post-depositional ion-exchange as with surficial sediments (Giovanoli & Brtsch 1979; Usui 1979; Arrhenius & Tsai 1981; Golden *et al.* 1987). It may rather reflect a physicochemical condition of sea water in which the colloidal particles of vernadite were formed. High Mn/Fe without Co and Ni enrichment in vernadite is typical of Pacific seamount crusts and nodules, but this deposit type does not occur in marginal deposits.

REE patterns

REE abundances and normalized patterns often reflect depositional processes and environment of formation. The mean total REE for selected deposits (more than eight elements analysed) from the northwest Pacific is about 1400 ppm for hydrogenetic deposits and about 40 ppm for hydrothermal deposits. The iron-rich hydrogenetic crusts and nodules show high total REE abundances but hydrothermal manganese deposits are significantly low, because REEs are scavenged from sea water by settling iron-manganese oxide (Elderfield *et al.* 1981). Distinct differences in abundance between hydrothermal and hydrogenetic deposits is noted in Fig. 10 compiled from 64 data sets.

The Ce anomaly, $Ce^* = 3 \times Ce / (2 \times La + Nd)$, shows discrete ranges for hydrogenetic and hydrothermal deposits. Ce^* for hydrogenetic crusts from seamounts (Pacific and marginal) ranges from 1.1 to 4.4 (average 2.0), while that of hydrothermal deposits ranges from 0.15 to 0.96 (average 0.57). Marginal basin nodules, presumably influenced by an early-diagenetic process (slight enrichment of Cu), have a negative Ce anomaly (average 0.66) despite high total abundance. These distinct differences in REE pattern with depositional environments agree with the idea that Ce anomaly is an indicator of redox condition of formation of marine manganese deposits (Glasby *et al.* 1987; De Carlo & McMurtry 1992). Hydrogenetic deposits may be related to oxygenated bottom water, diagenetic deposits to suboxic surface

sediments caused by decomposition of organic matter, and hydrothermal deposits to anoxic hydrothermal water supplied from substrate rocks.

Discussion and summary

The compositional variability with changing geological province was characterized for the northwest Pacific based on a manganese deposit database. The great variability of occurrences and compositions is largely controlled by topography and tectonic history, which affect sedimentary and oceanographic conditions. The characteristics of manganese deposits in the following geological environments are summarized in terms of deposit types, geochemical characteristics and growth history. Figure 11 summarizes the distribution of manganese deposits in terms of origin and geological provinces.

Marine manganese deposits in the area are classified broadly into (A) slowly deposited hydrogenetic iron-manganese deposits and (B) rapidly deposited hydrothermal manganese deposits. Each category is subdivided as follows.

(A1) *Pacific basin nodules*. Hydrogenetic manganese nodules are sparsely distributed on the abyssal sea floor with a few percent frequency of occurrence, despite the very old age of the lithosphere and great water depth (5500–6000 m). This paucity of nodules probably results from a very rapid sedimentation rate and subsequent burial of nodules by younger hemipelagic and biogenic sediments during the Neogene to Quaternary, as revealed in DSDP/ODP drill cores (Shipboard Scientific Party 1985; Usui & Ito 1994). The rarely occurring nodules are of hydrogenetic origin with moderate Cu, Ni and Co contents. Early-diagenetic influence is probably negligible, though cannot be ruled out.

(A2) *Pacific seamount crusts and nodules*. Hydrogenetic manganese crusts, nodules, and coated talus are nearly ubiquitously distributed over topographic highs at depths above 5000 m. The thickness of oxide layers is the greatest within the northwest Pacific, with an average of about 30 mm and up to a maximum 150 mm. The crest and flanks of seamounts, guyots, and plateaus are often covered with nodules and crust pavements at depths of 800–2500 m where calcareous sediments are absent or being eroded. The Cretaceous–Oligocene limestones, mostly phosphatized, often serve as substrates for crusts and as nuclei for nodules. Two distinct hydrogenetic components occur; normal Co- and Ni-rich young crusts (iron-rich vernadite) and

high Mn/Fe, Pt and P older crusts (iron-poor vernadite). REE patterns of both types show a high total abundance and a typical positive Ce anomaly. The iron-poor vernadite crust is unique, and common in the older generation crusts from the Mid-Pacific Mountains area (Halbach 1986b). This older-generation crust may reflect a specific palaeoceanographic environment, such as change in deep-water circulation, the extent of oxygen minimum zone, etc. Further global correlation of manganese deposits is needed to delineate paleoceanographic reconstructions in space and time.

(A3) *Marginal seamount crusts and nodules*. Crusts and nodules with moderately thick oxide layers are often associated with topographic highs on volcanically inactive ridges. No significant differences were found in the composition of hydrogenetic nodules and crusts among the three areas representative of this geological setting: Daito ridges, Kyushu–Palau ridge, and Nishi–Shichito ridge, with decreasing age. The chemical composition and appearance are similar to Pacific seamount crusts and nodules, except for lower Mn/Fe ratio and lower contents of Co, Pt and possibly Ni. These depletions may be related to poor development of an oxygen minimum zone at the middle depths in the western margin of the Pacific Ocean (Chester 1990). The mean maximum crust and nodule thickness increases with age of these remnant arcs. Despite fairly uniform chemical compositions throughout these environment, the local variations in mode of occurrence and thickness of oxide layers are great as revealed by submersible observations (Usui *et al.* 1994) on seamounts. The nuclei and substrates of the deposits are composed of various materials, such as volcanic rocks, sedimentary rocks, acidic plutonic rocks, etc.

(A4) *Marginal basin abyssal nodules*. Manganese oxide deposits rarely occur in marginal basins (Japan, Okhotsk, Shikoku, Parece Vela and Philippine basins), largely because the basins have been supplied with abundant terrigenous and volcanogenic input. Even though pelagic environments exist, for example in Shikoku basin, nodules are also rare. This paucity of abyssal nodules is probably related to topographic controls on water circulation since formation of the basins. The long and shallow island-arcs, now being transformed into remnant arcs, would have inhibited the northward inflow of oxygenated bottom waters into the basins, which is inferred from Oligocene and younger tectonic reconstructions (Seno & Maruyama 1984; Drummond *et al.* 1985). These closed basins can yield only local small manganese

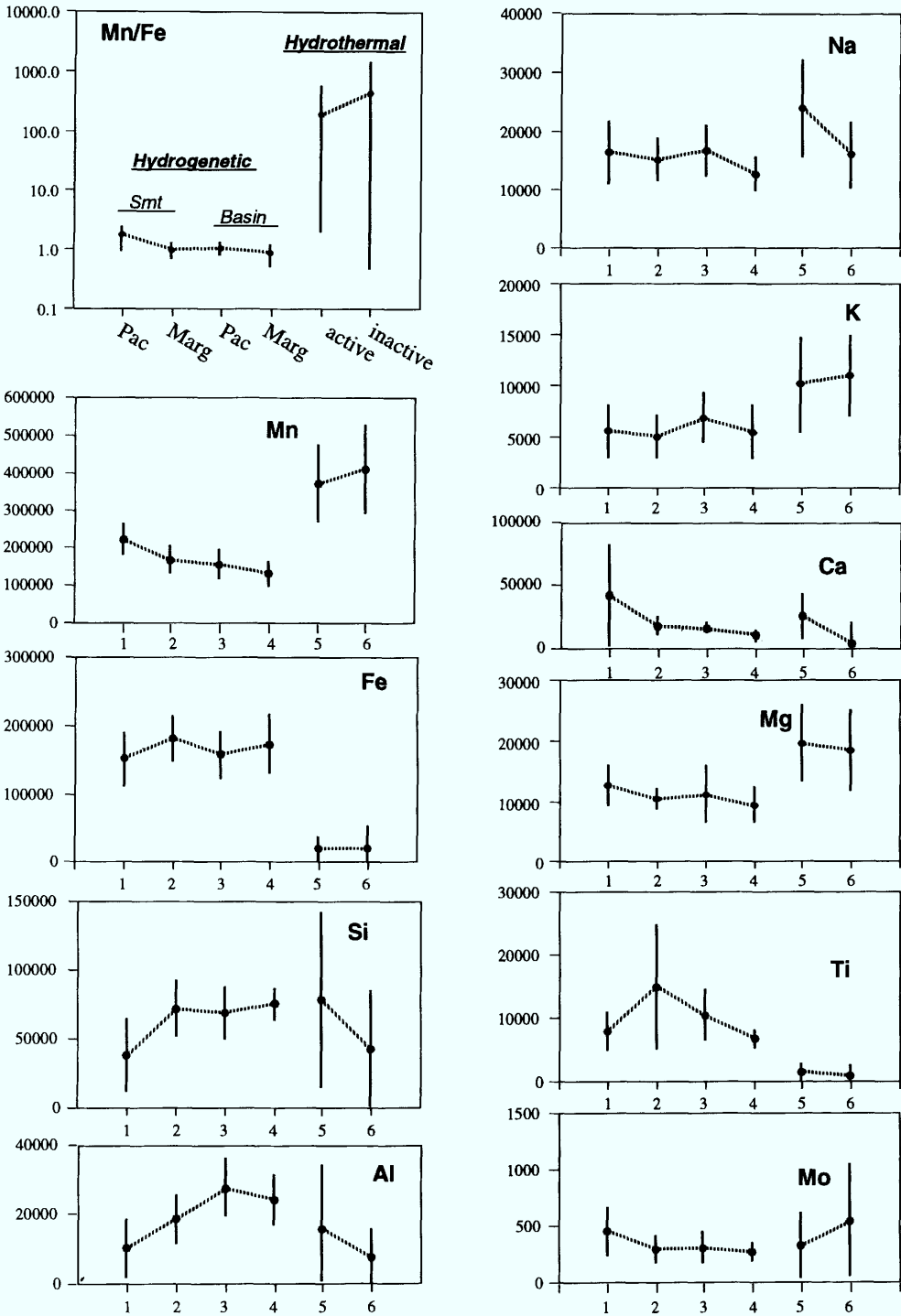


Fig. 8. Variation of element concentration with geological provinces. 'Pac' and 'Marg' mean Pacific Ocean and marginal seas, respectively. A vertical bar ranges between mean (dot) and ± 1 standard deviation. Numerical data are from Table 2.

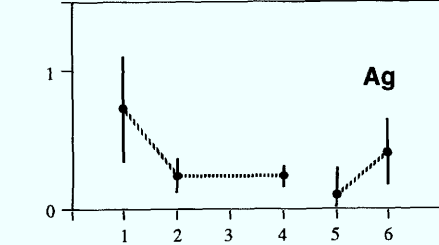
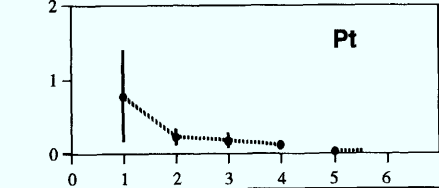
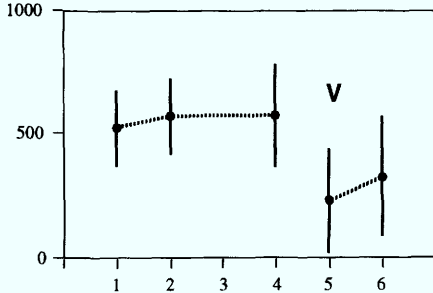
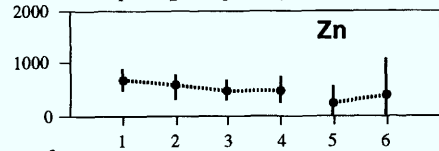
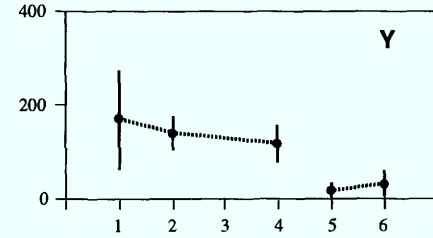
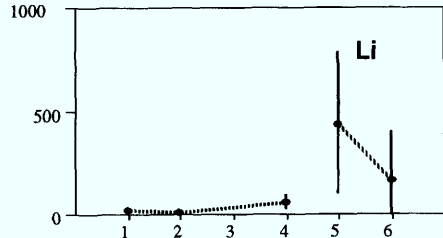
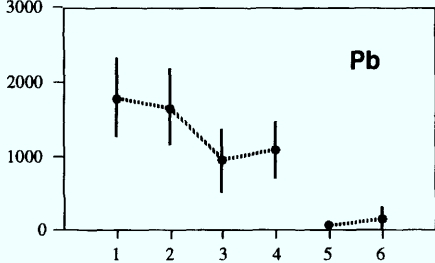
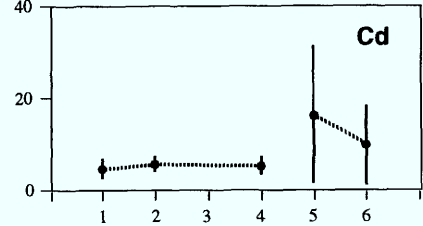
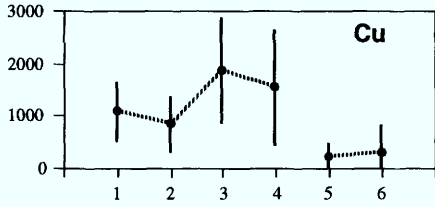
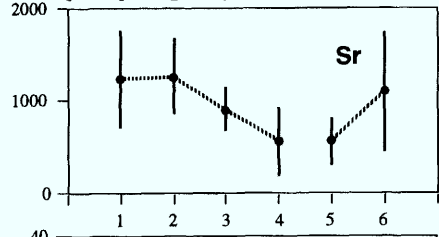
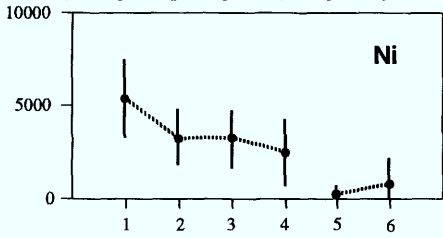
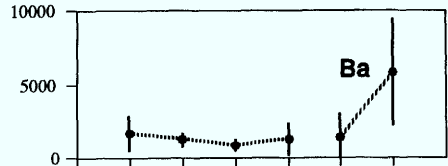
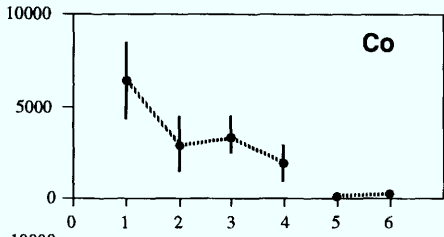


Table 2. Chemical composition of manganese deposits

Depth	Hydrogenetic																			
	Pacific seamounts					Marginal seamounts					Pacific abyssal plains					Marginal abyssal plain				
	Ave	Max	Min	SD	n	Ave	Max	Min	SD	n	Ave	Max	Min	SD	n	Ave	Max	Min	SD	n
Mn	220625	459000	72000	41947	1478	166001	319900	64078	36959	417	154441	272000	37600	39624	59	131328	210000	67378	35186	118
Fe	150866	360264	28800	40029	1478	179896	322000	85500	33937	417	156906	218900	25000	34962	59	172266	321000	97400	43381	118
Cu	1075	5600	50	561	1418	847	5382	130	527	417	1864	5000	400	1001	57	1540	5470	370	1096	118
Ni	5403	14400	340	2020	1427	3277	10000	230	1479	417	3238	7080	210	1534	59	2488	7500	380	1747	118
Co	6371.8	14200.0	300.0	2042.2	1440	2905.2	10218.0	131.0	1515.6	416	3320.7	6060.0	700.0	1396.3	59	1861.1	5380.0	90.0	1009.2	117
Zn	680	1500	294	215	335	606	1480	312	162	296	487	810	200	179	17	491	1480	90	237	103
Pb	1777	3200	150	526	307	1643	3510	94	521	265	930	2090	200	422	25	1070	1650	238	392	50
Si	36924	127376	1000	26416	273	70962	128732	34300	19841	178	67792	140900	41400	18872	35	74220	102800	62400	12135	13
Al	10164	53000	1100	8308	328	18192	45968	4800	6982	218	27322	49000	12400	8578	39	23590	38600	11300	7253	34
Na	16321	47000	7641	5416	175	15046	34816	3330	3720	125	16486	28116	11276	4442	21	12530	23700	9600	2868	29
K	5568	15800	1502	2541	177	5049	18275	1982	2112	157	6877	14445	4200	2448	25	5436	18200	2900	2666	35
Ca	41384	23500	1700	40679	374	17161	90000	800	8171	237	15477	22513	1450	4793	35	9431	20000	1000	5291	42
Mg	12612	35000	3200	3367	342	10390	19951	6400	2276	176	11133	30880	3200	4817	30	9378	16000	5300	3053	37
Ti	7736	20800	400	2938	370	14678	38400	2100	9829	165	10331	15105	1800	3933	20	6561	11014	4000	1422	28
Ba	1695	18000	500	1224	266	1285	3314	690	389	99	853	1300	448	273	15	1326	5800	594	1091	20
Sr	1212	2900	135	536	166	1248	1860	54	407	131	887	1110	150	309	10	546	1163	32	364	31
V	515	1019	93	152	163	566	1062	284	150	101	-	-	-	-	-	570	992	301	209	28
Mo	455	1530	3	223	172	297	643	80	119	97	313	560	180	144	6	273	385	128	77	20
Li	63	110	16	66	2	4	9	3	2	8	-	-	-	-	-	15	45	3	15	10
Zr	172	602	4	153	76	135	528	2	178	43	650	650	650	-	1	207	541	3	207	27
B	115	206	57	40	37	-	-	-	-	-	-	-	-	-	-	-	-	-	-	-
Y	166.3	700.0	15.5	104.6	104	135.6	198.0	41.2	36.0	45	-	-	-	-	-	117.1	195.8	22.4	40.0	28

Table 2. (continued)

	Hydrothermal										All data				
	Modern					Fossil					Ave	Max	Min	SD	n
	Ave	Max	Min	SD	n	Ave	Max	Min	SD	n					
Depth	1294	2975	172	389	132	1739	8350	110	1101	116	2089	8350	110	1150	2317
Mn	369749	550100	105000	102369	132	410764	804000	113500	120221	118	222735	804000	37600	83291	2322
Fe	18703	91000	190	20053	132	18349	256600	100	34318	118	143073	360264	100	58605	2322
Cu	228	1700	18	239	130	322	2870	5	511	103	993	5600	5	672	2243
Ni	287	2400	1	429	132	765	9750	10	1369	110	4279	14400	1	2450	2263
Co	72.3	1103.0	2.0	159.3	128	162.2	1350.0	0.5	230.2	107	4774.7	14200.0	0.5	2860.9	2267
Zn	238	1427	8	299	132	395	5330	1	697	98	547	5330	1	336	981
Pb	45	460	1	69	99	126	815	1	162	72	1310	3510	1	808	818
Si	77316	184000	1700	63286	25	41717	144400	900	42068	27	52828	184000	900	32339	551
Al	15697	73000	300	18670	90	7203	45400	350	8188	77	14166	73000	300	11076	786
Na	23710	41700	5700	8167	86	15957	42879	4080	5780	73	16995	47000	3300	6370	509
K	10130	20300	1600	4611	69	10947	23400	332	4007	66	6733	23400	332	3749	529
Ca	24838	97600	6900	17947	90	19302	218000	2400	32113	84	28236	235000	800	31809	862
Mg	19513	35000	6800	6182	90	18336	36000	2400	6692	79	13300	36000	2400	5219	754
Ti	1466	4300	85	1278	48	792	9700	60	1554	42	8585	38400	60	6803	673
Ba	1376	9800	242	1727	86	5871	18000	358	3538	63	2014	18000	242	2156	549
Sr	555	1890	280	249	90	1080	3500	240	640	71	1036	3500	32	545	499
V	225	926	5	209	63	322	1110	47	239	47	464	1110	5	217	402
Mo	327	1840	27	289	90	533	2500	60	517	72	399	2500	3	297	457
Li	436	1090	4	342	35	164	1210	8	240	44	230	1210	3	304	99
Zr	23	88	4	19	35	29	340	8	57	33	125	650	2	162	215
B	—	—	—	—	—	100	100	100	—	1	115	206	57	39	38
Y	17.1	75.0	0.7	14.0	59	29.6	140.0	1.9	26.9	33	106.5	700.0	0.7	93.5	269

Table 2. (continued)

	Hydrogenetic																				
	Pacific seamounts					Marginal seamounts					Pacific abyssal plains					Marginal abyssal plain					
	Ave	Max	Min	SD	n	Ave	Max	Min	SD	n	Ave	Max	Min	SD	n	Ave	Max	Min	SD	n	
As	165.0	385.1	9.0	77.3	106	148.2	288.8	13.0	61.5	41	-	-	-	-	-	145.6	232.6	77.0	38.7	19	
W	93.3	250.0	14.0	56.8	44	33.6	83.0	11.0	18.7	30	-	-	-	-	-	25.0	38.0	10.0	9.5	11	
Cr	22.4	60.0	2.6	12.3	67	25.2	62.0	6.7	8.8	51	-	-	-	-	-	26.8	65.0	8.6	9.3	30	
Sb	24.4	48.8	13.0	8.1	47	24.3	39.7	7.0	7.8	39	-	-	-	-	-	25.2	33.0	11.0	6.0	18	
Nb	-	-	-	-	-	31.4	50.5	4.2	19.4	7	-	-	-	-	-	43.0	51.0	29.6	7.9	9	
Rb	-	-	-	-	-	18.4	40.0	10.0	12.5	5	-	-	-	-	-	17.5	33.0	10.0	8.8	8	
Th	32.97	64.00	9.43	15.27	12	28.68	35.40	15.70	6.86	6	-	-	-	-	-	65.55	88.50	42.60	32.46	2	
Cd	4.6	15.0	1.5	2.0	63	5.5	10.0	2.3	1.6	38	-	-	-	-	-	4.9	12.0	2.0	2.0	20	
Hf	7.4	10.0	5.1	2.0	6	-	-	-	-	-	-	-	-	-	-	-	-	-	-	-	-
Sc	6.4	20.9	0.5	3.6	64	7.6	11.9	4.9	1.8	40	-	-	-	-	-	10.2	16.4	7.0	2.9	18	
U	9.6	9.7	9.4	0.2	2	9.6	11.3	8.3	1.1	5	-	-	-	-	-	7.5	8.6	6.4	1.6	2	
Ag	0.717	1.200	0.015	0.381	32	0.239	0.500	0.100	0.124	18	-	-	-	-	-	0.229	0.300	0.100	0.076	7	
Pt	0.777	3.100	0.060	0.613	113	0.218	0.710	0.070	0.114	82	0.165	0.330	0.080	0.112	4	0.119	0.190	0.080	0.036	7	
F	0.34	1.30	0.01	0.48	8	-	-	-	-	-	-	-	-	-	-	-	-	-	-	-	-
Se	0.40	1.20	0.05	0.34	23	-	-	-	-	-	-	-	-	-	-	-	-	-	-	-	-
La	202.2	450.0	21.5	79.3	66	228.2	538.0	62.0	114.6	46	-	-	-	-	-	228.4	525.0	55.0	122.2	27	
Ce	1104.6	2100.0	173.9	371.3	48	740.6	1028.0	355.0	214.3	15	-	-	-	-	-	918.4	1427.0	132.0	381.0	12	
Pr	106.2	122.0	82.0	11.8	11	51.4	58.6	43.3	7.7	3	-	-	-	-	-	47.9	55.2	40.5	10.4	2	
Nd	162.4	360.0	94.0	68.0	25	259.4	356.0	140.0	79.9	12	-	-	-	-	-	220.8	358.0	34.0	91.2	11	
Sm	41.58	74.00	24.00	12.61	26	45.58	57.70	30.80	9.46	6	-	-	-	-	-	47.50	55.70	39.30	11.60	2	
Eu	9.90	19.00	4.30	3.23	26	10.40	13.70	6.58	2.59	6	-	-	-	-	-	11.38	13.40	9.35	2.86	2	
Gd	26	96	4	29	13	57	64	47	9	3	-	-	-	-	-	53	60	45	10	2	
Tb	7.53	12.80	1.90	3.21	26	6.86	9.00	4.42	1.67	6	-	-	-	-	-	7.25	8.60	5.90	1.91	2	
Dy	57.8	102.0	4.0	32.4	11	46.3	52.1	38.9	6.7	3	-	-	-	-	-	40.5	48.8	32.1	11.8	2	
Ho	6.6	15.0	3.0	2.8	19	8.9	10.0	7.6	1.2	3	-	-	-	-	-	7.3	8.9	5.7	2.3	2	
Er	31.9	35.0	26.0	2.7	11	24.7	27.8	21.0	3.4	3	-	-	-	-	-	20.2	24.6	15.8	6.2	2	
Tm	4.3	8.0	2.0	2.4	19	3.5	3.9	3.0	0.5	3	-	-	-	-	-	2.9	3.5	2.2	0.9	2	
Yb	17.66	34.00	5.00	8.51	27	19.37	23.90	16.80	2.83	6	22.00	22.00	22.00	-	1	17.85	21.70	14.00	5.44	2	
Lu	3.34	6.60	0.98	1.21	26	3.22	3.72	2.93	0.29	6	-	-	-	-	-	2.77	3.32	2.22	0.78	2	
P	11773	125000	200	16175	332	3895	19013	900	1920	165	2033	4801	1004	1140	19	2258	3551	1300	488	24	
S	3053	4448	1842	12	-	-	-	-	-	-	-	-	-	-	-	-	-	-	-	-	-
Mn/Fe	1.63	9.16	0.27	0.76	1478	0.95	2.32	0.24	0.28	417	1.01	1.71	0.55	0.26	59	0.81	2.07	0.23	0.32	118	

Table 2. (continued)

	All data														
	Hydrothermal						Fossil								
	Ave	Max	Min	SD	n		Ave	Max	Min	SD	n				
As	33.1	160.0	0.8	36.4	78	52.5	170.0	4.0	38.9	58	105.8	385.1	0.8	82.4	302
W	31.6	144.0	9.8	23.7	59	56.8	149.0	1.3	30.5	48	52.0	250.0	1.3	42.5	192
Cr	47.8	127.0	1.0	42.9	68	63.7	114.0	2.0	34.9	51	37.8	127.0	1.0	31.8	267
Sb	25.5	130.0	0.8	31.7	60	27.1	108.0	5.4	21.6	53	25.4	130.0	0.8	20.4	217
Nb	9.9	28.1	4.6	3.8	34	9.9	14.7	6.0	2.3	31	15.4	51.0	4.2	13.2	81
Rb	—	—	—	—	—	—	—	—	—	—	17.8	40.0	10.0	9.9	13
Th	0.65	6.63	0.03	1.58	24	0.97	3.17	0.02	0.99	17	11.98	88.50	0.02	19.05	61
Cd	16.1	62.0	0.2	14.9	49	9.6	33.0	1.0	8.4	42	8.4	62.0	0.2	9.4	212
Hf	—	—	—	—	—	3.7	4.8	1.4	2.0	3	6.1	10.0	1.4	2.6	9
Sc	3.8	17.6	0.5	3.8	57	2.1	14.5	0.1	2.5	54	5.3	20.9	0.1	3.9	233
U	2.1	10.1	0.2	2.6	27	2.4	11.0	0.1	2.8	16	3.4	11.3	0.1	3.6	52
Ag	0.283	1.700	0.100	0.371	18	0.400	0.700	0.100	0.233	8	0.448	1.700	0.015	0.374	83
Pt	0.015	0.064	0.005	0.020	13	—	—	—	—	—	0.490	3.100	0.005	0.537	219
F	—	—	—	—	—	—	—	—	—	—	0.34	1.30	0.01	0.48	8
Se	0.12	0.35	0.02	0.13	5	0.11	0.19	0.02	0.12	2	0.33	1.20	0.02	0.33	30
La	18.9	70.8	0.2	15.8	61	27.7	84.0	1.2	19.3	50	130.2	538.0	0.2	122.6	250
Ce	16.3	160.0	0.2	28.7	76	25.8	160.0	0.9	34.0	34	417.6	2100.0	0.2	539.3	185
Pr	—	—	—	—	—	—	—	—	—	—	88.6	122.0	40.5	28.0	16
Nd	7.2	35.7	0.7	10.4	16	24.4	82.7	1.7	32.0	9	136.1	360.0	0.7	113.7	73
Sm	0.99	7.46	0.08	1.66	27	4.24	21.30	0.12	6.96	12	20.92	74.00	0.08	22.17	73
Eu	0.28	2.10	0.03	0.45	27	1.05	5.06	0.02	1.72	12	4.97	19.00	0.02	5.28	73
Gd	—	—	—	—	—	—	—	—	—	—	34	96	4	28	18
Tb	0.25	2.13	0.02	0.44	27	0.78	5.06	0.02	1.47	12	3.66	12.80	0.02	4.07	73
Dy	—	—	—	—	—	—	—	—	—	—	53.5	102.0	4.0	27.6	16
Ho	—	—	—	—	—	—	—	—	—	—	7.0	15.0	3.0	2.7	24
Er	—	—	—	—	—	—	—	—	—	—	29.1	35.0	15.8	5.4	16
Tm	—	—	—	—	—	—	—	—	—	—	4.1	8.0	2.0	2.2	24
Yb	0.78	4.46	0.11	0.95	27	2.84	13.00	0.12	4.11	13	9.32	34.00	0.11	9.99	76
Lu	0.14	0.74	0.03	0.16	27	0.28	1.11	0.02	0.39	12	1.63	6.60	0.02	1.73	73
P	1272	4700	250	750	59	2326	29600	131	4458	42	7515	125000	131	12558	641
S	640	1100	200	358	5	1500	2200	800	990	2	2255	4448	200	1318	19
Mn/Fe	188.50	2421.00	1.88	378.48	132	423.08	4893.00	0.44	939.04	118	33.49	4893.00	0.23	250.07	2322

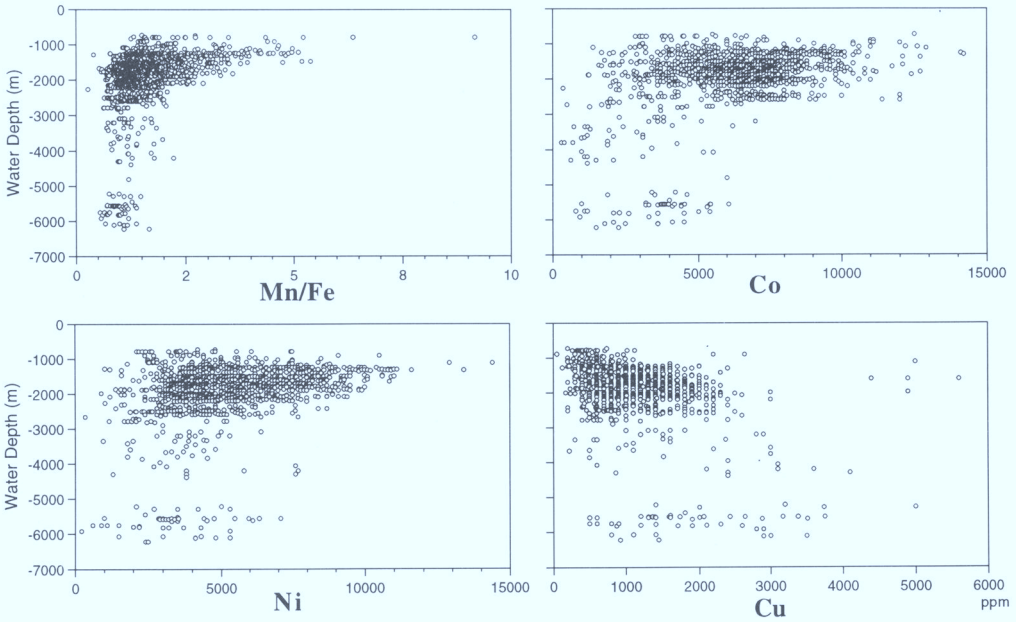


Fig. 9. Variation of element concentration with water depth. Note the different ranges of enrichment between (Co, Ni) and Mn/Fe. Cu shows no correlation.

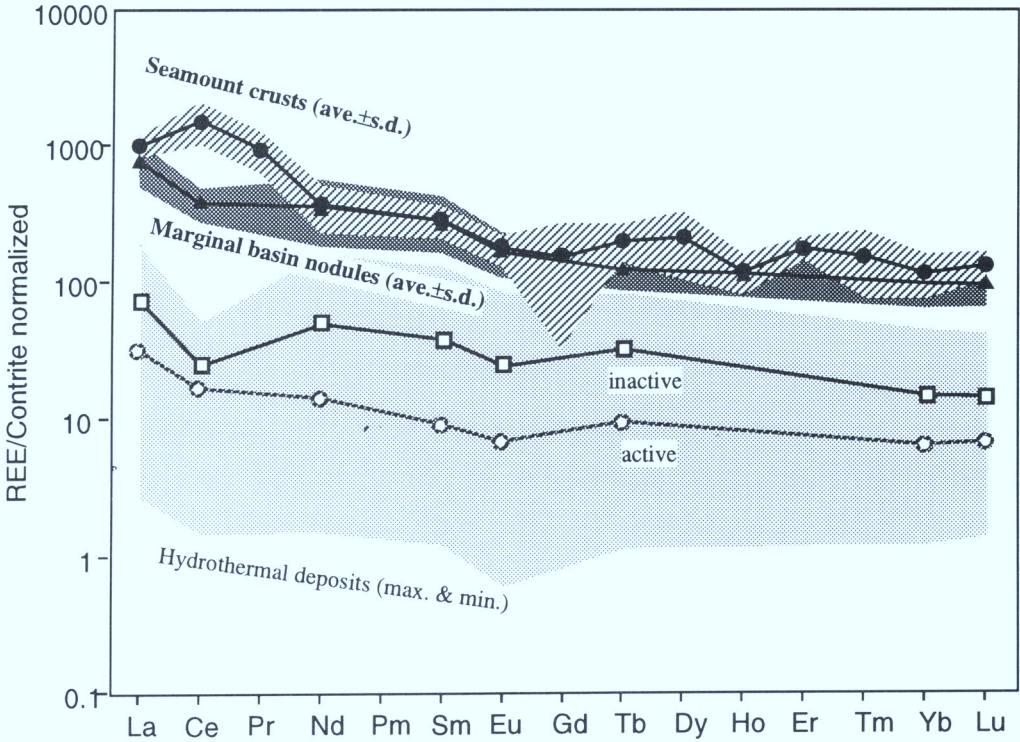


Fig. 10. REE patterns of hydrogenetic and hydrothermal deposits ($n = 64$). Note the marked differences in abundance and Ce anomaly with genetic types.

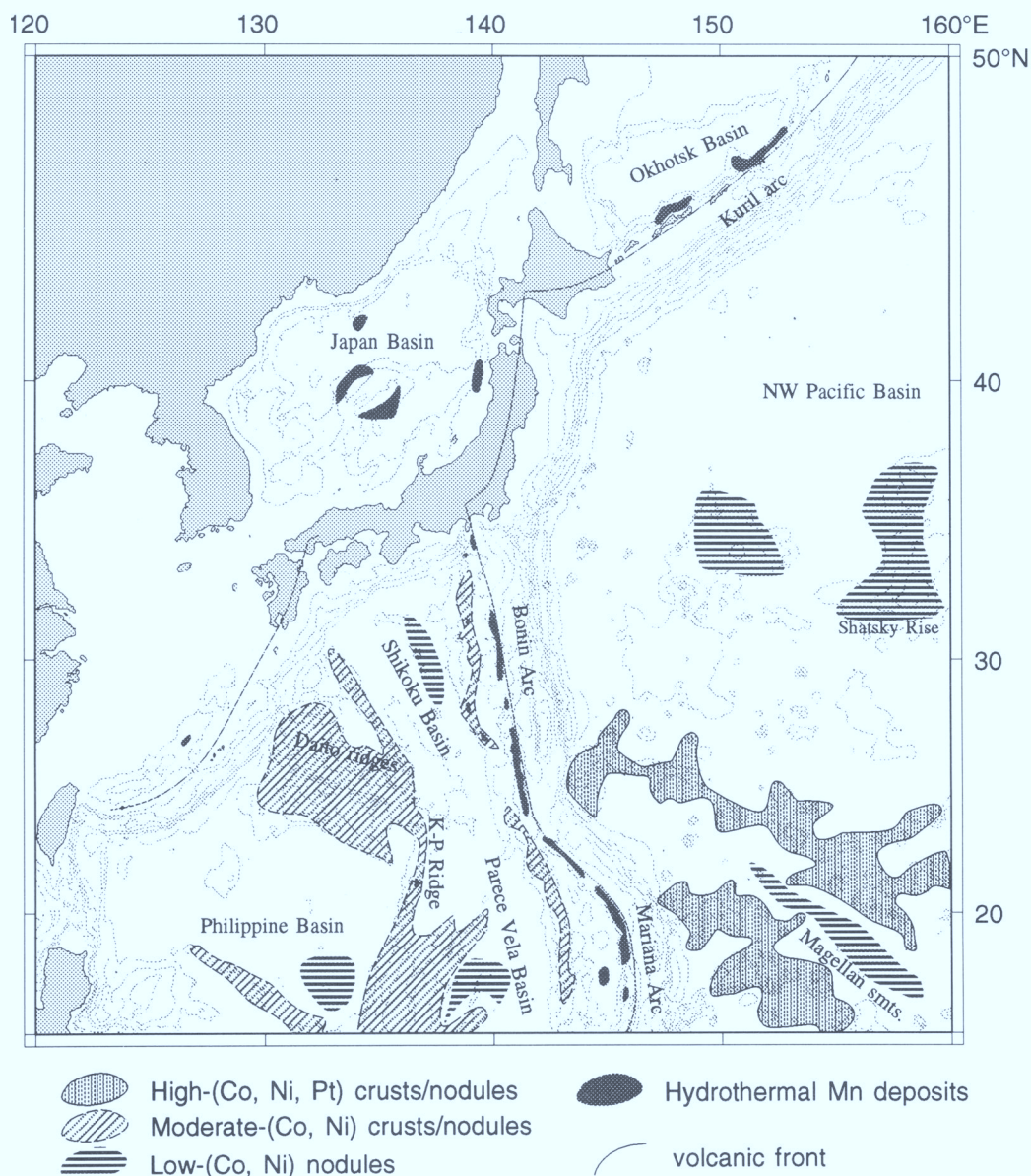


Fig. 11. Summary of distribution of hydrogenetic and hydrothermal manganese deposits in terms of geological provinces. Blank regions denote non- or rare occurrence.

oxide deposits. For example, no substantial hydrogenetic manganese nodules or crusts occur in the Japan Sea, where the deep waters have been reducing since the Miocene (Matsumoto 1992). When present in marginal basins, the hydrogenetic deposits are almost similar in composition to those from the Pacific basins. Cu is relatively enriched in Pacific basin nodules,

but 4–5 times more depleted than typical high-grade nodules from the central and northeast Pacific, suggesting a very slight early-diagenetic influence.

(B1) *Hydrothermal Mn deposits from volcanically active ridges and rifts.* Hydrogenetic nodules and crusts are scarce due to the young age of the sea floor. Thickness of the oxide layers

is less than 1 mm, if present. By contrast, hydrothermal manganese deposits with distinct chemistry, mineralogy, and morphology are common in active submarine volcanoes and rift areas. The deposits are composed of pure manganate minerals (series of todorokite and Cu-Ni poor busserite), with very low contents of Fe, other heavy metals, and silicates (Hein *et al.* 1987; Usui *et al.* 1989; Usui & Nishimura 1992). The hydrothermal manganese minerals display crystal sizes ranging from clay size to as large or silt size, which is clearly larger than hydrogenetic vernadite. The textures are variable; commonly forming dense homogeneous layers, dispersed in a matrix of sandstone, as network, veinlets, infilling of fossils, stalactite-like cusps, hardpan, etc. Despite their variable textures, the chemical composition is fairly constant within the areas. Alkali and alkali earth elements are minor, and Ba, Li, Mo, Zn and Cd are high in some deposits. The extent of the manganese deposits is often large and spatially continuous (e.g. Kaikata seamount, Usui & Nishimura 1992), probably due to large-scale subbottom circulation of low-temperature hydrothermal waters. The measured temperature of discharging water ranges from nearly that of bottom water to 40°C (Usui & Nishimura 1992; Kimura *et al.* 1988). The manganese deposits are sometimes associated with hydrothermal iron oxide deposits, and in some places surround sulphide mineralization.

(B2) *Fossil hydrothermal Mn deposits from inactive ridges and rifts.* Since iron and manganese oxides are relatively stable under bottom water conditions and usually within sediments, they record past hydrothermal activity. The fossil hydrothermal manganese deposits have been recorded sporadically from remnant arc seamounts (Nishi-Shichito and Kyushu-Palau ridges) and abandoned spreading centers (Japan Sea and Shatsky rise). Deposits of unknown extent were reported to occur in ODP drill cores (Usui 1992). The age of the fossil hydrothermal manganese deposits ranges from late Oligocene to Pliocene. The major mineral component is todorokite and/or Cu-Ni poor busserite, often containing high Ba and Li. The chemical characteristics are generally similar to those of modern hydrothermal deposits.

Conclusions

Based on compiled data of occurrence and composition of northwest Pacific samples, the marine manganese deposits are characterized in relation to geological settings. Hydrogenetic and

hydrothermal deposits dominate over this area. The hydrogenetic nodules and crusts occur nearly ubiquitously on topographic highs in the Pacific and the marginal seas where younger sediments are absent or being eroded. Oxide layers of hydrogenetic nodules and crusts are generally thicker in deposits on older basement. The Pacific seamount crusts and nodules are characterized by higher Pt and P and by a unique high Mn/Fe component that comprises the old crust generation. Nodules rarely occur in marginal basins and the Pacific basin probably because of recent high sedimentation rates and a lack of oxygenated deep waters owing to topographic and tectonic settings.

Hydrothermal manganese deposits are found commonly on submarine volcanoes along the modern active oceanic arcs and less frequently in backarc rifts. The deposits have a unique mineralogical and chemical composition; very high Mn/Fe ratios and very low minor elements except for Ba and Li. Manganese deposits similar in occurrence and composition were also observed in the inactive submarine volcanoes on remnant arcs and in abandoned backarc spreading centers, thereby indicating past low-temperature hydrothermal activity.

The present analysis and summary of manganese deposits show promise of economic potential of some areas on a regional scale. We can single out the hydrogenetic crusts and nodules of the Pacific seamounts and plateaus, and secondly the marginal seamounts as potential metal resources of Co, Ni and Pt. REE in these deposits may be of possible interest, though the abundance is hardly competitive with land ores. More detailed study may be focused on the marginal seamounts, such as remnant arcs on the Philippine Sea Plate, where sample locations are sparse. Hydrothermal manganese deposits seem economically less important, but can be an indicator for exploration for polymetallic sulfide deposits. Local-scale variability and comprehensive economic assessments await future detailed surveys.

The authors would like to acknowledge Carla Moore, National Geophysical Data Center, National Oceanic & Atmospheric Administration for her collaboration and efforts on their invaluable NOAA databases of marine minerals. Our data include some unpublished data provided by personal communication from the following organizations: Geological Data Center of Scripps Institution of Oceanography, US Geological Survey at Woods Hole & Menlo Park, Russian Far East Geological Institute, Institut Francais de Recherche pour l'Exploitation de la Mer (IFREMER), and Japanese organizations such as Ocean Development Office of Ministry of International Trade and Industry,

Tokai University, and University of Tsukuba. We thank workers at the Geological and Palaeontological Institute and Museum of Kiel University, Ocean Research Institute of University of Tokyo, Hydrographic Office of Maritime Agency of Japan, National Institute for Resources and Environment, Akita University, Yamagata University, and colleagues from MMAJ and GSI for helpful information. Correspondence to A. Usui (e. mail: akirau@gsj.go.jp).

References

- APLIN, A. C. & CRONAN, D. S. 1985. Ferromanganese oxide deposits from the Central Pacific Ocean, I. Encrustations from the Line Islands archipelago. *Geochimica et Cosmochimica Acta*, **49**, 427–436.
- ARRHENIUS, G. & TSAI, A. G. 1981. Structure, phase transformation and prebiotic catalysis in marine manganese minerals. *Scripps Institution of Oceanography Reference Series*, **81**–28.
- BURNS, R. G., BURNS, V. M. & STOCKMAN, H. W. 1985. The todorokite-buserite problem: further considerations. *American Mineralogist*, **70**, 205–208.
- CHESTER, R. 1990. *Marine Chemistry*. Unwin Hyman, London, 243–247.
- CRONAN, D. S., GLASBY, G. P., MOORBY, S. A., THOMSON, J., KNEDLER, K. E. & MCDUGALL, J. C. 1982. A submarine hydrothermal manganese deposit from the S. W. Pacific Island Arc. *Nature*, **298**, 456–458.
- DE CARLO, E. H. 1987. Geochemistry of ferromanganese deposits from the Kiribati and Tubalu region of the West Central Pacific Ocean. *Marine Mining*, **6**, 301–321.
- & MCMURTRY, G. M. 1992. Rare earth element geochemistry of ferromanganese crusts from the Hawaiian Archipelago, central Pacific. *Chemical Geology*, **95**, 235–250.
- DRUMMOND, K. J., NISHIWAKI, C., CORVALAN, J., DOUTCH, H. F. & CRADDOCK, C. 1985. *Plate-Tectonic Map of the Circum-Pacific Region: Pacific Basin Sheet*. Circum-Pacific Council for Energy and Mineral Resources, Houston.
- ELDERFIELD, H., HAWKESWORTH, C. J. & GREAVES, M. J. 1981. Rare earth element geochemistry of oceanic ferromanganese nodules and associated sediments. *Geochimica et Cosmochimica Acta*, **45**, 513–528.
- GIOVANOLI, R. 1985a. Layer Structures and Tunnel Structures in Manganates. *Chemie der Erde*, **44**, 227–244.
- 1985b. A review of the todorokite-buserite problem: implications to the mineralogy of marine manganese nodules: discussion. *American Mineralogist*, **70**, 202–204.
- & BRÜTSCH, R. 1979. L'échange des ions de transition par le manganate-10Å et le manganate-7Å. In: LALOU, C. (ed.) *La Genèse des Nodules de Manganèse*. Colloques Internationaux du Centre National de la Recherche Scientifique, **289**, 305–313.
- GLASBY, G. P. 1978. Deep-sea manganese nodules in the stratigraphic records: evidence from DSDP cores. *Marine Geology*, **28**, 51–64.
- , GWOZDZ, R., KUNZENDORF, H., FRIEDRICH, G. & THIJSSSEN, T. 1987. The distribution of rare earth and minor elements in manganese nodules and sediments for the equator and S. W. Pacific. *Lithos*, **20**, 97–113.
- GOLDEN, D. C., CHEN, C. C. & DIXON, J. B. 1987. Transformation of birnessite to buserite, todorokite, and manganite under mild hydrothermal treatment. *Clays & Clay Minerals*, **35**, 271–280.
- , DIXON, J. B. & CHEN, C. C. 1986. Ion exchange, thermal transformations, and oxidizing properties of birnessite. *Clays & Clay Minerals*, **34**, 511–520.
- HALBACH, P. 1986a. Processes controlling the heavy metal distribution in Pacific ferromanganese nodules and crusts. *Geologisches Rundschau*, **75**, 235–247.
- 1986b. Cobalt-rich and platinum-bearing manganese crusts: nature, occurrence, and formation. In: JOHNSON, C. L. & CLARK, A. L. (eds) *Pacific Mineral Resources – Physical, Economic, and Legal Issues*. E-W Resources System Institute, University Hawaii, 137–160.
- & ÖZKARA, M. 1979. Morphological and geochemical classification of deep-sea ferromanganese nodules and its genetical interpretation. In: LALOU, C. (ed.) *La Genèse des Nodules de Manganèse*. Colloques Internationaux du Centre National de la Recherche Scientifique, **289**, 77–89.
- , SEGL, M., PUTEANUS, D. & MANGINI, A. 1983. Co-fluxes and growth rates in ferromanganese deposits from central Pacific seamount areas. *Nature*, **304**, 716–719.
- HEIN, J. R., AHN, J. H., WONG, J. C., et al. 1992. *Geology, Geophysics, Geochemistry, and Deep-sea Mineral Deposits, Federated States of Micronesia: KORDI-USGS R. V. Farnella Cruise F11–90-CP*. US Geological Survey Open File Reports, 92–218.
- , FLEISHMAN, C. L., MORGENSTEIN, L. A., BLOOMER, S. H. & STERN, R. J. 1987. *Submarine ferromanganese deposits from the Mariana and Volcano volcanic arcs, West Pacific*. US Geological Survey Open File Reports, 87–281.
- , MORGENSON, L. A., CLAGUE, D. A. & KOSKI, R. A. 1987. Cobalt-rich ferromanganese crusts from the exclusive economic zone of the United States and nodules from the oceanic Pacific. In: SCHOLL, D. W., GRANTZ, A. & VEDDERM, J. G. (eds) *Geology and Resource Potential of the Continental Margin of Western North America and Adjacent Ocean Basins*. Circum-Pacific Council for Energy and Mineral Resources, Houston, 753–771.
- HONZA, E. & TAMAKI, K. 1985. The Bonin arc. In: NAIRN, A. E. & STEHLI, F. G. (eds) *The Ocean Basins and Margins*. Plenum, NY, 7, 459–502.
- IZASA, K., TERASHIMA, S., SASAKI, M. & MARUMO, K. 1993. Hydrothermal mineralization in the Kita-Bayonnaise submarine caldera, Izu-Ogasawara arc. *Proceedings of Japan Marine Science and Technology Center Symposium of Deep Sea Research*, **6**, 105–115.

- KIMURA, M., UYEDA, S., KATO, Y., TANAKA, T., YAMANO, M., GAMO, T., SAKAI, H., KATO, S., IZAWA, E. & OOMORI, T. 1988. Active hydrothermal mounds in the Okinawa Trough backarc basin, Japan. *Tectonophysics*, **145**, 319–324.
- MANHEIM, F. T. & LANE-BOSTWICK, C. M. 1989. *Chemical composition of ferromanganese crusts in the world ocean: A review and comprehensive data base*. US Geological Survey Open File Reports, 89–020.
- MATSUMOTO, R. 1992. Diagenetic dolomite, calcite, rhodochrosite, magnesite, and landforcite from site 799, Japan Sea – Implications for depositional environments and the diagenesis of organic-rich sediments. *Proceedings of Ocean Drilling Program Scientific Results Part I* National Science Foundation, **127/128**, 75–98.
- MCKELVEY, V. E., WRIGHT, N. A. & BOWEN, R. W. 1983. *Analysis of the World Distribution of Metal-Rich Subsea Manganese Nodules*. US Geological Survey Circular, 886.
- MELLIN, T. A. M. & LEI, G. 1993. Stabilization of 10 Å – manganates by interlayer cations and hydrothermal treatment: Implications for the mineralogy of marine manganese concretions. *Marine Geology*, **115**, 67–83.
- OSTWALD, J. 1984. Ferruginous vernadite in an Indian Ocean ferromanganese nodule. *Geological Magazine*, **121**, 483–488.
- POST, J. E. & BISH, D. L. 1988. Rietveld refinement of the todorokite structure. *American Mineralogist*, **73**, 861–869.
- SENO, T. & MARUYAMA, S. 1984. Paleogeographic reconstruction and origin of the Philippine Sea. *Tectonophysics*, **102**, 53–84.
- SHIPBOARD SCIENTIFIC PARTY 1985. Site 578. In: *Initial Reports of Deep Sea Drilling Project*, **86**, 139–173.
- SHTERENBERG, L. E., ALEKSANDROVA, V. A., GABLINA, I. F., LELIKOV, E. P., SIVTISOV, A. V. & STEPANETX, M. I. 1990. Composition and structure of manganese crusts from the Sea of Japan. *Geology of Pacific Ocean*, **5**, 232–237.
- , GORSHKOV, A. I., SIVTISOV, A. V., STEPANOV, S. S., IL'INSKAYA, M. N. & ILICHEVA, L. V. 1989. Sedimentary and hydrothermal ferromanganese on the Shatskiy Rise. *Izvestia Akademia Nauka*, **5**, 112–119 [in Russian].
- TAMAKI, K. 1985. Two modes of back-arc spreading. *Geology*, **13**, 475–478.
- TURNER, S. & BUSECK, P. R. 1981. Todorokites: A new family of naturally occurring manganese oxides. *Science*, **203**, 456–458.
- USPENSKAYA, T. YU, GORSHKOV, A. I., GAVRILENKO, G. M. & SIVTISOV, A. V. 1990. Ferromanganese crusts and nodules in the Kurile Island arc: Structure, composition, and origin. *Lithology and Mineral Resources*, **24**, 330–338.
- USUI, A. 1979. Nickel and copper accumulation as essential elements in 10 Å manganite of deep-sea manganese nodules. *Nature*, **279**, 411–413.
- 1992. Hydrothermal Manganese Minerals in Leg 126 cores. In: TAYLOR, B. *et al.* (eds) *Proceedings of Ocean Drilling Program Scientific Results*, **126**, 113–123.
- & ITO, T. 1994. Fossil manganese deposits buried within DSDP/ODP cores. Legs 1–126. *Marine Geology*, **119**, 111–136.
- & NISHIMURA, A. 1992. Submersible observations of hydrothermal manganese deposits on the Kaikata Seamount, Izu-Ogasawara (Bonin) Arc. *Marine Geology*, **106**, 203–216.
- , MELLIN, T. A., NOHARA, M. & YUASA, M. 1989. Structural stability of marine 10 manganates from the Ogasawara (Bonin) Arc: Implication for low-temperature hydrothermal activity. *Marine Geology*, **86**, 41–56.
- , NISHIMURA, A. & IIZASA, K. 1994. Submersible observations of manganese nodules and crusts on the Tenpo seamount, Northwest Pacific. *Marine Georesources and Geotechnology*, **11**, 263–291.
- , YUASA, M., YOKOTA, M., NISHIMURA, A. & MURAKAMI, F. 1986. Submarine hydrothermal manganese deposits from the Ogasawara (Bonin) Arc, off the Japan Islands. *Marine Geology*, **73**, 311–322.

Geochemical constraints on the hydrothermal origin of ferromanganese encrustations from the Rodriguez Triple Junction, Indian Ocean

B. NAGENDER NATH¹, W. L. PLÜGER² & I. ROELANDTS³

¹ *Geological Oceanography Division, National Institute of Oceanography, Dona Paula, GOA-403 004, India*

² *Abteilung für Angewandte Lagerstättenlehre, der RWTH, Süsterfeldstrasse 22, D-52012 Aachen, Germany*

³ *Department of Geology, Petrology and Geochemistry, University of Liège, Sart Tilman, B-4000 Liège, Belgium*

Abstract: Ferromanganese crusts recovered from a spreading ridge north of the Rodriguez Triple Junction in the Indian Ocean were studied for their mineral and geochemical compositions. The crusts are highly porous, have maximum thickness of 2 cm, and occur on basaltic substrates. The composition of the crusts resembles that of hydrothermal ferromanganese crusts from other oceanic spreading centres. Compared to hydrogenous ferromanganese crusts and nodules, the hydrothermal crusts exhibit very low Mn/Fe ratios, lower transitional metal contents, low Σ REE contents and negative Ce anomalies, which are all characteristics of hydrothermal origin. Geochemical discriminant plots of crust data show similarities to data for metalliferous sediment and hydrothermal deposits recovered from other areas. Shale-normalized REE patterns indicate that the hydrothermal contribution to the crusts is between 60 and 92%. Crusts have rarely been reported to occur at Indian Ocean spreading centers, and those described here are consistent with the earlier findings on water column temperature and chemical anomalies indicative of hydrothermal activity in the region.

Some aspects of the crusts, such as δ -MnO₂ mineralogy and middle REE enrichment, are not typical of hydrothermal Fe–Mn oxides. Microprobe studies show that some layers within the crusts have Mn/Fe ratios close to unity, suggesting a significant input from normal seawater.

Growth rates, estimated from an algorithm based on Mn, Fe and Co contents, are orders of magnitude faster than rates determined for hydrogenous Fe–Mn oxides. The outer layers and some internal layers of the crust had relatively faster growth rates indicating that the crusts precipitated from distinct hydrothermal episodes.

Hydrothermal deposits of various types are frequently found at or near actively spreading mid-ocean ridges (e.g. Rona 1984). Hydrothermal ferromanganese-oxide crusts have been recovered from many localities such as oceanic spreading centres (mid-Atlantic Ridge, Scott *et al.* 1974; the Galapagos Ridge, Moore & Vogt 1976; Corliss *et al.* 1979; East Pacific Rise, Lonsdale *et al.* 1980; Explorer Ridge, Grill *et al.* 1981; in volcanic arc–back-arc basin settings (Tonga–Kermadec Ridge, Cronan *et al.* 1982; Moorby *et al.* 1984; Manus Basin, Bolton *et al.* 1988; Lau Basin, Hein *et al.* 1990; Herzig *et al.* 1990; North Fiji Basin, Murphy *et al.* 1991; Izu–Ogasawara (Bonin) and Mariana Arc, Usui *et al.* 1986; Usui & Nishimura 1992) and in mid-plate seamount and guyot regions (Futa *et al.* 1988; Ingram *et al.* 1990; Puteanus *et al.* 1991; Hodkinson *et al.* 1994). Despite so many reports from a variety of locations and geological settings, hydrothermal ferromanganese-oxide crusts from Indian Ocean spreading centres

have been rarely documented (Lisitzyn 1986; Lisitzyn & Gurvich 1987; Murdmaa *et al.* 1989). This is because, until the late 1980s, exploration efforts were concentrated on fast-spreading centres of the Pacific, while the slow- and medium-spreading centres of Atlantic and Indian Oceans were considered less favourable targets (Plüger *et al.* 1990). A serious effort to explore the mid-Indian Oceanic ridge for hydrothermal activity (Herzig *et al.* 1988; Rao & Pattan 1989; Plüger *et al.* 1990; Chaubey *et al.* 1990, Rao 1992; Nath 1993) occurred only after the discovery of massive sulphides, black smokers and vent biota at the slow-spreading TAG area of the Mid-Atlantic ridge in 1985 (Rona *et al.* 1986). One of these cruises (GEMINO 3) yielded ferromanganese encrustations that exhibited hydrothermal chemical signatures. This paper forms one of the few reports of hydrothermal ferromanganese mineralization found along the mid-Indian Ocean ridge.

Previous reports on Indian Ocean hydrothermal activity

Only sporadic investigations have been carried out on the mineralization of Indian Ocean ridges. Rozanova & Baturin (1971) and Baturin & Rozanova (1971) found indications of hydrothermal activity near the Vityaz fracture zone in the NW Indian Ocean. Lisitzyn & Gurvich (1987) reported the occurrence of metalliferous sediments at RTJ with Fe and Mn contents reaching to about 25% and 5% respectively. Rona *et al.* (1981) noted manganese coatings on basalt walls of the Carlsberg ridge. Colley *et al.* (*In: Cronan 1979*) also recovered ferromanganese crusts from the Carlsberg ridge crest and attributed their formation to hydrogenetic precipitation; they suggested that the crusts are indistinguishable from those forming in non-volcanic areas. During the first large scale exploration programme GEMINO (geothermal metallogenesis Indian Ocean) for polymetallic sulphides in the Indian Ocean, four areas along the Carlsberg ridge and Central Indian Ridge were surveyed (Herzig *et al.* 1988) based on the

above-mentioned reports. Among the four sites surveyed, only one site at the Rodriguez Triple Junction (RTJ) indicated hydrothermal activity. At the RTJ station were recovered metalliferous sediments, hydrothermally altered basalts, and other indicators of hydrothermal activity. Udintsev (1975) reported that high thermal gradients occur in the sediments of the RTJ. Later, three more cruises by Germans (under project GEMINO) revealed photographic evidence of neo-tectonic activity at one site and high concentrations of methane (maximum of 202 ml l^{-1}), high TDM (total dissolved manganese – maximum of $23.1 \text{ nmol kg}^{-1}$, and a temperature anomaly of $\pm 0.05^\circ\text{C}$ at $24^\circ 00.3' \text{ S}$ (hydrothermal plume site, Plüger *et al.* 1990), all indicators of hydrothermal activity. Two short cruises by Indians to the RTJ delineated an undiscovered transform fault (Chaubey *et al.* 1990) and found very thin oxide coatings on basalt (Rao & Pattan 1989; Rao 1992). The exploration activity carried out by French investigators also discovered a hydrothermal ^3He plume north of the RTJ at $19^\circ 29' \text{ S}$. Water-column ^3He anomalies showed a spike of 33.8% at 2460 m depth, the highest ^3He

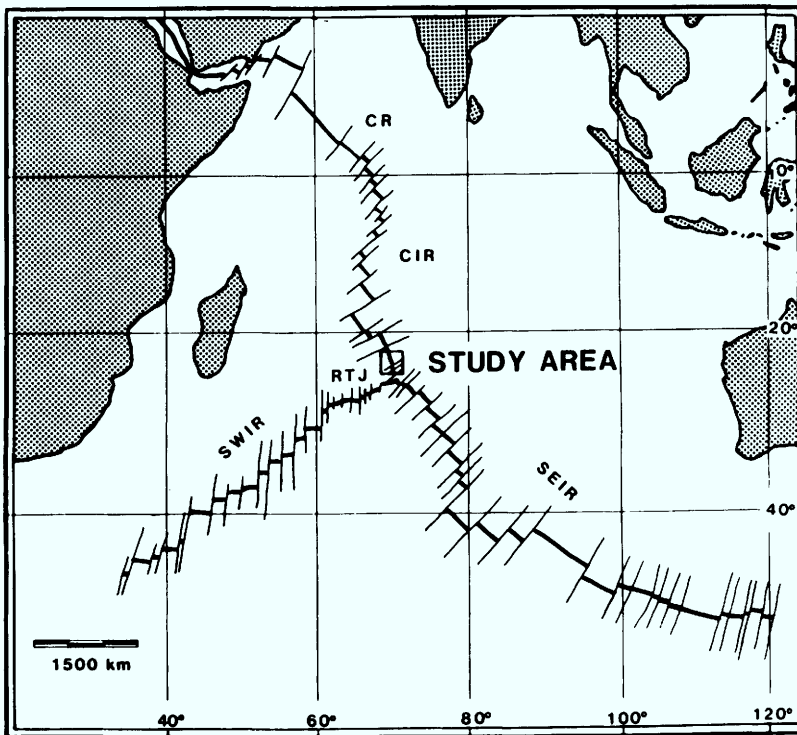


Fig. 1. Location map of the study area. Crusts have been recovered from the walls of the rift valley of the Central Indian Ridge (CIR); SWIR, Southwest Indian Ridge; SEIR, Southeast Indian Ridge; RTJ, Rodriguez Triple Junction; CR, Carlsberg Ridge.

anomaly recorded so far in the Indian Ocean (Jean-Baptiste *et al.* 1992). However, hydrothermal ferromanganese oxides have rarely been reported. Recently, Halbach *et al.* (1994) reported the first recovery of massive sulphides at RTJ.

Tectonic setting

The RTJ is the junction of three Indian Ocean spreading ridges and also the Indian–Australian, African and Antarctic lithospheric plates (Patriat & Parson 1989). The RTJ is located near 25°30' S and 70° E, 900 km southwest of Rodriguez Island (Munsch & Schlich 1989). The three spreading ridges are central (CIR), Southeast (SEIR) and Southwest (SWIR) Indian ridges. SEIR and CIR have intermediate spreading rates, whereas SWIR is a slow-spreading ridge. The CIR from where the samples were recovered (Fig. 1) trends nearly N–S from near the equator to the Rodriguez Triple Junction (Chaubey *et al.* 1990). The ridge is highly segmented and is bounded on the east by the Chagos–Laccadive Ridge and on the west by the Mascarene Plateau. The half-spreading rates progressively change from 2.5 cm a⁻¹ at RTJ to about 1.8 cm a⁻¹ at the equator (Munsch & Schlich 1989).

Sample description and methods

The samples were collected from the western wall of the rift valley at an area designated LX on the CIR (Fig. 1; locations in Table 1). They were collected

during cruise SO-52 of FS *Sonne* (GEMINO-3). The samples comprise basalt substrates with ferromanganese encrustations having a maximum thickness of about 2 cm (Table 1). The crusts are highly porous and show dendritic growth, both of which are characteristic of fast growth rates (Halbach & Puteanus 1988). Bulk chemical analyses were carried out on five Fe–Mn crusts using X-ray fluorescence spectrometry. Small-scale compositional variations were studied in one crust using an electron microprobe (Table 2). In all, 42 spots were selected on this particular crust (Plüger 1990). Five bulk crusts were also analysed for rare-earth elements using ICP-AES after ion-exchange separations following Roelandts (1992) and Nath *et al.* (1994). Mineralogy was studied using a Siemens X-ray diffractometer with a molybdenum target.

Results

The dominant mineral phase present in the ferromanganese crusts is δ -MnO₂ (vernadite). The mineral is identified from XRD *d*-spacings of 1.42 and 2.44 Å. Although iron contents are higher than Mn contents, X-ray diffractograms do not show iron-oxides (such as goethite), indicating that most of the Fe may be present as amorphous iron-oxyhydroxides.

Mn contents range from 1.1 to 12.7% and are lower than iron contents (Table 2). Fe contents range from 14% to 39%; Fe/Mn varies from 35 to 1, certainly not as fractionated as in other hydrothermal iron-manganese crusts (cf. Moorby *et al.* 1984; Hein *et al.* 1994). The concentrations of trace elements Cu, Co, Ni and Pb (Table 2) are generally low, below concentrations in hydrogenous crusts. Zn concentrations

Table 1. Sample locations and descriptions

Station	Latitude (S)	Longitude (E)	Depth (m)	Description
112 DR	24°05.30'	69°32.03'	2954	Dark brown to black Fe–Mn crusts with oxide thickness to 7 mm. Associated with basalts, pillow lavas with glass.
138 DR	24°06.25'	69°32.79'	2925	Black coloured Fe–Mn crusts, oxide thickness to 20 mm. Associated with brown thick iron-oxides, basalts, pillow lavas with glass.
151 DR	24°14.30'	69°40.92'	3730	Black Fe–Mn crusts, thickness variable and >10 mm. Associated with basaltic talus, pillow lavas and sheet flows.
159 DR	24°05.20'	69°41.65'	2466	Black Fe–Mn crusts, thickness to 10 mm in depressions and some basaltic surfaces with thickness to 2 mm. Associated with phryic basaltic talus, pillows etc.
168 DR	24°00.03'	69°37.7'	3598	Black Fe–Mn crusts associated with hydrothermally altered basalt.

Table 2. Chemical composition of the crusts

Sample No.	Type	Mn	Fe	Mn/Fe	Si	Al	Ca	Na	P	Co	Ni	Cu	Zn	Pb	Co/Zn	Zn/Fe	Gr
112DR	Bulk	11.3	29.5	0.38	4.9	1.33	1.96	na	0.55	0.07	0.01	0.05	0.07	0.017	1.06	0.0024	41
138DR	Bulk	9.9	29.1	0.34	5.3	1.57	2.90	na	0.50	0.06	0.01	0.05	0.07	0.021	0.91	0.0024	49
151DR	Bulk	11.5	23.7	0.49	5.0	1.05	4.71	na	0.52	0.09	bd	0.03	0.06	0.023	1.55	0.0025	21
159DR	Bulk	11.6	22.8	0.51	5.1	1.13	5.66	na	0.57	0.09	0.01	0.03	0.11	0.023	0.83	0.0048	20
168DR	Bulk	9.3	20.9	0.44	6.2	1.63	7.81	na	0.48	0.07	bd	0.03	0.08	0.021	0.92	0.0038	25
<i>Microprobe analyses</i>																	
69601	A	8.7	32.8	0.27	8.8	1.79	0.04	2.97	0.58	0.05	0.05	0.09	0.07	na	0.71	0.0021	74
69602	A	5.9	28.5	0.21	7.4	1.45	1.65	1.32	0.36	0.04	0.04	0.06	0.07	na	0.57	0.0025	79
69603	B	15.9	18.3	0.87	5.7	1.79	1.77	0.91	0.37	0.06	0.12	0.08	0.07	na	0.86	0.0038	40
69604	A	12.4	25.7	0.48	10.2	2.34	1.62	1.62	0.38	0.09	0.05	0.07	0.02	na	4.5	0.0008	24
69605	A	10.4	23.4	0.44	9.8	2.50	1.16	0.98	0.23	0.10	0.09	0.12	0.06	na	1.67	0.0026	17
69607	A	7.9	31.9	0.25	9.3	1.95	1.56	1.57	0.51	0.04	bd	0.09	0.06	na	0.67	0.0019	101
69608	B	17.0	16.9	1.00	5.2	1.97	1.84	1.25	0.40	0.02	0.13	0.09	0.05	na	0.40	0.0029	244
69609	B	15.4	19.7	0.78	6.2	1.74	1.73	0.79	0.38	0.08	0.07	0.08	0.08	na	1.00	0.0040	26
69610	B	15.7	22.6	0.70	8.9	2.44	2.02	0.06	0.47	0.12	0.07	0.09	0.06	na	2.00	0.0027	9
69611	B	15.9	23.2	0.69	8.4	2.54	1.96	0.41	0.50	0.12	0.03	0.06	0.03	na	4.00	0.0013	16
69612	A	12.1	27.8	0.44	9.5	2.03	1.68	0.62	0.50	0.07	0.02	0.06	0.07	na	1.00	0.0025	40
69613	B	18.3	22.1	0.33	8.2	2.67	2.01	0.67	0.51	0.14	0.05	0.10	0.06	na	2.30	0.0027	13
69614	A	12.6	26.3	0.48	8.2	2.45	1.56	1.28	0.44	0.10	0.06	0.08	0.10	na	1.00	0.0038	21
69615	D	13.7	19.1	0.71	6.4	2.17	1.62	13.94	0.45	0.07	0.03	0.10	0.05	na	1.40	0.0026	29
69616	A	8.6	24.0	0.36	7.9	1.97	1.10	1.10	0.37	0.08	0.04	0.06	0.04	na	2.00	0.0017	23
69617	D	10.1	24.3	0.41	7.8	1.81	1.31	8.06	0.46	0.06	0.03	0.06	0.06	na	1.00	0.0025	40
69618	A	11.8	21.8	0.54	5.2	1.22	2.21	1.13	0.45	0.07	0.03	0.04	0.06	na	1.17	0.0028	30
69619	C	2.5	35.0	0.07	8.0	1.43	1.76	0.92	0.48	0.10	0.04	0.11	0.05	na	2.00	0.0014	20
69620	B	14.4	17.3	0.83	4.0	1.09	5.03	0.98	0.38	0.19	0.13	0.09	0.02	na	9.50	0.0012	5
69621	B	15.5	19.1	0.81	4.2	1.12	1.73	1.27	0.45	0.08	0.09	0.06	0.06	na	1.33	0.0031	25

69 622	B	15.8	19.5	0.81	4.4	1.04	1.76	0.77	0.47	0.06	0.12	0.06	0.06	0.06	na	1.00	0.0031	42
69 623	B	18.8	18.3	1.03	3.6	1.30	1.91	1.31	0.46	0.03	0.18	0.11	0.11	0.03	na	1.00	0.0016	144
69 624	B	18.3	18.6	0.98	3.9	1.36	1.94	1.31	0.46	0.06	0.17	0.08	0.10	0.10	na	0.60	0.0054	45
69 625	B	17.1	20.0	0.85	4.5	1.39	1.92	1.46	0.44	0.09	0.11	0.07	0.04	0.04	na	2.25	0.0020	23
69 626	B	16.0	22.0	0.73	4.9	1.50	1.93	1.37	0.50	0.08	0.06	0.06	0.06	0.04	na	2.00	0.0018	29
69 627	A	7.5	31.2	0.24	7.3	1.36	1.91	1.15	0.45	0.06	0.04	0.09	0.05	0.05	na	1.20	0.0016	49
69 628	A	12.1	25.7	0.47	5.9	1.50	1.45	0.82	0.46	0.04	0.08	0.10	0.09	0.09	na	0.44	0.0035	92
69 629	B	14.3	20.9	0.68	4.4	1.33	1.59	0.98	0.41	0.10	0.09	0.11	0.06	0.06	na	1.67	0.0029	18
69 630	C	5.5	35.4	0.16	7.8	1.56	2.77	1.02	0.51	0.07	0.02	0.08	0.02	0.02	na	3.50	0.0006	41
69 631	A	10.5	26.8	0.39	6.6	1.77	1.42	0.91	0.44	0.07	0.03	0.04	0.06	0.06	na	1.17	0.0022	35
69 632	B	14.7	21.1	0.70	5.5	1.93	1.64	0.65	0.37	0.07	0.04	0.05	0.04	0.04	na	1.75	0.0019	33
69 633	A	13.1	23.5	0.56	7.1	1.97	1.55	0.12	0.41	0.06	0.07	0.08	0.06	0.06	na	1.00	0.0026	44
69 634	B	10.1	14.0	0.72	11.9	5.26	2.03	2.71	0.32	0.03	0.06	0.03	bd	bd	na	bd	bd	70
69 635	C	5.2	38.9	0.13	7.9	1.95	1.53	0.95	0.55	0.06	bd	0.10	0.08	0.08	na	0.75	0.0021	22
69 636	C	3.9	33.0	0.12	7.2	1.85	6.04	1.03	0.47	0.06	0.07	0.07	0.08	0.08	na	0.75	0.0024	45
69 637	C	1.1	38.5	0.03	8.0	2.49	1.16	0.71	0.58	0.03	0.02	0.11	0.05	0.05	na	0.60	0.0013	161
69 638	C	1.7	38.9	0.04	7.4	2.21	0.92	0.53	0.57	0.05	0.02	0.10	0.07	0.07	na	0.71	0.0018	72
69 639	C	5.2	31.2	0.17	6.0	1.68	2.05	0.91	0.46	0.04	0.02	0.08	0.04	0.04	na	1.00	0.0013	86
69 640	B	15.2	22.0	0.69	5.2	1.60	2.22	0.69	0.43	0.08	0.06	0.05	0.06	0.06	na	1.33	0.0027	28
69 641	B	15.0	22.1	0.68	5.6	1.60	2.11	1.24	0.45	0.06	0.02	0.01	0.07	0.07	na	0.86	0.0032	45
69 642	A	11.5	26.0	0.44	6.1	1.64	1.54	0.91	0.42	0.07	0.07	0.10	0.06	0.06	na	1.17	0.0023	37
69 643	B	15.0	19.6	0.76	4.4	1.43	1.67	0.83	0.42	0.09	0.17	0.08	0.06	0.06	na	1.50	0.0031	20
Avg.	A	10.4	26.8	0.39	7.8	1.85	1.56	1.18	0.43	0.07	0.05	0.08	0.06	0.06	na	1.17	0.0022	35
Avg.	B	15.7	19.9	0.79	5.7	1.85	2.04	1.03	0.43	0.08	0.09	0.07	0.05	0.05	na	1.60	0.0025	26
Avg.	C	3.6	35.9	0.10	7.5	1.88	2.31	1.31	0.52	0.06	0.03	0.09	0.06	0.06	na	1.00	0.0017	50
Avg.	D	11.9	21.7	0.55	7.1	1.99	1.47	11.00	0.45	0.07	0.03	0.08	0.06	0.06	na	1.17	0.0028	31

Elemental data in %.

Microprobe data from a traverse across one Fe-Mn crust.

A, B, C and D represent layers with different colour intensities under a microscope.

GR, Growth rate (mm Ma^{-1}) calculated following Mannheim & Lane-Bostwick (1988).

na, not analysed; bd, below detection.

Table 3. Rare earth element concentrations in ferromanganese crusts (ppm)

	La	Ce	Nd	Sm	Eu	Gd	Dy	Yb	Lu	ΣREE	La*/Lu*	Ce*
112DR	204	187	183	39.8	10.14	42.8	40.3	21.41	3.16	732	0.96	-0.34
138DR	183	195	168	36.1	9.20	37.5	34.1	16.86	2.42	682	1.12	-0.28
151DR	202	173	179	37.4	9.59	37.9	35.0	16.37	2.37	693	1.27	-0.37
159DR	151	117	135	28.8	7.59	30.5	28.4	14.04	2.00	514	1.12	-0.41
168DR	176	147	157	34.6	8.86	37.3	35.7	19.45	2.95	619	0.89	-0.38

La* and Lu* are shale-normalized values.

Ce*, cerium anomaly calculated using the formula of Elderfield & Greaves (1981) ($\log 3\text{Ce}/2\text{La} + \text{Nd}$).

are high and comparable to abyssal crusts of the Central Indian Basin (Rao 1992; Nath 1993) and other parts of the ocean (Moorby *et al.* 1984). Combined Cu + Ni + Co concentrations are very low, ranging from 0.05 to 0.49% with a mean of 0.21%. CaO contents are generally low, with the exception of three crusts (#151, #159 and #168 DR), where higher concentrations were observed. XRD show some calcite peaks in samples 168 DR and 159 DR suggesting that Ca is present both in biogenic and non-biogenic phases.

ΣREE contents range between 514 ppm and 732 ppm (Table 3), lower than ΣREE of hydrogenous crusts from the Central Indian Basin and the Central Pacific which range between 1188 and 2757 ppm (Nath 1993), but much higher than for stratabound hydrothermal Mn deposits (e.g. Hein *et al.* 1990). The shale-normalized patterns display strong negative Ce anomalies and middle (MREE) enrichment with convex up shape. La_n/Lu_n ($\text{La}_{\text{sample}}/\text{La}_{\text{shale}}/\text{Lu}_{\text{sample}}/\text{Lu}_{\text{shale}}$) ranges from 0.89 to 1.27 (Table 3), with a mean close to 1, which means that there is no significant LREE or HREE fractionation.

Discussion

Geochemical discriminants for a hydrothermal origin

Mn/Fe ratios. Several investigators (Dymond & Eklund 1978; Dymond 1981; Graybeal & Heath 1984; Ruhlin & Owen 1986; Owen & Olivarez 1988) have demonstrated that the hydrothermal component of metalliferous sediments can be distinguished by Mn/Fe ratios (c. 0.3–0.4). However, pure hydrothermal iron and manganese oxide deposits are much more fractionated in Fe and Mn (Moore & Vogt 1976; Grill *et al.* 1981; Cronan *et al.* 1982; De Carlo *et al.* 1987; Hein *et al.* 1990, 1994; von Stackelberg *et al.* 1990; Hodkinson *et al.* 1994; and references therein). Chen & Owen (1989) delineated a large area in the Pacific dominated

by hydrothermally influenced manganese nodules based on a characteristic Mn/Fe ratio of 0.3. Mn/Fe ratios of GEMINO crusts (bulk analyses) range between 0.3 and 0.5 (Table 2). Microprobe analyses reveal Mn/Fe ratios as low as 0.07 in some layers suggesting variations in hydrothermal (Fe-rich) and hydrogenetic input. Fe and Mn fractionate during precipitation from hydrothermal fluids because of their different solubilities, with Fe species being less soluble than Mn (Krauskopf 1957; Toth 1980; Hein *et al.* 1994). The ratios of GEMINO crusts may indicate a relatively distal hydrothermal deposit following Owen & Olivarez (1988). During their studies on EPR metalliferous sediments, Owen & Olivarez (1988) found a Mn/Fe ratio of 0.43 to be a characteristic of distal hydrothermal deposits.

Trace elements Cu, Ni and Co. The trace metal concentrations (Cu, Ni and Co) are comparable with other marine hydrothermal Fe–Mn oxide deposits (Moore & Vogt 1976; Grill *et al.* 1981; Cronan *et al.* 1982; Usui *et al.* 1986; Hein *et al.* 1994), one or more orders of magnitude lower than that of hydrogenous Fe–Mn crusts and manganese nodules (Nath *et al.* 1992). The ternary diagram of Fe–Mn–Co + Ni + Cu (Fig. 2) shows interpreted hydrothermal and hydrogenous fields (Bonatti *et al.* 1972). A third field based on the studies of Fe–Mn crusts was included by Toth (1980). This field lies midway between the Fe end member and the nodule field demonstrating the enrichment and depletion of Fe and trace elements respectively. GEMINO crusts data fall in the hydrothermal field below the field defined by Toth (1980) for Fe–Mn crusts and close to the area occupied by EPR metalliferous sediments (Fig. 2). This further supports a hydrothermal origin of these crusts.

Silica and aluminium. The Si/Al ratios in these GEMINO crusts are mostly higher than 3 with a mean of 3.8. Many nodules are reported to have

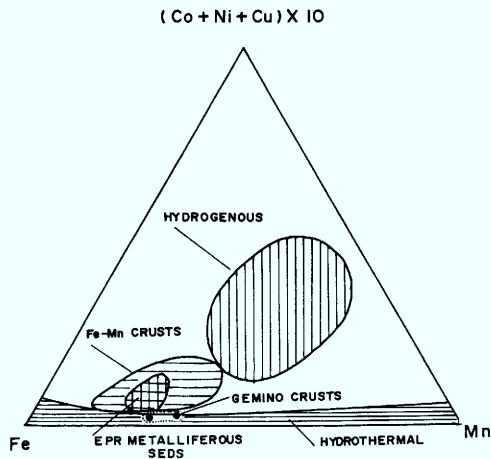


Fig. 2. Ternary diagram of Fe-Mn-(Cu + Ni + Co) × 10 (Bonatti *et al.* 1971; modified by Toth 1980). Illustrated are (1) low trace-metal content of GEMINO crusts and (2) similar Fe-enriched trace-metal depleted compositions of ferromanganese crusts and EPR metalliferous sediments. GEMINO samples fall just at the base of EPR metalliferous data and in hydrothermal field. All field interpretations are from Bonatti *et al.* (1971) and Toth (1980).

Si/Al ratios of approximately 3 (which is a crustal ratio), suggesting that Si reflects detrital input (Toth 1980). Si/Al ratios greater than 3 indicate an additional source of Si in these crusts, which could possibly be X-ray amorphous hydrothermal silica. Excess Si (over that contained in aluminosilicate phase) combined with Fe in the hydrothermal iron-oxyhydroxide deposits from the South Pacific hot spot areas has been attributed to nontronite (Puteanus *et al.* 1991). We have no evidence for assigning the excess Si to nontronite in our samples. A plot of Si versus Al (Fig. 3) indicates that the GEMINO crust values fall closer to the line defining Fe-Mn crusts and close to Fe-rich crusts described by Toth (1980). In a ternary diagram of Fe:Mn:Si (adopted from Toth 1980), the values of GEMINO crusts fall in an area occupied by EPR metalliferous sediments and Fe-Mn crusts, but are not as fractionated as in Galapagos and Lau basin crusts (Nath 1993; Fig. 4).

Co/Zn and Zn/Fe ratios. Co/Zn ratios were used by Toth (1980) as an indicator of hydrothermal mineralization, with the mean value for hydrothermal deposits being 0.15, and that for hydrogenous deposits being 2.5. Experimental work has shown that, after Mn and Fe, Zn is the trace metal that is most enriched in seawater

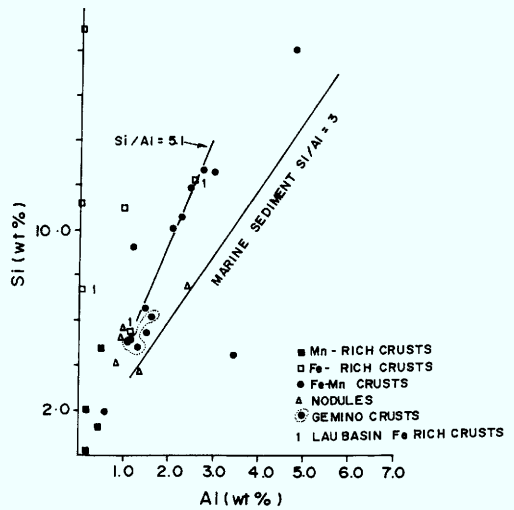


Fig. 3. A plot of Si versus Al concentrations (from Toth 1980). Ferromanganese crusts and Fe-rich crusts show enrichment in Si. The line defining Si/Al ratio of 5.1 encompasses many Fe-Mn deposits and different from typical marine sediment ratio of 3. GEMINO values fall close to the line defining Fe-rich crusts. All data from Toth (1980).

having undergone reaction with hot basalt (Seyfried & Mottl 1982). Zn has been found to be enriched in proximal hydrothermal deposits (Rona 1984). Co/Zn ratios in RTJ crusts range

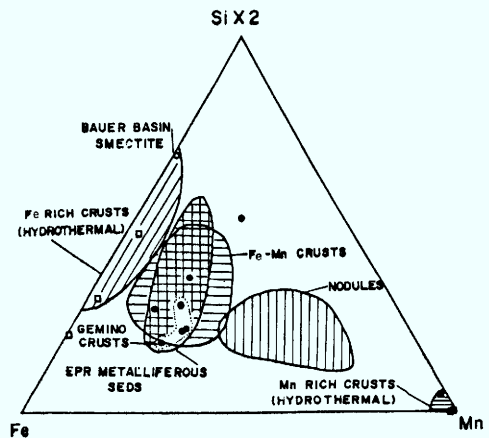


Fig. 4. Ternary diagram of Fe versus Mn versus Si × 2 (adopted from Toth 1980). GEMINO crusts fall in the EPR metalliferous sediment data. The open squares in the hydrothermal Fe-rich crusts/oxides field are hydrothermal iron-oxides of the Lau Basin (Nath 1993). The filled squares in the field described as Mn-rich crusts are from Galapagos, EPR and Lau Basin (Nath 1993). The GEMINO crusts are enriched in Fe but not as fractionated as the Fe-rich and Mn-rich crusts of Galapagos, EPR and Lau Basin.

between 0.83 and 1.55 (Table 2) and indicate a mixed hydrothermal–hydrogenous origin. A plot of $\text{Cu} + \text{Ni} + \text{Co}$ versus Co/Zn was used by Toth (1980) to indicate the relative contribution of hydrothermal deposition in ferromanganese deposits. The GEMINO values fall close to hydrothermal Fe–Mn crusts and only at the lower end of hydrogenous values (Fig. 5). Mean Zn/Fe ratios are 0.0024 (Table 2) and are also close to the hydrothermal end-member ratios (0.022) suggested by Graybeal & Heath (1984).

Rare-earth elements. The most striking feature of the REE patterns for these crusts is the strong negative cerium anomaly (Fig. 6). Negative Ce anomaly is a characteristic feature of hydrothermal Fe–Mn deposits as well as seawater (Elderfield & Greaves 1981; Fleet 1983). The Ce anomaly may or may not occur depending on the temperature of the fluid, proximity to the hydrothermal source, and amount of hydrogenetic contamination (Clauer *et al.* 1984; Hein *et al.* 1994 and references therein). Ce anomalies calculated with the formula $(\log 3\text{Ce}/2\text{La} + \text{Nd})$ suggested by Elderfield & Greaves (1981) range between -0.277 and -0.411 (Table 3). In contrast, typical hydrogenetic crusts from the basal parts of the Indian Ocean have strong positive Ce anomalies ranging from 0.352 to 0.637 (Nath 1993). Therefore, the negative Ce anomalies of the GEMINO crusts are consistent

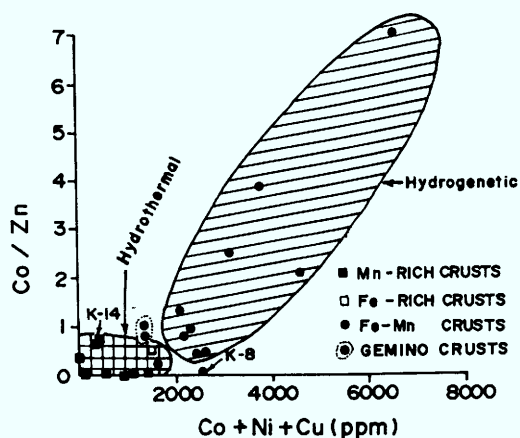


Fig. 5. Co/Zn versus $\text{Cu} + \text{Ni} + \text{Co}$ contents (from Toth 1980). The low contents for hydrothermal crusts indicate low hydrothermal input of Co, Ni and Cu, but relatively high hydrothermally derived Zn contents. Dots represent Fe–Mn crusts of mostly hydrogenous origin (Toth 1980). GEMINO data fall between the two fields but somewhat close to the hydrothermal crusts. #K14 and #K8 are from Galapagos spreading centre (data from Nath 1993).

with a hydrothermal origin. The fractionation of Ce in the marine environment has been attributed to its oxidation from Ce^{3+} to Ce^{4+} and subsequent removal by suspended Fe and Mn particles in the water column or the solid phases residing on the seafloor (Goldberg 1961). The behaviour of Ce in these crusts is illustrated by a plot between La and Ce (Fig. 7). La/Ce ratios of GEMINO crusts are high and close to the seawater ratio and the line defining hydrothermal Mn-rich, Fe-rich and Mn-Fe-rich crusts (Fig. 7). On the other hand, Ce enrichments are evident for hydrogenous crusts (including those from Central Indian Basin) by their low La/Ce values (generally <1). Furthermore, a comparison of $\text{Cu} + \text{Ni} + \text{Co}$ concentration with ΣREE concentrations provides a means of characterizing the hydrothermal and hydrogenous Fe–Mn deposits (Clauer *et al.* 1984). Hydrothermal deposits have REE and Cu, Ni and Co concentrations that are distinctly lower than those of hydrogenous deposits. The GEMINO crusts data fall in the field defined as metalliferous deposits (Fig. 8).

Hydrothermal and hydrogenetic contributions

The hydrothermal contribution to crusts can be roughly estimated by comparison of the shale-normalized REE patterns with those presented by Fleet (1983) for mixtures of hydrogenous and hydrothermal ferromanganese oxides, and by comparisons with the chemical composition of pure hydrogenetic and hydrothermal end members determined for deposits from other areas. Fleet (1983) determined the shale-normalized REE patterns for hypothetical mixtures of the hydrogenous and hydrothermal end-members. Comparison of our REE patterns with Fleet's indicates that the hydrothermal contribution to the GEMINO crusts may range from 60 to 92%.

Although the crusts seem to be predominantly hydrothermal, additions of hydrogenous material are likely. The basic evidence comes from the mineralogy and the incomplete fractionation of Fe and Mn. The crusts show no todorokite or birnessite which are typical of hydrothermal deposits, instead they consist solely of $\delta\text{-MnO}_2$. $\delta\text{-MnO}_2$ is a characteristic feature of hydrogenous crusts. Secondly, the shale-normalized REE patterns show middle REE enrichment, which is typical of hydrogenous nodules and crusts (Nath *et al.* 1992 and references therein). The ΣREE contents are neither as high as in hydrogenous crusts nor as low as in other hydrothermal Fe–Mn deposits

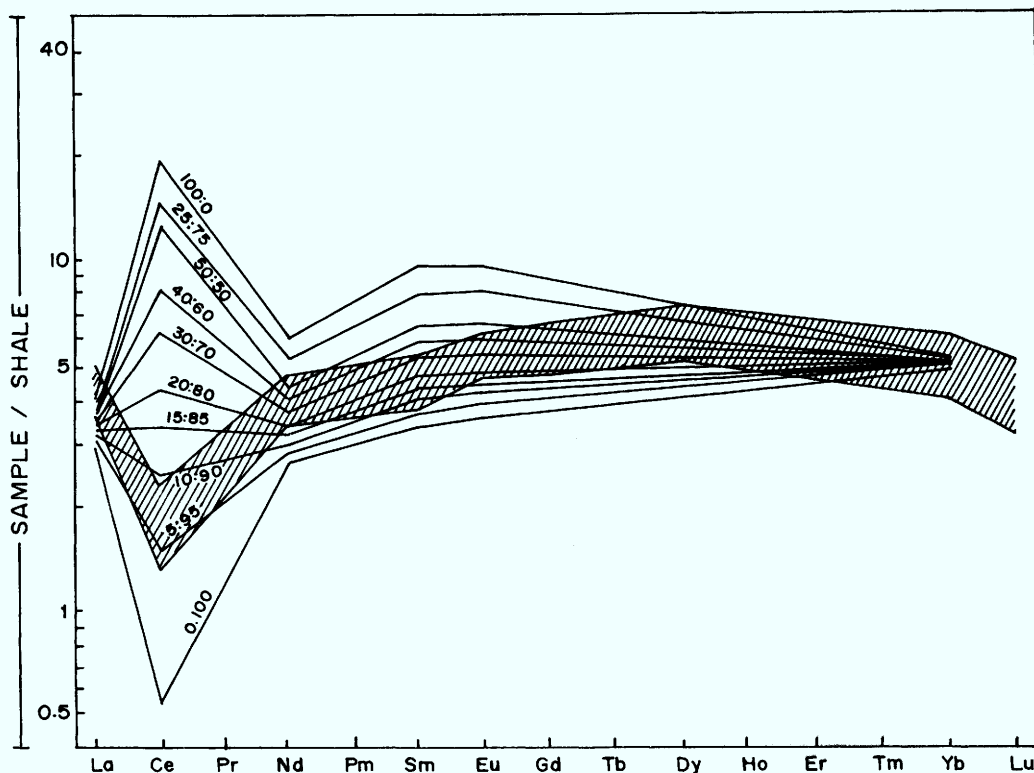


Fig. 6. Range of shale-normalized REE patterns of ferromanganese crusts recovered from the Rodriguez Triple Junction (hatched area). All samples typically display strong negative Ce anomaly, middle REE enrichment, and no significant LREE/HREE fractionation. The patterns of the GEMINO samples are superimposed on the hypothetical mixtures of average hydrothermal material and average hydrogenous ferromanganese material proposed by Fleet (1983). The first and second values in ratios represent the percentages of hydrogenous and hydrothermal material respectively. GEMINO crusts reflect about 60–92% hydrothermal input.

(Hein *et al.* 1990, 1994; Nath 1993). These considerations indicate that the crusts studied here are a mixture of hydrothermal and hydrogenous input, very similar to mixed crusts studied from the Tonga–Lau, Mariana and Yap arcs (Moorby *et al.* 1984; Hein *et al.* 1990, 1992; Schulz & Hein 1991).

Age of mineralization

In the absence of radiometric dating, the growth rates of marine ferromanganese oxides have been calculated by various workers in the past using the empirical formulas proposed by Scott *et al.* (1976), Lyle (1982), Sharma & Somayajulu (1987), Putaenus & Halbach (1988) and Manheim & Lane-Bostwick (1988). These equations are based on the chemical composition of the deposits with different assumptions in each case. Among these, the formulas proposed by Lyle (1982), Sharma & Somayajulu (1987) and

Putaenus & Halbach (1988) are more suitable for hydrogenous or diagenetic ferromanganese oxides. Therefore, we have used the equations proposed by Scott *et al.* (1976) and Manheim & Lane-Bostwick (1988) to determine the growth rate and the derived ages for these crusts. Among the two, we prefer the Manheim & Lane-Bostwick 'Cobalt chronometer', because three important hydrothermal discriminant elements Co, Mn and Fe are used to compute the growth rates ($R = 6.8 \times 10^{-1} / (\text{Co}^n)^{1.67}$ where R is the growth rate in mm Ma^{-1} , $\text{Co}^n = \text{Co} \times 50 / (\text{Fe} + \text{Mn})$). The growth rates for bulk crusts range between 20 and 49 mm Ma^{-1} (Table 2) which are higher than the usual growth rates of about $1\text{--}15 \text{ mm Ma}^{-1}$ (4–6 being most common) for hydrogenous crusts. Considering an oxide thickness of 2 cm, the maximum age of this crust could range from 0.4 to 1 Ma. Because this method is not sensitive to hiatuses, calculated rates should be considered as maximum values and the derived ages as minimum values

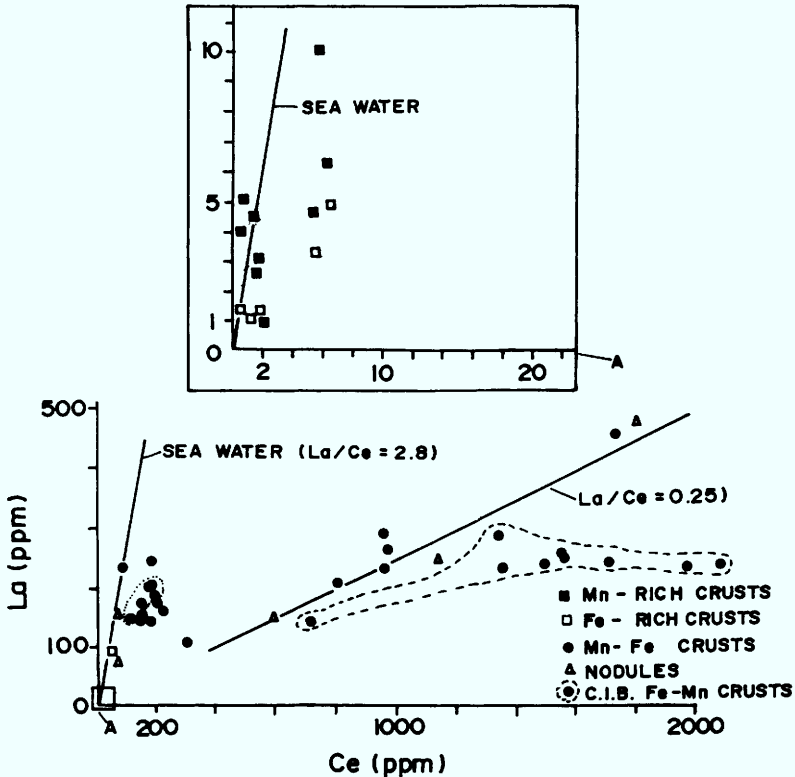


Fig. 7. A plot of La versus Ce concentrations (from Toth 1980). Hydrothermal crusts have low La/Ce ratios and are similar to seawater (2.8) compared to the La/Ce ratio of hydrogenous Fe-Mn crusts which are as low as 0.25. The GEMINO crusts (field encircled with small dots close to the line defining seawater ratio) are depleted in Ce and fall close to other hydrothermal deposits. For comparison, data of purely hydrogenous crusts from the Central Indian Basin (data from Nath 1993 are shown - data points circled with dashes). They are extremely enriched in Ce and plot distinctively away from GEMINO crusts.

(McMurtry *et al.* 1994). The growth rates determined from the microprobe data reveal the outer few layers had faster growth rates, ranging between 74 and 243 mm Ma⁻¹ (Table 2), which are about 2-10 times faster than the interior layers. In addition, few internal layers yielded relatively fast growth rates (fastest 160 mm Ma⁻¹) indicating some episodic hydrothermal input. Hydrothermal activity may not be extinct in this area, because thin ferromanganese coatings on basalts have been reported from Rodriguez Triple Junction which were found to have hydrothermal signatures (Rao & Pattan 1989; Rao 1992). Additionally, water-column geochemical tracers of hydrothermal activity such as methane, total dissolved manganese (TDM), and helium have been found (Plüger *et al.* 1990; Jean-Baptiste *et al.* 1992) at the Rodriguez Triple Junction. The GEMINO crusts probably grew by a combination of hydrogenous precipitation (about 1-15 mm Ma⁻¹) and precipitation from diffuse

hydrothermal plumes that originated at a hydrothermal vent and travelled some distance through the water column.

Summary

Low trace element contents, δ -MnO₂ mineralogy, Mn/Fe, Co/Zn, Zn/Fe, La/Ce, Si/Al ratios, ternary diagrams, Σ REE contents, negative cerium anomalies, middle REE enrichment and the porous texture indicate that the ferromanganese crusts recovered from the Rodriguez Triple Junction are predominantly hydrothermal in origin with variable, but significant (<40%) additions of hydrogenous oxides. Consequently, the crusts are transitional between hydrothermal and hydrogenous ferromanganese oxides and probably represent deposition during a period of fluctuating hydrothermal activity. The ferromanganese deposits of the type described here

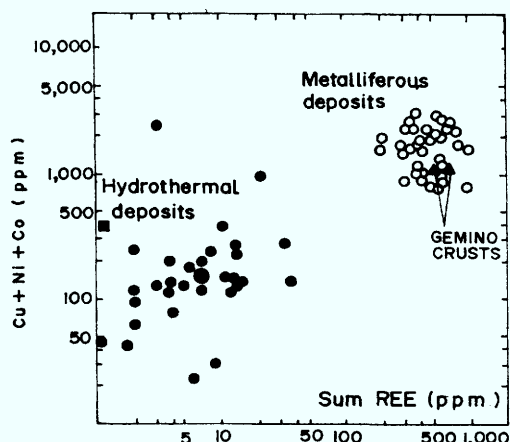


Fig. 8. Correlation between Σ REE and Cu + Ni + Co concentrations in hydrothermal deposits and metalliferous sedimentary deposits (adopted from Clauer *et al.* 1984). Data represented by smaller open and filled circles corresponds to hydrothermal and metalliferous material from FAMOUS, Galapagos, Cyprus, DSDP leg 54, Bauer deep, Marquesas zone and N. Pacific (Clauer *et al.* 1984 and references therein). GEMINO data (closed triangles) fall in the field of metalliferous deposits. Big closed circle and square denote Galapagos data from Clauer *et al.*

and also found in other areas such as Red Sea, Galapagos, Tonga-Kermadec etc., are the last phase (most distal) to precipitate in a hydrothermal fractionation sequence. More proximal members of such sequence include iron silicates and polymetallic sulphides (Cronan *et al.* 1982).

B.N. wishes to thank R. R. Nair, project Co-ordinator (PMN) and E. Desa, Director, NIO for their encouragement and permission to publish. S. Jaishankar is thanked for his help during the data analyses and typing the manuscript. Two anonymous reviewers and Editor in-charge for this manuscript J. Hein (USGS) considerably improved the text, and our sincere thanks to them.

GEMINO cruises were organized with the financial assistance from German Research Foundation (DMG). The ICP-AES equipment used in this work for REE analyses was purchased with funds from the Belgian Fonds de la Recherche Fondamentale Collective under contract No. 9.4569.83. Research completed in co-operation with IGCP Project 318 on Marine Polymetallic oxides.

References

- BATURIN, G. N. & ROZANOVA, T. V. 1975. Ore mineralization in the rift zone of the Indian Ocean. In: VINOGRADOV, A. P. & UDINTSEV, G. B. (eds) *Rift zones of the world ocean*. Wiley-Halsted, New York, 431–441.
- BOLTON, B. R., BOTH, R., EXON, N. F., HAMILTON, T. F., OSWALD, J. & SMITH, J. D. 1988. Geochemistry and mineralogy of seafloor hydrothermal and hydrogenetic Mn oxide deposits from the Manus Basin and Bismarck Archipelago region of the southwest Pacific Ocean. *Marine Geology*, **85**, 65–87.
- BONATTI, E., KRAEMER, T. & RYDELL, H. 1972. Classification and genesis of submarine iron-manganese deposits. In: HORN, D. R. (ed.) *Ferromanganese deposits of the ocean floor*. Aren House, Harriman, 473–489.
- CHAUBEY, A. K., KRISHNA, K. S., RAJU, L. V. S. & RAO, D. G. 1990. Magnetic anomalies across the Southern Central Indian Ridge: evidence for a neo-transform fault. *Deep-sea Research*, **37**, 647–656.
- CHEN, J. C. & OWEN, R. M. 1989. The hydrothermal component in ferromanganese nodules from the southeast Pacific Ocean. *Geochemical Cosmochimica Acta*, **53**, 1299–1305.
- CLAUER, N., STILLE, P., BONNOT-COURTOIS, C. & MOORE, W. S. 1984. Nd-Sr isotopic and REE constraints on the genesis of hydrothermal manganese crusts in the Galapagos. *Nature*, **311**, 743–745.
- CORLISS, J. B., DYMOND, J., GORDON, L. I., EDMOND, J. M., VON HERZEN, R. P., BALLARD, R. D., GREEN, K., WILLIAMS, D., BAINBRIDGE, A., CRANE, K. & VAN ANDEL, T. H. 1979. Submarine thermal springs on the Galapagos rift. *Science*, **203**, 1073–1083.
- CRONAN, D. S. 1979. Metallogensis at oceanic spreading centres. *Journal of the Geological Society, London*, **136**, 621–626.
- , GLASBY, G. P., MOORBY, S. A., THOMSON, J., KNEDLER, K. E. & McDougall, J. C. 1982. A submarine hydrothermal manganese deposit from the south-west Pacific island arc. *Nature*, **298**, 456–458.
- DE CARLO, E. H., MCMURTY, G. M. & KIM, K. H. 1987. Geochemistry of ferromanganese crusts from the Hawaiian Archipelago. I. Northern survey areas. *Deep-Sea Research*, **34**, 441–467.
- DYMOND, J. 1981. The geochemistry of Nazca Plate surface sediments: an evaluation of hydrothermal, biogenic, detrital, and hydrogenous sources. In: KULM, L. D., DYMOND, J., DASCH, E. J. & HUSSONG, D. M. (eds) *Nazca plate: Crustal formation and Andean convergence*. Geological Society of America Memoirs, **154**, 133–174.
- & EKLUND, W. 1978. A microprobe study of metalliferous sediment components. *Earth and Planetary Science Letters*, **40**, 243–251.
- ELDERFIELD, H. & GREAVES, M. J. 1981. Negative cerium anomalies in the rare earth element patterns of oceanic ferromanganese nodules. *Earth Planetary Science Letters*, **55**, 163–170.
- FLEET, A. J. 1983. Hydrothermal and hydrogenous ferromanganese deposits: Do they form a continuum? The rare earth element evidence. In: RONA, P. A., BOSTROM, K., LOUBIER, L. & SMITH, K. L. (eds) *Hydrothermal processes at seafloor spreading centers*. NATO Conference series, **12**. Plenum, New York, 535–555.

- FUTA, K., PETERMAN, Z. E. & HEIN, J. R. 1988. Sr and Nd isotopic variations in ferromanganese crusts from the central Pacific: Implications for age and source provenance. *Geochimica et Cosmochimica Acta*, **52**, 2229–2233.
- GOLDBERG, E. D. 1961. Chemistry in the oceans. In: SEARS, M. (ed.) *Oceanography*. American Association for the Advanced Science Publications, **67**, 583–597.
- GRAYBEAL, A. L. & HEATH, G. R. 1984. Remobilization of transition metals in surficial pelagic sediments from the Eastern Pacific. *Geochimica et Cosmochimica Acta*, **48**, 965–975.
- GRILL, E. V., CHASE, R. L., MACDONALD, R. D. & MURRAY, J. W. 1981. A hydrothermal deposit from Explorer ridge in the Northeast Pacific Ocean. *Earth and Planetary Science Letters*, **52**, 142–150.
- HALBACH, P. & PUTEANUS, D. 1988. Internal Texture. In: HALBACH, P., FREIDRICH, G. & VON STACKELBERG, U. (eds) *The Manganese Nodule Belt of the Pacific Ocean, Geological Environment, Nodule formation, and Mining aspects*. Ferdinand Enke, Stuttgart, 51–56.
- , BLUM, N., VAN GERVEN, M. & PLÜGER, W. L. 1994. Massive sulfides from the central Indian Ocean Ridge. *EOS* **75**, 204.
- HEIN, J. R., AHN, J.-H., WONG, J. C. et al. 1992. *Geology, geophysics, geochemistry, and deep-sea mineral deposits, Federal States of Micronesia: KORDI-USGS, R.V. Farnella Cruise F11-90-CP*. United States Geological Survey Open File Reports, 92–218.
- , SCHULZ, M. S. & KANG, J.-K. 1990. Insular and submarine ferromanganese mineralization of the Tonga-Lau region. *Marine Mining*, **9**, 305–354.
- , YEH, H.-W., GUNN, S. H., GIBBS, A. E. & WANG, C.-H. 1994. Composition and origin of hydrothermal ironstones from central Pacific seamounts. *Geochimica et Cosmochimica Acta*, **58**, 179–189.
- HERZIG, P. M., PLÜGER, W. L. & SHIPBOARD SCIENTIFIC PARTIES. 1988. Exploration for hydrothermal mineralization near the Rodriguez Triple Junction, Indian Ocean. *Canadian Mineralogist*, **26**, 721–736.
- , VON STACKELBERG, U. & PETERSEN, S. 1990. Hydrothermal mineralization from the valu Fa ridge, Lau back-arc basin (SW Pacific). *Marine Mining*, **9**, 271–301.
- HODKINSON, R. A., STOFFERS, P., SCHOLTEN, J., CRONAN, D. S., JESCHKE, G. & ROGERS, T. D. S. 1994. Geochemistry of hydrothermal manganese deposits from the Pitcairn Island hotspot, south-eastern Pacific. *Geochimica et Cosmochimica Acta*, **58**, 5011–5029.
- INGRAM, B. C., HEIN, J. R. & FARMER, G. I. 1990. Age determination and growth rates of Pacific ferromanganese deposits using strontium isotopes. *Geochimica et Cosmochimica Acta*, **54**, 1709–1721.
- JEAN-BAPTISTE, P., MANTIS, F., PAUWELLS, H., GRIMAUD, D. & PATRIAT, P. 1992. Hydrothermal ³He and manganese plume at 19°29'S on the Central Indian Ridge. *Geophysical Research Letters*, **19**, 1787–1790.
- KRAUSKOPF, K. B. 1957. Separation of manganese from iron in sedimentary processes. *Geochimica et Cosmochimica Acta*, **12**, 61–84.
- LONSDALE, P., BURNS, V. M. & FISK, M. 1980. Nodules of hydrothermal birnessite in the caldera of a young seamount. *Journal of Geology*, **88**, 611–618.
- LISITZYN, A. P. (ed.) 1986. *Transform rifts in the Indian Ocean* [in Russian]. Nauka, Moscow.
- & GURVICH, E. G. (eds) 1987. *Metalliferous sediments in the Indian Ocean* [In Russian]. Nauka, Moscow.
- LYLE, M. 1982. Estimating growth rates of ferromanganese nodules from chemical compositions: implications for nodule formation processes. *Geochimica et Cosmochimica Acta*, **46**, 2301–2306.
- MANHEIM, F. T. & LANE-BOSTWICK, C. M. 1988. Cobalt in ferromanganese crusts as a monitor of hydrothermal discharge on the Pacific seafloor. *Nature*, **335**, 59–62.
- MCMURTRY, G. M., VONDERHAAR, D. L., EISENHAUER, A., MAHONEY, J. J. & YEH, H.-W. 1994. Cenozoic accumulation history of a Pacific ferromanganese crust. *Earth and Planetary Science Letters*, **125**, 105–118.
- MOORBY, S. A., CRONAN, D. S. & GLASBY, G. P. 1984. Geochemistry of hydrothermal Mn-oxide deposits from the SW Pacific island arc. *Geochimica et Cosmochimica Acta*, **48**, 433–441.
- MOORE, W. S. & VOGT, P. R. 1976. Hydrothermal manganese crusts from two sites near the Galapagos spreading axis. *Earth and Planetary Science Letters*, **29**, 349–356.
- MUNSCHY, M. & SCHLICH, R. 1989. The Rodriguez Triple Junction (Indian Ocean): Structure and evolution for the past one million years. *Marine Geophysical Researches*, **11**, 1–14.
- MURDMAA, I. O., ZHITKOVSKI, YU. YU. & SKORNYAKOVA, N. S. (eds) 1989. *Zelezno-mangantsevye konkrezii Zentral'noi Kitloviny Indijskogo Okeana*. Nauka, Moscow.
- MURPHY, E., MCMURTRY, G. M., KIM, K. H. & DE CARLO, E. H. 1991. Geochemistry and geochronology of a hydrothermal ferromanganese deposit from the N. Fiji Basin. *Marine Geology*, **98**, 297–312.
- NATH, B. N. 1993. *Rare earth element geochemistry of the sediments, ferromanganese nodules and crusts from the Indian Ocean*. PhD thesis, Goa University.
- , BALARAM, V., SUDHAKAR, M. & PLÜGER, W. L. 1992. Rare earth element geochemistry of ferromanganese deposits of the Indian Ocean. *Marine Chemistry*, **38**, 185–208.
- , ROELANDTS, I., SUDHAKAR, M., PLÜGER, W. L. & BALARAM, V. 1994. Cerium anomaly variations in ferromanganese nodules and crusts from the Indian Ocean. *Marine Geology*, **120**, 385–400.
- OWEN, R. M. & OLIVAREZ, A. M. 1988. Geochemistry of rare earth elements in Pacific hydrothermal sediments. *Marine Chemistry*, **25**, 183–196.

- PATRIAT, PH. & PARSON, L. 1989. A survey of the Indian Ocean triple Junction trace within the Antarctic plate. Implications for the junction evolution since 15 Ma. *Marine Geophysical Researches*, **11**, 89–100.
- PLÜGER, W. L. 1990. *Abschlussbericht SO-52 GEMINO-3 Geothermal Metallogenesis Indian Ocean*. RWTH, Aachen.
- , HERZIG, P. M., BECKER, K. P., DEISSMANN, G., SCHOEPS, D., LANGE, J., JENISCH, A., LADAGE, S., RICHNOW, H. H., SCHULZE, T. & MICHAELIS, W. 1990. Discovery of hydrothermal fields at the Central Indian Ridge. *Marine Mining*, **9**, 73–86.
- PUTEANUS, D. & HALBACH, P. 1988. Correlation of Co concentration and growth rate – a method for age determination of ferromanganese crusts. *Chemical Geology*, **69**, 73–85.
- , GLASBY, G. P., STOFFERS, P. & KUNZENDORF, H. 1991. Hydrothermal iron-rich deposit from the Teahita-Mehitia and Macdonald hot spot areas, southwest Pacific. *Marine Geology*, **98**, 389–409.
- RAO, P. S. 1992. Composition and origin of ferromanganese crusts from the central Indian Basin. In: *Proceedings of the Eighth Quadrennial IAGOD symposium*. Schweizerbart'sche Verlagsbuchhandlung, Stuttgart, 585–596.
- & PATTAN, J. N. 1989. Ferromanganese oxides from Mid-Indian Ridge, seamounts and abyssal plains from the Indian Ocean. *Indian Journal of Marine Sciences*, **18**, 11–15.
- ROELANDTS, I. 1992. Inductively coupled plasma determination of nine rare-earth elements in five ferromanganese nodule reference samples. *Spectrochimica Acta*, **47B**, 947–955.
- RONA, P. A. 1984. Hydrothermal mineralization at seafloor spreading centers. *Earth-Science Reviews*, **20**, 1–104.
- , BOSTROM, K., WILDENFALK, L. E. G., MALLETTE, M. & MELSON, W. B. 1981. Preliminary reconnaissance of the Carlsberg Ridge, northwestern Indian Ocean for hydrothermal mineralization. *Transactions American geophysical Union*, **62**, 914.
- , KLINKHAMMER, G., NELSEN, T., TREFRY, J. H. & ELDERFIELD, H. 1986. Black smokers, massive sulphides and vent biota at the Mid-Atlantic Ridge. *Nature*, **321**, 33–37.
- ROZANOVA, T. V. & BATURIN, G. N. 1971. Hydrothermal ore shows on the floor of the Indian Ocean. *Oceanology*, **11**, 874–879.
- RUHLIN, D. E. & OWEN, R. M. 1986. The rare earth element geochemistry of hydrothermal sediments from the East Pacific Rise: Examination of a seawater scavenging mechanism. *Geochimica et Cosmochimica Acta*, **50**, 393–400.
- SCHULZ, M. S. & HEIN, J. R. 1991. *Petrography and chemistry of hydrothermal manganese oxyhydroxides from the Mariana and Izu-Bonin volcanic arcs, west Pacific*. United States Geological Survey Open File Reports, **91-557**.
- SCOTT, R. B., MALPAS, J., RONA, P. A. & UDINTSEV, G. B. 1976. Duration of hydrothermal activity at an oceanic spreading center, mid-Atlantic Ridge (Lat. 26° N). *Geology*, **4**, 233–236.
- SCOTT, R. M., SCOTT, R. B., RONA, P. A., BUTLER, L. W. & NALWALK, A. J. 1974. Rapidly accumulating manganese deposit from the median valley of the Mid-Atlantic ridge. *Geophysical Research Letters*, **1**, 355–358.
- SEYFRIED, W. & MOTTIL, M. J. 1982. Hydrothermal alteration of basalt by seawater under seawater dominated conditions. *Geochimica et Cosmochimica Acta*, **46**, 985–1002.
- SHARMA, P. & SOMAYAJULU, B. L. K. 1987. Composition, mineralogy and depositional history of ferromanganese nodules from World oceans. In: RAO, T. S. S., NATARAJAN, R., DESAI, B. N., NARAYANASWAMY, C. & BHAT, S. R. (eds) *Contributions in Marine Sciences*. Dr. S. Z. Qasim Sastyabhdapurti felicitation vol. National Inst. Oceanography, Dona Paula, Goa, 335–390.
- VON STACKELBERG, U., MARCHIG, V., MÜLLER, P. & WEISER, T. 1990. Hydrothermal mineralisation in the Lau and North Fiji Basins. *Geologisches Jahrbuch*, **D92**, 547–613.
- TOTH, J. R. 1980. Deposition of submarine crusts rich in manganese and iron. *Geological Society of America Bulletin*, **91**, 44–54.
- UDINSTEV, G. B. 1975. *Geological-Geophysical Atlas of the Indian Ocean*. Pergamon, London.
- USUI, A. & NISHIMURA, A. 1991. Hydrothermal manganese oxide deposits from the Izu-Ogasawara (Bonin) – Mariana Arc and adjacent areas. *Bulletin of Geological Society Japan*, **43**, 247–284.
- , YUASA, M., YOKOTA, S., NOHARA, M., NISHIMURA, A. & MURAKAMI, F. 1986. Submarine hydrothermal manganese deposits from the Ogasawara (Bonin) Arc, off the Japan Islands. *Marine Geology*, **73**, 311–322.

Environments of formation of ferromanganese concretions in the Baltic Sea: a critical review

G. P. GLASBY¹, E. M. EMELYANOV², V. A. ZHAMOIDA³,
G. N. BATURIN⁴, T. LEIPE, R. BAHLO¹ & P. BONACKER¹

¹ *Institute für Ostseeforschung, Seestr. 15, 18119 Warnemünde, Germany*

² *Atlantic Branch, P. P. Shirshov Institute of Oceanology, 1, Prospect Mira, Kaliningrad, Russia*

³ *All-Russia Geological Institute (VSEGEI), Sredny Prospect 74, 19026 St Petersburg, Russia*

⁴ *P. P. Shirshov Institute of Oceanology, 23 Krasiknov Street, 117851 Moscow, Russia*

Abstract: Ferromanganese concretions from the Baltic sea can be divided into three main types based on their abundance, morphology, composition and mode of formation; those from the Gulfs of Bothnia, Finland and Riga, from the Baltic Proper and from the western Belt Sea.

Concretions from the Gulf of Bothnia are most abundant in Bothnian Bay where the abundance reaches 15–40 kg m⁻² in an area of about 200 km². This is equivalent to about 3 million tonnes of concretions and has led to these deposits being evaluated as an economic resource. These concretions are mainly spheroidal up to 25–30 mm in diameter and are formed in the uppermost water-rich sediment layers at well-oxidized sites. They are most abundant where sedimentation rates are <0.4 mm a⁻¹. In the Bothnian Sea, flat crusts with low Mn/Fe ratios are widely distributed.

Concretions from the Gulf of Finland are abundant in the eastern half of the gulf with a maximum abundance of 18–24 kg m⁻². One area of about 300 km² in the Russian sector of the gulf contains about 6 × 10⁶ tonnes of spheroidal concretions and is receiving serious attention as an ore resource. These concretions frequently occur in the upper brown oxidized layer of the sediment.

Concretions from the Gulf of Riga are most abundant (up to 17 kg m⁻²) around a central depression containing muddy sediments. Spheroidal concretions occur adjacent to the depression and discoidal concretions and crusts further away.

Concretions from the Baltic Proper are found mainly around the margins of the deep basins in a depth range 48–103 m. The concretions are mainly discoidal 20–150 mm in diameter and crusts. Their abundance is mainly sporadic and more rarely common to abundant. Locally, abundances of 10–16 kg m⁻² are attained. Their formation is the result of the build up of Mn and Fe in the anoxic waters of the deep basins of the Baltic Proper. During major inflows of North Sea water (>100 km³) into the Baltic which occur on average once every 11 years, the anoxic waters are flushed out of the basins. Mn and Fe precipitate out as an unstable gel and are ultimately incorporated into the concretions. The concretions occur mainly on lag deposits in the vicinity of the halocline where strong bottom currents occur.

Concretions from Kiel Bay in the western Belt Sea occur in a narrow depth range of 20–28 m at the boundary between sands and mud in zones of active bottom currents. They occur as coatings on molluscs and as spheroidal and discoidal concretions. In Lübeck–Mecklenburg Bay, the concretions are restricted to limited areas where glacial till is exposed through the mud. The formation of the concretions is influenced by the development of summer anoxia which leads to the diagenetic remobilization and lateral transport of Mn. This accounts for the high Mn/Fe ratios of these concretions.

Increasing attention is being directed to the use of concretions for the long-term monitoring of heavy-metal pollution in the Baltic. The method shows considerable promise. Zn profiles have already been used to monitor such pollution in concretions from Kiel Bay. However, there remain a number of difficulties such as the lack of knowledge of concretion growth rates, the fragmentary knowledge of the input and fate of heavy metals in the Baltic and the different periods of industrialization in the various parts of the Baltic. Such a monitoring techniques would be of considerable value if the Baltic is going to be cleaned up over the next century. A more detailed evaluation of the mode of formation of the ferromanganese concretions and their uptake of heavy metals would therefore appear to be an important next step in developing a strategy for monitoring pollution in the Baltic Sea.

Early reports of ferromanganese concretions from the Baltic Sea include those of Grewingk (1884), Samoïlov & Titov (1922), Hessle (1924) and Gripenberg (1934); the most significant of these have been listed by Manheim (1965) and Ingri (1985). However, it was not until the 1960s and 1970s that major studies on Baltic concretions were carried out. These resulted in the publication of a number of classic papers which described the distribution, morphology, mineralogy and composition of these deposits and gave some insight into their genesis (Manheim 1965; Varentsov & Blashchishin 1976; Winterhalter 1980; Winterhalter *et al.* 1981) as well as a number of overviews of their characteristics (Calvert & Price 1977; Roy 1981). In 1976, a major Swedish programme was initiated to study the behaviour of manganese in the Baltic (Ingri 1985). As part of this programme, a detailed study of concretions from the Gulf of Bothnia was made (Boström *et al.* 1982; Ingri 1985; Ingri & Ponter 1986a, 1987). In part, the aim of these early studies was to evaluate the concretions as a commercial resource (Boström *et al.* 1982; Ingri 1985). This period of activity was followed by a substantial hiatus in which relatively little work was carried out. However, there now appears to be a resumption of interest in the concretions focusing on their possible use in monitoring anthropogenic pollution in the Baltic Sea (Hlawatsch 1993) as well as on more detailed local surveys of these deposits such as in the Polish Exclusive Economic Zone (Glasby *et al.* in press) and in the Gulf of Finland (Zhamoida *et al.* 1996). It is hoped that the present phase of activity will give a much more detailed insight into the origin of the concretions within the various basins of the Baltic Sea as well as into the mode of transport of manganese, iron and other elements to the concretions.

In this study, we review data on the distribution, mineralogy and geochemistry of ferromanganese concretions in the various basins of the Baltic Sea concentrating on published and unpublished Russian material where available. We will then summarize some recent data on the internal structure and uptake of anthropogenic elements in Baltic Sea concretions based on work carried out in Kiel and Warnemünde.

Geological and hydrographic setting

The Baltic Sea can be divided into four main basins, namely the Gulf of Bothnia (comprising Bothnian Bay and the Bothnian Sea), the Gulf of Finland, the Gulf of Riga and the Baltic Proper. The Baltic Proper can be further divided

into the Arkona Sea, Bornholm Sea and Gotland Sea (Wattenberg 1949). In addition, the western Belt Sea can be considered to be a transition zone between the North Sea and Baltic Sea (Wattenberg 1949). For the purposes of classifying ferromanganese concretions, these areas must be treated separately. In the following account, the geological characteristics of the basins are described based mainly on the chapter of Winterhalter *et al.* (1981) and the hydrological characteristics on the chapters of Ehlin (1981), Grasshoff & Voipio (1981) and Kullenberg (1975, 1981). In addition, there are a large number of relevant background papers including Maggaard & Rheinheimer (1974), Gudelis & Emelyanov (1976), Lisitzin & Emelyanov (1981), Voipio (1981), Lisitzin (1984), Anon (1990), Emeis *et al.* (1992), Perttilä & Brüggmann (1992), HELCOM (1994) and Emelyanov (1995). A schematic map showing the principal areas mentioned in the text is shown in Fig. 1.

The Baltic Sea has an area of 374 000 km² of which the Gulf of Bothnia makes up 27.7%, the Gulf of Finland 8.0%, the Gulf of Riga 4.8% and the Baltic Proper 56.0%. The Baltic is a shallow sea; the average depth of the Baltic Proper is 65 m, of the Bothnian Sea 68 m and of Bothnian Bay 43 m. The bathymetry of the sea floor is complex. Its morphology is mainly preglacial in origin with glacial erosion and deposition and subsequent current- and wave-induced sediment transport having had only limited roles in influencing topography.

Bothnian Bay has a maximum depth of 120 m and is separated from the Bothnian Sea by a sill with a depth <40 m. The Bothnian Sea has a number of deeps along its axis, the deepest being the Harnosand Deep (max. depth 230 m). It is separated from the Baltic Proper by the Aland Sea which includes a local tectonic depression (max. depth 290 m). The Gulf of Finland has a maximum depth of c. 80 m. The Gulf of Riga is much shallower (max. depth 54 m) and has a restricted entrance (>20 m). The Baltic Proper is separated from the North Sea by the Kattegatt and the Danish Straits with a minimum depth of 18 m. It may be divided into the western Belt Sea and the southern and central Baltic. The latter is characterized by a number of deeps including the Arkona Basin (55 m), the Bornholm Basin (105 m), the Gdansk Basin (116 m), the Gotland Basin (249 m), the Landsort Basin (459 m) and the Faro Basin (208 m). These basins occupy about 18 000 km² (about 4.8%) of the area of the Baltic. There are also four main shoals in the southern Baltic with large areas less than 20 m deep. The western Belt Sea includes Kiel Bay and Lübeck-Mecklenburg Bay (Seibold *et al.* 1971).

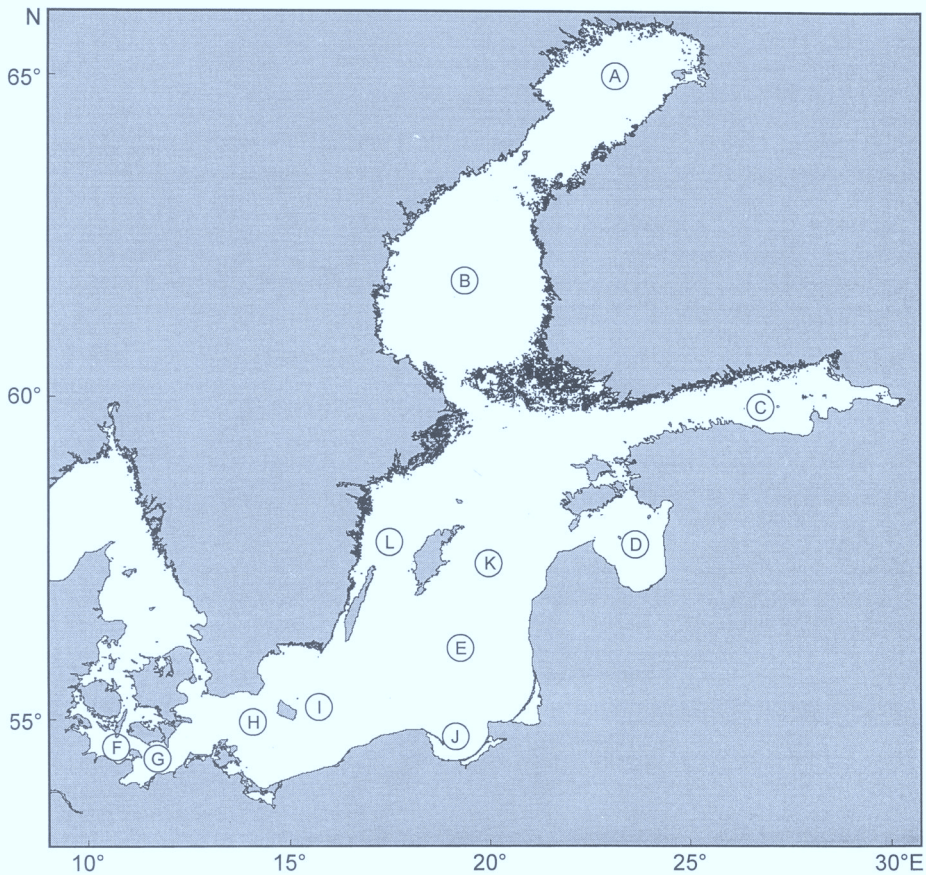


Fig. 1. Schematic map showing the principal areas of interest in the Baltic Sea. A, Bothnian Bay; B, Bothnian Sea; C, Gulf of Finland; D, Gulf of Riga; E, Baltic Proper; F, Kiel Bay; G, Mecklenburg Bay; H, Arkona Basin; I, Bornholm Basin; J, Gdansk Deep; K, Gotland Deep; L, Landsort Deep.

In terms of basement geology, the Baltic may be divided into two regions. Precambrian crystalline basement (Baltic Shield) underlies most of Sweden and Finland whereas Phanerozoic sedimentary rocks underlie the Baltic States, Russia, Poland and Germany. The Gulf of Finland is the dividing line between the two. Proterozoic sedimentary rocks underlie parts of the Gulf of Finland.

The Baltic Sea underwent repeated glaciations during the Pleistocene. Deglaciation of the Baltic took place between 15 000 years BP in the southern Baltic and 9 000 years BP in the Bothnian Bay. The history of the Baltic was then determined by its connection with the sea. The main periods of Baltic evolution are Baltic Ice-Lake (until 10 250 years BP), Yoldia Sea (until 9 500 years BP), Ancylus Lake (until 8 000 years BP), Litorina Sea (until 4 000–3 500 years BP) and the present Baltic (Damm 1992; Witkowski 1994).

Quaternary sedimentation in the Baltic Sea has been described in some detail by Winterhalter *et al.* (1981), Emelyanov (1992, 1995), Raukas & Hyvarinen (1992), Winterhalter (1992) and Harff *et al.* (1995) and sediment charts prepared by Winterhalter *et al.* (1981) and Nielsen (1992). Five major zones of sedimentation were identified (coastal sands, relict clastic deposits, sediment non-deposition, sediment erosion and silts and clays). Factors affecting the distribution of the sediments include the differential post-glacial uplift of the Baltic Sea basin and the multiple transgressions and regressions during the various phases of basin evolution.

In Bothnian Bay, sedimentation is dominated by resedimented material derived from shallower areas as a result of very rapid uplift in the area and the large shallow areas exposed to wave erosion. In the Bothnian Sea, large

areas are dominated by hard bottoms. Extensive deposits of glacial drift occur in the northwest of the sea off the coast of Sweden. The Gulf of Finland is notable for its dissected topography and sedimentation is very variable. The northern part consists of rocky areas alternating with clay sediments. The south-eastern part includes large deposits of glacial drift. Black muds containing H_2S are frequently found in local depressions (Varentsov 1973). A detailed study of sedimentation in a small area of the western Gulf of Finland has recently been carried out by Nuoteva (1994). The influence of bottom currents on sediments was inferred from acoustic profiles. It was shown that erosion takes place at depths less than 40–42 m and that about 23.5% of postglacial sediment has been eroded. In the Gulf of Riga, large deposits of sands and till occur. In the Baltic Proper, there are large areas of hard bottoms and sand.

In the western Belt Sea, sediment is derived mainly from erosion and redeposition of sea-floor material (Seibold *et al.* 1971) (cf. Nielsen 1992). The distribution of sediments in Kiel Bay is mainly dependent on water depth (Heuser 1988). In general, there is a decrease in sediment grain size with increasing distance from shore and with increasing water depth. Sediments from shallow water areas consist mainly of redistributed material from glacial moraines. Sandy sediments displaying ripple marks are found at a depth of about 21 m and muds in the channels. Mixed sediments consisting of coarse sand, fine sand and mud occur at depths of 22–26 m in areas characterized by high bottom current velocities. These areas are particularly favourable for the occurrence of ferromanganese concretions. In Lübeck–Mecklenburg Bay, the water depth lies in the range 20–26 m. Sediment characteristics are dependent on water depth and are similar to those found in Kiel Bay except that a much larger area is covered by mud (Schulz 1969; Lange 1984, 1987; Niedermeyer & Lange 1989, 1990; Eronen *et al.* 1990; Nielsen 1992).

In all parts of the Baltic Sea, zones of mud accumulation are located well below the permanent halocline and the wave-base level including the level of internal waves in the halocline (50–80 m). Emeis *et al.* (1992) have reported average sedimentation rates of about 1 mm a^{-1} for the Baltic over the last 100 years (cf. Boström *et al.* 1983). However, this figure is based on studies at selected sites and should be treated with caution, particularly since concretions generally form in areas of sediment non-deposition.

At present, the Baltic Sea is the largest body of brackish water on earth (Boesen & Potsma 1989). The runoff of river water to the Baltic is about $430 \text{ km}^3 \text{ a}^{-1}$. Runoff to the Gulf of Bothnia makes up about 43% of the total, to the Gulf of Finland about 25%, to the Gulf of Riga about 6% and the Baltic Proper about 26%. It is therefore seen that the Gulfs of Finland, Bothnia and Riga receive a disproportionate amount of the river runoff. In the case of the Gulf of Finland, this is principally due to the presence of the Neva River which is the largest river flowing into the Baltic. The runoff of river water to the Gulf of Bothnia is double that of the Baltic Proper per unit area. There are also seasonal differences in river water runoff to the Baltic. The maximum runoff takes place between April and June and the minimum runoff between November and January. As a consequence, there is a marked variability in the salinity of surface waters in the Baltic, particularly in Spring and Summer. This varies from <3‰ in Bothnian Bay and <5‰ in the Gulf of Finland to <7‰ in the southwestern Baltic in June. The salinity variation is much less in December (<6–8‰). There is also a greater temperature difference in June (<3–14°C) than in December (0–>6°C).

The water balance of the Baltic (in km^3) has been calculated as follows (Winterhalter 1980)

$$\begin{array}{r} \text{Runoff + precipitation + Inflow} \\ 470 \quad 200 \quad 430 \\ \\ = \text{Evaporation + Outflow} \\ 180 \quad 920 \end{array}$$

In fact, there is a large variability in the inflow of water into the Baltic through the Kattegat and Danish Straits both annually and interannually. Maximum inflows occur during the autumn and winter. Interannual inflow can vary by a factor of 1.54.

Because the salinity of the inflowing North Sea water is greater (15–20‰) than that of Baltic surface waters (6.5–7.5‰), the incoming water sinks resulting in stratification of the water column and development of a halocline. The depth of this halocline increases from west to east. It is about 30–40 m in the Arkona Basin, 40–50 m in the Bornholm Basin, 60–70 m in the Baltic Proper and 80 m in the northern part of the Landsort Deep. Anoxia is a common feature below the halocline and nutrients are trapped there. Studies have indicated a marked deterioration of the oxygen content in the waters of the Gotland Deep since the last century (Gerlach 1990; Helcom Experts 1990a). The inflow of North Sea water through Danish Straits is the major source of oxygen in these basins.

The hydrology of Kiel Bay, western Belt Sea, has been summarized by Seibold *et al.* (1971) and Heuser (1988). The salinity of surface water in the bay varies between 9 and 22‰ and of deep water between 14 and 30‰. In Summer, the temperature of surface water reaches 17°C whereas that of bottom water reaches only 12–13°C. In Summer, layering of the water column takes place with a boundary at 16–20 m. This leads to depletion of oxygen in the bottom waters with H₂S development locally in depressions. The conditions required for the development of anoxia in such continental shelf settings have been described in detail by Tyson & Pearson (1991). Severe autumn and winter storms together with cooling of the surface waters destroy this stratification. This leads to a mixed water column with a mean temperature of about 2°C in February–March. All these hydrological conditions are dependent on weather conditions, particularly on wind speed and direction. In Lübeck–Mecklenburg Bay, hydrological conditions are very much less dynamic because the bay is essentially protected on three sides.

The importance of periodic major inflows of North Sea water (>100 km³) into the Baltic has been discussed at length in a previous publication (Glasby *et al.* in press). Such inflows occur sporadically, about 9 times per century on average. This inflow is restricted to the Baltic Proper and does not penetrate into the Gulfs of Bothnia, Finland and Riga because of topographic constraints (Franck *et al.* 1987; Matthäus 1992, 1993a, b; cf. Nausch & Nehring 1994; Nehring & Matthäus 1994). These large inflows are also erosive events due to the generation of internal waves at the halocline. According to Seibold *et al.* (1971), these major inflows of water can lead to bottom water velocities in excess of 1.2 m s⁻¹ through the Fehmarn Belt in Kiel Bay and result in erosion of channels and the generation of megaripples. These inflows reach the eastern Baltic some 16–18 months later.

Within the Gulf of Bothnia, stratification of the water column is much weaker than in the Baltic Proper. This is because Baltic bottom water is unable to penetrate into the Gulf of Bothnia. Instead, Baltic surface water is the main source of bottom water in the gulf. The salinity of the bottom water in the Gulf of Bothnia is therefore only 1.3‰ greater than that of the surface water. Stratification is stable throughout the year but there is no sharp halocline and its depth varies widely. In contrast to the situation in the Baltic Proper, the basins of the Bothnian Bay and Bothnian Sea are well oxygenated and the oxygen level seldom falls

below 60–80%. In parts of the Gulf of Finland, convectational overturn of the water column also occurs during winter which leads to loss of the halocline (Grasshoff 1975; cf. Talpsepp 1990).

A major study of the oxygen content of Baltic Sea water has been undertaken by HELCOM (1990). The oxygen content in the bottom waters of the Bothnian Bay (70 m to bottom) was shown to be in excess of 8 ml l⁻¹ and of Bothnian Sea (100 m to bottom) in excess of 6 ml l⁻¹. The oxygen content in the bottom waters of the Gulf of Finland (50 m to bottom) is very variable (2–10 ml l⁻¹) but no systematic long-term trend was noted. However, the oxygen content of the bottom waters of the Gulf of Riga has declined from about 6 ml l⁻¹ in 1965 to about 5 ml l⁻¹ in 1985 and that in the bottom waters of Kiel Bay declined from about 3 ml l⁻¹ in 1979 to about 2 ml l⁻¹ in 1990 with periods of anoxia increasing over the last decade. The area of 'dead bottoms' in the Gulf of Finland, Baltic Proper, Belt Sea and Kattegatt is now estimated to be about 100 000 km² corresponding to about one third of the seafloor (HELCOM 1993).

The principal factor controlling the distribution of manganese and iron within the Baltic system is the redox characteristics of the environment. These have been well described by Ingri (1985, 1993) and Heuser (1988; cf. Burige 1993; Davison 1993; Thamdrup *et al.* 1994a, b). According to Ingri (1985), sediments from the open Bothnian Bay are characterized by a thick oxidized surface layer up to 0.15 m thick with reducing conditions below this (Ingri & Ponter 1986b). Because Bothnian Bay seawater is well oxygenated, much of the Mn and Fe in the pore waters is fixed within the sediment column. Five layers can be recognized; a brown water-rich surface layer containing spheroidal concretions, a black Mn-rich layer, a brown, hard Fe-rich crust, an orange-brown Fe-rich layer and a yellow-grey transition zone. The Mn-rich surface layer is common in Bothnian Bay sediments but much rarer in those from the Bothnian Sea. Fe-rich strata are, however, common in the Bothnian Sea. This reflects the lower redox level in the Bothnian Sea sediments compared to those from Bothnian Bay. In the Gulf of Finland, the bottom waters display a more variable oxygen content and anoxic zones are developed. In the Baltic Proper, anoxic conditions develop in the basins below the halocline. This leads to a build up of Mn and Fe in the water column there as a result of diffusion from the underlying sediments (Emelyanov *et al.* 1982; Lein 1983; Emelyanov 1986, 1995; Boström *et al.* 1988; Brüggemann 1988; Bernard *et al.* 1989; Dyrssen & Kremling

1990; Ingri *et al.* 1991; Brüggmann *et al.* 1992; Kravtsov 1992; Belmans *et al.* 1993; Neumann *et al.* in press. Dissolved Mn and Fe contents in these waters attain values $<700 \mu\text{g l}^{-1}$ and $120 \mu\text{g l}^{-1}$ respectively (Dyrssen & Kremling 1990; Ingri *et al.* 1991). Mn is also enriched in the basin sediments and occurs mainly as Ca-rhodochrosite (Manheim 1961, 1982; Hartmann 1964; Belmans *et al.* 1993; Huckriede 1993) and Fe as sulphides (Boesen & Potsma 1989). At the borders of these basins, there is a zone of Mn enrichment in the sediments in the vicinity of the halocline as a result of oxidation of the Mn. Mn, Fe and other transition elements contained in the basinal waters may be flushed out during major inflows of seawater from the North Sea, thereby providing a major source of these elements during these events. Layers of gelatinous Mn and Fe oxyhydroxides 10–15 mm thick can form in these circumstances (Emelyanov 1986). These are unstable and become a source of these elements in the adjacent concretions. Higher abundances of ferromanganese concretions have been reported around stagnant depressions by Manheim (1965). However, part of the particulate manganese oxides remains in the basin and is fixed in the sediment column as Ca-rhodochrosite, although this process is much slower (Huckriede 1993). The relationship between manganese oxide deposition and anoxia in adjacent basins is well known in the case of ancient stratiform manganese deposits (Sapozhnikov 1967, 1984; Okita *et al.* 1987; Force & Cannon 1988; Jenkyns *et al.* 1991; Kukul 1991; Frakes & Bolton 1992; Roy 1992; Polgari 1993; Brüchert *et al.* 1994). For the areas lying above the halocline, layered oxidized sediments are very rare in the Baltic Proper and ferromanganese concretions are much less

abundant than in the Gulf of Bothnia. Figure 2 summarizes the pathways of Mn and Fe into the Baltic Sea based on the data of Ingri (1985).

The importance of seasonal effects on manganese and iron mobilization in sediments from Kiel Bay has been demonstrated experimentally by Heuser (1988). Other studies of Mn and Fe cycling in the Bay have been presented by Hartmann (1964), Djafari (1976), Balzer (1982, 1989), Balzer *et al.* (1983, 1987) and Lapp & Balzer (1993). Similar effects have been observed in lakes (Sigg *et al.* 1995; Wehrli *et al.* 1995).

The low inflow of North Sea water into Kiel Bay in Summer and Autumn leads to a layering in the water column. As a result of the Spring plankton bloom, an oxygen-minimum zone develops in the bottom waters in Summer which leads to an increase in the dissolved Mn and Fe contents of the bottom waters. The maximum dissolved Mn content of $>100 \mu\text{l}^{-1}$ is attained in October/November somewhat after the minimum oxygen and maximum H_2S ($700\text{--}1000 \mu\text{g l}^{-1}$) contents of the waters are achieved. The maximum dissolved Fe content of $<1000 \mu\text{g l}^{-1}$ occurs about two months later. Similar studies in the Skaggeak show that the cycling of Mn and Fe in the sediment column is very rapid (Canfield *et al.* 1993a) (cf. Canfield *et al.* 1993b; Bakker & Helder 1993). The cooling of the surface waters and the onset of storms in late Autumn results in a mixing of the water masses. As a consequence, the bottom waters become well oxygenated in Winter and Spring such that the redox boundary lies below the sediment–water interface. In this situation, migration of Mn and Fe from the sediments into the bottom waters is limited by a millimetre-to-centimetre-thick layer of oxidized sediment. Within Kiel Bay, porewater fluxes of Cd, Cu and

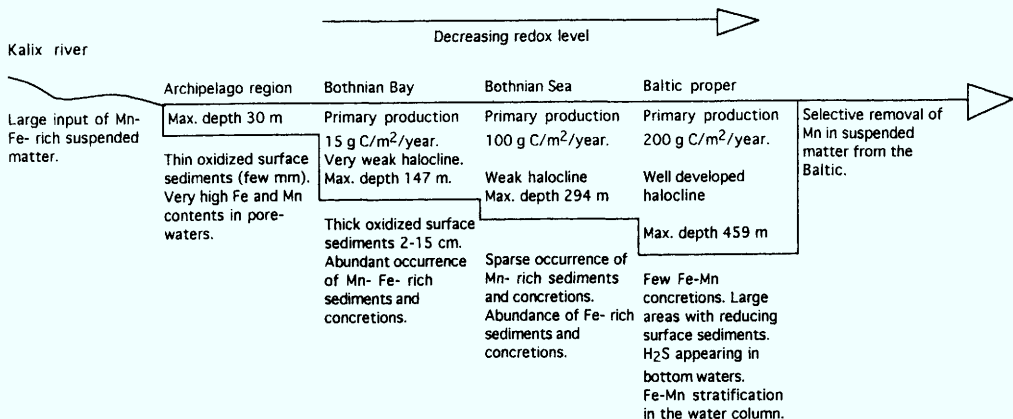


Fig. 2. Schematic representation of the pathways of Mn and Fe in the Baltic Sea after Ingri (1985).

Ni are higher in shallower (20–21 m) (more oxic) sediments than in deeper (24–25 m) anoxic sediments (Lapp & Balzer 1993). This may influence the uptake of these elements into the concretions.

Similar seasonal variations in hydrological conditions occur in Mecklenburg Bay. The enrichment of Mn in the pore waters of the organic-rich muds is less than that found in Kiel Bay but that of iron is similar (Niedermeyer & Lange 1989).

Ferromanganese concretions

The general characteristics of the morphology, mineralogy and composition of Baltic ferromanganese concretions have been well described in a number of major papers (Manheim 1965; Varentsov & Blashchishin 1976; Calvert & Price 1977; Winterhalter 1980; Winterhalter *et al.* 1981; Ingri 1985) and it is not the intention to repeat these descriptions. Rather attention will be focused on the nature of the concretions in each of the major basins within the Baltic. Because of its relative inaccessibility, particular attention will be directed towards the Russian literature. 80 Soviet cruises have been undertaken to carry out geological investigations in the Baltic since 1965 and half the scientific publications on the Baltic are in Russian. This has resulted in a large Russian literature on concretions (Samoilov & Titov 1922; Gorshkova 1961, 1963, 1967; Shterenberg *et al.* 1968, 1975; Strakhov *et al.* 1968; Putans *et al.* 1968; Shterenberg 1971; Varentsov 1973, 1975; Varentsov & Blashchishin 1974, 1976; Strakhov 1976; Varentsov *et al.* 1977; Butylin *et al.* 1985; Shnukov *et al.* 1987; Baturin 1988; Baturin *et al.* 1988; Butylin & Zhamoida 1988; Zhamoida 1989; Gorshkov *et al.* 1992; Zhamoida & Butylin 1992, 1993; Zhamoida *et al.* 1996; Baturin & Emelyanov in press).

Three principal types of ferromanganese concretions occur within the Baltic (spheroidal, discoidal and crusts) (Manheim 1965; Djafari 1976; Varentsov & Blashchishin 1976; Winterhalter 1980; Ingri 1985; Heuser 1988; Zhamoida *et al.* 1996). Figure 3 is a schematic representation of the distribution of concretions throughout the Baltic based on the work of Manheim (1965), Winterhalter (1966), Varentsov (1975), Djafari (1976), Varentsov & Blashchishin (1976) and Ingri (1985). The following section will not describe the principal characteristics of concretions from each of the main basins of the Baltic.

Ferromanganese concretions from the Gulf of Bothnia have been studied by Gripenberg

(1934), Winterhalter (1966, 1980), Winterhalter & Siivola (1967), Boström *et al.* (1982), Ingri (1985, 1993), Ingri & Ponter (1986a, 1987), Mellin (1987), Sanchez *et al.* (1988), Kimberley (1989) and Amakawa *et al.* (1991).

Within the Gulf of Bothnia, spheroidal concretions are the most abundant (Ingri 1985). These are formed within the uppermost water-rich sediment layer at well-oxidized sites and have maximum diameters of 25–30 mm. They display the highest Mn/Fe ratios of the various concretion types (av. 0.70). Mo, Ba, Ni, Cu, Co and Zn are closely associated with the Mn-rich phase. Buried concretions contain lower contents of Ni, Cu, Zn, Y and REE than the surface concretions. They are found in high abundance in Bothnian Bay but in much lower abundance in the Bothnian Sea.

About 30% of Bothnian Bay is characterized by an abundance of spheroidal concretions in the range 0.5–2 kg m⁻² and a further 5% in the range 5–15 kg m⁻². An abundance in the range 15–40 kg m⁻² is found in an area of 200 km². This corresponds to about 3 million tonnes of concretions or 0.2 × 10⁶ t of Mn on a dry weight basis. In all, about 21 × 10⁶ t of concretions are found in Bothnian Bay and these deposits have attracted economic attention. These concretions occur in a depth range 35–115 m.

Discoidal concretions are the least abundant of the three concretion types. These display somewhat lower Mn/Fe ratios (av. 0.55) than the spheroidal concretions but display negative Ce anomalies suggesting that they are found at a lower redox level in the vicinity of the redox boundary.

Flat slabs and crusts have very low Mn/Fe ratios (av. 0.09) and somewhat higher contents of P (3.1% P₂O₅) which is associated with the Fe-rich phase.

Mineralogically, the concretions appear to contain 7 Å manganese as the principal Mn oxide mineral (Ingri 1985). However, no attempt was made to prevent drying of the concretions prior to study and it could be that the 7 Å peak is simply an artefact caused by the collapse of the original 10 Å phase.

The average sedimentation rate of post-glacial sediments in Bothnian Bay has been calculated to be 0.15 mm a⁻¹. Concretions are most abundant at this sedimentation rate but are absent at rates greater than 0.4 mm a⁻¹. Under optimal conditions in which spheroidal concretions grow in oxidized surface sediments containing high contents of Mn and Fe in the interstitial waters, concretions grow at a rate of about 0.15 mm a⁻¹. When concretions form at erosive sites and are exposed to bottom waters, growth rates are

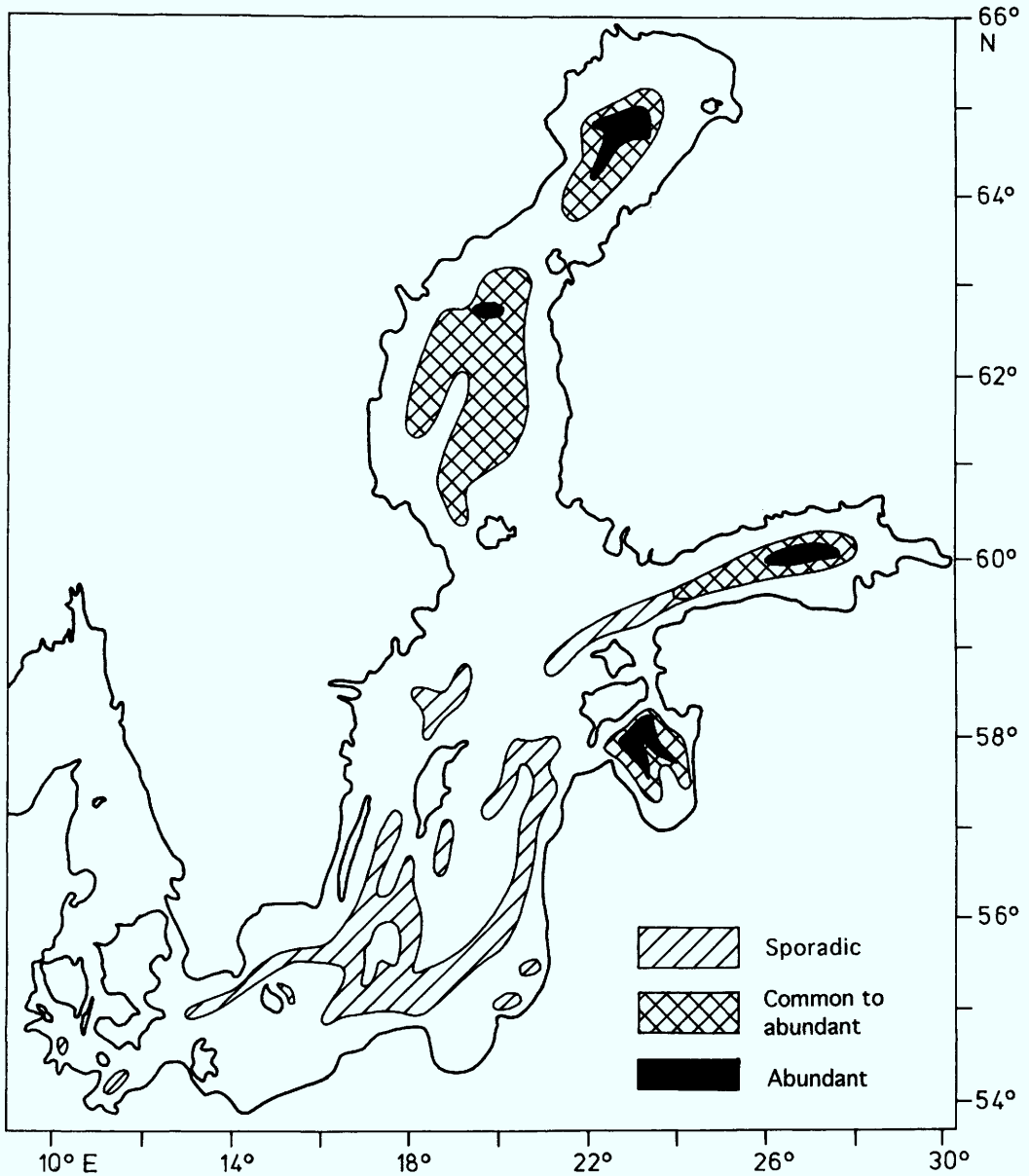


Fig. 3. Schematic map showing the distribution of ferromanganese concretions in the Baltic (after Ingri 1985). Data based on Manheim (1965), Winterhalter (1966), Varentsov & Blashchishin (1976), Kulesza-Owsikowska (1981), Heuser (1988) and Leipe *et al.* (1994). In the abundant areas of the Gulfs of Bothnia, Finland and Riga, Mn-rich spheroidal concretions predominate but, in the Bothnian Sea, Fe-rich discoidal concretions. In the Baltic Proper, Mn-rich concretions are mainly of the girdle type but the deeper areas are barren of concretions. In the Kiel Bay, sporadic to common occurrences of concretions are found.

much lower. The maximum age of the concretions is thought to be about 3000 years. This date corresponds to the age of the proposed dissolution event in the early Littorina Sea which resulted from the development of a permanent halocline in the Gulf of Bothnia.

However, most concretions are undoubtedly much younger than this.

Rare earth element distribution patterns for Gulf of Bothnian concretions have been shown to be dependent on the morphology of the concretions (Ingri & Ponter 1987). The spher-

oidal concretions have higher abundances of REE than the discoidal and flat concretions and display positive rather than negative Ce anomalies. Nonetheless, all display relative enrichments of LREE and negative Eu anomalies. This is taken to indicate that the REE are transported into the gulf on river-derived particulate material. The study of Nd isotope ratios in the concretions lends support to the role of Baltic shield rocks as a source of elements in these concretions (Amakawa *et al.* 1991). This finding is in agreement with the conclusion of Ingri (1985) that till is the main source of Mn, Fe and some associated trace elements in Gulf of Bothnian concretions (cf. Dean & Ghosh 1980).

In the Bothnian Sea, stiff varved glacial clay is exposed to submarine erosion. The varves are easily separated and become encrusted with a few mm of ferromanganese oxides. These crusts have low Mn/Fe ratios, are widely distributed and occur in the depth range 35–170 m.

Ferromanganese concretions from the Gulf of Finland have been studied by Gripenberg (1934), Varentsov (1973), Varentsov & Blashchishin (1974, 1976), Varentsov *et al.* (1977), Butylin *et al.* (1985), Butylin & Zhamoida (1988), Zhamoida (1989), Gorshkov *et al.* (1992), Zhamoida & Butylin (1992, 1993), Zhamoida *et al.* (1996) and Baturin & Emelyanov (in press).

The morphology of concretions in the Gulf of Finland takes many forms. Baturin & Emelyanov (in press) have described the concretions as spheroidal, buckshot, discoidal, rod-like and irregular. In addition, they also reported the occurrence of crusts and coatings on shells of mussels and rock fragments. V. A. Zhamoida classified the concretions into 18 types, although this was summarized to three major types for publication (Zhamoida *et al.* 1996. He considered the morphology of the concretions to be the result of environmental factors as follows:

zero rate of sedimentation	discoidal concretions
low rates of sedimentation	concave (saucer) concretions
pulses of clastic sediments or erosion	penny-shaped concretions with clastic nuclei
low rates of erosion	crusts incorporating clastic material or cementation of superficial deposits
high bottom currents	spheroidal concretions with gravel nuclei

covering by mud	dissolution of concretions; loss of clastic nuclei results in penny-shaped concretions without nuclei
redistribution of concretions by bottom currents or slumping	very concave concretions; aggregates of concretions

The morphology of the concretions is therefore seen to be influenced by their position in the sediment column (i.e. whether in the oxidizing or reducing layers of the sediment), by sediment slumping or by coverage by mud.

The morphology of the concretions has been described in more detail by Varentsov & Blashchishin (1976). The concretions were classified as follows.

Spheroidal concretions. Buckshot concretions 1–10 mm in diameter by typically 2–5 mm, also silt- to sand-sized, with irregular spheroidal shape, occurring in the central part of the gulf in water depths of 54–77 m. Bean-shaped concretions 10–50 mm in diameter spheroidal to ellipsoidal to irregularly-shaped, occurring principally in the central and eastern part of the gulf in water depths of 40–62 m, although mainly 40–45 m.

Discoidal concretions. Concentric horizontal banding around erratic nuclei consisting mostly of granite fragments; irregular round shapes up to 10 × 7 × 0.5 mm to 50 × 35 × 3 mm (penny-shaped) and 100 × 70 × 3 mm (discoidal) occurring in water depths of 31–52 m at the surface and within olive-green, brownish silt layers in the eastern part of the gulf.

Crusts (Fe-rich, low Mn). Small crusts with Fe-Mn oxyhydroxide layers 5–7 mm thick on the upper surfaces of rock fragments (mostly granite) found at the sediment-water interface, no growth on the underside, transitional to discoidal form where oxide layer >5 mm thick, occurring in water depths 24–48 m, although seldom in depths greater than 30 m. Large crusts flat and irregular up to 200–300 mm in diameter, cavernous surface texture, growth rings, possible coalescence of several crusts, predominantly found to the north of the central part of the gulf in water depths of up to 70 m.

The concretions occur in elevated areas characterized by slow sedimentation (Varentsov 1973). Concretions, crusts and microconcretions are found mainly in the upper brown oxidized sediment layer (Baturin & Emelyanov in press). The concretions are frequently overlain by a 60–100 mm thick mud layer and have a size range

<1–30 mm. They form layers several centimetres thick where they coalesce to produce various morphological types. The abundance of the concretions in these zones lies in the range 18–24 kg m⁻² with a maximum surface coverage of 25%. The associated microconcretions tend to be concentrated in the 0.05–0.10 mm size class.

Mineralogically, the concretions consist dominantly of quartz with lesser amounts of alkali feldspar, montmorillonite and traces of chlorite and kaolinite (Varentsov & Blashchishin 1976). 7 Å manganite is the principal Mn oxide phase. 10 Å manganite occurs rarely. Traces of Carhodochrosite are also observed. In terms of composition, spheroidal concretions display the highest Mn contents (28.8%) and penny-shaped concretions from greater depths the highest Fe contents (37.5%) (Baturin & Emelyannov in press). Co tends to be associated with Mn and Sc and Th with Fe in these concretions.

The abundance of the concretions has been mapped by Varentsov & Blashchishin (1976). The highest abundances were shown to occur in the eastern half of the gulf, particularly north of the axis of the gulf. The concretions occur in a depth range 29–78 m. According to Zhamoïda *et al.* (1996), the area rich in concretions within the Russian sector of the Gulf of Finland occupies about 300 km² and contains about 6 × 10⁶ t of concretions equivalent to 1 × 10⁶ t of Mn. Because of recent events which have restricted supplies of Mn from the Ukraine, these deposits are now seen as commercially attractive. The deposits consist of spheroidal concretions which are rich in Mn (21.4%) and contain no discernible foreign nuclei (Ingri 1985). However, they do contain appreciable P (2.7% P₂O₅). A St Petersburg firm, Hypronikel, has developed a technique for removing the P from the concretions. The deposits can therefore be regarded as a low-grade Mn ore with an economic lifetime of perhaps 100 years. There appears to be considerable interest in exploiting this field at present.

Buried concretions from the Russian sector of the Gulf of Finland (60°09' N 28°12' E) were also studied by Gorshkov *et al.* (1992). These authors found a layer of concretions 30–40 mm thick overlain by 30–60 mm of clayey mud at a water depth of 45 m. The concretions had diameters ranging from a few millimetres to 30 mm and were closely packed forming complex agglomerations or pavements. The smaller concretions had relatively smooth surfaces whereas the larger concretions (15–30 mm in diameter) had botryoidal surfaces with many cracks. Under the microscope, the botryoids were seen to be agglomerations of microconcretions. The interiors of

the concretions contained mud but no distinct nuclei. The bridges between the agglomerated concretions consisted of friable black to brown black material overlain by a veneer of orange to red material.

The mineralogy of the concretions was studied by electron microscopy and diffraction as well as energy dispersive analysis. The orange to red material on the surface of the concretions was shown to be a mixture of Mn-feroxyhyte and protoferrihydrite with lesser amounts of vernadite. The smaller concretions consisted of brown to dark red material (Mn-feroxyhyte, protoferrihydrite and sometimes goethite) or black to brown black material (birnessite and Mn-feroxyhyte). The surfaces of the larger concretions are made up of botryoids consisting of finely dispersed birnessite with lesser amounts of Mn-feroxyhyte together with Fe-poor and Fe-rich vernadite. The interiors of these concretions consist mainly of brown black material (finely dispersed birnessite, disordered todorokite and Mn-feroxyhyte) interspersed with thin layers (<1 mm) or spots (1–2 mm) of orange material (Mn-feroxyhyte and protoferrihydrite with rare goethite and hematite). The Mn contents of the larger concretions increase towards the interior of the concretion. It was concluded that the larger concretions are formed by agglomeration and recrystallization of smaller concretions. This is shown by the formation of layers within these concretions, the increasing Mn contents in the interiors of the concretions, the increasing Mn contents in the interiors of the concretions and the formation of bridges between the various accreted smaller concretions. Microbiological investigations indicated that *Siderocapsa* bacteria play an important role in the oxidation of Mn and Fe in these concretions.

Ferromanganese concretions from the Gulf of Riga have been studied by Putans *et al.* (1968), Shterenberg *et al.* (1968), Shterenberg (1971), Varentsov (1973), Varentsov & Blashchishin (1976) and Varentsov *et al.* (1977).

The concretions occur in water depths of 19–37 m with an abundance of up to 17 kg m⁻² around a central depression (>40 m) containing muddy sediments. The most abundant deposits are confined to the gently sloping sides of this depression and occur in the western and central part of the gulf away from the influence of the Daugava River.

The morphology of the concretions has been described in more detail by Varentsov & Blashchishin (1976). The concretions were classified as follows.

Spheroidal concretions. Buckshot concretions 1–10 mm in diameter but typically 2–5 mm, also

smaller to 0.016 mm, with irregular spheroidal shape, predominant form in the Gulf of Riga. Bean-shaped concretions 10–50 mm in diameter with irregular spheroidal, sometimes ellipsoidal, shape, concentrically layered around a lithogenous, usually clay, nucleus, rarer than buckshot concretions).

Discoidal concretions. Concentric horizontal banding around erratic nuclei, Fe > Mn, size up to 10 × 0.5 mm to 50 × 3 mm (penny-shaped) and 150 × 5 mm (discoidal) occurring in shallower water depths of 31–52 mm, rare.

Crusts (Fe-rich, low Mn). Small crusts formed predominantly on the upper surfaces of rock fragments (mostly glacial clay) and above the sediment–water interface with only limited growth occurring on the underside, uneven, flat 40–200 × 10 mm, occurring in water depths 24–48 m, although rarely in depths greater than 30 m. Large crusts mostly occurring with abundant deposits of bean-shaped spheroidal concretions.

Mineralogically, the concretions consist dominantly of quartz with feldspar, heavy minerals from the granitic complex and clay minerals from the associated sediment as well as traces of Ca-rhodochrosite. The principal Mn oxide minerals are 7 Å manganite and poorly crystalline 10 Å manganite.

Spheroidal concretions have high Mn contents (>15%) and low Fe contents (<15–20%) and are associated with muddy, organic-rich sediments adjacent to the depression. Discoidal concretions and crusts occur at shallower depths away from the depression and are associated with silts and sands. They have higher Fe contents (>30%) but lower Mn contents (<5%). This compositional trend has been mapped by Varentsov & Blashchishin (1976, figs 133 and 134). According to Varentsov (1973), the concretions tend to form in brown watery muds (up to 50 mm thick) overlying rather thin (70–100 mm) dark grey silts containing H₂S. These muds can contain up to 80% by volume of concretions.

In the Baltic Proper, the concretions appear to be distributed mostly around the margins of the basins as previously described by Manheim (1965) and Varentsov (1973). The abundance of the concretions has been charted as being in the range sporadic or more rarely common to abundant (Varentsov & Blashchishin 1976; Ingri 1985). The abundance therefore never reaches the levels encountered in the Gulfs of Bothnia, Finland and Riga. The concretions are found in the depth range 48–103 m and attain abundances of 10–16 kg m⁻² locally (Varentsov & Blashchishin 1976).

The morphology of the concretions has been described in detail by Varentsov & Blashchishin (1976). The concretions were classified as follows.

Discoidal concretions. Concretic horizontal banding around erratic nuclei, irregular round to ellipsoidal in shape, diameter 20–150 mm, thickness 20–70 mm.

Crusts (Fe-rich, low Mn). Small crusts <1–15 mm in diameter formed on exposed gravel and rocks, also occurring as thin margins 1–3 mm wide around nuclei (girdle form), sometimes the margins are mushroom shaped and curve towards the underside, then 3–10 mm wide and 10–20 mm thick; large crusts widely distributed on brown-grey glacial clay, irregular, bizarre forms or plate shaped, upper surface concave, cavernous with holes 5–20 mm in diameter, Fe–Mn oxyhydroxide crust layer 5–50 mm thick, underside hard substrate material with only thin Fe–Mn coating, size range of sample 100–170 mm, sometimes 25–400 mm.

The concretions occur mainly in the transition zone between shallow sands and silts and deep-water terrigenous muds. Late Quaternary oxidized brown clays and the erosion products of moraines-gravels with boulders and pebbles occur in this zone and ferromanganese concretions are widespread there (Emelyanov *et al.* 1982). According to Varentsov (1973), the concretions generally occur on coarse clastic sediments and not infrequently on the eroded surfaces of glacial clays. The nature of the concretions in the Polish Exclusive Economic Zone has been described in detail recently (Glasby *et al.* in press). It is not proposed to repeat these descriptions here.

In Kiel Bay, some of the most detailed descriptions of concretions and their mode of formation have been undertaken (Seibold *et al.* 1971; Djafari 1976; Suess & Djafari 1977; Hueser 1988; Hlawatsch 1993). The concretions occur under a narrow range of conditions, in a depth range of 20–28 m at the boundary between sands and muds. The most favourable substrate appears to be a mixed sediment which consists mainly of mud intermixed with coarse material of variable grain size (including gravel) and forms as thin deposits on Pleistocene surfaces bordering mud areas. Benthic fauna are rich on this substrate.

Three types of ferromanganese deposits were identified by Djafari (1976) as follows:

(a) Ferromanganese coatings on the surface of mussels and crabs. These deposits grow rapidly as shown by the occurrence of 2 mm thick layers of ferromanganese oxides on living molluscs.

(b) Spheroidal concretions with diameters of 10–30 mm. These concretions sometimes have a small nucleus of feldspar, quartz or flint. However, 80% have no discernible nucleus but instead loose, clayey material. Bottom currents in the areas where these form are typically in the range 0.18–0.28 m s⁻¹.

(c) Discoidal concretions with diameters of 20–100 mm. These are generally formed around a nucleus of flint or granite. The upper surfaces are convex and the lower surfaces concave. Bottom currents are typically in the range 0.24–0.45 m s⁻¹.

The concretions have high Mn/Fe ratios varying from 3.5 for deposits on mussels to 2.5 for discoidal concretions. Zn contents are much higher in the deposits formed on mussels (av. 1128 ppm) than in the other types (av. 166 ppm in spheroidal concretions and 188 ppm in discoidal concretions). These high Zn contents on the mussel shells could reflect the very recent deposition of the ferromanganese oxides there. Mineralogically, both 10 Å manganite and 7 Å manganite were identified in the concretions.

Heuser (1988) made a more detailed study of the concretions at three localities on the western side of Kiel Bay, Breitgrund, Schleimünde and Hausgarten. The areas were chosen to be in a restricted depth range on the margins of the bay. A different pattern of distribution of concretions in each of these areas was established. At Breitgrund to the north, spheroidal and discoidal concretions occur on an elevated area of stiff glacial till whereas ferromanganese deposits on mussels are found on soft mixed sediments. At Schleimünde on the other side of the channel, ferromanganese deposits on mussels and discoidal concretions as well as transitional forms occur on muddy fine sand. The sediments become finer with depth and the concretions cease to occur at a depth of 27 m. At Hausgarten to the south, only ferromanganese deposits on mussels are found. This reflects the weaker currents occurring there as well as the proximity of the area to an actively eroding coastline which results in a high rate of sediment supply. These deposits are restricted to a limited area of lag sediments. The ferromanganese oxides are deposited on the mussel *Astarte* which is capable of keeping at the sediment surface in a high sedimentation regime.

In Lübeck–Mecklenburg Bay, much less information is available on the distribution and characteristics of ferromanganese concretions (Wenk 1981; Moenke-Blankenburg *et al.* 1989; Leipe *et al.* 1994). The concretions are restricted to the relatively small areas where glacial till (boulder clay) is exposed through the mud

(Wenk 1981; Lange 1987; Nielsen 1992). The concretions occur at the boundary of the till and mud and have a light covering of mud (Leipe *et al.* 1994). The concretions occur in water depths of 20–25 m (Wenk 1981). They are generally asymmetrical and discoidal and have a maximum diameter of 170 mm and a maximum thickness of 20 mm. They form on substrates of erratic rock. Their colour varies from light to dark brown. The surface of the concretions is mainly porous but can be smooth. The larger concretions are usually cracked. Leipe *et al.* (1994) has calculated the enrichment of various elements in these concretions relative to the underlying sediment to be in the order

$$\text{Mn}(646) > \text{Fe}(3.6) > \text{Co}(3.4) > \text{Ni}(2.9) > \text{Zn}(1.9) \\ > \text{Cu}(0.8) > \text{Pb}(0.5) > \text{Cr}(0.2).$$

This emphasizes the importance of diagenetic enrichment of Mn in the formation of these concretions.

The average compositional data for the concretions from the various basins of the Baltic is presented in Table 1. The Mn/Fe ratios in concretions from Kiel and Lübeck–Mecklenburg Bays are seen to be much higher than those in concretions from the rest of the Baltic. This presumably reflects the greater diagenetic contribution of Mn to the concretions as a result of the anoxic conditions developing in the sediments during the Summer. The ratio shows no major difference throughout the rest of the Baltic suggesting similar patterns of deposition of Mn and Fe there. Variations in the contents of heavy metals are apparent but are difficult to interpret because of analytical differences. Nonetheless, Varentsov *et al.* (1985) have interpreted the increase in Cu content in concretions in the sequence Gulf of Finland → Gulf of Riga → Baltic Proper to be a consequence of the increasing salinity (and therefore of the ionic strength) of the bottom waters in these basins (cf. Varentsov 1972a; Zaitseva & Varentsov 1990).

There has been considerable debate as to whether the diagenetic contribution of Mn and Fe to the concretions takes place directly from the underlying sediments or involves lateral transport of the remobilized elements (Varentsov 1973; Winterhalter 1980; Boström *et al.* 1982; Heuser 1988). The frequent occurrence of concretions on eroded lag deposits adjacent to mud fields suggests that these elements are mobilized out of the muds, transported by bottom currents and deposited in the concretions. Remobilization of Mn appears to be more important than that of Fe. Lateral transport of

Table 1. Average chemical composition of ferromanganese concretions from various basins of the Baltic Sea

	Gulf of Bothnia (1)	Gulf of Finland (2)	Gulf of Riga (2)	Gotland Region (3)	Gdansk Bay (2)	Kiel Bay (4)	Kiel Bay (5)
Mn	14.6	13.3	9.7	14.0	8.7	29.3	26.4
Fe	16.6	19.7	22.8	22.5	18.5	10.1	10.0
Zn	200	113	135	80	137	340	527
Co	140	96	64	160	91	77	96
Ni	260	35	47	750	148	97	61
Cu	80	9	17	48	42	21	27
Mn/Fe	0.88	0.68	0.43	0.62	0.47	2.90	2.64

Data sources: (1) Winerhalter (1980); (2) Varentsov (1973); (3) Manheim (1965); (4) Djafari (1976); (5) Heuser (1988).

Data compiled by Heuser (1988); other compilations by Djafari (1976) and Ingri (1986). Mn and Fe in %; other elements in ppm.

diagenetically mobilized Mn and, to a lesser extent, Fe therefore appears to be an important source of these elements in the concretions (Glasby *et al.* in press). A similar process has been invoked in the formation of lake (e.g. Strakhov 1966; Cronan & Thomas 1972; Callender & Bowser, 1976; Sozanski & Cronan 1979; Dean *et al.* 1981; Saufer & Armstrong 1986), fjord (Grill 1978) and deep-sea (Calvert & Piper 1984) concretions as well as in sediments from a Japanese hydrothermal lake (Tanaka *et al.* 1994). Nonetheless, a riverine source of these elements may be important (Varentsov 1973). It has been shown that the Fe/Mn ratio of concretions decreases markedly away from river mouths as in the case of Eningi-Lampi Lake, Central Karelia (Varentsov 1972*a, b*) and Green Bay, Lake Michigan (Callender & Boser 1976). Another factor explaining the variations in composition of concretions in the Gulfs of Finland and Riga could be the inflow the Neva and Daugava Rivers respectively and the interactions of the metals in the freshwater with seawater.

Internal structure and dating

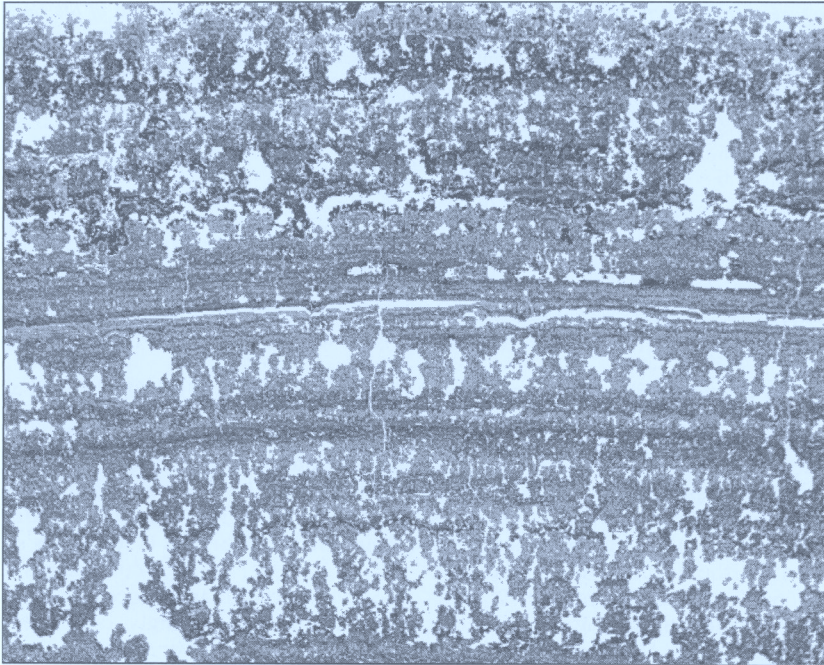
The concretion growth pattern of alternating iron- and manganese-rich layers in Baltic Sea ferromanganese concretions is well known and has been attributed to cyclic variations in bottom water conditions (Varentsov & Blashchishin 1976; Winterhalter 1980). Winterhalter (1980) described three types of layers:

- an iron-rich phase practically devoid of manganese;
- a manganese phase containing at most only minor quantities of iron;
- an intermediate layer consisting of both iron and manganese phases possibly as mixed layer minerals.

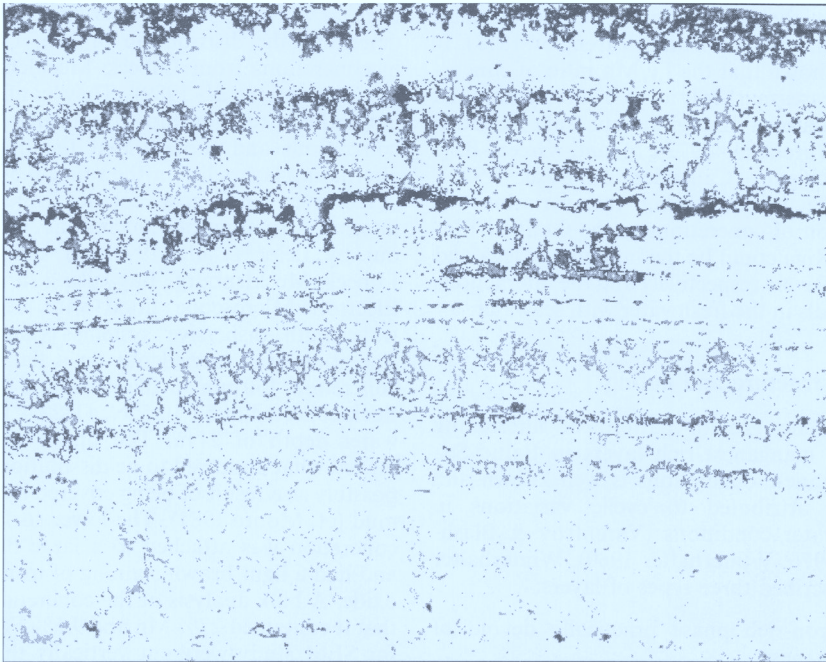
The internal structure of the concretions was first studied by electron microprobe and the distribution of Mn, Fe and P determined by Winterhalter & Siivola (1967). This showed that P is present in the concretions in higher concentrations than in oceanic and lacustrine deposits and is strongly correlated with Fe. Similar patterns were observed in Finnish (Halbach 1975), Russian (Strakhov 1954, 1968) and American (Stauffer & Armstrong 1986) lake concretions. Subsequently, Moenke-Blankenburg *et al.* (1989) used laser microanalysis to determine the distribution of Mn, Fe and Ba in concretions from Lübeck-Mecklenburg Bay (cf. Adeberg *et al.* 1989). They confirmed the antipathetic relationship of Mn and Fe in the concretions and showed that the thickness of alternating layers lies in the range 0.5–10 mm.

However, the most detailed study of the internal structure of concretions was carried out by Leipe *et al.* (1994) on samples from Lübeck-Mecklenburg Bay using a Scanning Electron Microscope fitted with energy and wavelength dispersive systems (CamScan-44). The study was carried out on a flat, discoidal concretion 150 mm in diameter and 20–30 mm thick collected at 54°10.5' N, 11°22.4' E and at a water depth of 21 m. The upper surface displayed what appeared to be dissolution features, possibly as a result of being covered by a layer of mud (cf. Moore 1981). The lower surface of the concretion was attached to a large flint erratic and had a light brown staining of iron oxyhydroxide. A bulk analysis of the concretion showed that it contained 27% Mn and 9.5% Fe. Samples for SEM study were cut vertically through the concretion. Figures 4 and 5 show the distributions of Mn and Fe in the upper and lower sections of the concretion.

The upper section of the sample is characterized by parallel banding in which Mn-rich layers

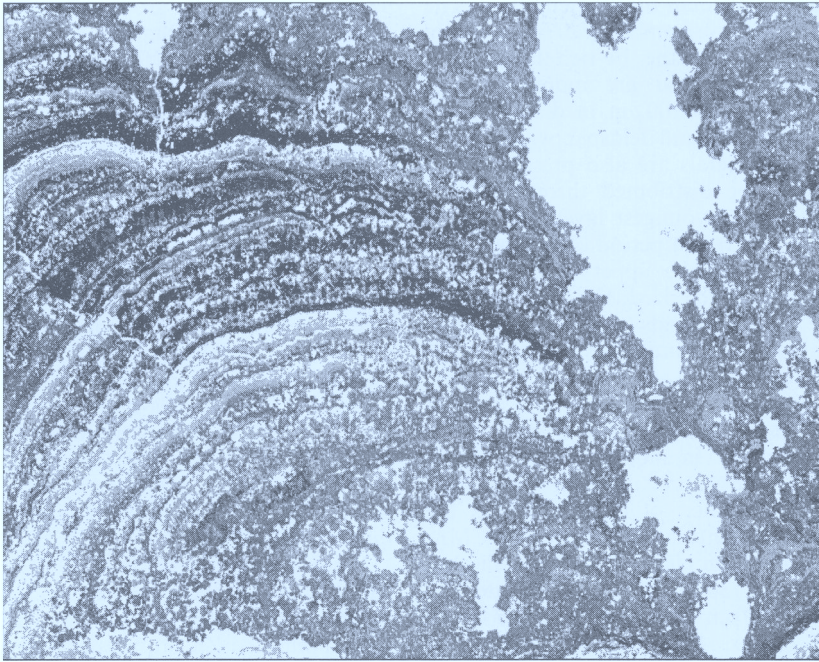


Mn

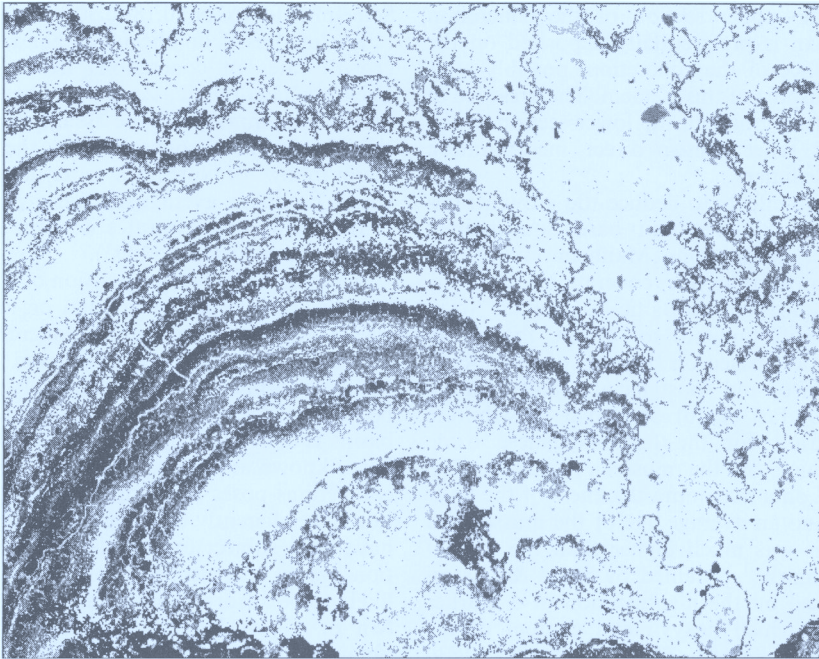


Fe

Fig. 4. Digital X-ray pictures showing the distribution of Mn and Fe in the upper section of a discoidal concretion taken from Mecklenburg Bay at a water depth of 21 m. Image taken from Leipe *et al.* (1994).



Mn



Fe

Fig. 5. Digital X-ray pictures showing the distribution of Mn and Fe in the lower section of a discoidal concretion taken from Mecklenburg Bay at a water depth of 21 m. Image from the Leipe *et al.* (1994).

are more abundant than the Fe-rich layers. The Mn-rich layers vary from 60–720 μm and are more diffuse whereas the Fe-rich layers vary from 15 to 60 μm and are more compact. Detrital grains up to 100 μm in diameter and consisting of quartz and feldspar with smaller illite-rich clay minerals are also present. These grains tend to be distributed throughout the growth layers. The youngest layer is iron-rich which points to a recent period of stagnation in concretion growth. The upper section of the concretion is characterized by high porosity within the growth bands which may reflect post-depositional dissolution of the upper surface of the concretion.

The lower section of the concretion shows a quite different cusped structure in which Mn and Fe are present in more similar amounts. These bands are more irregular suggesting perhaps the influence of movement of the concretion on its internal structure. The Mn-rich layers vary from 60 to 370 μm and the Fe-rich layers from 30 to 80 μm . Large detrital grains up to 2000 μm in diameter and consisting mainly of quartz, feldspar, mica, illite and dolomite with minor apatite (bone material) are also present and tend to occur between cusps. P tends to follow Fe. The higher Mn/Fe ratio in the upper section of the concretion suggests Mn is preferentially deposited on the upper surface of the concretion, possibly after lateral transport of this element. The presence of larger detrital grains in the lower section of the concretion reflects their direct incorporation from the sediment.

So far, all efforts to deduce the growth rates of concretions have been based on indirect evidence or assumptions. Manheim (1965) estimated growth rates for concretions from the northern and central Baltic as well as from the Gulf of Finland to be in the range 0.02–1 mm a^{-1} based on the ages of Pleistocene sea-level rise and postglacial uplift. Subsequently, Djafari (1976) derived a growth rate of 0.6 mm a^{-1} for the ferromanganese oxide layer forming on the mussel *Astarte* in Kiel Bay based on a maximum thickness of the layer of 2 mm and an average age of the mussel of 3 years. This was much higher than the rate of 0.02–0.12 mm a^{-1} obtained by Suess & Djafari (1977) based on the identification of a marker horizon at which heavy-metal content of the concretions increased. This was dated at 1830 based on the study of heavy-metal distribution in an adjacent sediment core (Erlenkeuser *et al.* 1974). However, it should be noted that the rates calculated by Suess & Djafari (1977) actually represent concretion growth in both directions.

The unidirectional growth rates are 0.01–0.06 mm a^{-1} . Winterhalter & Siivola (1967) derived a growth rate for concretions of 0.15–0.2 mm a^{-1} from electron microprobe measurements based on the assumption that the alternate Mn- and Fe-rich layers in the concretions reflect seasonal variations. Winterhalter (1980) subsequently modified this value to 0.05–0.2 mm a^{-1} . On these figures, a spheroidal concretion 20 mm in diameter was assumed to have formed over a period of several hundred years. Heuser (1988) determined the growth rates of ferromanganese oxides on artificial substrates at the Hausgarten site. He determined an average growth rate of the concretions of 0.02 mm a^{-1} but with a marked seasonal variation. The growth rates were highest in Summer and Autumn when the waters are stratified. In general, the Fe content of the layers exceeds that of Mn. Only in July did the Mn content exceed that of Fe.

More recently, Hlawatsch (1993) has compared heavy-metal profiles in concretions collected in 1973–74, 1978–82 and 1992–93. By overlapping the Zn profiles for the concretions collected at different times, she was able to deduce growth rates for concretions from Breitgrund to be 0.13–0.16 mm a^{-1} and from Schleimünde to be 0.18–0.30 mm a^{-1} . Glasby *et al.* (in press), on the other hand, proposed growth rates of concretions from the Polish Exclusive Economic Zone of the order of 0.013–0.018 mm a^{-1} on the assumption that the layering in these concretions is the result of major inflows of North Sea water into the Baltic which occur on average 11 times per century. A full listing of these rates is given by Heuser (1988) and Hlawatsch (1993).

In order to resolve the question of whether the growth layers represent annual or longer-term events, radiometric dating of concretions from the various basins of the Baltic and displaying various morphologies is required. It could well be that concretion formation in the various basins is controlled by different factors but this is not known at present. However, dating of the concretions poses problems because the concretions are inherently unstable and could therefore have been subject to post-depositional dissolution events and also because radioisotopes are likely to be adsorbed preferentially on either the Mn or Fe oxyhydroxide phase. Nonetheless, obtaining meaningful growth rates for concretions throughout the Baltic should be a major goal of future studies. The lack of such information remains a limitation on our understanding of the mode of formation of the concretions at present.

Mass balance

In order to understand fully the origin of these concretions, it is necessary to determine the source of elements forming them. A number of studies have been dedicated to that task (Pustelnikov 1976; Varentsov & Blashchishin 1976; Boström *et al.* 1983; Blashchishin 1984; Healy & Werner 1987; Emeis *et al.* 1992; HELCOM 1993; Emelyanov 1992, 1995; Schneider 1993).

A balance of terrigenous and organic material in the Baltic Sea based on the data of Pustelnikov (1976) shows that 217 million tonnes of sedimentary material are introduced into the Baltic Sea annually. 80% of this material is biogenic in origin. However, 97% of this is mineralized and therefore not permanently incorporated in the sediment column. For terrigenous sediments, the redistribution of material from the coast and seafloor by erosion and abrasion is greater by a factor of 8 than the input of material from rivers. 83% of the material on the sea floor is therefore supplied by erosional processes, 11% by rivers and 6% is biogenic in origin. These figures have been modified somewhat by later workers (Emelyanov 1992, 1995) but show the same general trends.

Data on the mass balance of manganese and iron in the Baltic Sea are relatively limited (Varentsov & Blashchishin 1976; Boström *et al.* 1983; Blashchishin 1984; Emelyanov 1995). Unfortunately, these elements were not included in major studies of heavy-metal pollution in the Baltic which seems surprising in view of their key role in controlling the distribution of these elements (Emeis *et al.* 1992; HELCOM 1993).

Varentsov & Blashchishin (1976) estimated the inputs of Mn and Fe into the various basins of the Baltic (in t a^{-1}) as follows: Gulf of Finland (340 and 61 700), Gulf of Riga (634 and 48 800), Baltic Proper (Vistula River 290 and 35 200; Neman River 30 and 15 000). This gives a total for Mn of 1564 t a^{-1} and for Fe of $160 700 \text{ t a}^{-1}$.

Subsequently, Blashchishin (1984) calculated that the amount of Mn deposited in the Baltic (excluding the Gulf of Bothnia) during the Holocene (the last 8000 years) as follows: 43.6×10^6 tonnes in clastic material, 8.2×10^6 tonnes in authigenic Ca-rhodochrosite, 2.6×10^6 tonnes in phosphates and sulphides and 8.3×10^6 tonnes in ferromanganese concretions. These figures indicate that the deposition rate of Mn in the Baltic Sea has averaged about 7800 t a^{-1} during the Holocene. The much higher deposition rate for Mn compared to the input rate reflects the fact that most of the Mn is present in clastic sediments.

Blashchishin (1984) also estimated the absolute amounts of Mn and Fe in ferromanganese concretions in the various basins of the Baltic (in Mt) as follows: Gulf of Bothnia (7.06 and 11.27), Gulf of Finland (3.79 and 6.51), Gulf of Riga (2.18 and 4.25) and Baltic Proper (2.33 and 5.35) making totals of 15.36 and 27.38 Mt of Mn and Fe respectively. This corresponds to about 130 million tonnes of concretions. It was also shown that the amount of Mn in the concretions makes up about 70% of the total Mn in sediments, authigenic minerals and concretions in the Gulf of Finland, 50% in the Gulf of Riga and 30% in the Baltic Proper. A mass balance for the Baltic was computed but it showed a deficit of input relative to output of 5% for Mn and 8% for Fe.

Other calculations by Boström *et al.* (1983) indicated a supply of Mn and Fe from rivers to be 13 000 and $310 000 \text{ t a}^{-1}$. The figures compared with a deposition rate of these elements in postglacial clays of $43 000$ and $2 800 000 \text{ t a}^{-1}$ and a loss of these elements through the Danish Straits are 8000 and $32 000 \text{ t a}^{-1}$ respectively. These calculations are clearly not in balance, the riverine input supplying only 25% and 11% of the output of these elements respectively.

Perhaps the most detailed studies of riverine input of Mn and Fe to the Baltic Sea have been carried out on the Kalix River in northern Sweden (Burman 1983; Ponter *et al.* 1990, 1992; Ingri & Widerlund 1994; Widerlund 1994). This is one of the last unregulated rivers in the region. As noted by Boström *et al.* (1983), the Fe/Al ratio in suspended matter in the Kalix river is very high (5.0) compared to that of 0.5 for regulated rivers. The distribution of Mn in the river is markedly seasonal. Dissolved Mn contents are high during the spring flood. Particulate Mn then increases and reaches a peak in July–August. The particulate Mn is probably added to the river from the local lakes during this period. For May–September, the total Fe in the river water (5418 t) exceeds the total Mn (144 t) by a factor of 38 (Ponter *et al.* 1990). The Boreal region is characterized by coniferous forests and cold continental climates. High Fe contents are typical of rivers from this region, possibly as a result of leaching of till by humic acids (Ingri 1985; cf. Andersson *et al.* 1992, 1994). Similar conditions are known in Finland (Carlson 1982; Virtanen 1994) and lead to the formation of iron-rich lake ores (Halbach 1975). This mobilization of Fe may explain the presence of iron-rich concretions in the northern Gulf of Bothnia and Gulf of Finland. By contrast, southern Sweden and central Europe are characterized by mixed forests and

semi-continental climates. The adjacent regions of the Baltic are much poorer in ferromanganese concretions.

The mass balance for heavy metals has been reported by Brüggmann (1986a), Brüggmann & Lange (1990), HELCOM Experts (1990b), Michaelis (1990), Emeis *et al.* (1992), Stryuk (1993), HELCOM (1993) and Schneider (1993). Emeis *et al.* (1992) have summarized the data for the inputs of the heavy-metals into the various basins of the Baltic. Total loads of metals into the Baltic are Zn 3890 t a^{-1} , Pb 1740 t a^{-1} , Cd 56 t a^{-1} and Hg 4.8 t a^{-1} . On this basis, the Baltic Proper accounts for the input of 19%, 47%, 82% and 23% of these elements respectively (in comparison its area accounts for 56% of the total). By contrast, 50% of the Zn is discharged into the Gulf of Bothnia. However, these figures are somewhat misleading since they represent average values calculated for the period 1900–1983 (Brüggmann & Lange 1990). As such, they do not accurately represent the present situation. More recent figures for the loading of these elements from the atmosphere and waste water effluents give values of Zn 10004 t a^{-1} , Pb 1878 t a^{-1} , Cd 114.5 t a^{-1} and Hg 16.3 t a^{-1} (HELCOM Experts 1990b). These metals are believed to be transported into the Baltic Sea dominantly by atmospheric transport (HELCOM Experts 1990b; Brüggmann *et al.* 1992; Schneider 1993). The most comprehensive compilation of the data is that of HELCOM (1993) but this reveals many gaps in the data.

The above data give some insight into the mass balance of elements into the Baltic Sea. However, the mass balance of Mn and Fe, in particular, appears to be poorly constrained and needs to be much better understood if the source of these elements in ferromanganese concretions is to be properly ascertained. More complete information on the input of the heavy-metals into the Baltic Sea is required if ultimate repositories are to be evaluated and the role of ferromanganese concretions in their uptake understood.

Environmental monitoring

The increasing pollution of the Baltic Sea is a serious problem which has received considerable attention (Suess & Erlenkeuser 1975; HELCOM 1987, 1993, 1994; Brüggmann & Lange 1990; Ergin 1990; HELCOM Experts 1990a, b; Brüggmann *et al.* 1992; Damm 1992; Emeis *et al.* 1992; Perttilä & Brüggmann 1992; Brüggmann 1993; Schneider 1993). According to Perttilä & Brüggmann (1992),

the data collected so far on Baltic Sea contaminants are very fragmentary. The use of ferromanganese concretions to monitor the input of heavy metals into the Baltic Sea was first suggested nearly 20 years ago. The object of this section is to evaluate the viability of such a method. The need for such a method can be seen by considering the goal of 'Forward to 1950', which aims to reduce pollution in the Baltic to its level in 1950, a target which may take a century to achieve (The Stockholm Environment Institute 1990). For this, reliable environmental monitoring will be required.

The fact that the outer layers of Baltic Sea ferromanganese concretions contain anomalously high concentrations of Zn, Pb, Cd and Cu of possible anthropogenic origin was first reported by Djafari (1976) and Suess & Djafari (1977). They showed that these elements were enriched in the outer layers of concretions from Kiel Bay. From previous studies of element distribution and age dating of a nearby sediment core, they were able to deduce that the anthropogenic input of metals in the area began about 1830 (Erlenkeuser *et al.* 1974). The thickness of the heavy-metal enriched layers in the concretions was 8–9 mm in the direction of fastest growth and 2–3 mm in the direction of slowest growth. From this, they were able to conclude that the concretions grow at a rate of $0.02\text{--}0.12 \text{ mm a}^{-1}$. Ferromanganese oxide layers on mussels were shown to have much higher Zn contents than those in spheroidal and discoidal concretions (see earlier) reflecting the more rapid growth of the oxide layers in these samples in the more polluted present-day conditions. Heuser (1988) similarly reported higher Zn contents in ferromanganese oxides growing on artificial substrates in the same region. Interestingly, mussels from Kiel Bay have already been used for monitoring Cd pollution in the bay (Fischer 1986).

A more detailed study of this problem has been undertaken by Hlawatsch (1993). She used the increased Zn contents in the outer layers of the concretions to date the concretions and proposed the use of the concretions for monitoring the depositional environment of the concretions by means of laser ablation ICPMS and Scanning Electron Microscopy.

A critique of this method has already been presented by Ingri & Ponter (1986a). These authors showed that the contents of several elements (including Zn) increase with decreasing size of the concretions with most of this increase occurring within microconcretions <2 mm in diameter. In addition, the composition of the concretions is markedly dependent on the depth of burial of the concretions. They therefore

concluded that concretions are poor sampling objects for pollution investigations because element enrichments are dependent on the redox level of the environment and it is difficult to determine what this is. In addition, there are large variations in the Mn/Fe ratios and Zn contents within the Baltic. For example, the average Zn content of concretions varies from 80 ppm in the Gotland region to 527 ppm in Kiel Bay (Table 1).

Furthermore, it is well known that the onset of pollution is different in the various basins of the Baltic. For example, the onset of Zn pollution is recorded in sediment cores at about 1830 in Kiel Bay, 1900 in Bornholm Basin, 1910 in Gotland Deep, 1940 in the northern Baltic and Bothnian Sea and 1950 in Bothnian Bay (Niemestö 1986; cf. Hlawatsch 1993). Emeis *et al.* (1992) reported a clear increase in Zn and Pb in sediment cores from the southern Baltic about 1875 and in the Gotland deep about 1920.

The fate of heavy metals in the Baltic Sea is also not well known. The role of Mn and Fe oxyhydroxides in scavenging and redistributing heavy metals has been emphasized by Brüggmann (1986b) and Brüggmann *et al.* (1992). Although the principal phases occurring in Baltic sediments are known (Emelyanov 1986, 1995; Belmans *et al.* 1993), no mass balance for the distribution of heavy metals within the various mineral and sediment types in the Baltic exists. It is therefore not clear at present what proportions of heavy metals entering the Baltic Sea are incorporated into ferromanganese concretions. Hakansson (1990), for example, considered that the deep-water zone is the ultimate repository for many types of pollutants in the Baltic. Ferromanganese concretions may therefore play only a minor role in the mass balance of heavy-metals in the Baltic.

Finally, the thickness of the outer layer of the concretion contaminated by heavy metals is very dependent on the concretion growth rate which has not yet been measured directly. It is therefore not possible to develop a standard profile for heavy-metal distribution in the concretions. Rather, such a distribution will be dependent on the precise mode of formation of the concretions and therefore on such secondary parameters as concretion size and morphology.

In spite of these limitations, Baltic Sea ferromanganese concretions do have potential as environmental monitors. Nonetheless, it is clear that they can only be used under controlled circumstances and that much more needs to be known about the pathways of heavy metals through the Baltic (both inputs and modes of deposition) before this method can be universally accepted.

Summary

The data presented above show that the character (abundance, type, composition) of Baltic Sea ferromanganese concretions is very dependent on the environment of formation. Three main types of environment are proposed; the Gulfs of Bothnia, Finland and Riga, the Baltic Proper and the western Belt Sea. The characteristics of the concretions is dependent on the sedimentological, hydrological and above all redox characteristics of the environment. The use of the concretions for monitoring the level of heavy-metal pollution of the Baltic Sea appears to be possible. However, substantial investigation is required to put this method on a sound scientific basis.

The senior author (GPG) wishes to thank the European Environmental Research Organization (EERO) which supported his involvement in this project and Professor J. Harff who organized his stay at IOW Warnemünde and encouraged this work. He also thanks S. Hlawatsch, W. Lemke, T. Neumann, S. Roy and I. M. Varentsov for helpful discussions.

References

- ADEBERG, V., BRÜGMANN, L., DOERFFEL, K. & MONKE, L. 1989. Detection of periodicities in a line-scan with high noise by means of correlation functions. *Fresenius Zeitschrift für Analytische Chemie*, **333**, 143 [in German].
- AMAKAWA, H., INGRI, J., MASUDA, A. & SHIMIZU, H. 1991. Isotopic compositions of Ce, Nd and Sr in ferromanganese nodules from the Pacific and Atlantic Oceans, the Baltic and Barents Seas, and the Gulf of Bothnia. *Earth and Planetary Science Letters*, **105**, 554–565.
- ANDERSSON, P. S., WASSERBURG, G. J. & INGRI, J. 1992. The sources and transport of Sr and Nd isotopes in the Baltic Sea. *Earth and Planetary Science Letters*, **113**, 459–472.
- , —, & STORDAL, M. C. 1994. Strontium, dissolved and particulate loads in fresh and brackish waters: the Baltic Sea and Mississippi Delta. *Earth and Planetary Science Letters*, **124**, 195–210.
- ANON 1990. *Status of the Baltic Sea – A sea in transition*. Ambio Special Reports. 7.
- BAKKER, J. F. & HELDER, W. 1993. Skagerrak (northeastern North Sea) oxygen microprofiles and porewater chemistry in sediments. *Marine Geology*, **111**, 299–321.
- BALZER, W. 1982. On the distribution of manganese and iron at the sediment/water interface: Thermodynamic versus kinetic control. *Geochemica et Cosmochimica Acta*, **46**, 1153–1161.
- 1989. *Chemical reactions and transport processes in surface sediments in boreal and polar marine environments*. Habilitation-Schrift (Universität Kiel) [in German].

- , ERLKENUSER, H., HARTMANN, M., MÜLLER, P. J. & POLLEHNE, F. 1987. Diagenesis and exchange processes at the benthic boundary. In: RUMOHR, J., WALGER, E. & ZEITZSCHEL, B. (eds) *Seawater-Sediment Interactions in Coastal Waters*. Lecture Notes on Coastal and Estuarine Studies, 13. Springer-Verlag, Berlin, 111–161.
- , GRASSHOFF, K., DIECKMANN, P., HAARDT, H. & PETERSOHN, U. 1983. Redox-turnover at the sediment/water interface studied in a large bell jar system. *Oceanologica Acta*, **6**, 337–349.
- BATURIN, G. N. 1988. *The Geochemistry of Manganese and Manganese Nodules*. D. Reidel, Dordrecht.
- & EMEL'YANOV, E. M. In press. Manganese concretions in the Gulf of Finland. In: DAVIDAN, I. N. (ed.) *Gulf of Finland, Baltica*, **5** [in Russian].
- , ROGINSKAYA, I. S., RAKOVSKIY, E. YE. & KULIGIN, V. M. 1988. Composition of iron-manganese and sulphide nodules in sediments of the Baltic Sea. *Oceanologia*, **28**, 478–481.
- BELMANS, F., VAN GRIEKEN, R. & BRÜGMANN, L. 1993. Geochemical characterization of recent sediments in the Baltic Sea by bulk and electron microprobe analysis. *Marine Chemistry*, **42**, 223–236.
- BERNARD, P. C., VAN GRIEKEN, R. E. & BRÜGMANN, L. 1989. Geochemistry of suspended matter from the Baltic Sea. I. Results of individual particle characterization by automated electron microprobe. *Marine Chemistry*, **26**, 155–177.
- BLASHCHISHIN, A. I. 1984. Balance of Fe, Mn and P in the Baltic Sea. In: LISITZIN, A. P. (ed.) *Geological History and Geochemistry of the Baltic Sea*. Nauka, Moscow, 122–129 [in Russian].
- BOESEN, C. & POTSMAN, D. 1989. Pyrite formation in anoxic environments of the Baltic Sea. *American Journal of Science*, **288**, 575–603.
- BOSTRÖM, K., WIBORG, L. & INGRI, J. 1982. Geochemistry and origin of ferromanganese concretions in the Gulf of Bothnia. *Marine Geology*, **50**, 1–24.
- , BURMAN, J.-O. & INGRI, J. 1983. A geochemical massbalance for the Baltic. *Ecological Bulletin (Stockholm)*, **35**, 39–58.
- , INGRI, J. & PONTER, C. 1988. Origin of iron-manganese-rich suspended matter in the Landsort Deep, NW Baltic Sea. *Marine Chemistry*, **24**, 93–98.
- BRÜCHERT, V., DELANO, J. W. & KIDD, W. S. F. 1994. Fe- and Mn-enrichment in middle Ordovician hematitic argillites preceding black shale and flysch deposition: the Shoal Arm Formation, north-central Newfoundland. *Journal of Geology*, **102**, 197–214.
- BRÜGMANN, L. 1986a. The influence of coastal zone processes on mass balances for trace metals in the Baltic Sea. *Rapports et Procès-verbaux des Réunions Conseil International Pour l'Exploration de la Mer*, **186**, 329–342.
- 1986b. Particulate trace metals in waters of the Baltic Sea and parts of the adjacent NE Atlantic. *Beiträge zur Meereskunde*, **55**, 3–18.
- 1988. Some peculiarities of the trace-metal distribution in Baltic waters and sediments. *Marine Chemistry*, **23**, 425–440.
- 1993. *Meeres-Verunreinigung*. Akademie Verlag, Berlin [in German].
- & LANGE, D. 1990. Metal distribution in sediments of the Baltic Sea. *Limnologia (Berlin)*, **20**, 15–28.
- , BERNARD, P. C. & VAN GRIEKEN, R. 1992. Geochemistry of suspended matter from the Baltic Sea 2. Results of bulk trace metal analysis by AAS. *Marine Chemistry*, **38**, 303–323.
- BURDIGE, D. J. 1993. The biogeochemistry of manganese and iron reduction in marine sediments. *Earth-Science Reviews*, **35**, 249–284.
- BURMAN, J.-O. 1983. Element transports in suspended and dissolved phases in the Kalix River. *Ecological Bulletin (Stockholm)*, **35**, 99–113.
- BUTYLIN, V. P. & ZHAMOIDA, V. A. 1988. Zonation of modern, shallow water ferromanganese concretions in the Gulf of Finland. In: *Geology and Geochemistry of Ferromanganese Concretions in the World Ocean*, Sevmoregeologia, Leningrad, 93–107 [in Russian].
- , — & KOSIN, M. B. 1985. Distribution of chemical elements and concretion formation in the Quaternary deposits of the Gulf of Finland. In: *Glacial Shelves; Problems of Geology and Methods of Investigation*. VESEGEI, Ministry of Geology, Leningrad, 43–54 [in Russian].
- CALLENDER, E. & BOWSER, C. J. 1976. Freshwater ferromanganese concretions. In: WOLF, K. H. (ed.) *Handbook of Strata-Bound and Stratiform Ore Deposits*, 7. Elsevier, Amsterdam, 341–394.
- CALVERT, S. E. & PIPER, D. Z. 1984. Geochemistry of ferromanganese nodules from DOMES Site A, Northern Equatorial Pacific: Multiple diagenetic metal sources in the deep sea. *Geochimica et Cosmochimica Acta*, **48**, 1913–1928.
- & PRICE, N. B. 1977. Shallow water, continental margin and lacustrine nodules: Distribution and geochemistry. In: GLASBY, G. P. (ed.) *Marine Manganese Deposits*. Elsevier, Amsterdam, 45–86.
- CANFIELD, D. E., THAMDRUP, B. & HANSEN, J. W. 1993a. The anaerobic degradation of organic matter in Danish coastal sediments: iron reduction, manganese reduction, and sulfate reduction. *Geochimica et Cosmochimica Acta*, **57**, 3867–3883.
- , JORGENSEN, B. B., FOSSING, H., GLUD, R., GUNDERSEN, J., RAMSING, N. B., THAMDRUP, B., HANSEN, J. W., NIELSEN, L. P. & HALL, P. J. 1993b. Pathways of organic carbon oxidation in three continental margin sediments. *Marine Geology*, **113**, 27–40.
- CARLSON, L. 1982. *Oxide minerals of iron in oxidate accumulations in Finland*. Unpublished PhD thesis (University of Helsinki), 24pp + 4 papers.
- CRONAN, D. S. & THOMAS, R. L. 1972. Geochemistry of ferromanganese oxide concretions and associated deposits in Lake Ontario. *Geological Society of America Bulletin*, **83**, 1493–1502.
- DAMM, E. 1992. *Early diagenetic distribution of heavy metals in muds of the western Baltic Sea*. Berichte Fachbereich Geowissenschaften Universität Bremen, **31** [in German].
- DAVISON, W. 1993. Iron and manganese in lakes. *Earth-Science Reviews*, **34**, 119–163.

- DEAN, W. E. & GHOSH, S. K. 1980. Geochemistry of freshwater ferromanganese deposits in North America. In: VARENTSOV, I. M. & GRASSELLY, GY. (eds) *Geology and Geochemistry of Manganese*, 3. Hungarian Academy of Sciences, Budapest, 255–277.
- , MOORE, W. S. & NEALSON, K. H. 1981. Manganese cycles and the origin of manganese nodules, Oneida Lake, New York, U.S.A. *Chemical Geology*, **34**, 53–64.
- DJAFARI, D. 1976. *Manganese-iron accumulates in Kiel Bay*. Dr. rer. nat. thesis (Universität Kiel) [in German].
- DYRSSEN, D. & KREMLING, K. 1990. Increasing hydrogen sulfide concentration and trace metal behavior in the anoxic Baltic waters. *Marine Chemistry*, **30** 193–204.
- EHLIN, U. 1981. Hydrology. In: VOIPIO, A. (ed.) *The Baltic Sea*. Elsevier, Amsterdam, 123–134.
- EMEIS, K.-C., LARSEN, B. & SEIBOLD, E. 1992. What is the environmental capacity of enclosed marginal seas? Approaches to the problem in the Baltic, North, and Mediterranean Seas. In: HSÜ, K. J. & THIEDE, J. (eds) *Use and Misuse of the Seafloor*. John Wiley, New York, 181–211.
- EMEL'YANOV, E. M. 1986. Basins of the Baltic Sea. *Finnish Marine Research*, **253**, 79–96.
- 1992. The Baltic Proper. In Review of Contaminants in Baltic sediments. *ICES Cooperative Research Report*, **190**, 16–19.
- 1995. *Baltic Sea Geology, Geochemistry, Paleo-oceanography, Pollution*. P. P. Shirshov Institute, Kaliningrad
- , PILIPCHUK, M. F., VOLOSTNYKH, B. V., KHANDROS, G. S. & SHADUROV, YU. O. 1982. Fe and Mn forms in the geochemical profile of the Baltic Sea. *Baltica*, **7**, 153–171.
- ERGIN, M. 1990. Pre-civilizational and civilizational layers in two sediment cores from the western Baltic Sea. *Bollettino Oceanologia Teoretica e Applicata*, **8**, 41–50.
- ERLENKEUSER, H., SUESS, E. & WILLKOMM, H. 1974. Industrialization affects heavy metal and carbon isotope concentrations in recent Baltic sediments. *Geochimica et Cosmochimica Acta*, **38**, 823–842.
- ERONEN, M., RISTANIEMI, O. & LANGE, D. 1990. Analysis of a sediment core from the Mecklenburg Bay, with a discussion on the early history of the southern Baltic Sea. *Geologiska Föreningens i Stockholm Förhandlingar*, **112**, 1–8.
- FISCHER, H. 1986. Cadmium in Kieler Förde mussels: An innovative monitoring programme. *Rapports et Procès-verbaux des Réunions Conseil International Pour l'Exploration de la Mer*, **186**, 468–474.
- FORCE, E. R. & CANNON, W. F. 1988. Depositional model for shallow-marine manganese deposits around black shale basins. *Economic Geology*, **83**, 93–117.
- FRAKES, L. & BOLTON, B. 1992. Effects of ocean chemistry, sea level and climate on the formation of primary sedimentary manganese ore deposits. *Economic Geology*, **87**, 1207–1217.
- FRANCK, H., MATTHÄUS, W. & SAMMLER, R. 1987. Major inflows of saline water into the Baltic Sea during the present century. *Gerlands Beiträge für Geophysik*, **96**, 517–531.
- GERLACH, S. A. 1990. *Nitrogen, phosphorus, plankton and oxygen deficiency in the German bight and in Kiel Bay*. Kieler Meeresforschung Sonderheft, 7.
- GLASBY, G. P., USCINOWICZ, SZ. & SOCHAN, J. in press. Marine ferromanganese concretions in the Polish Exclusive Economic Zone: Influence of major inflows of North Sea water. *Marine Georesources and Geotechnology*.
- GORSHKOV, A. I., BATURIN, G. N., BERESOVSKAYA, V. V., DUBININA, G. A. & SITSOV, A. V. 1992. Mineralogy and genesis of the buried concretions of the Baltic Sea. In: *Geology of the Oceans and Seas. Abstracts 10th International Marine Geology School, Moscow*, 3, 78–79 [in Russian].
- GORSHKOVA, T. I. 1961. *Sediments of Riga Bay*. Proceedings of the Research Institute of Fishing, Latvian SSSR, 3.
- 1963. Bottom deposits of the Baltic Sea. *Baltica (Vilnius)*, **1**, 189–210.
- 1967. Manganese in bottom sediments of northern seas. In: SAPOZHNIKOV, D. G. (ed.) *Manganese Deposits of the USSR*. Nauka, Moscow, 125–145 [in Russian].
- GRASSHOFF, K. 1975. The hydrochemistry of landlocked basins and fjords. In: RILEY, J. P. & SKIRROW, G. (eds) *Chemical Oceanography* 2nd Edition, 2. Academic Press, London, 455–597.
- & VOIPIO, A. 1981. Chemical oceanography. In: VOIPIO, A. (ed.) *The Baltic Sea*. Elsevier, Amsterdam, 183–218.
- GREWINGK, C. 1984. Submarine exposure of eastern Baltic dolomite. *Sitzungsberichte der Naturforscher-Gesellschaft der Universität Dorpat*, **6**, 83–87 [in German].
- GRILL, E. V. 1978. The effect of sediment-water exchange on manganese deposition and nodule growth in Jervis Inlet, British Columbia. *Geochimica et Cosmochimica Acta*, **42**, 485–494.
- GRIPENBERG, S. 1934. A study of the sediments of the North Baltic and adjoining seas. *Merentutkimuslaitoksen Julkaisu Havsforskningsinstitutets Skrift*, **96**, 1–231.
- GUDELIS, V. & EMEL'YANOV, E. (eds) 1976. *Geology of the Baltic Sea*. Mokslas Publishers, Vilnius [in Russian].
- HAKANSSON, L. 1990. *Baltic research developments*. Ambio Special Report, 7.
- HALBACH, P. 1975. Mineralogical and geochemical investigation of Finnish lake ores. *Bulletin of the Geological Society of Finland*, **43**, 33–42.
- HARFF, J., LEMKE, W., TAUBER, F. & EMEL'YANOV, E. M. 1995. Geological mapping in the Baltic Sea. *Geowissenschaften*, **13**, 442–447 [in German].
- HARTMANN, M. 1964. On the geochemistry of manganese and iron in the Baltic Sea. *Meyniana*, **14**, 3–20 [in German].
- HEALY, T. M. & WERNER, F. 1987. Sediment budget for a semi-enclosed sea in a near homogenous lithology example of Kieler Bucht, western Baltic. *Senckenbergiana Maritima*, **19** 195–222.

- HELCOM 1987. *Progress reports on cadmium, mercury, copper and zinc*. Baltic Sea Environmental Proceedings, **24**.
- 1990. *Second periodic assessment of the state of the marine environment of the Baltic Sea, 1984–1988; Background document*. Baltic Sea Environmental Proceedings, **35B**.
- 1993. *Second Baltic Sea pollution load compilation*. Baltic Sea Environmental Proceedings, **45**.
- 1994. *The Baltic Sea Joint Comprehensive Environmental Action Programme*. Baltic Sea Environmental Proceedings, **48**.
- HELCOM Experts 1990a. Oxygen conditions. *Ambio Special Report*, **7**, 3–4.
- 1990b. Metals. *Ambio Special Report*, **7**, 7–9.
- HESSLE, C. 1924. Evaluation of the bottom deposits of the inner Baltic Sea. *Meddelanden fran Kungliga Lantbruksstyrelsen*, **250**, 1–52 [in Swedish]
- HEUSER, H. 1988. *Observations and investigations on the genesis of shallow-water manganese nodules in Kiel Bay (western Baltic)*. Berichte-Reports, Geologisch-Paläontologisches Institut Universität Kiel, **26** [in German].
- HLAWATSCH, S. 1993. *Growth of manganese-iron accumulates in the western Baltic Sea Indicator for environmental change*. Diplom thesis, Universität Kiel, [in German].
- HUCKRIEDE, H. 1993. *Manganese enrichment in anoxic marine basins: examples from the central Baltic Sea and the Lower Carboniferous II. Middle and West Europe*. Cuvillier Verlag, Göttingen [in German].
- INGRI, J. 1985. *Geochemistry of ferromanganese concretions and associated sediments in the Gulf of Bothnia*. PhD thesis, University of Lulea.
- 1993. Redox potential, a significant factor in regulating the uptake of Cu, Ni and Zn in Mn-oxyhydroxide at the sediment-water interface in the northern Baltic Sea (Abstract). *EOS Transactions of the American Geophysical Union*, **74(16)** Supplement, 326–327.
- & PONTER, C. 1986a. Scavenging properties of ferromanganese nodules in the Gulf of Bothnia. *Rapports et Procès verbaux des Réunions Conseil International Pour l'Exploration de la Mer*, **186**, 234–243.
- & — 1986b. Iron and manganese layering in Recent sediments in the Gulf of Bothnia. *Chemical Geology*, **56**, 105–116.
- & — 1987. Rare earth abundance patterns in ferromanganese concretions from the Gulf of Bothnia and the Barents Sea. *Geochimica et Cosmochimica Acta*, **51**, 155–161.
- & WIDERLUND, A. 1994. Uptake of alkali and alkaline-earth elements on suspended iron and manganese in the Kalix River, northern Sweden. *Geochimica et Cosmochimica Acta*, **58**, 5433–5442.
- , LÖVENDAHL, R. & BOSTRÖM, K. 1991. Chemistry of suspended particles in the southern Baltic Sea. *Marine Chemistry*, **32**, 73–87.
- JAKOBSEN, R. & POSTMA, D. 1989. Formation and solid solution behavior of Ca-rhodochrosite in marine muds of the Baltic Deep. *Geochimica et Cosmochimica Acta*, **53**, 2639–2348.
- JENKYN, H. C., GECZY, B. & MARSHALL, J. D. 1991. Jurassic manganese carbonates of Central Europe and the early Toarcian anoxic event. *Journal of Geology*, **99**, 137–149.
- KIMBERLEY, M. M. 1989. Exhalative origins of iron-formations. *Ore Geology Reviews*, **5**, 13–145.
- KRAVTSOV, A. A. 1992. Forms of Fe, Mn, Zn, Cd, Pb and Cu in the Baltic Sea water (Abstract). *Institut für Ostseeforschung Warnemünde Marine Scientific Reports*, **4**, 84–85.
- KUKAL, Z. 1991. Anoxic microenvironment-Main factor in the formation of manganese. In: PAIGAL, M. & LEROY, J. L. (eds) *Source, Transport and Deposition of Metals*. A. A. Balkema, Rotterdam, 545–547.
- KULESZA-OWSIKOWSKA, G. 1981. Mineralogical and geochemical studies of iron-manganese nodules from the southern Baltic Sea. *Archiwum Mineralogiczne*, **37**, 149–216 [in Polish].
- KULLENBERG, G. 1981. Physical oceanography. In: VOIPIO, A. (ed.) *The Baltic Sea*. Elsevier, Amsterdam, 135–181.
- LANGE, D. 1984. *Geological investigations of late Glacial and Holocene sediments in Lübeck and Mecklenburg Bays*. Dr. habil. thesis, Univ. Rostock [in German].
- 1987. *Mecklenburg Bay Sediments 1:100 000*. Hydrographic Office, German Democratic Republic.
- LAPP, B. & BALZER, W. 1993. Early diagenesis of trace metals used as an indicator of past productivity changes in coastal sediments. *Geochimica et Cosmochimica Acta*, **57**, 4639–4652.
- LEIN, A. YU. 1983. Biogeochemistry of the anaerobic diagenesis of recent Baltic sediments. *Ecological Bulletin (Stockholm)*, **35**, 441–461.
- LEIPE, T., BAHLO, R., DAHMKE, A. & HARFF, J. 1994. *Iron-manganese crusts from Mecklenburg Bay, western Baltic Microstructure, chemical compilation and element distribution*. Final Report to BMFT (BMFT-FK 03 F 0077A) [in German].
- LISITZIN, A. P. (ed.) 1984. *Geological History and Geochemistry of the Baltic Sea*. Nauka, Moscow [in Russian].
- & EMELYANOV, E. M. 1981. *Formation of sediments in the Baltic Sea*. Akademia nauk SSSR, Moscow [in Russian].
- MAGAARD, L. & RHEINHEIMER, G. (eds) 1974. *Meereskunde der Ostsee*. Springer-Verlag, Berlin.
- MANHEIM, F. T. 1961. A geochemical profile in the Baltic Sea. *Geochimica et Cosmochimica Acta*, **25**, 52–70.
- 1965. Manganese-iron accumulations in the shallow marine environment. In: SCHINK, D. R. & CORLESS, J. T. (eds) *Symposium on Marine Geochemistry*. Occasional Publications of the Narragansett Marine Laboratory, University of Rhode Island, **3**, 217–276.
- 1982. Geochemistry of manganese carbonates in the Baltic Sea. *Stockholm Contributions in Geology*, **37**, 145–159.
- MATTHÄUS, W. 1992. Water exchange between the North Sea and Baltic Sea. *Geographische Rundschau*, **44**, 626–631 [in German].

- 1993a. Major inflows of highly saline water into the Baltic Sea. *Paper presented at the ICES Statutory Meeting 1993*.
- 1993b. Salt water influx and its significance for marine environment in the Baltic Sea. *Wasser + Boden*, **12**, 922–928 [in German].
- MELLIN, T. 1987. Investigations of manganese nodule occurrences in the Gulf of Bothnia. *Cruise Rep. Res. Rep. 1, Havsmineralgruppen. R. Inst. Technol., Sweden* [in Swedish].
- MICHAELIS, W. 1990. Balancing of suspended and trace material in the tidal zone of the Elbe. In: BEYER, M., PETZOLD, S., PRANGE, A. & WILKEN, R.-D. (eds) *3. Magdeburger Gewässerschutzseminar-Zur Belastung der Elbe*. GKSS, Geesthacht, 70–82 [in German].
- MOENKE-BLANKENBURG, L., JAHN, K. & BRÜGMANN, L. 1989. Laser-micro-analytical studies on distribution patterns of manganese, iron and barium in Fe/Mn-accumulates of the western Baltic Sea. *Chemie der Erde*, **49**, 39–46.
- MOORE, W. S. 1981. Iron-manganese banding in Oneida Lake ferromanganese nodules. *Nature*, **292**, 233–235.
- NAUSCH, G. & NEHRING, D. 1994. Nutrient dynamics in the Gotland Deep—reactions to the major salt water inflow in 1993. In: *Proceedings of the 19th Conference of the Baltic Oceanographers 29 August–1 September 1994*, 551–559.
- NEUMANN, T., CHRISTIANSEN, C., CLASEN, S., EMEIS, K.-C. & KUNZENDORF, H. in press. Geochemical records of salt-water inflows into the deep basins of the Baltic Sea. *Continental Shelf Research*.
- NIEDERMEYER, R.-O. & LANGE, D. 1989. Modern mud deposits of the western Baltic Sea (Mecklenburg Bight). Sedimentary environment and diagenesis. *Beiträge zur Meereskunde, Berlin* **60**, 5–20.
- & —1990. An actualistic model of mud deposition and diagenesis for the western Baltic Sea. *Limnologica (Berlin)*, **20**, 9–14.
- NIELSEN, P. E. 1992. *Bottom sediments around Denmark and western Sweden*. Geological Surveys of Denmark and Sweden.
- NIEMISTO, L. 1986. Monitoring sediments in the Baltic Sea. *Baltic Sea Environment Proceedings*, **19**, 175–180.
- NVORTEVA, J. 1994. Topographically influenced sedimentation in Quaternary deposits—a detailed acoustic study from the western part of the Gulf of Finland. *Geological Survey of Finland Report of Investigation*, **122**, 1–88.
- OKITA, P. M., MAYNARD, J. B., SPIKER, E. C. & FORCE, E. R. 1987. Isotopic evidence for organic matter oxidation by manganese reduction in the formation of stratiform manganese carbonate ore. *Geochimica et Cosmochimica Acta* **52**, 2679–2685.
- PERTTILA, M. & BRÜGMANN, L. 1992. *Review of contaminants in Baltic sediments*. International Council for the Exploration of the Sea Cooperative Research Report, **180**.
- POLGARI, M. 1993. *Manganese Geochemistry – Reflected by Black Shale Formation and Diagenetic Processes Model of formation of the Carbonatitic Manganese Ore of Urkut*. Hungarian Academy of Sciences, Budapest.
- PONTER, C., INGRI, J. & BOSTRÖM, K. 1992. Geochemistry of manganese in the Kalix River, northern Sweden. *Geochimica et Cosmochimica Acta*, **56**, 1485–1494.
- , —, BURMAN, J.-O. & BOSTRÖM, K. 1990. Temporal variations in dissolved and suspended iron and manganese in the Kalix River, northern Sweden. *Chemical Geology*, **81**, 121–131.
- PUSTELNKIOV, O. S. 1976. Absolute value of the mass of sediment material and the rate of recent sedimentation in the Baltic Sea. *Beiträge zur Meereskunde, Berlin*, **38**, 81–93 [in German].
- PUTANS, B. D., UL'ST, V. G. & EMSS, V. B. 1968. Ferromanganese concretions in the sediments of the Gulf of Riga. In: *Lithology, Geochemistry and Economic Minerals of Byelorussia and Baltic States*. Minsk, 249–255 [in Russian].
- RAUKAS, A. & HYVARINEN, H. (eds) 1992. *Geology of the Gulf of Finland*. Estonian Academy of Sciences, Tallinn. [in Russian, English summary].
- ROY, S. 1981. *Manganese Deposits*. Academic Press, London.
- 1992. Environments and processes of manganese deposition. *Economic Geology*, **87**, 1218–1236.
- SAMOILOV, Y. V. & TITOV, A. G. 1922. Iron-manganese rich nodules of the Black, Baltic and Barents Seas. *Trudy Geologo-Mineralogicheskogo Muzeya*, **3**, 25–112 [in Russian].
- SANCHEZ, A. L., GASTAUD, J., HOLM, E., INGRI, J. & LÖFENDAHL, R. 1988. Fallout Pu and Am in Baltic Sea ferromanganese concretions: implications regarding their interactions in sediments. *Radiochimica*, **44/45**, 153–157.
- SAPOZHNIKOV, D. G. 1967. Some geological conditions of formation of manganese ore deposits. In: SAPOZHNIKOV, D. G. (ed.) *Manganese Deposits of the USSR*. Nauka, Moscow, 11–33 [in Russian].
- 1984. Possible sources of metals during formation of manganese ore deposits. In: SAPOZHNIKOV, D. G. (ed.) *Manganese ore Formation in the Territory of the USSR*. Nauka, Moscow, 4–13 [in Russian].
- SCHNEIDER, B. 1993. *Investigation and assessment of the entry of pollutants from the atmosphere in the framework of PARCOM (North Sea) and HELCOM (Baltic Sea)—Partial plans: measurements of heavy metals*. GKSS Report (Geesthacht), **93/E/53** [in German].
- SCHULZ, S. 1969. Benthos and sediments in Mecklenburg Bay. *Beiträge zur Meereskunde, Berlin*, **24/25**, 15–55 [in German].
- SEIBOLD, E., EXON, N., HARTMANN, M., KÖGLER, F.-C., KRUMM, H., LUTZE, G. F., NEWTON, R. S. & WERNER, F. 1971. Marine geology of Kiel Bay. *Sedimentology of parts of Central Europe Guidebook VIII. International Sedimentology Congress 1971*, 209–235.
- SHNUKOV, E. F., OGORODNIKOV, V. I. & KRASOVSKIY, K. S. 1987. Ferromanganese concretions in the sea basins of the USSR. *Geological Magazine (Ukrainian Academy of Science)*, **47(1)**, 32–43 [in Russian].

- SHTERENBERG, L. Y. 1971. Some aspects of the genesis of iron-manganese concretions in the Gulf of Riga. *Doklady Akademii Nauk SSSR*, **201**, 252–255 [in Russian].
- , DUBINA, G. A. & STEPANOVA, K. A. 1975. The formation of Fe–Mn nodules of a flattened form. In: *Problems of Lithology and Geochemistry of Sedimentary Rocks and Ores to the 75-th Anniversary of Academician N.M. Strakhov*. Nauka, Moscow, 166–181 [in Russian].
- , GORSHKOVA, T. I. & NAKTINAS, E. M. 1968. Manganese carbonates in ferromanganese concretions in the Gulf of Riga. *Lithology and Economic Resources*, **4**, 63–69 [in Russian].
- SIGG, L., KUHN, A., XUE, H., KIEFER, E. & KISTLER, D. 1995. Cycles of trace elements (copper and zinc) in a eutrophic lake. Role of speciation and sedimentation. In: HUANG, P. C., O'MELIA, C. R. & MORGAN, J. J. (eds) *Aquatic Chemistry: Interfacial and Interspecies Processes*. ACS Advances in Chemistry Series, **224**, 177–1194.
- SOZANSKI, A. G. & CRONAN, D. S. 1979. Ferromanganese concretions in Shebandowan Lakes, Ontario. *Canadian Journal of Earth Science*, **16**, 126–140.
- STAUFFER, R. E. & ARMSTRONG, D. E. 1986. Cycling of iron, manganese, phosphorus, calcium and potassium in two stratified basins of Shagawa Lake, Minnesota. *Geochimica et Cosmochimica Acta*, **50**, 215–229.
- STRAKHOV, N. M. 1966. Types of manganese accumulation in present-day basins: their significance in understanding manganese mineralization. *International Geological Reviews*, **8**, 1172–1198.
- & TRAKHOV, N. M. 1976. Conditions of formation of nodulous manganese ores on Recent Basins. *Lithology and Mineral Resources*, **1**, 3–19 [in Russian].
- , BRODSKAYA, N. G., KNYAZEVA, L. M., RAZZHIVINA, A. I., RATEEV, M. A., SAPOZHNIKOV, D. G. & SHISHOVA, E. C. 1954. *Formation of Sediments in Recent Basins*. USSR Academy of Sciences, Moscow [in Russian].
- , SHTERENBERG, L. E., KALINENKO, V. V. & TIKHOMIROVA, E. S. 1968. *Geochemistry of a Sedimentary Manganese Ore-Forming Processes*. Nauka, Moscow [in Russian].
- STRYUK, V. L. 1992. Sedimentary matter supply and transformation in geochemical barrier zones of the Baltic Sea (Abstract). *Institut für Ostseeforschung Warnemünde Marine Scientific Reports*, **4**, 142.
- SUESS, E. 1979. Mineral phases formed in anoxic sediments by microbial decomposition of organic matter. *Geochimica et Cosmochimica Acta*, **43**, 339–352.
- & DJAFARI, D. 1977. Trace metal distribution in Baltic Sea ferromanganese concretions: inferences on accretion rates. *Earth and Planetary Science Letters*, **35**, 49–54.
- & ERLKENKUSER, H. 1975. History of metal pollution and carbon input in Baltic Sea sediments. *Meyniana*, **27**, 63–75.
- TALPSEPP, L. 1990. Hydrophysical processes in the Gulf of Finland and their influence on the distribution of hydrochemical and hydrobiological fields. Overview of investigations in 1986–1990. *Proceedings of the 17th Conference of the Baltic Oceanographers*, 000–000.
- TANAKA, A., SEYAMA, H. & SOMA, M. 1994. Iron- and manganese-rich sediments as an indicator of hot spring activities at the bottom of Lake Mashu, Japan. *Geochemical Journal*, **28**, 289–306.
- THAMDRUP, B., FOSSING, H. & JORGENSEN, B. B. 1994a. Manganese, iron and sulfur cycling in a coastal marine sediment, Aarhus Bay, Denmark. *Geochimica et Cosmochimica Acta*, **58**, 5115–5129.
- , GLUD, R. N. & HANSEN, J. W. 1994b. Manganese oxidation and in situ manganese fluxes from a coastal sediment. *Geochimica et Cosmochimica Acta*, **58**, 2563–2570.
- THE STOCKHOLM ENVIRONMENT INSTITUTE 1990. "Forward to 1950": Policy considerations for the Baltic environment. *Ambio Special Report*, **7**, 21–24.
- TYSON, R. V. & PEARSON, T. H. 1991. Modern and ancient continental shelf anoxia: an overview. In: TYSON, R. V. & PEARSON, T. H. (eds) *Modern and Ancient Continental Shelf Anoxia*. Geological Society London, Special Publications, **58**, 1–24.
- VARENTSOV, I. M. 1972a. On the main aspects of formation of ferromanganese ores in Recent basins. *International Geological Congress twenty-fourth session*, **4**, 395–403.
- 1972b. Geochemical studies on the formation of iron-manganese nodules and crusts in Recent basins I. Eningi-Lampi Lake, Central Karelia. *Acta Mineralogica-Petrographica, Szeged*, **20**, 363–381.
- 1973. Geochemical aspects of formation of ferromanganese ores in shelf regions of Recent seas. *Acta Mineralogica-Petrographica, Szeged*, **21**, 141–153.
- 1975. Geochemical aspects of formation of iron-manganese ores in Recent shelf seas. In: *Problems of Lithology and Geochemistry of Sedimentary Rocks and Ores to the 75th Anniversary of Academician N.M. Strakhov*. Nauka, Moscow, 150–165 [in Russian].
- & BLASHCHISHIN, A. I. 1976. Iron and manganese concretions. In: GUEDELIS, V. & EMEL'YANOV, E. (eds) *Geology of the Baltic Sea*. Mokslas Publishers, Vilnius, 307–348 [in Russian].
- , — & SOKOLOVA, G. B. 1977. Original variations of the mineral composition of the ferromanganese concretions and crusts, Baltic Sea. In: *Concretions and Concretion Analysis*. Nauka, Moscow, 180–187 [in Russian].
- & BLAZHCHISHIN, A. I. 1974. Ferromanganese nodules from the Gulf of Finland. *Acta Mineralogica-Petrographica, Szeged*, **21**, 303–304.
- , ZAITSEVA, L. V. & PUTILINA, V. S. 1985. On the geochemistry of nodular polymetallic ore formation in Recent basins: Experimental data on the role of major ions in seawater in the process of copper sorption manganese hydroxides. *Chemie der Erde*, **44** 193–225.
- VIRTANEN, K. 1994. Geological control of iron and phosphorus precipitation in mines of Ruukki-Vihanti area, Central Finland. *Geological Survey of Finland, Bulletin*, **375**, 1–69.

- VOIPIO, A. (ed.) 1981. *The Baltic Sea*. Elsevier, Amsterdam.
- WATTENBERG, H. 1949. Sketch of a natural division of the Baltic Sea. *Kieler Meeresforschungen*, **6**, 10–15 [in German].
- WEHRLI, B., FRIEDL, G. & MANCEAU, A. 1995. Reaction rates and products of manganese oxidation at the sediment-water interface. In: HUANG, P. C., O'MELIA, C. R. & MORGAN, J. J. (eds) *Aquatic Chemistry: Interfacial and Inter-species Processes*. ACS Advances in Chemistry Series, **224**, 111–134.
- WENK, B. 1981. *Comparison of geochemical investigations of iron-manganese concretions from the Baltic Sea, the Pacific and Atlantic Oceans*. Final Report (Institut für Meereskunde, Warnemünde) [in German].
- WIDERLUND, A. 1994. Geochemistry of iron and arsenic of the Kalix River estuary, northern Bothnian Bay (abstract). *3rd International Symposium on Environmental Geochemistry, Krakow*, 438–439.
- WINTERHALTER, B. 1966. Iron-manganese concretions from the Gulf of Bothnia and the Gulf of Finland. *Geoteknillisiä Julkaisuja*, No. **69**, 1–77 [in Finnish, English abstract].
- 1980. Ferromanganese concretions in the Baltic Sea. In: VARENTSOV, I. M. & GRASSELLY, GY. (eds) *Geology and Geochemistry of Manganese*, **3**. Hungarian Academy of Sciences, Budapest, 227–254.
- 1992. Late-Quaternary stratigraphy of Baltic Sea basins – a review. *Bulletin of the Geological Survey of Finland*, **64**, 189–194.
- & SIIVOLA, J. 1967. An electron microprobe study of the distribution of iron, manganese, and phosphorus in concretions from the Gulf of Bothnia, northern Baltic Sea. *Comptes Rendus de la Société Géologique de la Finlande*, **39**, 161–172.
- , FLODEN, T., IGNIATUS, H., AXBERG, S. & NIEMISTO, L. 1981. Geology of the Baltic Sea. In: VOIPIO, A. (ed.) *The Baltic Sea*. Elsevier, Amsterdam, 1–121.
- WITKOWSKI, A. 1994. *Recent and fossil diatom flora in the Gulf of Gdansk, southern Baltic Sea*. *Bibliotheca Diatomologia*, **28**.
- ZAITSEVA, L. V. & VARENTSOV, I. M. 1990. Influence of major ions of seawater (chloride systems) on Cu(II) sorption by manganese oxyhydroxides: Use of experimental data in a model of poly-metallic ore formation in Recent basins. *Chemie der Erde*, **50**, 225–268.
- ZHAMOIDA, V. A. 1989. Ferromanganese concretions: morphology and genesis. In: *Geology of the Submarine Sector of the Baltic Shield and Russian Platform as far the Gulf of Finland*. VESEGEL, Leningrad, 70–83 [in Russian].
- & BUTYLIN, W. P. 1992. Distribution of Fe–Mn nodules fields at the bottom of the Gulf of Finland, and the variety of nodules (abstract). *Institut für Ostseeforschung Warnemünde Marine Scientific Reports*, **4**, 169.
- & — 1993. Differentiation of the ferromanganese nodules from the eastern part of the Gulf of Finland by their chemical composition (abstract). *Third Marine Geological Conference Spot, 21–24 September 1993*, 63.
- , — GLASBY, G. P. & POPOVA, I. A. 1996. Ferromanganese concretions of the Gulf of Finland, Baltic Sea. *Marine Georesources and Geotechnology*, **14**, 161–176.

Deception Island (Antarctica): a new target for exploration of Fe–Mn mineralization?

J. REY¹, L. SOMOZA², J. MARTÍNEZ-FRÍAS³,
R. BENITO² & S. MARTÍN-ALFAGEME²

¹ *Instituto Español de Oceanografía, Centro Oceanográfico de Málaga, Fuengirola, Aptdo. 285, Málaga, Spain*

² *Marine Geology Division, ITGE (Geological Survey of Spain), Rios Rosas, 23, 28003 Madrid, Spain*

³ *Departamento de Geología, Museo Nacional de Ciencias Naturales, CSIC, José Gutierrez Abascal, 2 28006 Madrid, Spain*

Abstract: This work correlates the submarine volcanic and hydrothermal structures detected through seismic profiles on Deception Island (DI) with geochemical distribution patterns of the volcanic sediments which make up the seafloor of the island. A comparison of subaerial and submarine volcanic events is also carried out and three groups of submerged seismo-depositional units are defined. A model is proposed according to which the highest contents of Fe–Mn–Zn are related to volcanic cones, mounds and vents formed in relation with extensional normal low-angle faults. The As–Ba anomalies, active fumaroles and hot-springs are associated to later tensional faults.

Deception Island (DI) is a complex and intermittently active volcanic area located at the west end of the volcanic ridge of the Bransfield Trough (BT) between the South Shetland Islands (SSI) and the Antarctica Peninsula. A simplified plates scheme (Fig. 1) shows the complex relationships between the Drake, Scotia and Antarctic plates. The Drake plate and the Bransfield Trough became part of the Antarctic plate when sea-floor spreading stopped in Drake Passage 4 Ma ago (Barker 1982) making subduction of the SSI thrust inactive. The rifting of the BT is a Late Cenozoic tensional structure produced as a consequence of a back-arc spreading process (Gonzalez Ferrán 1985). Traditionally, all authors, except Hawkes (1961), assume the caldera to be the result of the collapse of just one volcanic cone, caused by concentric faults (ring faults). However, recent geophysical studies have shown that the gravimetric and magnetic anomalies are not related to a typical circular structure of a classic volcanic caldera, but reveals a lineal trend in the crustal mass expansion in a NE–SW direction (Ortiz *et al.* 1992). At present, the volcanic ridge of the BT is divided by faults (orientated mainly NW–SE) that compartmentalize and move it (Fig. 1) (Grad *et al.* 1992). DI is the only point on this ridge with active volcanic and hydrothermal emissions.

Deception Island is ring-shaped and encircles an elongated bay of 6 × 10 km in diameter (Fig. 2a and b), which opens onto the sea

(Bransfield Strait) through the strait of Neptune's Bellows (Fig. 3). The maximum depth of the bay is about 160 m, the deepest part being in the centre (Fig. 4a). The surface temperature of the water varies between 0°C and –1°C in the area of Neptune's Bellows and above 1°C in the central part of the bay (Fig. 4b). Exceptionally high temperatures (above 90°C) have been observed associated with the presence of fumaroles and hot springs.

Submarine volcanic morphology and geotectonic setting

In order to understand the physiographical characteristics and the structure of the submerged volcanic sediments in the interior of the DI caldera a series of seismic reflection profiles (Sparker, Geopulse) were carried out in N–S and NW–SE directions. These profiles indicate that there is a deep basin in the centre of the island, bordered by walls which display slope instabilities and slumping processes towards the basin (Rey *et al.* 1992). In the southern part of the island the bottom is characterized by a group of volcanic cones which, in some cases, stand up from the seafloor up to more than 50 m (Fig. 3). In addition, the joint interpretation of the fault systems and the subaerial and submarine volcanic cones shows the existence of three main tectonic systems which control the architecture of the island (Rey *et al.* 1995).

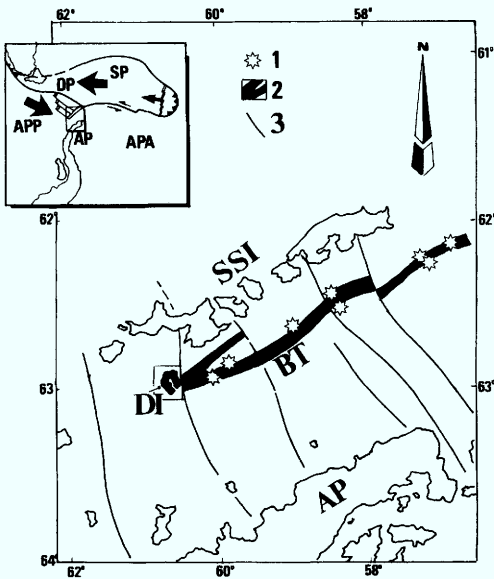


Fig. 1. Tectonic and geographical location of Deception Island. SP, Scotia Plate; DP, Drake Plate; APP, Antarctic Pacific Plate; APA, Antarctic Atlantic Plate. Regional framework: Deception Island (DI) is situated along the spreading axis of the Bransfield Trough (BT) located between the South Shetland Islands (SSI) and the Antarctic Peninsula (AP). Legend: (1) submarine sea-mounts; (2) volcanic spreading axis; (3) main faults crossing the BT (partly modified from the compilation of Grad *et al.* 1992).

(a) Normal faults which strike NE–SW and which act as vents for the fumarole activity between Fumarole Bay and Pendulum Cove.

(b) A N115–N120 axis, with which the submarine volcanic cones are associated.

(c) The N160 Macaroni fault which controls the shape of the eastern part of the island, just between Macaroni Point and Bally Head.

Subaerial and submarine volcanic series

In relation to the structuring of the submarine volcanic Formations and their relation to the subaerial volcanic series, traditionally the different volcanic rocks which crop out on the island have been simply subdivided into pre-caldera and post-caldera deposits. The ages obtained by K/Ar for the pre-caldera deposits were $150\,000 \pm 46\,000$ years (Keller *et al.* 1992), thus the island began to form 0.2 Ma ago. On an anecdotal note, historical texts from whaler ships indicate that the south of the island saw numerous eruptions in 1842. The recent eruptions of 1967, 1969 and 1970 have drastically changed

the configuration of the coast line of the bay, including the destruction of two scientific stations.

The work which, in our opinion, best defines the spatial and temporal position of the subaerial volcanic Formations on DI is that of Birkenmajer (1992). This author collects all the existing data and proposes some lithostratigraphic patterns to explain this volcanic succession dividing the Formations into an old group, which includes the pre-caldera deposits (Foster Group), and a more recent one (Hawkes Group), which includes both the syn-caldera and post-caldera deposits. This last group includes seven formations:

- (1) andesitic lapilli tuff (Murature Fm);
- (2) trachydacite lavas and plugs (Ronald Fm);
- (3) trachydacite lava flows (Collins Fm);
- (4) basaltic andesite tephra cones and maars (Chacao Fm);
- (5) basaltic andesite tephra cones with craters (Casco Fm);
- (6) basaltic lavas and tephra (Kirkwood Fm);
- (7) the modern andesitic tephra cones and lavas of the Telefon Bay (Telefon Fm).

In this way, the seismo-depositional units, B1 to B5 (Fig. 5) correspond to the first five Formations that Birkenmajer (1992) includes in Hawkes Group, while unit C corresponds to the Kirkwood and Telefon Fm. More specifically, unit B1, which displays deformed syn-tectonic reflectors, correlates with the andesitic Murature Fm. It is interpreted as being generated synchronously with the beginning of the collapse of the caldera, subsequent to the flooding of the internal bay of the island. Units B2 and B3 correspond with the Collins and Ronalds Formations, dating from the Holocene. Volcanic structures, intercalated in these Formations, are observed associated with the fault situated to the south. Seismic units B4 and B5 display the largest volcanic structures on the profile (Fig. 6). Unit B4 is characterized by containing a large volcanic cone made up by the superimposition of several small cones. The alignment of these submarine cones with the great crater of Chacao Point, to the west of Telefon Bay (Fig. 3), allows the correlation of this unit with the Chacao Fm. Unit B5, which fills a depression created by the rotation of normal faults, is mainly made up of mound-type structures associated with the same fault that generates the B2 and B3 deposits. These mounds, which intercalate with well stratified parallel deposits, are formed from the same centre of emission, opening upwards into a 'positive-flower' structure. Unit B5 correlates with the Casco Fm, the most significant deposits

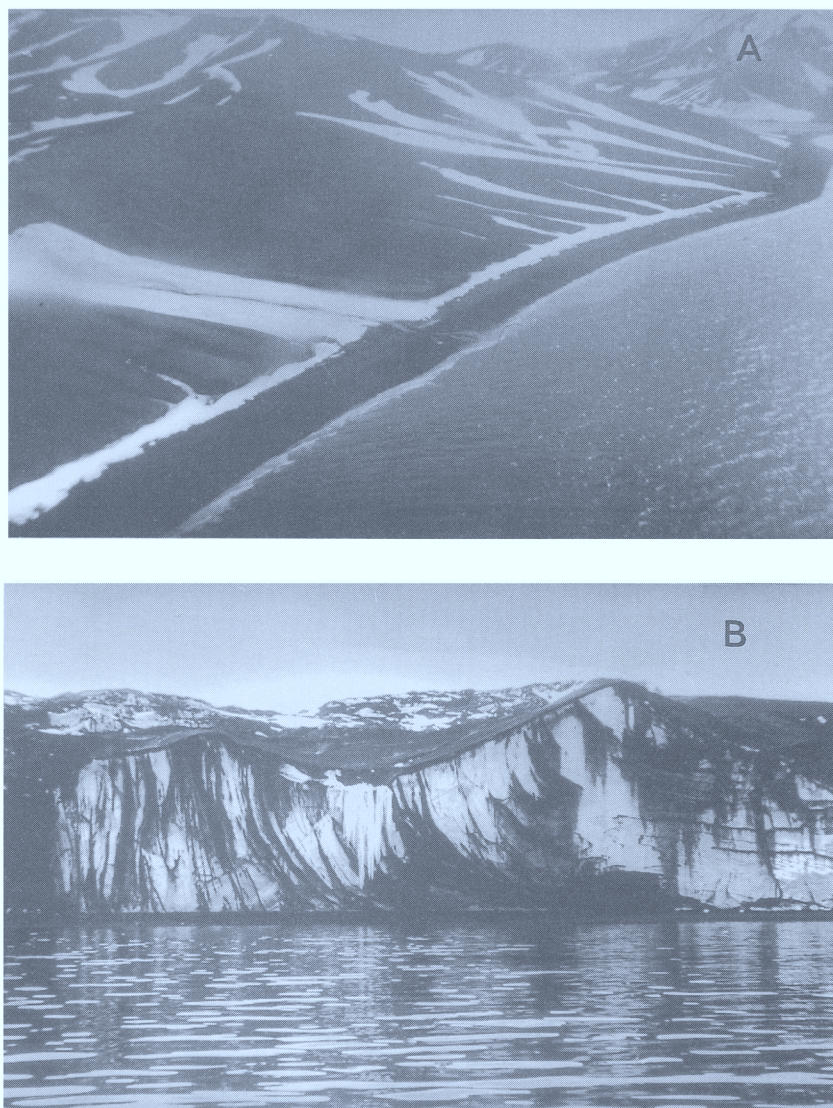


Fig. 2. Panoramic views of various parts of Deception Island. (a) Fumarole Bay, in the northwest of the island. (b) Glacial front to the northeast, covered with intercalations of volcanic ash pertaining to the most recent volcanic episodes.

of which are found in Charco Point, just to the north of Mount Kirkwood, as basaltic andesite tephra cones. The unit which is discordantly superimposed is C1, which correlates with the Kirkwood Fm. It is deformed by the intrusion of vents and small volcanic cones. The Kirkwood Fm is dated through historical writings as between 1829 and 1912. Lastly, unit C2 correlates with the Telefon Fm, the principal eruptions of which took place in three phases (1967,

1969 and 1970) which show a clock-wise progression of the caldera subsidence during these recent eruptions (Orheim 1972).

Geochemical characteristics of the DI seafloor

The general characteristics of magmatism developed in the BR, and more specifically in the area

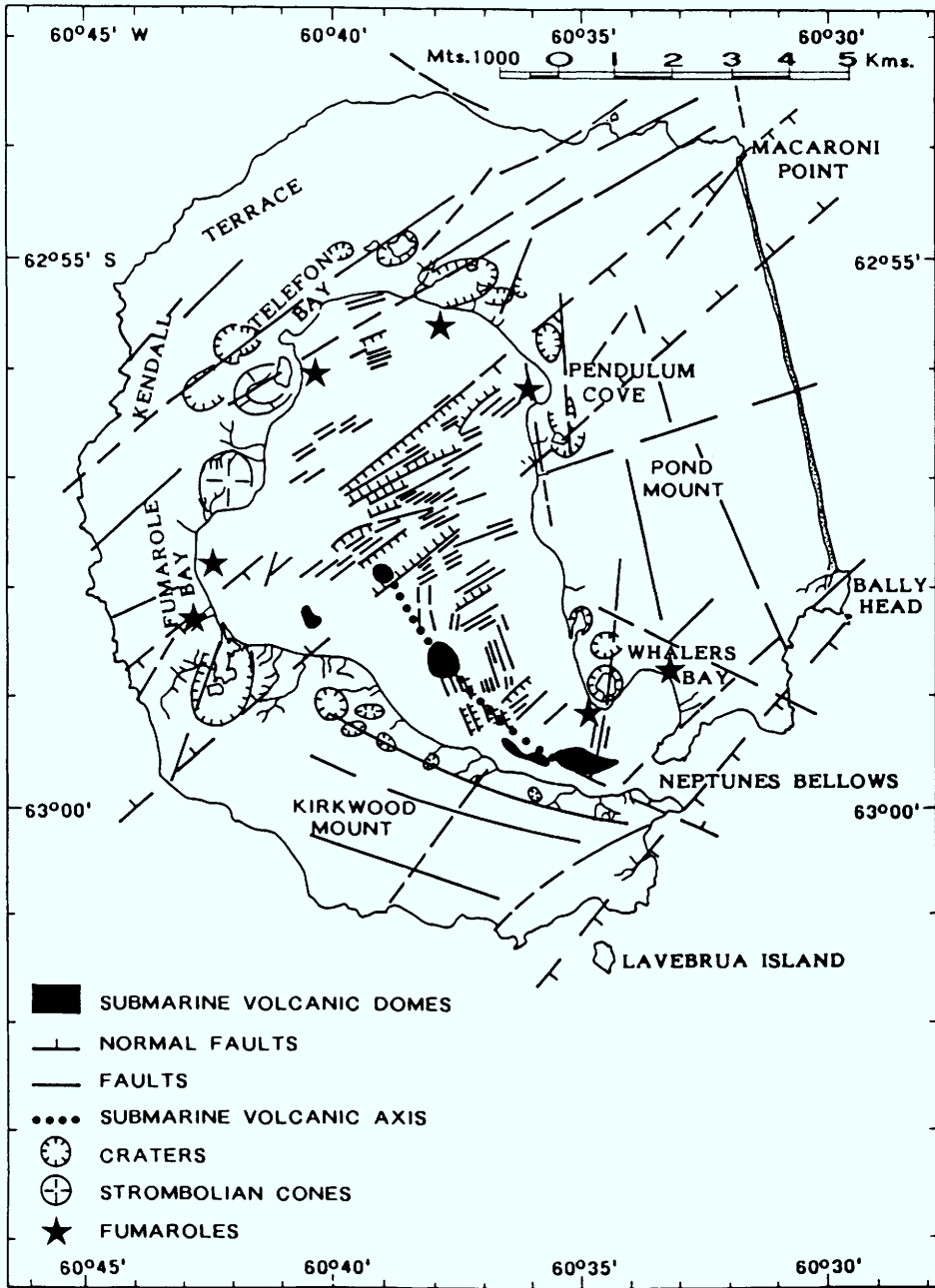


Fig. 3. Fault system and position of the volcanic cones and fumarole areas of Deception Island.

of DI, have been studied by a great number of authors (González-Ferrán & Katsui 1970; Barker *et al.* 1975; Smellie 1981, 1988; González-Ferrán 1985; Marti *et al.* 1990; Keller *et al.* 1991; Peccerillo *et al.* 1991; Birkenmajer 1992). In general terms, this volcanism is geochemically

very varied, the characteristics of which have been studied directly on DI by using the data from the historical eruptions which affected the island in 1842, 1967, 1969 and 1970. This volcanism is represented by basalts, basaltic mugearites, andesitic benmoreites, and

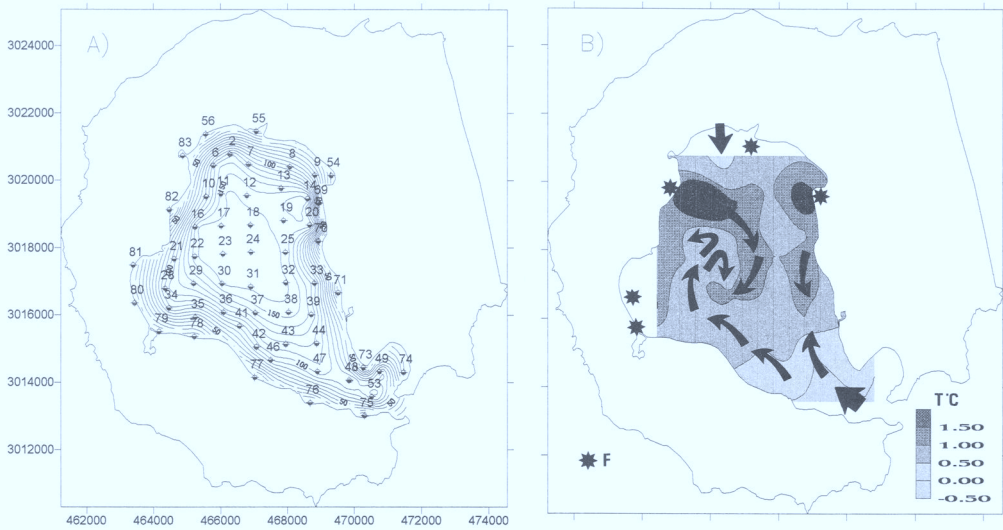


Fig. 4. (a) Water depth and position of the sampling stations in the interior of the island. (b) Surface temperatures of the water during the period of sample taking (Antarctic summer).

After Birkenmajer, 1992			This paper		
Formations	Age	Volcano-stratigraphy	Seismic Units	Tectonic events	Geochemical and structure
Telefon fm	1970 1969 1967	Andesitic tephra cones	C2	Post-bent	As-Ba hot-springs and fumaroles
Kirkwood	1829	Basaltic lavas	C1	Post-bent	Fissure and fluid vents
				Normal faulted NNE-SSW	
Casco	Late Holocene	Basaltic andesitic tephra cones	B5	Fill rotational block	Fe-Mn-Zn mounds
Chacao	Late Holocene	Basaltic andesitic tephra cones	B4	low-angle normal fault	Volcanic cones
Collins	Holocene	Trachydacite lava flows and plugs	B3	low-angle normal fault	Lava flows
Ronald			B2		
Bay Open			NW-SE Axis clockwise rotation		
Murature	Pleistocene	Andesitic lapilli tuff	B1	Sin-tectonic layers	
Pre-caldera formations			A		
Begin collapse					

Fig. 5. Correlation between the subaerial volcano-stratigraphic Formations defined by Birkenmajer (1992) and the submarine seismo-depositional units defined by Rey *et al.* (1995).

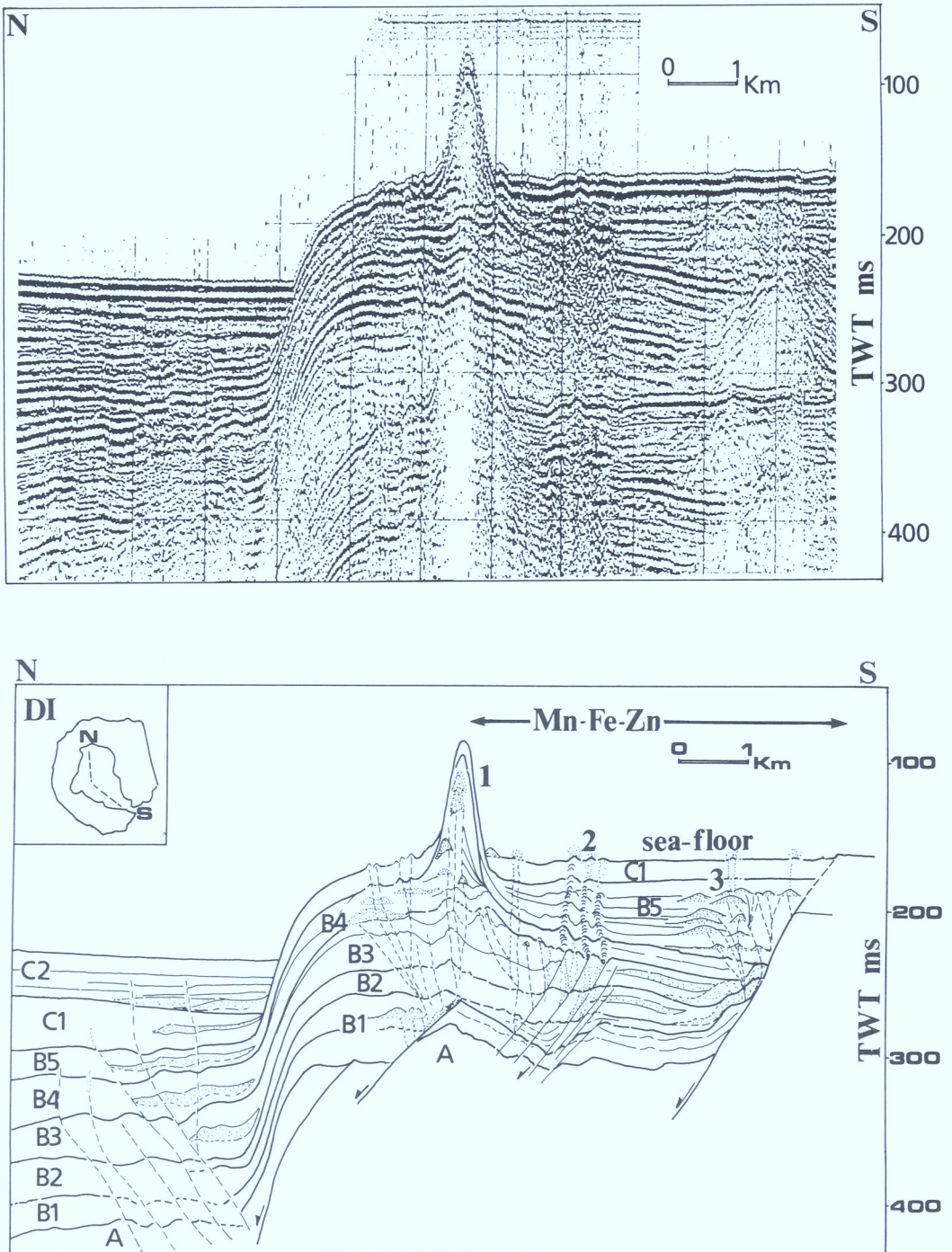


Fig. 6. (a) Continuous seismic reflection profile (Sparker) which crosses the bay. (b) Interpretation of the profile showing the position of the seismo-depositional units (A, B and C) and the associated volcanic and hydrothermal structures. 1, submarine volcanic cones; 2, vents; 3, mound-type structures.

dacites/trachytes. Peccerillo *et al.* (1991) indicates that these rocks define on DI a continuous Na-transitional series ranging from basalt to trachyte, the geochemical characteristics and Sr isotopic ratios of which show 'smooth variations from mafic to acidic rocks and are consistent with an evolution of the magma by closed-system crystal/liquid fractionation in a shallow-level magma chamber'. This same author proposes a model to explain the origin of these rocks according to which 'an island-arc component affected the source of the Deception magma, possibly by introduction within the mantle wedge of fluids or melts released from the oceanic slab which was subducting under the South Shetland during Tertiary times'.

All these papers cover the problem of DI volcanism by studying the subaerial volcanic rocks, and it is not until the works of Rey *et al.* (1992, 1994) and Somoza *et al.* (1994) that, for the first time, the geochemical characterization of the submerged volcanic formations was studied.

To sample the submarine sediments from the interior of DI, Shipex sediment samplers with digital metre counter pulleys were used on 54 sampling

stations (Fig. 4a) for non-consolidated sediments in combination with 39 oceanographic parameter stations. The submarine samples were collected from the actual ship. In all the points sampled the UTM and Geographic reference coordinates were registered, the thickness of the superficial water sheet was taken, and a correlative number was assigned for later identification. The ship's position was continuously supervised during the sampling using a Trisponder positioning system linked to a GPS.

In order to make the geochemical grid, 37 samples were selected by size. These were classified into 20 samples of whole rock, four of fine grain materials, nine of fraction >2mm and four blocks (several centimetres in size). The initial selection, grinding and desiccation of the samples was carried out in the 'Instituto Andaluz de Geología Mediterránea de Granada'. The analyses were carried out in the Centro de Laboratorios y Ensayos del ITGE de Madrid. Rb, Sr and Li were analysed by AAS using a Thermo Jarrell Asf Smith-Hieftje 8000, and major Al, Fe, Mn, Mg, Ca, Na, K Ti and P and trace Sc, V Cr, Co, Ni, Cu, Zn, Y Ba, Pb, As and W were determined by ICP-AES, using a multichannel Thermo Jarrell Ash ICAP61. Elemental dissolutions in HCl 10% and the SO-1, SO-2, NBS-2704 and BM reference standards were used for quality control of the analyses. The tables which contain all of the analytical results can be found in Rey *et al.* (1994).

Table 1. Statistical combinations and geochemical ranges obtained by the principal component factor analysis

Group	Ia	Ib	Ic	IIa	IIb	MGDS	BDS	FGDS
<i>Major elements (wt%)</i>								
TiO ₂	1.57-1.60	1.68-1.92	1.72-1.82	1.83-1.98	1.95-2.03	1.77-2.05	1.35-2.14	1.68-1.78
Al ₂ O ₃	14.06-14.27	14.95-16.24	14.72-15.46	16.18-16.59	15.84-16.35	15.37-16.14	16.08-16.95	14.38-15.06
Fe ₂ O ₃	8.39-8.59	9.52-10.11	9.64-10.00	10.12-10.48	10.48-10.70	9.15-10.10	8.09-10.24	9.48-9.88
MnO	0.16	0.15-0.18	0.15-0.16	0.15-0.16	0.15-0.16	0.14-0.16	0.12-0.15	0.15-0.16
MgO	2.99-3.06	3.06-3.51	3.02-3.36	3.81-4.39	3.72-3.92	3.14-4.36	5.11-5.76	3.26-3.44
CaO	5.74-5.92	5.91-6.61	6.22-6.43	7.63-8.40	7.25-7.87	6.58-8.32	9.02-9.66	5.81-6.33
Na ₂ O	4.86-5.01	5.05-5.27	4.85-4.98	4.34-4.70	4.73-4.85	4.54-5.17	3.91-4.15	4.46-4.70
K ₂ O	0.80	0.85-0.91	0.80-0.85	0.62-0.70	0.71-0.74	0.64-0.92	0.50-0.54	0.83-0.89
P ₂ O ₅	0.43	0.37-0.49	0.45-0.47	0.31-0.36	0.38-0.44	0.28-0.34	0.24-0.37	0.45-0.51
<i>Trace elements (ppm)</i>								
Li	12-13	13-14	13-14	11	11-12	10-13	8-9	13-14
Sc	14-15	16-18	16-17	19-22	20-21	16-22	21-25	16-17
V	228-294	180-215	181-214	236-259	233-252	205-262	188-250	192-208
Cr	26-29	15-27	20-27	24-42	24-34	23-45	86-88	24-25
Co	46-68	25-41	28-36	40-64	36-46	32-42	34-55	24-28
Ni	11-12	10-11	<10	10-21	12-13	10-20	39-48	11-12
Cu	33-35	35-56	34-49	47-59	47-48	35-63	33-59	45-47
Zn	86-91	96-101	91-98	90-95	96-97	84-94	70-87	91-102
Rb	5-6	4-7	4-7	<4	<4	<4	<4	8-9
Sr	321-322	337-361	348-362	380-394	377	351-399	416-475	321-345
Y	27	27-31	25-28	23-25	26-27	23-27	18-24	27-28
Ba	129-140	115-138	114-127	95-110	106-108	93-130	69-98	116-123
Pb	12	13-16	11-13	11-13	12-14	10-12	10-11	11-13
As	42-56	20-30	22-76	20-35	<20	<20	<20	25-33
W	140-155	10-142	13-76	91-198	89-148	79-158	63-211	10-29

Ia-IIb: geochemical groups and subgroups. MGDS, fraction >2mm; BDS, blocks; FGDS, fine-grained material.

Statistical study

A principal component factor analysis was carried out on the 37 samples. The variables included were the determined 24 chemical elements. The combinations obtained appear in table 1. From these combinations the following geochemical groups were established.

(a) Whole rocks: the results obtained have identified two groups of samples. Group I displays higher contents of Na_2O , K_2O , P_2O_5 , Li, Rb, Ba, Y and As, while group II has higher contents of Al_2O_3 , Fe_2O_3 , MgO, CaO, TiO_2 , Sr, Sc, Cr, Ni, Co, Cu, V and W.

(b) Fine-grained materials: only samples from group I were analysed, displaying a slight enrichment in P_2O_5 and Rb compared with the whole rocks.

(c) Fraction $>2\text{ mm}$: important geochemical variations are displayed, although its composition is similar to that of the whole rocks of group II.

(d) Blocks: these are of two types. One of the blocks is characterized by higher concentrations of the enriched elements in group I of the whole rocks, and lower concentrations of the elements of group II. The other three blocks analysed have high concentrations of some of the enriched elements in group II of the whole rocks (MgO, CaO, Sc, Cr, Ni and Sr).

A second principal component factor analysis was carried out on the analytical results for the whole rocks (20 samples), omitting Li, Ni, W and As as variables. The detailed analysis of the

distribution of the aforementioned geochemical groups allowed various subgroups to be distinguished (Fig. 7a). Within group I, three subgroups were identified: one with very low contents of all the major elements and with higher contents in Cr, Co and V (group Ia), a second with higher concentrations of Na_2O , K_2O , Y, Pb and Zn (group Ib), and a third intermediate subgroup (group Ic).

In group II two subgroups were identified: group IIa, with slightly higher contents of MgO, CaO and Sr and group IIb, with higher concentrations of Fe_2O_3 , Na_2O , K_2O , TiO_2 , P_2O_5 , Y and Zn (Fig. 7b).

Geochemical distribution patterns

The analytical results of the DI seafloor sediments demonstrate the existence of important chemical variations that, in our opinion, are the result of different submarine volcanic episodes. Thus, the sediment samples can be classified as: (1) metaluminous calc-alkaline according to their $\text{FeO}-\text{MgO}-(\text{Na}_2\text{O} + \text{K}_2\text{O})$ relationship and $\text{Al}_2\text{O}_3/(\text{CaO} + \text{Na}_2\text{O} + \text{K}_2\text{O})$ v. $\text{Al}_2\text{O}_3/(\text{Na}_2\text{O} + \text{K}_2\text{O})$ contents; (2) low K tholeiites, taking into account their $\log \text{Cr}/\log \text{Ti}$ ratios, and (3) ocean floor basalts in accordance with their $\text{Ti}/100$ v. V relations.

Geochemical distribution patterns show that, although very high amounts were not detected, the geochemical haloes of some elements are indicative of links between the geochemical

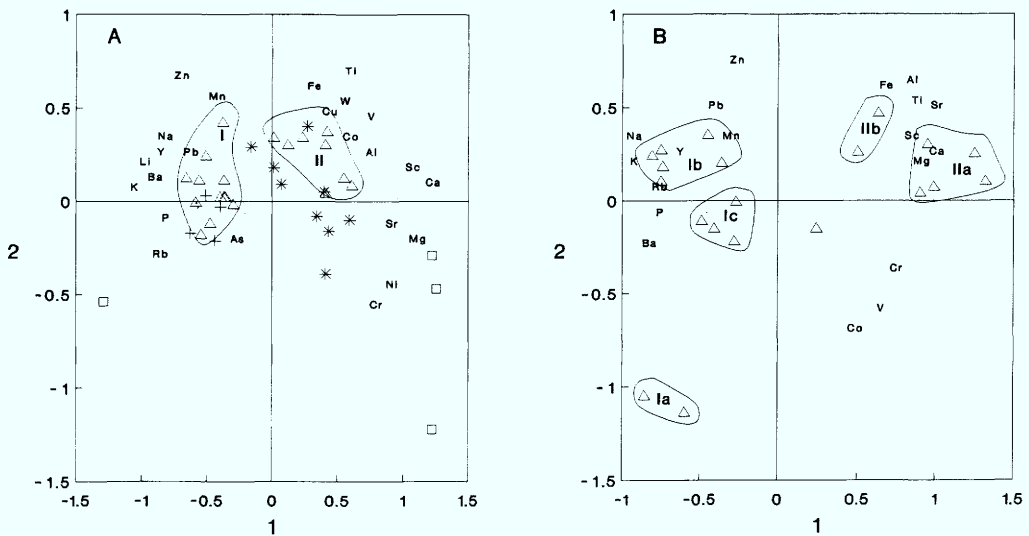


Fig. 7. Principal component factor analysis diagrams (see explanation in text) showing the geochemical groups and subgroups (triangles, whole rock; asterisk, fraction $>2\text{ mm}$; crosses, fine-grained materials; squares, blocks).

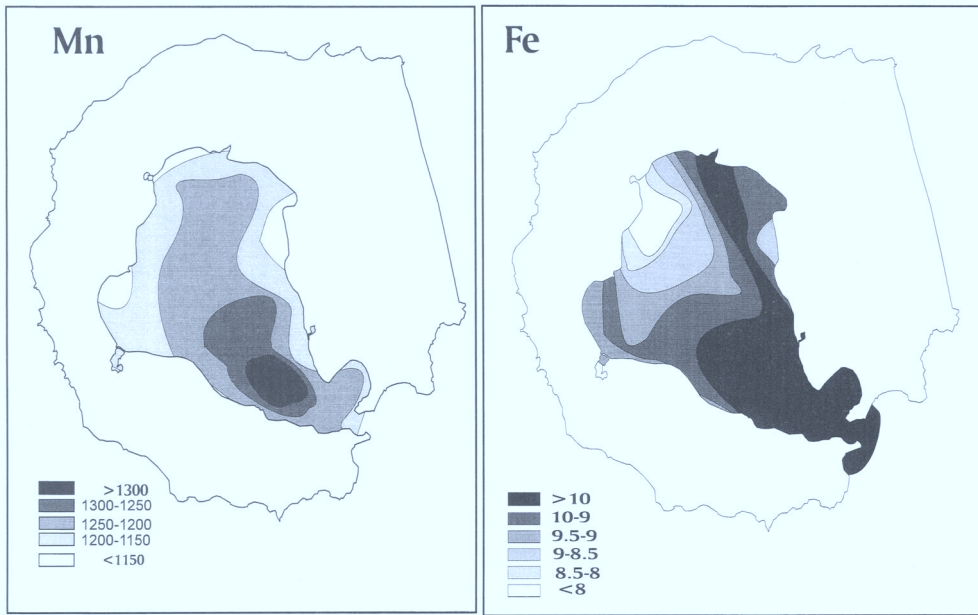


Fig. 8. Geochemical distribution maps of Mn and Fe in the interior of DI. Mn (ppm), Fe (Fe₂O₃, in wt%). Note that the highest contents coincide with the principal NW-SE alignment of submarine volcanic structures (see Fig. 3).

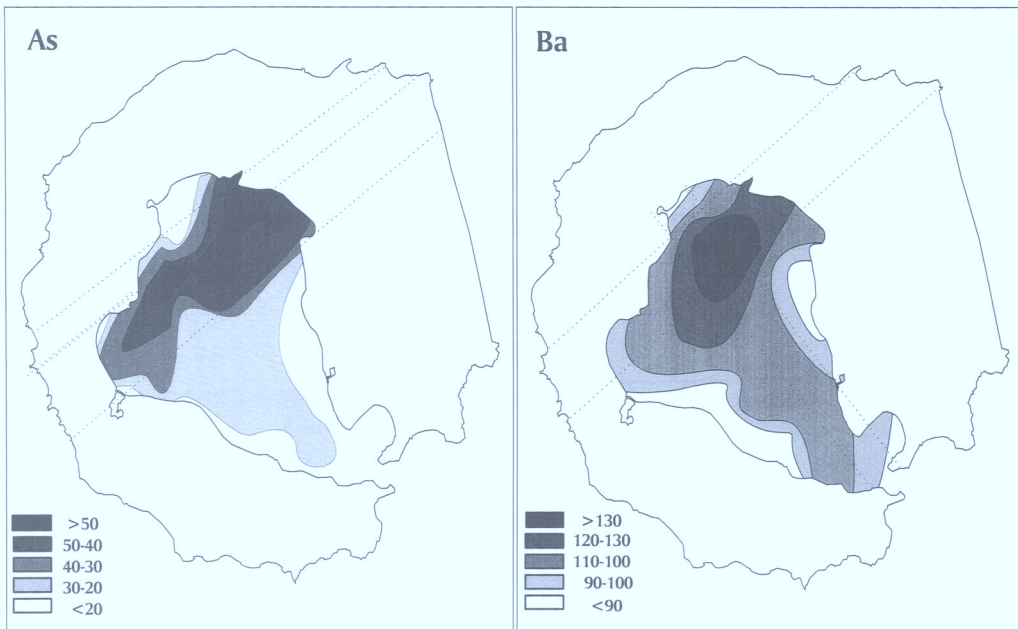


Fig. 9. Geochemical distribution maps of As and Ba (ppm) in the interior of DI. Note that the highest contents coincide with the NE-SW system of faults associated on the surface with the existence of fumaroles and hot springs (see Fig. 3).



Fig. 10. Fumarole vent (Fumarole Bay area).

values, the submarine volcanic units and the ancient and recent tectonic systems of DI. Thus, the highest contents of Mn, Fe and Zn coincide with the position of the mounds and volcanic cones (Fig. 8). These values decrease progressively from the axis to the boundaries of the flooded caldera and the lowest values were detected at the Telefon Bay area. So, it is possible that the hydrothermal fluids linked to the syncaldera volcanic episode (unit B) would be richer in metals than those of the more recent eruptions (unit C).

The highest values of As, Ba, Al, Ca, Mg and K are found between Fumarole Bay and Pendulum Cove, and coincide with the N60 axis that crosses the flooded caldera (Fig. 9). Currently active hydrothermal processes, such as fumaroles (Fig. 10) and hot springs, are associated with this axis in the areas of Fumarole Bay, Telefon Bay, Pendulum Cove and Whalers Bay (Ortiz *et al.* 1992). These authors propose that the fluids are produced by the venting of shallow aquifers heated by convective gaseous inflow from the underlying magma chamber. H₂ (0.010–0.066%), CH₄ (0.0010–0.066%), He (0.0010–0.019%), air and water vapour are the main components of fluids from the fumarole emissions.

Conclusions

In accordance with the seismic profiles and with the interpretation of the tectonic systems and

geochemical characteristics of the submarine volcanic Formations it is possible to establish the following final conclusions.

(1) Fundamentally, two main geotectonic directions exist on DI, one NW–SE, which includes the submarine volcanic cones and the mound-type structures, and another, NE–SW, which is associated with the presence of fumaroles and hot-springs. Both directions are related to a deformation ellipsoid, the major axis of which is along a NW–SE direction, produced as a consequence of a simple shear stress generated by a N–S strike dextral pair fault system. The evolution of this system (Fig. 11) gives rise to a clock-wise rotation of the main extensional axis. The piling of the mounds appears to be conditioned by the rapid subsidence produced by the rotation of normal faults, which subsequently generates a significant accumulation of material (maximum estimated thickness of 50–60 m).

(2) Three seismo-depositional units have been defined in the interior of the island which coincide with the subaerial volcanic Formations defined by Birkenmajer (1992). However, masking of parts of the seismic profiles has been detected in certain cases, probably due to fluid emissions associated with present volcanic activity. The simple analysis of the volcanic Formations which make up the seafloor of DI does not allow a valid geochemical classification of said rocks, given that they respond to the interference of different volcanic episodes.

(3) Although the geochemical values of some elements (Fe, Mn, Ba, As, Zn) cannot be

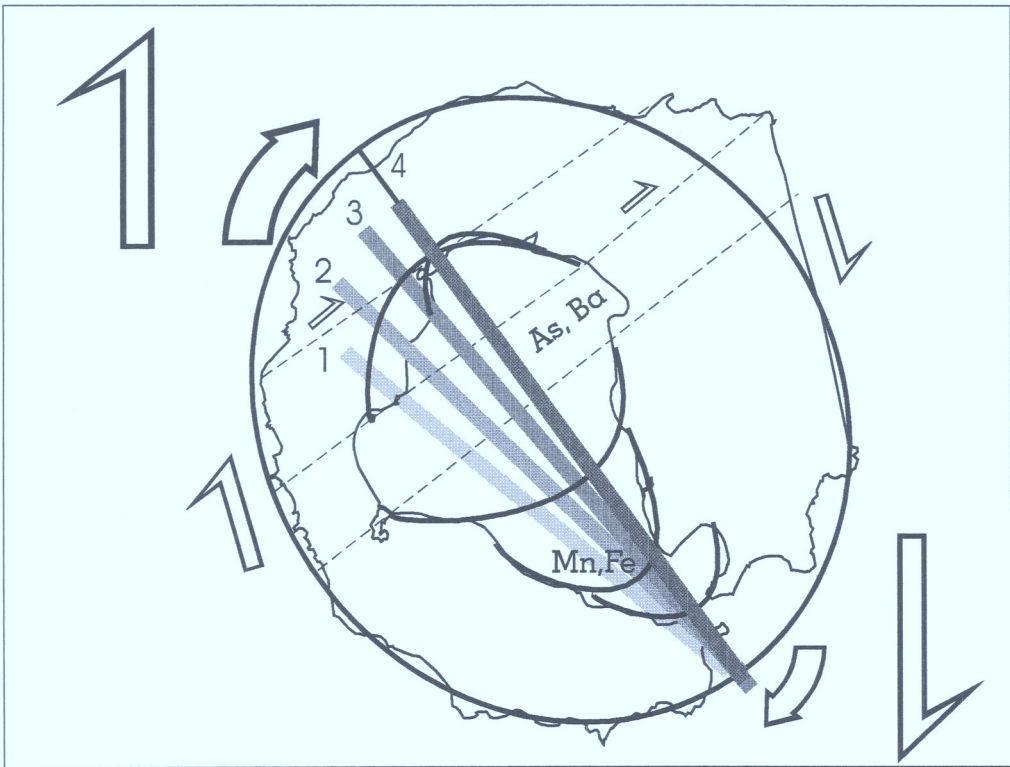


Fig. 11. Deformation ellipsoid superimposed onto DI where the major NW-SE ellipsoid axis and its evolution with respect to the model proposed to explain the rotation of the island can be seen. 1-4: Successive axes from the Murature Fm (1) to the Telefon Fm (4). The dotted lines correspond to the directions of the vertical tensional faults.

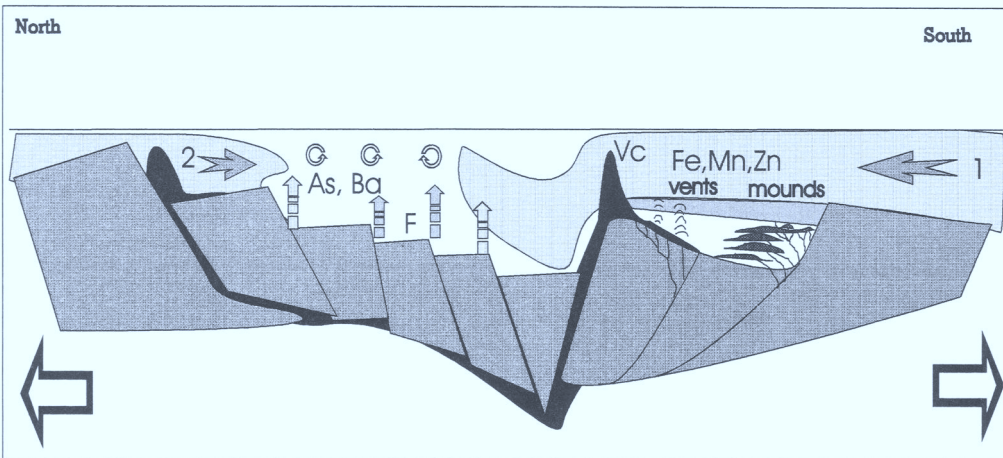


Fig. 12. Idealized synthetic profile of the bay. The highest values of Mn, Fe and Zn are associated with the volcanic cones and mound and vent structures located in the south of the island. These structures, in turn, are related with normal faults which were generated as a consequence of the great central flexing of the island, which gave rise to the volcanic cones (VC). The ingress of oceanic water (1) with temperatures of less than 0°C could speed up the oxidizing process of the mounds, the piling of which takes place through a rapid process of subsidence by rotation of the normal faults. In the centre of the bay, fumaroles (F) (controlled by almost vertical faults) raise considerably the water temperature and give rise to convection phenomena.

considered anomalously high, the distribution patterns of these and the position of the geochemical haloes with respect to the submarine structures indicate a clear relationship between submarine volcanism, tectonic systems and the probable existence of mineralizing hydrothermal processes (Fig. 12). In fact, the DI mounds resemble other Fe–Mn mound-shaped structures which have been described in other mineralized areas related with volcanism (e.g. Semail Nappe, Oman; Fleet & Robertson 1980; Robertson & Boyle 1983), Galapagos mounds area (Corliss *et al.* 1978).

(4) Supposing that, in accordance with the model proposed, the island has suffered a clockwise rotation and that the NW–SE structures are the oldest and the NE–SW are the most modern, it is possible to surmise that the first hydrothermal emissions were those enriched in Fe and Mn (vents and mounds) and that the latest were enriched in Ba and As. These last emissions coincide with the presence of the fumaroles and hot-springs.

(5) All things considered, DI is, in conclusion, an extraordinary natural laboratory where volcanism, tectonic systems and mineralizing hydrothermal processes can be studied in unison, and is an interesting target for the exploration of Fe–Mn structures similar to those of other mineralized areas.

We would like to thank the members of the Antarctic Spanish Expedition (Oceanographic Vessel *Las Palmas*) for their collaboration, especially the expedition chief, E. Moreau. Thanks also to IEO (Instituto Español de Oceanografía) and CSIC (Consejo Superior de Investigaciones Científicas) for financial support for part of the research. This work has been carried out in cooperation with the IGCP project 318 (IUGS/UNESCO), and with the Spanish Working Group on Geology and Metallogeny of Seafloor Hydrothermal Deposits. Special thanks to J. Hein for prompting the publication of this paper and to M. Harffy for his help with the English of the manuscript.

References

- BARKER, P. E., PIHIL, D., MAREATH, I., HARVEY, M. R., ROOBOL, M. J. & DAVIES, T. G. 1975. The geology of the South Shetland Islands: V. The volcanic evolution of Deception Island. *British Antarctic Survey Scientific Reports*, **78**, 1–81.
- BARKER, P. F. 1982. The Cenozoic subduction history of the Pacific margin of the Antarctic Peninsula: ridge crest-trench interactions. *Journal of the Geological Society, London*, **139**, 787–801.
- BIRKEMAJER, K. 1992. Volcanic succession at Deception Island, West Antarctica: A revised lithostratigraphic standard. *Studia Geologica Polonica*, **101**, 27–82.
- CORLISS, J. B., LYLE, M., DYMOND, D. J. & CRANE, M. 1978. The chemistry of hydrothermal mounds near the Galapagos rift. *Earth and Planetary Science Letters*, **40**, 12–24.
- FLEET, A. J. & ROBERTSON, A. H. F. 1980. Ocean-ridge metalliferous and pelagic sediments of the Semail Nappe, Oman. *Journal of the Geological Society, London*, **137**, 403–422.
- GONZALEZ-FERRÁN, O. 1985. Volcanic and tectonic evolution of the northern Antarctica Peninsula–Late Cenozoic to Recent. In: HUSEBYE, E. S., JOHNSON, G. L., & KRISTOFFERSEN, Y. (eds) *Geophysics of the polar regions. Tectonophysics*, **114**, 389–409.
- & KATSUI, Y. 1970. Estudio integral del vulcanismo cenozoico superior de las Islas Shetland del Sur, Antártica. *Instituto Antártico Chileno Serie Científica*, **1**, 123–174.
- HAWKES, D. D. 1996. *The geology of the South Shetland Islands. II. The geology and petrology of Deception Island*. Falkland Islands Dependencies Survey Scientific Report, **27**.
- GRAD, M., GUTERCH, A. & SRODA, P. 1992. Upper crustal structure of Deception Island area, Bransfield Strait, West Antarctica. *Antarctic Science*, **4**, 469–476.
- KELLER, R. A., FISK, M. R. & WHITE, W. M. 1991. Rifting of an island arc, Bransfield Strait and South Shetland islands, Antarctica. *Sixth International Symposium on Antarctic Earth Sciences*. National Institute of Polar Research, Japan, 298–303.
- , —, — & BIRKENMAJER, K. 1992. Isotopic and trace element constraints on mixing and melting models of marginal basin volcanism, Bransfield Strait, Antarctica. *Earth and Planetary Science Letters*, **111**, 287–303.
- MARTÍ, J., REY, J. & BARALDO, A. 1990. Origen y estructura de la isla Decepcion (Islas Shetland del Sur). *Actas del Tercer Simposium de Estudios Antárticos*. Comisión Interministerial de Ciencia y Tecnología, Madrid, Spain: 187–194.
- ORHEIM, O. 1972. Volcanic activity on Deception Island, South Shetland Islands. In: ADIE, R. J. (ed.) *Antarctic Geology and Geophysics*. Universitetsforlaget, Oslo, 117–120.
- ORTIZ, R., VILA, J., GARCIA, A. *et al.* 1992. Geophysical features of Deception Island. In: YOSHIDA, Y. *et al.* (eds) *Recent Progress in Antarctic Earth Science*. Terra Scientific Publications, Tokyo, 443–448.
- PECCERILLO, A., TRIPODO, A., VILLARI, L., GURRIERI, S. & ZIMBALATTI, E. 1991. Genesis and evolution of volcanism in back-arc areas. A case history, the island of Deception (Western Antarctica). *Periodico di Mineralogia*, **60**, 29–44.
- REY J., SOMOZA, L. & HERNANDEZ-MOLINA, F. J. 1992. Formas de los sedimentos submarinos superficiales en Puerto Foster, Isla Decepción, Islas Shetland del Sur. In: LÓPEZ-MARTINEZ, J. (ed.) *Geología de la Antártida Occidental*. III Congreso Geología de España & VIII Congreso Latinoamericano de Geología, Salamanca, España, Symposium **3**, 163–172.

- , — & MARTINEZ-FRIAS, J. 1995. Tectonic, volcanic and hydrothermal event sequence on Deception Island (Antarctica). *Geo-Marine Letters*, **15**, 1–8.
- ROBERTSON, A. H. F. & BOYLE, J. F. 1983. Tectonic setting and origin of metalliferous sediments in the Mesozoic Tethys ocean. In: RONA, P. A., BOSTRÖM, K., LAMBIER, L. & SMITH, K. L. JR (eds) *Hydrothermal processes at seafloor spreading centers*. NATO Conference Series.
- SMELLIE, J. L. 1981. A complete arc-trench system recognized in Gondwana sequences of Scotia Arc Region. *Geological Magazine*, **118**, 139–159.
- 1988. Recent observations on the volcanic history of Deception Island, South Shetland Islands. *British Antarctic Survey Bulletin*, **81**, 83–85.
- SOMOZA, L., REY, J., MARTINEZ-FRIAS, J. & BENITO, R. 1994. Fe-Mn distribution patterns on seafloor sediments related to the discovery of submarine volcanic cones, mounds and vent structures (Deception Island, Antarctica). *European Journal of Mineralogy*, **6**, 343–344.

Terrestrial hot-spring Co-rich Mn mineralization in the Pliocene–Quaternary Calatrava Region (central Spain)

A. CRESPO¹ & R. LUNAR²

¹ *Departamento de Geología Aplicada, INI Medioambiente S.A., Zurbarán 28, 28010 Madrid, Spain*

² *Departamento de Cristalografía y Mineralogía, Facultad de Ciencias Geológicas, Universidad Complutense, 28040 Madrid, Spain*

Abstract: Central Spain hosts a series of high-Co (up to 1.7% Co) Mn mineralizations displaying a variety of morphologies: spring aprons and feeders, pisolitic beds, wad beds and tufa-like replacements of plants and plant debris. The Mn mineralogy consist of cryptomelane, lithiophorite, birnessite and todorokite. The spring apron deposits formed in close proximity to Pliocene volcanic rocks (alkaline basaltic lava flows and pyroclastics) belonging to the so-called Calatrava Volcanic Field. The spring aprons are found along or near to normal faults bounding small basins and topographic highs. Mn tufa-like deposits are found near to the spring sources, while both pisolitic and wad beds are clearly distal facies occurring well within the Pliocene basins. The two latter are interbedded with clastic lacustrine and fluvial sediments. Collectively, these deposits contain a complex suite of Mn–(Co) mineralization ranging from proximal, hot-spring-type Mn facies, grading into more distant sedimentary, stratabound mineralization. Volcanism, basin formation and Mn deposition took place within a failed rift environment which triggered hydrothermal activity and Mn–(Co) deposition as proximal (near to the volcanic axes) and distal (of sedimentary affinities, within the basins) facies.

The Calatrava region in central Spain (Fig. 1) hosts one of the most outstanding volcanic fields of the Iberian peninsula. The volcanic rocks were extruded from more than 240 emission centres (craters, vents, etc.) forming the so-called Calatrava Volcanic Field (CVF), of late Miocene–Quaternary age. The volcanism developed under extensional conditions that led to the formation of a series of fault-bounded continental basins receiving fluvial and lacustrine sediments and volcanic rocks. A variety of Mn–(Co) mineralizations developed within this realm, some in close proximity to the volcanic emission centers and normal faults (proximal facies), the others within the continental clastic sedimentary basins (distal facies).

Under the geochemical point of view these manganese deposits are to be regarded as unusual, as high Co content in Mn ores are not found in terrestrial but in marine deposits either of the supergene or hydrothermal type. The Calatrava deposits were mined in the past (1885–1965), and more recently (1985–1991) received a renewed interest in terms assessing the possibilities of Co extraction from the manganese ores.

Geological framework

The Calatrava region is located in the boundary between the Centro-Iberian subdivision of the

Hesperian Variscan Massif to the west, and a series of neogene sedimentary basins to the east. This part of the Variscan Massif is characterized by Palaeozoic rocks, predominantly quartzites of the so-called Armorican facies (Lower Ordovician), as well as limestones (Upper Ordovician) and slates (Ordovician–Silurian), variably affected by Hercynian deformations, resulting in a series of NW–SE- to W–E-oriented folds. This basement is unconformably overlain by Upper Miocene to Quaternary fluvial and lacustrine sediments and alkaline basaltic volcanic rocks (Figs 1 & 2).

Two tectonic episodes can be recognized in the CVF (López Ruíz *et al.* 1993): (a) late Miocene to Pliocene extension leading to the opening of the sedimentary basins, and the extrusion of the volcanic rocks, and (b) a Quaternary compressional regime giving rise to gentle undulatory deformations. This scheme results from a geotectonic scenario with NW-directed convergence/indentation, taking place in the SE tip of the Iberian Peninsula, and acting upon the Iberian foreland.

The Pliocene sediments are continental derived, with initial arid deposits of alluvial fans, showing transition towards the center of the basins to more distal fluvial and/or lacustrine sediments. These molasse-type sedimentary series consist of the following: (1) heterochronous basal alluvial-fan-type deposits (conglomerates, clays and sands),

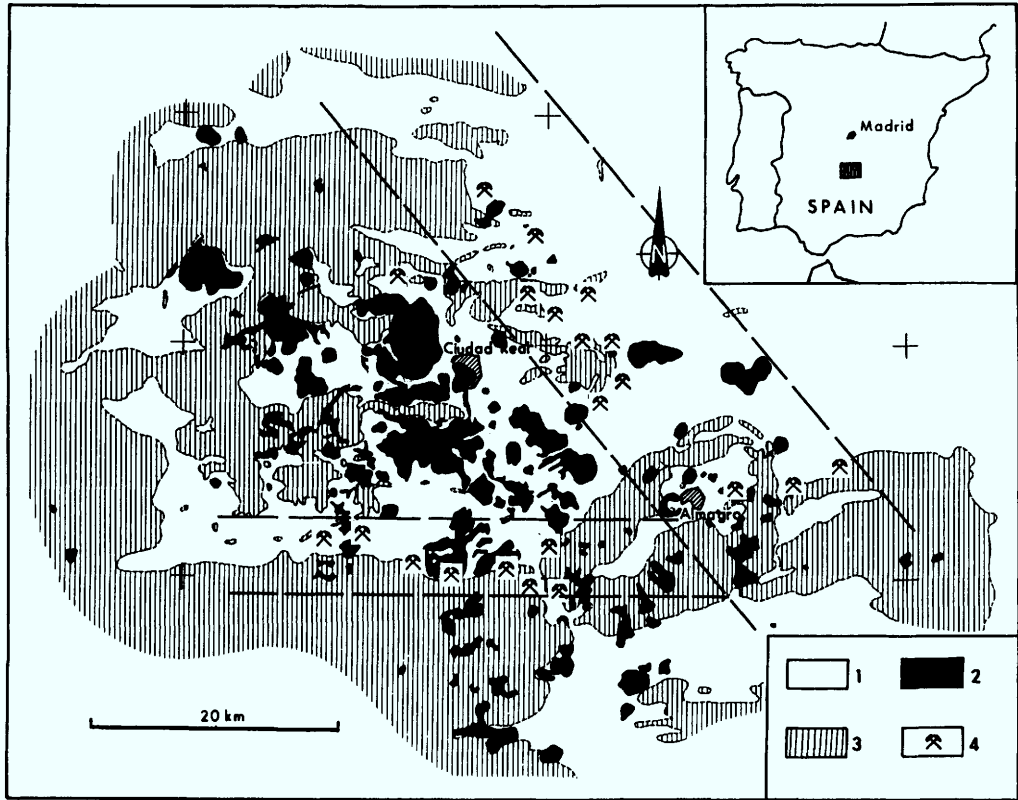


Fig. 1. Location map of the CVF and its Mn (Co) deposits. 1, Neogene and Quaternary sediments; 2, volcanic outcrops (Pliocene–Quaternary); 3, Palaeozoic basement (Ordovician to Silurian quartzites, slates, limestones); 4, Mn–(Co) deposit. Dashed lines indicate the preferred trends of the Mn deposits.

which are always found in the borders of the basins; (2) thick deposits with red lutites, and occasional fine-grained sands, carbonates, and gypsum; (3) palustrine/lacustrine carbonates on top of the series. The marginal basin areas show important lateral facies variations, as related to the presence of local depocenters, as well as to the Palaeozoic reliefs, and the activity of the bordering faults. These Pliocene sediments are covered by Plio-Quaternary glacial sediments, and Quaternary calcareous crusts, conglomerates, and endorreic valley deposits.

A characteristic feature of this zone is the existence of an important volcanic activity, coeval with the Neogene–Quaternary deposits. The volcanic edifices and their products are scattered all around the region (lava flows, lapilli, ashes, etc; Fig. 2). These volcanoes are essentially of the explosive/strombolian type, with some strongly explosive cases giving rise to maars. The volcanic materials are found interstratified with the Plio-Quaternary sediments. Alkaline volcanism began by late Miocene time

(8.7–6.40 Ma; Ancochea 1982; López Ruíz *et al.* 1993) with the extrusion of leucites. Most of the volcanic activity concentrated during the Pliocene–Quaternary (4.7–1.6 Ma) with olivine leucitites, olivine nephelinites, and alkali olivine basalts. Volcanism and sedimentary processes developed contemporaneously within the extensional basins. The chemical composition of the volcanic rocks of this area does not show important differences regarding the distribution of Mn, Co and Ni, as compared to other similar volcanic regions. The composition of the volcanic rocks is given in Table 1.

Pyroclasts and lavas were ejected from more than 240 emission centres within a subcircular-shaped area where dominant NW–SE and E–W volcanic trends can be recognized. As shown by mining/exploration works in the CVF, volcanism was related to extensional faults, which also acted as preferred conduits (feeders) for the migration of hydrothermal fluids leading to the formation of the Mn–(Co) deposits. A waning geothermal activity within the area is shown by

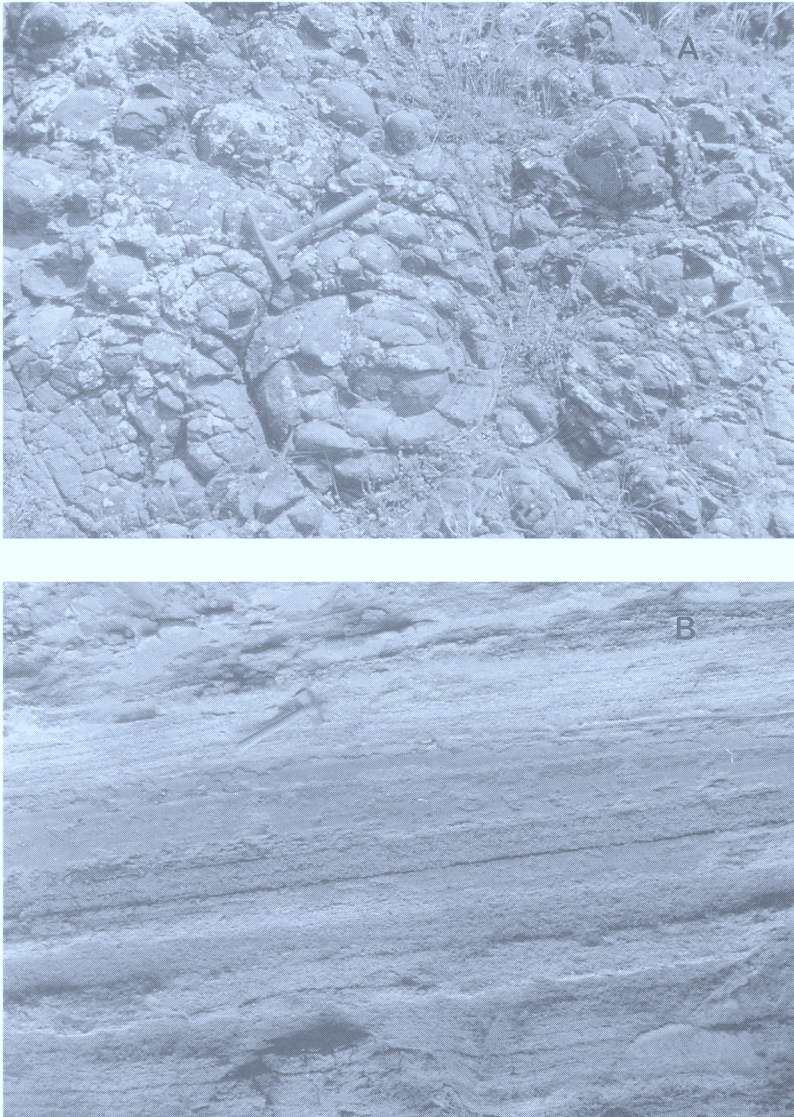


Fig. 2. (a) Basaltic lava-flows in the CVF showing spherical-like erosional features. (b) Subhorizontal lapilli deposits of the CVF.

the existence of the so called 'herverideros' (boiling spots), even though no deposition of Mn is recorded at present.

Mn-(Co) mineralization

Age

The age of the Mn deposits ranges from Pliocene to Lower Pleistocene, as can be deduced from a

series of mammal fossil remains found within the mineralized horizons (Crespo 1992). This coincides well with the radiometric ages of the volcanic rocks (concentrated in the time-span 4.7–1.6 Ma; Ancochea 1982; Bonnadona & Villa 1986; López Ruíz *et al.* 1993). The Mn deposits are aligned along two main fault trends (Fig. 1): NW–SE (corresponding to the Iberian range Alpine Trend) and E–W (corresponding to the Toledo Range Alpine Trend).

Table 1. Ranges in major (%) and trace elements (ppm) of the alkaline basaltic rocks and leucitites from the Calatrava Volcanic Province

	M (n = 38)	N (n = 8)	OB (n = 16)	L (n = 5)
SiO ₂	36.17–40.71	41.00–43.96	42.73–46.85	42.80–47.49
TiO ₂	2.46–3.78	0.65–3.78	2.15–3.63	1.80–2.35
Al ₂ O ₃	8.97–13.15	10.76–13.12	11.00–3.19	8.29–11.11
Fe ₂ O ₃	3.11–9.72	3.16–6.14	2.54–6.42	2.82–6.57
FeO	2.63–8.98	5.81–9.05	5.46–8.38	4.31–6.73
MnO	0.16–0.22	0.17–0.21	0.13–0.19	0.14–0.16
MgO	9.08–16.70	9.03–13.81	8.69–12.68	10.06–17.56
CaO	10.22–17.08	11.13–13.21	10.20–12.42	9.90–11.80
Na ₂	2.12–4.84	3.02–5.21	2.23–5.60	1.50–2.8
K ₂ O	0.38–2.27	0.45–2.24	0.46–1.90	1.87–4.34
P ₂ O ₅	0.78–1.72	0.51–1.08	0.53–0.84	0.67–1.20
LOI	0.37–3.05	1.24–3.19	0.03–3.14	0.66–2.72
Rb	14–113	5–78	24–116	241–303
Ba	566–1597	635–1213	446–1298	845–1175
Sr	784–2347	530–1088	579–1243	879–1090
La	56.4–106	57.4–67.5	33.6–56.0	64.6–80.0
Ce	112–230	112–128	66.4–108	140–176
Nd	57.2–104	51.6–62.6	35.6–51.2	78.4–105.0
Sm	10.7–19.6	10.2–11.8	7.3–10.6	14.9–19.3
Eu	3.50–5.66	3.09–3.83	2.57–3.27	3.24–4.26
Gd	9.2–15.6	8.3–10.7	7.4–8.8	9.0–12.7
Dy	6.1–10.4	5.7–7.5	5.3–6.4	4.8–7.0
Yb	1.79–2.67	1.76–2.16	1.69–2.03	1.64–2.13
Lu	0.27–0.37	0.24–0.29	0.24–0.30	0.25–0.29
Y	28–44	28–34	25–33	9–21
Zr	241–424	239–331	169–311	351–449
Nb	58–144	61–98	42–82	54–69
Zn	77–118	83–11	88–108	64–79
Co	28–52	31–47	30–47	32–73
Ni	99–428	113–354	105–308	182–746
V	220–298	220–296	196–284	169–213
Cr	192–750	261–625	250–557	798–853

M, Melilitites; N, nephelinites; OB, olivine basalts; L, leucitites (based on data from López Ruiz *et al.* 1993).

Mineralogy

The mineralogy of the CVF deposits is formed by four tetravalent oxides: cryptomelane, lithiophorite, todorokite and birnessite. Two of these minerals have tunnel-type structures (cryptomelane and todorokite) while the two other ones have layered structures (lithiophorite and birnessite). Most of the manganese oxides of the area display important Co contents (0.02–2.0%), and minor quantities of Ni. As seen in microprobe studies, Co does not form individual minerals, and it is incorporated within the structure of the Mn oxides. All of these oxides are structurally based on [MnO₆] octahedral

units sharing either corners or edges. The todorokite with tunnel structure has cation exchange properties and it can admit Co²⁺, Ni²⁺ and Cu²⁺ in the M2-type octahedral sites (Roy 1981, 1992; Burns & Burns 1978*a, b*). The proposed mechanisms of capture of these elements, for layered structures (Burns 1976), include a first stage during which the cations are adsorbed on the surfaces of the Mn oxides. The Co²⁺ which appear near the vacancies in the [MnO₆] layer, and oxidates to Co³⁺, occupies finally the octahedral sites. This mineralogy is accompanied by iron oxides, and variable amounts of detrital quartz, clay minerals, carbonates and phosphates. Mineralogical studies

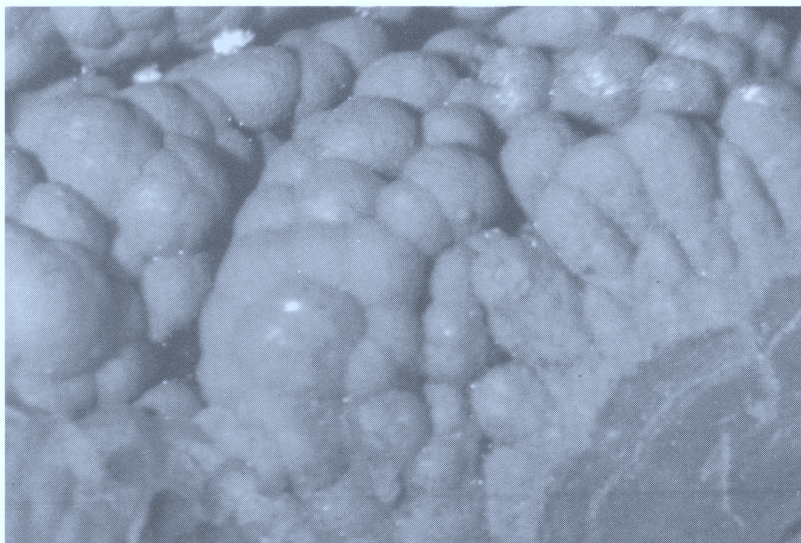


Fig. 3. Botroidal texture of cryptomelane. La Zarza mine.

undertaken (in more than 900 samples) include XRD, transmitted and reflected light microscopy, SEM, electron microprobe and infrared spectroscopy.

Cryptomelane is the most abundant Mn oxide at the CVF, and it is found in the mineralized

bodies in association to all types of textures and structures (except pisolites). The textural aspect varies from heavy, hard reniform-botroidal specimens (Fig. 3) commonly found in proximal facies, and light earthy masses (wads) present in the distal facies. The chemical composition of

Table 2. Selected chemical analyses of cryptomelane in the CVF

	M8DC	M10DC	M77DC	M11DC	M47DC	M58DC	M40DC
<i>Major elements (wt%)</i>							
SiO ₂	4.73	1.00	2.00	1.12	4.00	5.00	3.42
TiO ₂	0.28	0.08	0.08	0.07	0.06	0.18	0.41
Al ₂ O ₃	2.76	1.02	1.16	2.40	1.96	1.40	3.68
Fe ₂ O ₃	2.06	0.08	0.50	0.34	1.69	1.37	2.00
MnO ₂	73.04	76.42	75.86	75.12	69.71	71.79	68.91
MgO	0.31	0.17	0.20	0.20	0.34	0.37	0.26
CaO	0.23	0.51	0.32	0.38	0.59	0.59	0.46
BaO	0.84	0.05	0.43	0.38	9.22	1.00	2.04
Na ₂ O	0.26	0.15	0.15	0.18	0.10	0.18	0.23
K ₂ O	3.10	5.36	2.40	2.60	1.56	4.70	3.54
P ₂ O ₅	0.32	0.58	0.23	0.16	0.41	0.28	0.72
LOI	12.14	12.63	13.04	15.04	9.86	11.61	13.03
<i>Trace elements (ppm)</i>							
Co	2200	5400	5400	11 400	1700	6400	4100
Ni	210	710	278	2 070	244	590	485
Cu	57	880	35	2 800	250	1055	145
Zn	230	790	440	1 550	192	625	810
Cr	64	150	56	54	34	68	56
Sr	405	2800	2260	1 360	1680	2400	2200
V	168	2060	738	280	4240	888	1295
Be	9	28	5	2	34	6	12
Li	22	22	88	848	44	63	120

the CVF cryptomelane samples falls within the expected range (with the exception of Co which ranges from 0.2% to 1.1%). Table 2 includes seven analyses selected from different zones of the CVF.

Lithiophorite is second to cryptomelane in order of abundance and is typically found in pisolitic (Fig. 4) or nodular Mn beds, commonly associated with cryptomelane, birnessite, hematite, goethite, calcite and apatite. This mineral has not been found in the wads. Table 3 includes the chemical composition of some lithiophorite samples of the CVF. No chemical analyses could be performed in either birnessite or todorokite as they occur intermixed with other minerals. Birnessite occurs in close association with clays and calcite in the Mn wads, and to a lesser extent within scattered Mn concretions found in the Pliocene sediments. Todorokite is the least abundant Mn oxide at the CVF, and it has been found in the wads associated with carbonates and phosphates.

Morphology of the mineralization

The mineralized bodies display different morphologies that can be grouped into five types: disseminations, wad beds, pisolitic beds, spring aprons and veins. Gradual transitions have been found between some of them. The morphological differences have no chemical expression in terms of Mn, Fe and Co, as might be seen in Fig. 5, where we have represented the mean values of Mn, Fe, Co, and Ni (from 579 mineralized manganese levels). Depending on the spatial relationships between the mineralized bodies and the hydrothermal vents, the Mn deposits can be grouped into two categories (Fig. 6): proximal and distal facies (Crespo *et al.* 1995):

Proximal facies. These facies (spring aprons, Fig. 7; veins; Mn tufa-like replacements) developed in close association with fault-controlled hydrothermal vents (the so-called 'hervideros'; Fig. 8) that formed along the margins of the different basins. Part of the Mn was deposited *in situ* as spring aprons, in the areas surrounding the vents. The higher levels are Fe-rich and of Quaternary age. The Mn-(Co) spring aprons overlap laterally with volcanoclastic and sedimentary facies and display average thicknesses of 0.7 m, extending up to a 100 m. Analyses of spring apron are shown in Table 4. The evolution of the hydrothermal systems led to early Mn-(Co) oxide mineralization, followed in time by the deposition of Fe oxides (Fig. 8). The

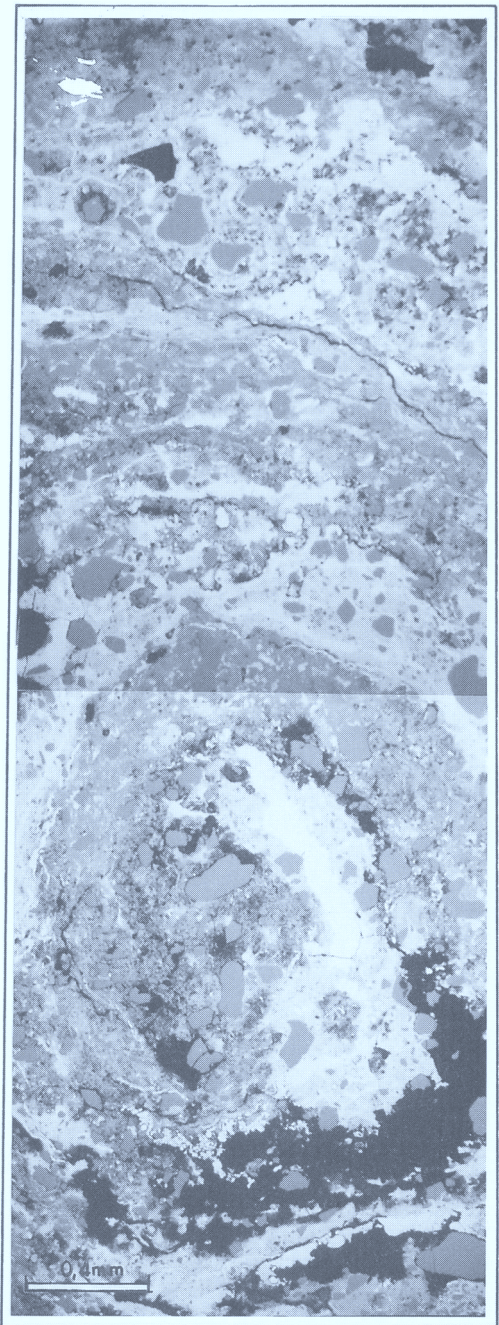


Fig. 4. Section of a pisolite. Note the different growing sequences constituted by lithiophorite (white), and clays (kaolinite and illite). The brecciated texture is due to the presence of quartz grains within the pisolite.

Table 3. Chemical analyses of lithiophorite

	(1)	(2)	(3)	(4)	(5)	C-3	M-3DC
<i>Major elements (wt%)</i>							
SiO ₂	0.67	8.25	3.08	bd	4.00	7.70	29.80
TiO ₂	0.00	0.07	0.08	bd	bd	0.90	0.57
Al ₂ O ₃	22.21	18.30	15.53	15.70	25.29	12.00	9.68
Fe ₂ O ₃	0.45	4.95	2.43	7.70	0.20	5.00	12.30
MnO	3.88	na	15.42	na	na	na	na
MnO ₂	51.56	48.50	42.22	55.82	46.00	53.34	33.16
MgO	0.02	0.49	bd	1.60	bd	bd	0.56
CaO	0.15	0.20	bd	bd	bd	1.00	0.34
BaO	0.05	0.49	1.26	bd	bd	bd	1.70
Na ₂ O	0.12	0.05	bd	0.10	bd	bd	0.10
K ₂ O	0.21	0.21	1.50	1.20	bd	2.20	1.24
P ₂ O ₅	0.00	bd	0.23	bd	bd	bd	0.46
LOI	15.32	bd	15.42	14.40	14.30	bd	10.24
<i>Trace elements (ppm)</i>							
Co	16820	504	5030	25164	56137	81100	6800
Ni	11900	10490	2358	bd	10970	29000	3000
Cu	3100	15908	7680	798	bd	bd	2000
Zn	bd	21700	bd	1600	bd	bd	1020
Sr	bd	84	bd	bd	bd	bd	450
V	bd	bd	bd	bd	bd	bd	276
Li	9007	5200	8633	bd	1824	bd	980

(1) Tennessee (Hewett & Fleischer 1960); (2) Banffshire (Wilson *et al.* 1970); (3) Sajonia (Frenzel 1980); (4) Australia (Ostwald 1988); (5) N. Caledonia (Manceau *et al.* 1987). C-3 and M-3DC, this work (C-3, La Zarza area; M-3DC; Ardales area, CVF). na, not available; bd, below detection.

vertical passage from the Mn to the Fe facies is not only marked by a drastic change in mineralogy (goethite dominates the oxide mineralogy), but also by a chemical threshold which separated Co-rich Mn oxide facies from Co-poor Fe oxide facies (Table 4).

The scarce veins are found within marls and limestones in the Pliocene rocks. The grades include 3.7% Mn, 0.9% Fe, 0.24% Co and 0.05% Ni, with mean thicknesses of 7 cm. In all cases the veins wedge out in depth and the Mn oxides are transformed into Fe oxides. Other forms of the Mn mineralizations which are not very important, but are typical of the CVF, are tube-like structures so-called 'canutillos' (a local mining term; Fig. 9), which are originated by tufa-like replacements of plants and plant debris by Mn (cryptomelane in all the cases studied).

Distal facies. These are typical stratabound deposits of sedimentary affinities. Grades are generally low (average: 3.4% Mn). Three subtypes of distal facies are recognized; disseminations, wad beds and pisolitic beds. Disseminations are the most common morphologies and constitute stratabound deposits. Mn deposition occurred as a combination of detrital, chemical and biochemical processes. The Mn oxides, with

varied structures, are included within the detrital Pliocene sediments of the basins. The wad beds, constitute about 16% of the distal facies. The beds are formed by an earthy variety of wad, and typically display lensoid morphologies. The mineralized bodies (criptomelane, birnessite and todorokite) can extend for several hundred meters, with an average thickness of 0.7 m. Average grades have values of 5.85% Mn,

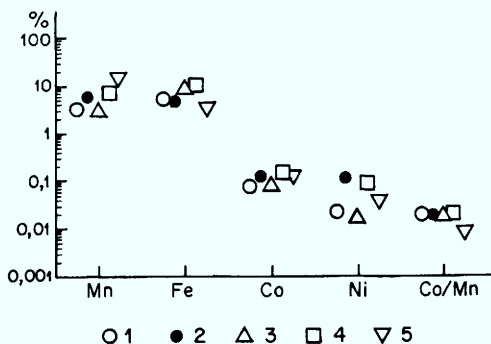


Fig. 5. Mean grades of Mn, Fe, Co and Ni in the different types of mineralized bodies. 1, Disseminations; 2, wad beds; 3, pisolitic beds; 4, spring aprons; 5, veins.

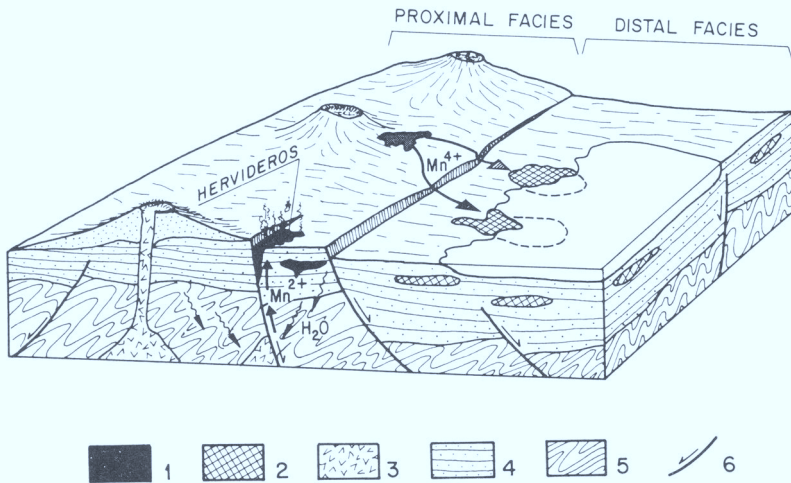


Fig. 6. Idealized sketch depicting Mn deposition (proximal and distal facies) during Pliocene–Quaternary time in the CVF. 1, Proximal Mn facies; 2, distal Mn facies; 3, undersaturated alkaline mafic rocks; 4, Pliocene–Quaternary fluvio-lacustrine sedimentary facies; 5, Hercynian basement; 6, fault.

4.96% Fe, 0.13% Co, and 0.001% Ni. They are often associated with clay deposits, and they are frequently interbedded with neoformed fibrous clays (paligorskite and sepiolite).

Pisolitic beds (Fig. 4) are not abundant, as they constitute less than 4% of the distal facies. The beds are formed by pisolitic Mn oxides embedded within a clay/sandy matrix. The

mineralized bodies might reach sizes up to 200 m. The average thickness of these bodies is 0.96 m, and grades are 3.21% Mn, 8.47% Fe, 0.07% Co and 0.02% Ni. Lihioforite is the only manganese oxide which has been found in the pisolites of the CVF. The associated clay minerals are illite and kaolinite. We suggest that the genesis of the pisolites in the zone is related



Fig. 7. Mn spring apron (cryptomelane–lithiophorite) with a high content in Co (up to 2%), and an outer Fe coating. Zarza mine.

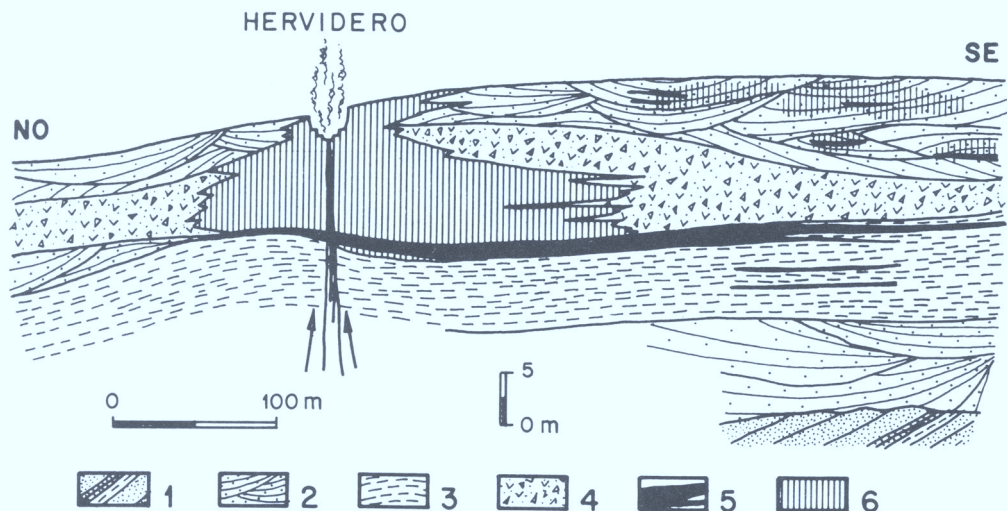


Fig. 8. Geological cross-section showing the morphology of one of the CVF 'Hervidero' (Los Baños del Villar). 1, Palaeozoic basement; 2, alluvial fans; 3, lutites; 4, hydromagmatic deposits; 5, Mn spring apron; 6, Fe crust. (Crespo 1992).

to the presence of shallow water bodies of small sizes, possibly in the sectors between alluvial fans. These small basins were probably the site of frequent changes in the chemical conditions and the energy of the fluids, thus inducing frequent variations in the concentration of the dissolved Mn. These changes triggered the alternating deposits of clays and manganese oxides.

A genetic model for the CVF Co-rich Mn deposits

Several data favour a volcanogenic-hydrothermal origin for part of the CVF Mn deposits: (a) the proximal facies formed in close association with the volcanic facies; (b) clear evidences of hydrothermal activity of the hot-spring-type still exists at the CVF as shown by the presence of the

Table 4. Chemical analyses of Calatrava Volcanic Field Mn spring apron (M-3 to M-96) and Fe Iron Caps (Fe-1 and Fe-2)

	M-3	M-9	M-19	M-68	M-69	M-88	M-96	FE-1	FE-2
<i>Major elements (wt%)</i>									
Fe ₂ O ₃	11.62	5.75	10.24	0.84	1.16	2.32	0.17	42.15	73.33
MnO	23.88	56.97	26.56	62.48	5.55	45.41	66.24	0.93	0.37
<i>Trace elements (ppm)</i>									
Co	5900	7400	16000	7000	990	9000	11000	22	14
Ni	2758	2027	3297	456	240	6207	2121	89	103
Cu	254	1750	8729	1246	56	118	288	155	24
Zn	812	386	441	157	28	276	353	66	76
Pb	12	7	<5	15	6	12	<5	9	8
Sb	5.8	2.8	1.4	4.3	1.8	2.3	1.9	2.1	1.1
As	22	30	14	12	8	17	15	8	115
Ag	<0.4	<0.4	0.4	<0.4	0.5	<0.4	<0.4	<0.4	<0.4
<i>Trace elements (ppb)</i>									
Au	5	5	5	5	5	25	12	6	<5
Hg	530	505	655	10	345	105	4580	155	150

Based on data from Crespo *et al.* (1995).

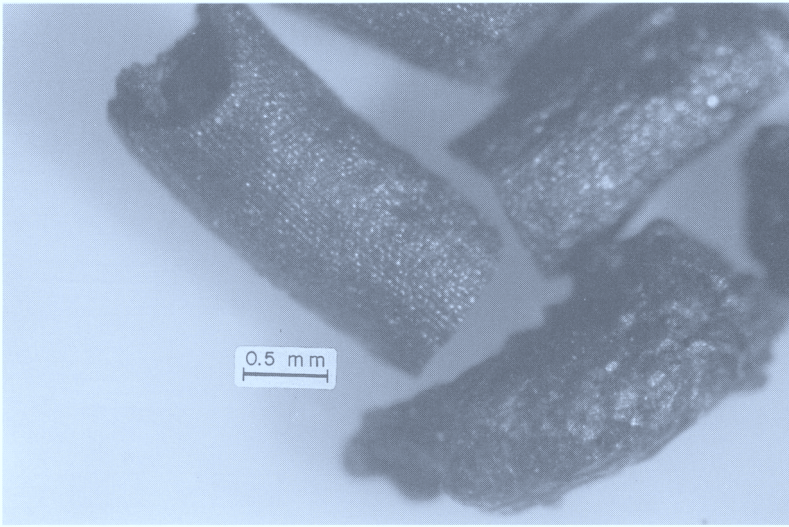


Fig. 9. Tufa-like replacement of plant debris by manganese (cryptomelane).

'hervideros'; (c) volcanism, Mn-(Co) mineralization, and sedimentation developed within a generalized extensional framework, and (d) on a global geotectonic scale, the CVF seems to have formed within a failed rift scenario.

The CVF Mn-(Co) deposits have a clear link with volcanism and extensional tectonics, which is often the case with these types of mineralizations. However, the high Co contents makes the CVF Mn-(Co) deposits rather unusual. The

most common examples of high-Co Mn oxides are those found in the present-day manganiferous nodules formed in seamounts and active hydrothermal vents in mid-oceanic ridges (1.15% Co and 0.40% Co respectively; Glasby 1977; Roy 1992; Nicholson 1992). Furthermore, only hydrogenous ferromanganese deposits are clearly Co-rich (as compared to the submarine hydrothermal deposits). In this sense, the geological framework of the CVF Co-rich Mn

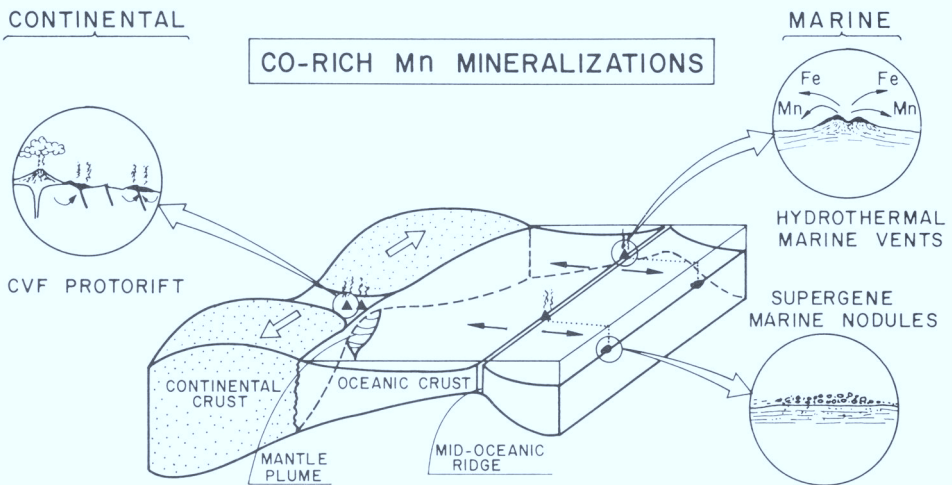


Fig. 10. Idealized sketch depicting the main environments in which Co-rich Mn mineralizations might be found (marine), including the one proposed here for the CVF (continental).

deposits is completely different from these environments, and it might constitute a new type of Mn mineralization, previously unrecognized, associated with a shallow continental scheme (lacustrine and fluvial basis), with alkaline mafic volcanism (Fig. 10).

One answer to the problem can be addressed in terms of the mineralogy of the CVF Mn-(Co) deposits. As shown earlier, the four Mn oxides found in the CVF can either admit or adsorb high amounts of Co. Since the alkaline volcanic rocks of the CVF are neither enriched nor depleted in Co, the key to the question might not be the source, but the ability of some minerals to scavenge Co from solution. Both the tunnel and layered structure minerals (todorokite-cryptomelane, lithiophorite-birnessite respectively) have this potential ability. This constitutes the mineralogical approach to the problem. However, even if this apparently explains the Co-rich Mn oxides facies, a major problem still remains to be solved. None of these minerals are common within environments such as the CVF (hot springs). In fact, only birnessite and cryptomelane have been observed in such environments (Nicholson 1992). Nevertheless, they can hardly be regarded as common in hot-spring deposits. The CVF Mn oxides are more usually found in association with weathering deposits under arid climates (supergene terrestrial; birnessite, cryptomelane), soil profiles including swamp and bog deposits (supergene terrestrial; birnessite, lithiophorite), weathering of mineralized sequences (supergene terrestrial; cryptomelane), or seawater nodules (supergene marine, hydrothermal marine; todorokite) (Nicholson 1992). Since the CVF Mn-(Co) deposits have clear-cut indicators of a hot-spring source, their origin is rare and therefore quite unique in terms of the high-Co values and Mn-oxide mineralogy.

The following points summarize our ideas regarding the genesis of the CVF (Mn-(Co) deposits).

(a) The deposits formed within a volcanosedimentary environment during Pliocene-Quaternary time, near to hot-spring sources ('hervideros') and within lacustrine-fluvial extensional basins; (b) transport mechanisms for the metals were epithermal hydrothermal solutions with high- f_{O_2} , that precipitated their metal load as tetravalent Mn oxides near the 'hervideros' (spring-apron-type deposits, in proximal facies); (c) part of the manganese migrated towards the inner parts of the basins forming stratabound deposits (wad and pisolitic beds in distal facies); (d) Co was most probably scavenged from the solutions and incorporated to the CVF Mn oxides; (e) a final decrease in the f_{O_2} conditions would have resulted

in the precipitation of iron within near surface levels, and the washing away of the manganese as soluble Mn^{4+} .

The tectonic scenario of the Calatrava region (Fig. 10) provides another insight into the problem. The CVF can be understood as the result of distal disturbances of the Iberian foreland, as related to compressional/indentation effects taking place in the eastern Betics (Doblas *et al.* 1991; López Ruíz *et al.* 1993). In this sense, the CVF might be explained as related to an impactogen scheme (Şengör 1976), where the NW-directed compressional stresses would have favoured the opening of the NW-SE-oriented Variscan trends, thus triggering a passive rifting arm, associated to mantle diapirism and upwelling, and possibly to a hot-spot. This might be similar to other late Cenozoic volcanic provinces of western Europe (e.g. Rhône, Rhine), which developed as a consequence of extensional processes taking place in the foreland, directly driven by compressions happening in orogens located in their southern borders (Şengör 1976; Illies & Greiner 1978). A tectonic approach to the problem of these anomalous Co-rich Mn mineralizations comes from the fact that the continental-related CVF constitutes an unique scenario involving a protorift or failed rift with a mantle diapir underneath (López-Ruiz *et al.* 1993). We suggest that failed rifts, possibly associated with triple junctions and/or hot-spots, might constitute potential targets for Co-rich Mn mineralizations within continental scenarios associated to the initial stages of oceanic opening. In this sense, it is noticeable that the mid-oceanic central Atlantic Fe-Mn hydrothermal deposits (Famous and TAG vents, Lalou 1983) seem to outcrop where the former Central Atlantic triple junction/hot-spot existed. In this sense, the CVF continental mineralizations might contribute to shed new lights upon the genesis of the Mn deposits worldwide. Furthermore, anomalous concentrations of the Mn-hydrothermal vents in certain sectors of mid-oceanic ridges might be indicative of former sites of hot-spots and proto-rift environments.

Financial support was provided by ENADIMSA through the Project Reserve Bolaños no. 237, with partial funding also from the Grant GEO-91-0055 (Ministry of Education and Science, Spain). This work has been carried out in cooperation with the IGCP project 318, and with the Spanish Working Group on Geology and Metallogeny of Seafloor Hydrothermal Deposits. Thanks to J. Hein for prompting the publication of this paper and special thanks to M. Doblas and R. Oyarzun for their critical review of tectonic setting.

References

- ANCOCHEA, E. 1982. *Evolución espacial y temporal del volcanismo reciente de España Central*. PhD Thesis, UCM, Madrid.
- BONADONNA, F. P. & VILLA, I. 1986. Estudio geocronológico del volcanismo de Las Higueruelas. *Actas Castilla-La Mancha: Espacio y Sociedad*, **3**, 249–253.
- BURNS, R. G. 1976. The uptake of cobalt into ferromanganese nodules, soils, and synthetic manganese (IV) oxides. *Geochimica et Cosmochimica Acta*, **4**, 95–102.
- BURNS, V. M. & BURNS, R. G. 1978a. Post-depositional metal enrichment processes inside manganese nodules from the north equatorial Pacific. *Earth and Planetary Science Letters*, **39**, 341–348.
- & — 1978b. Authigenic todorokite and phillipsite inside deep-sea manganese nodules. *American Mineralogist*, **63**, 827–831.
- CRESPO, A. 1992. *Geología, mineralogía y génesis de los yacimientos de manganeso cobaltíferos del Campo de Calatrava (Ciudad Real)*. PhD Thesis, UCM, Madrid.
- , LUNAR, R., OYARZUN, R. & DOBLAS, M. 1995. Unusual case of hot-springs-related Co-rich Mn mineralization in central Spain: the Pliocene calatrava deposits. *Economic Geology*, **90**, 433–437.
- DOBLAS, M., LÓPEZ RUÍZ, J., HOYOS, M. MARTÍN, C. & CEBRIA, J. M. 1991. Late Cenozoic indentation/escape tectonics in the eastern Betin cordilleras and its consequences on the Iberian foreland. *Estudios Geológicos*, **47**, 193–205.
- FRENZEL, G. 1980. The manganese ore minerals. In: VARENTSOV, I. M. & GRASSELLY, G. (eds) *Geology and Geochemistry of Manganese*. Schweizerbart'sche, Stuttgart, **1**, 25–158.
- GLASBY, G. P. 1977. *Marine Manganese Deposits*. Elsevier, Amsterdam.
- HEWETT, D. F. & FLEISCHER, M. 1960. Deposits of the manganese oxides. *Economic Geology*, **55**, 1–55.
- ILLIES, J. H. & GREINER, G. 1978. Rhinegraben and the Alpine system. *Geological Society of America Bulletin*, **89**, 770–782.
- LALOU, C. 1983. Genesis of ferromanganese deposits: hydrothermal origin. In: RONA, P. A., BOSTRÖM, K., LAMBIER, L. & SMITH, K. L. JR (eds) *Hydrothermal processes at seafloor spreading centers* NATO Conference Series, 503–535.
- LÓPEZ RUÍZ, J., CEBRIA, J. M., DOBLAS, M., OYARZUN, R., HOYOS, M. & MARTÍN, C. 1993. The late Cenozoic alkaline volcanism of the Central Iberian Peninsula (Calatrava Volcanic Province, Spain): intraplate volcanism related to extensional tectonics. *Journal of the Geological Society, London*, **150**, 915–922.
- MANCEAU, A., LLORCAS, S. & SALAS, G. 1987. Crystalchemistry of cobalt and nickel in lithiophorite and asbolane from New Caledonia. *Geochimica et Cosmochimica Acta*, **51**, 105–113.
- NICHOLSON, K. 1992. Contrasting mineralogical-geochemical signatures of manganese oxides: guides to metallogenesis. *Economic Geology*, **87**, 1253–1264.
- OSTWALD, J. 1988. Mineralogy of the Groote Eylandt manganese oxides: A review. *Ore Geology Reviews*, **4**, 3–45.
- ROY, S. 1981. *Manganese Deposits*. Academic Press, London.
- 1992. Environments and processes of manganese deposition. *Economic Geology*, **87**, 1218–1236.
- ŞENGÖR, A. M. C. 1976. Collision of irregular continental margins: Implications for foreland deformation of Alpine-type orogens. *Geology*, **4**, 779–782.
- WILSON, M. J., BERROW, M. L. & MCHARDY, W. 1970. Lithiophorite from the Lecht Mines, Tomintoul, Bannfshire. *Mineralogical Magazine*, **37**, 618–623.

An EPMA and SEM study of the Mn-oxide mineralization of Kato Nevrokopi, Macedonia, northern Greece: Controls on formation of the Mn⁴⁺ oxides

K. M. MICHAILIDIS¹, K. NICHOLSON²,
M. K. NIMFOPOULOS³ & R. A. D. PATTRICK⁴

¹ *Department of Mineralogy, Petrology & Economic Geology, Aristotle University, 540 06 Thessaloniki, Macedonia, Greece*

² *Environment Division, School of Applied Sciences, The Robert Gordon University, Aberdeen AB1 1HG, UK*

³ *Institute of Geology & Mineral Exploration, Thessaloniki Branch, 1 Fragon Street, 546 26 Thessaloniki, Macedonia, Greece*

⁴ *Department of Geology, The University, Manchester M13 9PL, UK*

Abstract: EPMA and SEM studies of tunnel-structured todorokite and nsutite and layer-structured chalcophanite and birnessite from the Kato Nevrokopi battery grade Mn-mineralization were performed. The chemistry of todorokite, formed at hypogene and supergene environments in an increasing order of weathering, reflects different pH and oxidation conditions. The data also point to a clear dependence of the development of late stage hypogene and early supergene Mn⁴⁺-oxide paragenesis on the host rock and protore composition and the mobilities of base metals (mainly Zn), alkalis and alkaline earths (mainly Ca).

The chemistry and development of (large cation-bearing) nsutite as *in situ* oxidations and banded poorly crystalline (with structural defects) aggregates in veins and associated karstic cavities, together with birnessite, indicates the influence of climate, oxidation and water table fluctuations. The data on chalcophanite revealed a deposition, under low f_{O_2} conditions, from acid meteoric fluids produced by weathering of vein sulphides. Birnessite formation reflects a prevalence of higher f_{O_2} in weathered veins and the karstic cavities.

The evolution of well developed layer structures through poorly crystalline to amorphous tunnel-structured nsutite is probably controlled by a Zn-saturation of the ore fluids.

The economic (currently mined) manganese mineralization of Kato Nevrokopi, Drama region, in Macedonia northern Greece, contains supergene ores predominantly composed of Mn-oxides. They have developed by weathering of vein mineralization of rhodochrosite and todorokite with minor base metal sulphides.

The Mn-oxides at Kato Nevrokopi are suitable for use as the cathodic material in dry cell cylindrical and flat battery manufacturing because they contain nsutite and its chemically formed natural analogues. Nsutite and its analogues (e.g. todorokite and birnessite) constitute a good battery material because they are able to allow proton diffusion to the interiors of their grains (Turner & Buseck 1983).

The geological setting and the description of the orebodies is given in Nimfopoulos *et al.* (this volume). The manganese mines are either located along an east-west-trending thrust zone that divides the Lower Palaeozoic marbles and Precambrian gneisses or form a distinct north-

west-trending line (Fig. 1). The latter series of mines are associated with veins which occupy small faults in the marbles. The mineralization is spatially and genetically related to the Oligocene granodiorite intrusives and andesite subvolcanics and has been confirmed as part of the mid-Tertiary hydrothermal event in northern Greece (Nimfopoulos *et al.* 1988).

Previous studies referred on descriptions of the mineralogy, mineral chemistry, textures, and parageneses of representative ore samples (Spathi 1964; Podufal 1971; Giovanoli 1980; Vacondios 1982; Nimfopoulos 1988, Nimfopoulos & Patrick 1991).

On the basis of their setting and mineralogy, the ore zones have been divided into three categories (Nimfopoulos & Patrick 1991).

(a) The deeper mineralized sulphide-carbonate-rich zones which at the time of the primary hypogene mineralization were situated at significant depth. They are currently exposed only in deeply eroded areas such as in the Pyrgi mines (Fig. 1).

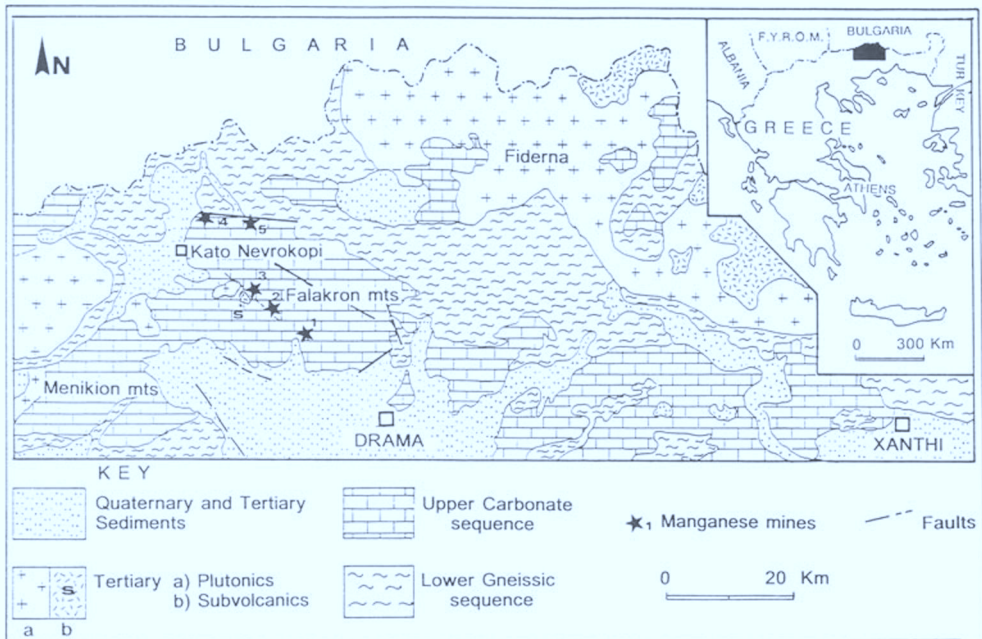


Fig. 1. Geology (redrawn from Dimadis & Zachos 1986) and mineralization of the Kato Nevrokopi, Drama area in Macedonia, northern Greece. Manganese mines: 1, Pyrgi; 2, 25th km and Mavro Xylo; 3, 28th km; 4, Karposluk; and 5, Tartana.

(b) The upper mineralized Mn-oxide rich zones which at the time of the primary mineralization were located close to the surface (25th km, Mavro Xylo; 28th km, Karposluk and Tartana mines). These zones are exposed in the higher altitude regions of the Falakron mountains.

(c) Secondary Mn-oxide in karstic cavities. In most mining areas the weathering products of the primary mineralization were concentrated in karsts. These karstic orebodies have originated mainly from the upper zone type mineralization and therefore types (b) and (c) are found together.

In the present report, a more detailed study of the tunnel-structured minerals todorokite and nsutite and the layer structured birnessite and chalcophanite was performed by means of a combined optical, EPMA, XRD and SEM investigation. For the first time, each mineral was collected and studied from different localities representing different weathering conditions relative to the protore and the host-rock lithologies. The aim of this paper is to clarify controls, exercised by local environments of weathering and the kind of mineral protore, on variations in chemistry, crystallinity and mineral textures of the secondary Mn⁴⁺-oxides.

Experimental methods

Polished sections of selected samples were first thoroughly examined by transmitted and reflected light microscopy and areas rich in the studied minerals were identified. Special care was taken to locate areas totally free of any optically visible nearby calcite and other gangue in order to avoid analysing any calcite-Mn oxide mineral mixtures. EPMA were carried out by a CAMECA-CAMEBAX instrument fitted with both energy dispersive (EDS) and wavelength dispersive spectrometers (WDS) (University of Manchester, UK) and a JEOL JSM-840 A instrument fitted with a LINK EDS analytical system (University of Thessaloniki, Greece). First, the EDS spectrum of the analysed mineral was obtained and the major elements (>1000 ppm) identified. The identity and possible existence of trace elements (<1000 ppm) was also checked by WDS peak-seeking. Standards included pure metals, synthetic and natural minerals all of international suppliers.

An identification by X-ray powder diffraction of the analysed by EPMA area was then performed by scraping off material from the polished section according to the method of Sorem & Fewkes (1980). The XRD patterns (Fig. 2) were recorded at $1^\circ 2\theta \times \text{min}^{-1}$ with Cu-K α radiation filtered with a curved graphite crystal monochromator. SEM was performed on small chips of selected hand specimens containing the desired minerals using the ISI Super II model (Manchester) for three-dimension

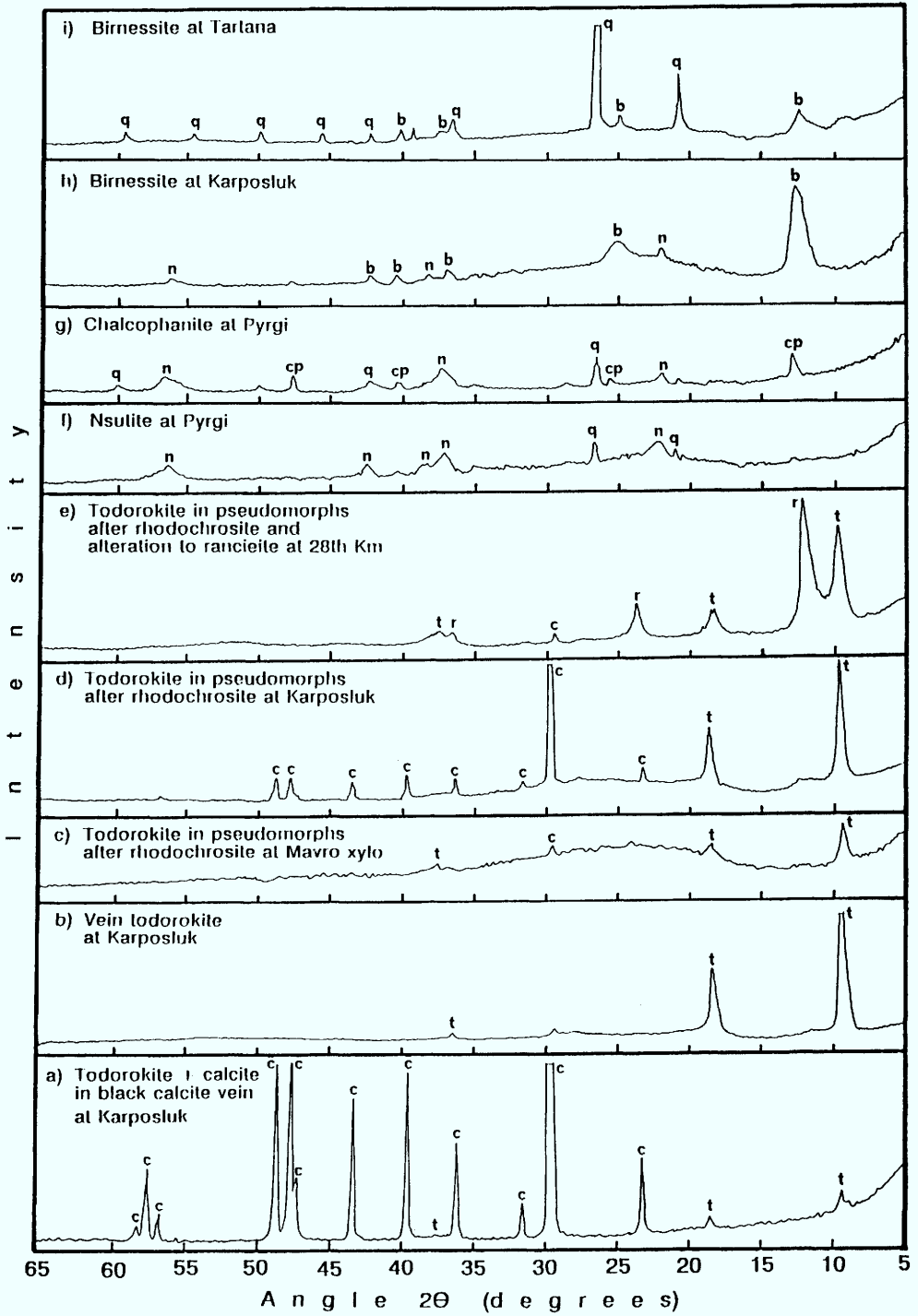
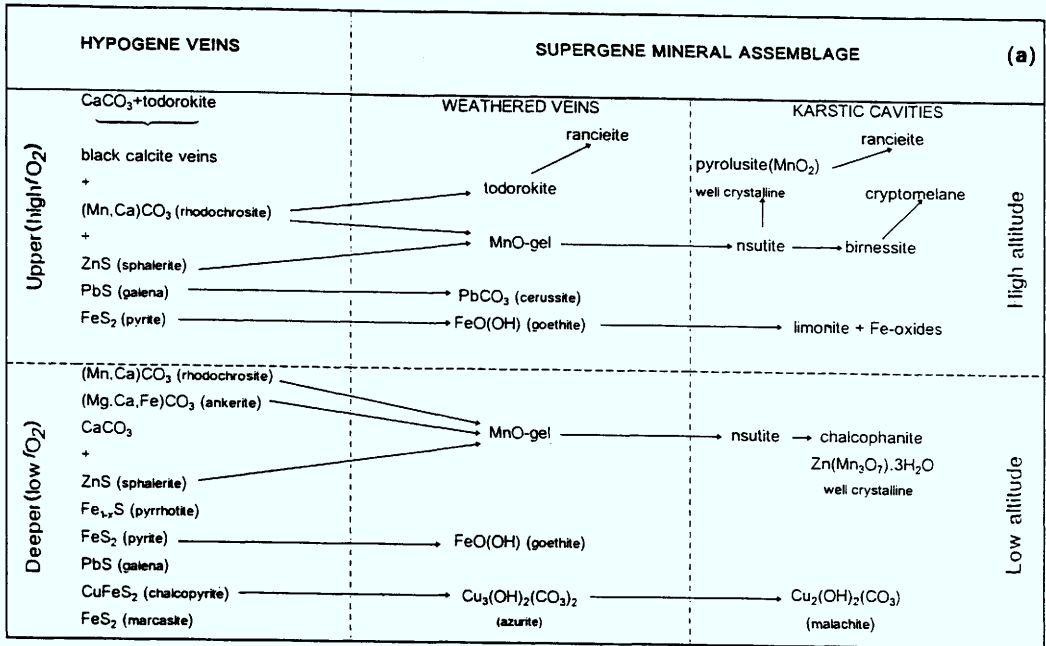


Fig. 2. Representative XRD diagrams of the Mn-oxides found at Kato Nevrokopi: t, todorokite; c, calcite; r, rancieite; n, nsutite; cp, chalcophanite; q, quartz; and b, birnessite.



	HYDROTHERMAL PROCESS	WEATHERING PROCESS		
	STAGE 1 <i>Hypogene veins</i>	STAGE 2 <i>In situ oxidation (a) or replacement (b)</i>	STAGE 3 <i>Infiltration and oxidation</i>	STAGE 4 <i>Karst mineralisation</i>
MINERAL				
Todorokite	Associated with dolomitisation in the upper parts of vein protopes: A) Finely crystalline in black calcite veins B) Well crystalline in quartz-calcite veins	a Finely crystalline "ghost" textures after oxidation of rhodochrosite in the upper parts of vein protopes Partial dissolution and replacement by cryptomelane and rancieite	Well crystalline dendritic forms in marble in the footwall of the weathered veins	
Nsutite		b <i>In situ</i> replacement of stage 2a todorokite (or MnO-gel) pseudomorphs after rhodochrosite Cleavage controlled replacement of marble wall rock Replacement by microcrystalline pyrolusite in vugs		Cryptocrystalline layers and encrustations with birnessite in partly developed karstic cavities Alternation with fibrous cryptomelane in well developed karsts
Chalcophanite				Well crystalline Replacing nsutite (stage 2b) in the beginning of karstic cavity formation
Birnessite				Concentric bands with nsutite or "stripe-like" aggregates in partly developed karsts Fine grained encrustations with nsutite in well developed karsts Replaced by cryptomelane

Fig. 3. (a) Evolution of the supergene mineral assemblage from the hypogene veins at Kato Nevrokopi, Macedonia. Redrawn and modified from Nimfopoulos & Patrick (1991). (b) Stages of evolution of Mn^{4+} -oxides at Kato Nevrokopi.

(3D) microscopic pictures, or on polished microscopic flat sections by the back-scattered electron technique (2D) using the JEOL JSM-840 A (Thessaloniki).

Mineralogy

The mineralogical evolution of the Kato Nevrokopi manganese mineralization, as given by Nimfopoulos & Patrick (1991) and Nimfopoulos *et al.* (this volume), is summarized in Fig. 3a. From the mineral paragenesis found in the area, todorokite, nsutite, chalcophanite and birnessite were selected for the present detailed study, because they are found in different evolutionary stages of the weathering process which affected the protore assemblage.

The stages of evolution of the studied Mn⁴⁺-oxides are (Fig. 3b): (1) hypogene veins; (2) *in situ* oxidation (a), or replacement (b); (3) infiltration and oxidation; and (4) karst mineralization. Hypogene veins of stage 1 constitute the upper parts of a vein mixed sulphide mineralization. The *in situ* oxidation produces 'ghost' textures after rhodochrosite (and pyrite) in the initial stages of weathering. Stage 3 is characterized by a more advanced weathering, in which a small downward mobility of the dissolved Mn (infiltration) is followed by oxidation. Finally, in stage 4 Mn dissolved from the weathered veins is deposited in karstic cavities formed at various distances from the original hydrothermal veins.

Todorokite

Formation of todorokite (orthorhombic or monoclinic $3 \times n$; commonly 3×3 tunnel; Turner & Buseck 1981) is bimodal, taking place from stage 1 to stage 3. Characteristic forms of the mineral are given in Fig. 4.

Nsutite

Nsutite (hexagonal $1 \times n$ tunnel; Faulring 1965; Turner & Buseck 1983), is the most abundant Mn⁴⁺-oxide found in the majority of mineralized places resulting from the weathering of hypogene veins (Fig. 5). It forms during the stages 2b to 4, and is the most abundant Mn-oxide in the stage 4.

Chalcophanite

Chalcophanite (trigonal layer structure stacked along the c axis in the sequence O-Mn-O-Zn-H₂O-Zn-O-Mn-O; Wadsley 1955; Post & Appleman 1988) is closely related to the

weathered parts of the sphalerite-rich deeper hypogene veins.

Chalcophanite replaces nsutite in low altitude weathered veins in the beginning of karstic cavity formation, growing in veinlets at the expense of nsutite (Fig. 3b). The platelet crystals of chalcophanite (Fig. 6) are hexagonal (Post & Appleman 1988) not triclinic as determined by Wadsley (1955). They show an excellent basal cleavage and grow perpendicular to the veinlet walls. They represent localized reaction of nsutite with Zn-rich fluids. Weathered sulphides are represented by goethite and malachite but no sphalerite or galena oxidation products were identified.

Birnessite

Birnessite (monoclinic layer structure similar to chalcophanite with additional cations; Post & Veblen 1990) is related to more advanced stages of weathering.

In embryonic karsts, occurring mainly at high altitudes, nsutite is interlayered with birnessite. Birnessite forms concentric bands with nsutite (Fig. 7a) and 'stripe-like' aggregates lining cavities (Fig. 7b). The stripe-like textures in 3D SEM show clearly a platy crystal morphology indicating a layer structure with multiple layers of birnessite forming each stripe (Fig. 7c). The observed morphology together with XRD (Fig. 2h) indicate similarities to chalcophanite (Fig. 2g), although birnessite is monoclinic. Large voids occur between the observed stripes (Fig. 7d) and these could be the result of shrinkage during dehydration, something common in the supergene Mn⁴⁺-oxides (Hewett & Fleischer 1960; Hewett *et al.* 1963; Sorem & Fewkes 1980 and others).

The Mn-oxide ore in well formed karstic cavities (prolonged stage; Fig. 3b) contains nsutite, birnessite and cryptomelane. Relics of nsutite have been used for nucleation of birnessite.

Mineral chemistry

Todorokite

Hypogene todorokites (Table 1; 1-8) of stage 1 are characterized by a distinctly high Ca content (compared to todorokites in Roy 1981, Ostwald 1986 and Carlos *et al.* 1993), which is similar to that of Falotta Switzerland (Perseil & Giovanoli 1989). The large Ca cation ($r = 0.99 \text{ \AA}$), together with the similar ionic size Ba²⁺ ($r = 1.34 \text{ \AA}$),

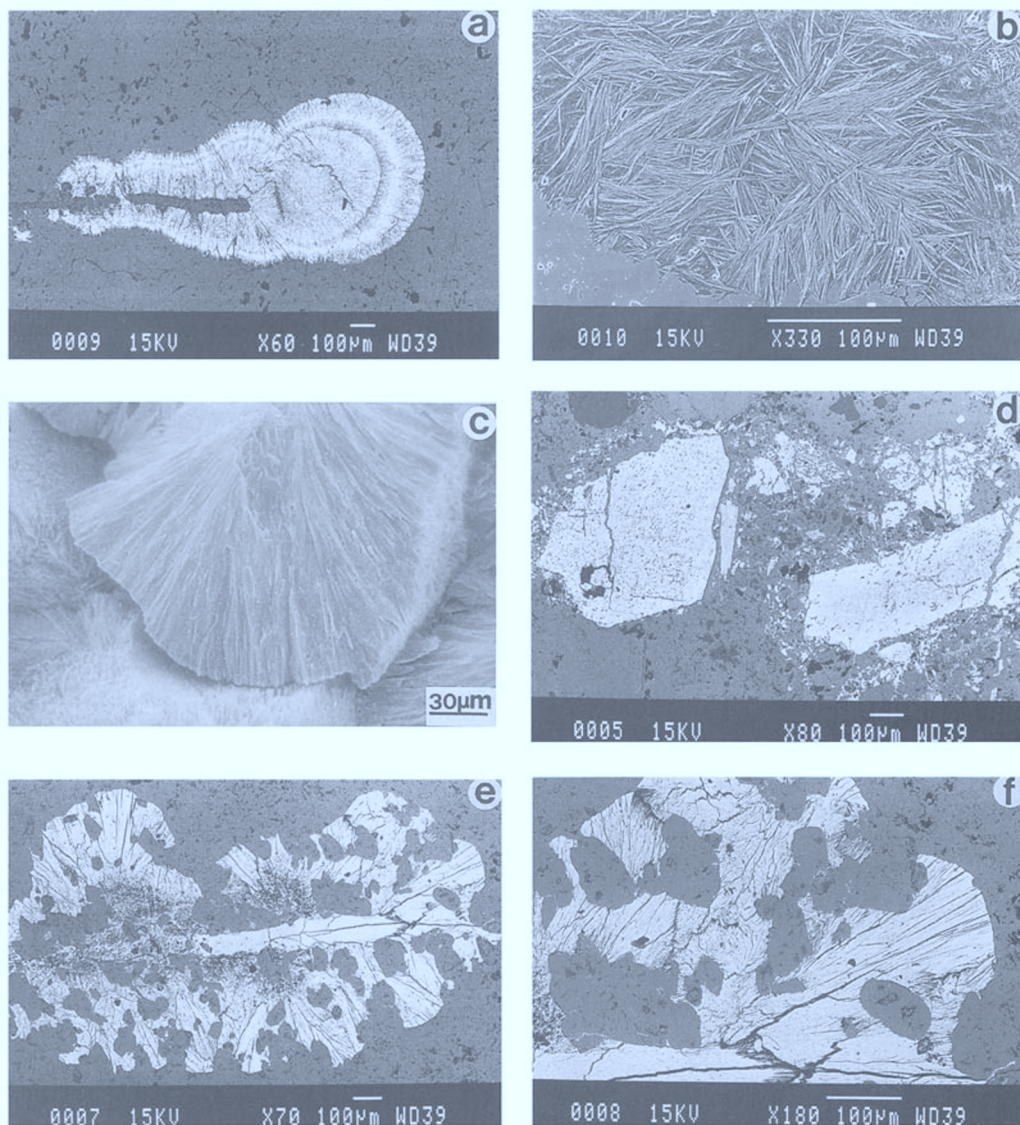


Fig. 4. SEM photomicrographs of fresh to variably weathered todorokite at Kato Nevrokopi: (a) 'Fossil-like' aggregate nucleated in amorphous silica (quartz-calcite vein) after black-calcite formation (Karposluk). (b) Fibrous grain morphology of the above todorokite in contact with host calcite. (c) 3D image of fan-shaped, highly pure todorokite grains (quartz calcite vein). (d) *In situ* formed pseudomorphous microcrystalline todorokite controlled by the crystal shape of the precursor rhodochrosite in weathered quartz vein (Mavro Xylo). (e) Fibrous todorokite forming spectacular dendrites which replace the host calcite in a weathered vein bearing mixed sulphides (Karposluk). (f) Higher magnification of e, showing the best crystallinity and the strong fibrous character.

Na^{2+} ($r = 0.97 \text{ \AA}$) and K^+ ($r = 1.33 \text{ \AA}$) cations and H_2O molecules, occupy the tunnels between the $[\text{Mn}^{4+}\text{O}_6]$ chains (Burns *et al.* 1983). Since the contents of the other tunnel cations are minimal (K and Na) to below detection (Ba), such Ca-contents (c. 8 wt% CaO) are reasonable.

While Mg^{2+} ($r = 0.66 \text{ \AA}$) and Zn^{2+} ($r = 0.74 \text{ \AA}$) substitute for Mn^{2+} in the tunnel 'walls' of the todorokite structure (Burns *et al.* 1985), the Zn content is low in the vein todorokites varying from below detection (black calcite vein) up to c. 1 wt% on average (quartz-calcite vein).

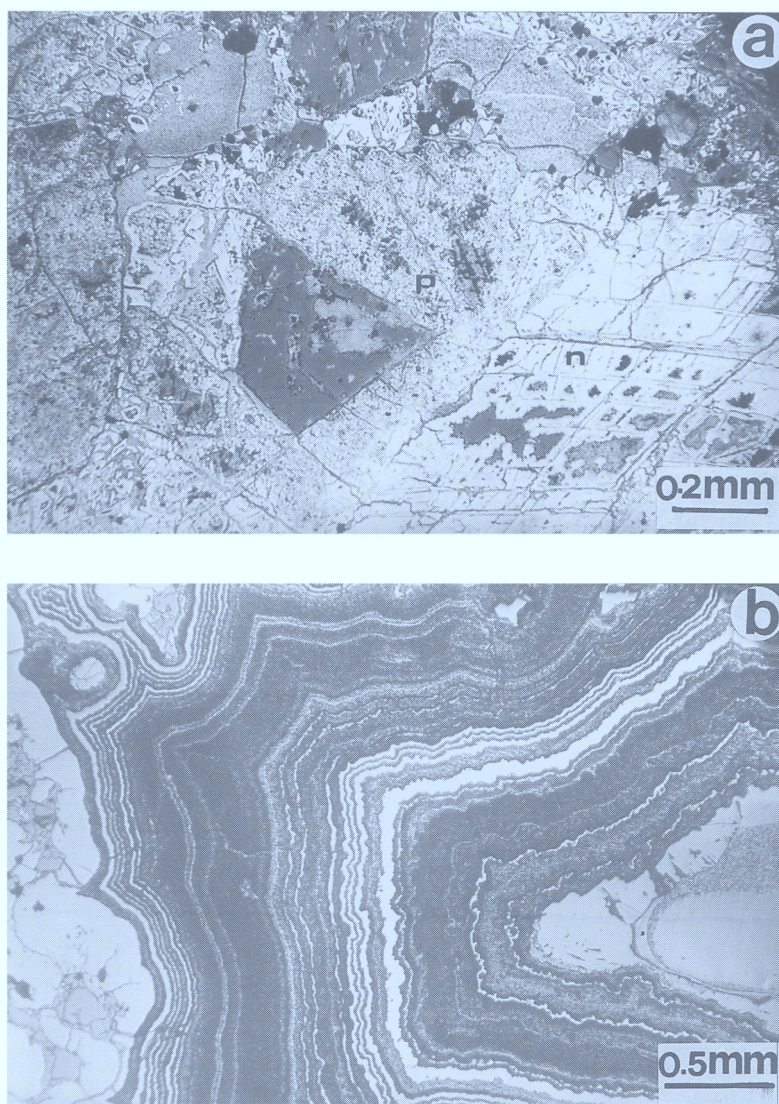


Fig. 5. Reflected light photomicrographs of nsutite from weathered veins and karstic cavities (Karposluk). (a) Cleavage-controlled replacement of wallrock calcite by nsutite (n) and replacement of nsutite by pyrolusite (p) in vugs after dissolution of calcite in long weathered vein. (b) Deposition of nsutite (white) in alternating bands with other amorphous Mn-oxides in a karstic cavity adjacent to a weathered vein.

Contrary to stage 1 todorokite; in pseudomorphs of todorokite after rhodochrosite (stage 2a) the Ca content which is located in the tunnels varies considerably but is distinctly lower on average (Table 1; 9–13). Ca was retained in todorokite after the oxidation of precursor Ca-bearing rhodochrosite. The lower Ca content is balanced by an increased K (and part of the increased Mg) at Mavro Xylo or by other large cations (all detected by WDS)

such as Ba, Pb ($r = 1.20 \text{ \AA}$) and minor Ag ($r = 1.26 \text{ \AA}$) at Karposluk in the more weathered veins. These long weathered (partly dissolved) argentiferous todorokite (Radtke *et al.* 1967) pseudomorphs represent the advanced stage 2a (Table 1; 12–13), forming in the proximity of weathered mixed-sulphide assemblages. They have also a distinctly lower Mn content (expressed as MnO_2) and higher amounts of molecular water (low EPMA totals), displaying

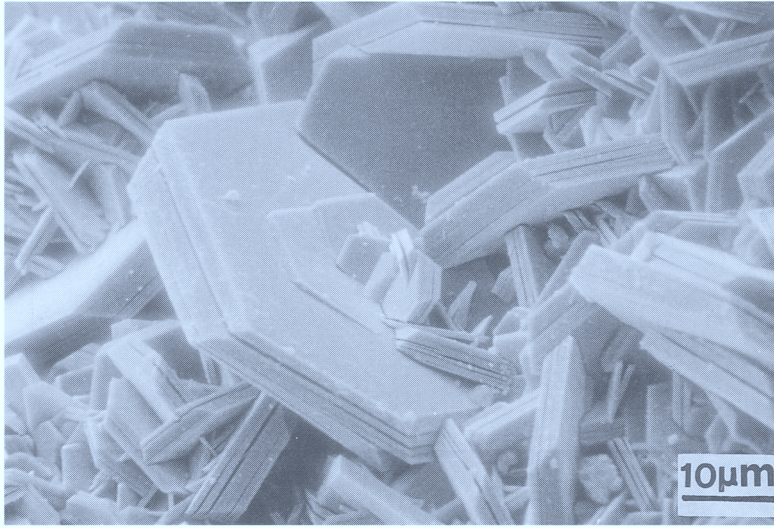


Fig. 6. 3D SEM of multiply twinned and well crystalline platelets of chalcophanite forming in veinlets in contact with amorphous oxide of nsutite composition.

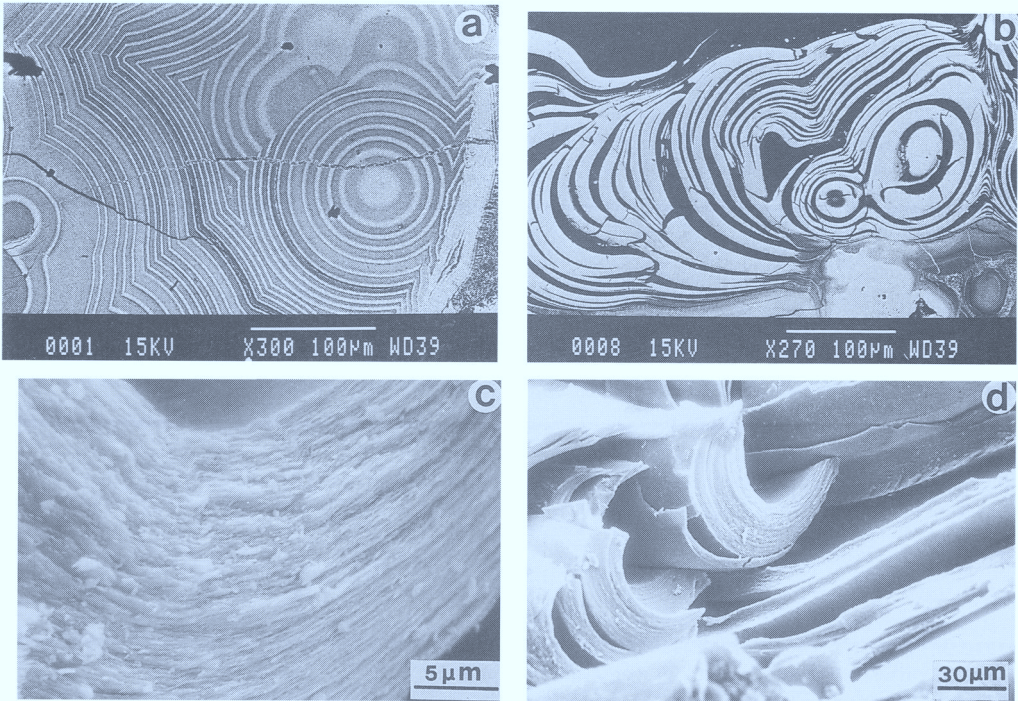


Fig. 7. SEM photomicrographs of birnessite in strongly weathered veins (Karposluk). (a) Concentric growth of intermixed nsutite (white) and birnessite (grey) in a weathered vein bearing mixed sulphides in parts. A shrinkage crack runs across both minerals. (b) 'Stripe-like' birnessite in cavities formed after dissolution of other Mn-oxides. Shrinkage cracks can also be seen. (c) 3D higher magnification indicating the innumerable layers of birnessite forming each stripe. (d) 3D showing large voids between stripes.

Table 1. Representative electron probe microanalyses of Kato Nevrokopi todorokite from different environments of formation

	MnO ₂	Fe ₂ O ₃	SiO ₂	Al ₂ O ₃	CaO	MgO	SrO	ZnO	BaO	PbO	CuO	Na ₂ O	K ₂ O	Ag ₂ O	Total
1	75.00	0.59	0.34	bd	8.01	1.30	0.08	bd	bd	bd	bd	0.14	0.25	bd	85.70
2	74.40	0.58	0.23	bd	7.80	1.31	0.05	bd	bd	bd	bd	0.14	0.24	bd	84.75
3	74.76	0.55	0.38	bd	7.83	1.26	0.03	bd	bd	bd	bd	0.11	0.24	bd	85.16
4	75.22	0.81	0.20	0.39	7.76	0.69	bd	0.11	bd	bd	bd	bd	0.34	bd	85.52
5	75.80	0.58	0.38	0.37	8.05	0.44	bd	0.01	bd	bd	bd	bd	0.33	bd	85.96
6	74.87	1.34	0.25	0.38	7.07	0.74	bd	0.13	bd	bd	bd	bd	0.35	bd	85.13
7	74.96	0.58	0.18	bd	5.98	1.35	0.09	0.59	bd	bd	bd	0.15	0.50	bd	84.38
8	72.79	bd	0.19	bd	4.01	1.94	0.21	1.78	bd	bd	bd	0.51	0.61	bd	82.04
9	79.93	bd	0.43	bd	3.46	2.15	bd	bd	bd	bd	bd	bd	1.17	bd	87.14
10	77.64	bd	0.30	bd	4.11	1.91	bd	bd	bd	bd	bd	bd	1.07	bd	85.02
11	78.68	bd	0.49	bd	3.82	1.78	bd	bd	bd	bd	bd	bd	1.08	bd	85.84
12	57.01	bd	0.54	0.59	4.55	0.71	bd	7.92	1.54	0.19	1.01	bd	bd	0.02	74.08
13	54.93	0.77	0.32	0.71	9.27	0.96	bd	6.45	1.59	0.15	1.17	bd	bd	0.02	76.34
14	70.42	bd	0.26	0.36	5.30	bd	bd	7.57	bd	bd	bd	bd	0.18	bd	84.98
15	70.53	0.63	0.27	0.83	5.34	0.37	bd	6.81	bd	bd	bd	bd	0.20	bd	84.98
16	72.10	0.47	0.32	0.65	4.01	0.76	bd	5.70	bd	bd	bd	bd	0.55	bd	84.56
17	69.41	0.47	0.27	bd	7.03	0.98	0.02	2.22	0.58	bd	bd	0.22	0.16	bd	81.45
18	70.72	0.65	0.23	bd	7.19	1.18	0.09	2.67	0.68	bd	bd	0.31	0.15	bd	84.02
19	73.85	bd	0.31	bd	7.55	1.27	0.01	2.70	0.56	bd	bd	0.46	0.13	bd	86.90

bd, Below detection limit (0.01) by both EDS and WDS methods.

1-3, Todorokite from black calcite vein (Karposluk); 4-6, quartz-calcite vein (25th km); 7-8, quartz-calcite vein (Karposluk); 9-11, supergene todorokite pseudomorphs after rhodochrosite in weathered veins (Mavro Xylo); 12-13, supergene todorokite pseudomorphs after rhodochrosite in weathered veins (Karposluk); 14-16, todorokite dendrites (Karposluk); 17-19, todorokite pseudomorphs replaced by nsutite (28th km).

poor textures compared to most other todorokites (Fig. 4d). However, they contain significant Zn, Cu and Ba, are more crystalline compared with less-weathered pseudomorphs (Mavro Xylo) and black calcite todorokites, and depleted in K and Mg. Zn^{2+} ($r = 0.74 \text{ \AA}$) and Cu^{2+} (0.73 \AA) cations are not susceptible to oxidation, have a similar ionic size and substitute for Mn^{2+} in the $[3 \times n]$ tunnel 'walls' of $[\text{Mn}^{4+}\text{O}_6]$ octahedra, thus stabilizing the structure of todorokite (Burns *et al.* 1983) under highly oxidizing environments (Post & Bish 1988). In this way the low Mn content of the extensively weathered todorokite pseudomorphs is balanced by the elevated content of the above cations.

Todorokite formed by infiltration and oxidation (stage 3) has a similar composition to todorokite in quartz-calcite veins but a lower Mn content (Table 1; 14–16). On the other hand, the Zn content is significantly higher. Since this metal can substitute for Mn^{2+} in tunnel walls of the todorokite structure (Burns *et al.* 1985) it balances for the relevant depletion of Mn and may be the cause for the good crystallinity.

Hence, todorokite changes in composition from Ca, Mn-rich (stage 1) to locally enriched in K, H_2O and/or Zn (stage 2) and finally to Zn-rich (Mn-poor) forms (stage 3).

Nsutite

Nsutite, replacing *in situ* (stage 2b) prismatic to rhombic hexagonal pseudomorphs of todorokite after rhodochrosite (weathered veins adjacent to subvolcanics at the 28 km mine), retains significant As and Ba content, traces of Hg (detected by WDS), and a portion of Ca of the precursor todorokite (Tables 1; 17–19 and 2; 1–2). While As^{5+} is a small cation ($r = 0.46 \text{ \AA}$) and could possibly substitute for Mn in the tunnel walls, Ba^{2+} and Ca^{2+} are large cations and it is questionable how they could be accommodated in the $[1 \times n]$ nsutite structure (Ostwald 1984). However, Turner & Buseck (1983) using a detailed HRTEM investigation revealed relicts of todorokite structures (3×3) in nsutite explaining the presence of significant water in the mineral. These todorokite structures are favourable for locations of large cations such as those found in the Kato Nevrokopi nsutite. However, Turner & Buseck (1983) assumed that todorokite is an alteration product of nsutite, whereas, at Kato Nevrokopi the reverse process took place. In these weathered veins the precursor MnO gel contains traces of Hg and significant As (detected by WDS).

Nsutite from the weathered rhodochrosite-mixed sulphide veins of Pyrgi (stage 2b) contains significant amounts of Pb^{2+} , K^+ , Ca^{2+} and Na^+ (Table 2; 3–6). Since these metals are large cations and can only be located in large tunnels, their presence indicates the existence of larger tunnel structures in nsutite (Turner & Buseck 1983). The presence of large cations is inhibitive of good crystallinity (Ostwald 1984). Therefore, defects and structural disorders of the todorokite (3×3), coronadite or cryptomelane (2×2) type should be present in the nsutite at Pyrgi. These defects cause the optically observed low to minimal crystallinity, because the structure ($1 \times n$) cannot accommodate large cations. The low Mn content reflects the probable substitution of Zn^{2+} ($r = 0.74 \text{ \AA}$) for Mn^{2+} ($r = 0.84 \text{ \AA}$) in the 'walls' of the tunnels thus stabilizing the structure and preventing it from further oxidation (Burns *et al.* 1985).

Rhombic pseudomorphs of nsutite after calcite (advanced stage 2b-stage 3?) in marble vugs adjacent to veins (Karposluk) have similar chemistry (Table 2; 11–12) but lower Zn and Pb (below detection) content and minimal amounts of large cations (except Ca). Therefore, further weathering of them results in the formation of free from lattice defects pyrolusite (1×1 tunnels, Table 2; 13–15) which is structurally stable under oxidation (Ostwald 1984).

Nsutite layers from the karst-hosted mineralization (stage 4) contains variable Zn^{2+} and significant but low Ca^{2+} (Table 3; 1–3). Nsutite found in karsts located adjacent to weathered veins (e.g. Karposluk mines) is on average richer in Zn compared to nsutite found in karstic cavities (Table 3; 4–6 and 9–11) away from the veins (e.g. Tartana mines). The latter carries also elevated Ba content (Table 3; 4–6).

Hence, nsutite with poor crystallinity (structurally defected) contains large cations such as Ca, K, Na (and base metals) while well crystalline (structurally ordered) nsutite is depleted in these elements. The latter nsutite leads to pyrolusite formation.

Chalcophanite

Chalcophanite in veinlets replacing nsutite in the beginning of karstic cavity formation (stage 4) is depleted in Pb^{2+} , K^+ and Ca^{2+} (Table 2; 7–10) compared to the nsutite it replaces (Tables 2; 3–6). This indicates a gradual loss of large cations at the same time with the change from a tunnel to a layer structure (Burns & Burns 1977; Potter & Rossman 1979). The low SiO_2 content is part of the chalcophanite composition and does not

Table 2. Representative electron probe microanalyses of Kato Neurokopi Mn-oxides in different stages of progressive weathering

	MnO ₂	Fe ₂ O ₃	SiO ₂	Al ₂ O ₃	CaO	MgO	NiO	SrO	ZnO	BaO	PbO	Na ₂ O	K ₂ O	As ₂ O ₅	Total
1	96.45	bd	0.50	bd	0.73	bd	bd	0.02	bd	0.34	bd	0.05	0.02	0.08	98.19
2	93.36	bd	0.22	bd	1.25	bd	bd	0.07	0.68	0.64	bd	0.05	0.05	0.48	96.80
3	85.79	bd	0.41	bd	0.75	0.01	bd	0.13	2.93	bd	2.17	0.35	1.81	bd	94.35
4	87.87	0.80	0.28	bd	0.84	bd	bd	0.01	3.71	bd	2.63	0.38	1.88	bd	98.40
5	85.01	0.60	0.39	bd	0.76	bd	bd	0.08	3.17	bd	1.82	0.44	2.34	bd	94.61
6	88.57	0.79	0.32	bd	0.83	bd	bd	0.05	3.11	bd	2.09	0.40	2.25	bd	98.41
7	72.98	bd	0.24	bd	bd	0.03	bd	bd	19.06	bd	bd	0.73	bd	bd	93.04
8	74.89	bd	0.22	bd	0.27	0.03	bd	bd	18.18	bd	bd	0.67	0.11	bd	94.37
9	76.26	bd	0.21	bd	bd	0.01	bd	0.04	19.85	bd	bd	0.75	0.07	bd	97.19
10	75.26	bd	0.23	bd	bd	0.01	bd	bd	21.65	bd	bd	0.89	bd	bd	98.04
11	93.79	bd	0.37	0.02	1.33	0.09	bd	bd	1.27	bd	bd	0.09	0.17	bd	97.13
12	92.83	0.55	0.38	0.01	1.34	0.08	0.02	bd	1.69	bd	bd	0.10	0.11	bd	97.11
13	94.58	bd	0.51	0.03	0.59	bd	0.08	bd	1.26	bd	bd	0.06	bd	bd	97.11
14	96.28	bd	0.59	0.08	0.64	bd	bd	bd	0.89	bd	bd	0.05	bd	bd	98.53
15	93.97	0.69	0.60	0.07	0.61	bd	0.01	bd	1.32	bd	bd	0.05	bd	bd	97.32
16	91.32	bd	0.12	bd	1.01	bd	2.42	bd	bd	0.77	bd	0.14	0.04	bd	95.82
17	94.19	bd	0.13	bd	0.75	bd	1.97	bd	bd	0.58	bd	0.09	0.02	bd	97.73
18	94.02	bd	0.13	bd	0.71	bd	2.18	bd	bd	0.64	bd	0.09	0.02	bd	97.79
19	90.71	bd	0.10	bd	1.24	bd	2.54	bd	bd	0.70	bd	0.21	0.06	bd	95.98
20	77.80	bd	0.09	bd	2.12	bd	bd	bd	5.87	2.19	bd	0.32	0.18	bd	88.57
21	78.27	bd	0.13	bd	1.14	bd	bd	bd	9.26	1.06	bd	0.60	0.08	bd	90.54
22	74.23	bd	0.20	bd	0.89	bd	bd	bd	15.61	0.97	bd	0.72	0.07	bd	92.69
23	70.92	bd	0.03	bd	3.31	bd	bd	bd	12.77	1.73	bd	0.53	0.30	bd	89.59
24	68.63	bd	0.03	bd	3.12	bd	bd	bd	12.34	1.74	bd	0.51	0.27	bd	86.64

bd, Below detection limit (0.01) by both EDS and WDS methods.

1-2, Nsutite replacing todorokite and MnO-gel (28th km); 3-6, nsutite from weathered veins (Pyrgi); 7-10, chalcophanite veinlets replacing nsutite in weathered veins (Pyrgi); 11-12, nsutite pseudomorphs after rhodochrosite in weathered vein (Karposluk); 13-15, pyrolusite replacing nsutite in cavity from weathered vein (Karposluk); 16-19, nsutite concentric with birnessite in weathered vein (Karposluk); 20-21, concentric birnessite intermixed with nsutite (Karposluk); 22-24, birnessite stripe-like aggregates in cavities adjacent to weathered veins (Karposluk).

Table 3. Representative electron probe microanalyses of Kato Nevrokopi Mn-oxides in karstic cavities

	MnO ₂	Fe ₂ O ₃	SiO ₂	Al ₂ O ₃	CaO	MgO	NiO	ZnO	BaO	PbO	Na ₂ O	K ₂ O	As ₂ O ₅	Total
1	89.80	bd	0.43	0.01	1.20	0.08	bd	2.72	0.11	bd	0.14	0.06	bd	94.55
2	83.49	bd	0.53	0.38	1.16	0.14	bd	5.63	0.12	bd	0.43	0.30	bd	92.18
3	90.96	bd	0.58	0.20	0.82	0.11	bd	1.69	0.08	bd	0.15	0.16	bd	94.75
4	82.03	bd	0.18	0.87	0.27	0.73	bd	2.21	1.43	bd	0.36	0.54	1.86	93.48
5	80.61	bd	0.14	0.63	2.98	0.78	bd	2.44	1.35	bd	0.33	0.54	1.34	91.14
6	77.52	bd	0.05	0.87	2.89	0.72	bd	4.62	0.55	bd	0.33	0.36	2.02	89.93
7	77.13	bd	0.18	0.50	2.89	0.97	bd	1.83	1.10	bd	0.73	0.85	1.50	87.68
8	79.76	bd	0.21	0.65	2.88	0.98	bd	2.36	1.09	bd	0.43	0.57	1.15	90.08
9	93.59	bd	0.08	0.03	1.10	0.30	bd	bd	0.48	bd	bd	0.15	bd	95.73
10	94.53	0.39	0.09	0.06	1.11	0.29	bd	bd	0.49	bd	bd	0.10	bd	97.18
11	95.41	bd	0.08	0.07	1.02	0.26	bd	bd	0.38	bd	bd	bd	bd	97.25

bd, Below detection limit (0.01) by both EDS and WDS methods.

1-3, Nsutite bands: partly developed karstic cavity (Karpouluk); 4-6, nsutite and 7-8, birnessite. Partly developed karstic cavity (Tartana); 9-11, nsutite bands in well developed karstic cavity (Tartana).

come from silicate impurities, substituting for Mn^{4+} in the octahedral $[\text{MnO}_6]$ layers (Ostwald 1985). Assuming the difference of the EPMA total to 100 wt% as the H_2O -content, the empirical formula of chalcophanite from Pyrgi is: $[(\text{Zn}_{0.83}\text{Mn}_{3.04}^{4+}\text{Na}_{0.08}\text{Si}_{0.02}\text{Ca}_{0.01})\text{O}_7 \cdot 0.91\text{H}_2\text{O}]$ (Nimfopoulos & Pattrick 1991). This compared to the theoretically ideal formula ($\text{ZnMn}_3\text{O}_7 \cdot 3\text{H}_2\text{O}$; Wadsley 1955) is deficient in Zn^{2+} ($r = 0.74 \text{ \AA}$), which should have been at least partly replaced by Mn^{2+} ($r = 0.80 \text{ \AA}$) and partly by Na and Ca in the H_2O interlayers (Radtke *et al.* 1967; Ostwald 1985; Post & Appleman 1988). The mineral is indeed enriched in Mn. However, it is difficult to trace the location of large and significantly enriched cations such as Na and explain their presence without assuming a hybrid structure (Ostwald 1985), something not observed by XRD (Fig. 2) at Pyrgi mines. High resolution transmission electron microscopy (HRTEM) and selected area electron diffraction (SAED) are needed for this purpose. The observed low water content compared to the theoretical values may be the result of dehydration along cleavage (Fig. 6) after breaking of hydrogen bonds (binding force between layers) between water molecules and between the water oxygen atom and the two oxygen atoms in the octahedral sheets (Post & Appleman 1988).

Birnessite

EPMA of birnessite found in partly developed karstic cavities (stage 4) at high altitudes reveal high Zn contents as well as significant Ca, Ba, Na and K (Table 2; 20–21) compared to the nsutite it replaces (Table 2; 16–19). These large interlayer cations cause at least part of the observed (XRD; Fig. 2) structural disorder in birnessite (Post & Veblen 1990). The analogy of birnessite structure to that of chalcophanite (Giovanoli 1969; Burns & Burns 1977; Post & Veblen 1990) is probably responsible for the incorporation of such high, and very uncommon, Zn contents in birnessite from the weathered veins. Chalcophanite has not formed together with birnessite at Karposluk but Burns & Burns (1977) proposed that Na, Ca, Ba, K, etc. replace Zn atoms in chalcophanite structure to form birnessite. The position of each cation is a function of its type. It is not clear so far where exactly in the interlayers of birnessite these cations are located (Post & Veblen 1990).

In the same karstic cavities, the stripe-like aggregates of finely crystalline birnessite (Fig. 7)

are more enriched in Zn (Table 2; 22–24) compared to early birnessite in concentric bands with nsutite. These stripe-like aggregates show better crystallinity as a result of the increasing substitution of Zn for Mn (Giovanoli & Brutsch 1979).

Finally, birnessite alternated with nsutite in crusts in well-developed karstic cavities (stage 4; Tartana mines) has a lower Zn-content but increased As, Mg, Al and K contents (Table 3; 7–8) than the birnessite in partly developed karstic cavities. The significant occurrence of these variable type cations in the water interlayers of birnessite probably contributes to the observed, under the microscope and in XRD, poor crystallinity.

Thus, birnessite with better crystallinity is characterised by very high Zn contents.

Controls on the mineral chemistry

The evolution of Mn oxide mineralization is largely controlled by pH-Eh conditions in natural waters. The chemistry of the solution, the length of weathering period, the climatic conditions and the presence of special structures available to induce crystallization are also critical factors (Ostwald 1992). The chemistry of the Mn^{4+} -oxide depositing solutions mainly constrains the mineralogy of the Mn-oxide mineral assemblage.

The evolution of Mn-oxide mineralogy at Kato Nevrokopi is diagrammatically given in Fig. 3b.

The studied Mn-mineral assemblages at Kato Nevrokopi cover a range from the late hydrothermal (stage 1) to the advanced weathering cycle (stage 4; karstic cavity ore). The combined optical, XRD, SEM and EPMA data of the four Mn-oxides examined in this study were used for defining the controls exercised by the chemistry of the depositing fluids on the Mn-assemblages according to Ostwald's (1992) and Nicholson's (1992) suggestions.

Black calcite veins (stage 1) at Kato Nevrokopi occur only in the upper zones indicating an increase in the oxidation state (low positive Eh; Brannath & Smykatz-Kloss 1992) of the hydrothermal fluids ($\text{pH} \approx 4$) towards the surface. Hewett (1964) demonstrated that the black calcite veins are typically found in a hot spring environment. The occurrence of Ca-rich, Zn-poor, todorokite from Karposluk black calcite indicate a formation after sphalerite deposition just below the discharge points of hot springs in a zone of mixing with overlying oxygenated meteoric water (Nimfopoulos & Pattrick 1991).

As the pH and Eh (or f_{O_2}) of these fluids increased after mixing, further deposition of todorokite was induced by the presence of SiO₂ (silica or quartz) directly from the hydrothermal fluids, followed by calcite deposition in quartz-calcite veins.

The breakdown of rhodochrosite and associated mixed sulphides in the veins was aided by the circulation of O₂- and CO₂-rich meteoric water (Bricker 1965). Slow oxidation of the breakdown products resulted in the formation of MnO-gel. However, in areas of fast oxidation, Mn²⁺ in rhodochrosite was directly oxidized to Mn⁴⁺ and formation of todorokite took place (stage 2a) retaining the precursor shape (pseudomorphs), in near neutral pH and high f_{O_2} (Mavro Xylo). K (from mica) and Mg (dolomite or ankerite) were adsorbed even at this stage, and todorokite becomes enriched in the above elements.

In the partly dissolved, weathered veins (stage 2a), todorokite pseudomorphs are enriched in base metals. This reflects an oxidation under the continuous action of air-bearing meteoric water which infiltrated through the veins of the mixed sulphide-rhodochrosite protore. Acid fluids with low positive Eh were released at this stage and probably caused leaching of Mn and Ca from the pseudomorphs (Brannath & Smykatz-Kloss 1992). As the predominant base metals in the system were those coming from the vein sulphide protore, the mobility of each metal could be approximately indicated from the composition of long weathered todorokite pseudomorphs (Karposluk mines). The obtained order Zn > Cu > Fe > Pb > Ag is in full agreement (for Zn, Cu and Pb) with the data of Mann & Deutscher (1980) for pH < 6 and high Eh environments on weathered base metal sulphide ores. In the same pseudomorphs (Karposluk) a depletion trend in alkalis (K, Na) and alkaline earths (Ca, Mg) is observed (except for Ba which shows enrichment). As the order of mobility in weathered veins was geochemically indicated as Na > K > Mg > Ca > Ba (Nimfopoulos 1988) this behaviour is expected during supergene weathering of 'dubhites' (Crerar *et al.* 1980; Nicholson 1992).

Similar behaviour of Mn, Ca and other alkaline earths and alkalis is observed in todorokite dendrites (stage 3; infiltration-oxidation), the formation of which indicates a precursor process of Mn²⁺ dissolution (after breakdown of rhodochrosite and sulphides) and its transport in acidic fluids, together with Zn. Dendrites occur in weathered veins, not far from the original Mn²⁺ position and were deposited

in a Ca-rich environment due to dissolution of the marble by acidic meteoric fluids. Their composition should reflect the control exercised by the chemistry of the host rock and the mobility of the protore metals (e.g. Zn) onto the formation of well crystalline todorokite. In this case, the host marble has also caused the deposition of todorokite probably by slow reaction with Mn²⁺ (and Zn²⁺)-bearing meteoric fluids.

Nsutite pseudomorphic textures with poor crystallinity, which replaced *in situ* precursor todorokite (stage 2b), are characterised by significant alkali and alkaline earth contents, suggesting incomplete leaching of these elements (large cations) in the process of nsutite formation. The presence of such cations prevents the formation of well crystalline nsutite, in a process called 'reverse diadochy' (Ostwald 1992).

Nsutite replacing MnO-gel in weathered rhodochrosite-mixed sulphide veins (stage 2b) contains significant large cations such as Pb, K, Ca and Na. These elements are released from the protore and host rock, enter the structure of nsutite and control its structural defects and poor crystallinity.

The low large cation contents of rhombic pseudomorphs of nsutite after calcite in weathered veins indicate that a prolonged weathering and oxidation process (prolonged stage 2b) has taken place. The depletion of large cations enhances the crystallinity of nsutite. Such environment explains the presence of pyrolusite as the stable mineral by further oxidation in semi-arid seasons (Ostwald 1992).

A general observation on todorokite and nsutite composition concerns the increase in substitution of Zn for Mn with progressive weathering. Zn²⁺ has a similar ionic size to Mn²⁺, but is less mobile during weathering of the veins. In these conditions Zn²⁺ substitutes for Mn²⁺ in the tunnel 'walls' of both todorokite and nsutite preventing them from further oxidation (Burns *et al.* 1983, 1985; Turner & Buseck 1983). The adsorption of Zn in todorokite and nsutite, combined with the predominance of sphalerite in the hypogene assemblage indicates the percolation of meteoric fluids through the veins and an associated dissolution of sphalerite.

Mobilized manganese during weathering processes was concentrated in the adjacent located proximal or distal karsts. The formation of these karsts has been largely dependent on the weathering of hypogene veins and the resulting release of acidic fluids. The present siting of karstic mineralization above a highly fluctuating water table is a probable combination of erosion and

the fact that the water table was higher in the recent past, for instance during the ice age. The observed encrustations and layers also indicate that Mn-bearing groundwaters were periodically flushed through the veins and karsts (Nimfopoulos & Pattrick 1991).

The chemistry of nsutite (formed at stage 2b) found at the beginning of karst formation (embryonic stage 4) in the veins reflects semi-humid conditions with low positive Eh (Brannath & Smykatz-Kloss 1992) caused by flushing of meteoric fluids. These fluids may still have been periodically acidic, dissolving the protore and the host rocks.

The progressive leaching of Mn, Pb, K and alkaline earths (large cations), and the replacement of Mn by Zn from dissolved sphalerite, resulted in the breakdown of tunnel structure nsutite and the formation of layer structure chalcophanite or birnessite veinlets in cavities through a cryptocrystalline to amorphous nsutite phase. The layer structures are also formed by reaction of crystalline nsutite with Zn-rich acidic fluids ($\text{pH} < 6$, f_{O_2} low). It appears therefore, that chalcophanite and birnessite probably form through an entire breakdown of precursor nsutite and complete restructuring of the amorphous nsutite product. However, the mechanism of structural transition from any amorphous nsutite to chalcophanite or birnessite has not been studied experimentally so far.

Chalcophanite is present within embryonic karsts (stage 4) close to the deeper seated weathered veins, where circulation of oxygen-rich meteoric water has been restricted. These conditions may probably have been responsible for the incomplete oxidation of Mn to Mn^{4+} and the enrichment of chalcophanite in Mn^{2+} compared to its ideal formula. The low but significant Na and Ca contents may have also been caused by the same mechanism and incomplete leaching of these large cations from the precursor nsutite.

Contrary to chalcophanite; birnessite is found dominant in the upper seated weathered veins and the related karstic cavities (intermediate stage 4), where more oxidizing conditions have prevailed. This indicates that a larger portion of Mn should have been oxidized to Mn^{4+} . Therefore, the interlayer Mn^{2+} -content of birnessite is expected to be low. The deficiency of Mn^{2+} should be balanced by the presence of other cations (e.g. Ca, Ba, Na, Zn). However, birnessite shows a remarkable increase only in its Zn content from co-banded to stripe textures, whereas the other large cations remain fairly constant. The increase in the Zn content is combined with a higher crystallinity and may

have been caused by the circulation of periodically flushed (Zn-saturated) acid fluids coming from the dissolution of the vein sulphides. On the other hand, within the karstic cavities, under alkaline conditions the oxidation of Mn can proceed at lower Eh values. This is consistent with the development of birnessite with a very low Zn content and a poor crystallinity.

The composition of nsutite in associated karsts distal to the veins (prolonged stage 4; Tartana) reveals the high mobility of Mn compared to Zn in humid conditions and that Mn may be transported as bicarbonate complex in the meteoric fluids (Borchert 1970). Ba and Al contents probably indicate the circulation of the Mn-mineralizing fluids through the adjacent schist and deposition of Mn-minerals in alkaline conditions ($\text{pH} \approx 7-8$).

Nsutite is the predominant mineral in the exploited ores at Kato Nevrokopi. It has been indirectly observed (XRD and chemistry) to have structural defects and disorders of todorokite-type (single, double and triple $[\text{MnO}_6]$ chains) and a significant water content. As it was demonstrated by Turner & Buseck (1983) the combination of these two characteristics may in fact facilitate an enhanced proton diffusion and therefore a greater efficiency for the ore material which is currently used in dry cell cylindrical and flat battery manufacturing.

We would like to express our sincere appreciation for a financial support donated by the British Council, enabling the presentation of this paper. We would also like to thank J. Zussman for permission to do a great part of the research at the University of Manchester UK, D. A. Polya, J. Esson and G. T. R. Droop of the above institution for fruitful discussions and two anonymous Geological Society referees for invaluable criticism. Thanks are also due to D. A. Plant and T. C. Hopkins for assistance with the EPMA, S. Caldwell (Manchester) and V. Kyriakopoulos (Thessaloniki) for SEM analysis.

References

- BORCHERT, H. 1970. On the ore deposition and geochemistry of manganese. *Mineralium Deposita*, **5**, 300-314.
- BRANNATH, A. & SMYKATZ-KLOSS, W. 1992. Mineralogical investigations on manganese-iron ores from Hesse, Germany. *Chemie Erde*, **52**, 3-31 [German with English abstract].
- BRICKER, O. 1965. Some stability relations in the system $\text{Mn-O}_2\text{-H}_2\text{O}$ at 25° and one atmosphere total pressure. *American Mineralogist*, **50**, 1296-1352.
- BURNS, R. G. & BURNS, V. M. 1977. Mineralogy. In: GLASBY, G. P. (ed.) *Marine Manganese Deposits*. Elsevier, New York, 185-248.

- , — & STOCKMAN, H. W. 1983. A review of the todorokite–buserite problem: implications to the mineralogy of marine manganese nodules. *American Mineralogist*, **68**, 972–980.
- , — & STOCKMAN, H. W. 1985. The todorokite–buserite problem: further considerations. *American Mineralogist*, **70**, 205–208.
- CARLOS, B. A., CHIPERA, S. J., BISH, D. L. & CRAVEN, S. J. 1993. Fracture-lining manganese oxide minerals in silicic tuff, Yucca Mountain, Nevada, U. S. A. *Chemical Geology*, **107**, 47–69.
- CRERAR, D. A., CORMICK, R. K. & BARNES, H. L. 1980. Geochemistry of manganese: an overview. In: VARENTSOV, I. M. & GRASSELLY, G. (eds) *Geology and Geochemistry of Manganese*. Schweizerbart'sche, Stuttgart, **1**, 293–334.
- DIMADIS, E. & ZACHOS, S. 1986. *Geological map of Rhodope massif (1:200,000)*. IGME, Athens.
- FAULRING, G. M. 1965. Unit cell dimension and thermal transformation of nsutite. *American Mineralogist*, **50**, 170–179.
- GIOVANOLI, R. 1969. A simplified scheme for polymorphism in the manganese dioxides. *Chimia*, **23**, 470–472.
- 1980. On natural and synthetic manganese nodules. In: VARENTSOV, I. M. & GRASSELLY, G. (eds) *Geology and Geochemistry of Manganese*. Schweizerbart'sche, Stuttgart, **1**, 159–202.
- & BRUTSCH 1979. Über oxidhydroxide des Mn(IV) mit schichtengitter. 5. Mitteilung: Stochiometric, ausverhalten und die rolle bei der bildung von tiefsee-mangankonkretionen. *Chimia*, **33**, 372–376.
- HEWETT, D. F. 1964. Veins of hypogene manganese oxide minerals in the southwestern United States. *Economic Geology*, **59**, 1429–1472.
- & FLEISCHER, M. 1960. Deposits of the manganese oxides. *Economic Geology*, **55**, 1–55.
- , — & CONKLIN 1963. Deposits of the manganese oxides: Supplement. *Economic Geology*, **58**, 1–51.
- MANN, A. W. & DEUTSCHER, R. L. 1980. Solution geochemistry of lead and zinc in water containing carbonate, sulphate, and chloride ions. *Chemical Geology*, **29**, 293–311.
- NICHOLSON, K. 1992. Contrasting mineralogical-geochemical signatures of manganese oxides: Guides to metallogenesis. *Economic Geology*, **87**, 1253–1264.
- NIMFOPOULOS, M. K. 1988. *Manganese mineralization near Kato Nevrokopi, Drama, Greece*. PhD thesis, University of Manchester UK.
- & PATRICK, R. A. D. 1991. Mineralogical and textural evolution of the economic manganese mineralisation in western Rhodope massif, N. Greece. *Mineralogical Magazine*, **55**, 423–434.
- , MICHAILIDIS, K. M. & CHRISTOFIDES, G. 1997. Zincian rancieite from the Kato Nevrokopi manganese deposits, Macedonia, northern Greece. *This volume*.
- , REX, D. & PATRICK, R. A. D. 1988. Age of hydrothermal manganese mineralization near Kato Nevrokopi, Drama, northern Greece. *Transactions of the Institution of Mining and Metallurgy*, **97(B)**, 193–195.
- OSTWALD, J. 1984. Some observations on the genesis of nsutite. *Neues Jahrbuch für Mineralogie Monatshefte*, **9**, 385–392.
- 1985. Some observations on the chemical composition of chalcophanite. *Mineralogical Magazine*, **49**, 752–755.
- 1986. Some observations on the chemical composition of todorokite. *Mineralogical Magazine*, **50**, 336–340.
- 1992. Genesis and paragenesis of the tetravalent manganese oxides of the Australian continent. *Economic Geology*, **87**, 1237–1252.
- PERSEIL, E. A. & GIOVANOLI, R. 1989. L'association todorokite–birnessite dans les concentrations manganésifères de Falotta et Parsettens (Grisons-Suisse) et sa place dans la paragenese. *Schweizerische Mineralogische und Petrographische Mitteilungen*, **69**, 283–288.
- PODUFAL, P. 1971. *Zur geologie und lagerstättenkunde der manganvorkommen bei Drama (Griechisch-Makedonien)*. Clausthaler Geologische Abhandlungen, **10**.
- POST, J. E. & APPLEMAN, D. E. 1988. Chalcophanite, $ZnMn_3O_7 \cdot 3H_2O$: New crystal-structure determinations. *American Mineralogist*, **73**, 1401–1404.
- & BISH, D. L. 1988. Rietveld refinement of the todorokite structure. *American Mineralogist*, **73**, 861–869.
- & VEBLEN, D. R. 1990. Crystal structure determinations of synthetic sodium, magnesium, and potassium birnessite using TEM and the Rietveld method. *American Mineralogist*, **75**, 477–489.
- POTTER, R. M. & ROSSMAN, G. R. 1979. The tetravalent manganese oxides: Identification, hydration and structural relationships by infrared spectroscopy. *American Mineralogist*, **64**, 1199–1218.
- RADTKE, A. S., TAYLOR, C. M. & HEWETT, D. F. 1967. Aurorite, argentinian todorokite and hydrous silver-bearing lead manganese oxide. *Economic Geology*, **62**, 182–206.
- ROY, S. 1981. *Manganese deposits*. Academic Press, London.
- SOREM, R. K. & FEWKES, R. H. 1980. Distribution of todorokite and birnessite in manganese nodules from the "Horn Region", Eastern Pacific Ocean. In: VARENTSOV, I. M. & GRASSELLY, G. (eds) *Geology and Geochemistry of Manganese*. Schweizerbart'sche, Stuttgart, **1**, 203–229.
- SPATHI, C. 1964. *The mineralogical composition of the Greek manganese ores*. Ph D thesis, University of Thessaloniki [in Greek with English abstract].
- TURNER, S. & BUSECK, P. R. 1981. Todorokites: a new family of naturally occurring manganese oxides. *Science*, **212**, 1024–1027.
- & — 1983. Defects in nsutite (γ - MnO_2) and dry cell battery efficiency. *Nature*, **304**, 143–146.
- VACONDIOS, I. 1982. *Preliminary geological and metallogenetic study of the Falakron region (Drama district)*. DA study, France [in French].
- WADSLEY, A. D. 1955. The crystal structure of chalcophanite $ZnMn_3O_7 \cdot 3H_2O$. *Acta Crystallographica*, **8**, 165–172.

Recent manganese oxide deposits in Hokkaido, Japan

HIROYUKI MIURA¹ & YU HARIYA²

¹ *Department of Earth and Planetary Sciences, Graduate School of Science, Hokkaido University, 060, Sapporo, Japan*

² *Hokkaido Institute of Technology, 006, Teine-ku, Sapporo, Japan*

Abstract: Recent manganese oxide deposits and manganese-bearing hot-spring waters from Hokkaido, Japan have been studied. There are many active hot-springs in the volcanic zones in Japan and stable isotope data (δD) show that the hot-spring water is derived from surface water. Some hot-spring waters precipitate manganese oxides. They are black, soft and muddy. SEM micrographs show a pipe structure coated by manganese oxides which indicates the role of microorganisms in manganese precipitation. X-ray powder diffraction reveals that they consist of todorokite or birnessite. Pyrolusite is not a primary product from hot-spring waters, but a recrystallized product in the post-depositional environment. Manganese oxides alternated with calcareous sinter and are crusty and consist of rancieite. The concentration of heavy metal elements in manganese oxide is controlled by the crystal structure of manganese oxide minerals present in the deposits and todorokite contains the most heavy metal elements. REE concentration varies widely and the negative Ce anomaly is an indicator of depositional rate.

There are many manganese deposits in Hokkaido, the northern island of Japan, most of which are of sedimentary origin (Yoshimura 1952, 1967, 1969). They occur predominantly in the Tokoro and Setana areas of NE and SW Hokkaido, respectively. Choi & Hariya (1990*a, b*) showed that manganese deposits in the Tokoro area are of Cretaceous age and that they are of hydrothermal origin showing limited hydrogenetic effects. Manganese oxide deposits in the Setana area are believed to be volcanogenic submarine deposits formed during the Tertiary (Doi 1958; Miura *et al.* 1992). In addition, many Recent manganese oxide deposits occur in Hokkaido. There are many active volcanoes in Hokkaido some of which are associated with hot-springs. Several hot-springs precipitate manganese oxides. Although these are usually much smaller than the Cretaceous or Tertiary ore deposits, some are being mined. However, Recent manganese deposits are important not because of their economic value, but because of their unique characteristics. We can directly observe the depositional process of manganese oxides from hot-spring waters. We can see not only the solid phase but also the ore solution, which is unknown in older manganese deposits. We can see the manganese minerals at an early stage of deposition before they change to another, more stable, phase. Further, the role of algae and microorganisms in the process of manganese deposition can be determined (Hariya & Kikuchi 1964; Hariya *et al.* 1992). Deep-sea manganese deposits also provide information about manganese deposition. However, it is difficult to observe them because they

are located deep in the sea. By contrast, Recent manganese deposits on land are easy to observe and study. Here, we will show that the distribution of Recent manganese deposits in Hokkaido, their occurrence, mineral morphology and the chemistry of manganese minerals and hot-springs enables us to understand the nature of manganese deposits and minerals. Recent manganese deposits are useful indicators of mineralization processes in ancient manganese deposits.

Recent manganese deposits and volcanic zones in Japan

There are many active volcanoes in Japan, which occur in several volcanic zones. These zones, from north to south, are Chishima, Nasu, Chokai, Norikura, Hakusan, Fuji and Kirishima (Fig. 1). In these volcanic zones, Recent manganese oxide deposits occur. There are three such areas in Honshu island. In Fujikoto, Akita prefecture, a Recent manganese deposit exists on the slope of Komagatake volcano. The orebody is currently being mined and hot-spring activity has ceased (Saito 1951). At Shigakonsen hot-spring, which is located at the foot of Sambe volcano in Sambe area, Shimane prefecture, large amounts of manganese oxides are deposited. However, the hot-springs which precipitated the deposit are no longer active (Yoshimura 1969). In Hokkaido, the Chishima Volcanic zone extends from the Tokachi area (central Hokkaido) to the Shiretoko peninsula (eastern Hokkaido). The Nasu volcanic zone extends from Honshu island to south-western

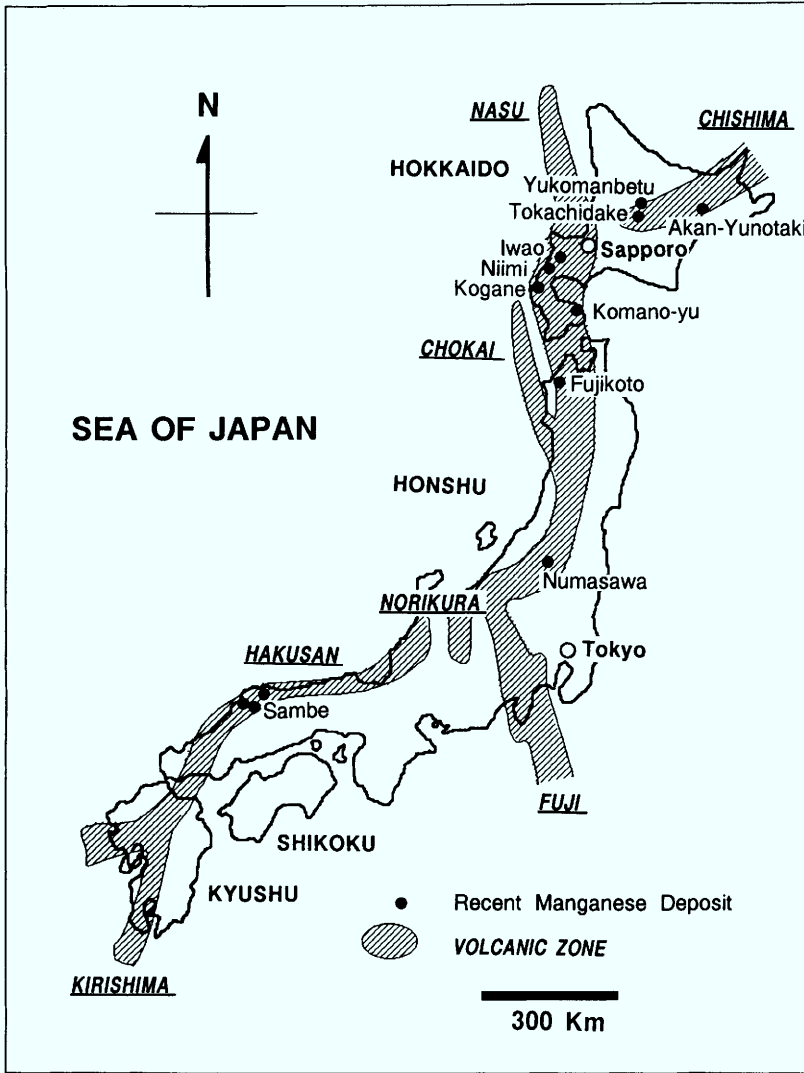


Fig. 1. Distribution of Recent manganese deposits and volcanic zones in Japan. Active volcanoes are located in seven volcanic zones (underlined). Recent manganese deposits (black dots) occur in these volcanic zones. The distribution of volcanic zones are quoted from Minato (1977).

part of Hokkaido. There are many active volcanoes accompanied by hot-spring activity in these areas. In some of the hot-springs, iron oxyhydroxide and manganese oxide precipitate to form economic ore deposits (Table 1).

Iwao mine

Ogawa-onsen is located on the northeastern slope of Mt Iwaonupuri, Niseko area, 60 km SW of Sapporo. The iron deposit that is precipitated from the hot-spring is distributed in area

c. 300 m × 200 m, south of Ogawa-onsen. The estimated amount of the iron deposit is 100 000 t. In the last stage of hot-spring activity, manganese oxide was precipitated. It is distributed east of the iron deposit and 2500 t of manganese wad was mined (Saito 1954). Samples (IW-1, IW-3) were collected from the outcrop located about 500 m west of Ogawa-onsen. Alternating layers of goethite and manganese oxides were observed. Manganese oxide layers of pyrolusite contain quartz, plagioclase and montmorillonite as impurities. The observed manganese beds are 2–6 cm thick. Manganese oxides are black and

Table 1. Recent manganese deposits in Hokkaido, Japan

Mn deposit	Volcano/locality	Minerals	Activity*	Micro. org.†	Assoc. dep.‡	Remarks
Iwao-mine	Mt Iwaonupuri Niseko area	Pyrolusite	Not active	—	Fe	Ore reserve of Fe is 100 000 t; 2500 t of Mn wad was mined
Niimi-onsen	Mt Shyakunage Niseko area	Pyrolusite, todorokite, birnessite	Not active	—	—	Western deposit is 40 × 10 × 3 m and covered by soil; Eastern deposit is 50 × 20 × 5 m
Kogane-onsen	— Setana area	Rancieite, birnessite	Active	—	S, Ca	Hot-spring water runs down river terrace, orebodies are 100 × 60 × 3 m and 140 × 60 × 2 m
Komanoyu-onsen	Mt Komagatake Oshima peninsula	Birnessite	Active	Mn bacteria	—	Hot-spring water runs about 50 m and deposits Mn wad
Tokachidake Mn dep.	Mt Tokachidake Hidaka area	Vernadite	Not active	—	—	Mn precipitated from spring water emerged through tuff
Akan-Yunotaki	Mt Meakandake Akan National Park	Todorokite, birnessite	Active	Mn bacteria	Ca	Hot-spring water runs down the slope, orebody is 150 m × 70 m; 1500 t of Mn wad was mined
Yukomanbetu-onsen	Mt Asahidake Hidaka area	Todorokite, birnessite	Active	Algae are observed	Fe	Fe deposit at the upper side of the mountain slope and Mn at the lower side

* Present activity of manganese deposition.

† Microorganism activity in the process of manganese deposition.

‡ Associated phase in deposit.



Fig. 2. Occurrence of recent manganese deposits in Hokkaido, Japan. **(a)** Hot spring-water runs down the river terrace at Kogane-onsen. The river terrace near the vent is covered by sulphur. **(b)** Alternation of manganese oxide and calcium carbonate layers at the edge of ore body at Kogane-sawa river. Mn, manganese oxide; Ca, calcium carbonate. **(c)** Manganese oxide deposit in the stream at Komanoyu-onsen. **(d)** Manganese wad precipitated from hot-spring water covering the wall of Akan-Yunotaki. **(e)** Hot-spring water discharged from the vent in the stream of Yukomanbetu river and forming manganese wad in bog. White vapour caused by a drop of hydrogen peroxide shows the existence of manganese dioxide.

soft. The hot-spring that deposited this manganese oxide is no longer active and the manganese layers are covered by soil 10–40 cm thick.

Niimi-onsen

Niimi-onsen is located on the foot of Mt Shyakunage, an active volcano in the Niseko area, about 65 km SE of Sapporo city. The area is covered by pyroclastic materials erupted from Mt Shyakunage in the Quarternary. There are two manganese oxide orebodies, separated by about 150 m. The northwestern orebody is about 40 m × 100 m with a thickness of about 3 m, most of which has already been extracted. The annual production was 150 t in 1951 (Sakou *et al.* 1977). Two to four layers of manganese oxide sandwiched between clay beds can be seen at three outcrops. The orebody was covered by clay and soil with thicknesses of 15–100 cm. Soft black samples (NI-11–NI-32), one from each layer, were collected for analysis. The hot-spring which generated the orebody can no longer be observed. The eastern orebody located near the Niimi-onsen hotel, is about 50 m × 20 m with a maximum thickness of 5 m (Igarashi & Yokota 1970). The orebody is not observed now and the present hot-spring does not precipitate manganese.

Kogane-onsen

Kogane-onsen hot-spring is located about 110 km SW of Sapporo. There are many Tertiary manganese deposits in the area. The hot-spring discharges at five points in the terrace of Kogane-sawa river and runs down the surface (Fig. 2a). The orebody which precipitates from these hot-springs covers the river terrace. The orebody consists of manganese oxide and calcareous sinter and is about 100 m × 60 m with a thickness of about 2–3 m (Yamaguchi *et al.* 1977). The calcareous sinter deposit is dominant in the central part of the orebody and manganese oxide is dominant at the rim part. Very close to the vents, sulphur deposits are present, while 2–3 m away from the vents calcium carbonate starts to deposit. Manganese oxide deposits over 8 m from vents. At the outcrop of orebody, alternate layers of manganese oxide and calcium carbonate are observed (Fig. 2b) Samples were collected from manganese deposits precipitated from three hot-springs (KG-1, KG-4 and KG-5). There is another orebody along the Kogane-sawa River about 500 m west of Kogane-onsen. This orebody also consists of manganese oxide and calcareous sinter and is about 140 m × 60 m with a thickness of about 2 m (Yamaguchi *et al.* 1977). The hot-spring that precipitated this deposit is extinct.

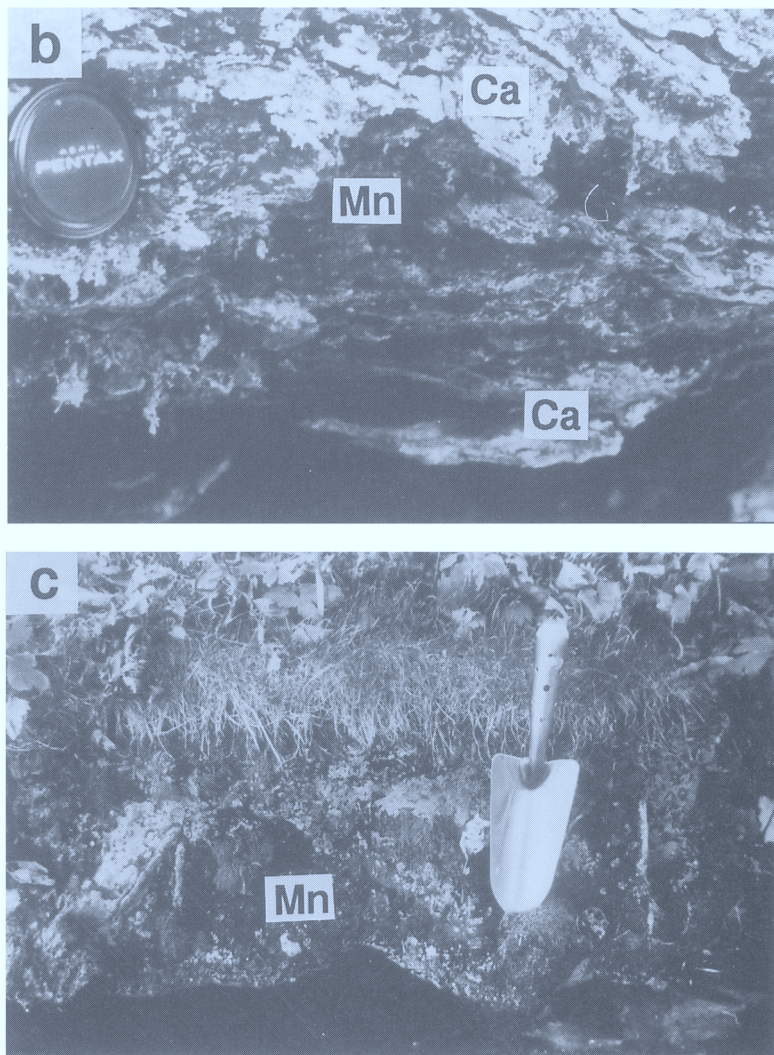


Fig. 2. (continued)

Sample (KG-6) was collected from the orebody. Samples are greyish black and very hard compared with other manganese wads from Recent manganese deposits in Hokkaido.

Komanoy-onsen

The Komanoyu-onsen hot-spring is located on the southwestern foot of Mt Komagatake, 120 km SW of Sapporo. It percolates through the volcanic breccia of Mt Komagatake, which is a very active volcano. Hot-spring water runs about 50m and flow into a small stream. The width of the flow is about 50 cm and pebbles in

the flow are covered by manganese oxides. Many spherical manganese micronodules of about 1 mm diameter were found in stream. About 40m from the vent, the width of the flow increases to 2m, which slows down the flow, and a deposit of manganese wad, 10 cm thick, is formed (Fig. 2c). Black or brownish black and muddy samples (KM-0, KM-4) were collected from there. Manganese bacterial activity has been reported by Hariya & Kikuchi (1964). There were several cold springs that precipitated a manganese deposit with a thickness of 1–1.5 m (Hariya & Harada 1957). The area has been cultivated with loss of the deposit.

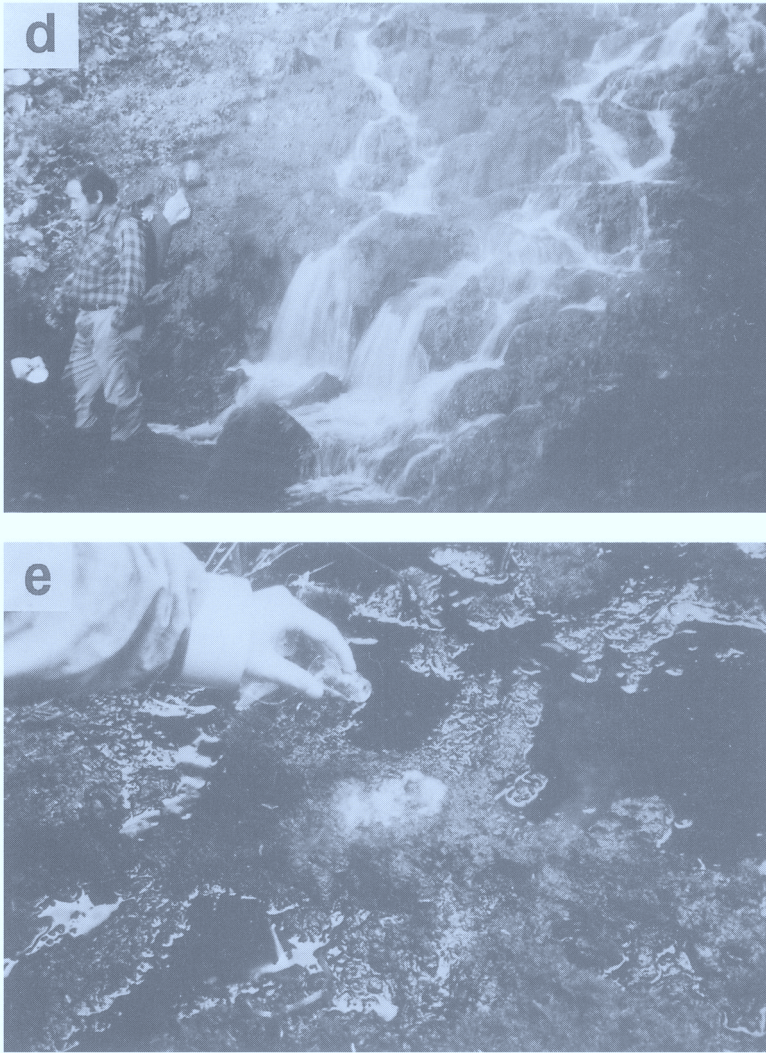


Fig. 2. (continued)

Tokachidake manganese deposit

The Tokachidake manganese deposit is located 2.5 km NW of Shirogane-onsen, central Hokkaido 120 km NE of Sapporo. Hot-springs flow from the northwestern slope of Mt Tokachidake and manganese oxide ore is precipitated from the spring water. Mt Tokachidake is an active volcano and the spring water comes up through a welded tuff layer of late Tertiary or early Quaternary age (Fujiwara 1959). A sample collected by Fujiwara was used for measurement.

Akan-Yunotaki

Akan-Yunotaki located to the SW of Meakan volcano, close to Lake Onneto in Akan National Park, about 240 km east of Sapporo. The area contains andesite erupted from Mt Meakan. A large amount of hot water emerges from the mountain slopes and forms a pair of waterfalls. In 1941, manganese wad deposits were found around the falls, in an ore zone of approximately 150 m × 70 m. Annual manganese production was 1500 t in 1952 and 1953. In 1954, 495 t of 48% Mn was worked and then mining stopped

Table 2. Temperature, pH and chemical concentration of hot-spring waters from Hokkaido

Deposit	Kogane-1 Mn	Kogane-1 Mn	Kogane-2 Mn	Kogane-2 Mn	Kogane-3 Mn	Koma. Mn	Yuko. Mn	Akan. Mn	Nishi-1 Fe	Nishi-2 Fe	Ogawa* Fe	Kajika* Fe	Niimi Nothing
Temp.(°C)	44.2	64.4	64.4	64.4	42.0	50.0	30.0	36.0	10.4	10.0	32.1	67.5	42.9
pH _T	5.9	5.9	5.9	5.9	6.5	6.8	5.9	6.4	4.0	6.5	6.0	6.5	7.5
Mn ppm	4.4	4.6	4.6	4.6	5.3	4.9	5.6	4.5	2.3	1.05	1.88	1.05	1.10
Fe ppm	0.40	0.48	0.48	0.48	0.48	0.02	0.20	0.05	20	3.36	20.69	3.36	0.02
Na ppm	580	580	580	580	540	178	110	170	24	619	137.2	619	305.7
K ppm	560	480	480	480	430	21	31	49.0	4	101	33.8	101	5.5
Ca ppm	57	59	59	59	61	97	175	210.0	110	287.5	248.0	287.5	305.7
Mg ppm	8.9	9.0	9.0	9.0	9.0	57	86	160.0	25	39.6	154.1	39.6	8.0
Cr ppm	<0.001	<0.001	<0.001	<0.001	<0.001	0.001	<0.02	0.006	0.020	0.014	na	na	<0.001
Co ppm	<0.001	<0.001	<0.001	<0.001	<0.001	0.004	<0.002	<0.001	<0.001	0.020	na	na	<0.001
Ni ppm	na	na	na	na	na	na	<0.002	na	0.018	0.018	na	na	<0.001
Cu ppm	0.002	0.003	0.003	0.003	0.003	0.004	<0.002	0.018	0.016	0.014	0.001	0.003	0.006
Zn ppm	0.006	0.006	0.006	0.006	0.006	0.012	<0.002	0.030	0.056	0.006	0.046	0.012	0.001
As ppm	0.030	0.060	0.060	0.060	0.040	0.010	na	<0.001	0.032	0.000	0.017	0.772	0.254
Sb ppm	<0.001	<0.001	<0.001	<0.001	<0.001	0.011	na	<0.001	0.014	0.006	na	na	na
Ag ppm	<0.001	<0.001	<0.001	<0.001	<0.001	<0.001	<0.001	<0.001	<0.001	<0.001	na	na	na
Pb ppm	<0.001	0.002	0.002	0.002	0.001	0.034	0.004	0.012	0.006	0.008	na	na	na

Kogane, Kogane-onsen; Koma., Komanoyu-onsen; Yuko, Yukomanbetu; Akan., Akan-Yunotaki; Nishi., Nishikinuma; Ogawa, Ogawa-onsen; Kajika, Kajika-onsen; Niimi, Niimi-onsen.

pH_T = pH at measured temperature.

na, not analysed.

* From Matsunami *et al.* (1979).

Table 3. Chemical composition of Recent manganese oxides from Hikkaido

Sample	IW-1	IW-3	NI-11	NI-13	NI-15	NI-21	NI-22	NI-31	Ni-32	KG-1	KG-4	KG-5
Mn %	49.0	48.0	49.0	36.0	50.0	61.0	60.0	45.0	57	56.0	54.0	54.0
Fe %	0.04	0.05	5.0	8.3	1.8	3.6	0.34	9.4	2.5	2.2	2.1	2.5
Ca %	0.30	0.38	0.80	0.74	0.50	0.64	0.27	0.6	1.50	2.1	1.6	2.0
Mg %	0.42	0.37	0.30	0.44	0.17	0.35	0.04	0.34	0.24	0.28	0.31	0.67
Na %	0.044	0.025	0.24	0.11	0.15	0.20	0.058	0.18	0.085	0.039	0.025	0.025
K %	0.10	0.08	1.00	0.59	0.60	0.55	0.26	0.76	0.63	0.35	0.26	0.35
Cu ppm	60	42	8.3	65	8.5	18	4.8	22	27	93	62	20
Cr ppm	27	7.4	4.2	17	2.2	5.8	1.9	7.9	0.86	8.2	21	2.3
Ni ppm	27	14	4.9	32	2.8	10	1.0	10	6.2	12	32	14
Co ppm	<1	<1	12	100	11	57	17	34	250	<1	15	2.0
As ppm	160	160	5300	6600	5600	3000	4400	5700	2500	420	140	260
Sb ppm	7.9	3.1	350	310	2100	210	1000	20	170	8.2	4.6	6.7
Pb ppm	16	6.1	2.5	9.2	7.1	12	0.2	3.9	3.4	140	54	6.7
Ag ppm	<0.4	<0.4	<0.4	<0.4	<0.4	<0.4	<0.4	<0.4	<0.4	<0.4	<0.4	<0.4
Zn ppm	55	64	45	200	60	170	58	100	180	56	na	na

Sample	KG-6	KM-0	KM-4	TO-1	AK-1	AK-2	AK-31	AK-32	AK-33	UK-1	UK-1	UK-4
Mn %	59.0	45.0	23.9	41.0	41.0	33.0	36.0	36.0	37.0	39.2	37.8	50.7
Fe %	2.2	2.0	3.80	0.23	0.19	0.09	0.04	0.01	0.02	1.4	6.52	0.0
Ca %	2.2	3.1	2.56	0.26	1.5	2.7	3.8	4.1	3.6	1.7	1.45	1.2
Mg %	0.56	0.69	0.52	0.36	1.4	4.5	2.3	2.0	2.0	0.76	0.30	0.30
Na %	0.029	0.19	0.37	0.075	0.039	0.048	0.20	0.14	0.20	0.21	0.30	0.04
K %	0.27	0.45	0.20	0.20	0.62	0.40	0.44	0.56	0.44	0.57	0.70	0.72
Cu ppm	290	46	75	240	460	350	260	370	490	133	11	179
Cr ppm	48	0.18	3.0	0.19	2.4	32	3.0	3.4	11	5.9	3.7	1.9
Ni ppm	76	<1	3.0	300	130	220	140	96	160	2	4	4
Co ppm	52	110	1.3	14	35	79	23	38	23	35.2	5.9	6.9
As ppm	100	270	212	18	95	100	70	98	110	95	4	95
Sb ppm	1.9	<0.2	0.2	<0.2	3.3	22	4	4.6	6.2	<0.5	<0.5	<0.5
Pb ppm	38	80	6	7.0	<0.2	<0.2	20	42	75	1.2	0.3	0.3
Ag ppm	<1.2	<0.4	<0.4	<0.4	<0.4	<0.4	0.81	<0.4	2.5	0.4	<0.4	<0.4
Zn ppm	na	300	57	3900	390	270	290	320	440	na	na	na

IW, Iwao mine; NI, Niimi-onsen; KG, Kogane-onsen; KM, Komanoyu-onsen; TO, Tokachidake manganese deposit; AK, Akan-Yunotaki; UK, Yukomanbetsu. na, not analysed.

Table 4. REE composition (ppm) of Recent manganese oxides from Hokkaido

Sample	NI-11	NI-22	NI-32	KG-1	KG-4	KG-6	KM-4	TO-1	AK-31	AK-32	AK-33	UK-1	UK-3	UK-4
La	31.7	7.6	19.3	0.3	0.2	9.6	3.5	249	4.0	17.6	11.7	4.1	6.2	1.2
Ce	34	10	172	2	<1	20	6	1410	3	4	4	8	10	2
Nd	44	8	26	<1	<1	10	5	394	3	11	9	3	5	1
Sm	9.81	1.17	8.00	0.13	0.08	2.18	1.13	121	0.84	2.05	1.99	0.78	1.39	0.27
Eu	3.20	0.87	2.59	0.06	0.05	0.93	0.33	19.4	0.17	0.43	0.39	0.23	0.28	0.06
Tb	1.9	0.2	1.3	<0.1	<0.1	0.6	0.3	20	0.3	0.8	0.7	0.3	0.3	<0.1
Yb	6.78	1.83	5.02	0.28	0.20	2.31	0.32	91.0	1.53	3.92	3.08	1.00	1.07	0.37
Lu	0.97	0.28	0.65	0.04	0.03	0.34	0.18	14.5	0.26	0.63	0.51	0.19	0.18	0.06

Abbreviations are the same as in Table 3.

Table 5. Hydrogen isotope ratios and equilibrium coefficient of hot-spring waters, surface waters and manganese oxides from Hokkaido

Sample	δD (‰)			$\alpha_{\text{mineral-water}}$
	Hot-spring water	Surface water	Manganese oxide	
Akan	-73 to -74	-76	-98 to -106	0.969
Komanoyu	-64 to -67	-66	-98 to -106	0.961
Pirika (Tertiary Mn dep.)	(-56*)	-	-89	(0.965†)

SMOW, Standard mean ocean water.

* Calculated data.

† Average of Akan and Komanoyu.

(Umemoto *et al.* 1956). Hot spring-water overflowing from the right side spring was measured as 1370 l per min in 1990 and the annual amount of deposition is about 1100 kg (Hariya *et al.* 1992). This is the largest manganese deposit in Hokkaido, and perhaps the world, where we can see the process of deposition (Fig. 2d). Alternate layers of manganese oxide and calcite (about 1.5 m thick), observed in the outcrops near the streams, indicate that the chemical conditions of hot-spring water have changed periodically. Manganese bacterial activity has been reported by Hariya *et al.* (1992) and Usui & Mita (1995). Dried samples of AK-1 (under the calcite layer) and AK-2 (above the calcite layer) were collected from the outcrop. They are black or greyish black and crusty. Samples of wet manganese wads were collected from the deposits in the waterfall (AK-31-33). They are black, soft and produce a very fine powder when dried.

Yukomanbetu-onsen

Yukomanbetu-onsen is located in central Hokkaido, 140 km NE of Sapporo on the slopes of Mt Asahidake volcano. There are about 30 hot-springs associated with iron and manganese deposits along the tracks. At the higher part of the mountain slope, the deposits consist of iron oxyhydroxide and, at the lower part, of manganese oxide (Ueno & Igarashi 1957). At the start point of the track at the foot of the mountain, manganese deposits were observed adjacent to the Yukomanbetu River. There are several hot-springs situated near the Yukomanbetu River. Hot water discharged from the vent into the stream and formed a manganese deposit in the stream or a manganese wad in the bog (Fig. 2e). UK-1 and UK-3 were collected from the stream and UK-4 from the bog.

Analytical methods

Collected samples were dried at 40°C for 24 hours in air and screened before XRD or chemical analysis. Impurities such as grains of rocks or grass roots were removed under the microscope. XRD profiles from $2\theta = 4-70^\circ$ in 0.05 steps were obtained using Cu-K α radiation (35 kv, 40 mA) with graphite monochromator. Mn, Fe, Na, K, Ca and Mg were measured by Hitachi 170-30 flame atomic absorption spectrometer (AAS). Heavy metal elements were analysed by Hitachi 180-70 flameless atomic absorption spectrometer. 100 mg of sample was dissolved in 30 ml of 12N HCl and dried. For flame AAS, 30 ml 1N HCl was added to the sample and filtered to remove silicate and/or clay minerals. To prevent interference of Na, Mg, K and Ca, 4000 ppm Sr solution was added to the solution for Ca, Mg and K determination (Terashima 1970). For flameless AAS, 1N HNO₃ was used instead of HCl. The solutions were diluted with distilled water to the concentration range of standard solution. Water samples from the hot-spring were treated in the same manner. The REE concentrations of selected samples were determined by neutron activation analysis. Hydrogen isotopes were measured by mass spectrometry. The equilibrium coefficient of hydrogen isotope between the hot-spring water and manganese oxide is given by

$$\alpha_{\text{mineral-water}} = \frac{\{1 + \delta D_{\text{mineral}}/1000\}}{\{1 + \delta D_{\text{water}}/1000\}}$$

where δD is given in the permil deviation relative to standard mean ocean water (SMOW) and expressed by

$$\delta D = \left(\frac{D/H_{\text{sample}}}{D/H_{\text{SMOW}}} - 1 \right) \times 1000\text{‰}$$

Results

Chemical composition and isotopic data

Table 2 shows data for temperature, pH and chemical concentration of the hot-spring waters. The hot-springs associated with manganese deposits occur at Kogane-onsen, Komanoyu-

Table 6. Mineral assemblages of Recent manganese oxides from Hokkaido

Sample	IW-1	IW-3	NI-11	NI-13	NI-15	NI-21	NI-22	NI-31	NI-32	KG-1	KG-4	KG-5
Todorokite			+++	++				+				
Birnessite				+		+		++	+++	+++		
Rancietite											+++	+++
Pyrolusite	+++	+++		+++	++	+++	+++					
Vernadite												
Sample	KG-6	KM-0	KM-4	TO-1	AK-1	AK-2	AK-31	KA-32	AK-33	UK-1	UK-3	UK-4
Todorokite					+	+	+++		+++	+++		
Birnessite		+++	+++		++	++		+++			+++	+++
Rancietite	+++											
Pyrolusite												
Vernadite				+++								

Abbreviations same as in Table 2.

+, Present; ++, Common; +++, Dominant.

Samples are measured after being dried at room temperature and Wet samples of KM-4, AK-32, UK-3 and UK-4 are todorokite.

Table 7. X-ray diffraction data for manganese wad from Kogane-onsen

KG-1		KG-4		KG-5		KG-6		Birnessite		Rancieite	
$d(\text{\AA})$	I	$d(\text{\AA})$	I	$d(\text{\AA})$	I	$d(\text{\AA})$	I	$d(\text{\AA})$	I	$d(\text{\AA})$	I
7.07	100	7.45	100	7.45	100	7.44	100	7.09	100	7.49	100
3.55	50	3.71	60	3.71	60	3.71	60	3.56	80	3.73	50
2.45	50	2.46	40	2.46	30	2.46	50	2.51	70	2.46	30
		2.36	10			2.34	30	2.47	10		
		2.29	10	2.28	20			2.26	10		
				1.91	20			2.09	10	2.05	10
		1.82	8	1.87	20			1.82	40		
								1.77	10	1.76	5
		1.54	8					1.55	10	1.54	5
				1.47	8			1.47	60		
		1.42	10	1.42	10	1.42	30	1.43	50	1.42	30
		1.38	10	1.39	8	1.38	10	1.37	20	1.39	5

XRD data of birnessite and rancieite after Burns & Burns (1979).
KG, Kogane-onsen.

onsen, Yukomanbetu-onsen and Akan-Yunotaki. The hot-springs at Nishikinuma, Iwao (Ogawa-onsen) and Kajika-onsen are associated with iron deposits. Chemical data of hot-spring water from Iwao (Ogawa-onsen) and Kajika-onsen are quoted from Matsunami *et al.* (1979). Chemical concentrations of the oxides are listed in Table 3 and Table 4. Fe/Mn ratios of recent manganese deposits in Hokkaido which lie between 0.002 and 0.23, indicate that the manganese and iron are well fractionated. Table 5 shows the hydrogen isotope ratios of hot-spring water and nearby surface water from Niimi-onsen, Akan-Yunotaki, Komanoyu-onsen and associated manganese oxides. The equilibrium coefficients of hydrogen isotope between the hot-spring water and manganese oxide are also given in Table 5.

X-ray diffraction data

X-ray diffraction data show that the main manganese minerals in oxide from Hokkaido are todorokite, birnessite, rancieite and pyrolusite (Table 6). The 9.6 and 7.1 Å basal diffraction peaks are regarded as indicative of todorokite and birnessite respectively. The samples from Kogane-onsen hot-spring show a diffraction peak at 7.44–7.45 Å (KG-4, 5, 6). From the d -value of the basal diffraction peak, this phase was confirmed to be rancieite (Table 7). The sample from Akan-Yunotaki consists of two minerals, birnessite and todorokite. The results of the heat treatment of manganese oxide from

Yukomanbetu-onsen are shown in Fig. 3. The diffraction profile of wet UK-4 show a typical 9.6 Å basal diffraction peak and broad diffraction peak ranges from $2\theta = 20^\circ$ – 50° (Cu-K α) which may derived from the disorder in the structure. After drying at room temperature, the crystal structure deforms and the diffraction peak of 9.6 Å shifts to 7.3 Å, while the broad diffraction peak disappeared. The XRD profile is similar to that of birnessite. At 300°C, UK-4 shows only two diffraction peaks of 2.4 and 1.4 Å and identical to vernadite (Chukhrov *et al.* 1979). Above 650°C, UK-4 changes to Mn₂O₃ + Mn₃O₄. Wet samples of AK-33, UK-3, and KM-4 also show the basal diffraction peaks of 9.8–9.7 Å and shift to 7.2 Å after drying or heating. These data suggest that birnessite in these manganese oxide deposit is a desiccation product of todorokite. In the Komanoyu-onsen hot-spring, manganese micronodules occur in the stream (Fig. 4). They usually have a plagioclase grain at their centre and show concentric oxide zonation. XRD shows the constituent of the micronodule is birnessite. XRD data of the sample TO-1 from Tokachidake shows only 2.4 Å and 1.4 Å peaks, which is due to vernadite (Chukhrov *et al.* 1979).

Morphology

Wet samples collected from stream are very soft and when dried become very fine. From the SEM micrographs, aggregates of a pipe structure coated by manganese oxides can be

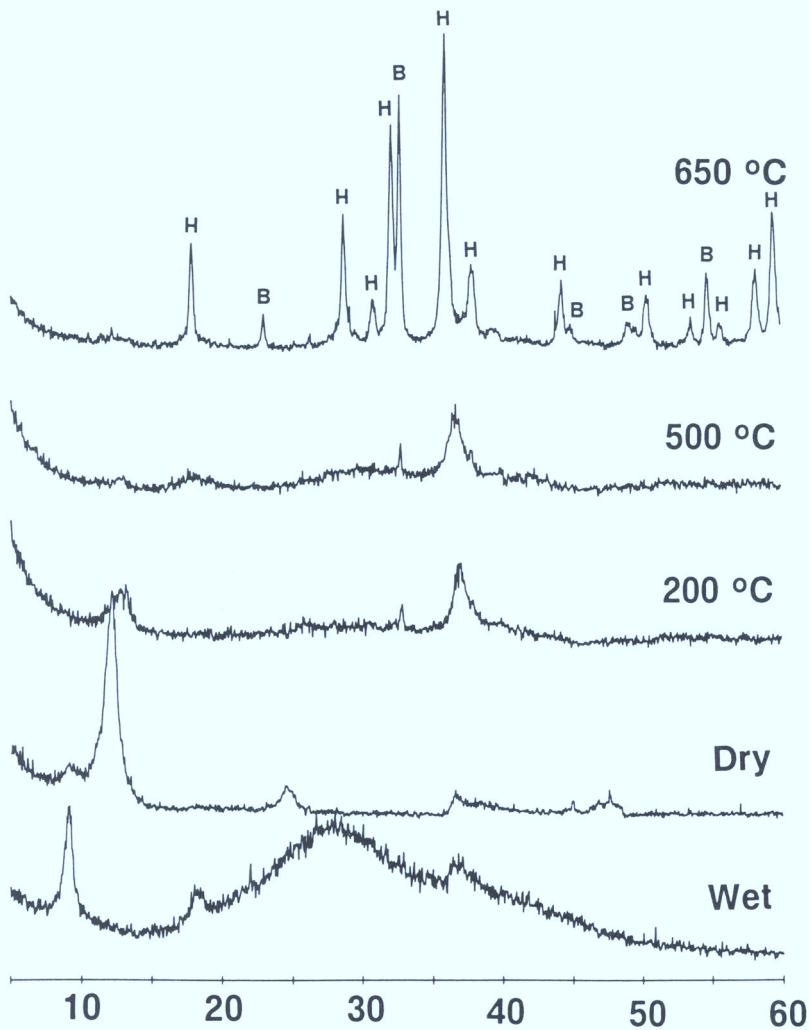


Fig. 3. X-ray diffraction profiles of todorokite from Yukomanbetu-onsen at different temperatures showing the deformation from todorokite to birnessite and more reduced form of manganese oxides. B, bixbyite; H, hausmannite.

seen from Komanoyu-onsen and Yukomanbets-onsen (Fig. 5a–d). These pipes are considered to be of algal origin and very similar to the algae reported from Akan-Yunotaki (Fig. 5e & f) by Usui & Mita (1995). The surface of the algae is covered by very fine networks of manganese minerals and these textures were common to all manganese minerals precipitated from hot-spring waters (Fig. 3b, d, f & h). Manganese minerals from Kogane-onsen (KG-6) are hard and crusty. Aggregates of hemispherical crystals were observed by SEM

and the existence of algae was not confirmed (Fig. 5g). They are identified as rancieite by XRD. These results agree well with the fact that this mineral contains 1.6–2.2 wt% Ca and their occurrence (alternating with calcium carbonate). The morphology of NI-22 is quite different from that of manganese minerals from Akan-Yunotaki (AK-33), Komanoyu-onsen (KM-4) and Yukomanbetu-onsen (UK-4). NI-22 shows aggregates of small crystals with sharp surfaces. They are well crystallized pyrolusite.

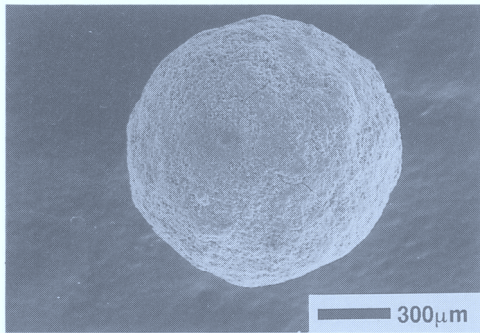


Fig. 4. SEM micrograph of manganese-micro nodule from Komanoyu-onsen. They usually have a plagioclase grain at their centre and show concentric zonation of vernadite.

Discussion

The origin of the hot-spring water

White (1967) demonstrated that the D/H and $^{18}\text{O}/^{16}\text{O}$ ratios of the cold surface waters of each area differ from each other depending on latitude, distance from the ocean and other climatic factors. The D/H ratios of hot-spring waters are usually identical to those of the cold surface waters of each particular area. However, the hot-spring waters are enriched in ^{18}O relative to ^{16}O . The data are not explained by the mixing of magmatic waters and the hot-spring waters are regarded as being derived from surface water. The enrichment in ^{18}O is explained by the reaction with silicate and/or carbonate rocks. The D/H ratios (δD) of hot-spring water from Hokkaido range from -74‰ to -64‰ , which is very similar to that of nearby surface water (-72 to -66‰), indicating that the hot-spring water is derived from local surface waters. The δD values of manganese oxide lie

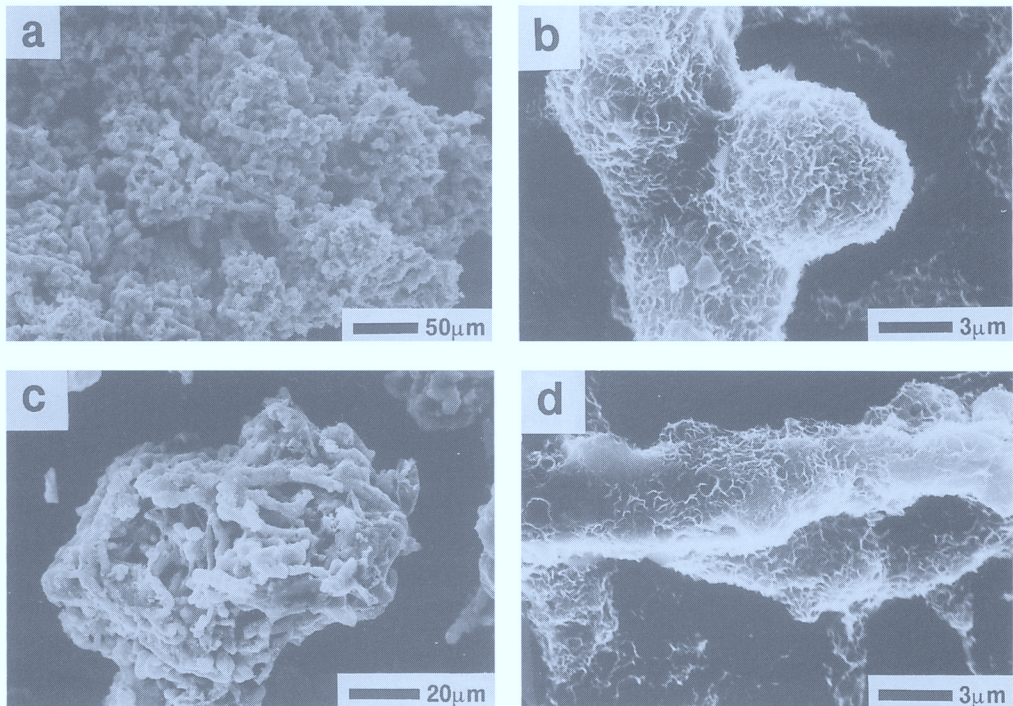


Fig. 5. Morphology of manganese minerals from Recent manganese wads. (a, b) Komanoyu-onsen (KM-4), (c, d) Akan-Yunotaki (AK-33), (e, f) Yukomanbetu-onsen (UK-4), (g, h): Kogane-onsen (KG-6), (i, j) Niimi-onsen (NI-22). (a, c, e) Pipe structure of algae coated by manganese oxides are observed in manganese wads from Komanoyu-onsen, Akan-Yunotaki and Yukomanbetu-onsen. (g) The crusty sample from Kogane-onsen shows aggregates of spherical form of rancieite crystals. (b, d, f, h, j) The surface of algae coated by very fine crystals of manganese minerals. These surface structures are common to all samples precipitate from hot-spring waters.

between -98% and -106% . The equilibrium coefficients ($\alpha_{\text{mineral-water}}$) for Akan-Yunotaki and Komanoyu-onsen are 0.969 and 0.961 respectively. The coefficients, which are lower than 1.00, demonstrate that spring-water is deuterium-enriched relative to manganese oxide. We can calculate the δD of the water which precipitated the manganese minerals on the basis of the equilibrium coefficient and δD of Recent manganese oxides. The δD value of manganese oxy-hydroxide minerals from Pirika mine of Tertiary age is -89% . This value is slightly lower than that of Recent manganese deposits (Table 5) and indicates that the water that precipitated this mineral contains more

deuterium than the Recent surface water (the calculated δD is -56%). The isotopic data of Recent manganese deposits thus indicates the nature of hydrothermal or hot-spring water that precipitated manganese oxides in the geological past.

Deposition of manganese

An inorganic process of manganese deposition is controlled by pH and Eh of solution (Crerar *et al.* 1980). We can see the effect of Eh in Kogane-onsen hot spring. When the hot-spring water emerges on the surface, the Eh is very low

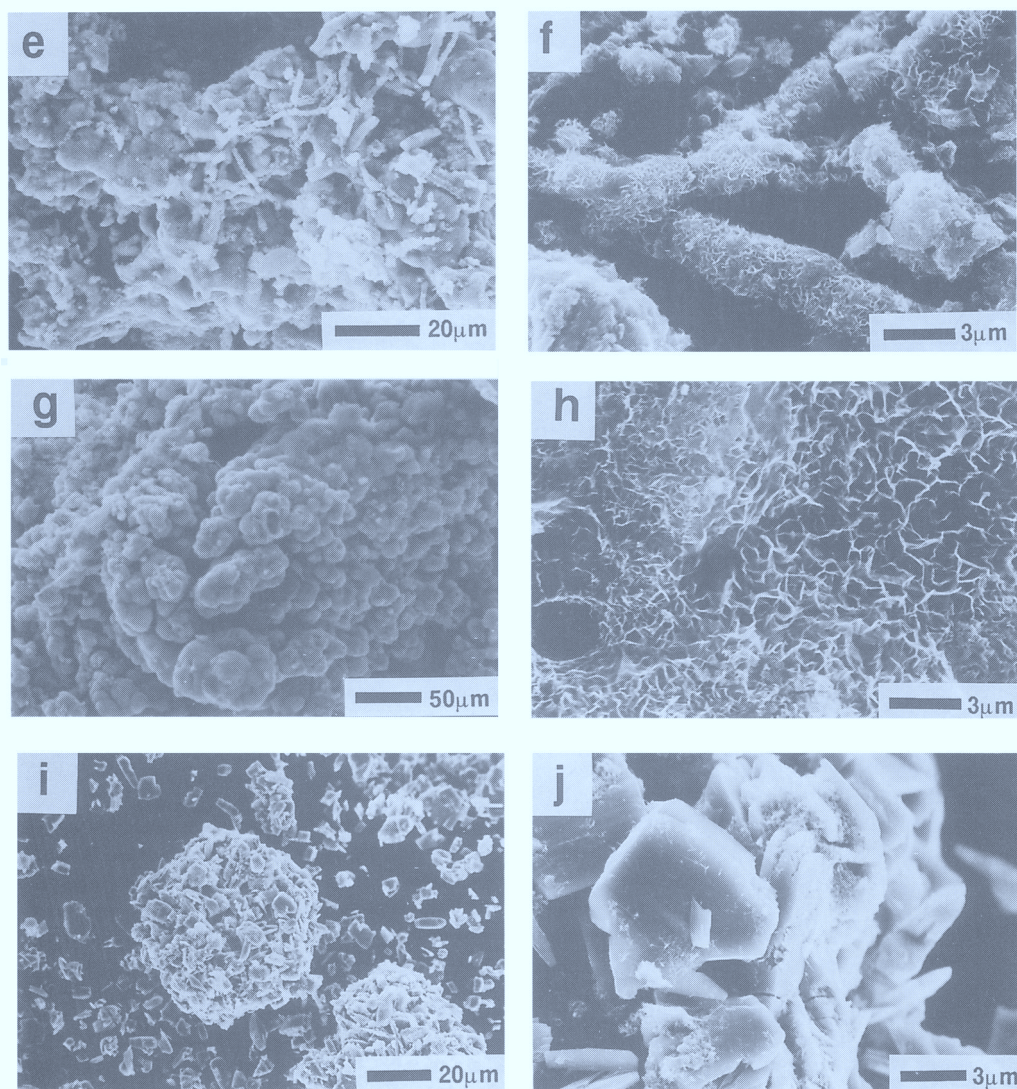


Fig. 5. (continued)

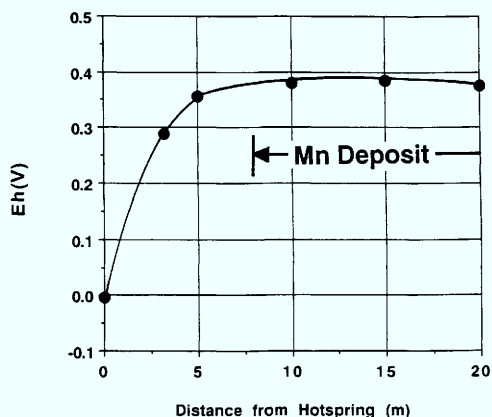


Fig. 6. Relationship between the Eh of hot-spring water and the distance from the spring. Manganese oxide starts to deposit when Eh exceeds 0.38 V.

(-0.05 V) and it can contain dissolved Mn^{2+} ion. Aerial oxidation increases the Eh to 0.38 V and precipitates Mn^{2+} as MnO_2 (Fig. 6). As the field of Fe^{2+} in the Eh-pH diagram exists in a lower Eh region than Mn^{2+} , even if the hot-spring water contained Fe^{2+} originally, it should be oxidized and precipitated before the deposition of manganese. Consequently, the hot-spring waters which precipitate manganese oxides have low Fe concentrations. The manganese oxides therefore also have low Fe contents (Fig. 7).

The existence of algae in three Recent manganese deposits (Akan-Yunotaki, Komano-yu-onsen and Yukomanbetu-onsen) indicate the importance of microorganisms in the process of manganese oxide deposition. The mineral phase in these three deposits is todorokite or birnessite and that in KG-6, which did not indicate the existence of algae, is rancieite. The difference of the morphology and hardness of manganese minerals among KG-6, AK-33, KM-4 and UK-4 derived from the difference of mineral phase. However the Ca concentration in hot-spring water is the same in these four hot-springs and Ca concentration is not the factor in determining the mineral phase. The mineral species in manganese wad precipitated from hot-spring water is therefore dependent on the presence or absence of microorganisms in the wad. It is therefore possible to conclude that the activity of the microorganisms controls the mineral phase and the absence of microorganisms in KG-6 indicates the inorganic process of deposition in Kogane-onsen. The absolute age of the manganese deposit of Niimi-onsen and Iwao-mine is not clear. However, the deposit

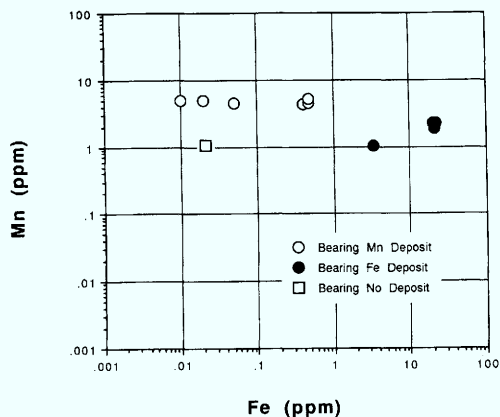


Fig. 7. Mn v. Fe concentrations of hot spring waters from Hokkaido. Hot spring waters contain 1 to 5 ppm Mn and up to 20 ppm Fe. The low Fe concentrations of hot spring water producing manganese oxide deposits. Open circle, hot-spring precipitating Mn oxide; filled circle, hot-spring precipitating Fe oxide; open square, no Fe or Mn oxide deposition.

must be old because the manganese layers were overlain by 15–100 and 10–40 cm of clay and soil respectively. The fact that pyrolusite is observed only in these old manganese deposits indicates that pyrolusite is not a primary mineral precipitated directly from hot-spring water. It might be recrystallized from manganese wads in the post-depositional period.

Mineral phase and heavy metal concentration

Recent manganese oxides in Hokkaido consist of todorokite, birnessite, rancieite and pyrolusite and the relative proportions vary with locality. The most probable reason for the variability is the characteristics of hot-spring water, such as Eh and pH and trace element concentration. There is no clear correlation between the concentration of heavy metals in hot-spring water and mineral species. Figure 8 shows the concentrations of Cu, Ni, Zn and Co in different mineral species of Recent manganese oxide from Hokkaido. Todorokite contains the highest amounts of these elements and pyrolusite the least. The concentrations of heavy metal elements in birnessite and rancieite are intermediate between todorokite and pyrolusite. Pyrolusite has a rutile-type structure and consists of close packing of oxygen atoms (Burns & Burns 1977). There is no space to incorporate trace element atoms, so they have to replace

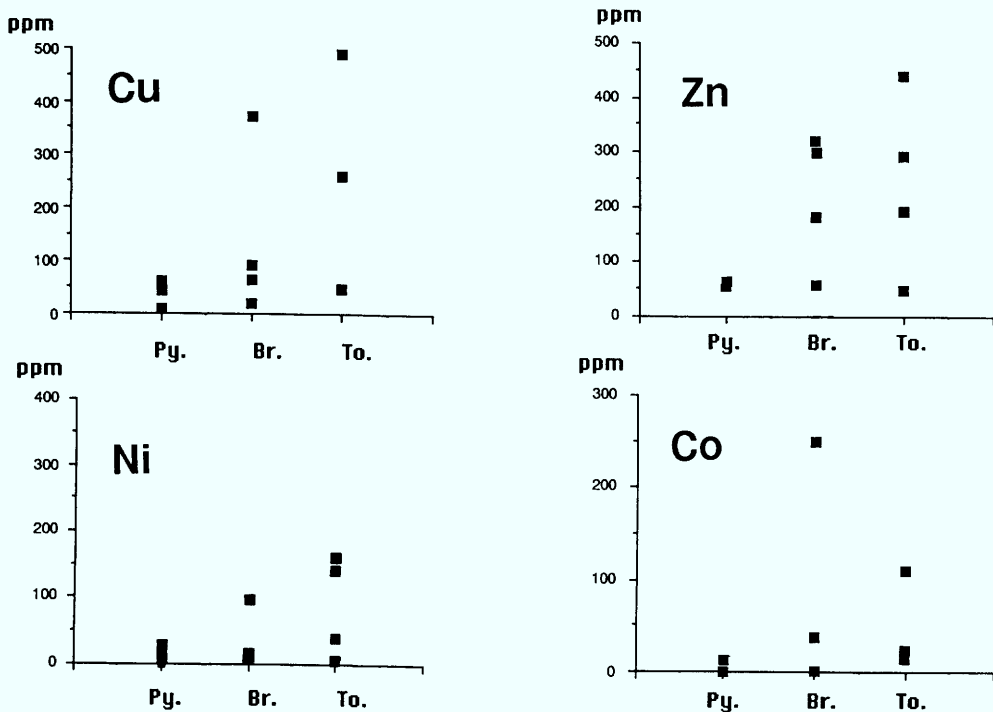


Fig. 8. Concentrations of Cu, Zn, Ni and Co in different mineral species of manganese oxide from Hokkaido. Py, pyrolusite; Br, birnessite and rancieite; To, todorokite.

manganese. On the other hand, todorokite and birnessite have structures capable of trapping trace elements (Burns and Burns 1977). The crystal structure of todorokite has space to hold large amounts of trace elements (Burns *et al.* 1983; Giovanoli 1985; Post & Bish 1988; Miura 1991). Birnessite has a layer structure consisting of $[\text{MnO}_6]$ layers separated on 7.2 Å. Between these two layers, H_2O and Ca exist. As the inter-layer distance of birnessite is smaller than that of todorokite (9.6 Å), the concentration of trace elements that exist in birnessite is lower than that of todorokite. The crystal structure of individual manganese oxide species controls the heavy metal element concentrations in manganese oxide deposit.

REE concentrations in manganese deposits

REE concentrations in manganese were very widely from very low concentrations such as in KG-1 and KG-4 to very high concentrations such as in TO-1, which are comparable to those of deep-sea manganese nodules. Chondrite-normalized REE patterns of AK-31-33

and NI-11 & 22 show a clear negative Ce anomaly. NI-32 and TO-1 show a clear positive anomaly and KG-6, and UK-1, 3 & 4 show neither a negative nor a positive anomaly (Fig. 9). Takematsu *et al.* (1989) pointed out that the incorporation of Ce into ferromanganese concretions is controlled by the redox potential of the depositional environment. The redox potential of hot-spring waters at the point where manganese oxides are precipitated are 0.29 V (AK-31), 0.13 V (UK-4) and 0.38 V (KG-1) and there is no clear relationship between the Ce anomaly and the redox potential. Hence, the Ce anomaly does not indicate the redox potential of the depositional environment. Manganese oxides of Akan-Yunotaki accumulated rapidly ($2-3 \text{ cm a}^{-1}$, Mita *et al.* 1994) and show a clear negative Ce anomaly. The deposits of UK-3, UK-4 and KM-4 are covered by moss indicating a slow depositional rate. These samples do not show any Ce anomaly. The difference in the Ce anomaly may therefore be a result of differences in the rate of deposition, similar to that found in Recent hydrothermal and hydrogenic manganese deposits described by Goldberg *et al.* (1963).

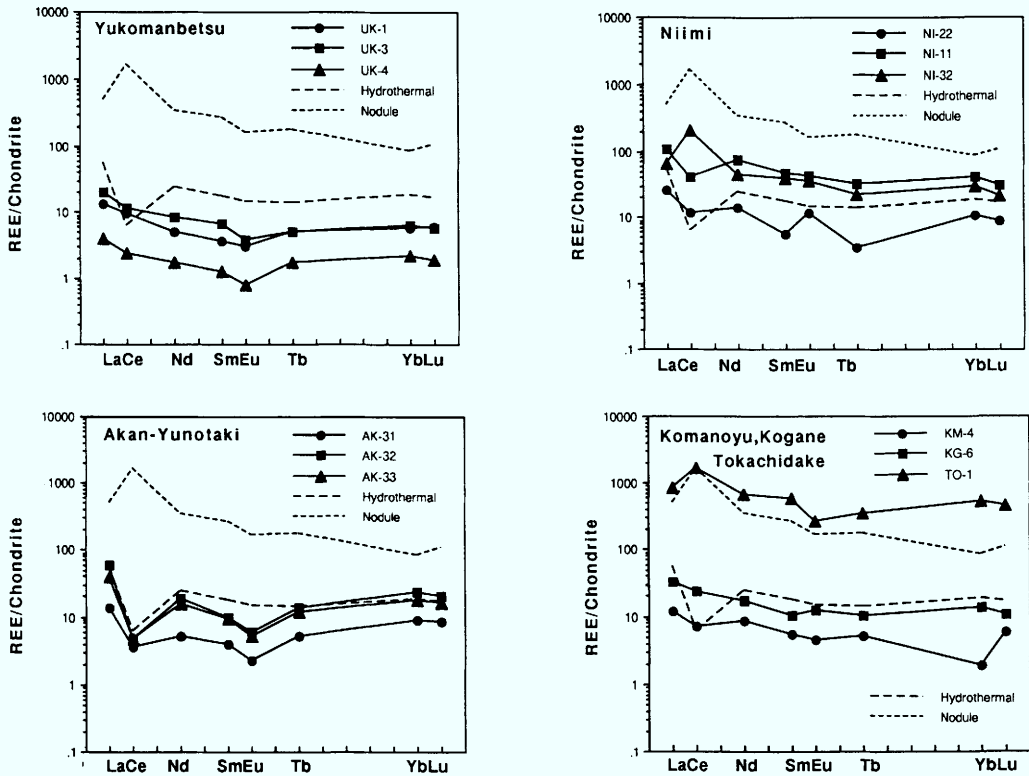


Fig. 9. Chondrite-normalized REE pattern of recent manganese deposits from Hokkaido. KG-1 and KG-4 are eliminated because their Nd and Tb concentrations are less than the detection limits. Hydrothermal and nodule data are quoted from Haskin *et al.* (1966) and Bender *et al.* (1971).

We wish to thank M. Tsutumi of Tokyo University for hydrogen isotope measurements and Y. Iwabuchi, M. Kamoi and M. Katake for chemical analyses of manganese oxides and hot-spring waters. Constructive suggestions by D. K. Mukhopadhyay of University of Roorkee and J. Ostwald of BHP Co. Ltd helped us to improve the manuscript.

References

- BENDER, M., BROECKER, W., GARNITZ, V., MIDDEL, U., KAY, R., SUN, S. S. & BISCAYE, P. 1971. Geochemistry of three cores from East Pacific Rise. *Earth and Planetary Science Letters*, **12**, 425–433.
- BURNS, R. G. & BURNS, V. M. 1977. Mineralogy of manganese nodules. In: GLASBY, G. P. (ed.) *Marine Manganese Deposits*. Elsevier, Amsterdam, 185–248.
- & — 1979. Manganese Oxides. Mineralogical Society of America short course notes. *Marine minerals*, **6**, 1–46.
- , — & STOCKMAN, H. W. 1983. A review of the todorokite-buserite problem: implications to the mineralogy of marine manganese nodules. *American Mineralogist*, **68**, 972–980.
- CHOI, J. H. & HARIYA, Y. 1990a. Trace element concentrations of manganese deposits in the Tokoro belt, Hokkaido, Japan. *Journal of Faculty of Science, Hokkaido University*, **22**, 553–564.
- & — 1990b. Geochemistry of manganese deposits in the Tiloro belt, north-eastern Hokkaido, Japan. *Mining Geology*, **40**, 159–173.
- CHUKHROV, F. V., GORSHKOV, A. I., RUDNITSKAYA, E. S., BEREZOVSKAYA, V. V. & SIVTSOV, A. V. 1979. New Mineral names, Vernadite. *American Mineralogist*, **64**, 1334.
- CRERAR, D. A., CORMICK, R. K. & BARNES, H. L. 1980. Geochemistry of manganese: An overview. In: VARENTSOV, I. M. & GRASSELLY, G. Y. (eds) *Geology and Geochemistry of Manganese*. E. Schweizerbart'sche Verlagsbuchhandlung, Stuttgart, **1**, 293–234.
- DOI, S. 1958. *Manganese deposits in the Imagane area*. Report of Geological Survey of Hokkaido, **20** [in Japanese].
- FUJIWARA, T. 1959. Recent manganese deposit on the northwestern slope of Mt. Tokachidake, Biei Town. *Bulletin of the Geological Survey of Hokkaido*, **21**, 61.

- GIOVANOLI R. 1985. A review of the todorokite-buserite problem: implications to the mineralogy of marine manganese nodules: discussion. *American Mineralogist*, **70**, 202–204.
- GOLDBERG, E. D., KOIDE, M., SCHMIT, R. A. & SMITH, R. H. 1963. Rare-earth distribution in marine environments. *Journal of Geophysics Research*, **68**, 4209–4217.
- HASKIN, L. A., WILDEMAN, T. R., FREY, F. A., COLLINS, K. A., KEEDY, C. R. & HASKIN, M. A. 1966. Rare earths in sediments. *Journal of Geophysical Research*, **71**, 6091–6105.
- HARIYA, Y. & KIKUCHI, T. 1964. Precipitation of manganese by bacteria in mineral springs. *Nature*, **202**, 416–417.
- & HARADA, Z. 1957. On manganese wads from some localities in Hokkaido, Studies on manganese oxide minerals (Report No. 1). *Journal of the Mineralogical Society of Japan*, **3**, 300–313 [in Japanese].
- , MIURA, H. & MITA, N. 1992. *Manganese and manganese-iron deposits of northeastern Hokkaido (CO4)*. 29th IGC Field Trip Guide Book, **6**, 1–15.
- IGARASHI, T. & YOKOTA, S. 1970. Quaternary Mineralization in the Niseko volcano area, western Hokkaido, Japan. *Bulletin of geological Survey of Japan*, **21**, 361–385 [in Japanese with English abstract]
- MATSUNAMI, T., WAKE, T., HAYAKAWA, F., FUTAMASE, T., YOKOYAMA, E., SAKOU, T., SAITO, N. & UCHIDA, Y. 1979. *Geothermal indications and hot springs of Hokkaido, Japan, (C)*; Central Hokkaido. Geological Survey of Hokkaido, Special Reports.
- MINATO, M. (ed.) 1977. *Japan and its nature*. Heibonsya, Tokyo [in Japanese].
- MITA, N., HARIYA, Y., USUI, A., MARUYAMA, A., HIGASHIHARA, T., NAKAJIMA, T., KANAI, Y., MIURA, H. & ITO, T. 1994. A living manganese deposit, the Yuno-Taki Falls. *Journal of the Geological Society of Japan*, **100**, XXV–XXVI [in Japanese].
- MIURA, H. 1991. Structure model of todorokite. *Journal of Faculty of Science, Hokkaido University, Series. IV*, **23**, 41–51.
- , ONISHI, M., CHOI, J. H. & HARIYA, Y. 1992. Geochemical study of Manganese oxide deposits in the Setana area, southwestern Hokkaido, Japan. *Mining Geology*, **42**, 165–173 [in Japanese with English abstract]
- POST, J. E. & BISH, D. L. 1988. Rietveld refinement of the todorokite structure. *American Mineralogist*, **73**, 861–869.
- SAITO, M. 1951. Geology of the upper Fujikoto-river district, northern Akita prefecture. *Bulletin of Geological Survey of Japan*, **2**, 247–253 [in Japanese with English abstract].
- 1954. *Goethite, manganese and sulfur deposits in the Niseko area*. Reports of Geological Survey of Hokkaido, **16** [in Japanese].
- SAKOU, S., WAKE, T., HAYAKAWA, F., FUTAMASE, T., YOKOYAMA, E., MATSUNAMI, T., SAITO, N. & UCHIDA, Y. 1977. *Geothermal indications and hot springs of Hokkaido, Japan, (B)*; Niseko Area. Geological Survey of Hokkaido, Special Reports **4**.
- TAKEMATSU, N., SATO, Y. & OKABE, S. 1989. Mechanisms of incorporation of rare earth elements into ferromanganese concretions. *La Mer*, **27**, 41–52.
- TERASHIMA, S. 1970. Determination of sodium, potassium, magnesium, calcium, manganese and iron in the silicate rocks and terrestrial water by atomic absorption spectrophotometry. *Bulletin of the Geological Survey of Japan*, **21**, 693–707.
- UMEMOTO, S., MATSUMURA, A., YAMAYA, M. & ISHIBASHI, Y. 1956. Sulphur, iron and manganese deposit around the Mt. Meakan-dake. *Bulletin of the Geological Survey of Hokkaido*, **24**, 21–35 [in Japanese].
- UENO & IGARASHI, 1957. Sulphur and bog-iron deposits in the Daisetzu and Tokachi area. *Bulletin of the Geological Survey of Hokkaido*, **32**, 1–24 [in Japanese].
- USUI, A. & MITA, N. 1995. Geochemistry and mineralogy of a modern buserite from a hot spring in Hokkaido, Japan. *Clay and clay Minerals*, **43**, 116–127.
- WHITE, D. E. 1967. Some principles of geyser activity, mainly from Steamboat springs, Nevada. *American Journal of Science*, **265**, 641–684.
- YAMAGUCHI, S., SAKAI, A. & IGARASHI, T. 1977. *Investigation report of hydrothermal alteration haloes – Mt. Obira. An investigation report of the exploitation of geothermal energy resources*. **8** [in Japanese].
- YOSHIMURA, T. 1952. *Manganese Deposits in Japan*. Kyushu University, Fukuoka, [in Japanese].
- 1967. *Supplement to Manganese Deposits in Japan, part 1*. Special Issue No. 1 of the Science Reports of the Faculty of Science, Kyushu University, Geology, **9** [in Japanese].
- 1969. *Supplement to Manganese deposits in Japan, part 2*. Special Issue No. 2 of the Science Reports of the faculty of Science, Kyushu University. Geology, **9** [in Japanese].

Formation of solid phases of manganese in oxygenated aquatic environments

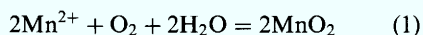
LEV M. GRAMM-OSIPOV

Pacific Oceanological Institute, Far Eastern Branch, Russian Academy of Sciences, Vladivostok 690041, Russia

Abstract: The article describes a thermodynamic analysis of the formation process of solid manganese phases in oxygenated aquatic environment. The first step of this process is the formation of the compound MnOOH. In the second step the latter in a disproportionation reaction is transformed into a complicated oxhydroxide $[(\text{MnO}_2)_{2n-3} (\text{MnOOH})_{4-2n}]$ with O/Mn ranging from 1.700 to 1.999. As an example of using results of thermodynamic analyses the behaviour Mn system in the ocean is described. It is shown that Mn_3O_4 and MnOOH respectively control concentrations and distribution of the manganese in the upper (150–600 m) and lower oceanic water column.

There is considerable interest in understanding manganese behavior and formation of its solid phases in oxygenated aquatic environments, as these phases form terrestrial ore deposits and nodules and crusts in the ocean. Various hypothesis have been proposed to explain the origin of manganese solid phases. In this paper an attempt is made to approach the problem by physico-chemical analysis of the origin of solid Mn-phase formations in oxygenate aquatic environments.

Notwithstanding a wide range of manganese mineral varieties found in the nature (e.g. pyrolusite, ramsdellite, vernadite, buserite 1 and 2 asbolanbuserite, birnessite 1 and 2, and todorokite (Gramm-Osipov *et al.* 1989) their chemical composition is given by the formula MnO_2 . However this formula is only a first approximation and represents the composition of the minerals and their artificial analogs (Rode, 1952; Giovanoli, 1969). In this paper, the oxidation number (degree of oxidation) n (O/Mn) of the oxide is 2, and a charge on manganese is +4. Yet complete stoichiometry in these compounds is not achieved and oxidation number ranges from 1.800 to 1.999. Investigations of Mn dioxide have shown (Rode, 1952) that these compounds have properties of polymorphism and nonstoichiometry. The region of homogenic of the same compounds depends on type of crystalline lattice (Euler 1982), and the oxidation number for some modifications is able to change from 1.5 to 2.0 (Vetter 1961). Thus, manganese in the minerals has a charge of +4 and less. Thus the reaction:

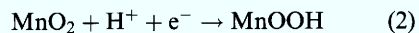


governs neither the process of nonstoichiometric manganese oxide formation nor Mn concentrations in the natural waters. For example, the

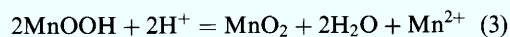
equilibrium concentrations in the ocean calculated from this formula are 10^4 – 10^5 times higher than those observed (Sillen 1961; Gramm-Osipov & Shul'ga 1980). Thus, one of the most important problems in the geochemistry of manganese in aquatic environment is to select the solid phase that would control the concentration and distribution of the element in natural waters, and to understand the mechanism for the formation of nonstoichiometric manganese oxides compositionally close to MnO_2 .

Manganese solid phase formation

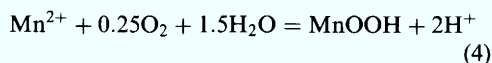
Electrochemical studies show (Kozawa & Yeager 1965; Kozawa & Powers 1967, 1968; Gabano *et al.* 1967; Maskell *et al.* 1981) that during cathode reduction of σMnO_2 (and other modifications) the compound MnOOH is formed:



The reaction proceeds with no manganese ions transferring into solution. Chemical reduction of Mn dioxides also occurs in the homogenic phase and results in MnOOH formation (Feitknecht *et al.* 1960; Giovanoli *et al.* 1968; Maskell *et al.* 1981). This testifies that Mn has a valence of +3 and +4 in nonstoichiometric dioxides (Caudle *et al.* 1973; Tye 1976, 1985). In addition it has been found (Vetter, 1961) that manganese oxide can be in equilibrium with the electrolyte Mn^{2+} and H^+ pre-set concentrations only if it has a definite oxidation number n . Provided that the initial degree of oxidation (n^*) is higher (or lower) than equilibrium n , then n^* will change until equilibrium n is achieved. These changes are associated with the disproportionation reaction in the system:



The change of oxidation state in manganese oxide with ions Mn^{2+} and H^+ activity in the solution suggests (Tishchenko & Gramm-Osipov 1985) that manganese solid phase formation in the nature waters should be a two-step process. First, the compound $MnOOH$ is formed:



The compound $MnOOH$ has degree of oxidation $n = 1.5$, but with respect to Mn^{2+} concentrations and pH in the solution, n in freshly precipitated $MnOOH$ increases up to 1.800–1.999, that is it forms a nonstoichiometric compound because of disproportionation reaction (3). The reaction (3) is a second stage formation of solid phase in aqueous solution. The thermodynamic formation of the same nonstoichiometric solid phase was carried out (Tishchenko & Gramm-Osipov 1985; Tishchenko *et al.* 1985) on the example of γMnO_2 which was well investigated by Tye (1976). As was shown by Tye (1976), γMnO_2 in the homogenic region is like a solid electrolyte with ions Mn^{4+} , Mn^{3+} , O^{2-} and OH^- . This solid electrolyte can be expressed as MnO_2 and $MnOOH$ components. The formula of this compound is $\gamma[(MnO_2)_{2n-3}(MnOOH)_{4-2n}]$, where $2 \geq n \geq 1.5$. The chemical potentials of the components of this solid solution are

$$\mu_{MnO_2} = \mu_{MnO_2}^\circ + RT \ln(2n-3)(n-1)^2 \quad (a)$$

$$\mu_{MnOOH} = \mu_{MnOOH}^\circ + RT \ln(4-2n)^2(2n-2) \quad (b)$$

In these equations included within the (ln) symbol the activity of corresponding components are as follows: in (a) this is $a_{Mn^{4+}}$ and $a_{O^{2-}}$ in (b) $a_{Mn^{3+}}$, $a_{O^{2-}}$, a_{OH^-} , where n is the oxidation number n , R is the gas constant and T is the temperature in Kelvin.

Standardization of chemical potentials in (a) and (b) were carried out with $\mu_{MnO_2}^\circ$ and μ_{MnOOH}° as the Gibbs free energy of formation the oxides from pure matter, when $n = 2$, and 1.5, that is as solid solution is transformed in pure MnO_2 and $MnOOH$. From reaction (3) and equations (a) and (b) it is possible to get analytical expression which will connect the degree of oxidation (n) of solid solution $\gamma[(MnO_2)_{2n-3}(MnOOH)_{4-2n}]$ with pH and concentration of Mn^{2+} ions in the liquid phase:

$$(2-n)^4/(2n-3) = (a_{Mn^{2+}}/64a_{H^+}^2) \times \exp[2\Delta G_{H_2O}^\circ + \Delta G_{Mn^{2+}}^\circ + \Delta G_{MnO_2}^\circ - 2\Delta G_{MnOOH}/RT] \quad (5)$$

where $\Delta G_{MnO_2}^\circ$ and ΔG_{MnOOH}° are the standard Gibbs free energies of formation of corresponding pure components, which form solid solution, $\Delta G_{H_2O}^\circ$ and $\Delta G_{Mn^{2+}}^\circ$ are standard Gibbs free energies of formation water and Mn^{2+} . After inserting ΔG° numbers (Table 1) of each components into reaction (3) equation (4) at $T = 298.15$ K, $P_{tot} = 1$ atm becomes:

$$\ln(a_{Mn^{2+}}/a_{H^+}^2) = 25.056 + \ln[(2-n)^2/(2n-3)] \quad (6)$$

Tye (1976) has determined standard Gibbs free energies of $MnOOH$ (he named this compound

Table 1. Thermodynamica data

Formula	State	$-\Delta G_{298}^\circ$ (kJ mol ⁻¹)	$-\Delta H_{298}^\circ$ (kJ mol ⁻¹)	S_{298}° (J/mol ⁻¹)	V_{298}° (cm ³ mol ⁻¹)	References
O _{2w}	Oxygen, in water solution	-16.318	11.715	110.876	32	1
H ₂ O	Water, liquid	237.191	285.851	-69.998	18.063	1
H ⁺	Aqueous	0.000	0.000	0.000	0.000	1
OH ⁻	-	137.293	229.994	10.753	-3.98	1
Mn ²⁺	-	227.610	223.007	-83.68	-17.60§	2
Mn ³⁺	-	81.923*				
Mn ⁴⁺	-	-74.852†				
δMnOOH	Solid	553.543	623.92		20‡	3
MnO ₂	Solid	456.893	511.10			3
Mn ₃ O ₄	Solid	1280.304	1386.578		47.28‡	2

* Our calculation from $E_{Mn^{3+}/Mn^{2+}}^\circ$ (Sukhotin 1981).

† Our calculation from $E_{Mn^{4+}/Mn^{3+}}^\circ$ (Vetter 1961).

‡ Gramm-Osipov *et al.* (1989).

§ Milero (1971).

References: 1, Naumov *et al.* (1971); 2, Latimer (1952); 3, Tye (1976).

σMnOOH) and MnO_2 in solid solution $\gamma[(\text{MnO}_2)_{2n-3}(\text{MnOOH})_{4-2n}]$. This equation is deduced only for γMnO_2 . It will be different for other modifications of manganese dioxides, which require other solid solution models. However, their behaviour will not differ from that of γMnO_2 at the same concentrations of Mn^{2+} and H^+ ions in the solution.

The above shows that the behaviour on manganese dioxides in aqueous solution is not described by reaction (1), which is usually employed to describe the formation of those compounds, as it does not reflect the processes that occur in the system. In reaction (1) the degree of oxidation remains 2 for any Mn^{2+} and H^+ contents in the solution, which is not so as shown above. Further, there are reasons for thinking that reaction (1) does not occur at all (Tye 1976). When manganese dioxides react with solutions, we need to consider reaction (3), analysis of which gives equation (6). Equation (6) is tested by experiments described below. The experiment (Table 2) was designed as follows. We prepared a series of MnCl_2 solutions with given pH and concentrations, which were used to treat solid γMnO_2 . After interaction of a solid phase with the solution, the Mn content and pH of the latter were determined. Then the solution was removed and the solid was treated with a new batch of the initial solution. This procedure was continued until there was no difference between the compositions of the treated and initial solutions. We then determined the degree of oxidation in the solid.

Table 2 shows that the agreement between the calculated and observed concentrations is satisfactory. An exact agreement is difficult to attain because equation (6) has been deduced on the assumption that $\gamma[(\text{MnO}_2)_{2n-3}(\text{MnOOH})_{4-2n}]$ is an ideal solid solution. Nevertheless it describes quite satisfactorily the relation between Mn^{2+} and H^+ in the solution on the one hand and n in the solid on the other. The experiment showed

that 'high solubility' (Savenko 1985, 1990; Swain *et al.* 1975) is displaced not by MnO_2 , the compound with a stoichiometry of 2, but by manganese oxide with a particular degree of oxidation for particular concentrations of Mn^{2+} and H^+ in the solution. Neglect of this has led the authors of (Savenko 1985, 1990; Swain *et al.* 1975) to erroneous conclusions. They used a non-stoichiometric oxide (they neglected the deviation from stoichiometry) and assigned it the formula MnO_2 on the assumption that the composition of the compound did not alter during the experiment and that equilibrium is established relative to MnO_2 . Errors of that kind had been made previously, which led Latimer (1954) to note that the difficulties in researching the reaction (1) system (written, it is true, as a half-reaction) arise not from its being irreversible, but from differences in the thermodynamic parameters of different manganese dioxide specimens.

Above we have discussed a theoretical approach to the problem formation of some manganese solid phases whose composition is close to MnO_2 in oxygenated aquatic environment. Below we will show how it was used to describe the problem formation of oceanic nodules and crusts.

In order to understand the process of Mn nodule formation, it is necessary to find solid phases of manganese and the reactions governing their formation, which may describe the distribution and concentration of this element in the oceanic water column. It is essential to define physico-chemical conditions in environments where nodules and crusts develop and to assess whether or not oceanic water is saturated with manganese in relation to minerals of nodules.

Thermodynamics data

To calculate chemical equilibrium we used thermodynamic equilibrium constants (K_{298})

Table 2. Equilibrium Mn concentrations in a solution in contact with γMnO_2

Degree of oxidation	pH	Activity coefficient	Mn concentration (M)	
			Observed	Calculated
1.938	3.33	0.611	0.0503	0.460
1.927	3.44	0.607	0.284	0.550
1.920	4.30	0.674	0.0142	0.0138
1.919	4.52	0.705	0.0057	0.0051
1.925	4.62	0.666	0.0147	0.0024
1.891	4.90	0.689	0.0108	0.0032
1.647	7.86	0.741	0.0000020	0.00000103
1.519	7.90	0.660	0.0000051	0.0000258

deduced from the known ratios (Lewis & Randal 1961):

$$\ln(K_{298} = -\Delta G_r^\circ / RT$$

where: ΔG_r° is the change in Gibbs energy in the reaction ($T = 298 \text{ K}$, $P = 1 \text{ atm}$), R is the gas constant and T is the temperature in Kelvin.

The equilibrium constant in the reaction at temperature T was calculated by Vant-Hoff isotherm (Garrels & Christ 1965) considering that temperature in oceanic conditions has a narrow range (0–30°C) and any drastic change in warmth capacity can be assumed to be zero:

$$\ln(K_T / K_{298}) = -\Delta H_{298} / R(1/T - 1/298.15)$$

where ΔH_{298} = change in enthalpy in the reaction under standard conditions. The thermodynamic constants used for the analyses are given in Table 1. Using Kharapetjants' method (Karapetjants 1965) (bond $\Delta G^\circ - \Delta H^\circ$), we obtained (Gramm-Osipov *et al.* 1989) enthalpies metahydroxide of Mn (III). This allowed us to study the Mn system under *in situ* conditions.

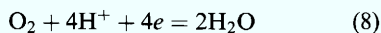
To correct for the effect of temperature on molal volume Mn^{2+} and isothermic compressibility we used the relationships given in Millero (1982). To estimate the effect of temperature and pressure on pure water molal volume we (Gramm-Osipov *et al.* 1989) used the IUPAC density equation (Anon 1982).

Physico-chemical environment

The major geochemical environment, that Fe–Mn crusts are formed, is known to be oxidizing conditions (Strakhov 1976). As a proof of the oxidizing nature of seawater, some researchers have provided data not only on concentrations of oxygen dissolved in seawater (2.8–8.0 ml/l⁻¹), but also on oxidation potentials (0.25–0.45 V) measured with a platinum electrode (Baas-Becking *et al.* 1960). However it was shown (Peshchevitsky *et al.* 1970; Gramm-Osipova 1982), that this potential is stationary, and cannot be used for physicochemical calculations. True oxidation potential (more correctly equilibrium) is deduced from the formula (Peshchevitsky *et al.* 1970; Gramm-Osipova 1982):

$$\text{Eh} = E^\circ - 0.059 \text{ pH} + 0.0147 \log P_{\text{O}_2} \quad (7)$$

where: P_{O_2} = partial pressure of oxygen; E° = standard potential of reaction



With $T = 298 \text{ K}$, $P_{\text{tot}} = 1 \text{ atm}$, $P_{\text{O}_2} = 0.21 \text{ atm}$ and pH 8, oxidation potential equals 0.74 V. At

the depth of 6000 m ($P_{\text{tot}} = 600 \text{ atm}$, $T = 273 \text{ K}$) it equals 0.81 V (Gramm-Osipov *et al.* 1983). As the oxidation potential in sea water is given by the redox system (8), so thermodynamic analysis of the manganese system in the ocean in the present work is made through the reaction of its direct interaction with the system (8).

Bottom sediments underlying nodules are also characterized by oxidizing conditions – no reduction processes take place at their depths, the oxidation potential measured by the platinum electrode is 0.5–0.6 V (pH 6.8–7.8) (Zheleznova & Shishkina 1964; Hartman & Muller, 1982). The application of the technique for potential-measurements with the help of mediators (ferri-ferrocyanide system, Shultz *et al.* 1984) makes it possible to prove that equilibrium potentials are 80–100 mV higher than in direct measurements (Pisarevsky *et al.* 1989). Besides it has been shown that the solid phase of pelagic sediments is oxidative as opposed to pore water. That invokes a conclusion that oxidation potential in strongly oxidized pelagic sediments is determined by the heterogenic redox system MnO_2 (sediment)/ Mn^{2+} (interstitial water) (Pisarevsky *et al.* 1989).

Manganese in sea water

Dissolved manganese in oceanic water ranges from 0.2 to 5.0 nmol kg⁻¹ and averages 0.5 nmol kg⁻¹ (Bruland 1983). In recent years the most important discovery on manganese distribution in water column has been its high concentration in the oxygen-minimum layer (Klinkhammer & Bender 1980; Bruland 1983; Martin *et al.* 1985). As we know, there is a surface maximum of 0.8–2.3 nmol kg⁻¹ seawater; subsurface minimum of 0.24 nmol, maximum concentration related to the oxygen minimum is 3.7 nmol, at depths of over 2000 m manganese concentration is about 0.5 nmol kg⁻¹ sea water. Particulate manganese occurs throughout the oceanic water column.

From the Eh–pH plot of Mn-ion stability (Fig. 1) it follows that Mn^{2+} is the most common oxidation state of dissolved Mn in oceanic water. Our experiments also support this conclusion (Gramm-Osipov *et al.* 1991, 1992). Therefore it is conceivable that Mn dissolved in oceanic water occurs in the form of Mn(II) compounds. An assessment of possible influence of dissolved organic matter on the distribution of manganese-forms in seawater shows that manganese metal–organic compounds are insignificant (Gramm-Osipov *et al.* 1989). Direct analytical determinations are also in good agreement with

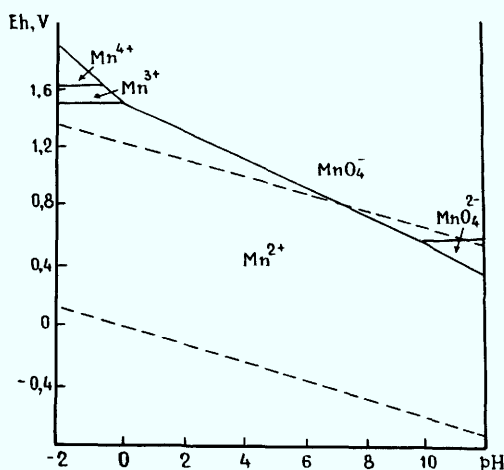


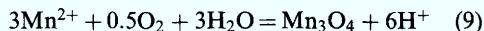
Fig. 1. Eh-pH stability diagram of Mn ions in water solution for 25°C and 1 atm.

this conclusion (Bruland 1983). Calculations show that 90% of dissolved manganese is in form of Mn^{2+} ions and $MnCl^+$ (Gramm-Osipov & Shul'ga 1980; Gramm-Osipov *et al.* 1989).

Manganese solid phase formation in the ocean

It has been found experimentally (Giovanoli *et al.* 1976; Hem & Lind 1983; Murray *et al.* 1985) that at the temperatures of 20–25°C

the primary oxidation product of Mn(II) is Mn_3O_4



below 10°C- $MnOOH$ (Hem & Lind 1983; Hem *et al.* 1982).

That is why the description of Mn depth-variation was made for Mn_3O_4 and $\sigma MnOOH$. The latter is a final product of chemical and electrochemical reduction of γMnO_2 (nsutite) for which we obtained equation (6). Solid phases of manganese are formed in the ocean most probably in the way typical of γMnO_2 with the only difference in quantity. The required data on distribution of pH, O_2 , manganese, temperature, and depths for which our calculations are made, have been taken from GEOSECS stations (Klinkhammer & Bender 1980). Keeping all the aforementioned in mind equilibrium manganese concentrations are calculated from reactions (6) and (9), using an activity coefficient of Mn^{2+} equal to 0.210 (Whitfield 1975).

It is shown in Fig. 2, that in the upper (150–600 m) ocean horizons (where the temperature is over 10°C) manganese concentrations computed against Mn_3O_4 are 0.76–3.36 $nmol\ kg^{-1}$ and differ from those defined analytically by 0.3–2.0 $nmol$. At lower horizons (temperature is below 10°C) equilibrium concentrations computed against $\sigma MnOOH$ are about 0.8–8.3 $nmol\ kg^{-1}$ and differ from those observed by 0.45–4.0 $nmol$. As to the dissolved manganese distribution obtained through chemical analysis (Klinkhammer & Bender 1980)

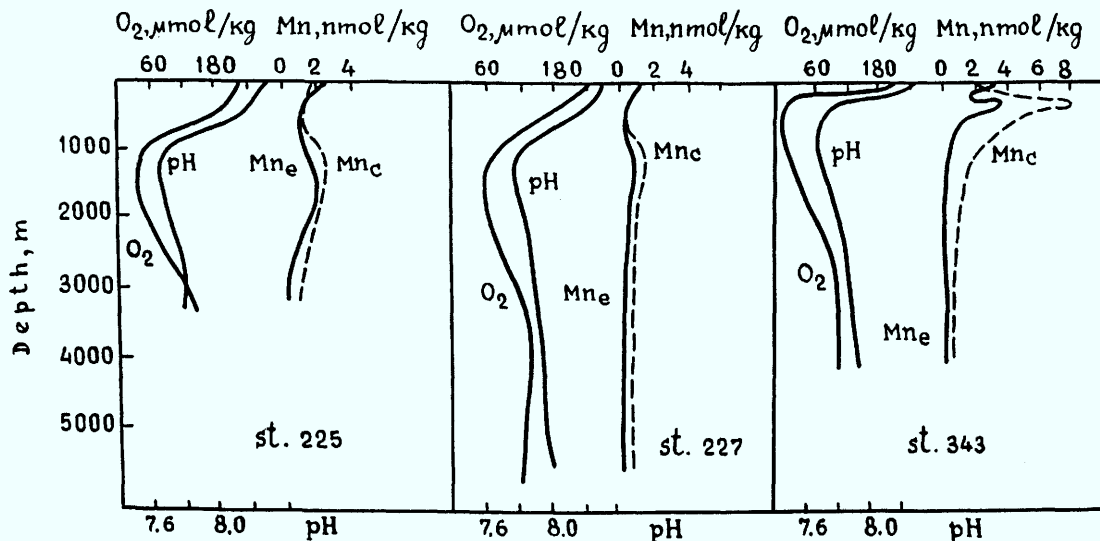


Fig. 2. Distribution of dissolved manganese in seawater column (concentration of manganese: Mn_c , calculated (Gramm-Osipov *et al.* 1989); Mn_e , analytically determined (Klinkhammer & Bender 1980)).

and through computation, it is practically the same. This indicates that we have made a correct choice of the controlling reactions (6) and (9). Fresh metahydroxide σMnOOH transforms through the reaction (3) into a complicated oxohydroxide with oxidation number (n) 1.800–1.999. As for the discrepancy between the computed manganese concentrations and those observed, they are due to the uncertainty in the calculated activity coefficient of Mn^{2+} , pH, O_2 , manganese, ΔH° values of σMnOOH , and, largely, to insufficient data on Gibbs' energies of natural MnOOH . Oxidation number measurements in particulate matter from offshore Canada equaling 1.500–1.700 (Grill 1982) sustain the suggestion that it is MnOOH that is the early stage of solid Mn oxide formation in the ocean (below 150–600 m).

Manganese in diagenetic processes

It has been said above that the use of mediators make it possible to obtain equilibrium Eh values in strongly oxidized pelagic sediments underlying Fe–Mn nodules, and that $\text{MnO}_2/\text{Mn}^{2+}$ is a potential-defining system there. As a result it becomes possible to calculate manganese concentrations in the pore waters of these accumulations, based on published electrochemical properties of manganese dioxide electrode (Tye 1976, 1985). According to these views, the

oxidation potential in the system $\text{MnO}_2/\text{Mn}^{2+}$ is given by the reaction (2). In turn, the degree of oxidation of manganese oxide (i.e. sediment) depends on concentrations of Mn^{2+} and H^+ in the solution (reaction 3). With data available on Eh, pH and n values the Mn^{2+} concentrations in solution are deduced:

$$\begin{aligned} \text{Eh} = & (\Delta G_{\text{sample}} - \mu_{\text{MnO}_2}^\circ - 2\mu_{\text{H}_2\text{O}}^\circ)/2(n-1)F \\ & - [n\Theta/(n-1)]\text{pH} \\ & - [\Theta/2(n-1) \times \log a_{\text{Mn}^{2+}}] \end{aligned}$$

where:

$$\begin{aligned} \Delta G_{\text{sample}} = & (2n-3)\mu_{\text{MnO}_2}^\circ + (4-2n)\mu_{\text{MnOOH}}^\circ \\ & + RT[(2n-3)\ln(2n-3) \times (n-1)^2 \\ & + (4-2n)\ln(4-2n)^2(2n-2)] \end{aligned}$$

and $\Theta = 2.303RT/F$. F is the Faraday constant.

The data of measurements Eh, pH, degree of oxidation and concentrations Mn in interstitial water of red clays are presented in Table 3 (Pisarevsky *et al.* 1989). A correlation between the results of calculation with analytically defined Mn concentrations in pore water of pelagic clays is satisfied.

Summary

As it was shown above there are strong reasons to think that the formation process of

Table 3. Redox potential, pH, degree of oxidation (n), and concentration of manganese in interstitial water of pelagic (red clays) sediments

Station no. and depth horizon (cm)	Eh (direct measurements by Pt electrode) (mV)	Eh (by mediator) (mV)	pH	n	Concentration of Mn (nmol l ⁻¹)	
					Calc.	Meas.
838 (0–1)	543	630	7.34	1.69	154	35.6
858 (1–2)	565	664	7.40	1.90	12	16
860 (46–49)	569	650	7.31	1.98	21.9	41.7
(200)	530	651	7.10	1.94	42	23
861 (15)	560	650	7.30	1.94	71	55
870 (0–3)	479	650	7.36	1.83	17.8	27.8
(52)	555	670	7.15	1.92	68	53
874 (0–1)	582	645	7.34	1.78	62.9	24
(9–10)	574	665	7.34	1.89	6.2	62
880 (2–3)	556	651	7.38	1.82	14.3	15.3
881 (7)	560	645	7.45	1.78	50	24

manganese solid phases in oxygenated aquatic environments is two stage. In the first stage formation of compound MnOOH take place. During second stage the latter in a result disproportionation reaction is transformed into a complicated oxhydroxide $[(\text{MnO}_2)_{2n-3}(\text{MnOOH})_{4-2n}]$ with O/Mn ranging from 1.700 to 1.999. In the example of the behaviour of Mn system in the ocean, it was shown that Mn_3O_4 and MnOOH are compounds controlling concentrations and distribution of the manganese in the upper (150–600 m) and lower oceanic water column respectively. Physico-chemical analysis of the manganese system in pore water of bottom sediments have shown that the source of Mn is manganese oxides that are formed in sea water. As they enter the sediment and get buried at a pH lower than in sea water, the disproportionation reaction continues to deepen causing a consequent 'discharge' of manganese into pore water and an increase in Mn concentration.

References

- ANON, 1982. On the introduction of the Practical salinity scale, 1978 and new International equation at the sea water state, 1980. *Oceanology*, **22**, 337–343.
- BAAS-BECKING, L. G. M., KAPLAN, I. E. & MOORE, D. 1960. Limits of the natural environment in terms of pH and oxidation-reduction potentials. *Journal of Geology*, **8**, 243–284.
- BRULAND, K. W. 1983. Trace elements in seawater. In: RILEY, G. P., CHESTER, R. L. *et al.* (eds) *Chemical Oceanography*. Academic Press, **8**, 157–221.
- CAUDLE, J., SUMMER, K. G. & TYE, F. L. 1973. Manganese dioxide electrode. Part 2. Hydrogen ion Response in the Presence of Manganese (II) ions. *Journal of the Chemical Society Faraday Transactions*, **69**, 885–893.
- EULER, K. J. 1982. Manganese dioxide in dry cell electrodes. *Materials Chemistry*, **7**, 291–312.
- FEITKNECHT, W., OSWALD, H. R. & FEITKNECHT-STEINMAUN, U. 1960. Über die topochemische einphasige Reduction von γMnO_2 . *Helvetica Chimia Acta*, **43**, 1947–1950.
- GABANO, J. P., MORIGNAT, B. & LAURENT, J. F. 1967. Chemical and Electrochemical Reductions of Manganese dioxide. *Electrochemistry Technology*, **5**, 531–535.
- GARRELS, R. M. & CHRIST, C. J. 1965. *Solutions, Minerals and Equilibria*. Harper and Row, New York.
- GIOVANOLI, R. 1969. A simplified scheme for polymorphism in the manganese dioxides. *Chimia*, **23**, 470–472.
- , BERNHARD, K. & FEITKNECHT, W. 1968. Über ein- und zweiphasige Reduction von MnO_2 durch Zimtalkohol. *Helvetica Chimia Acta*, **51**, 355–366.
- , FEITKNECHT, W., MAURER, R. *et al.* 1976. Über die Reaction von Mn_3O_4 mit Sauren. *Chimia*, **30**, 307–309.
- GRAMM-OSIPOV, L. M. & SHUL'GA, YU. M. 1980. Elements of Manganese Equilibrium in Ocean Water. *Geochemistry International*, **17**, 134–140.
- , BYCHKOV, A. S., VOLKOVA, T. I., TISHCHENKO, P. YA. & SHUL'GA, YU. M. 1983. Ferrum-manganese nodules as products of sedimentation and diageneses (physico-chemical analyses). *Dokladi Akademii Nauk SSSR*, **270**, 1471–1474 [in Russian].
- , VOLKOVA, T. I. & CHICHKIN, R. V. 1992. Laboratory data on the Behavior of Manganese dioxide in Aqueous Solution. *Geochemistry International*, **7**, 28–36.
- , SHARIPOV, R. Z. & VOLKOVA, T. I. 1991. Oxidation states of Mn in Aqueous solution. *Geochemistry International*, **2**, 151–154.
- , TISHCHENKO, P. YA., STASHCHUK, M. F., VOLKOVA, T. I. *et al.* 1989. Ferrum-manganese system. In: ILYICHEV, V. I. (ed.) *Chemistry of sea water and authigenic mineralization*. Science, Moscow, 112–203 [in Russian].
- GRAMM-OSIPOVA, V. N. 1982. On oxidation-reduction potential of oceanic water. *Dokladi Akademii Nauk SSSR*, **267**, 457–459 [in Russian].
- GRILL, K. V. 1982. Kinetic and thermodynamic factors controlling manganese concentrations in oceanic waters. *Geochimica et Cosmochimica Acta*, **46**, 2435–2446.
- HARTMANN, M. & MULLER, P. J. 1982. Trace metals in interstitial waters from central Pacific Ocean sediments. In: FANNING, U. A. & MANHEIM, F. T. (eds) *The dynamic environment of the ocean floor*. Heath and Co., Lexington (Mass.), 285–301.
- HEM, J. D. & LIND, C. J. 1983. Nonequilibrium models for predicting forms of precipitated manganese oxides. *Geochimica et Cosmochimica Acta*, **47**, 2037–2046.
- , ROBERSON, C. E. & FOURNIER, R. B. 1982. Stability of MnOOH and Manganese Oxide Deposition from Springwater. *Water Resource Research*, **18**, 563–570.
- KARAPETJANTS, M. KH. 1965. *Methods of comparative calculation of physico-chemical properties*. Science, Moscow [in Russian].
- KLINKHAMMER, G. P. & BENDER, M. L. 1980. The distribution of manganese in the Pacific Ocean. *Earth and Planetary Science Letters*, **66**, 361–384.
- KOZAWA, A. & POWERS, R. A. 1968. The manganese dioxide electrode in alkaline electrolyte; the electron-proton mechanism for the discharge process from MnO_2 to $\text{MnO}_{1.5}$. *Journal of the Electrochemistry Society*, **113**, 870–878.
- & —— 1967. Cathodic reduction of βMnO_2 and γMnO_2 in NH_4Cl and KOH electrolytes. *Electrochemistry Technology*, **5**, 535–541.
- & YEAGER, J. F. 1965. The cathodic reduction mechanism of electrolytic manganese dioxide in alkaline electrolyte. *Journal of the Electrochemistry Society*, **112**, 959–963.

- LATIMER, W. M. 1952. *Oxidation Potentials* (2nd edition). Prentice-Hall.
- LEWIS, G. N. & RANDALL, M. 1961. *Thermodynamics* (2nd ed. revised by Pitzer, K. S. & Brewer, Z.), McGraw-Hill, New York.
- LAWN, D. A., THIRSK, H. R. & WYNNE-JONES, L. 1968. Effect of pressure on ionization equilibria in water at 25°C. *Transaction of the Faraday Society*, **64**, 2073–2080.
- MARTIN, J. H., KNAUER, G. A. & BROENKOW, W. W. 1985. VERTEX: the lateral transport of manganese in the northeast Pacific. *Deep-sea Research*, **32**, 1405–1427.
- MASKELL, W. C., CHAW, J. E. & TYE, F. L. 1981. Manganese dioxide electrode – IV. Chemical and electrochemical reduction of an electrolytic γ -MnO₂. *Electrochimica Acta*, **26**, 1403–1410.
- MILLERO, F. J. 1971. The molal volumes of electrolytes. *Chemical Reviews*, **71**, 147–176.
- 1982. The effect of pressure on solubility of minerals in water and sediments. *Geochimica et Cosmochimica Acta*, **46**, 11–22.
- MURRAY, J. W., DILLARD, J. G., GIOVANOLLY, R. et al. 1985. Oxidation of Mn(II): initial mineralogy, oxidation state and aging. *Geochimica et Cosmochimica Acta*, **49**, 463–470.
- NAUMOV, G. B., RYZHENKO, B. N. & KHODAKOVSKY, I. L. 1971. *Reference book of thermodynamic constants (for geologists)*. Atomizdat, Moscow [in Russian].
- PESHCHEVITSKY, V. I., ANOSHCHIN, G. N. & ERENBURG, A. M. 1970. Chemical forms of gold and questions of oxidation-reduction potential of sea water. In: *Chemical resources in seas and oceans*. Science, Moscow, 141–144 [in Russian].
- PISAREVSKY, A. M., TISHCHENKO, P. YA., GRAMM-OSIPOV, L. M. & NIKOLAYEV, YU. I. 1989. The MnO₂/Mn²⁺ system as a potential defining system for controlling Eh in pelagic deep-sea bottom accumulations. *Dokladi Akademii Nauk SSSR*, **306**, 195–198 [in Russian].
- RODE, E. YA. 1952. *Oxygen compounds of manganese*. USSR Academy of Sciences, Moscow [in Russian].
- SAVENKO, V. S., 1985. Dissolution of MnO₂ in water solutions. *Geochemistry*, **N3**, 416–419 [in Russian].
- 1990. About mechanism Fe–Mn nodules formation. *Geochemistry*, **N7**, 1040–1043 [in Russian].
- SHULTZ, M. M., PISAREVSKY, A. M. & POLOZOVA, I. P. 1984. *Oxidation potential*. Leningrad, Chemistry [in Russian].
- SILLEN, L. G. 1961. The physical chemistry of seawater. In: SEARS, M. (ed.) *Oceanography*. American Association to the Advancement of Science Publications, **67**, 549–581.
- STRAKHOV, N. N. 1976. *Problems of geochemistry of the recent oceanic lithogenesis*. Science, Moscow [in Russian].
- SUKHOTIN, A. M. (ed.) 1981. *Reference Book to Electrochemistry*. Chemistry, Leningrad [in Russian].
- SWAIN, H. A. JR, LEE, C. & HARWEY, G. R. 1975. Determination of the solubility of manganese hydroxide and manganese dioxide at 25°C by atomic absorption spectrometry. *Analytical Chemistry*, **301**, 234–236.
- TISHCHENKO, P. YA., VOLKOVA, T. I. & CHICHKIN, R. V. 1985. Interaction of complex manganese oxides with water solutions. Thermodynamic analyses. *Geochemistry*, **4**, 554–558 [in Russian].
- & GRAMM-OSIPOV, L. M. 1985. Manganese solid phase formations in the ocean. *Dokladi Akademii Nauk SSSR*, **280**, 231–232 [in Russian].
- TYE, F. L. 1976. Manganese dioxide electrode – III. Relationship between activities and stoichiometry for compositions near to MnO₂. *Electrochimica Acta*, **21**, 415–420.
- 1985. Manganese dioxide electrode – X. A theoretical treatment based on the concept of two solid solutions in the range MnO₂ to MnOOH. *Electrochimica Acta*, **30**, 17–23.
- VETTER, K. J. 1961. *Electrochemische kinetic*. Springer Verlag, Berlin.
- WHITFIELD, M. 1975. The extension of chemical models for seawater to include trace components at 25°C and 1 atm pressure. *Geochimica et Cosmochimica Acta*, **39**, 1545–1557.
- ZHELEZNOVA, A. A. & SHISHKINA, O. V. 1964. Oxidation-reduction potential and active reaction in sediments of the northern Indian Ocean. In: *Investigations in the Indian Oceans (R/V "Vityaz" cruise 33)*. Trudi instituta okeanologii Akademii Nauk SSSR, **64**, 236–243 [in Russian].

Geochemistry of manganese oxides: metal adsorption in freshwater and marine environments

KEITH NICHOLSON & MARK ELEY

*Environmental Geochemistry Research Group, School of Applied Sciences,
The Robert Gordon University, Aberdeen AB1 1HG, UK*

Abstract: The effect of pH and metal ion concentration on the adsorption of Cu, Co, Cd, Mn, Ni and Zn onto manganese oxides was investigated. The oxides used in the experiments were deposited around individual sand grains in water treatment filter beds in NE Scotland and show reproducible adsorption profiles regardless of location or age. The oxides remained amorphous throughout the four-year study period, and show an inferred pH_{ZPC} of 1.5. Metal adsorption increases towards more alkaline pH. The adsorption series $Co > Cu > Cd > Zn > Mn > Ni$ is shown at pH 3 and $Cu > Co > Cd > Mn > Zn > Ni$ at pH 6. Changing the concentration of the metal ions in solution leads to an increase in the mass of metal adsorbed, though the relationship is not linear as the proportion of metal taken up falls as concentration rises. Adsorption from an artificial seawater solution shows a significant reduction in the amount of metal taken up in all cases except Cu which shows an adsorption profile comparable with that in deionized water. The linear Freundlich isotherm accurately and reproducibly models the adsorption profile of all metals at each pH and concentration examined. The data do not, however, replicate the enrichment sequence observed in manganese nodules. The study demonstrates that for the enrichments observed in manganese nodules to be attained, the active oxide surface must be replenished by regular precipitation of fresh oxide material to enable continued adsorption to take place.

Since the pioneering work of Hewett & Fleischer (1960), it has been recognized that the geochemistry of manganese oxide deposits is a reflection of, and a guide to, their origin. Subsequent workers have developed geochemical enrichment signatures and diagnostic diagrams that aid metallogenesis interpretations (e.g. Bonatti *et al.* 1972; Meylan *et al.* 1981; Crerar *et al.* 1982; Nicholson 1992*a, b*). While this approach to identifying the origin of manganese mineralization has been widely employed for over three decades, the basis on which the signatures are developed has received less attention.

It is the surface chemistry of manganese oxides that permits the adsorption and subsequent incorporation of trace elements, and it is this process that lies behind the development of diagnostic geochemical signatures. At pH values above that of the zero point of charge (about pH 1.5–2) the oxides take up available cations from the surrounding fluid, thereby providing a fossil signature of the depositional fluid which is also a guide to their origin. These cations also act as a control on the oxide minerals that subsequently form on crystallization of the initial amorphous manganese oxide precipitate. In this way the development of the geochemistry and mineralogy of a deposit is an iterative process, since although the fluids contribute the necessary elements for the geochemical signature and the constituent elements of the minerals, once the minerals have formed the extent to

which further adsorption takes place is dependent on the surface chemistry of the minerals which varies between species and is different from that of the original amorphous oxides.

This paper describes experimental work performed to determine the relative adsorption of trace metals by manganese oxides in fluids simulating freshwater and marine environments. The work is directed towards developing a model that predicts the relative enrichments observed in modern deposits, such a model would additionally find application in interpreting the chemistry of fluids that deposited ancient manganese ores.

Adsorption of metals on manganese oxides

Deposits of manganese oxides have been shown to be one of the most important phases for adsorption of trace elements in soils and aquatic sediments (Jenne 1968; Young & Harvey 1992). Previous studies have shown that metals such as Co and Zn, are highly concentrated in hydrous manganese oxides (Loganathan & Bureau 1973). McKenzie (1978) reported that manganese oxides in soils play an important role in controlling Pb, Ni and Co uptake by clover by adsorbing and fixing these metals in the soil. Taylor & McKenzie (1966) found that manganese deposits in Australian soils contained most of the soil cobalt, with Ni, Mo, Cr, V and Zn

also showing higher concentrations in these deposits than in the surrounding soil. Sullivan & Koppi (1992) also found that most of the Co in their soil samples was associated with manganese oxide accumulations. Whitney (1975) studied Pb, Zn and Cd distributions in stream sediments and discovered that the substantial control on these metals was adsorption by manganese oxide coatings on sediments. Robinson (1981) found significant adsorption of Cu, Pb and Zn from solution by pebbles coated with a hydrous manganese oxide, taken from a stream in Virginia, USA. Takamatsu *et al.* (1985) concluded that arsenic adsorption by hydrous manganese oxides could play a significant role in the accumulation of As on the surface of lake sediments. Marine manganese deposits have also been found to contain large amounts of heavy metals such as cobalt, nickel and copper (e.g. Chao & Theobald 1976) and remain the focus of world-wide studies. In seawater, adsorption by these deposits is recognised as the most important mechanism in controlling the concentration of heavy metals (Krauskopf 1956; Murray 1975).

Adsorption of heavy metals by hydrous manganese oxides has been extensively examined in previous studies. These have attempted to explore metal adsorption from solution, by studying the influence of factors such as solution pH and metal concentration on the adsorption behaviour of manganese oxides. One of the difficulties in comparing these studies is the range of preparation methods employed and their influence on the adsorption properties of the oxide. Trends between studies are often not consistent, and it is consequently difficult to know how realistic these studies are in describing the behaviour of manganese oxides in the natural environment.

Effect of oxide preparation method

To obtain successful results for heavy metal adsorption studies from solution, it is vital for manganese oxides to be well characterized since adsorption behaviour is strongly determined by the method of preparation. The pH of zero point of charge (pH_{ZPC}) has been found to be affected by the crystal structure and chemical composition of the prepared oxide (Healy *et al.* 1966). The pH_{ZPC} represents the pH at which the overall charge on an oxide is zero and therefore affects the relationship between pH and adsorption for the oxide. The surface area of prepared oxides also depends on the method of production. It is also important that prepared oxides

are stored correctly if ageing effects on adsorption by the oxides are to be avoided (Stroes-Gascoyne *et al.* 1987).

Stroes-Gascoyne *et al.* (1987) used a range of methods for preparing manganese oxides, using them to study the effects of different preparation methods on surface properties and metal adsorption behaviour of the oxides. Copper adsorption at pH 6 was determined for each different manganese oxide preparation and on manganese oxides left to age. The redox, reduction and oxidizing methods discussed here are described elsewhere (van den Berg & Kramer 1979, Healy *et al.* 1966 and McKenzie 1971 respectively). Surface areas range between 145 and $245 \text{ m}^2 \text{ g}^{-1}$, depending on the oxide preparation method. Manganese oxides prepared using both redox and reduction methods gave similar adsorption results for copper at pH 6. However, copper adsorption by the oxide prepared using an oxidation method was found to be significantly lower than those prepared by redox and reduction. The amorphous oxide prepared by oxidation was found to transform to a cryptomelane or birnessite morphology on ageing, whereas oxides prepared by redox and reduction methods did not undergo such a transformation. All oxides were found to remain stable for at least four years if stored correctly at low temperature and neutral pH. Recommendations arising from this study included the use of the redox or reduction methods for preparing manganese oxides, along with employing suitable storage procedures if loss of adsorption capacity of around 50% on ageing is to be prevented (Stroes-Gascoyne *et al.* 1987).

McKenzie (1979) also demonstrated the impact of using different preparation methods for manganese oxides on metal adsorption. He prepared birnessite using four different methods and cryptomelane by three additional methods. Although these methods gave apparently the same two mineral forms of manganese, properties such as surface area were found to vary significantly ($75\text{--}220 \text{ m}^2 \text{ g}^{-1}$) within each mineral type depending on the method of formation used (table 6.2). The pH_{ZPC} shows a small spread of values, ranging from 1.8 to 2.4 which all lie well within the 1.5–7.3 range found by Healy *et al.* (1966). However, adsorption capacity was found not to be dependant on manganese oxide surface area, with identical cryptomelane preparations having similar surface areas yet one preparation adsorbed twice as much metal as the second under identical conditions. Other prepared samples identified as birnessite also had significantly different adsorption capacities depending

on the preparation method, with those being prepared using a reduction technique adsorbing twice as much as those formed by oxidation. This observation clearly highlights the difficulties in using precipitated manganese oxides for reproducible adsorption studies: even when apparently identical methods of oxide production are used, the resulting oxide characteristics can vary significantly. In addition, the adsorption capacity of prepared oxides decreases rapidly with time if they are not stored using the correct conditions (McKenzie 1979). Adsorption studies using manganese oxides prepared in the laboratory cannot therefore be used with confidence for predicting adsorption capacities of oxides deposited in the environment.

Effect of solution pH on adsorption by manganese oxides

The effect of pH on adsorption of metal ions by hydrous manganese oxides has been extensively examined. Posselt & Anderson (1968) found that adsorption of Ag, Mn, Ba, Ca, Mg, Sr and Nd increased with increasing solution pH. A linear relationship was developed to describe the effect of metal solution pH on adsorption from solution. Plotting the log of the equilibrium coefficient ($\log [Mn^{2+}]_{\text{solution}}/[Mn^{2+}]_{\text{adsorbed}}$) against solution pH resulted in a straight line for all the metals used in the investigation. Loganathan *et al.* (1977) studied adsorption of Co, Zn, and Ca from solution and found that the effect of pH on metal adsorption could also be described using Posselt & Anderson's model (1968). However, they reported significant deviation from linearity for Co and Zn at pH values greater than 5 when using this model. Murray (1975) studied Co, Mn, Zn, Ni, Ba, Sr, Ca and Mg adsorption and again found the relationship between adsorption and pH fitted Posselt & Anderson's model (1968).

Gadde & Laitinen (1974) compared the effect of increasing solution pH on adsorption of Pb, Zn and Cd by oxides of manganese and iron. They found a linear increase in Zn and Cd adsorption by manganese oxide between pH 2 and pH 8, with Pb being adsorbed most at all pH values in this range. Ferric oxide, however, was found to only have appreciable Zn, Cd and Pb adsorption capacity at pH values greater than 7 showing effectively the difference in adsorption behaviour of these two oxide types.

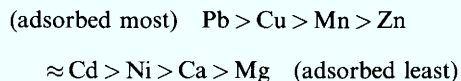
Loganathan *et al.* (1977) found that above pH 6, abrupt increases in adsorption occurred for Co and Zn over a very narrow pH range

(pH 5–7), whereas Ca showed no such marked increase. The authors explained adsorption at low pH ($pH < 5$) as being an ion exchange process of metals with surface hydrogen. At high pH, abrupt increases in adsorption were not accompanied by an abrupt change in the surface negative charge on the oxide, this abrupt increase being explained by suggesting that at high pH values $CdOH^+$ and $ZnOH^+$ hydroxy species may have formed in solution and these species may have a higher affinity for the oxide surface than simple Cd^{2+} or Zn^{2+} . This idea was reinforced by comparing adsorption of Ca on the same manganese oxide which was shown to undergo little hydroxylation between pH 2 and pH 9, hence explaining its different adsorption/pH behaviour when compared with Co and Zn. Gray & Malati (1979) studied Cu and Fe adsorption and found a rapid rise in adsorption at pH values greater than 2 which again was explained by metal hydrolysis as described in Loganathan *et al.*'s study. McKenzie (1979) compared adsorption of Mn, Ni, Co, Zn, Cu and Pb by goethite and birnessite prepared in the laboratory. Metal adsorption was found to increase in a linear fashion from pH 2–8 for birnessite, whereas for goethite it increased rapidly over a narrow pH range between pH 4 and pH 6. Traina & Doner (1985a) found a similar result for Co and Cu adsorption on prepared birnessite.

Murray (1974) examined the relationship between pH and the surface charge on four synthetic manganese oxides. All of the oxides were found to develop a more negative charge as pH was increased between 2 and 11, but the oxide preparations identified as birnessite were found to have a higher charge and increased charging rate (i.e. their charge increased more rapidly with increasing pH) when compared with the oxides identified as cryptomelane. Murray postulates that since birnessite is one of the most commonly found oxide minerals, its adsorption properties may be explained by this high surface charge if natural oxide deposits behave in the same way. Catts and Langmuir (1986) attempted to use a computer programme MINEQL to model the increasing adsorption of Cu, Pb and Zn with increasing pH. Up to about pH 6, metal adsorption was found to be best described using surface reactions of the oxide with divalent metal cations in solution. Above pH 6, model fits using metal hydroxyl complexes were found to provide best agreement with observed adsorption behaviour. The MINEQL model was found to be unsuccessful in modelling changes in metal adsorption profiles except under ideal laboratory conditions. In natural

systems, unless critical parameters such as pH and ion concentration could be accurately determined and controlled, then the authors state that the model may not provide good results. Manceau *et al.* (1992) used X-ray absorption spectroscopy to study Pb adsorption on birnessite at pH values of 3 and 6.5. Results suggested that the high affinity of manganese oxide for Pb was due to Pb being polymerized on the oxide surface, resulting in a highly charged Pb polymer with a high affinity for the oxide surface. Bhutani & Mitra (1992) examined chromate adsorption between pH 1 and pH 9. Adsorption of chromium anions was greatest at low pH values and decreased with increasing pH. This was explained by the manganese oxide having an increasingly negative surface charge as pH increased, hence adsorption of anions would not be favoured at higher pH values. Mukai & de Haan (1992) studied Fe adsorption onto a prepared hydrous manganese oxide from simulated lake waters under acidic conditions (pH 3–5). Adsorption was found to increase rapidly over this small pH range. Cd and Cu adsorption between pH 3 and pH 9 was studied by Fu (1991). Between pH 4 and 7 metal adsorption increased rapidly for both metals before levelling off between pH 7 and 8 giving the curves an S-shaped profile. This profile was thought to be due to an increase in surface charge and change in metal speciation as pH increased.

Most of the studies report an 'adsorption series' for the metals used in their work i.e. which metals were adsorbed most and which were adsorbed to a lesser extent. These are summarized in Table 1 and may be combined to give a more generalized metal adsorption series for manganese oxides, shown below.



This generalized series satisfies all the above experimental observations with the exception of Co which appears at different points in the series in some of the results listed in Table 1. For example, Traina & Doner (1985*a, b*) reported that Co was adsorbed more than Cu or Mn, whereas McKenzie (1979) found Co was adsorbed less than Cu or Mn. Other examples of this uncertainty in the position of Co in the series can also be seen, hence the exclusion of Co from the above adsorption series. The relative positions of Zn and Cd in the series also appear to be in some doubt, with Zn sometimes adsorbed more than Cd and vice versa. This interchange in relative adsorption intensity is most likely due to the prevalent conditions used in individual studies.

Adsorption modelling

Two of the most commonly reported and effective methods for obtaining a linear model for metal adsorption by manganese oxides are the Freundlich and Langmuir adsorption isotherms. A large number of studies have used the linear form of the Langmuir adsorption isotherm to describe metal adsorption (Posselt & Anderson 1968; Loganathan & Burau 1973; Gray & Malati 1979; Stroes-Gascoyne *et al.* 1986; Fu 1991; Mukai & de Haan 1992). The use of the Langmuir in all of these studies readily demonstrates its wide applicability to metal adsorption studies, since these studies encompass a wide range of metal species and experimental conditions. However, Zasoski & Burau (1988) and Bhutani (1992) found that a linear form of the Freundlich adsorption isotherm provided the best agreement with experimental data. Like the Langmuir, this model fitted a large range of metals and different experimental conditions.

Table 1 Reported metal adsorption series

Adsorption Series	pH Range	Reference
Co > Zn > Ca	4	Loganathan & Burau 1973
Pb > Zn > Cd	2–8	Gadde & Laitinen 1974
Cu > Co > Mn > Zn > Ni > Ca > Mg	2–8	Murray 1974
Mn > Zn > Cd > Co > Ni	6	Gray & Malati 1979
Pb > Cu > Mn > Co > Zn > Ni	1–8	McKenzie 1979
Cu > Co > Mn	4	Traina & Doner 1985 <i>b</i>
Pb > Cu > Zn	2–9	Catts & Langmuir 1986
Cd > Zn	4	Zasoski & Burau 1988
Zn > Cd	6–8	Zasoski & Burau 1988
Cu > Cd	5.5–8.0	Fu 1991

Freundlich and Langmuir models

The Langmuir model was developed for systems in which sorption leads to the deposition of a single monolayer of solute on the sorbent surface (Weber 1991). This model assumes that the energy of adsorption for each molecule is the same and independent of surface coverage, and that no interactions occur between sorbed molecules. Derivations of the model can be obtained from mass action, kinetic or statistical thermodynamic approaches. This results in the expression:

$$Q_e = Q^0 b C_e / (1 + b C_e)$$

Q^0 = sorbed solute concentration corresponding to monolayer coverage, b = sorption coefficient related to adsorption enthalpy, Q_e = amount of solute adsorbed per unit of sorbent, C_e = equilibrium solute concentration.

This expression can be put into a linear form which results in the equation:

$$1/Q_e = (1/Q^0) + (1/bQ^0)(1/C_e)$$

The Freundlich isotherm is also one of the most widely used adsorption equilibrium models. Although its origins are for the most part empirical, the model can be shown to be thermodynamically rigorous for cases of adsorption on heterogeneous surfaces (Weber 1991). The model has the general form:

$$Q_e = K_f C_e^b$$

K_f relates to adsorption capacity, b relates to adsorption potential. Other notation as for Langmuir equation earlier.

To determine K_f and b coefficients, data are normally fitted to the linear form of the equation:

$$\log Q_e = \log K_f + b \log C_e$$

This form of the equation gives reliable estimates of the Freundlich isotherm coefficients (Kinniburgh 1986).

There are several other models for adsorption (e.g. Vuceta & Morgan 1978; Murali & Aylmore 1983; Hayes & Leckie 1987; Smith & Jenne 1991) which are a great deal more complicated than the relatively simple models described here. These models too, however, have their limitations for use in natural environments because our ability to model metal behaviour using known, thermodynamic constants is severely limited. They also do not take into account interactive effects such as the differences in chemical composition of surfaces and coatings in the environment (Honeyman & Santschi 1988). It seems, therefore, that the use of a simple model for modelling adsorption processes in natural systems may achieve the desired

result, without entailing complex laboratory studies which may not take into account processes other than adsorption.

Adsorption experiments

The material used for the adsorption experiments described here was extracted from sand filters at water treatment plants in north-east Scotland (Eley & Nicholson 1992). These oxides, which coat each individual sand grain in the beds, showed several advantages for use in adsorption experiments over laboratory-prepared material. They have a relatively uniform morphology and chemical composition (Eley & Nicholson 1992) and showed comparable behaviour in adsorption experiments regardless of the source plant for the filter deposits. Ageing has also been shown to have no effect on the oxidation state or mineralogy of the oxides sampled over the three year period of this study. The oxides therefore provide an ideal medium for studying metal adsorption: they provide a stable medium showing consistent and uniform adsorption characteristics thus overcoming one of the main limitations of the previous studies with synthetic oxides. In addition, these thin (micron scale), amorphous oxide coatings on a sand substrate also better resemble manganese oxide coatings found in the natural environment, rather than the laboratory-precipitated colloidal manganese oxides used in the studies described above. It is likely therefore that the results of adsorption experiments with such material might better reflect the behaviour of the oxides in the natural environment.

The effect of three factors on metal adsorption are studied in this paper: solution pH, metal concentration and ionic strength. These series of experiments were performed using solutions of the metals Cu, Cd, Mn, Ni, Zn and Co, which were chosen because they have been examined the most in previous studies and hence their study here will facilitate comparison with earlier published adsorption data using precipitated oxides.

To ensure that all adsorption experiments performed during this study were allowed sufficient time to achieve equilibrium and hence provide reproducible experimental metal adsorption data, the adsorption equilibrium time was determined for different metal solution concentrations over a range of pH values. It was found that metal adsorption reached equilibrium very quickly, in less than 30 minutes. All solutions were therefore left for 30 minutes prior to metal determination.

Effect of solution pH on metal adsorption

Two different solution concentrations containing either 2 mg l^{-1} and 10 mg l^{-1} of each metal were used in these experiments to evaluate the impact of pH on adsorption. The variation in metal adsorption with pH for 2 mg l^{-1} solutions of Cu, Co, Cd, Mn, Zn and Ni is shown in Fig. 1a. The effect of increasing the metal solution pH can be clearly seen for all of the

metal solutions, with metal adsorption being greatly enhanced when pH values were greater than pH 3. Cobalt, for example, increased from solution at pH 2.0 to around 85% adsorbed at pH 6.0. All of the metals have an S-shaped adsorption profile over the pH range of this study, with an almost linear rise in adsorption occurring between pH 3.0 and pH 5.0 before levelling off at around pH 6.0. Below pH 3.0 very little

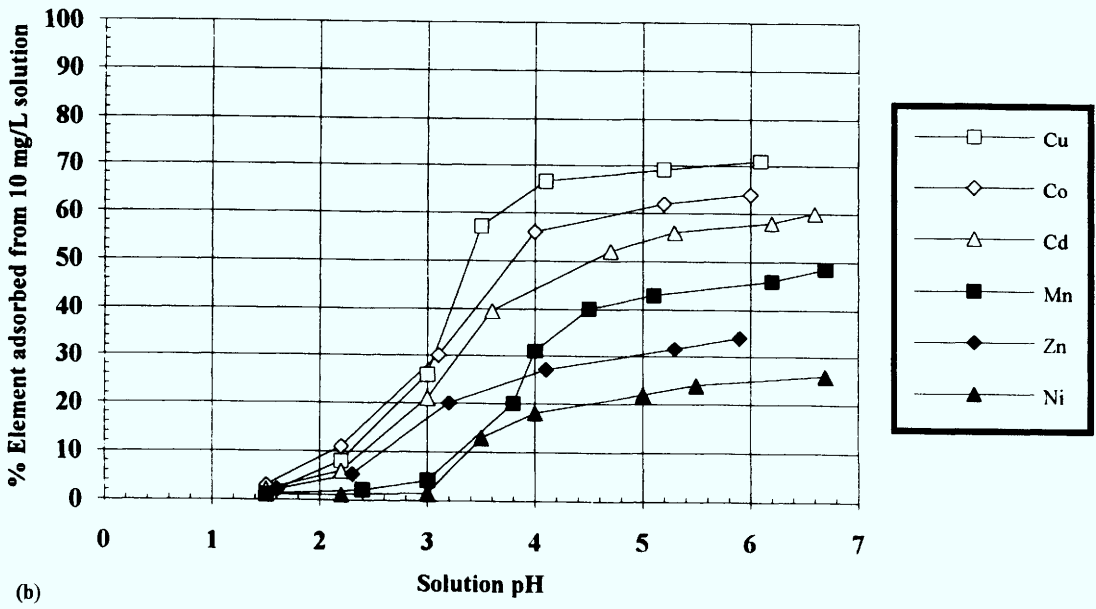
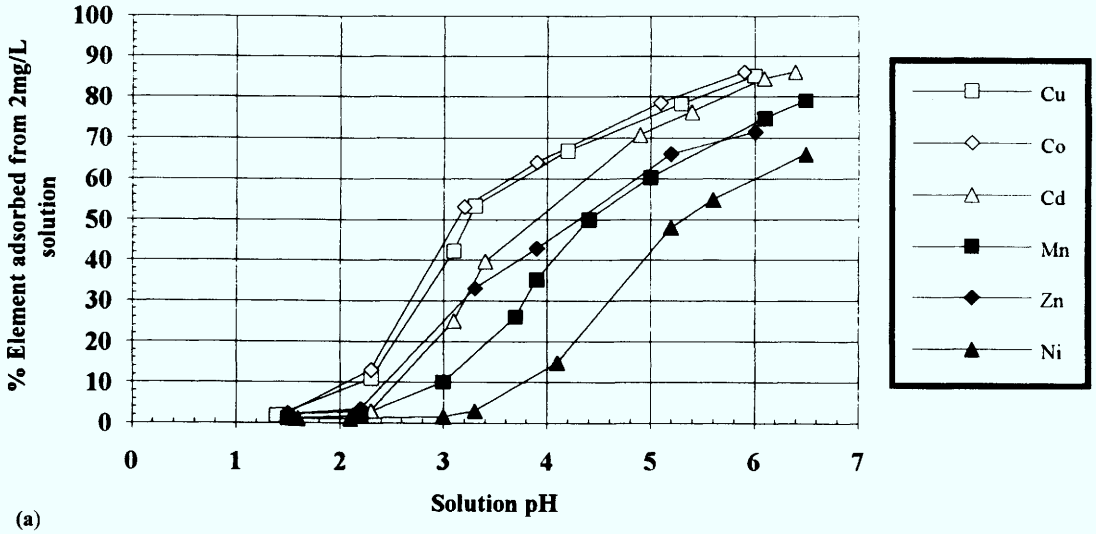


Fig. 1. (a) Variation in metal adsorption with solution pH using 2 mg l^{-1} metal solution concentrations. (b) Variation in metal adsorption with solution pH using 10 mg l^{-1} metal solution concentrations.

adsorption is found, with all metal adsorption profiles seeming to intercept at approximately pH 1.5 where <1% of metal in solution was adsorbed by the oxide-coated sand. The adsorption series found for these metal solutions at pH 3.0 can be seen from Fig. 1a to be $\text{Co} > \text{Cu} > \text{Zn} \approx \text{Cd} > \text{Mn} > \text{Ni}$, but at pH 6.0 the relative positions of Cd and Zn are changed resulting in an adsorption series $\text{Co} > \text{Cu} > \text{Cd} > \text{Zn} > \text{Mn} > \text{Ni}$.

Similar S-shaped adsorption profiles were found for 10 mg l^{-1} metal solutions, shown in Fig. 1b. The oxide coated sand showed a larger capacity for metal adsorption at this higher solution concentration, with up to 70% of some metals being removed at the highest pH values. As found for the 2 mg l^{-1} study, a rapid rise in adsorption occurred over a narrow pH range but this time it occurred more sharply between pH 3.0 and pH 4.0 before levelling off above pH 4.0–5.0. At around pH 1.5 the adsorption profiles of all the metals again seem to intercept with very little adsorption (<2%) occurring at this pH value. Examining the metal profiles at pH 3.0, the series of metal adsorption observed was $\text{Co} \approx \text{Cu} > \text{Cd} > \text{Zn} > \text{Mn} > \text{Ni}$ whilst at pH 6.0 it was $\text{Cu} > \text{Co} > \text{Cd} > \text{Mn} > \text{Zn} > \text{Ni}$.

The rapid increase in adsorption over a small pH range observed here for oxide coated sand has also been found in previous studies on precipitated manganese oxides, iron oxides, silicon oxides and titanium oxides. Loganathan *et al.* (1977) found a similar adsorption pH profile for Zn and Co on precipitated manganese oxide, but the region of rapid adsorption increase lay between pH 6.0 and pH 7.0 which is higher than that reported here. However, this difference may be attributed to the different metal solution concentrations used in their study, since this has been shown to affect the position of this pH region. This effect can be seen by comparing the difference in the pH position of this rapid rise in adsorption, as shown by comparing Fig. 1 and was also reported in Loganathan's study. This rapid increase in adsorption over a narrow pH is further emphasised by Fu (1991) who found the region of rapid adsorption increase lay between pH 3.0 and 5.0 which is very similar to the results of this study. Rapid changes in the amount of metal adsorbed are not found only for manganese oxides, with SiO_2 and TiO_2 oxides showing similar S-shaped pH-adsorption profiles (James & Healy 1972). This rapid increase in adsorption with pH is postulated by most of these earlier studies to be due to an increase in the hydroxylation of metals in solution resulting in a relatively greater affinity

of the metal for the oxide surface, but only qualitative data is reported due to the difficulty in determining the exact speciation of metals at the solution-oxide interface.

The position of pH_{ZPC} for the oxides used in this study could not be directly determined due to the relatively massive nature of the sand media, making the necessary electrophoretic studies impossible. However, the intersection of all the pH profiles at around pH 1.5 in this study implies that the pH_{ZPC} of these oxides must lie in the close vicinity of this value, since metal adsorption is mostly due to the surface charge on the oxide. We can presume, therefore, that if very little adsorption is occurring at pH 1.5 then the oxide charge must be very small and hence this value must be approaching the pH_{ZPC} of the oxide.

Effect of metal solution concentration on adsorption

A series of adsorption experiments were performed at pH 3.0 and pH 6.0 to determine the influence of metal solution concentration on adsorption. These pH values were chosen to allow comparisons to be made between adsorption at low pH and at higher pH for a wide range of solution concentrations between 0.5– 10 mg l^{-1} . The higher value of pH 6.0 was chosen because above this problems with precipitation of metals in high metal concentration solutions was found to occur. This choice of values also facilitates comparison with previous studies on precipitated manganese oxides which are predominantly performed around these pH values.

Effect of metal solution concentration at pH 3

The relationship between metal ion concentration in solution and mass of metal adsorbed is shown in Fig. 2 for the metals Co, Cu, Cd, Zn and Mn. Adsorption of Ni is not shown since no significant metal adsorption was found at pH 3 for any of the different Ni concentrations chosen. Fig. 2 shows the mass of each metal adsorbed per gram of oxide coated sand for each metal concentration used. The data used in this figure represent the mean value of three replicate studies for each metal. The plotted data show a similar curved profile for all the metals, with adsorption showing a relatively large increase at lower metal concentrations before tailing off slightly at higher solution concentrations. By examining Fig. 2 the adsorption series at pH 3

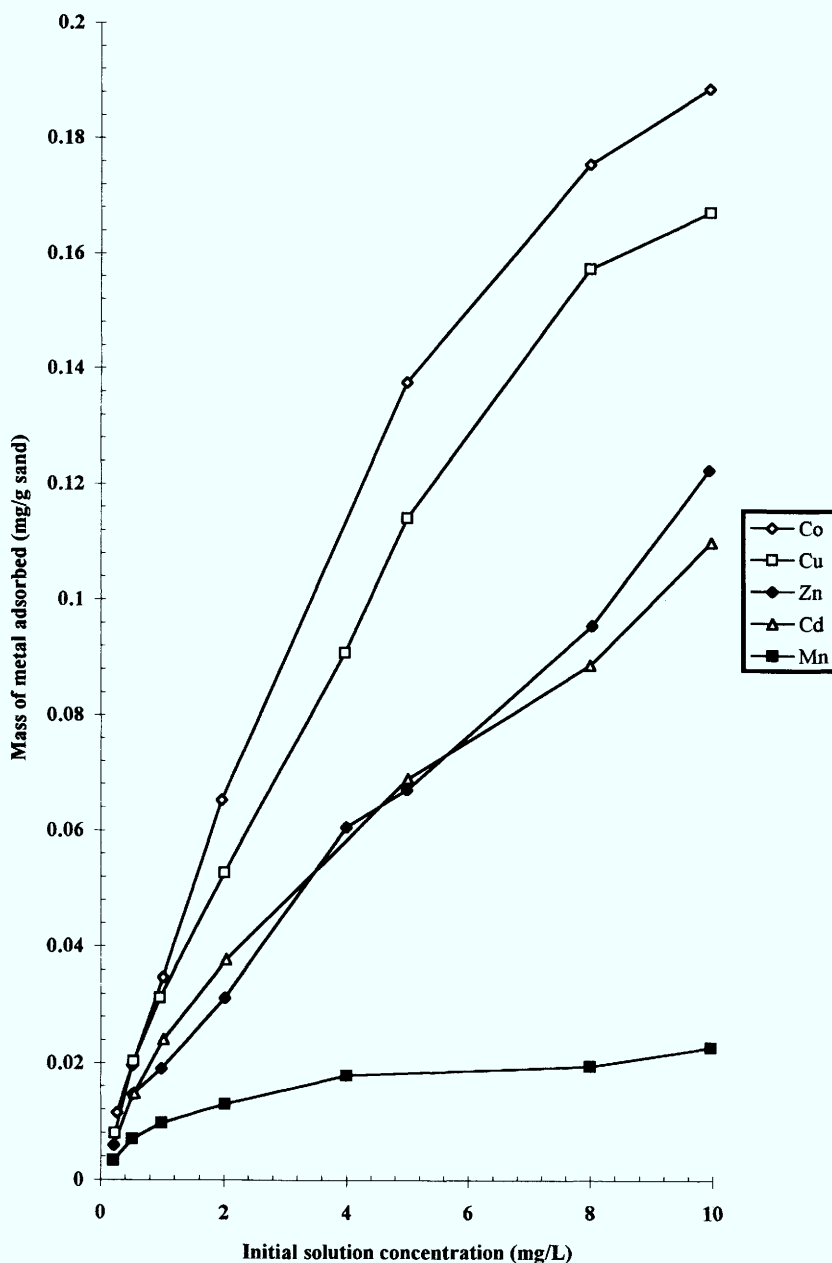


Fig. 2. Effect of metal solution concentration on mass of metal adsorbed at pH 3.

can be seen to be $\text{Co} > \text{Cu} > \text{Zn} \approx \text{Cd} > \text{Mn} > \text{Ni}$ which is similar to the general adsorption series described above except Mn is adsorbed less than Zn or Cd.

The Langmuir and Freundlich adsorption isotherm models were applied to this data. In the Langmuir isotherm, by plotting $1/Q$ (where

Q = mass of metal adsorbed per unit mass of sand) against $1/C$ (where C = equilibrium solution concentration), a linear relationship should be found. However, none of the metal adsorption profiles were accurately modelled by this isotherm. The linear form of the Freundlich adsorption isotherm was applied by plotting

log Q against log C. A straight line plot should be obtained if the expression correctly models the metal adsorption profile. Figures 3 and 4 show Freundlich plots for the adsorption data for Co and Mn at pH 3 and demonstrate the applicability of this model, since a good straight line fit is observed for both Co adsorption ($R^2 = 0.965$) and Mn adsorption ($R^2 = 0.983$). All of the replicate experimental data for each of these metal solutions (shown on each figure) fall

within the calculated 95% confidence limits of the linear regression line. The Freundlich adsorption model also accurately describes adsorption of Cu, Cd and Zn. The good fit of the regression line on all the Freundlich plots can best be seen by examining the R^2 regression coefficients for all of the metals studied (Table 2). The lowest R^2 value calculated is that for Cu adsorption, but even then a value of 0.960 is still acceptable. When the regression

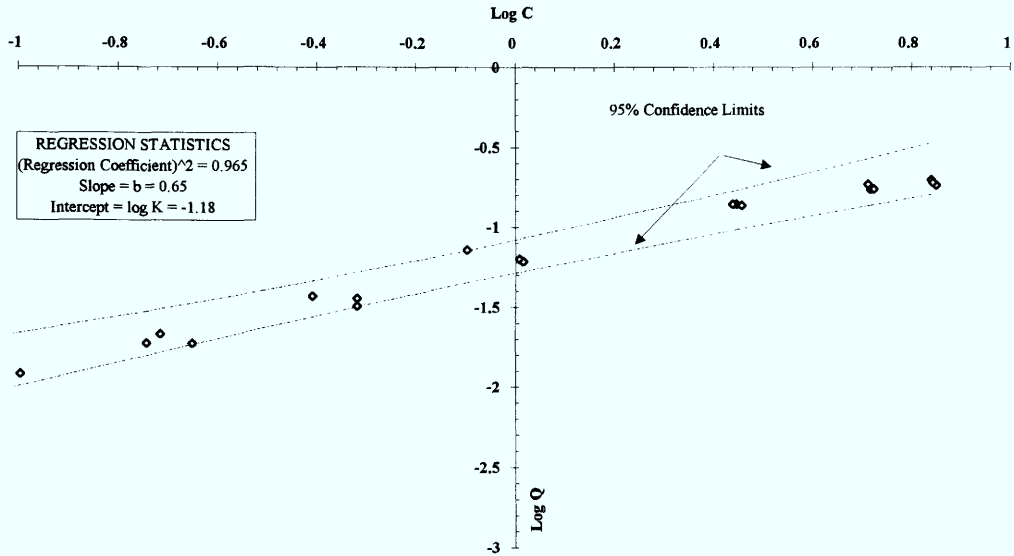


Fig. 3. Freundlich isotherm for Co adsorption at pH 3.

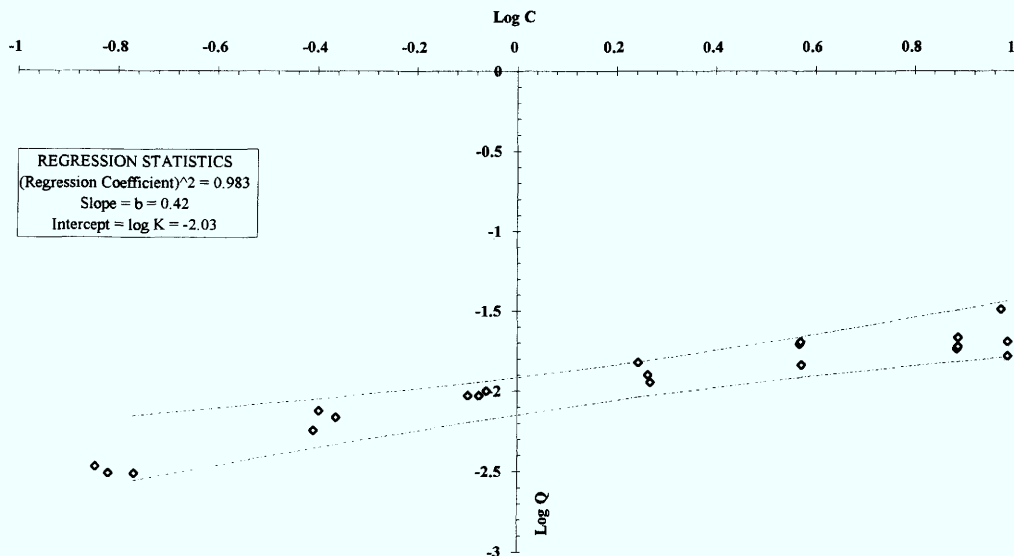


Fig. 4. Freundlich isotherm for Mn adsorption at pH 3.

Table 2. *Freundlich coefficients for metal adsorption at pH 3*

Metal	R^2	Slope (b)	Log K	$K(10^{-2})$
Co	0.965	0.65 ± 0.17	-1.18 ± 0.12	6.6 ± 1.6
Cu	0.960	0.68 ± 0.17	-1.29 ± 0.11	5.1 ± 1.2
Cd	0.981	0.69 ± 0.11	-1.58 ± 0.07	2.6 ± 0.5
Zn	0.997	0.58 ± 0.06	-1.52 ± 0.04	3.0 ± 0.3
Mn	0.983	0.42 ± 0.12	-2.03 ± 0.14	0.9 ± 0.3

lines are shown along with their calculated 95% confidence limits the ability of the Freundlich isotherm for modelling adsorption of Co, Cu, Mn, Ni and Zn by the oxide-coated sand is clear, with all subsequent replicate adsorption data for these metals lying within the calculated confidence limits.

As described above, the slope of a plotted linear Freundlich line (b) is related to the total potential for metal adsorption by the oxide. This calculated ' b ' value allows the relationship between adsorption and solution concentration to be examined. A low ' b ' value shows that the maximum adsorption potential of the oxide is approached at low solution concentrations, whereas a high ' b ' value means that the maximum adsorption potential is not approached until much higher solution concentrations. The K value (determined from the calculated intercept value = $\log K$) is related to the adsorption capacity of the oxides. Table 2 shows the results for b and K coefficients. The values for ' b ' all appear to all have a similar value of around 0.6–0.7, which would mean that the maximum adsorption potential of the oxide for all of the metals in this study is not reached over this concentration range. This implies that the adsorption maxima for these metals on the coated sand is not approached until high metal solution concentrations in are used. The reason why Mn does not lie within this range of b values is unclear, but examination of Fig. 2 shows that the shape of the Mn adsorption profile is clearly different to the other metals in studied. The Mn curve does not show the dramatic rise in adsorption with solution concentration that all of the other metals display, with adsorption levelling off quickly at a relatively low adsorption capacity indicating that the maximum adsorption potential of the oxide has nearly been reached.

The calculated Freundlich K values shown in Table 2 provide a useful tool for comparing the adsorption capacity of oxide for a variety of metals. Using the K values in Table 2 we would expect that Co would be the most adsorbed metal followed closely by Cu. The metals Zn and

Cd would be adsorbed to a much smaller extent but would have similar adsorption capacities themselves, with Mn being adsorbed far less than these metals. It appears, therefore, that using K values will allow comparisons to be made between adsorption of any metal on the oxide under any different solution condition e.g. at higher solution pH. This permits direct comparison of metal adsorption under a range of different adsorption conditions. By also considering the ' b ' values, which describe the shape of an adsorption capacity curve, a good picture of the complete adsorption profile over a wide concentration range can be described.

Effect of metal solution concentration at pH 6

Figure 5 shows the mean average of the adsorption data for each of the metals at pH 6. The initial point to note is the similarity in the shape of the adsorption curves to those found in Fig. 2, despite adsorption clearly being enhanced at this higher pH. For instance, Cu at pH 6 was adsorbed from solution more than twice as much across the entire concentration range when compared to adsorption at pH 3. The Langmuir model was again tested against the adsorption data for each of the metals. As found for adsorption at pH 3.0, the linear form of the Langmuir model fails to describe the adsorption profile and is an inappropriate model.

In contrast, the linear regression data for the Freundlich model show higher R^2 values than those fitted at pH 3, indicating an even better fit to this adsorption model. This is also reflected in much narrower 95% confidence limits on the data yet despite this, all the replicate data plots within these limits. Examples of the Freundlich plots at pH 6 are shown in Fig. 6. Table 3 shows the Freundlich coefficients obtained from the linear Freundlich plots discussed above. The K values are all clearly higher for each metal at pH 6 than at pH 3 due to the large increase in metal adsorption observed at this higher pH, as was anticipated from earlier studies. Two of the

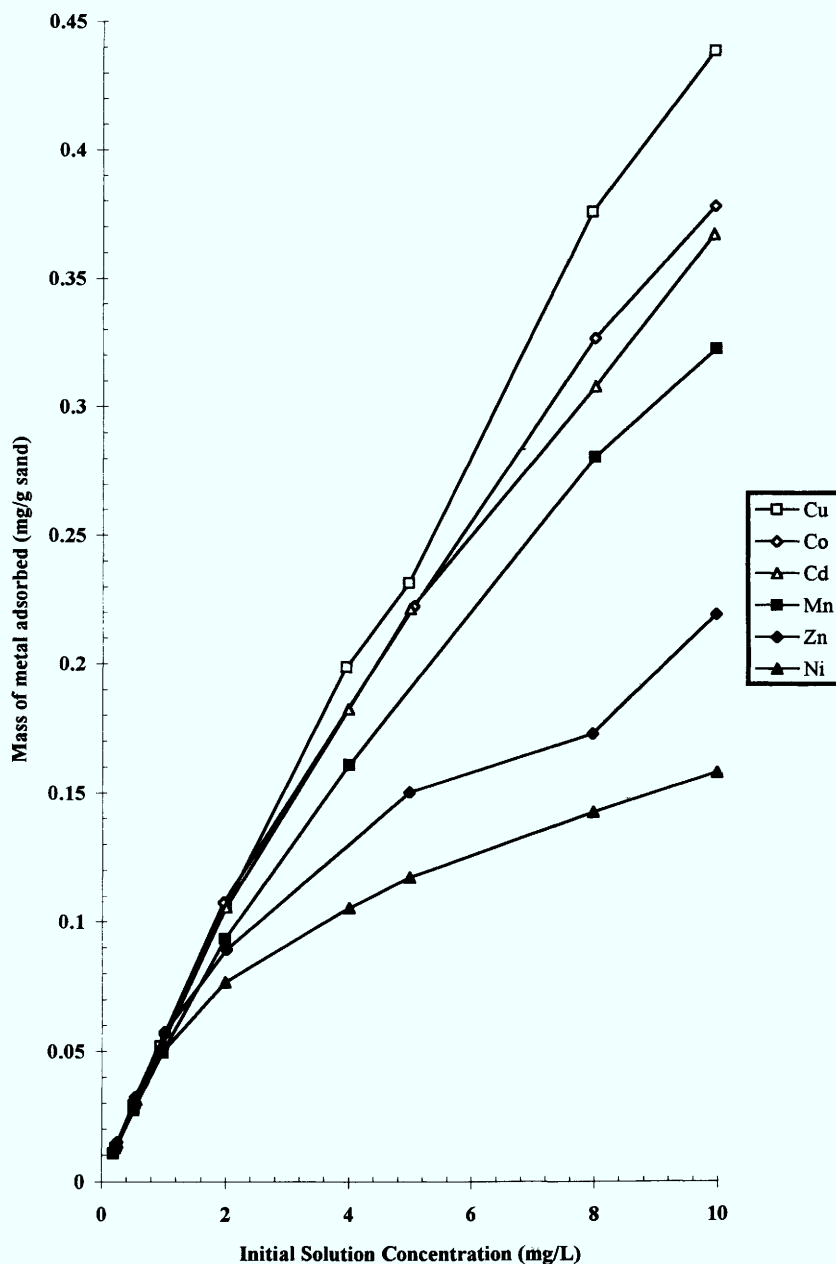


Fig. 5. Effect of metal solution concentration on mass of metal adsorbed at pH 6.

metals in particular have shown a more dramatic increase in adsorption than the others, which is reflected in their measured K values. The biggest overall increase in K value and hence adsorption capacity occurred for Mn, which has risen from an average K value of 0.9 at pH 3 to an average value of 13.2 at pH 6. This is almost a 15 times increase in K value at pH 6,

which is far greater than that shown by Cu, Co, Cd and Zn which all show an increase of between 3 and 6 times their value determined at pH 3. Clearly, manganese adsorption by oxide coated sand is greatly enhanced by increasing solution pH. The reason for this dramatic increase in adsorption capacity of Mn at higher solution pH could be due to the autocatalytic

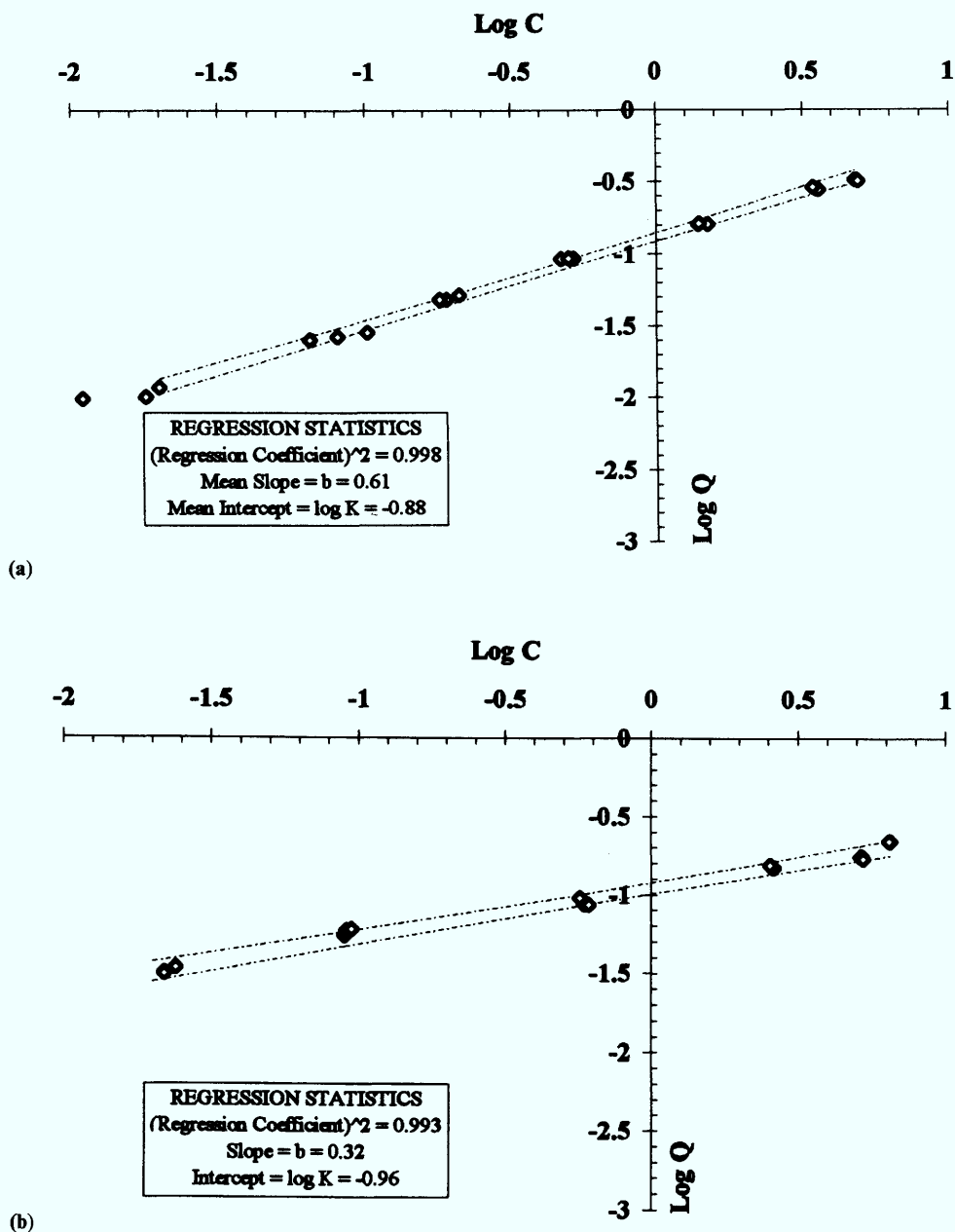


Fig. 6. Freundlich isotherms for (a) Mn and (b) Zn adsorption at pH 6.

behaviour of manganese oxide on the oxidation of adsorbed aqueous Mn, as described by the study of Davies & Morgan (1987). They found that oxidation of Mn on the oxide surface was very slow at low pH, but on increasing the solution pH this rate showed a significant increase.

The calculated slope values, b at pH 6 are also shown in Table 3 for the Freundlich isotherms. For Cu, Co and Cd they are not significantly different from those measured at pH 3, demonstrating that the maximum adsorption of these metals by the oxide is not approached until higher metal solution concen-

Table 3. *Freundlich coefficients for metal adsorption at pH 6*

Metal	R^2	Slope (b)	Log K	$K(10^{-2})$
Cu	0.993	0.70 ± 0.07	-0.65 ± 0.07	22.4 ± 3.9
Co	0.993	0.53 ± 0.06	-0.72 ± 0.06	19.1 ± 3.0
Cd	0.994	0.56 ± 0.05	-0.76 ± 0.05	17.4 ± 2.0
Mn	0.998	0.61 ± 0.04	-0.88 ± 0.04	13.2 ± 1.3
Zn	0.993	0.32 ± 0.04	-0.96 ± 0.04	11.0 ± 1.0
Ni	0.989	0.35 ± 0.04	-1.10 ± 0.04	7.9 ± 0.8

trations are used. The slope value for Mn, however, has increased slightly from 0.42 at pH 3 to 0.61 at pH 6. This apparent increase in adsorption potential may help explain the dramatic increase in Mn adsorption at pH 6 since it would mean that in addition to an increase in the overall adsorption capacity of the oxide, the actual maximum adsorption potential is not approached until higher metal solution concentrations are used. Conversely, the value of b for Zn has decreased from 0.58 to 0.32 which implies that although the oxide adsorption capacity for Zn has been found to be greater at higher pH (see previous discussion on K values), the adsorption potential has dropped and therefore the maximum adsorption potential is now approached at low solution concentrations. This may explain why the position of Zn in the observed adsorption series at pH 6 has changed when compared to that found at pH 3. At pH 3 the adsorption series of the metals was found to be $\text{Co} > \text{Cu} > \text{Cd} \approx \text{Zn} > \text{Mn}$ with Cd and Zn having very similar adsorption profiles (Fig. 2). At pH 6 the series changes to $\text{Cu} > \text{Co} > \text{Cd} > \text{Mn} > \text{Zn} > \text{Ni}$ and Zn no longer has an adsorption profile similar to that found for Cd (Fig. 5), with Zn adsorption tending to flatten off more quickly at higher solution concentrations than that found for Cd.

Adsorption from an artificial seawater solution

The affinity of the oxide for metals in a simulated freshwater solution (deionized water) was clearly demonstrated above. However, manganese oxides are frequently deposited in seawater environments, so the effects of using an artificial seawater solution for metal adsorption experiments was investigated. Adsorption studies were performed as in the earlier experiments to allow comparisons to be made between the different studies.

The mean average data for adsorption of Cu, Co, Mn, Cd, Zn and Ni from a seawater solution at pH 6 can be seen in Fig. 7. If this is

compared with adsorption at pH 6 from deionised water (Fig. 5), it is obvious that adsorption of all the metals except Cu is significantly lower from seawater solutions.

Although the adsorption of most of the metals was depressed by using a seawater solution, metal adsorption was still accurately modelled by applying the Freundlich adsorption isotherm as shown by the data in Table 4 and the exemplar plots of Fig. 8.

The K values for all the metals, with the exception of Cu, are significantly lower than those determined for metal adsorption from deionised water at the same pH. Even at pH 3 for adsorption experiments in deionised water most of the K values (Table 2) for the metals are higher than those found for pH 6 seawater experiments, showing the dramatic impact on adsorption of using a seawater solution. The exception to this rule is Cu, which appears to be adsorbed to a similar extent from both seawater and deionised water solutions.

The adsorption potential values, b in Table 4 show that no difference in b values can be seen when comparing calculated b values of Co and Cd in pH 6 seawater or pH 6 deionised water adsorption experiments (Table 3). This implies that although the adsorption capacity of the oxide drops for adsorption of these two metals from a seawater solution, it is not due to the total adsorption potential of the oxide being reached, i.e. the metal adsorption curves have not reached an adsorption plateau where the mass of metal adsorbed remains constant regardless of solution concentration (Fig. 7). This result implies that the decrease in adsorption capacity observed may be due to some form of chemical interaction of the metals in solution with the seawater solution, which results in adsorption of Co and Cd being decreased.

Contrary to the b results described above for Co and Cd, Mn, Zn and Ni show a significant increase in b values in seawater solution adsorption experiments. This increase in b indicates that the total adsorption potential of these metals is not even nearly approached over this concentration range, showing an almost

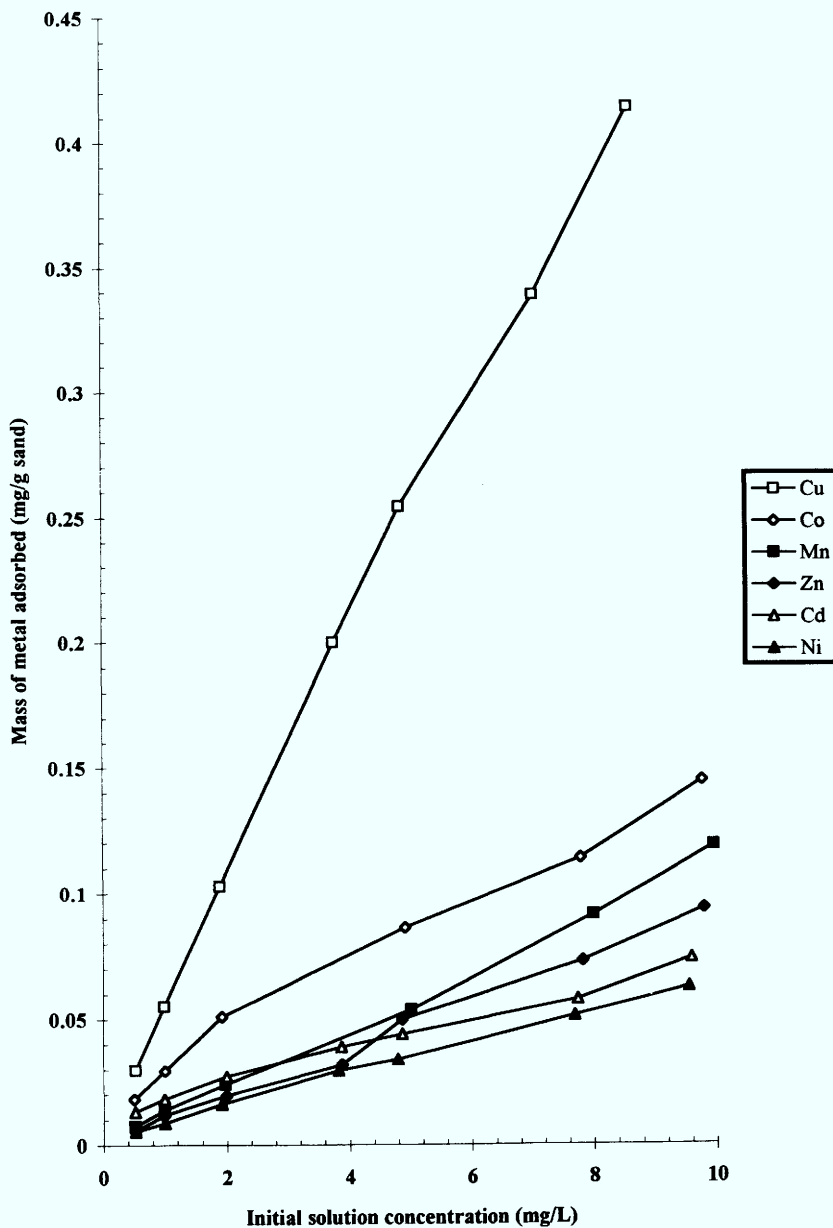


Fig. 7. Effect of metal solution concentration on mass of metal adsorbed at pH 6 in artificial seawater solution.

linear increase with increasing concentration. The decrease in adsorption cannot therefore be due to the total adsorption potential of the oxide being reached. As discussed for Co and Cd, this implies that adsorption of the metals is restricted because of metals in solution reacting with seawater, resulting in a metal species with a lower affinity for the oxide surface. This idea could also explain the reason for the anomalous

behaviour of Cu in seawater solutions which may form an aqueous species with a greater affinity for the oxide surface.

The adsorption series of metals in seawater is not as well defined as those for deionised water experiments with $\text{Cu} \gg \text{Co} > \text{Ni}$ being the only constant adsorption order observed across the entire metal concentration range. The other metals, Cd, Zn and Ni lie between Co and Ni

Table 4. Freundlich coefficients for metal adsorption from an artificial seawater solution at pH 6

Metal	R^2	Slope (b)	Log K	$K(10^{-2})$
Cu	0.990	0.70 ± 0.06	-0.56 ± 0.07	27.5 ± 5.0
Co	0.995	0.56 ± 0.08	-1.37 ± 0.06	4.3 ± 0.6
Cd	0.980	0.51 ± 0.09	-1.65 ± 0.06	2.2 ± 0.4
Mn	0.994	0.91 ± 0.05	-1.79 ± 0.07	1.6 ± 0.3
Zn	0.975	0.89 ± 0.12	-1.88 ± 0.13	1.3 ± 0.4
Ni	0.994	0.84 ± 0.08	-1.99 ± 0.03	1.0 ± 0.1

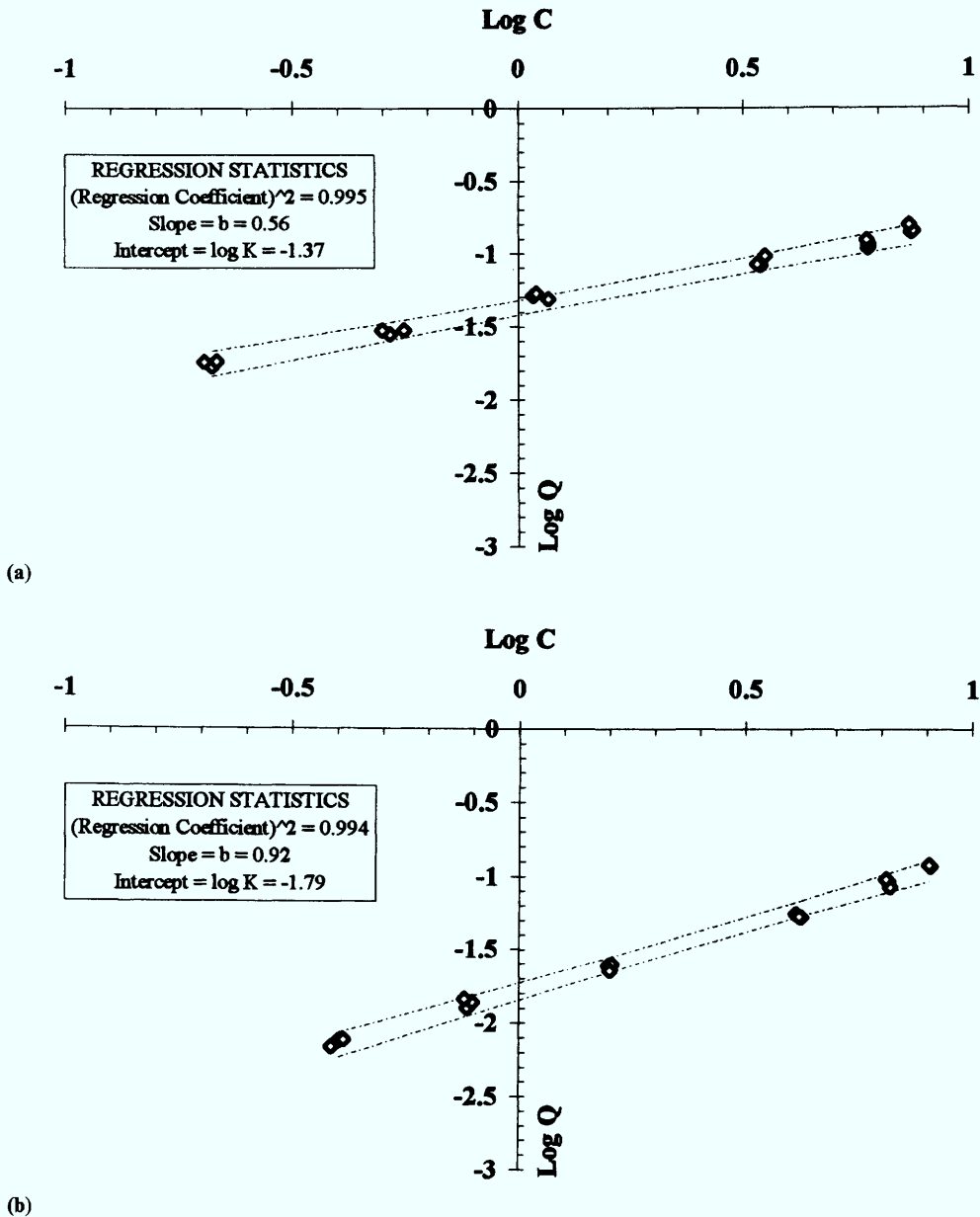


Fig. 8. Freundlich isotherm for (a) Co and (b) Mn adsorption at pH 6 from artificial seawater solution.

Table 5. Concentrations and abundance of metals in seawater and manganese oxides

	Mn	Co	Cu	Ni	Zn
seawater ($\mu\text{g kg}^{-1}$)*	0.2	0.05	0.5	0.5	2
marine nodules (mg kg^{-1})†	160 200	2840	2595	4800	780
nodule enrichment ($\times 10^6$)	801.0	56.8	5.19	0.030	0.005
freshwater oxides (mg kg^{-1})†	13 510	170	147	209	687
<i>Relative take up/abundance</i>					
seawater abundance Zn > Cu = Ni > Co					
nodule enrichments					
relative to seawater Co \gg Ni > Cu \gg Zn					
relative to Mn Co > Cu > Ni \gg Zn					
freshwater experiments Cu > Co > Zn > Ni					
seawater experiments Cu \gg Co > Zn > Ni or Cu \gg Co > Ni > Zn					

* Drever (1982)

† Nicholson (1992b)

in the adsorption series but interchange places in their relative adsorption order depending on the initial solution concentration used.

Adsorption of Co, Ni, Zn, Mn and Cd onto the oxide was greatly reduced when compared to adsorption from freshwater solutions. Adsorption of Cu, however, was unaffected and was adsorbed in similar amounts from both saline and freshwater solutions.

Implications for metallogenesis

Examination of the adsorption profiles in Fig. 5 show that although the mass of metal adsorbed increases concomitantly with solution concentration, the relative proportion or percentage of the original metal concentration taken up actually declines. For example at pH 6 Cu and Ni adsorption at 1 mg l^{-1} is around 5% for both metals while in 10 mg l^{-1} solutions this falls to 4.4% for Cu and 1.5% for Ni. There is therefore not a linear relationship between the mass of metal taken up and the initial metal concentration in solution.

A similar pattern is observed in seawater solutions (Fig. 7) with Cu adsorption falling from 5.5% to 4.7% over the same concentration range, while Ni shows a fall from 1% to 0.6%. A comparison between these two sets of data also shows that while the behaviour of Cu in freshwater and seawater shows minimal differences, the take up of Ni is up to 80% less in seawater solutions.

These experimental findings, taken in context with the discussion of the 'b' and 'K' coefficients of the Freundlich model, indicate that the metal concentrations and level of enrichments seen in manganese nodules (Table 5) require that the

active oxide surface of the nodule must be regularly replenished by fresh oxide precipitation to enable continued accumulation of the metals. The low metal concentration observed in freshwater oxides (Table 5) in spite of the relatively greater take up of most metals in such an environment, is a function of the water chemistry and possibly the reduced incidence of this oxide surface replenishment.

The adsorption profiles of the oxides are reproducible and can be effectively modelled by the Freundlich isotherm. However the above experiments do not successfully predict the metal relative enrichments seen in manganese nodules (Table 5). Further multi-element solution experiments are needed to refine and develop this aspect of the modelling.

References

- BHUTANI, M. M. 1992. Adsorption of ^{51}Cr (VI) on manganese dioxide from aqueous solution. *Mikrochimica Acta*, **107**, 19–26.
- & MITRA, A. K. 1992. Kinetic study of Cr (VI) sorption on MnO_2 . *Journal of Radioanalytical & Nuclear Chemistry*, **157**, 75–86.
- BONATTI, E., KRAEMER, T. & RYDELL, H. 1972. Classification and genesis of submarine iron-manganese deposits. In: HORN, D. R. (ed.) *Ferromanganese deposits on the ocean floor*. National Science Foundation, Washington, 149–166.
- CATTS, J. G. & LANGMUIR, D. 1986. Adsorption of Cu, Pb and Zn by MnO_2 : applicability of the site binding-surface complexation model. *Applied Geochemistry*, **1**, 255–264.
- CHAO, T. T. & THEOBALD, P. K. 1976. The significance of secondary iron and manganese oxides in geochemical exploration. *Economic Geology*, **71**, 1560–1569.

- CRERAR, D. A., NAMSON, J., CHYI, M. S., WILLIAMS, L. & FEIGENSON, M. D. 1982. Manganiferous cherts of the Franciscan assemblage: I. General geology, ancient and modern analogues and implications for hydrothermal convection at ocean spreading centres. *Economic Geology*, **77**, 519–540.
- DAVIES, S. H. R., & MORGAN, J. J. 1987. Manganese (II) oxidation kinetics on metal oxide surfaces. *Journal of Colloid & Interface Science*, **129**, 63–75.
- DREVER, J. I. 1982. *The geochemistry of natural waters*. Prentice Hall, New Jersey.
- ELEY, M. & NICHOLSON, K. 1993. Chemistry and adsorption-desorption properties of manganese oxides deposited in Forehill Water Treatment Plant, Grampian, Scotland. *Environmental Geochemistry and Health*, **15**, 85–91.
- FU, G. 1991. Adsorption of cadmium and copper by manganese oxide. *Soil Science*, **152**, 2 72–81.
- GADDE, R. R., & LAITENEN, H. A. 1974. Studies of heavy metal adsorption by hydrous iron and manganese oxides. *Analytical Chemistry*, **46**, 13, 2022–2026.
- GRAY, M. J. & MALATI, M. A. 1979. Adsorption from aqueous solution by manganese dioxide II. Adsorption of some heavy metal cations. *Journal of Chemical Technology Biotechnology*, **29**, 135–144.
- HAYES, K. F. & LECKIE, J. O. 1987. Modeling ionic strength effects on cation adsorption at hydrous oxide/solution interfaces. *Journal of Colloid & Interface Science*, **115**, 2 564–572.
- HEALY, T. W., HERRING, A. P. & FUERSTENAU, D. W. 1966. The effect of crystal structure on the surface properties of a series of manganese dioxides. *Journal of Colloid & Interface Science*, **21**, 435–444.
- HEWETT, D. F. & FLEISCHER, M. 1960. Deposits of the manganese oxides. *Economic Geology*, **61**, 431–461.
- HONEYMAN, B. D. & SANTSCHI, P. H. 1988. Metals in aquatic systems. *Environmental Science & Technology*, **22**, 862–871.
- JAMES, R. O. & HEALY, T. W. 1972. Adsorption of hydrolyzable metal ions at the oxide-water interface. *Journal of Colloid Interface Science*, **40**, 1 42–52.
- JENNE, E. A. 1968. Controls on Mn, Fe, Co, Ni, Cu, and Zn concentrations in soils and water: the significant role of hydrous Mn and Fe oxides. *Advances in Chemistry Series*, **73**, 337–387.
- KINNIBURGH, D. G. 1986. General purpose adsorption isotherms. *Environmental Science & Technology*, **20**, 895–904.
- KRAUSKOPF, K. B. 1956. Factors controlling the concentration of thirteen rare metals in seawater. *Geochimica et Cosmochimica Acta*, **9**, 1.
- LOGANATHAN, P. & BURAU, R. G. 1973. Sorption of heavy metal ions by a hydrous manganese oxide. *Geochimica et Cosmochimica Acta*, **37**, 1277–1293.
- , — & FUERSTENAU, D. 1977. Influence of pH on the sorption of Co^{2+} , Zn^{2+} and Ca^{2+} by a hydrous manganese oxide. *Soil Science Society America Journal*, **41**, 57–62.
- MANCEAU, A., CHARLET, M. C., BOISSET, B., DIDIER, B. & SPADINI, L. 1992. Sorption and speciation of heavy metals on hydrous Fe and Mn oxides. From microscopic to macroscopic. *Applied Clay Science*, **7**, 201–223.
- MEYLAN, M. A., GLASBY, G. P., KNEDLER, K. E. & JOHNSON, J. H. 1981. Metalliferous deep-sea sediments. In: WOLF, K. H. (ed.) *Handbook of strat-bound and stratiform ore deposits*. Elsevier, Amsterdam, **9**, 77–178.
- MCKENZIE, R. M. 1971. The synthesis of birnesite, cryptomelane and other oxides and hydroxides of manganese. *Minerological Magazine*, **38**, 493–502.
- 1978. The effect of two manganese dioxides on the uptake of lead, cobalt, nickel, copper and zinc by subterranean clover. *Australian Journal of Soil Research*, **16**, 209–214.
- 1979. Proton release during adsorption of heavy metal ions by a hydrous manganese oxide. *Geochimica et Cosmochimica Acta*, **43**, 1855–1857.
- MUKAL, T. & DE HAAN, H. 1992. Adsorptive characteristics of iron (III) onto hydrous manganese dioxide in model lake water under acidic conditions. *Hydrobiologica Bulletin*, **25**, 183–189.
- MURALI, V. & AYLMORE, L. A. G. 1983. Competitive adsorption during solute transport in soils: 2. Simulations of competitive adsorption. *Soil Science*, **153**, 203–213.
- MURRAY, J. W. 1974. The surface chemistry of hydrous manganese oxide. *Journal of Colloid Interface Science*, **46**, 3, 357–371.
- 1975. The interaction of metal ions at the manganese dioxide solution interface. *Geochimica et Cosmochimica Acta*, **39**, 505–519.
- NICHOLSON, K. 1992a. Genetic types of manganese mineralization in Scotland: Indicators of palaeo-ocean spreading rate and a Devonian geochemical mobility boundary. *Economic Geology*, **87**, 1301–1309.
- 1992b. Contrasting mineralogical-geochemical signatures of manganese oxides: guides to metallogenesis. *Economic Geology*, **87**, 1253–1264.
- POSSELT, H. S., & ANDERSON, F. J. 1968. Cation adsorption on colloidal hydrous manganese dioxide. *Environmental Science & Technology*, **2**, 1087–1093.
- ROBINSON, G. D. 1981. Adsorption of Cu, Zn and Pb near sulfide deposits by hydrous manganese-iron oxide coatings on stream alluvium. *Chemical Geology*, **33**, 65–79.
- SMITH, R. W. & JENNE, E. A. 1991. Recalculation, Evaluation and prediction of surface complexation constants for metal adsorption on iron and manganese oxides. *Environmental Science & Technology*, **25**, 525–531.
- STROES-GASCOYNE, S., KRAMER, J. R. & SNODGRAS, W. J. 1986. A new model describing the adsorption of copper on MnO_2 . *Environmental Science & Technology*, **20**, 1047–1050.
- 1987. Preparation, characterization and ageing of MnO_2 , for use in trace metal speciation studies. *Applied Geochemistry*, **2**, 217–226.

- SULLIVAN, L. A. & KOPPI, A. J. 1992. Manganese oxide accumulations associated with some soil structural pores. I. Morphology, Composition and Genesis. *Australian Journal of Soil Research*, **30**, 409–427.
- TAKAMATSU, T., KAWASHIMA, M. & KOYAMA, M. 1985. The role of Mn²⁺-rich hydrous manganese oxide in the accumulation of arsenic in lake sediments. *Water Research*, **19**, 8 1029–1032.
- TAYLOR, R. M., & MCKENZIE, R. M. 1966. The association of trace elements with manganese minerals in Australian soils. *Australian Journal of Soil Research*, **4**, 29–39.
- TRAINA, S. J. & DONER, H. E. 1985a. Heavy metal induced releases of manganese (II) from a hydrous manganese dioxide. *Soil Science Society America Journal*, **49**, 317–321.
- & — 1985b. Co, Cu, Ni and Ca sorption by a mixed suspension of smectite and hydrous manganese oxide. *Clays and Clay Minerals*, **33**, 118–122.
- VAN DEN BERG, C. M. G. & KRAMER, J. R. 1979. Determination of complexing capacities and conditional stability constants for copper in natural waters using MnO₂. *Analytica Chimica Acta*, **106**, 113–120.
- VUCETA, J., & MORGAN, J. J. 1978. Chemical modeling of trace metals in fresh waters: role of complexation and adsorption. *Environmental Science & Technology*, **12**, 1302–1309.
- WHITNEY, P. R. 1975. Relationship of manganese – iron oxides and associated heavy metals to grain size in stream sediments. *Journal of Geochemical Exploration*, **4**, 251–263.
- WEBER, W. J. 1991. Sorption phenomena in subsurface systems: concepts, models and effects on contaminant fate and transport. *Water Research*, **25**, 499–528.
- YOUNG, L. B. & HARVEY, H. 1992. The relative importance of manganese and iron oxide and organic matter in the sorption of trace metals by surficial lake sediments. *Geochimica et Cosmochimica Acta*, **56**, 1175–1186.
- ZASOSKI, R. J. & BURAU, R. G. 1988. Sorption and sorptive interaction of cadmium and zinc on hydrous manganese oxide. *Soil Science Society America Journal*, **52**, 81–87.

P–T–X relationships during metamorphism of manganese-rich sediments: Current status and future studies

SOMNATH DASGUPTA

*Department of Geological Sciences, Jadavpur University,
Calcutta 700 032, India*

Abstract: This paper aims at reviewing the mineralogy, mineral chemistry and petrology of metamorphosed manganese-rich sediments from occurrences described since 1988. It presents a summary of new experimental data and evaluates the merits and shortcomings of the petrogenetic grids so far proposed for Mn-rich metamorphic rocks. The paper focuses on the inadequacies of experimental data on Mn-rich systems and discusses the problems associated with further quantification of the petrogenetic grids. Finally, a few suggestions for future research on Mn-rich systems are put forward.

The intricacies of the interrelationships amongst the pressure–temperature–bulk compositional variables during metamorphism of manganese-rich sediments are significantly less understood than pelitic, sem pelitic and calcareous sediments and basic igneous rocks. In an earlier publication (Dasgupta *et al.* 1990) we attempted to summarize and synthesize the data both from natural occurrences and experimental studies available up to 1988 pertaining to the petrogenesis of metamorphosed manganese-rich sediments and had pointed out several inadequacies as well as gaps in knowledge. Since then some notable work has been carried out in these directions and interesting results have been obtained. The purpose of this communication is to evaluate the current status of the subject dealing with the petrogenesis of metamorphosed manganese-rich sediments based on the studies carried out since 1988 and to point out probable directions of future studies. Repetition of what has appeared in the previous review paper (Dasgupta *et al.* 1990) will be avoided as far as possible. At the very outset, let me emphasize that petrographic, mineral and bulk chemical data, and some stable isotopic data on natural occurrences have been generated in recent years, but we reversed phase equilibrium studies on manganese rich bulk compositions within the pressure–temperature limits of crustal metamorphism are far less in number. This has left a significant gap in our knowledge on the pressure–temperature–bulk compositional constraints of metamorphism of manganese rich sediments. Additional purpose of this communication will, therefore, be to point out gaps in the currently available dataset of manganese-rich bulk compositions towards which future experimental work should be directed.

Metamorphosed manganese-rich sediments in geological record: mineralogy and petrography

Dasgupta *et al.* (1990) proposed that the metamorphosed manganese rich sediments of the world can be classified into five distinct mineralogical types. These are:

- Type I, Mn-oxide rocks (ores) containing quartz;
- Type IIA, Mn-silicate rocks with minor Mn oxides;
- Type IIB, Mn-oxide dominated rocks inter-banded with IIA and [containing minor silicates;
- Type IIIA, Mn-silicate–carbonate rock with/without minor Mn-oxides;
- Type IIIB, Mn-oxide-dominated rock inter-banded with IIIA and containing minor Mn-carbonate.

Dasgupta *et al.* (1990) listed the mineral associations, metamorphic grade and geological setting of the important deposits of the world belonging to these five types. It was further suggested that types I, IIA and IIB were derived from Mn higher oxide precursor sediments with various degrees of admixtures of ferruginous oxides/hydroxides, silica and clay minerals. Types IIIA and IIIB were, on the other hand, derived from Mn (or Ca–Mn) carbonate precursor sediments with various degrees of admixture of similar materials. Both types of sediments are common in unmetamorphosed natural occurrences (Roy 1981). Interpretation of reaction textures in metamorphosed deposits reveals that types I, IIA and IIB evolved through prograde deoxidation reactions, while types IIIA and IIIB rocks resulted from prograde decarbonation with or without oxidation reactions.

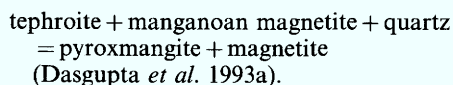
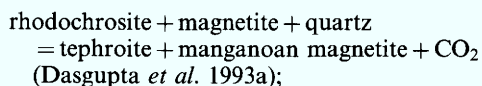
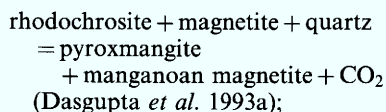
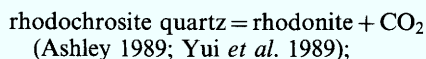
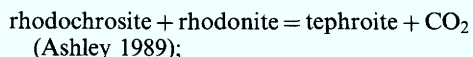
Table 1. Geological setting and mineral assemblages in different types of manganese formations of the world

Location	Geological setting, host rock	Metamorphic conditions	Major mineral assemblages	Probable precursor	Type of rock
Hoskins NSW Australia (Ashley 1989)	Oceanic submarine hydrothermal system, MORB basalts, chert	Greenschist facies	Tp + Rdh + Hs + Gt ± Rdn Rdn + Gt + Qz ± Bs ± Hdn ± Rdh	Carbonate ± oxide	IIIA, IIIB IIIA
Taiwan (Yu <i>et al.</i> 1989)	Eugeosynclinal, metachert, age unknown	450–500°C 3.5–4.5 kbar	Rdn + Qz ± Rdh + Gt + Amph Rdn + Qz + Rdh + Br + Hs + Amph	Carbonate Carbonate	IIIA IIIA & IIIB
Spain (Milland & Velilla 1994)	Eugeosynclinal, metatuffs, metacherts metabasics	450–500°C <4 kbar	Gt + Rdn + Hs + Tp + Mn-calcite Amph + Gt + Rdn + Qz + Mn-mica	Carbonate Oxide (?)	IIIA & IIIB IIA
Namibia (Bühn <i>et al.</i> 1995)	Iron-formations, glaciomarine sediments	660–700°C 3.5–4.5 kbar	Br + Hm + Jb + Hs ± silicates Br + Jb + Bx + Rdn + Cpx Gt + Cpx + Rdn + Qz ± Br ± Hm ± Hs	Oxide Oxide Oxide	I II B IIA
Sierra Nevada, California (Flohr & Huebner 1992)	Chert and shale, eugeosynclinal	325°C, 2 kbar	Hs + Rdh + Tp + Gt + Rdn ± Jb	Carbonate	IIIA & IIIB
Parseoni, India (Dasgupta <i>et al.</i> 1993a)	Metapelite and meta-calcareous	500–550°C 3–4 kbar	Pxm + Tp + Rdh + Mn-magnetite + Gt + Qz + Amph. Rdn + Pxm + Qz + Gt + Amph	Carbonate	IIIA
Wafangzi, China (Fan <i>et al.</i> 1992)	Shale, silty limestone	Thermally metamorphosed	Manganite + Br + Gt + Qz + Bx + Jb + Pxm Rdh + Tp + Jb + Bs + Cpx + Pxm	Oxide Carbonate	I, II B IIIA, IIIB

Tp, tephroite; Rdh, rhodochrosite; Hs, hausmannite; Gt, garnet; Rdn, rhodonite; Bs, bustamite; Hdn, hedenbergite; Amph, amphibole; Br, braunite; Bx, bixbyite; Jb, jacobite; Cpx, clinopyroxene; Hm, hematite; Qz, quartz, Pxm, pyroxmangite.

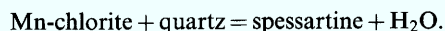
Numerous studies have shown that the manganese rich sediments, particularly types I, IIA, IIB and IIIB, were metamorphosed at considerably higher f_{O_2} than their enclosing rocks (Huebner 1967; Dasgupta *et al.* 1984, and the references cited therein). There is unanimity of opinion that oxygen behaves as an 'inert' component during metamorphism and considerable gradients in f_{O_2} exist between adjacent layers (Dasgupta *et al.* 1985). The latter conclusion has been confirmed by oxygen isotopic measurements (Bühn *et al.* 1995).

The geological setting, mineral associations, metamorphic conditions and probable precursor sediments of new occurrences of metamorphosed manganese rich rocks described since 1988 is given in Table 1. Most of these rocks are derived from carbonate precursors and textural features suggest the following mineral reactions during prograde metamorphism:



Reaction textures between different types of manganese silicates (amphiboles, pyroxenes and garnets) have not been studied in detail despite their ubiquitous presence in all these occurrences (Table 1). However, both prograde and retrograde phase relations between rhodochrosite, quartz, friedellites (friedellite, schallerite, manganopyrosmalite), caryopilite, tephroite and rhodonite have been interpreted on the basis of reaction textures in several very low grade metamorphosed deposits by Abrecht (1989) and Flohr & Huebner (1992). These studies are important because they bridge the gap of phase relations between the sedimentary/diagenetic stage and the greenschist facies and higher grades. There is, however, a major problem in the interpretation of phase relations involving these minerals. Some of these minerals contain As and Cl and the stability of these minerals will be enhanced by their presence in natural multi-component systems. Mineral reactions in nat-

ural rocks are expected to be multivariant and the simplistic phase relations deduced theoretically should be treated with caution. Abrecht (1989) and Ashley (1989) could document the reaction



All the workers since Huebner (1967) have predicted this reaction to account for the appearance of spessartine in a vast number of Mn-silicate rocks in the world conceivably by drawing analogy with the appearance of almandine-rich garnet in metapelites. However, clear-cut documentation was not available.

Another mineral which demands attention is caryopilite (with variable MgO, see Abrecht 1989) and Mn-talc, which could be precursor to Mn rich amphiboles and pyroxenes found in higher metamorphic grades. Experimental studies of Huebner (1986) indicated this possibility. Unfortunately, nearly all the caryopilites described from natural rocks are retrograde minerals.

Dasgupta *et al.* (1990) considered that calderite andradite garnets are restricted to type IIIA assemblages (also see Ashley 1989). They showed that stability of calderite-andradite garnet is an additional function of Ca content in the bulk. Bühn *et al.* (1995) have shown the presence of calderite-rich garnet from carbonate-free assemblages as well. This would imply a wider stability of calderite-andradite garnets in natural situations than believed earlier.

Dasgupta *et al.* (1989a) and Bühn *et al.* (1995) described Ba-Mn-Mg micas (kinoshitalite) from types IIIA and IIA manganese silicate rocks from India and Namibia respectively. These authors have not attempted to determine the phase relations of kinoshitalite and in the reported occurrences the mica has developed at the late stage of evolution (retrogression and water/granitic melt interaction?).

Mineral chemistry and element partitioning: Role of bulk and fluid compositions

Ostwald & Nayak (1993) described the so far highest Fe_2O_3 content in braunite (32.7 wt%) from Kajlidongri, India. In this deposit, braunite contains variable amounts of Fe_2O_3 (0–32.7 wt%), which the authors attributed to variable proportions of braunite and bixbyite modules in polysomatic braunite. The highly ferrian braunites have been characterized as 'primary metamorphic minerals'. The authors description shows presence of bixbyite along with these braunites. Although no bixbyite analysis is given, such wide variations

(7–32 wt.%) in Fe_2O_3 contents in braunites from the same sample are surprising. This can not be attributed to Mn–Fe partitioning between braunite and bixbyite (cf. Bhattacharya *et al.* 1984). Either the studied braunites are out of equilibrium or they consist of intergrowths of bixbyite and hematite.

Miscibility gaps between Mn-bearing ferromagnesian and alkali amphiboles have been documented by Shau *et al.* (1993). These authors were able to detect submicroscopic exsolution in Mn-rich alkali amphiboles, which they interpreted as results of spinoidal decomposition. The presence of such exsolution features in primary Mn-rich alkali amphiboles, however, raises the possibility that some amphibole analyses reported in the literature may represent bulk amphibole composition and should be treated with caution while interpreting phase relations.

Dasgupta *et al.* (1992) and Böhn *et al.* (1995) presented data on Mn-bearing alkali clinopyroxenes from types IIIA and IIA rocks from India and Namibia respectively. Compositionally these are manganoan aegirine-augites and in the occurrence described by Böhn *et al.* (1995) contain substantial acmite (up to 47 mol%). Compositional characteristics of these pyroxenes provide constraints on phase relationships under upper amphibolite facies conditions. The occurrence of these alkali pyroxenes is interesting because normal clinopyroxenes in metamorphosed Mn-silicate rocks are manganoan diopside–hedenbergite, kanoite and johannsenite (see review in Dasgupta *et al.* 1990). At the present stage data are inconclusive to suggest why alkali clinopyroxenes are stabilized in some occurrences that are not blueschist facies metamorphosed (Mottana 1986).

Several studies have documented the role of bulk composition (including the volatiles) in determining stabilization of Mn silicates and carbonates and partitioning of major elements amongst them. Millan & Velilla (1994) documented that X_{Mn} in the bulk controls stabilization of Mn garnet and tephroite, X_{Fe} controls tephroite and X_{CO_2} controls on the appearance of Mn carbonates in the rocks studied by them. Yui *et al.* (1989) corroborated the conclusion of Peters *et al.* (1974) and Winter *et al.* (1981) that carbonates strongly fractionate Ca over coexisting rhodonite under greenschist to amphibolite facies condition. However, under granulite-facies condition an opposite trend was noted by Dasgupta *et al.* (1993b) (Fig. 1). It is not yet resolved whether such reverse partitioning is due to the effect of increased temperatures under granulite facies condition or to the composition of the fluid phase and the nature of its buffering.

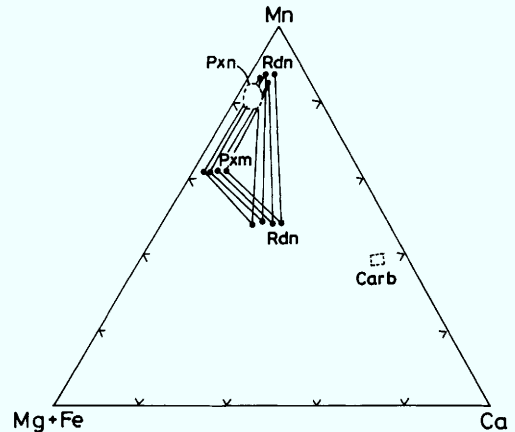


Fig. 1. Composition of carbonates and pyroxenoids in granulite facies plotted in Mn–(Mg + Fe)–Ca space. Dashed fields are the composition of these phases in amphibolite facies (after Winter *et al.* 1981). Rdh, rhodochrosite; Rdn, rhodonite; Pxm, pyroxmangite; Pxn, pyroxenoids.

In closely associated domains Dasgupta *et al.* (1993a) documented that pyroxmangite + tephroite assemblage was stabilized in relatively high-iron bulk compositions and low X_{CO_2} , and pyroxmangite (without tephroite) appeared at higher X_{CO_2} . This would additionally imply buffering of pore fluid composition by mineral reactions. That Mn–Fe partitioning between coexisting garnet, olivine, pyroxmangite and carbonates are functions of bulk composition under isothermal–isobaric condition has been documented from both amphibolite and granulite facies conditions (Dasgupta *et al.* 1993a, b). This would in turn imply non-ideal mixing of divalent Mn and Fe in these minerals. Lack of experimental data on distribution coefficients involving Mn amongst different phases prevents further quantification at this stage.

The compositions of coexisting rhodonite, pyroxmangite, bustamite, clinopyroxene and orthopyroxene define the miscibility gaps in the MnSiO_3 – FeSiO_3 – CaSiO_3 – MgSiO_3 system under ambient P – T conditions of metamorphism. New data on the compositional characteristics of these phases under granulite facies conditions (Dasgupta *et al.* 1993b) reveal some notable changes in the phase relationships, when compared with amphibolite facies conditions (Figs 2–4). The effect is more pronounced for rhodonite and clinopyroxene, the former becoming enriched in Ca and the latter more ferroan and less magnesian under granulite facies condition. This study demonstrated that, if properly

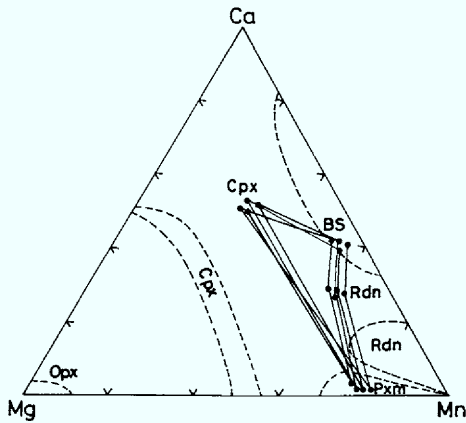


Fig. 2. Composition of coexisting pyroxenes and pyroxenoids plotted on the $\text{CaSiO}_3\text{-MnSiO}_3\text{-MgSiO}_3$ space in granulite facies. Cpx, clinopyroxene; Bs, bustamite; Rdn, rhodonite; Pxm, pyroxmangite; Opx, orthopyroxene. Dashed fields are after Brown *et al.* (1980) & Peterson *et al.* (1984).

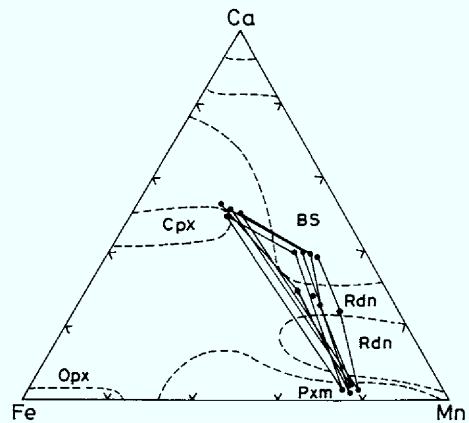


Fig. 4. Composition of coexisting phases in $\text{CaSiO}_3\text{-FeSiO}_3\text{-MnSiO}_3$ space in granulite facies. Abbreviations as in Figs 1 & 2.

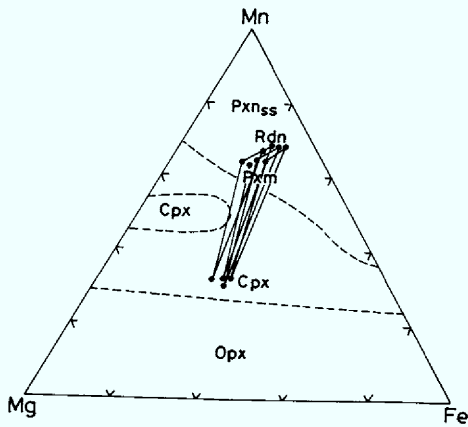


Fig. 3. Composition of coexisting phases plotted on $\text{MnSiO}_3\text{-MgSiO}_3\text{-FeSiO}_3$ space in granulite facies. Abbreviations as in Figs 1 & 2.

calibrated, the distribution coefficients can be used as geothermometers.

Preliminary data on oxygen isotopic fractionation between braunite and silicate minerals (garnet and feldspars) have been obtained by Böhn *et al.* (1995). This brings up a new avenue of research in case of metamorphosed Mn-rich rocks because of its potentiality as a temperature sensor.

It is evident from the above that fluid composition and the nature of its buffering and bulk X_{Mn} , X_{Fe} and X_{Mg} control the stabilization of manganese silicates and carbonates. There is, however, some evidence in

favour of temperature-dependence of the distribution coefficients involving Mn among coexisting phases.

Petrogenetic grids in Mn-rich systems

The pressure-temperature-bulk composition (including the fluids) dependence of the stabilization of Mn silicates, carbonates and oxides was first documented through the pioneering experimental work of Huebner (1967, 1969) in the system Mn-Si-C-O, which provided new directions of research on metamorphosed Mn-rich sediments. Subsequently, experimental studies by Peters (1971), Peters *et al.* (1974), Candia *et al.* (1975), Abrecht & Peters (1980), Abrecht (1980), Abs-Wurmbach *et al.* (1983) and Huebner (1986) provided further insights into the phase relationships in parts of the system Ca-Mn-Fe-Mg-Si-O. The effects of bulk composition ($X_{\text{CO}_2}^{\text{fl}}$, X_{Mg} , X_{Ca} , X_{Mn}) on the stabilization of Mn silicates and Mn carbonates, in addition to pressure and temperature, were clearly documented. These results have been reviewed in Dasgupta *et al.* (1990). Abrecht (1988) experimentally re-determined the equilibrium $\text{MnCO}_3 + \text{SiO}_2 = \text{MnSiO}_3 + \text{CO}_2$ at 1 Kb between 390 to 485°C in $\text{CO}_2\text{-H}_2\text{O}$ fluid mixtures. He confirmed that rhodonite and pyroxmangite have very small differences in entropy and Gibbs free energy of formation and, hence, metastable persistence of each of these phases is possible. He determined the entropy of formation and Gibbs free energy of formation of the pyroxenoid phase as $113 \pm 16 \text{ J mol}^{-1} \text{ K}$ and

$-1237 \pm 13 \text{ kJ/mol}^{-1}$ respectively. However, the discrepancy of this work with previous experimental studies on the same reaction is alarming. According to Abrecht (1988), no explanation can be offered for the discrepancy.

For low grade metamorphosed Mn silicate-carbonate rocks (Type IIIA) with rhodochrosite, friedelite, Mn-rich pyrosomalite, schallerite and caryopilite Abrecht (1989) constructed a partial petrogenetic grid in the system $\text{MnO-SiO}_2\text{-CO}_2\text{-H}_2\text{O}$ in the isobaric $T\text{-}X_{\text{CO}_2}$ space. Although this grid satisfactorily explains the sequence of mineral reactions involving these phases as functions of temperature and fluid compositions, the grid could not be quantified owing to the absence of thermochemical data. As pointed out earlier, the phase relationships in natural rocks will be far more complicated owing to the presence of additional components.

Dasgupta & Manickavasagam (1981) presented a qualitative petrogenetic grid in parts of the system Mn-Fe-Si-O . Combining available thermodynamic data and experimental data with mineral paragenesis in natural occurrences, Dasgupta *et al.* (1989b) constructed quantitative

petrogenetic grids in parts of the system Mn-Fe-Si-C-O (Fig. 5) and Mn-Fe-Si-O (Fig. 6) in $P\text{-}T\text{-}f_{\text{O}_2}$ space. Figure 5 shows that during prograde metamorphism from a carbonate precursor progressively oxidized phases will appear via decarbonation-oxidation reactions. Figure 6 shows that progressively reduced phases will appear from an oxide precursor with increase in temperature via deoxidation reactions. The nature of the reactions, the sequence of appearance of the phases and the temperatures of the reactions are consistent with those inferred from natural occurrences. Increase in pressure would shift all the invariant points to higher f_{O_2} . At constant f_{O_2} , mineral reactions in the system Mn-Fe-Si-C-O are relatively more sensitive to X_{CO_2} at lower temperatures. Dasgupta *et al.* (1989b) concluded that the Indian and South African Mn oxide (with/without carbonates) rocks equilibrated with an H_2O -rich fluid during progressive metamorphism. They have further shown that $X_{\text{Mn}^{3+}}$ in braunite is negatively correlated with $X_{\text{CO}_2}^{\text{fl}}$. Thus, unless the rocks equilibrate with a carbonic fluid, highly ferrian braunites

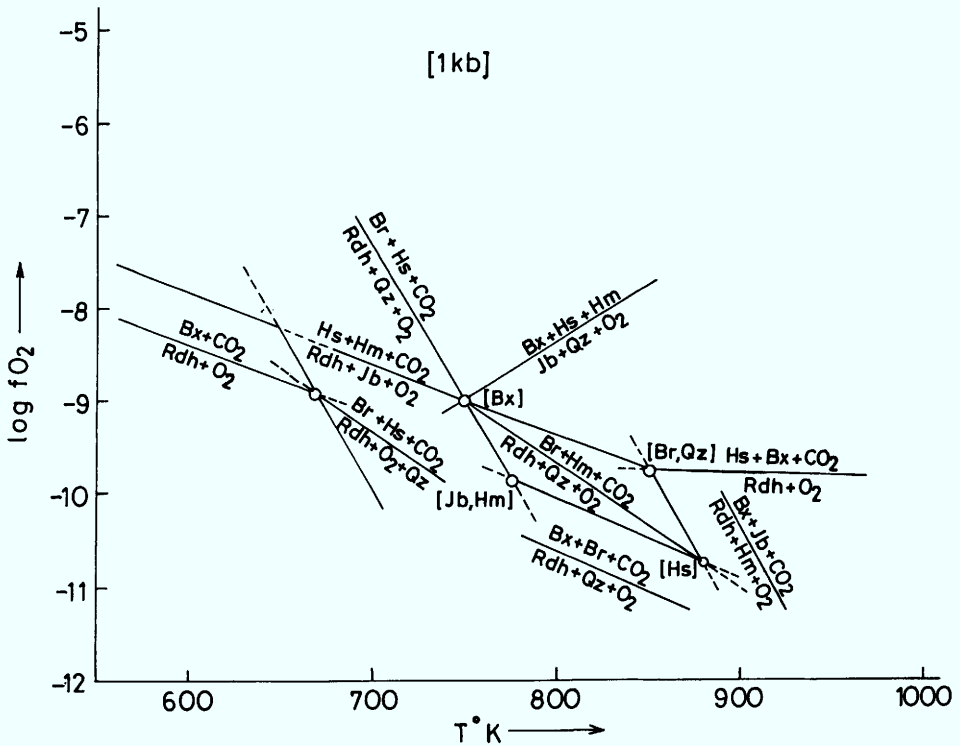


Fig. 5. Phase relations in part of the system Mn-Fe-Si-C-O at 1 kbar. Qz, quartz; Hs, hausmannite; Br, braunite; Jb, jacobsonite; Bx, bixbyite; Hm, hematite; others as in Figs 1 and 2.

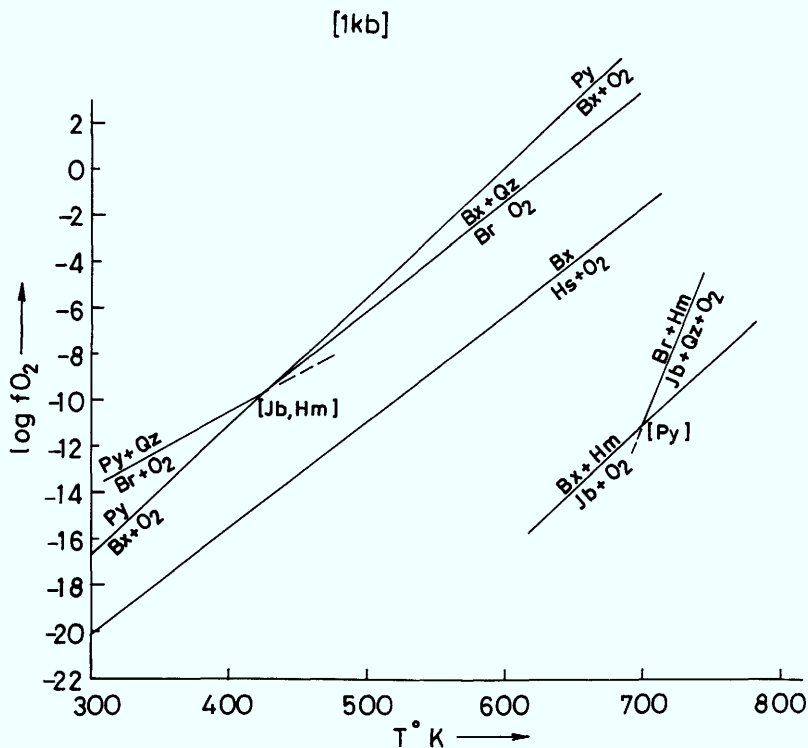


Fig. 6. Phase relations in parts of the system Mn-Fe-Si-O at 1 kbar. Py, pyrolusite; others as in Figs 1 and 2.

will not form. Although these grids correctly interpret the sequence of mineral reactions in many natural occurrences and temperature estimates tally well with those obtained from independent sources (see Bühn *et al.* 1995), these are not derived from internally consistent thermodynamic database. Hence, at the present stage these grids should be taken at best semi-quantitative.

Textual evidence from natural occurrences of Mn carbonate-oxide rocks (Type IIIB) indicate decarbonation-oxidation reactions during prograde metamorphism as discussed earlier. For a better understanding of the nature of inter-relationships between the two fugitive species, isothermal-isobaric μ_{CO_2} - μ_{O_2} diagrams need to be constructed. There are evidence for both buffered and unbuffered nature of X_{CO_2} during metamorphism of Mn-rich 2 sediments. In case of the former, μ_{CO_2} and μ_{O_2} could be mutually dependent variables. The slopes of the reactions would decide whether progressive oxidation (or deoxidation) of the assemblages could be the result of simply increasing (or decreasing) μ_{CO_2} under isothermal-isobaric conditions.

Problems associated with quantification of the petrogenetic grids

Any attempt to quantify the petrogenetic grids for Mn-rich systems is seriously handicapped by several crucial problems. In this section, I shall try to focus some of these major lacunae.

(A) Thermochemical parameters of some of the crucial Mn oxides and silicates are not known. One glaring example is braunite, one of the most common phases in metamorphosed Mn formations. Miyano & Beukes (1987) calculated the thermochemical parameters of braunite from oxides and these values were incorporated in the phase diagram computations of Dasgupta *et al.* (1989b). The values are obviously not internally consistent with those of the other phases, which were taken from other sources, principally from Robie *et al.* (1979). Despite several phase equilibrium studies involving braunite, no attempt has so far been made to retrieve standard state thermodynamic parameters of braunite. It is also not possible to do so from unreversed experiments. Standard state thermodynamic parameters are available for bixbyite, hausmannite, pyrolusite,

rhodochrosite, rhodonite, pyroxmangite and tephroite from various calorimetric and experimental studies and are available in parts in the compilations of Robie *et al.* (1979) and Holland & Powell (1990). However, one can easily observe significant discrepancies in the values given in the compilations. For Mn-rich amphiboles (both alkali and ferromagnesian), Mn-rich ortho- and clinopyroxenes, Mn-rich epidotes and complex hydroxyl bearing phases such as caryopilite, friedellite etc., no standard state thermodynamic data is available. As a result, no attempt can be made to calculate petrogenetic grids involving these phases.

(B) For common pelitic, sem pelitic, calcareous and basic rocks, the internally consistent database of Berman (1988) (TWEEQ) and Holland & Powell (1990) (THERMOCALC) have been proved to be extremely useful to calculate petrogenetic grids and to compute P - T - X relationships. Work on Mn-rich systems is hampered due to the non-availability of any internally consistent thermodynamic database. Development of an internally consistent database is obviously dependent on the availability of well-reversed experimental data. It is the paucity of the latter which is responsible for the lack of any acceptable database for Mn-rich systems.

(C) Many experimental studies in Mn-rich systems have been directed towards synthesis of the phases and determination of compositional limits of the phases in multicomponent systems. In most of these studies, the two- or three-phase fields have been delineated on the basis of XRD data of the coexisting phases and very few attempts have been made to determine the composition of the coexisting phases. As a result, it is impossible to determine whether any systematic pattern of exchange of major elements between coexisting phases as a function of temperature exists or not. Excepting a few cases (Huebner 1967; Abrecht 1988; Peters *et al.* 1974), reversal of experimental runs was not carried out. Unlike in normal pelite, basic and calcareous systems, very few mineral reactions in Mn-rich systems have been calibrated or experimentally reversed. Compositional limits of R (= Mn-Mg-Ca-Fe)SiO₃ phases under amphibolite and granulite facies conditions have been delineated on the basis of natural data (Brown *et al.* 1980; Petersen *et al.* 1984; Dasgupta *et al.* 1993b). These composition-paragenesis diagrams are obviously handicapped by the unknown degree of resetting of natural composition during cooling of the rocks and are again at best semi-quantitative. The results of Bhat-tacharya *et al.* (1984) indicated the possibility of formulation of a braunite-bixbyite Mn³⁺-Fe³⁺

exchange geothermometer. Formulation of a rhodonite-pyroxmangite geothermobarometer has been attempted by Maresch & Mottana (1976) and Schul Guttler & Peters (1988), with some degree of success. Sengupta *et al.* (1989) extended the Ellis & Green (1979) garnet-clinopyroxene geothermometer for Mn-rich bulk compositions and obtained reasonable results for several natural deposits. Therefore, there exist very limited means to calculate metamorphic pressure-temperature regimes of metamorphism directly from the Mn-rich rocks.

(D) Another major handicap bothering metamorphic petrologists working on Mn-rich systems is the non-availability of activity-composition relationships among common solid-solution phases. The situation is best for garnet solid solutions, where a reasonable amount of phase equilibria, calorimetric and natural data are available. It is now well known that mixing of Ca-Mn in garnet is ideal (Kozioł 1990). Mixing of Mn²⁺-Fe²⁺ in garnet is also close to ideality and can be expressed as a symmetric function of composition with $W_{\text{Mn-Fe}} \approx 300 \text{ cal mol}^{-1}$ (Powenceby *et al.* 1987). From natural compositional data, Sengupta *et al.* (1989) determined that Mn-Mg mixing in garnet is symmetric non-ideal with $W_{\text{Mn-Mg}} \approx 1600 \pm 500 \text{ cal mol}^{-1}$. Experimental data of Chakraborty & Ganguly (1992) corroborate the above value. Wood *et al.* (1994) have, on the other hand, experimentally obtained a value of $c. \approx 400 \pm 600 \text{ cal mol}^{-1}$. These workers have also determined that Mn-Mg mixing in olivine is also symmetric with $W_{\text{Mn-Mg}} \approx 1400 \pm 500 \text{ cal mol}^{-1}$. According to Wood *et al.* (1994), mixing of Mn and Mg in oxides is strongly asymmetrical with $W_{\text{Mn}} \approx 5000 \text{ cal mol}^{-1}$ and $W_{\text{Mg}} \approx 2500 \text{ cal mol}^{-1}$.

Activity-composition relationships in Mn-Mg-Fe-Ca pyroxenes/pyroxenoids and amphiboles are not known. Ideal on-site mixing of Mn in pyroxenoids has been assumed (Winter *et al.* 1981). Similarly, no reliable data exists regarding the mixing of trivalent Mn and Fe in oxides.

Suggestions for future work

In the previous sections I have tried to bring out the updated scenario regarding the pressure-temperature-compositional relationship of metamorphosed manganese rich sediments. If one combines the natural occurrence data on metamorphosed manganese rich rocks presented in this compilation and in Dasgupta *et al.* (1990), it becomes obvious that an adequate database is available to study the P - T - X evolution of such

rocks. The problem lies principally with inadequacies of experimental support to the predictions made from the study of natural deposits. Unless experimental studies are undertaken in future, P - T - X relationships during metamorphism of manganese rich sediments will remain semi-quantitative. Dasgupta *et al.* (1990) outlined some of the unsolved problems regarding petrogenesis of metamorphosed manganese rich sediments. To this list I may add here a few suggestions for further experimental studies: (a) to determine standard state thermodynamic parameters of braunite, Mn-Mg amphiboles, Mn-Mg clinopyroxenes, Mn-Mg-Fe orthopyroxene, Mn-micas; (b) to develop an internally consistent thermodynamic database in the system MnO-MgO-FeO-CaO-Al₂O₃-CO₂-SiO₂-H₂O-O₂; (c) to determine activity-composition relationships involving mixing of Mn in rock forming silicates, carbonates and oxides; (d) to determine the distribution coefficients of major elements with Mn as function of temperature in coexisting pyroxenes, garnets, pyroxenoids and olivines keeping in mind the possibilities of developing new geothermometers; and (e) to calibrate important mineral reactions deduced from textural relationships in natural rocks as functions of variable fluid compositions.

My grateful thanks go to M. Fukuoka who has supplied photocopies of recent publications on metamorphosed manganese deposits over the last five years. Because of this help I could venture into writing this paper. However, I am responsible for any inadvertent omission. Time and again P. Sengupta questioned my arguments and conclusions, which helped me substantially. B. Böhn kindly provided me a pre print of their forthcoming paper. Part of this paper was presented during the DMG Meeting held at Freiberg in 1994. Financial support to attend this meeting was given to me by the German Working Group of IGCP Project-318 and the Alexander Von Humboldt Stiftung. I acknowledge help from D. K. Mukhopadhyay and S. Pal while preparing the paper. My thanks are due to all the above mentioned persons and organizations. Reviews by two anonymous reviewers were helpful. This paper is a contribution to IGCP Project 318 (Polymetallic Marine Oxides).

References

- ABRECHT, J. 1980. Stability relations in the system CaSiO₃-CaMnSi₂O₆-CaFeSi₂O₆. *Contributions to Mineralogy and Petrology*, **74**, 253-260.
- 1988. Experimental evaluation of the MnCO₃+SiO₂=MnSiO₃+CO₂ equilibrium at 1 kbar. *American Mineralogist*, **73**, 1285-1291.
- 1989. Manganiferous phyllosilicate assemblages: occurrences, compositions and phase relations in metamorphosed Mn-deposits. *Contributions to Mineralogy and Petrology*, **103**, 228-241.
- & PETERS, T.J. 1980. The miscibility gap between rhodonite and bustamite along the join MnSiO₃-Ca_{0.40}Mn_{0.60}SiO₃. *Contributions to Mineralogy and Petrology*, **74**, 261-269.
- ABS WURMBACH, I., PETERS, T.J., LANGER, K. & SCHREYER, W. 1983. Phase relations in the system Mn-Si-O an experimental and petrological study. *Neues Jahrbuch für Mineralogie Abhandlungen*, **146**, 258-279.
- ASHLEY, P. M. 1989. Geochemistry and mineralogy of tephroite bearing rocks from the Hoskins manganese mine, New South Wales, Australia. *Neues Jahrbuch für Mineralogie Abhandlungen*, **161**, 85-111.
- BERMAN, R. G. 1988. Internally consistent thermodynamic data for the stoichiometric minerals in the system Na₂O-K₂O-CaO-MgO-FeO-Fe₂O₃-Al₂O₃-SiO₂-TiO₂-H₂O-CO₂. *Journal of Petrology*, **29**, 445-522.
- BHATTACHARYA, P. K., DASGUPTA, S., FUKUOKA, M. & ROY, S. 1984. Geochemistry of braunite and associated phases in metamorphosed non-calcareous manganese ores of India. *Contributions to Mineralogy and Petrology*, **87**, 65-71.
- BROWN, P. E., ESSENE, E. J. & PEACOR, D. R. 1980. Phase relations inferred from field data for Mn pyroxenes and pyroxenoids. *Contributions to Mineralogy and Petrology*, **74**, 1, 417-425.
- BÜHN, B., OKRUSCH, M., WOERMANN, E., LEHNERT, K. & HOERNES, S. 1995. Metamorphic evolution of Neoproterozoic manganese formations and their country rocks at Otjosondu, Namibia. *Journal of Petrology*, **36**, 463-496.
- CANDIA, M. A. F., PETERS, T.J. & VALARELLI, J. V. 1975. The experimental investigation of the reaction MnCO₃+SiO₂=MnSiO₃+CO₂ and MnSiO₃+MnCO₃=Mn₂SiO₄+CO₂ in CO₂/H₂O gas mixtures at a total pressure of 500 bars. *Contributions to Mineralogy and Petrology*, **52**, 261-266.
- CHAKRABORTY, S. & GANGULY, J. 1992. Cation diffusion in aluminosilicate garnets: experimental determination in spessartin almandine diffusion couples, evaluation of effective binary diffusion coefficients and applications. *Contributions to Mineralogy and Petrology*, **111**, 74-86.
- DASGUPTA, H. C. & MANICKAVASAGAM, R. M. 1981. Regional metamorphism of non-calcareous manganese rich sediments from India and the related petrogenetic grid for a part of the system Mn-Fe-Si-O. *Journal of Petrology*, **22**, 360-396.
- DASGUPTA, S., BANERJEE, H. & MAJUMDAR, N. 1984. Contrasting trends of mineral reactions during progressive metamorphism in interbanded pelite-manganese oxide sequence: Example from Precambrian Sausar Group, India. *Neues Jahrbuch Mineralogie Abhandlungen*, **150**, 95-102.
- & FUKUOKA, M. 1985. Oxidation gradients in metamorphosed non-carbonic manganese formations. *Contributions to Mineralogy and Petrology*, **90**, 258-261.

- , CHAKRABORTI, S., SENGUPTA, P., BANERJEE, H. & FUKUOKA, M. 1989a. Compositional characteristics of kinoshitalite from the Sausar Group, India. *American Mineralogist*, **74**, 200–202.
- , SENGUPTA, P., BANERJEE, H., ROY, S., FUKUOKA, M. & MUKHERJEE, M. 1989b. Mineral reactions in manganese oxide rocks: P–T–X phase relations. *Economic Geology*, **84**, 434–443.
- , BANERJEE, H., BHATTACHARYA, P. K., FUKUOKA, M. & ROY, S. 1990. Petrogenesis of metamorphosed manganese deposits and the nature of the precursor sediments. *Ore Geology Reviews*, **5**, 359–384.
- , FUKUOKA, M. & ROY, S. 1992. Depositional models for manganese oxide and carbonate deposits of the Precambrian Sausar Group, India. *Economic Geology*, **87**, 1412–1418.
- , SENGUPTA, P., FUKUOKA, M. & ROY, S. 1993a. Contrasting parageneses in the manganese silicate–carbonate rocks from Parseoni, Sausar Group, India and their interpretation. *Contributions to Mineralogy and Petrology*, **114**, 533–538.
- , HARIYA, Y. & MIURA, H. 1993b. Compositional limits of manganese carbonates and silicates in granulite facies metamorphosed deposits of Garbham, Eastern Ghats, India. *Resource Geology*, Special Issue 17, 43–49.
- ELLIS, E. J. & GREEN, D. H. 1979. An experimental study of the effect of Ca upon garnet–clinopyroxene Fe–Mg exchange equilibria. *Contributions to Mineralogy and Petrology*, **71**, 13–22.
- FAN, D., DASGUPTA, S., BOLTON, B. R., HARIYA, Y., MOMOI, H., MIURA, H., JIAJU, LI. & ROY, S. 1992. Mineralogy and geochemistry of the Proterozoic Wafangzi ferromanganese deposit, China. *Economic Geology*, **87**, 1430–1440.
- FLOHR, M. K. & HUEBNER, S. 1992. Mineralogy and geochemistry of two metamorphosed sedimentary manganese deposits, Sierra Nevada, California, USA. *Lithos*, **29**, 57–85.
- HOLLAND, T. B. J. & POWELL, R. 1990. An enlarged and updated internally consistent thermodynamic dataset with uncertainties and correlations: the system K_2O – Na_2O – CaO – MgO – MnO – FeO – Fe_2O_3 – TiO_2 – SiO_2 – C – H_2 – O_2 . *Journal of Metamorphic Geology*, **8**, 89–124.
- HUEBNER, J. S. 1967. *Stability relations of minerals in the system Mn–Si–C–O*. PhD Thesis, The Johns Hopkins University, Baltimore.
- 1969. Stability relations of rhodochrosite in the system Mn–C–O. *American Mineralogist*, **54**, 359–481.
- 1986. Nature of phases synthesized along the join $(Mg, Mn)_2Si_2O_6$. *American Mineralogist*, **71**, 111–122.
- KOZIOL, A. 1990. Activity–composition relationships of binary Ca–Fe and Ca–Mn garnets determined by reversed displaced equilibrium experiments. *American Mineralogist*, **75**, 319–327.
- MARESCH, W. V. & MOTTANA, A. 1976. The pyroxmangite rhodonite transformation for the $MnSiO_3$ composition. *Contributions to Mineralogy and Petrology*, **55**, 69–79.
- MILLAN, J. J. & VELILLA, N. 1994. Mineralogy and geochemistry of reduced manganese carbonate–silicate rocks from the Aracena area (Iberian Massif, SW Spain). *Neues Jahrbuch für Mineralogie Abhandlungen*, **166**, 193–209.
- MIYANO, T. & BEUKES, N. J. 1987. Physicochemical environments for the formation of quart free manganese oxide ores from the early Proterozoic Hotazel Formation, Kalahari manganese field, South Africa. *Economic Geology*, **82**, 706–718.
- MOTTANA, A. 1986. Blueschist facies metamorphism of manganese cherts: A review of the Alpine occurrences. *Geological Society of America Memoir*, **164**, 267–299.
- OSTWALD, J. & NAYAK, V. K. 1993. Braunite mineralogy and paragenesis from the Kajlidongri mine, Madhya Pradesh, India. *Mineralium Deposita*, **28**, 153–156.
- PETERS, Tj. 1971. Pyroxmangite, stability in H_2O – CO_2 mixtures at a total pressure of 2000 bars. *Contributions to Mineralogy and Petrology*, **32**, 267–273.
- , VALARELLI, J. V. & CANDIA, M. A. F. 1974. Petrogenetic grid from experimental data in the system Mn–Si–C–O–H. *Revista Brasileira Geociencias*, **4**, 15–27.
- PETERSEN, E. U., ANOVITZ, L. M. & ESSENE, E. J. 1984. Donpeacorite (Mn, Mg) $MgSi_2O_6$, a new orthopyroxene and the proposed phase relations in the system $MnSiO_3$ – $MgSiO_3$ – $FeSiO_3$. *American Mineralogist*, **69**, 472–480.
- POWENCEBY, M. I., WALL, V. J. & O'NEILL, H. ST. 1987. Fe–Mn partitioning between garnet and ilmenite: experimental calibration and applications. *Contributions to Mineralogy and Petrology*, **97**, 116–126.
- ROBIE, R., HEMMINGWAY, B. S. & FISHER, J. P. 1979. *Thermodynamic properties of minerals and related substances at 298.15°K and 1 bar (10⁵ pascals) pressure at higher temperatures*. United States Geological Survey Bulletin. **1452**.
- ROY, S. 1981. *Manganese Deposits*. Academic Press, London.
- SCHULZ–GÜTTLER, R. & PETERS, Tj. 1988. Coexisting rhodonite and pyroxmangite in the system $MnSiO_3$ – $MgSiO_3$ – $FeSiO_3$ – $CaSiO_3$ as a geothermometer. *Schweizerische Mineralogische und Petrographische Mitteilungen*, **67**, 47–51.
- SENGUPTA, P., DASGUPTA, S., BHATTACHARYA, P. K. & HARIYA, Y. 1989. Mixing behaviour in quaternary garnet solid solution and an extended Ellis and Green garnet–clinopyroxene geothermometer. *Contributions to Mineralogy and Petrology*, **103**, 223–227.
- SHAU, H., PEACOR, D. R., GHOSE, S. & PHAKEY, P. P. 1993. Submicroscopic exsolution in Mn-bearing alkali amphibole from Tirodi, Maharashtra, India. *American Mineralogist*, **78**, 96–106.
- WINTER, G. A., ESSENE, E. J. & PEACOR, D. R. 1981. Carbonates and pyroxenoids from the manganese deposits near Bald Knob, North Carolina. *American Mineralogist*, **66**, 276–289.

- WOOD, B. J., HACKLER, R. T. & DOBSON, D. P. 1994. Experimental determination of Mn-Mg mixing properties in garnet, olivine and oxide. *Contributions to Mineralogy and Petrology*, **115**, 438-448.
- YUI, T-F., LO, C-H. & LEE, C. W. 1989. Mineralogy and petrology of metamorphosed manganese rich rocks in the area of Santzan river, eastern Taiwan. *Neues Jahrbuch für Mineralogie Abhandlungen*, **160**, 249-268.

Zincian rancieite from the Kato Nevrokopi manganese deposits, Macedonia, northern Greece

M. K. NIMFOPOULOS¹, K. M. MICHAELIDIS² & G. CHRISTOFIDES²

¹ *Institute of Geology & Mineral Exploration, Thessaloniki Branch, 1 Fragon Street, 546 26 Thessaloniki, Macedonia, Greece*

² *Department of Mineralogy, Petrology & Economic Geology, Aristotle University, 540 06 Thessaloniki, Macedonia, Greece*

Abstract: At the 25th km main Mn-mine of Kato Nevrokopi, Macedonia, northern Greece, rancieite forms flaky to laminated aggregates encrusting vugs, and replacing pyrolusite and todorokite in massive deposits of the Falakron marbles. It has an unusually high ZnO (1.53–3.07 wt%) content and therefore it was named 'zincian rancieite'. The average (18 spots) chemical composition of rancieite by EPMA is (wt%): MnO₂ 62.01, CaO 6.83, ZnO 2.54, Al₂O₃ 1.18, MgO 0.63 plus minor oxides (Fe₂O₃, K₂O & SiO₂), total of 73.98. Assuming H₂O-content as 26.02 (100 – 73.98) wt%, these data reflect the following empirical formula: (Ca_{0.67}Zn_{0.17}Al_{0.12}Mg_{0.09} Fe_{0.02}³⁺K_{0.02}Si_{0.02})Mn_{3.90}⁴⁺O₉7.9H₂O. A high H₂O-content is also evidenced by the XRD pattern, which together with optical microscopy and SEM, indicates a poor structural order. Rancieite formation at Kato Nevrokopi belongs to the last stage of mineral genesis, which took place at ambient P, low T (around 25°C) by percolating oxygen bearing, Ca–Zn rich, meteoric water through the host marble.

Rancieite is a Ca-rich hydrated Mn-oxide mineral named after Rancie, France. It was first described from Devonian limestones of the French Pyrenees (Leymerie 1895). Its name was also used by Lacroix (1910) for chemically analysed Mn-oxide from other localities in the Pyrenees. Chemical analyses of rancieite from Cuba support the formula [(Ca,Mn²⁺) Mn₄⁴⁺O₉·3H₂O] (Richmond *et al.* 1969; Burns & Burns 1977).

Studies by Burns & Burns (1977), Bardossy & Brindley (1978) and Potter & Rossman (1979) showed that rancieite is an hexagonal phyllo-manganate, the structure of which consists of disorderly stacked layers of octahedral Mn⁴⁺O₆ or Mn(OH)₆ separated by interlayers of cations (predominantly Ca) and water. Other elements are present, but in minor amounts. Rancieite forms an isomorphous series with birnessite, in which Na predominates over Ca (Bardossy & Brindley 1978). Variations in the interlayer cations cause variability in the (001) spacing from 7 to *c.* 7.5 Å (Chukhrov *et al.* 1979). Data presented by Chukhrov *et al.* (1979) suggest that the series is not continuous, and they defined rancieite as those having the ratio Ca/(∑cations) in the range of 0.81 to 0.41, whereas for birnessite the ratio Ca/(∑cations) is in the order of 0.25 to 0.02. Bardossy & Brindley (1978) defined birnessite as those with Na > Ca. Kim (1980) suggested that there are two solid solution series, one for birnessite and one for rancieite; rancieite being more hydrated of the two, with an average of 2.8 water molecules per formula unit. Barrese *et al.* (1986) concluded

from the results of electron microprobe analysis and thermogravimetric studies that the correct formula for rancieite is CaMn₄O₉·4H₂O and noted some substitution of Mg and Ba for Ca in their samples. Carlos *et al.* (1993) found rancieite deficient in Mn and Ca, but with unusual concentration of Si, Ti, Fe, Mg, Zn, Ba, Ce and Pb. The name takanelite was also used to designate the Mn²⁺-analogue (Mn²⁺ substituting for Ca²⁺) of rancieite (Nambu & Tanida 1971; Kim 1991).

Rancieite has been described from a variety of supergene and sedimentary environments where it is a common mineral (see reviews by Frenzel 1980; Burns & Burns 1979). It is also rarely found in hot-spring environments (Hewett & Fleischer 1960; Hewett *et al.* 1963). Rancieite is characteristically found in Ca-rich environments such as weathered andesitic and basaltic tuffs (Cuba, Richmond *et al.* 1969; Italy, Barrese *et al.* 1986; Nevada USA, Carlos *et al.* 1993) and travertines, limestones or marbles (North Dakota USA, Hewett & Fleischer 1960; Itza Greece, Bardossy & Brindley 1978; Hesse Germany, Brannath & Smykatz-Kloss 1992).

This work is the first study of rancieite from the 25th km main manganese mine at Kato Nevrokopi, Drama district, northern Greece (Fig. 1). The Kato Nevrokopi mines, with over 4.5 Mt minimum total concentrate of Mn-oxide produced so far, constitute the largest manganese deposits in Macedonia, Greece (Nimfopoulos *et al.* 1988; Nimfopoulos & Patrick 1991). Rancieite was investigated using a variety of

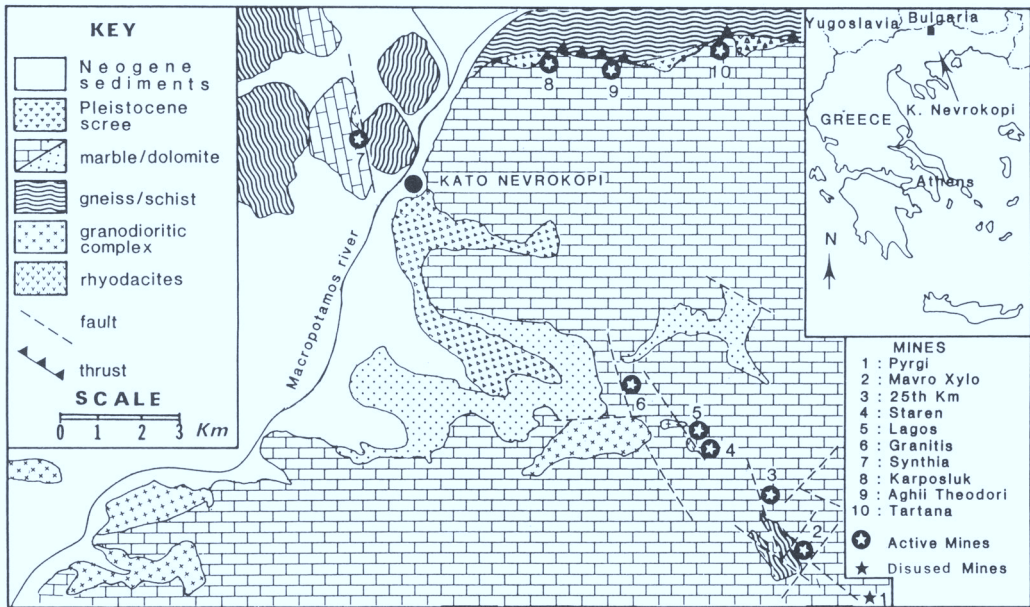


Fig. 1. Geology and mineralization at Kato Nevrokopi, in Macedonia, northern Greece.

techniques, such as optical microscopy, X-ray diffraction (XRD) electron probe microanalysis (EPMA), and scanning electron microscopy (SEM), in order to clarify its chemistry and occurrence, and its genetic relationship to the weathering process.

Geological setting

The Mn-mineralization of Kato Nevrokopi is scattered in an area of approximately 170 km² near to the Greek-Bulgarian border (Fig. 1), but the main mines (25th km and Mavro Xylo) are located adjacent to the Drama–Kato Nevrokopi main road, 25 km from Drama town (41°15'19" N, 23°58'23" E).

The study area geologically belongs to the Rhodope massif. The age of the Rhodope massif is uncertain. It has been suggested as Archaean to Proterozoic (Dimitrov & Zidarov 1969) and pre-Early Carboniferous on the basis of Rb/Sr dating on granitoids (342 ± 27 Ma) intruding the metamorphic basement (Moorbath & Zagorcev 1983).

The manganese mineralization is epigenetic, hosted by a thick sequence of Palaeozoic marbles (the Upper Carbonate Sequence) which has been thrust over a sequence of alternating gneisses, mica schists, amphibolites and marbles (the Lower Gneiss Sequence) (Papanikolaou & Panagopoulos 1981; Zachos

& Dimadis 1983). These two sequences form the Rhodope massif basement, which has experienced a complicated tectonometamorphic evolution. Alpine deformation is represented by small scale isoclinal folds and related northeast and northwest trending, steeply dipping, faults of Cretaceous to Oligocene age (Jordan 1969).

The mineralization at Kato Nevrokopi is confined to the intersections of the northeast- and northwest-trending faults and the thrust zone forming the junction between the Upper Carbonate and the Lower Gneissic unit (Fig. 1). The richest orebodies are found in places where the mineralization has extended laterally into the marble. Negligible mineralization occurs in the schist.

Primary orebodies are irregular in shape, with individual ore shoots being lenticular or tabular, sub-parallel to the bedding, up to 50 m in length, 20 m in width and 5–10 m in thickness. Secondary Mn-oxide orebodies have the shape of the karstic cavities (dolines or sinkholes, up to 100 m in diameter and 30 m depth).

Occurrence and association

The Kato Nevrokopi rancieite (Fig. 2a) occurs as aggregates of flakes or laminae encrusting small vugs (up to 2 cm in diameter) and/or filling open fissures in massive manganese dioxide deposited in large karstic cavities. The ore is

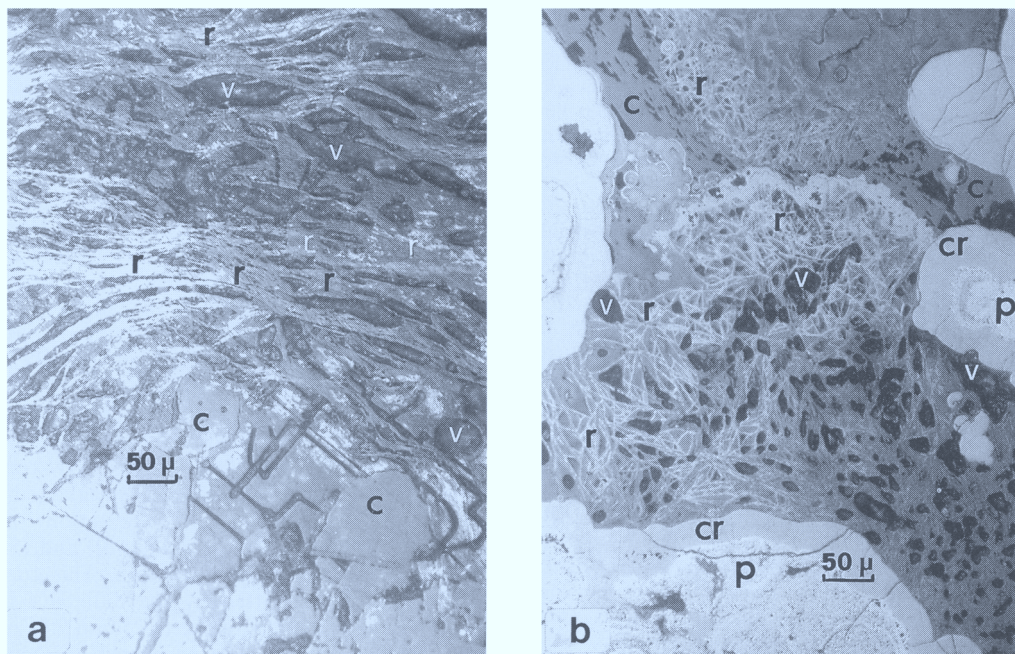


Fig. 2. Mineral texture photomicrographs in reflected light. (a) Flakes and fine laminae of rancieite (r), deposited in a karstic cavity in contact with marble calcite (c). Note the strong anisotropy (white to dark grey) of rancieite and the vugs (v) within the rancieite laminae. Partly crossed polars. Scale bar is 50 μ m. (b) Fine-grained pyrolusite (p) is partly replaced by encrustation of an amorphous cryptomelane type phase (cr) and this in turn by rancieite (r) flakes, leaving vugs (v) behind. Rancieite formation appears contemporary to the dissolution of pitted calcite (c). Plane polarized light. Scale bar is 50 μ m long.

dominated by the presence of subhedral to euhedral, coarse, tabular, pyrolusite (up to 50 μ m across), lining the margins of karstic cavities in contact with the marble calcite. Fine-grained (up to 15 μ m long) material resembling pyrolusite occurs in the interior (central part) of the cavities. This material gradually becomes coarsely crystalline and tabular in places, where it is in contact with late calcite (deposited in vugs of the cavities). The optical features, combined with the X-ray diffraction study, identified the coarse material as pyrolusite. Relict fibrous aggregates (up to 15 μ m across) of todorokite mixed with fine-grained pyrolusite also occur in the central part of the cavities, interbedded with mica. Finally, goethite forms subhedral to euhedral pseudomorphs after pyrite.

In the central part of karstic cavities, along fracture planes in the ore, fine-grained pyrolusite is locally replaced by irregular masses and encrustations of an amorphous to finely crystalline grey phase having a composition similar to that of cryptomelane (optical and EPMA evidence, Fig. 2b; XRD pattern without peaks). Breakdown of the grey phase and

dissolution of cavity calcite (evidenced by trigonal pits; Fig. 2b) resulted in their replacement by flaky or laminated rancieite aggregates, leaving behind vugs. Rancieite has also replaced fibrous todorokite (optical and XRD evidence) in the same part of the ore. This todorokite has been interpreted as the first formed Mn-oxide during the late hydrothermal to early supergene stage of mineralization (Nimfopoulos & Patrick 1991).

The margins of the karstic cavities also contain rancieite flakes and laminae, commonly replacing coarse-grained tabular pyrolusite and wallrock (marble) calcite along its cleavage planes.

Methodology

The samples were first thoroughly examined by transmitted and reflected light microscopy and areas rich in rancieite and free of other minerals were located. Special care was taken to locate areas totally free of any optically visible calcite, in order to avoid contamination. Analyses were, then, carried out in the same areas by a CAMECA-CAMEBAX instrument

fitted with both energy dispersive (EDS) and wavelength dispersive spectrometers (WDS) (University of Manchester, UK) and a JEOL JSM-840 A instrument fitted with a LINK EDS analytical system (University of Thessaloniki). The operating conditions for both instruments were 15 kV accelerating voltage, 3 nA beam current and 1 μ m beam diameter. Element concentrations were calculated with ZAF-4/FLS software provided by LINK systems. First, the EDS spectrum of the analysed mineral was obtained and the major elements (>1000 ppm) identified. The identity and possible existence of trace elements (<1000 ppm) was also checked by WDS peak-seeking. Absence of any nearby calcite and other Mn-oxides in the analysed area was also checked by back-scattered electron imaging. The following standards were used: wollastonite (Si, Ca), corundum (Al), periclase (Mg), orthoclase (K), albite (Na), olivine (Fe) and pure metals for Mn, Zn, Co and Ni.

X-ray powder diffraction of the area analysed by EPMA was then performed by scraping off material from the polished section according to the method of Sorem & Fewkes (1980). The XRD pattern was recorded at $1^\circ 2\theta \times \text{min}^{-1}$ with Cu-K α radiation filtered with a curved graphite crystal monochromator. SEM was performed on an ISI Super II model (University of Manchester).

X-ray crystallography

Data from the X-ray powder diffraction are presented in Table 1. Only two peaks, at 7.66 ($I = 100$) and 3.74 ($I = 20$) Å, stand out prominently, while a third peak, at 2.50 ($I = 8$) Å can be barely seen. These peaks correspond to the (001), (002) and (100) reflections respectively (Bardossy & Brindley 1978; Chukhrov *et al.* 1979).

Calculation of the hexagonal unit cell parameters cannot be done on the basis of the obtained X-ray pattern. The observed $d(001)$

value of 7.66 Å, however, is higher than most other studied rancieites which have $d(001)$ of 7.44 to 7.57 Å (Bardossy & Brindley 1978; Chukhrov *et al.* 1979; Barrese *et al.* 1986; Kim 1991; Brannath & Smykatz-Kloss 1992; Table 1). Since, according to Chukhrov *et al.* (1979) and Kim (1980), there is a positive correlation between the variations of $d(001)$ and the H₂O-content, the high $d(001)$ value of rancieite from Kato Nevrokopi can be mainly attributed to its high H₂O-content. This H₂O is located in the 'water interlayers' which contain cations (predominantly Ca) and H₂O molecules and separate the layers of edge sharing [Mn⁴⁺O₆] octahedra in the structure of rancieite (Giovannoli *et al.* 1970).

The observed basal reflection $d(002)$ of 3.74 Å indicates that rancieite from Kato Nevrokopi differs from its Mn²⁺-analogue called takanelite (Kim 1991), since no $d(002)$ reflections of takanelite [3.60 to 3.62 Å; Table 1: (4) and (5)] were observed in the XRD pattern. This conclusion is also supported by the difference in the $d(001)$ values of takanelite (7.25 and 7.31 Å) in respect of rancieite (7.66 Å) from Kato Nevrokopi. Therefore, the rancieite from Kato Nevrokopi should contain very little Mn²⁺, if any at all. Main reflections of calcite are absent from the XRD pattern of the microsample.

Chemical composition

The average of 18 spot analyses on different flakes and laminae of rancieite, performed by EPMA, the ranges, and the related standard deviations are reported in Table 2. The average empirical formula of the Kato Nevrokopi

Table 1. X-ray powder data for rancieite and takanelite

Rancieite			Takanelite						
1	2	3	4	5					
<i>I</i>	<i>d</i> (Å)	<i>hkl</i>	<i>I</i>	<i>d</i> (Å)	<i>I</i>	<i>d</i> (Å)	<i>I</i>	<i>d</i> (Å)	
100	7.66	001	100	7.56	100	7.44	s*	7.25	7.31
20	3.74	002	20	3.77	37	3.69	wb	3.62	3.60
8	2.50	100	12	2.46	22	2.46	m	2.45	2.44
		101	10	2.35			w	2.35	
		102	10	2.06					
		103	8	1.76					
		110	7	1.42			m	1.43	1.42
		111	5	1.40					

1, Kato Nevrokopi, Macedonia, Greece (this study); 2, Itea, Greece (Bardossy & Brindley 1978); 3, Mazzano, Latium, Italy (Barrese *et al.* 1986); 4, Janggun mine, Korea (Kim 1991); 5, Anson Betts, Ma, USA (Frondel *et al.* 1960).

*s, strong; m, medium; w, weak; b, broad.

Table 2. EPMA of rancieite from Kato Nevrokopi

Oxide	Mean (wt%)	Range (wt%)	SD (wt%)	Mean cation on O ²⁻ = 9	Range	
MnO ₂	62.01	56.80–68.61	3.38	Mn ⁴⁺	3.90	3.57–4.31
CaO	6.83	6.15–7.55	0.39	Ca ²⁺	0.67	0.60–0.74
ZnO	2.54	1.53–3.07	0.35	Zn ²⁺	0.17	0.10–0.21
Al ₂ O ₃	1.18	0.78–1.56	0.19	Al ³⁺	0.12	0.08–0.16
MgO	0.63	0.27–1.02	0.21	Mg ²⁺	0.09	0.04–0.14
Fe ₂ O ₃	0.30	0–0.72	0.16	Fe ³⁺	0.02	0–0.05
K ₂ O	0.25	0.14–0.41	0.07	K ⁺	0.02	0.01–0.05
SiO ₂	0.24	0–0.61	0.15	Si ⁴⁺	0.02	0–0.06
Total	73.98	68.33–81.13	4.07		5.01	4.95–5.04
H ₂ O*	c. 26.02			H ₂ O*	c. 7.90	

* The H₂O was estimated assuming 100 wt% total. Na, Co and Ni were not detected.
n = 18.

rancieite calculated to nine oxygen atoms gives 5.01 atoms total cation content, indicating the good agreement of the analytical data to those presented in the literature for rancieite. However, the rancieite from Kato Nevrokopi is slightly deficient in Mn, assumed to be mostly present as Mn⁴⁺ (free of takanelite member). On the other hand, rancieite has an unusually high Zn²⁺-content, which is higher than most other studied rancieites in the literature (Chukhrov *et al.* 1979; Kim 1980; Frenzel 1980; Carlos *et al.* 1993 and others). For this reason the prefix zincian is employed for the Kato Nevrokopi rancieite. Rancieite also contains significant Ca, and the estimated ratio of Ca/($\sum_{\text{cations}} - \text{Mn}^{4+}$) according to the method of Chukhrov *et al.* (1979) is 0.60; thus rancieite from Kato Nevrokopi excellently fits in the family of rancieites (range 0.81–0.41) and not that of birnessites (range 0.25–0.02) based on its Ca/(\sum_{cations}) ratio.

The positive correlation between Mn and Ca in the chemical analyses of the studied rancieite (Fig. 3a) just shows that Ca is essential for its structure and does not substitute for Mn. On the contrary, in the case of takanelite, the correlation between Mn and Ca ought to be negative, since Ca substitutes for Mn²⁺ (Kim 1991). Ca²⁺ ($r = 0.99 \text{ \AA}$) and K⁺ ($r = 1.33 \text{ \AA}$), because of their large size, cannot substitute for Mn in the layers of [MnO₆] octahedra of rancieite but possibly occupy places in the H₂O-interlayers, together with smaller cations such as Fe³⁺ and Si⁴⁺ (cf. Burns & Burns 1979).

On the other hand, by analogy to the crystal structure of birnessite which is also hexagonal and similar to rancieite (Kim 1980), it could reasonably be assumed that a large part, if not all, of the contained Zn may account for the deficiency of Mn (expressed as vacancies in the lattice), because of its similar ionic radius

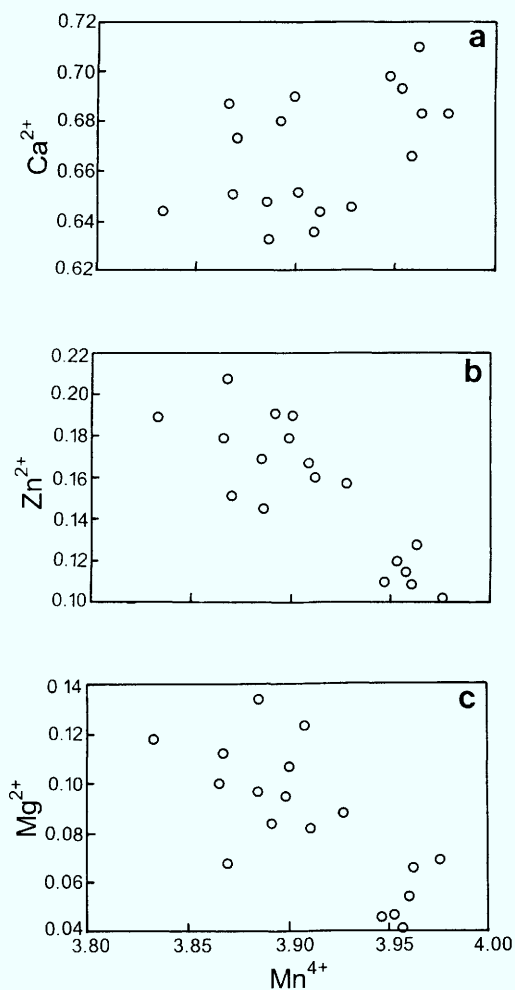
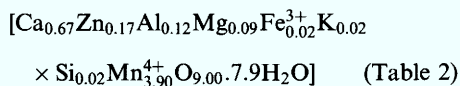


Fig. 3. Plots of cation concentrations in rancieite (found by EPMA), based on 9 oxygen atoms. (a) Mn⁴⁺ v. Ca²⁺; (b) Mn⁴⁺ v. Zn²⁺; (c) Mn⁴⁺ v. Mg²⁺.

(($r = 0.74 \text{ \AA}$ and chemical affinity. Zinc could take the place of Mn^{2+} ($r = 0.80 \text{ \AA}$) in the substitution above and below the vacant Mn^{4+} sites in the edge-sharing $[\text{MnO}_6]$ octahedral layers by the mechanism $\text{Mn}^{4+} + \text{vacancy} = 2 \text{ Zn}^{2+}$ (Burns & Burns 1979; Burns *et al.* 1983). This substitution can be evidenced by the negative correlation of the two metals (Fig. 3b). Indeed, the number of Zn atoms per formula unit (0.17) is nearly twice the deficiency of Mn (0.10) obtained by subtracting the analytical (3.90) from the theoretical (4.00) Mn^{4+} -atoms. This process stabilizes the structure of rancieite by not permitting further oxidation. A similar process could take place with Mg^{2+} ($r = 0.66 \text{ \AA}$), as evidenced by the negative correlation between Mn^{4+} and Mg^{2+} (Fig. 3c). Zn and Mg probably complement each other in the process of substitution for Mn. Other cations, such as the Al^{3+} ($r = 0.51 \text{ \AA}$), because of smaller ionic size could only sporadically substitute for Mn^{4+} ($r = 0.60 \text{ \AA}$) cations of $[\text{MnO}_6]$ octahedra.

Varying amounts of Al, Mg, Fe, K and Si also occur in rancieite. On the other hand, elements such as Ni and Co, which are characteristic of marine manganese nodules and concretions (Margolis & Burns 1976; Burns & Burns 1977) were not detected by EPMA. The Kato Nevrokopi rancieite is also free of Na, while Bardossy & Brindley (1978) found $\text{Na} < \text{Ca}$ for rancieites.

The low analytical totals obtained by EPMA (Table 2) are indicative of the presence of elements lighter than $Z = 11$ ($Z = \text{atomic number}$). The most likely of these to be present are H^+ and O^{2-} (as molecular water) and Li^+ , since calcite has been carefully avoided (no CO_2 was present) after a thorough examination. If Li^+ was present in the chemical composition of rancieite, and since Al^{3+} is already present, someone would expect the main reflections (4.72, 2.37 and 1.88 \AA) of lithiophorite (the Li-bearing Al-Mn⁴⁺-oxide with pseudohexagonal double-layer structure, Frenzel 1980) to show up at least weakly in the XRD patterns (for example see Yucca mountain, Nevada, USA, Carlos *et al.* 1993), because lithiophorite forms in similar thermodynamic conditions as rancieite. However, after a very thorough examination of the XRD diagrams no lithiophorite peaks have been identified. Thus, assuming that the difference of the analytical EPMA total to 100 wt% represents the molecular H_2O -content, the average empirical chemical formula of rancieite from Kato Nevrokopi could be written as:



Scanning electron microscopy

Figure 4a shows a scanning electron micrograph of rancieite. The layered structure of the mineral is clearly reflected in the appearance as laminated, sheeted grains with large cavities, although there is no evidence that the surfaces of laminae are the (001) planes (Bardossy & Brindley 1978). The thickness of individual lamina is as small as $0.5 \mu\text{m}$ or even lower as it can be seen in the micrograph. A magnified shot (Fig. 4b) of the same area reveals the flaky character of the rancieite laminae and gives a better estimate of their thickness (down to $0.2 \mu\text{m}$).

Both of the micrographs clearly support the optical, XRD and EPMA data which indicate a poor structural order for the rancieite from Kato Nevrokopi.

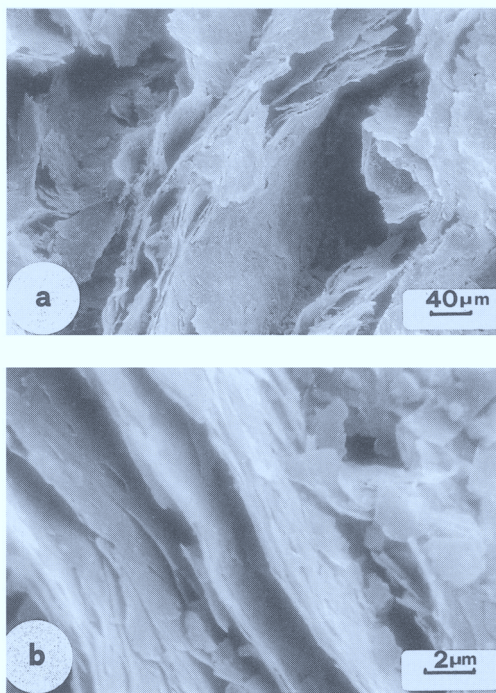


Fig. 4. SEM photomicrographs of rancieite. (a) Laminae of rancieite indicating the sheeted layer structure and the poor crystallinity. Note the large cavities between rancieite sheets. Scale bar is $40 \mu\text{m}$ long. (b) Higher magnification of (a) showing the flaky character of the laminae and the numerous cavities between packed rancieite sheets. The length of scale bar is $2 \mu\text{m}$.

Discussion

The replacement textures of Mn^{4+} -oxides by rancieite at Kato Nevrokopi, clearly indicate that rancieite formation is part of a late weathering process. Combining the conclusions of Nimfopoulos (1988) and Nimfopoulos & Patrick (1991) and the present results, the evolution of the Kato Nevrokopi manganese ores can be best expressed as follows:

- (a) hydrothermal deposition of minerals in veins;
- (b) supergene oxidation of hydrothermal minerals and enrichment to ore-grade, either *in situ* or after dissolution and redeposition in karstic cavities;
- (c) beginning of dissolution of Mn-oxides formed during stage b and deposition of rancieite.

During the first stage, a hypogene zoned vein system predominated by rhodochrosite and minor black calcite (mixture of todorokite and calcite) and mixed sulphides (mainly sphalerite, galena and pyrite) has developed in various locations of the Kato Nevrokopi area.

During the second stage, the hydrothermal minerals have undergone supergene oxidation and partial or total dissolution resulting in an associated enrichment to ore grade. The resulting paragenetic sequence is dominated by the formation of Mn^{4+} -oxides: MnO-gelnsutite-chalcophanite-birnessite-cryptomelane-pyrolusite (Nimfopoulos & Patrick 1991). Nevertheless, remnants of the hydrothermal mineralization (excluding rhodochrosite) are still present in most weathered veins. Rhodochrosite was identified by a variety of techniques, and occurs only in relatively unweathered, deeper parts of the veins.

Pyrolusite, the last mineral formed in the second stage, contains little water, alkalis and alkaline earths. The formation of pyrolusite can be favoured by semi-arid climatic and highly oxidizing conditions (Brannath & Smykatz-Kloss 1992). It requires very low foreign large cation (K, Ca, Ba etc.) concentration in the precipitating solution (Ostwald 1992).

The third stage begins with the replacement of pyrolusite by an amorphous cryptomelane type phase (Fig. 2b). This is followed by crystallization of rancieite in the remaining vugs of the karstic cavity ore. At the same stage, todorokite is replaced directly by rancieite. The process is also characterised by a decreasing Mn-content in the minerals but with increasing Ca and Al-contents as results from EPMA. According

to Brannath & Smykatz-Kloss (1992), cryptomelane formation is favoured by more humid climatic and less oxidised conditions than pyrolusite.

Crerar *et al.* (1980) concluded that such conditions exist in tundras of the northern temperate and subarctic zones, where rapid leaching of Mn occurs in acidic environment and moderate humidity. Thus, at Kato Nevrokopi, the formation of amorphous cryptomelane type material as encrustations (Fig. 2b) at lower Eh and pH may be indicative of periodical flushing of relatively reduced Mn-bearing meteoric fluids through the veins and karsts. These fluids can be produced by the dissolution of mixed sulphides, mainly pyrite (Nimfopoulos & Patrick 1991).

The chemical composition of Mn^{4+} -oxides is strongly influenced by the local variations in the chemistry of the percolating fluids (Nicholson 1992; Carlos *et al.* 1993), and this in turn by the composition of the dissolved host rock (marble and the hosted mineralization for Kato Nevrokopi). The composition of the amorphous cryptomelane and the following rancieite is controlled by the chemical composition of the mineralised marble (Ostwald 1992). Thus, the concentration of highly mobile Zn (Mann & Deutscher 1980), coming from the breakdown of sphalerite, and Ca in the depositional fluid probably controls zincian rancieite formation in a similar way to the Ca and Mg control on the formation of todorokite (Ostwald 1992). Hence, the observed replacement of todorokite fibres by rancieite flakes or laminae in places can be attributed to a continuous percolation of Ca-saturated, Zn-bearing and oxygenated meteoric fluids through the Mn^{4+} -ore and variable substitution of Zn for Mg.

Hence, rancieite was deposited under high humidity conditions, at atmospheric pressure and very low temperatures (around 25°C, see also Barrese *et al.* 1986) from cold meteoric waters, percolating through the marble and the associated orebodies for long periods. The dissolution of calcite, increases the concentration of Ca and the pH (to *c.* 7–8) of the fluids. These conditions are similar to the formation of karst bauxites and laterites (Crerar *et al.* 1980). As Bricker (1965) and Hem (1972) suggested that the Mn-dioxide minerals are stable under neutral to alkaline conditions (pH > 6), the equilibration of the depositing solutions with the host marble and the consequent increase in their pH to neutral may be the driving mechanism for the rancieite deposition.

J. Zussman is thanked for permission to do a great part of the research at the University of Manchester UK, K. Nicholson for invaluable collaboration and S. Roy, Y. Hariya and S. Dasgupta for thoroughly reviewing the manuscript. Financial support by the British Council is also gratefully acknowledged.

References

- BARRESE, E., GIAMPAOLO, C., GRUBESSI, O. & MOTTANA, A. 1986. Rancieite from Mazzano Romano (Latium, Italy). *Mineralogical Magazine*, **50**, 111–118.
- BARDOSSY, G. & BRINDLEY, G. W. 1978. Rancieite associated with a karstic bauxite deposit. *American Mineralogist*, **63**, 762–767.
- BRANNATH, A. & SMYKATZ-KLOSS, W. 1992. Mineralogical investigations on manganese-iron ores from Hesse, Germany. *Chemie Erde*, **52**, 3–31 [in German with English abstract].
- BRICKER, O. 1965. Some stability relations in the system Mn-O₂-H₂O at 25°C and one atmosphere total pressure. *American Mineralogist*, **50**, 1296–1354.
- BURNS, R. G. & BURNS, V. M. 1977. Mineralogy. In: GLASBY, G. P. (ed.) *Marine Manganese Deposits*. Elsevier, New York, 185–248.
- & — 1979. *Manganese oxides*. Mineralogical Society of America, Short Course Notes, 6.
- , — & STOCKMAN, H. W. 1983. A review of the todorokite-buserite problem: implications to the mineralogy of marine manganese nodules. *American Mineralogist*, **68**, 972–980.
- CARLOS, B. A., CHIPERA, S. J., BISH, D. L. & CRAVEN, S. J. 1993. Fracture-lining manganese oxide minerals in silicic tuff, Yucca Mountain, Nevada, U.S.A. *Chemical Geology*, **107**, 47–69.
- CHUKHROV, F. V., GORSHKOV, A. I., SVITSOV, A. V., BEREZOVSKAYA, V. V. & RUDNITSKAYA, YE. S. 1979. The nature of rancieite. *International Geology Reviews*, **23**, 115–124.
- CRERAR, D. A., CORMICK, R. K. & BARNES, H. L. 1980. Geochemistry of manganese: an overview. In: VARENTSOV, I. M. & GRASSELLY, G. (eds) *Geology and Geochemistry of Manganese*. Schweizerbart'sche, Stuttgart, 1, 293–334.
- DIMITROV, D. K. & ZIDAROV, N. 1969. *On the stratigraphy of the Archaic metamorphic complex in the Rhodope massif*. Reviews of the Geological Society of Bulgaria Report 303.
- FRENZEL, G. 1980. The manganese ore minerals. In: VARENTSOV, I. M. & GRASSELLY, G. (eds) *Geology and Geochemistry of Manganese*. Schweizerbart'sche, Stuttgart, 1, 25–158.
- FRONDEL, C., MARVIN, U. B. & ITO, J. 1960. New data on birnessite and hollandite. *American Mineralogist*, **45**, 871–875.
- GIOVANOLI, R., STAHLI, E. & FEITKNECHT, W. 1970. About the oxide-hydroxides of tetravalent manganese with layer structures. II. Manganite(III)-manganate (IV). *Helvetica Chimica Acta*, **53**, 453–456 [in German with English abstract].
- HEM, J. D. 1972. Chemical factors that influence the availability of iron and manganese in aqueous systems. *Geological Society of America Bulletin*, **83**, 443–450.
- HEWETT, D. F. & FLEISCHER, M. 1960. Deposits of the manganese oxides. *Economic Geology*, **55**, 1–55.
- , — & CONKLIN 1963. Deposits of the manganese oxides: Supplement. *Economic Geology*, **58**, 1–51.
- JORDAN, H. 1969. Geology and petrography of the Central Falakron (Drama, Greek-Macedonia). *Geotektonische Forschungen*, **31**, 50–85 [in German with English abstract].
- KIM, S. J. 1980. Birnessite and rancieite problem: their crystal chemistry and new classification. *Journal of the Geological Society of Korea*, **16**, 105–113.
- 1991. New characterization of takanelite. *American Mineralogist*, **76**, 1426–1430.
- LACROIX, A. 1910. *Mineralogy of France and her colonies*, 4. Nolle, Paris [in French].
- LEYMERIE, A. F. G. A. 1895. *Courses in mineralogy*, 8. Toulouse [in French].
- MANN, A. W. & DEUTSCHER, R. L. 1980. Solution geochemistry of lead and zinc in water containing carbonate, sulphate, and chloride ions. *Chemical Geology*, **29**, 293–311.
- MARGOLIS, S. V. & BURNS, R. G. 1976. Pacific deep-sea manganese nodules: their distribution, composition and origin. *Annual Reviews of Earth and Planetary Sciences*, **4**, 229–263.
- MOORBATH, S. & ZAGORCEV, I. 1983. Rubidium-Strontium isotopic data on the age of the first granitoid complex (Smilovene and Hisar plutons) in Sastinska Sredna Gora. *Geologica Balcanica*, **13**, 3–14.
- NAMBU, M. & TANIDA, K. 1971. New mineral takanelite. *Journal of the Japanese Association for Mineralogy Petrology and Economic Geology*, **65**, 1–15 [in Japanese with English abstract].
- NICHOLSON, K. 1992. Contrasting mineralogical-geochemical signatures of manganese oxides: Guides to metallogenesis. *Economic Geology*, **87**, 1253–1264.
- NIMFOPOULOS, M. K. 1988. *Manganese mineralization near Kato Nevrokopi, Drama, Greece*. PhD thesis, University of Manchester, UK.
- & PATRICK, R. A. D. 1991. Mineralogical and textural evolution of the economic manganese mineralization in western Rhodope massif, N. Greece. *Mineralogical Magazine*, **55**, 423–434.
- , REX, D. & PATRICK, R. A. D. 1988. Age of hydrothermal manganese mineralization near Kato Nevrokopi, Drama, northern Greece. *Transactions of the Institution of Mining and Metallurgy*, **97(B)**, 193–195.
- OSTWALD, J. 1992. Genesis and paragenesis of the tetravalent manganese oxides of the Australian continent. *Economic Geology*, **87**, 1237–1252.
- PAPANIKOLAOU, G. & PANAGOPOULOS, A. 1981. On the structural style of Southern Rhodopes, Greece. *Geologica Balcanica*, **11**, 13–22.

- POTTER, R. M. & ROSSMAN, G. R. 1979. The tetravalent manganese oxides: Identification, hydration and structural relationships by infrared spectroscopy. *American Mineralogist*, **64**, 1199–1218.
- RICHMOND, W. E., FLEISCHER, M. & MROSE, M. E. 1969. Studies on manganese oxide minerals, IX. Rancieite. *Bulletin of the French Society for Mineralogy and Crystallography*, **92**, 191–195.
- SOREM, R. K. & FEWKES, R. H. 1980. Distribution of todorokite and birnessite in manganese nodules from the "Horn Region", Eastern Pacific Ocean. In: VARENTSOV, I. M. & GRASSELLY, G. (eds) *Geology and Geochemistry of Manganese*. Schweizerbart'sche, Stuttgart, **1**, 203–229.
- ZACHOS, S. & DIMADIS, E. 1983. The geotectonic position of the Skaloti-Echinos granite and its relationship to the metamorphic formations of Greek Western and Central Rhodope. *Geologica Balcanica*, **13**, 17–24.

The determination of the valency of manganese in mineralogical and environmental samples by X-ray emission spectroscopy

S. D. GAMBLIN & D. S. URCH

*Department of Chemistry, Queen Mary and Westfield College – University of London,
Mile End Road, London E1 4NS, UK*

Abstract: The $K\beta$ X-ray emission spectrum arising from $3p \rightarrow 1s$ transitions in transition metal ions can be complicated by interaction between unpaired $3d$ electrons and the odd $3p$ electron in the final state. A non-diagram line, $K\beta'$ appears at lower emission energy than the diagram line $K\beta_{1,3}$. For lighter transition metals the intensity ratio of $K\beta'$ to $K\beta_{1,3}$ decreases with the number of unpaired $3d$ electrons. This enables this intensity ratio to be used to determine oxidation state.

This effect is demonstrated for the simple oxides MnO , Mn_2O_3 and MnO_2 , and for the anion MnO_4^- . Distinct spectra are obtained that can be related to the oxidation state of the manganese. The valency of manganese is then determined in mineral samples and in sand grains coated with manganese encrustations from water purification plants.

X-ray emission spectroscopy is widely used for the elemental analysis of mineral and environmental samples. Less widely appreciated is the fact that an emission line is not only indicative of an element's presence, but can exhibit structure that can be used to determine that element's chemical oxidation state.

In compounds containing first row transition metals with unpaired d electrons the $K\beta$ X-ray emission is split into a doublet composed of a main $K\beta_{1,3}$ line and a less intense low energy $K\beta'$ satellite. Since the relative intensity of these components can often be related to the number of unpaired d electrons (Tsutsumi & Nakamori 1968) accurate measurement of the $K\beta'/K\beta_{1,3}$ ratio is a potential valence and/or spin probe for the first row transition elements.

Manganese speciation is often a difficult task (Nicholson 1989) but the efficacy of this technique has been demonstrated using a double crystal spectrometer (Tsutsumi *et al.* 1976) and most recently using a synchrotron light source (Peng *et al.* 1994). This work will show how a simple, conventional single plane crystal instrument can be used for the same purpose without requirement for significant alteration of the spectrometer.

Experimental methods

Manganese $K\beta$ X-ray emission spectra were recorded from three groups of samples

A series of manganese oxides was studied using commercially available samples of MnO (Aldrich Chemical Company Inc.), Mn_2O_3 (Aldrich), MnO_2 (Aldrich) and $KMnO_4$ (Hopkin and Williams Ltd). The manufacturers quoted a

minimum purity of 99% for each of these samples.

A sample of the silicate mineral rhodonite, $MnSiO_3$, obtained from Broken Hill Australia, and a powdered sample of the mixed oxide spinel hausmannite, Mn_3O_4 , were also studied.

Four mineral samples were obtained from K. Nicholson of The Robert Gordon University Aberdeen. Two (designated in this paper as Vein #1 and Vein #2) were derived from a magnetite vein in Laeverock Braes granite. Two were derived from bulk ore of unknown composition (labelled Ore #1 and Ore #2) from India.

A number of water purification samples were also provided by Nicholson. These consisted of sand grains partly coated with manganese oxide as a consequence of their use in a water filtration process. The manganese was introduced into the water purification process as an impurity in ferrous sulphate. At a high pH the ferrous sulphate produced a flocculent precipitate. The supernatant liquid, in which the manganese was present as Mn^{2+} , was then dosed with chlorine gas before being passed over a sand filter bed. It is reasonable to assume that the chlorine oxidized the manganese to higher oxidation states and that it is in this form that it was deposited as oxide on the filter sand. Samples labelled Extracts #1, #2, and #3 were from three different water purification plants.

In all cases samples were prepared by pressing them onto polyethylene powder to form a coated disc.

Spectra were measured using a Philips PW 1410 spectrometer fitted with a tungsten anode X-ray tube operated at 40 mA and 50 kV. Optimum dispersion was achieved using second order reflection from a LiF (200) crystal ($2d=4.0267 \text{ \AA}$) and 'fine' collimation ($150 \mu\text{m}$,

angular dispersion $0.12\theta^\circ$) augmented by an extra collimator. This extra collimator was inserted with blades perpendicular to the primary collimator in order to restrict vertical divergence (Haycock & Urch 1982). The use of the extra collimator is essential to prevent spectral distortion caused by low energy tailing at high Bragg angles and accounts for the improvement of the present spectra over previous work (Urch & Wood 1978).

A gas flow proportional counter (utilising a 90% argon/10% methane mixture) and Harwell 2000 series counting equipment were used to detect Mn $K\beta$ radiation in the range $140\text{--}144\ 2\theta^\circ$. For the oxide and mineral samples the region of interest was scanned at a rate of $0.25\ 2\theta^\circ$ per minute. Extracts #1, #2 and #3 produced weak signals, so were step scanned at a rate of 30 s per $0.01\ 2\theta^\circ$ step.

The manganese $K\beta$ spectrum of MnF_2 (not shown) was recorded and used to calibrate the instrument against the most recent high resolution work (Peng *et al.* 1994).

Spectra were acquired under PC control and stored in digital form. All spectra were fitted with Voigt functions using a simple curve fitting package in which the position, intensity, width and Gaussian percentage of a number of mixed symmetric Gaussian/Lorentzian functions could be varied and their sum compared to the experimental spectrum.

Results

Manganese $K\beta$ spectra from MnO , Mn_2O_3 , MnO_2 and KMnO_4 are shown in Fig. 1. The doublet nature of the $K\beta$ emission is most clearly observed for the low valence oxides MnO and Mn_2O_3 with two resolved peaks clearly present.

There is also a clear trend for the $K\beta'$ satellite to decrease in intensity relative to the main $K\beta_{1,3}$ peak as the formal oxidation state of the manganese increases.

In an attempt to quantify these changes in profile each spectrum was subjected to curvefitting. It proved impossible to represent any spectrum by only two symmetric components. Any attempt to do so left a sizable residual approximately 5 eV to the low energy side of the main $K\beta_{1,3}$ peak. This residual intensity could be adequately fitted with a single peak and it is this combination of three peaks that has been used throughout this work. The third peak was considered to represent some asymmetry in the measured $K\beta_{1,3}$ spectrum caused by some residual low energy tailing. As such the area of

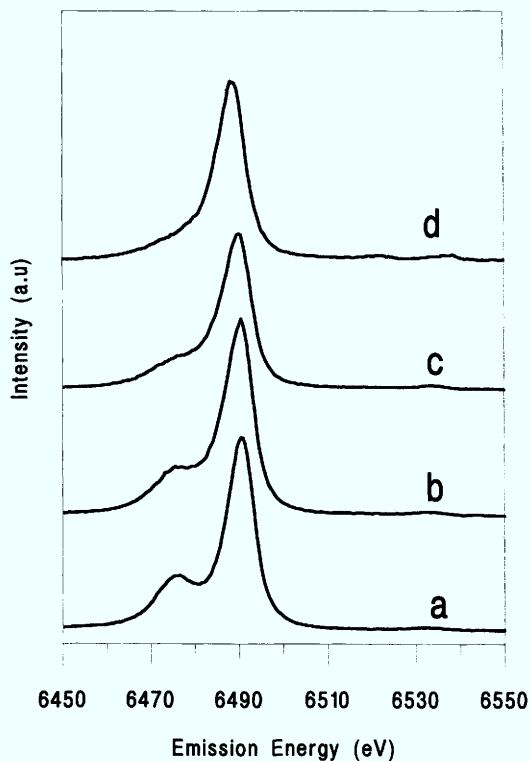


Fig. 1. Mn $K\beta$ X-ray emission spectra from MnO (a), Mn_2O_3 (b), MnO_2 (c) and KMnO_4 (d). Spectra have been approximately normalized for easy comparison of $K\beta'/K\beta_{1,3}$ ratios.

this peak was considered part of $K\beta_{1,3}$ for relative intensity calculations. The best fit to the experimental spectrum was obtained using a 45:55 Gaussian/Lorentzian mixture and peak widths in the ranges 9.5–14.8 eV for $K\beta'$ and 4.8–6.0 eV for $K\beta_{1,3}$.

Curve-fitted spectra corresponding to those in Fig. 1 are shown in Fig. 2. The peak positions and relative intensities thus obtained are listed in the upper third of Table 1. The $K\beta'$ and $K\beta_{1,3}$ peak positions are seen to shift towards one another so that the energy splitting decreases towards higher oxidation states. The width of the $K\beta'$ feature increases towards high oxidation states whilst that of the $K\beta_{1,3}$ component remains fairly independent of oxidation state.

The difference in the $K\beta'/K\beta_{1,3}$ intensity ratio between valence states is considerable and in excess of the possible error, which we estimate to be less than 2% when a consistent curve fitting procedure is followed.

Manganese $K\beta$ spectra from the four unknown mineral samples are shown in Fig. 3

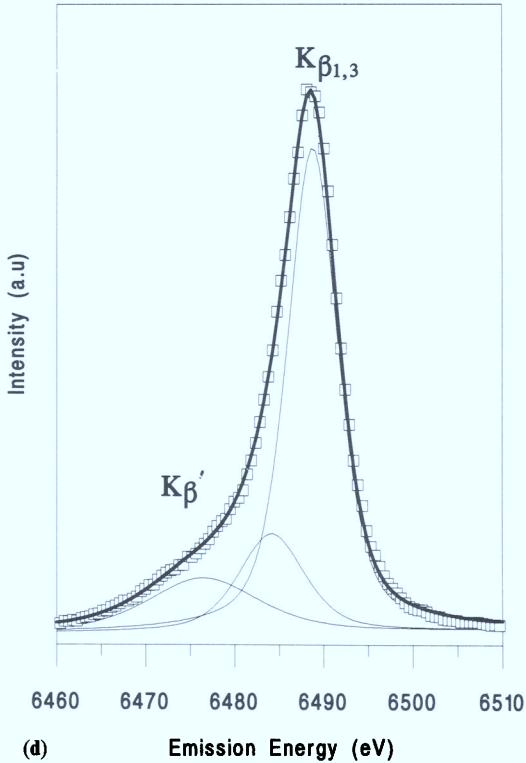
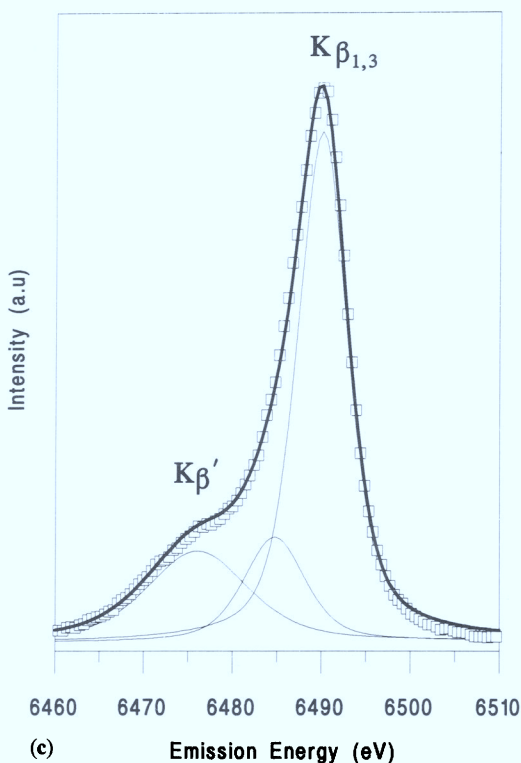
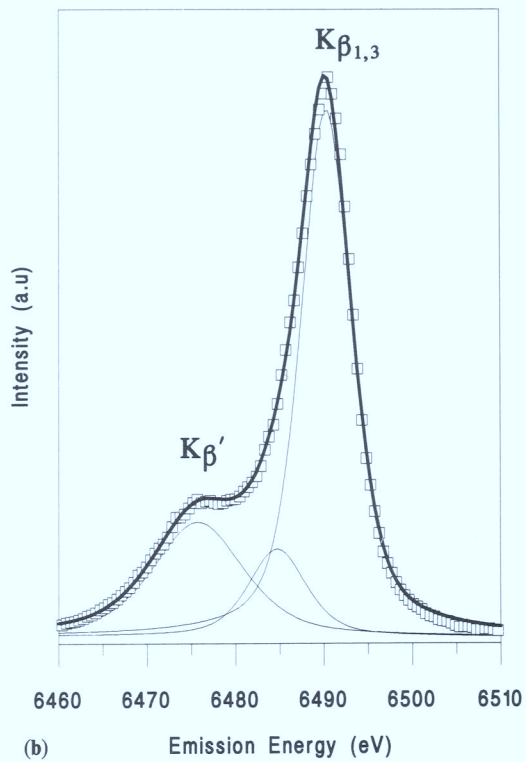
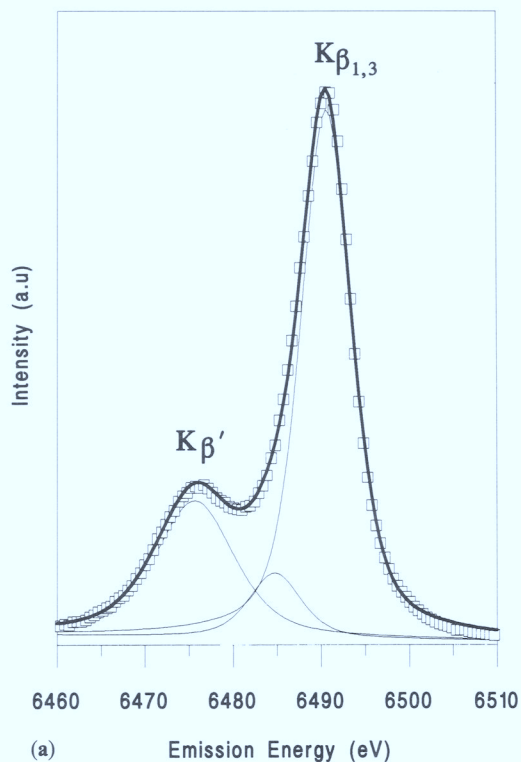
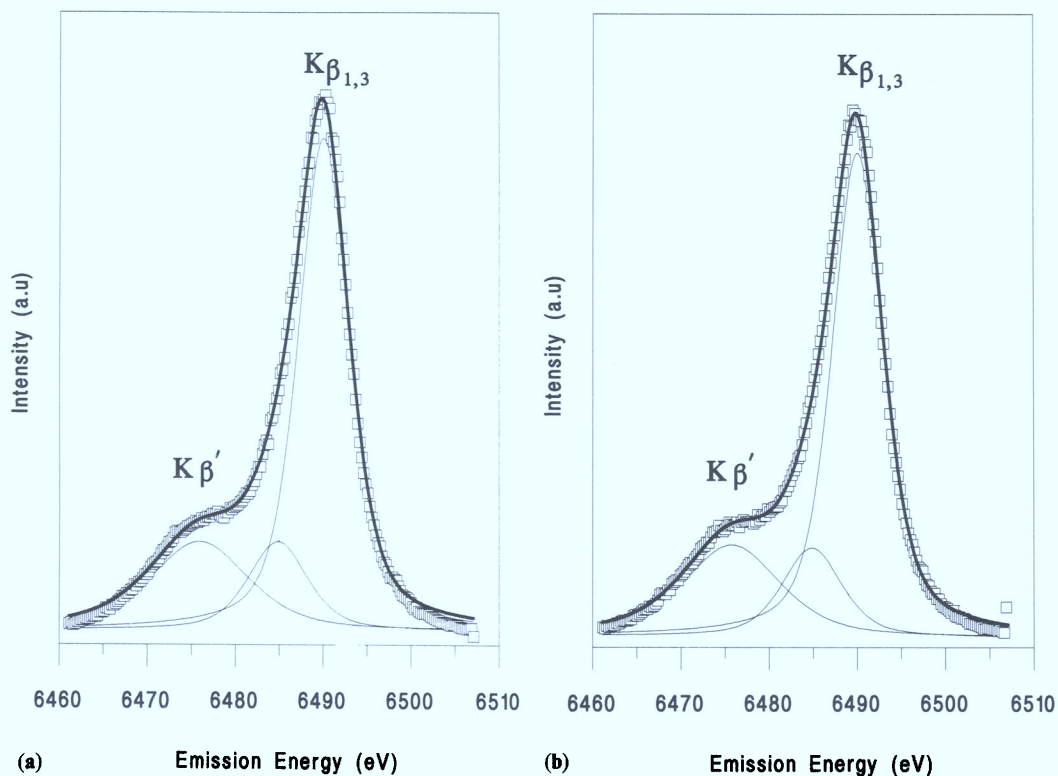


Fig. 2. Mn $K\beta$ spectra from MnO (a), Mn₂O₃ (b), MnO₂ (c) and KMnO₃ (d) showing experimental spectra (individual data points) and curvefit sum (bold line) produced from three component curves (feint line).

Table 1 $KK\beta_{1,3}$ and $K\beta'$ peak positions, widths and intensity ratios from the Mn $K\beta$ spectra of Figs 2, 3 and 4.

Fig.	Sample	$K\beta'$		$K\beta_{1,3}$		Int Ratio
		E_{\max} (eV)	FWHM (eV)	E_{\max} (eV)	FWHM (eV)	$K\beta'/K\beta_{1,3}$ (%)
2a	MnO	6476.0	10.0	6491.0	4.8	36.4
2b	Mn ₂ O ₃	6476.2	10.6	6490.7	5.1	32.7
2c	MnO ₂	6476.5	13.2	6490.3	5.7	28.6
2d	KMnO ₄	6477.0	14.8	6489.0	5.2	18.7
3a	Ore #1	6476.1	11.3	6490.7	5.6	33.1
3b	Ore #2	6476.4	11.2	6491.2	5.6	33.0
3c	Vein #1	6476.2	12.0	6490.6	6.0	29.2
3d	Vein #2	6476.2	12.1	6490.6	5.9	29.9
3e	Rhodonite	6475.5	9.5	6491.0	5.0	36.1
3f	Hausmannite	6476.4	12.8	6490.8	5.4	32.2
4a	Extract #1	6476.3	12.8	6490.8	6.1	29.4
4b	Extract #2	6476.2	13.0	6490.3	6.0	29.9
4c	Extract #3	6475.6	12.2	6490.0	6.1	29.6

**Fig. 3.** Mn $K\beta$ spectra from Ore #1 (a), Ore #2 (b), Vein #1 (c), Vein #2 (d), Rhodonite (e) and Hausmannite (f) showing experimental spectra (individual data points) and curvefit sum (bold line) produced from three component curves (feint lines).

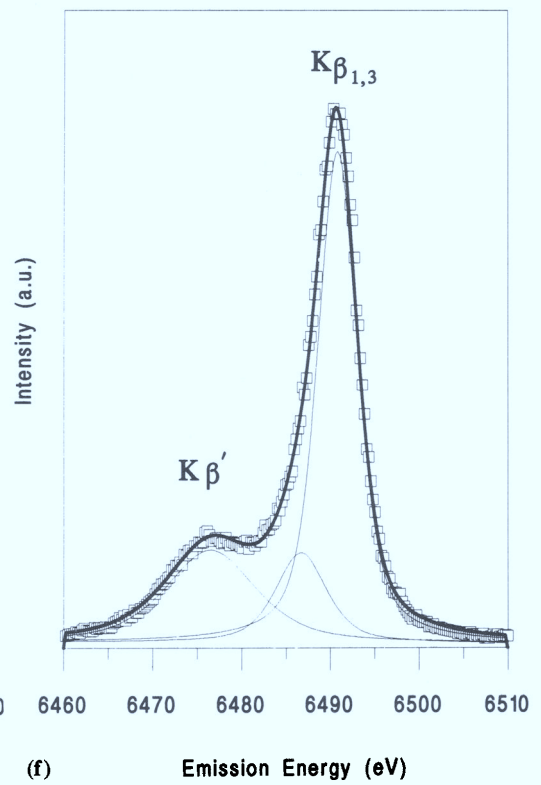
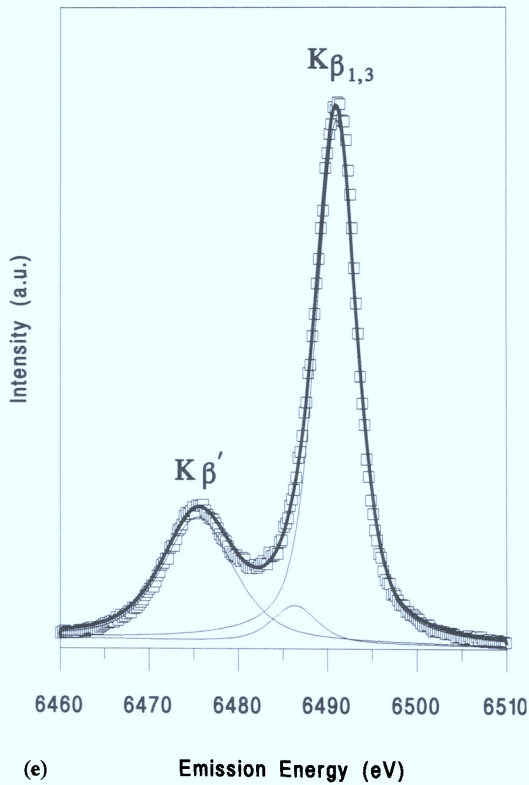
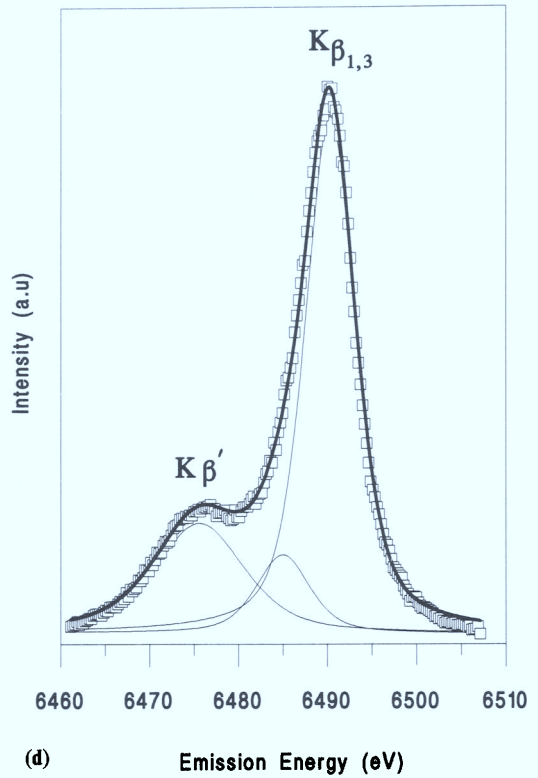
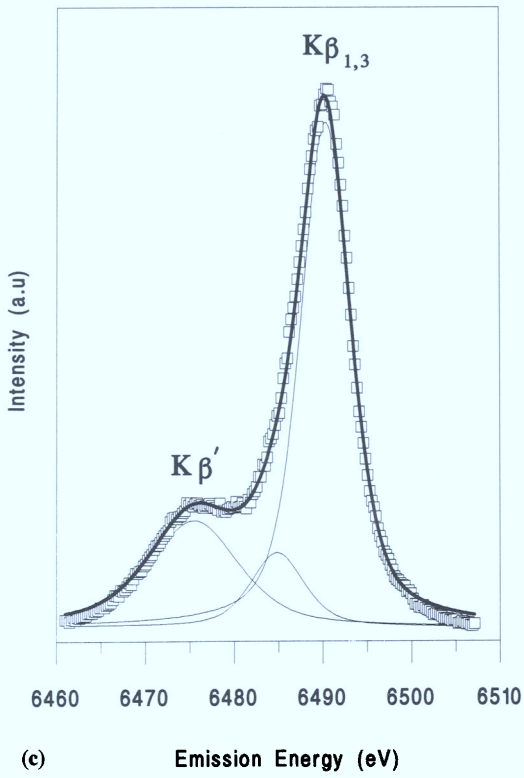


Fig. 3. (continued)

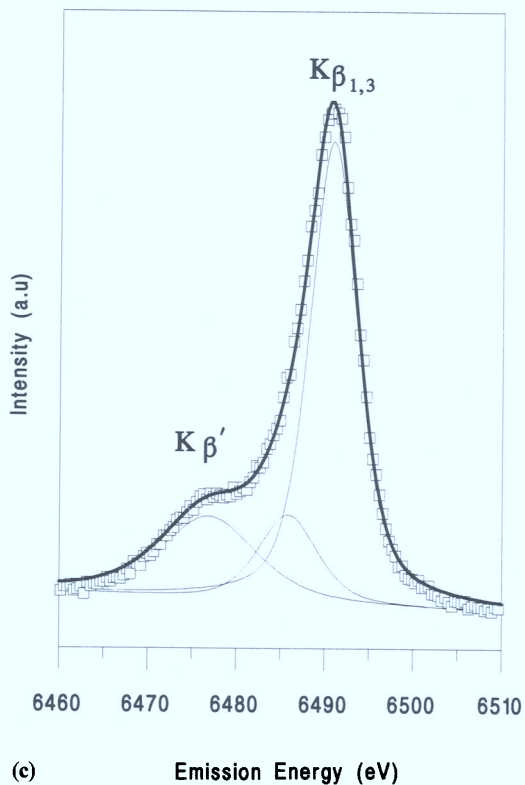
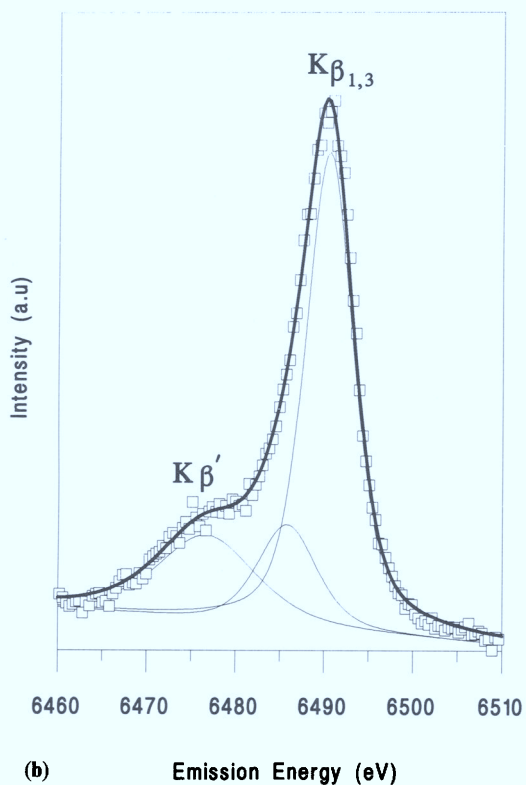
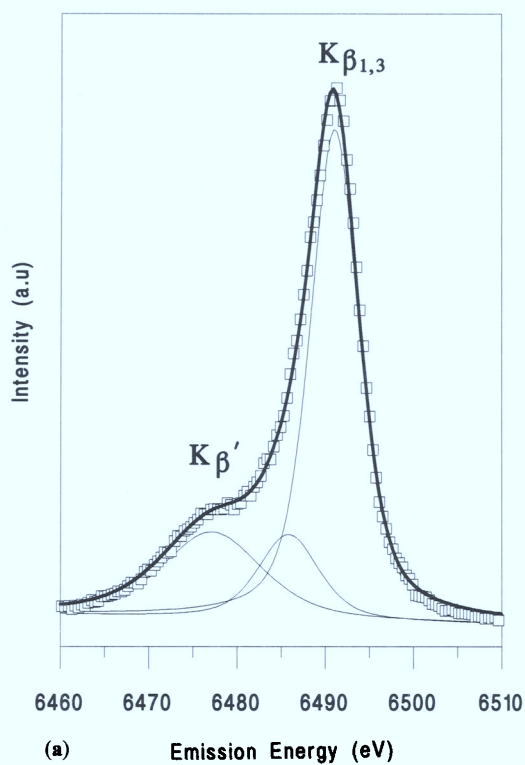


Fig. 4. Mn $K\beta$ spectra from Extract #1 (a), Extract #2 (b) and Extract #3 (c) showing experimental spectra (individual data points) and curvefit sum (bold line) produced from three component curves (feint lines).

together with those of rhodonite and hausmannite. Fitted curves are also shown and the consequent $K\beta'/K\beta_{1,3}$ ratios are listed in the second section of Table 1.

The Indian bulk ore spectra (Fig. 3a and b) closely resemble the spectrum of Mn_2O_3 and these ores are clearly quite different in composition to the vein samples derived from Scottish granite, the spectra of which (Fig. 3c and d) more closely resemble the spectrum of MnO_2 . By comparing the intensity ratios with those of the pure oxides we can confirm our judgement that the Indian samples are predominantly Mn^{3+} and the Scottish samples predominantly Mn^{4+} .

The manganese $K\beta$ spectrum of rhodonite (Fig. 3e) is most like that of the divalent oxide MnO . A comparison of $K\beta'/K\beta_{1,3}$ confirms the presence of Mn^{2+} in the silicate although it is interesting to note that the $K\beta'$ feature is narrower in rhodonite than in the oxide and that the $K\beta'/K\beta_{1,3}$ ratio is consequently somewhat smaller. This may be due to the silicate being more ionic than the oxide.

Hausmannite is a mixed oxide spinel of the type $Mn^{2+}Mn_3^{3+}O_4$ and as such might be expected to produce a $K\beta$ spectrum intermediate between that of MnO and Mn_2O_3 . Contrary to this expectation the spectrum of Mn_3O_4 (Fig. 3f) is much like that of Mn_2O_3 in appearance and $K\beta'/K\beta_{1,3}$ ratio.

Manganese $K\beta$ spectra and curve fitted simulations of Extracts #1, #2 and #3 are shown in Fig. 4. In each case the profile resembles that of MnO_2 . These extraction samples consist largely of silica grains acting as the substrate for a thin coating of metal oxide. The low concentration of manganese accounts for the poorer signal to noise ratio in these spectra, even after some step scanning improvement. The rising baseline towards 6450 eV is probably due to the presence of iron.

The $K\beta'/K\beta_{1,3}$ ratios were calculated from the deconvolved peaks and are listed in the last section of Table 1. They indicate that all extraction samples contain Mn^{4+} .

Discussion

A simple theoretical model is sufficient to explain the observed trend in the $K\beta'/K\beta_{1,3}$ ratio.

Consider, for example, a d^5 ion such as Mn^{2+} . $K\beta$ X-ray emission accompanies the transition of a $3p$ electron to a $1s$ core vacancy and a final state ($1s^2 3p^5 3d^5$) with net electron spin in the $3p$ level ($3p^{-1}$) is produced. For a first row

transition metal this is sufficiently close in energy to the valence $3d$ band for strong final state exchange coupling to occur. This coupling splits the $K\beta$ emission into two components $K\beta_{1,3}$ and $K\beta'$, corresponding to cases where the $3p$ and $3d$ spins in the final state are parallel and anti-parallel respectively. More formally, a 6S ground state is split by interaction with a $3p$ hole to produce 5P and 7P final states.

Using this simple model (Tsutsumi *et al.* 1976) the $K\beta'/K\beta_{1,3}$ intensity ratio should be that of the final state multiplicities; *i.e.* 5:7, 4:6 and 3:5 for d^5 , d^4 and d^3 ions respectively.

A great number of effects are, however, ignored by the simple model. The imposition of a ligand field, consideration of the intermediate ($1s^{-1}$) state, configuration interaction and charge transfer all *modify* the predicted ratio, **but** they do *not alter* the trend. This is dominated by exchange interaction and therefore by the number of unpaired d electrons. It is interesting to note that using a more sophisticated model Peng *et al.* (1994) predict a broadening of the $K\beta'$ emission for the higher oxidation states. This may be responsible for the wide range of half widths (9.5–14.8 eV) required to fit the $K\beta'$ emission as compared to the fairly constant (4.8–6.0 eV) $K\beta_{1,3}$ width. Using very high resolution Peng *et al.* observe an additional 5P state only some 2–3 eV less in energy than $K\beta_{1,3}$. This may be partly responsible for our need to use an additional feature for complete curve fitting. It may be noted in passing that the $K\beta'/K\beta_{1,3}$ ratios experimentally observed by Peng *et al.* are far less than their own prediction or any so far reported (including this work). The origin of this discrepancy is not known.

The observed results, therefore, follow a rational trend which can be reliably related to oxidation state. The absolute ratios are not predictable by a simple model but these are not necessary for analytical use. In any case the absolute value of the $K\beta'/K\beta_{1,3}$ ratio was found to depend greatly on the method employed for curvefitting. Other methods, such as considering the $K\beta'$ emission to be the difference between a particular spectrum and a normalised permanganate profile, or considering the third peak to be partly $K\beta'$, were found to respectively lower or raise the characteristic ratio values of both the standard oxides and the analysed samples. This did not alter the outcome of the analysis but does indicate the necessity of using a consistent technique on both analysed samples and reference standards. For this reason the simplest curvefit with the minimum number of peaks was adopted as a standard procedure as it is the easiest to apply consistently.

Manganese minerals are perhaps the ideal samples for this type of analysis. Manganese is particularly responsive to tungsten excitation and the emission from this element can be diffracted at the highest possible angle (around $140.2\theta^\circ$) measurable by the PW1410 spectrometer using LiF (200). The oxygen ligand and spin environment of manganese are almost constant amongst its minerals therefore comparison to a series of oxide references is a valid procedure. Work is, however, in progress to extend this $K\beta$ x-ray emission technique to other transition metals of the first row.

Conclusion

The $K\beta$ X-ray emission spectra of transition metals can be split by final state $3p3d$ exchange coupling into two components, $K\beta_{1,3}$ and $K\beta'$. Even the simplest theoretical explanation of this effect predicts that the $K\beta'/K\beta_{1,3}$ intensity ratio should increase with the number of unpaired d electrons, that is towards lower oxidation states.

A series of manganese oxides have been studied using a conventional single crystal X-ray spectrometer. A connection between valence state and the $K\beta'/K\beta_{1,3}$ intensity ratio is clearly seen.

The analytical potential of this profile change has been demonstrated using a number of manganese minerals, ores and thinly coated silicates produced during water purification.

Little difficulty was encountered in determining the dominant oxidation state of manganese in each case.

The authors wish to thank the Royal Society and the Central Research Fund of London University for grants for the purchase of equipment. S. D. G. acknowledges funding from the EPSRC and Philips. Thanks are also given to K. Nicholson for the provision of samples.

References

- HAYCOCK, D. E. & URCH, D. S. 1982. Resolution enhancement for a commercial X-ray fluorescence spectrometer. *Journal of Physics E: Scientific Instruments*, **15**, 40–43.
- NICHOLSON, K. 1989. Manganese minerals in Scotland. *Scottish Journal of Geology*, **25**, 125–142.
- PENG, G., DE GROOT, F. M. F. *et al.* 1994. High resolution manganese X-ray fluorescence spectroscopy. Oxidation state and spin state sensitivity. *Journal of the American Chemical Society*, **116**, 2914–2920.
- TSUTSUMI, K. & NAKAMORI, H. 1968. X-ray K emission spectra of chromium in various chromium compounds. *Journal of the Physical Society of Japan*, **25**, 1418–1423.
- , — & ICHIKAWA, K. 1976. X-ray Mn $K\beta$ emission spectra of manganese oxides and manganates. *Physical Review B: Condensed Matter*, **13**, 929–933.
- URCH, D. S. & WOOD, P. R. 198. The determination of the valency of manganese in minerals by X-ray fluorescence spectroscopy. *X-ray Spectrometry*, **7**, 9–12.

Index

- abyssal hills and ridge deposits, Peru Basin, 154
abyssal nodules, Pacific, 126, 132, 140, 187
abyssal plain deposits, Pacific, 124, 125, 190, 192
accretion rate
 of nodules, Peru basin, 153, 167, 174
 see also growth rates; sedimentation rates
acidic fluids, leaching by, Kato Nevrokopi, 278, 279
acidic soil, effects of, 14, 23
acmite, 330
active tectonic environment deposits, 5
 Pacific, 124, 125, 129
 northwest, 180, 183, 195–6
 South, 140
adsorption capacity, 319, 320, 321
adsorption of metals *see* metal adsorption on
 manganese oxides
adsorption series, 312, 315, 322, 324
Aitutaki–Jarvis Transect, manganese nodules, 145–9,
 166
Akan–Yunotaki deposits, 283, 284, 286–7, 288, 289,
 290, 291, 292, 293, 295, 296, 297, 298
alabandite, 7
Albian, Late, deposits, 21–2
algae
 Hokkaido, 291, 293, 295
 oxidation of ferrous iron by, 29, 34
alkali amphiboles, 330
aluminium (Al), 23
 Deception Island, 248, 249
 Indian Ocean, 202–3, 204–5
 Kato Nevrokopi, 273, 277, 279, 345
 Krivoy Rog basin, 61, 63
 Orissa, 119
 Pacific, 131, 132, 183, 188, 190, 191
aluminosilicates, Krivoy Rog Supergroup, 65–6
amphiboles, 328, 330, 334
anaerobic ocean waters, 29, 35
anoxic atmospheres, 85, 101
anoxic events, 12, 13, 19
anoxic waters, 16, 17, 119, 120, 187
 Baltic Sea, 216, 217
 dissolved elements in, 13–14, 15–16, 17, 19, 20, 22,
 34, 35, 69
 hydrothermal deposits related to, 187
 precipitation from, 29, 34, 35, 119
anoxic/suboxic diagenesis, 7
Antarctic Bottom Water, 142
anthropogenic pollution, Baltic Sea, 214, 230
antimony (Sb), 261, 288, 289
Archaean, 13, 35
 atmospheres, 12, 100–1
 banded iron formations, 29, 30, 31, 32, 33, 45, 66, 69
 deposits, 11, 14–15, 48, 49, 51, 97, 114
 hydrothermal activity, 30–1, 36
 see also Dharwar Craton, Archaean greenstone belt
 formations and deposits
Arkona Basin, 214, 216, 218
arsenic (As), 31, 134
 adsorption, 310
 Calatrava Region, 261
 Deception Island, 245, 246, 247, 248, 250
 Hokkaido, 288, 289
 Kato Nevrokopi, 274, 277
 Krivoy Rog basin, 73
 Orissa, 119, 120
 Pacific, 132, 192, 193
 Peru Basin, 168, 169
Astarte, ferromanganese deposits on, 223, 225
asymmetric growth of nodules, 173, 174
asymmetric rhythms, 73
atmosphere, 5, 14, 17, 19, 29, 33, 34, 36
 climate and, 84
 early, 91
 evolution, 10–13
 manganese depositon and, 15
 primitive, Archaean, 11, 100–1
atmospheric inputs to oceans, 31

Ba–Mn–Mg micas, 329
Bababudan Group, 91, 92
back-arc deposits, 7, 125, 180, 181, 183, 195, 196, 199
bacteria activity, Hokkaido, 286, 287
bacterial oxidation, 34, 221
Baltic Sea, 70, 71, 73, 74, 213–18, 227
 ferromanganese concretions, 214, 218–31
 pollution, 214, 227, 230
banded iron formations, 14, 16, 17, 18, 61
 Archaean, 100
 Dharwar Craton, 92, 95, 98
 formation, rate determining step, 29
 Krivoy Rog basin, *see under* Krivoy Rog basin
 Krivoy Rog Supergroup, 45, 50, 51, 64, 65, 66, 67
 manganese in, 31–2, 36, 63–4, 75, 100
 origin, 32–4, 35
 Palaeoproterozoic, 43
 precipitation mechanisms, 101
 Proterozoic, 29, 30, 31–6
banding and cyclicity, 50–61, 67
barium (Ba), 8, 10
 adsorption, 311
 Baltic Sea, 219, 224
 Calatrava Region, 256
 Deception Island, 245, 246, 247, 248, 250
 Dharwar Craton, 98
 Kato Nevrokopi, 271, 273, 274, 277, 278, 279
 Krivoy Rog basin, 49, 51, 70, 73
 Pacific, 129, 131, 132, 133
 northwest, 182, 183, 184, 189, 190, 191, 196
 Peru Basin, 168, 169
 precipitation, 87
basin nodules
 northwest Pacific, 186
 Peru Basin, 167, 173, 174
basin-centred volcanism, 18
battery grade manganese oxides, 265
bean-shaped concretions, 220, 222
Belt Sea, 214, 215, 216, 231
benthic organisms, 157, 173, 174
benthic release, 70, 71, 73, 74
beryllium (Be), Calatrava Region, 257
bicarbonate complex, transport by, 279
bicarbonate degradation, 23
biochemical mediation, 19
biogenic lifting, 172–3, 174
biogenic minerals, South Pacific, 149, 150
biogenic processes, Archaean, 97, 101

- biological productivity, Pacific, 129, 130, 142, 143, 146, 149, 150
- biological reduction of sulphate, 35
- bioproduction, 71
- bioturbation, 166, 172, 173
- Birimian Supergroup, 16, 17
- birnessite, 19, 310, 344
adsorption by, 312
Baltic Sea, 221
Calatrava Region, 256, 258, 259, 263
Hokkaido, 283, 291, 292, 293, 294–5, 296, 297
Kato Nevrokopi, 265, 266, 267, 268, 269, 272, 275, 277, 279, 345
Pacific, 128, 130, 183
Penganga Group, 108
Peru Basin, 164, 171, 172
structure, 295
- birnessite/rancieite series, 339, 343
- bismuth (Bi), South Pacific, 139
- bixbyite, 7 16, 17, 19, 24
Orissa, 118, 119
Penganga Group, 108
phase relations, 328, 329, 332, 333
- Black Sea, 13, 70, 73
- black shale deposition, 13
- Blue Jay hydrothermal deposits, 6 7, 8
- blue-green algae, 29, 34
- bog deposits, 30, 263, 284, 287
- Bonin, arcs, 178, 181, 183
- Boreal region, 227–8
- Bornholm Basin, 214, 216, 218, 231
- boron (B), northwest Pacific, 190, 191
- Bothnian Bay, 21, 214, 215, 216, 217, 218, 219, 231
- Bothnian Sea, 215, 216, 218, 219, 220, 226, 231
- bottom transport, 19, 20
- bottom waters, precipitation in, 74
- braunite, 7 15, 16, 17, 19, 24, 330
Dharwar Craton, 94
Orissa, 118, 119
Penganga Group, 108
phase relations, 328, 329–30, 332, 333
- braunite-bixbyite geothermometer, 334
- Breitgrund, 223, 225
- broom effect, 19, 20, 23
- Buckeye, hydrothermal deposits, 6 7, 9
- buoyant plumes, in dispersal of manganese, 13
- buried concretions, Baltic Sea, 217, 221, 231
- buried nodules
northwest Pacific, 180
Peru Basin, 162–3, 164, 166, 172, 173, 174
- burrowing organisms, Peru Basin, 173, 174
- buserite
Cu–Ni poor, 196
Cu–Ni rich, 183
Pacific, 128, 140, 182, 183, 186, 196
- bustamite, 7
phase relations, 328, 330, 331
- $\delta^{13}\text{C}$ anomaly, 35
- $\delta^{13}\text{C}$ values, 12, 16, 17, 19, 20, 22, 64
Dharwar Craton, 95, 97, 101
- Ca–Mg carbonate, Krivoy Rog basin, 64
- Ca-rhodochrosite, 17, 217, 221, 222, 227
- cadmium (Cd)
adsorption, 310, 311, 312, 313–24
Baltic Sea, 217–18, 230
Pacific Ocean, 132, 133, 139, 183, 189, 192, 193, 196
- caesium (Cs), 51
- Calatrava Region, 34, 253–5
Co-rich manganese mineralization, 254, 255–63
- calcite compensation depth (CCD)
Peru Basin, 166–7, 171, 172, 173, 174
South Pacific, 141, 142, 144, 146, 148, 149
- calcium (Ca)
adsorption, 310, 311, 312
Deception Island, 248, 249
fractionation, 330
Hokkaido, 283, 288, 289, 293
Indian Ocean, 202–3
Kato Nevrokopi, 270, 271, 273, 274, 277, 278, 279, 345, 346
Krivoy Rog basin, 61
Pacific Ocean, 119, 131, 132, 183, 186, 187, 188, 190, 191
Peru Basin, 168, 169
- calderite–andradite garnet, 329
- 'canutillos', Calatrava Region, 259
- carbon, derivation, 23
- carbon dioxide, 11, 12, 13, 19, 72, 73, 87
benthic release, 73
bioproduction related to, 71
climate related to, 10, 12, 84
from organic matter, 94, 97
- carbon isotope data, 22, 64, 95
- carbonates, seawater precipitation, 12
- caryopillite, 329, 332
- Casco Formation, 240, 243
- CaSiO₃–FeSiO₃–MnSiO₃ systems, 331
- CaSiO₃–MnSiO₃–MgSiO₃ systems, 331
- cation exchange, 269–71, 274, 277, 278
in rancieite, 339, 343–4
in todorokite, 256
- cauliflower-shaped nodules, Peru Basin, 162
- CdOH⁺, 311
- Ce anomaly, 6 10, 18
Baltic Sea, 219, 220
Dharwar Craton, 100
Hokkaido, 296, 297–8
Indian Ocean, 204, 206, 207, 208
Krivoy Rog basin, 50, 69
Pacific, 131, 133, 186, 187, 194
- cements, 124, 125
- Cenomanian deposits, 22
- Cenozoic
atmospheric composition, 12
deposits, 24, 29
- Central India Ridge, 200, 201
- Central Indian Basin, 204, 206, 208
- cerium (Ce)
Indian Ocean, 204, 206, 208
Krivoy Rog basin, 49
Pacific, 129, 130, 131, 132, 133, 192, 193
Peru Basin, 171
see also Ce anomaly
- Chacao Formation, 240, 243
- chalcophanite, Kato Nevrokopi, 266, 267, 268, 269, 272, 274, 275, 277, 279, 345

- Chanda Limestone Formation, 107, 108, 113
 chemical composition of minerals
 Calatrava, 256, 257, 259, 262
 Deception Island, 245, 246
 Dharwar Craton, 96, 98
 Kato Nevrokopi, 273, 275, 276, 343
 Krivoy Rog basin, 50, 51, 52, 59, 63, 64
 Peru, 168
 chemical sedimentation, 98
 chemogenic metasediments, Krivoy Rog Supergroup, 50–66
 chert-manganese oxide deposits, Penganga group, 114
 Chitura deposits, 21, 22
 chimneys, 124, 125
 Chitradurga Group, 14, 15, 114
 Chitradurga schist belt, 91, 92, 93, 101
 chromium (Cr)
 adsorption, 312
 Baltic Sea, 223
 Calatrava Region, 256, 257
 Deception Island, 245, 246
 Dharwar Craton, 98, 99
 Hokkaido, 288, 289
 Krivoy Rog basin, 49, 51, 63, 67
 Pacific, 131, 132, 133, 136, 192, 193
 Chuos Formation, 18
 Clarion–Clipperton Zone, 124, 129, 149, 171, 173, 174
 classification of sediments, 327
 climate, 84
 effects of, 14, 17–18, 23, 88, 174
 clinopyroxenes, 328, 330, 331, 334
 closed basins, 74, 187–8
 Co-rich manganese mineralization, Calatrava Region, 255–63
 Co/Zn, ratios Indian Ocean, 202–3, 205–6, 208
 coastal deposits, 14, 23
 coated talus, northwest Pacific, 187
 'cobalt chronometer', 207
 cobalt (Co), 6 8, 9 134
 adsorption, 310, 311, 312, 313–24
 Baltic Sea, 219, 221, 223
 Deception Island, 245, 246
 Dharwar Craton, 98
 Hokkaido, 288, 289, 295, 297
 Indian Ocean, 201, 202–3, 204, 206
 Krivoy Rog basin, 49, 51, 67, 73
 Orissa, 119, 120
 Pacific, 129, 131, 132
 northwest, 182, 183, 184, 185, 186, 187, 189, 190, 191, 194, 195, 196
 South, 139, 140, 141, 143, 145, 148
 Peru Basin, 168, 169
 cobalt-rich manganese mineralization, Calatrava Region, 255–63
 cold-spring deposits, Hokkaido, 286
 Collins Formation, 240, 243
 colloidal chemistry, 133–6
 colloidal manganese, 14
 commercial deposits, Baltic Sea, 221
 complexes, inorganic, in seawater, 134, 135, 136
 concretions
 Baltic Sea, 214, 218–31
 buckshot, 220, 222
 concave, 220
 spheroidal, 220
 continental breakup, deposition related to, 83, 84, 85, 86
 continental deposits, 7
 continental margins deposits, 7 23, 125, 131, 140
 continental shelf deposits, 17, 19, 20
 converging plate boundary deposits, 7
 copper (Cu), 6 8, 9 10, 31
 adsorption, 310, 311, 312, 313–24
 Baltic Sea, 217–18, 219, 223, 230
 Calatrava Region, 257, 259, 261
 Deception Island, 245, 246
 Dharwar Craton, 98
 Hokkaido, 288, 289, 295, 297
 Indian Ocean, 201, 202, 203, 204, 205, 206
 Kato Nevrokopi, 274, 278
 Krivoy Rog basin, 49, 51, 63, 73
 Orissa, 119, 120
 Pacific, 129, 132, 133, 136
 northwest, 182, 183, 184, 185, 186, 187, 189, 190, 191, 194, 195, 196
 South, 139, 140, 141, 143, 145, 147, 148, 149, 150
 Peru Basin, 153, 164, 168, 169, 170, 171, 172
 coronadite, 22
 crabs, ferromanganese coatings, 223
 Cretaceous deposits, 6 8, 9 10, 21, 87, 177, 180
 Cretaceous–Oligocene limestones, northwest Pacific, 187
 crusts, 124, 177
 Baltic Sea, 219, 220–1, 222
 formation, 304
 model for, 135
 Indian Ocean, 206, 207, 208
 Pacific, 125, 127, 129–33, 134, 135
 northwest, 180, 183, 184, 187, 196
 Peru Basin, 154, 172
 Rodriguez Triple Junction, 199, 201–9
 see also hydrogenetic deposits; hydrothermal deposits
 cryptomelane, 7 15, 17, 311, 345
 Calatrava Region, 256, 257, 258, 259, 260, 263
 Dharwar Craton, 92, 94
 Orissa, 118, 119
 Penganga Group, 108
 cummingtonite, 55
 cyanobacteria, 96
 cyclic contrast banding, 55
 cyclic uniform banding, 55
 cyclicity and banding, Krivoy Rog supergroup, 50–61, 67
 cycling of manganese and iron
 Baltic Sea, 217
 Krivoy Rog basin, 71, 74–5
 D/H ratios, 291, 293
 Daito ridge, 181, 187
 Damara Sequence, 18, 82, 84, 87, 105, 114
 Danish Straits, 214, 216, 227
 Datangpo black shale sequence, 18
 Daugava River, 222, 224
 'dead bottoms', Baltic Sea, 216–17
 decarbonation–oxidation reactions, 332, 333
 Deception Island, mineralization, 239–50

- deep-water deposits, 32
 Baltic Sea, 224
 Pacific, 123, 124–36, 141
 Penganga Group, 105, 107–8, 113–14
 Peru basin, 167, 171, 173
- degree of burial of nodules, 167
- degree of oxidation of manganese oxide, 301–2, 303, 306
- dendritic nodules, Peru Basin, 160, 161, 162–3, 164, 167, 168, 169, 170, 171, 172
- Deogiri Formation, 92, 93, 94, 95
- deoxidation reactions, 332, 333
- deposition *see* sedimentation
- deposition rate *see* accretion rate; growth rates; sedimentation rates
- depositional environments, nodule composition related to, 140
- depth of burial of concretions, 231
- deuterium enrichment, Hokkaido, 293
- Dharwar Craton, Archaean greenstone belt formations and deposits, 91
- geochemistry, 97–100
- geology, 91–4
- minerology, 94–5
- palaeobiology, 95–7
- Dharwar Supergroup, 23, 91
- diagenesis, anoxic/suboxic, 7
- diagenetic deposits
- Baltic Sea, 223, 224
- Pacific, 124, 125, 128, 130, 131, 133, 136
- northwest, 183, 186, 187, 195
- South, 140, 141, 146, 147, 148, 149, 166
- Peru Basin, 161, 164, 167, 170, 171, 172, 174
- diagenetic processes, 22, 23, 306
- diagenetic remobilization, Peru Basin, 153, 166
- differential precipitation, 17, 36, 82
- differential (selective) dissolution, 72–4, 75, 82, 85, 141, 163
- discoidal concretions, 220
- Baltic Sea, 219, 220, 222, 223, 225, 228–9, 230
- discoidal nodules, 159, 167
- DISCOL experiment, 153
- disordered graphite (graphite), 64
- disseminations, Calatrava Region, 258, 259
- dissolution, differential (selective), 72–4, 75, 82, 85, 141, 163
- distribution coefficients, 74
- dolomite, 2, 17, 22, 24
- Dongri Buzurg, deposit, 23–4
- Donimalai Formation, 92, 93, 94, 96
- dysaerobic waters, 19
- Eh**
- conditions, 124, 172, 278, 279, 293, 297
- effect of, 22, 23
- formulae for, 304, 306
- see also* redox potentials
- Eh–pH and manganese stability, 304–5
- electrochemical reactions, 23
- ellipsoidal nodules, 159, 167
- enzymatic microbial reduction, 23
- Eocene deposits, 6, 8
- EPMA analysis, Kato Nevrokopi manganese oxides, 265, 269, 271, 275, 276, 277
- equilibrium concentrations of dissolved manganese, 305
- equilibrium constants, 303–4
- erosion rates, 83
- Eu³⁺, reduction, 83
- Eu anomaly, 31, 33, 50, 67, 69, 82–3
- Baltic Sea, 220
- Dharwar Craton, 100
- euxinic sedimentation, 13, 19, 21
- evaporites, 84, 85
- event asymmetric banding, 55
- Exclusive Economic Zones (EEZ)
- Poland, 214, 222, 225
- South Pacific, 145
- United States, 124
- Fe** *see* iron
- Fe²⁺, 11, 12, 14, 23, 72
- as oxygen sink, 11, 12, 33, 36
- transport, 17
- see also* ferrous iron
- Fe₂O₃, 10, 329, 330
- Fe carbonate, 31, 34, 43, 74
- Fe hydroxide, Hokkaido, 282
- Fe oxides, 10, 21, 32, 33, 34, 36, 75
- Calatrava Region, 259
- Dharwar Craton, 96–7, 98, 101
- Pacific, 124
- Fe oxyhydroxide, 32, 73
- Baltic Sea, 217, 231
- Indian Ocean, 201
- Pacific, 128, 130
- Peru Basin, 158
- Fe silicates, 31, 74, 159, 209
- Fe sulphides, 31, 70, 73, 217
- Fe–Cu sulphides, 10
- Fe–Cu–Zn sulphide, 6
- Fe–Mn**
- crusts, 129, 304
- deposits, northwest Pacific, 187
- formations, Dharwar Craton, 97–100
- mineralization, Deception Island, 239–50
- nodules, 128, 157
- partitioning, 330
- see also* ferromanganese concretions; ferromanganese deposits; fractionation of manganese and iron
- Fe–Mn argillites, Dharwar Craton, 94, 99
- Fe–Mn carbonates**
- Dharwar Craton, 94, 97, 99
- Krivoy Rog basin, 73, 74, 77
- Fe–Mn oxides, 18, 70, 94, 95, 97, 182
- Fe–Mn oxyhydroxides, 97, 124, 220–1, 222
- Fe/Al ratio, Baltic Sea, 227
- Fe/Mn ratios *see* Mn/Fe ratios
- Fe(II)** *see* ferrous iron
- Fe(II) silicate precipitation, in BIF sediments, 74
- Fe(III) hydroxide**, Krivoy Rog basin, 64, 68, 72, 73, 74, 77
- Fe(III) oxide (ferric oxide)**, 75, 311
- ferric oxide, (iron(III) oxide)**, 75, 311
- ferroan dolomite**, 95
- ferromagnesian amphiboles**, 330
- ferromanganese concretions**, Baltic Sea, 214, 218–31

- ferromanganese deposits
 Indian Ocean, 199, 201–9
 Pacific, 123, 124–36
 Peru Basin, 172
- ferrous iron (iron(II)), 32, 34
 from oceanic ridges, 31
 in oceanic waters, 35, 36
 oxidation, 25, 29, 33, 34, 72, 73
see also dissolved iron; Fe²⁺
- ferruginous quartzites and schists, Krivoy Rog basin, 59
- ferruginous vernadite, 127
- filamentous structures, 96–7
- fjord-like basins, deposition in, 17
- flat concretions, Baltic Sea, 220
- flocculant fall out (veil effect), 19, 20
- flocculation, 14, 73
- fluvic acid, 23
- fossil deposits, northwest Pacific, 177, 183, 184, 191, 193, 196
- fractionation of manganese and iron, 29, 31–2, 34–6, 204
 Dharwar Craton, 101
 Orissa, 120, 121
 Pacific, 129, 136
see also partitioning
- fractionation sequences, 209
- fracture infillings, 124, 125
- fragment nuclei, Peru Basin, 157, 171
- Francevillian Series, 16, 17
- Franciscan Assemblage, 6 7, 8
- freshwater environments, metal adsorption in, 309–21
- Freundlich adsorption isotherm, 312, 313, 316–21, 323, 324
- friedellites, 329, 332
- fumaroles, Deception Island, 239, 240, 243, 247, 248, 249, 250
- gallium (Ga), 51, 98, 139
- Gangpur Series, 117, 118
- garnet, phase relations, 328, 330, 334
 garnet–clinopyroxene geothermometer, 334
- Gdantsev Group, 45, 46, 49, 52, 64, 67
- gelsutite, 345
- GEMINO programme, 200, 204, 205, 206, 207, 208, 209
- geothermobarometer, 334
- geothermometers, 331, 334
- Ghaap (Ghap) Group, 16, 24, 68
- Ghoriakhor–Monmunda area, India, 117, 118–21
- Gibbs free energies of formation of oxides, 302–3
- girldle type concretions, 226
- glaciation, deposition during, 17, 18, 33, 83, 85–6
- glaciogenic sediments, 84, 85
- Gleevat Group, 45, 46, 49, 52, 64, 67
- global temperatures, effects of, 12
- goethite, 127, 128, 130, 159, 221, 256, 282, 311, 341
- gold (Au), Calatrava Region, 261
- gonditic-type ores, 117, 118, 119
- Gondwana, break-up, 87
- Gotland deeps, 70, 74, 216, 218, 219, 231
- graphite, 64
- greenhouse conditions, 12, 19, 23, 87
- Groote Eylandt deposit, 19, 21, 23, 87
- ground water–seawater mixing zone, 23
- growth patterns, of ferromanganese concretions, 224
- growth rates, 136
 of ferromanganese concretions, 220, 225, 226, 230, 231
 of ferromanganese hydroxides, 207–8
 of nodules, 164–7, 184
see also accretion rates; sedimentation (deposition) rates
- Guatemala Basin, nodules, 173
- Gulf of Bothnia, 70, 214, 215, 216, 217, 219, 220, 226, 227, 230, 231
- Gulf of Finland, 214, 215, 216, 217, 218, 219, 220, 221, 223, 224, 225, 226, 227, 230, 231
- Gulf of Riga, 214, 215, 216, 218, 219, 221–2, 223, 224, 226, 227, 231
- guyots, northwest Pacific, 187
- hafnium (Hf), 98, 99, 192, 193
- halmyrolytic processes, 140
- halocline, Baltic Sea, 216, 217, 220
- Hamersley Basin, 33, 56, 66, 68, 71
- Hausgarten, 223, 225
- hausmannite, 7 16, 17, 328, 332, 333
 X-ray emission spectra, 352, 353, 355
- Hawaii rift zones, 124, 132, 133
- ³He plume, 200–1
- heat production of earth, mineralization and, 30
- hedenbergite, 328
- helium (He), 208, 248
- hematite, 16, 32, 95
 Baltic Sea, 221
 Calatrava Region, 258
 Krivoy Rog Basin, 77
 solid solutions, 328, 332
- 'hervideros', 255, 261, 262, 263
- high-temperature alteration, 33
- high-temperature hydrothermal fluids, 33, 83
- Hokkaido, manganese oxide deposits, 7 281–98
- hollandite, 7 17, 22, 118, 119
- Holocene deposits, 13, 227, 240
- Horizon Guyot seamount, 130
- hot springs
 Co-rich manganese mineralization, Calatrava Region, 255–63
 Deception Island, 239, 243, 247, 248, 250
 deposits, 7
 Hokkaido, 7 281–98
 Kato Nevrokopi, 277
- Hotazel Formation, South Africa, 16, 35, 75, 77, 85
- huebnerite, 7
- humic acid, 23
- hydrogen, Deception Island, 248
- hydrogen isotope ratios, Hokkaido, 291
- hydrogen sulphide, 13, 215, 216, 222
- hydrogenetic deposits, 6 262
 controls on element concentrations, 134–6
 Indian Ocean, 204, 206, 207, 208
 Orissa, 120
 Pacific, 123, 124, 125, 127, 129–30, 132, 133
 northwest, 180, 181, 183, 184, 185, 186, 187, 194, 195–6
 South, 140, 141, 146, 149
 Peru Basin, 161, 162, 164, 167, 170, 171, 172, 174

- hydrogenetic–diagenetic deposits, Pacific, 133
hydrogenetic–hydrothermal deposits
 Indian Ocean, 206, 208
 Pacific, 120, 125, 127, 136
hydrosphere, 5 16
 anoxic–oxic evolution, 10–13
 Archaean, 15
 early, oxygen content, 14, 91
hydrothermal deposits, 5–7, 8–9, 16, 18, 23, 35
 Calatrava Region, 254, 258, 261–2
 Deception Island, 244, 249, 250
 growth rate, 181
 Hokkaido, 281–98
 Indian Ocean, 120, 199, 200, 201–9
 Pacific, 124, 125, 128, 129–30, 131, 132, 133, 134, 136
 northwest, 180, 182, 183, 185, 186, 187, 191, 193, 194, 195–6
 South, 140, 141, 146
 see also hot springs
hydrothermal fluids, 31, 100
 high temperature, 33, 83
 low temperature, 33, 83, 196
hydrothermal inputs to oceans, 31, 33, 83, 120
hydrothermal material nuclei, Peru Basin, 157, 158
hydrothermal–hydrogenetic deposits, Pacific, 125, 127, 136
hydrothermalism, 29, 30–1, 35, 36, 88, 100
 Kato Nevrokopi, 268
hypogene veins, Kato Nevrokopi, 268, 269
- ice retreat, deposition during, 84
ice-cap, effect of changes, 18
igneous-hosted hydrothermal vein deposits, 7
Imini–Tasdremt deposits, 21, 22, 23
immobilization of iron, 29, 36
inactive ridge and rift deposits, 181, 183, 196
inauguration of manganese deposits, 14–15
Indian Ocean, 199
 ferromanganese encrustations, 199, 201–9
 nodules, 140
Inghoul–Inghoulets Supergroup, 45, 65
inorganic complexes, 134, 135, 136
interglacial periods, deposition during, 18, 19, 84, 86
intracratonic basins, deposition in, 23, 69–70
inverse-graded oolites and pisolites, 22
iridium (Ir), 139
iron (Fe), 7 9, 31
 adsorption, 312
 in anoxic waters, 17, 34, 69
 Baltic Sea, 217, 219–20, 221, 222, 223, 224, 225, 227, 228–9
 Calatrava Region, 258, 259, 260
 cycling, 74–5
 Deception Island, 248, 249
 deposition rate, in banded iron formations, 32, 33
 fractionation, 29, 31–2, 34–6
 Dharwar Craton, 101
 Indian Ocean, 204
 Orissa, 119
 Pacific, 129, 136
 Hokkaido, 282, 283, 288, 289, 293, 297
 hydrothermal, 29, 30, 33
 immobilization, 29, 36
 Indian Ocean, 201, 202–3, 204, 205, 206
 Kato Nevrokopi, 275, 278
 Krivoy Rog basin, 68, 69, 70, 71, 72, 73, 74, 77
 Krivoy Rog BIF, 67–9
 leaching, 23, 83
 northwest Pacific, 183, 184, 187, 188, 190, 191
 Orissa, 119
 oxidation, 35, 70, 82, 86
 pathways, 43
 Peru Basin, 153
 precipitation, 14, 17, 33, 35, 36, 70, 82, 263
 release, 71, 73, 77
 South Pacific, 139, 141, 148
 in suboxic water, 72, 74
 transport, 34, 73, 77
 see also banded iron formations; dissolved iron; Neoproterozoic manganese and iron formations
iron compounds *see* corresponding Fe compounds
iron and manganese deposits, distribution, 29
Iron Ore Group, 15, 23
Iron Ore Series, 117
iron/manganese ratios *see* Mn/Fe ratios
ironstones, Pacific, 132
irregular nodules, 159, 167
island-arc deposits, 5 6, 8–9
Isua iron formation, 31, 33
Iwao mine, 282, 283, 284, 285, 287, 289, 292, 294
- Jacadigo Group, 17, 18
jacobsonite, 16, 17, 118, 119, 328, 332
janggunite, 22
Japan Basin, 180, 183, 187
Japan Sea, 181, 183, 195, 196
johannsenite, 330
Jurassic deposits, 6 8, 9 21, 87, 88
- Kajika-onsen deposits, 287, 288
Kalahari manganese field, 16, 29, 35
Kalix River, 14
kanoite, 330
Karposluk mines, 266, 267, 277
Kato Nevrokopi, manganese oxides, 265–6, 268
 mineral chemistry, 269–79
 zincian rancieite, 339–46
K β X-ray emission spectra, 349, 350–5
Kiel Bay, 21, 214, 215, 216, 217, 218, 219, 222, 223, 226, 230
kinoshitalite, 329
Kirkwood Formation, 240, 241, 243
KMnO $_4$, X-ray emission spectra, 350–5
Kogane-onsen deposits, 283, 284, 287, 288, 290, 291, 292, 293, 294, 295, 296, 298
Kogane-sawa river, 284, 285
Komanoyu-onsen deposits, 283, 284, 285–6, 287, 288, 289, 290, 291, 293, 295, 297, 298
Kremenchug section, Ukraine, 44, 45, 46, 47, 57, 64
Krivoy Rog basin, 43–7
 banded iron formations, 43, 45, 47, 66
 chemogenic metasediments, 50–66, 67
 pathways of iron, silicon and manganese, 69–77
 siliciclastic metasediments, 48–50, 65, 67
 palaeoenvironmental model, 71–4
 tectonic setting, 66–7
Krivoy Rog Supergroup, 45, 46, 50, 51, 64, 65, 66, 67

- kutnohorite, 16, 19, 95, 96
 Kyushu-Palau ridge, 181, 183, 187, 196
- La anomaly, 100
 La/Ce ratios, Indian Ocean, 206, 208
 Labrador Trough, 75
 lake deposits, 5 36, 224
 land-based deposits, distribution, 29, 30, 32
 land-locked basins, modern, 70–1
 Landsort deeps, 70, 74, 216, 218
 Langmuir adsorption isotherm, 312, 313, 316, 318
 lanthanum (La), Peru Basin, 100, 168, 169
 latitude, nodule variation related to, 143–5
 Laurentia, break-up, 85
 layer-structured minerals
 Calatrava Region, 263
 Kato Nevrokopi, 266, 279
 leaching, 14, 23, 85, 120, 124, 136, 230, 345
 by acidic fluids, 278, 279
 selective, 82, 83
 lead (Pb), 31, 134
 adsorption, 311, 312
 Baltic Sea, 223, 230, 231
 Calatrava Region, 261
 Deception Island, 245, 246
 Hokkaido, 288, 289
 Indian Ocean, 202–3
 Kato Nevrokopi, 271, 274, 278, 279
 Krivoy Rog basin, 49, 51
 Orissa, 119, 120
 Pacific, 129, 131, 132, 136
 northwest, 182, 183, 184, 186, 189, 190, 191
 South, 139
 lithiophorite, Calatrava Region, 256, 258, 263
 lithium (Li)
 Calatrava Region, 257, 259
 Deception Island, 245, 246
 Krivoy Rog basin, 49, 51
 Pacific, 133, 183, 189, 190, 191, 196
 low-temperature alteration, 33, 83, 140
 low-temperature hydrothermal waters, 33, 83, 183, 196
 Lübeck–Mecklenburg Bay, 214, 215, 216, 223, 224
- maghemite, 21
 magnesium (Mg), 75
 adsorption, 311
 Deception Island, 248, 249
 Hokkaido, 288, 289
 Kato Nevrokopi, 270, 271, 274, 277, 278
 Krivoy Rog basin, 61, 63, 75
 Orissa, 119
 Pacific, 132, 182, 183, 187, 188, 190, 191
 magnetite, 21, 32, 50, 74, 77, 329
 Mamatwan-type ores, 16
 Manga Chrome, Smith Prospect, Sierra Nevada, 6 9
 manganese, 13, 15–16, 17, 18, 22, 23, 293
 in anoxic waters, 13–14, 15–16, 17, 20, 22, 69
 Baltic Sea, 217, 227
 Indian Ocean, 200, 208
 Krivoy Rog Basin, 69, 70, 71, 72, 74, 75
 levels, Palaeoproterozoic, 43
 oxidation, 70
 oxidation and precipitation, 15, 101
 Pacific, 136, 183
 in periods of greenhouse warming, 19
 release, 70, 71
 in seawater, 304–6
 solid phases, 75, 301–7
 sources, 69
 in suboxic water, 72, 74
 transport, 13–14, 18
 manganese compounds *see* corresponding Mn compounds
 manganese and iron formations, Neoproterozoic, *see under* Neoproterozoic
 manganese oxides *see* metal adsorption on manganese oxides; Mn oxides; specific minerals
 manganese pathways, Krivoy Rog basin, 69–77
 manganese/iron ratios *see* Mn/Fe ratios
 manganiferous dolomites, 24
 manganiferous sandstone, 124
 manganite, 15, 19, 108
 Pacific, 140, 146, 183
 Penenga Group, 108
 7 Å manganite
 Baltic Sea, 219, 221, 222, 223
 Pacific, 128
 10 Å manganite
 Baltic Sea, 221, 222, 223
 Pacific, 128, 140, 146, 148, 149, 150
 manganite aegirine-augites, 330
 manganite diopside-hedenbergite, 330
 manganite magnetite, 329
 mangrecite, 23
 mantle redox conditions, 11
 marginal deposits, 7 23
 Pacific, 125, 131
 northwest, 186, 187, 190, 192, 194, 195, 196
 South, 140
 Mariana arc, 128, 132, 133, 181, 183, 207
 Mariana Islands, 124
 Mariana ridge, 181
 Marshall Islands, 124, 127
 mass balance, for heavy metals, Baltic Sea, 227–30
 massive, non-directional nodules, Peru Basin, 160, 161–2, 167, 169, 170, 171
 Mavro Xylo mines, 266, 267, 271, 274, 278
 Mecklenburg Bay, 218, 228, 229
 mercury (Hg), 31, 230, 261, 274
 mesobands, 53–5, 56, 57–8, 61, 64, 65–6, 68, 73, 74, 76, 77
 Mesozoic deposits, 30, 100
 metal adsorption on manganese oxides, 309–10
 adsorption modelling, 312
 in freshwater, 309–321
 metal concentration and, 315–21
 pH and, 311–12, 314–15
 preparation method and, 310–11
 in seawater solution, 321–4
 metal adsorption series, 312, 322, 324
 metal–organic complexes, 87
 metamorphism, regional, 117, 119
 metamorphosed manganese-rich sediments, P-T-X relationships, 327–35
 metasedimentary rocks, Krivoy Rog Supergroup, 52
 metavolcanics, Krivoy Rog Supergroup, 52
 meteoric fluids, Kato Nevrokopi, 278, 279, 345
 methane, 200, 248

- Mg-Fe carbonate, Krivoy Rog basin, 64-5, 73, 74, 75
 Mg-Fe silicate, 73, 74
 microbands, 34, 50, 53, 54, 55-7, 58, 66, 68
 microbial oxidation, 70
 microconcretions, Baltic Sea, 221
 micronodules, 124, 291
 microorganisms, in control of mineralization, 294
 mid-ocean ridge deposits, 5 6, 10
 Middle Dnieper granite-greenstone terrain (MDGGT),
 43, 45, 46, 48, 69
 midplate volcanic edifices, precipitation on, 124, 125
 mineral composition, calculation of, 56-7
 mineral compositions *see* chemical composition of
 minerals
 Miocene deposits, 8 9
 mixing of waters, 23, 35, 119, 136, 224
 precipitation and, 74, 86, 120
 mixing zone model, 22, 23
 Mn *see* manganese
 Mn²⁺, 13, 14, 15-16, 23, 43, 72, 302
 oxidation, 13, 14, 33-4, 82, 278, 293, 305
 transport, 17
 Mn³⁺, 302
 Mn⁴⁺, 23, 24, 73, 279, 302
 Calatrava Region, 263
 Mn⁴⁺ oxides, 24
 Kato Nevrokopi, 266-9, 345
 mineral chemistry, 269-77
 Mn⁴⁺O₆, 274
 Mn carbonate-oxides, 333
 Mn carbonates, 7 16, 17, 20, 21, 70, 77
 formation, 14, 15, 17, 18, 19, 22, 23, 75
 metamorphosis, 14
 oxidation, 17, 23, 24
 stabilization, 331
 Mn chlorite, 329
 Mn dioxides, 301, 302-3
 Mn feroxyhyte, 127, 130, 221
 Mn oxide/hydroxides, 15, 17, 19, 24
 Mn oxides, 7 10, 14, 16, 19, 21, 23, 327
 Baltic Sea, 215, 217, 219
 Calatrava Region, 257, 258, 259
 Dharwar Craton, 94, 95, 96-7, 98, 101
 dissolution, 73
 formation, 15, 17, 22, 24
 Hokkaido, 281-98
 Krivoy Rog Basin, 77
 Orissa, 119, 120
 Penganga Group, 105
 Peru Basin, 158, 161, 162, 166, 174
 precipitation, 22, 35, 75-6, 97, 101, 120, 166
 X-ray emission spectra, 350-5
 Mn oxyhydroxide, MnOOH, 13, 20, 23, 73
 Baltic Sea, 217, 231
 disproportionation, 301, 307
 Hokkaido, 293
 Pacific, 124, 134
 solid phases, 301, 302-3, 305, 306, 307
 Mn protoferrihydrite, Baltic Sea, 221
 Mn siderite, 94, 95, 97
 Mn silicate-carbonates, 14, 15, 17, 24, 327, 332
 Mn silicate-oxide, 17
 Mn silicates, 7 16, 24, 327, 330, 331
 Mn sulphide, 7
 Mn-calcite, 16, 19, 22
 Mn-Fe-Si-C-O system, 332
 Mn-Fe-Si-O system, 332, 333
 Mn-impregnated nuclei, Peru Basin, 157
 Mn-rich dolomite, 17
 Mn-Si-C-O system, 331
 Mn/Fe ratios, 31, 34, 82
 Baltic Sea, 219, 220, 223, 224, 225, 231
 Hokkaido, 287, 297
 Indian Ocean, 201, 202-3, 204, 208
 Orissa ores, 120, 121
 Pacific, 124, 128, 129, 135
 northwest, 182, 183, 184, 186, 187, 188, 192, 193,
 196
 South, 140, 141, 147
 Peru Basin nodules, 171, 172
 MnO, 10
 X-ray emission spectra, 350-5
 MnO₂, 19, 21, 135, 293, 301, 302, 303, 306
 X-ray emission spectra, 350-5
 δMnO₂
 Indian Ocean, 201, 206, 208
 Peru Basin, 171, 172
 in South Pacific nodules, 140, 142, 146
 ΓMnO₂, 302, 303
 σMnO₂, 301, 303
 MnO₂/Mn²⁺ system, 306
 Mn₂O₃, X-ray emission spectra, 350-5
 Mn₃O₄, 73, 302, 305, 307
 MnO-SiO₂-CO₂-H₂O system, 332
 MnOOH *see* manganese oxyhydroxide; σMnOOH
 σMnOOH, 303, 305, 306
 MnSiO₃-FeSiO₃-CaSiO₃-MgSiO₃ system, 330
 MnSiO₃-MgSiO₃-FeSiO₃ system, 331
 MnSiO₃-MgSiO₃-FeSiO₃ systems, 331
 Moanda deposit, 17, 24
 mobility of metals, 23, 36, 217, 278, 279
 mobilization of metals, 141, 153, 217, 224, 230
 Molango deposit, 20, 21, 23, 24, 88
 molybdenum (Mo)
 Baltic Sea, 219
 Krivoy Rog basin, 49, 51
 Orissa, 119
 Pacific, 129, 131, 132, 133, 139
 northwest, 183, 188, 190, 191, 196
 South, 139
 Peru Basin, 168, 169
 MOR hydrothermal solutions, oxidation, 100
 morphology of concretions, 220, 221, 222
 mould formation, 171
 mounds
 Deception Island, 243, 244, 248, 250
 Pacific, 124, 125
 Murature Formation, 240, 243, 249
 mussels, ferromanganese coatings, 220, 223, 225,
 230
 Nandihalli Formation, 92, 93, 94
 Nantuo ice age, 18
 neodymium (Nd)
 adsorption, 311
 isotope values, 12
 Neogene deposits, 187
 Neogene Green Tuff Belt, hydrothermal deposits, 9

- Neoproterozoic
 banded iron formations, 31
 manganese and iron formations, 35, 81–2, 87–8
 depositional sequences, 86–7
 geotectonic setting, 83–4
 source of metals, 82–3
 tectonics and climate, 84–6
- New Krivoy Rog Group, 44, 45, 46, 47, 48, 64, 66, 69
- nickel (Ni), 6, 8, 9, 10, 134
 adsorption, 310, 311, 313–24
 Baltic Sea, 217–18, 219, 223
 Calatrava Region, 254, 256, 257, 258, 259, 260, 261
 Deception Island, 245, 246
 Dharwar Craton, 96, 98, 99
 Hokkaido, 288, 289, 295, 297
 Indian Ocean, 201, 202, 203, 204, 205, 206
 Krivoy Rog basin, 49, 51, 63, 67, 73
 in nodules, Peru Basin, 153, 164
 Orissa, 119, 120
 Pacific, 129, 131, 132, 133, 136
 northwest, 182, 183, 184, 185, 186, 187, 189, 190, 191, 194, 195, 196
 South, 139, 140, 141, 143, 145, 147, 148, 149, 150
 Peru Basin, 168, 169, 170, 171
- Niimi-onsen deposits, 283, 284, 287, 288, 289, 290, 292, 294, 295, 296, 298
- Nikopol deposits, 21, 22, 23
- niobium (Nb), 49, 51, 98, 192, 193, 256
- Nishi-Shichito ridge, 179, 183, 187, 196
- Nishikinuuma deposits, 287, 288
- nitrogen (N), 51
- nodular ores, 22, 132
- nodule nuclei, 157–9, 163
- nodules, 177
 abyssal, 126, 132, 140, 187
 buried, 162–3, 164, 166, 172, 173, 174, 180
 composition, 139–41, 168–9, 171–2
 deep-sea, 32, 167, 171, 173
 diagenetic, 128
 distribution in geological time, 29
 formation, 303
 fragmentation, 167
 Indian Ocean, 206
 lake, 36
 metal accumulation by, 324
 movement, 172–3, 174
 orientation, 167
 Pacific, 16, 124, 125, 126, 128, 129, 132, 134, 135
 northwest, 184, 187, 196
 South, 143–50
 Peru Basin, laminated, 160, 162, 163, 164, 168, 169, 170, 171, 172, 174
 Peru Basin, pillar, 160, 162, 167, 169, 170, 171
 seamount, 126
 shallow marine, 36, 167, 170, 173
 spherical, 159, 167, 173
 on topographic highs, 166, 167, 174
see also hydrogenetic deposits; Peru Basin, manganese nodules
- nonstoichiometric oxides and hydroxides, 301, 302, 307
- normal-graded pisoliths and oololiths, 22
- Northern Apennine Ophiolitic Complex, 6
- northwest Pacific manganese deposits, 177–8
 compositional characteristics, 181–96
 occurrence and distribution, 178–81
- nsutite
 Kato Nevrokopi, 265, 266, 267, 268, 269, 270, 272, 274, 275–6, 278, 279
 reduction, 305
- $\delta^{18}\text{O}$ values, 23
- $^{18}\text{O}/^{16}\text{O}$ ratios, 291, 293
- ocean basin deposits
 Pacific, 124–36, 131
see also deep-water deposits
- ocean waters, Archaean, 97
- oceanic metal fluxes, 31, 33, 35
- Ogawa-onsen deposits, 282, 287, 288
- Okhotsk basin, 180, 187
- Okinawa Trough deposits, 178, 181, 183
- Oligocene deposits, 8, 9, 21, 22, 181, 187, 196
- olivine, solid solutions, 334
- Olympic Peninsula, 5, 6
- ooliths, 22
- Ordovician deposits, 19, 21
- organic acids, leaching by, 14, 23
- organic carbon/organic matter
 atmospheric composition and, 10–13, 19
 burial, 13, 17
 and black shale formation, 13
 hydrospheric composition and, 10–13
 degradation, 23, 141, 146, 148, 149–50, 187
 oxidation, 17, 20, 21, 23, 70, 74, 77, 97
 Peru Basin, 173
 in production of Fe–Mn carbonates, 94, 97
 South Pacific, 146, 149–50
- organic productivity, 72
- organic remains nuclei, Peru Basin, 157
- organic-rich black shale deposition, 13
- organo-metal complexes, 87
- Orissa deposits, 117, 118–21
- orthopyroxene, 330, 331, 334
- Othris Zone, plate margin deposits, 5, 6
- outer shelf deposition, 87
- oxic diagenesis, South Pacific, 141, 148
- oxic waters, 29, 35, 72, 75, 166
- oxidation, 97
 bacterial, 221
 of hydrothermal solutions, 100
 microbial, 70
 pH-related, 320
 precipitation and, 82
- oxidation number (state), 301–2, 303, 306, 349–56
- oxidation potentials, 304, 306
see also Eh; redox potentials
- oxidising conditions, precipitation in, 87, 124
- oxygen
 atmospheric, 29, 73, 75, 76, 87
 banded iron formations and, 36
 control, 33, 36
 in control of sedimentation, 11, 34, 35, 71
 early, 11, 91
 tectonic processes and, 84
 deep water flux and organic productivity, 72
 dissolved, Archaean, 101
 hydrospheric

- oxygen, hydrospheric (*continued*)
 Baltic Sea, 216, 217
 in control of sedimentation, 11
 early, 91
 Pacific, 129, 130, 186
 production, 11, 101
oxygen isotope data, 22–3
oxygen minimum zone
 Baltic Sea, 217
 concentrations in, 304
 Pacific, 136, 186, 187
oxygen oases, 12, 14, 15
oxygen sinks, Fe²⁺ as, 11, 12, 33, 36
oxygenated aquatic environments, 301–7
- P–T–X* relationships, 327–35
Pacific basin deposits, 181, 187
Pacific Ocean
 deposits, 166, 180, 181
 deep water, 123–6, 127–36
 nodule compositional variability, 141, 143–50
see also northwest Pacific manganese deposits
palaeobiology, Sandur schist belt, 95–7
Palaeoproterozoic, 69
 banded iron formations, 30, 31, 33, 43, 66, 71, 72
 deposits, 29, 34, 35
 hydrothermalism, 31
 iron and manganese formations, 82, 83, 86
Palaeozoic
 carbon dioxide values, 13
 climate, 12
 deposits, 19, 23
Pangaea, break-up, 87, 88
Parece Vela Basin deposits, 181, 187
particulate manganese, 14, 19, 304
 Baltic Sea, 217, 227
partitioning, 74, 329–31
see also fractionation of manganese and iron
pathways of elements
 Baltic Sea, 217, 218, 231
 Krivoy Rog basin, 43, 69–77
pavements, 124
Panganga Group, 18, 19, 87, 105–7
 deep-water deposits, 105, 107–8, 113–14
 siliceous grey limestones, 108–113
penny-shaped concretions, 220, 221
Permian oceans, 35
Peru Basin, manganese nodules, 153–7, 166–74
 composition, 163–4
 growth rates, 164–7, 170, 171–2, 174
 internal growth structures, 160
 nuclei, 157–9, 163
 size distribution, 163
 surface features, 159–60, 167
petrogenetic grids, 331–4
pH, 304–5, 306
pH-related adsorption of metals, 310, 311–12, 314–15
pH-related deposition of sediments, 23, 74, 278, 346
Phanerozoic, 12, 36, 73
 atmospheric composition, 12, 19, 34
 deposits, 5 19–23, 29, 34, 35, 81, 82
 oceans (seawater), 101, 120, 121
phase relations, 74, 329–34
 of manganese in aquatic environments, 301–4, 305–7
 Philippine basin deposits, 181, 187
 Philippine Sea deposits, 181, 183
 Philippine Sea Plate deposits, 196
phosphorus (P)
 Baltic Sea, 219, 221, 224, 225
 Indian Ocean, 202–3
 Krivoy Rog basin, 63, 73
 Orissa, 119
 Pacific, 131, 132, 133
 northwest, 183, 186, 187, 192, 193, 196
photic zone, precipitation in, 74, 75, 76
photo-oxidation, 14, 29, 33–4, 72, 73, 82
photoreduction of particulate manganese, 73
photosynthesis, 36
 Archaean, 97
 atmospheric composition and, 10–13
 hydrospheric composition and, 10–13
 precipitation and, 101
 Proterozoic, 35
photosynthetic oxidation, 29, 33, 34, 72, 73
phyllomanganate, 339
Pindos Geotectonic Zone, 5 6
pipe structures, Hokkaido, 291, 295
pisoliths, 22
pisolitic beds, Calatrava Region, 258, 259, 260–1, 263
plankton, Baltic Sea, 217
plateaus, northwest Pacific, 187, 196
platinum (Pt)
 Pacific, 129, 131, 132, 133
 northwest, 183, 184, 186, 187, 189, 191, 193, 196
Pleistocene deposits, 7 181, 223
Pliocene deposits, 196
Pliocene–Quaternary mineralization, Calatrava
 Region, 255–63
‘point of reversal’, 171
Polish Exclusive Economic Zone, 214, 222, 225
pollution, Baltic Sea, 214, 227, 230
polymetallic sulphides, 209
polyoblate nodules, 167
pore water, manganese concentrations in, 306, 307
potassium (K)
 Deception Island, 248
 Hokkaido, 288, 289
 Kato Nevrokopi, 271, 274, 277, 278, 279
 Krivoy Rog basin, 61, 63
 Orissa, 119
 Pacific, 132, 139, 188, 190, 191
Pranhita Sandstone Formation, 107
Pranhita–Godavari Valley, 105–6
Precambrian, 46
 atmosphere-ocean system, 11
 deposits, 29, 31, 34, 35, 82, 83
 oceans, 71, 121
precipitation
 in anoxic waters, 29, 34, 35, 119
 differential, 17, 36, 82
 during marine regressions, 20
 Eh and, 22, 23, 293
 hydrogenous, Indian Ocean, 208
 in low oxygen waters, 136
 mechanisms, 72–4
 in mixing zones, 22, 74, 86
 in oxic waters, 17, 33
 in oxidizing conditions, 82, 87

- precipitation (*continued*)
 pH and, 23, 74, 278, 346
 photochemical, 33
 photosynthetic, 101
 redox potentials and, 91, 101
 in reducing waters, 22, 29, 75
see also sedimentation
- present day deposits, 5
- preservation potential, 88
- pressure–temperature–bulk composition (*P–T–X*)
 relationships, 327–35
- Proterozoic, 12, 24, 36, 88
 atmosphere, 12, 34
 banded iron formations, 31–6
 deposits, 6 29, 30, 31, 33, 34, 35, 91
 Krivoy Rog basin, 82
 Orissa, 118, 120
 development, 15–19
 hydrothermal activity, 13, 36
 oceans, 35, 120
 Penganga Group *see* Penganga Group
- psilomelane, 7 16, 24, 94, 108
- Pyrgi mines, 265, 266, 267, 274, 277
- pyrite, 17, 20, 29, 35, 36
 Cu-rich, 6
- pyritiferous Mn carbonate, 21
- pyrolusite, 7 15, 16, 22, 24, 333
 Dharwar Craton, 94
 formation, 345
 Hokkaido, 282, 283, 291, 292, 293, 295, 297
 Kato Nevrokopi, 274, 275, 278, 341, 345
 Mexico, 7
 Orissa, 118, 119
 Pacific, 128, 130, 183
 Penganga Group, 108
- pyrosmalite, 332
- pyroxenes, 330, 331, 334
- pyroxenoid phase, free energy, 331–2
- pyroxenoids, 331, 334
- pyroxmangite, 328, 329, 330, 331–2, 334
- Quaternary deposits, 153, 166, 180, 187, 215, 222
- rancieite
 formula of, 339, 344
 Hokkaido, 283, 291, 292, 293, 294–5, 297
 Kato Nevrokopi, 267
see also zinc rancieite
- Rapitan Group, 83, 87
- Rapitan iron formation, 84
- rare earth elements, 6 83, 86–7
 Baltic Sea, 219, 220
 Calatrava Region, 256
 Dharwar Craton, 100
 Hokkaido, 290, 296, 298
 Indian Ocean, 204, 206, 207, 208
 Krivoy Rog basin, 50, 67, 69
 Pacific, 132, 133, 136
 northwest, 183, 184, 186, 192, 193, 194, 196
 Peru Basin nodules, 164, 170, 171, 172
 Sandur schist belt, 98
- Recent manganese deposits, Hokkaido Japan,
 281–98
- Red beds, 36, 101
- redox boundary
 Baltic Sea, 217
 Guatemala Basin, 172
 Peru Basin, 171, 173, 174
- redox characteristics, sediments and, Baltic Sea, 217
- redox potentials, 304, 306
 Archaean oceans, 100
 deposition related to, 91, 101
 effects of, 29, 75, 217, 278, 296–7
 hot springs, Hokkaido, 296–7
 Pacific, 75, 129, 131
 Phanerozoic, 101
 transport related to, 91
see also Eh
- redox redistribution, 77
- reducing conditions
 Archaean and Proterozoic, 31
 Neoproterozoic, 85, 86
 precipitation in, 22, 29, 75
- regional metamorphism, 117, 119
- regional variability, of nodule composition, 139, 140, 141
- regression, deposition during, 19, 20, 21, 22, 34, 84
- regression–transgression cycles, 12, 18, 23, 66
 deposition during, 86, 114
- remnant arc deposits, Pacific, 180, 183, 187, 196
- remobilization of manganese, 224
- replacement of rocks, 124, 125
- ‘reverse diadochy’, 278
- rhodite, Orissa, 118
- rhodochrosite, 17, 19, 20, 21, 22
 Baltic Sea, 217
 Kato Nevrokopi, 265, 273, 274, 275, 278, 345
 Krivoy Rog basin, 74, 75
 northwest Pacific, 183
 phase relations, 328, 329, 330, 332, 334, 345
- rhodonite, 7
 phase relations, 328, 329, 330, 331, 334
 X-ray emission spectra, 352, 353, 355
- rhodonite–pyroxmangite geothermobarometer, 334
- ridges, nodules in, Peru Basin, 165, 167, 173
- riebeckite, 85
- rift-related deposits, 83, 195–6
- rifted basins
 deposition in, 17, 19, 23
 dissolution in, 85
- Rio das Velhas Supergroup, 14, 15
- ripidolite, Dharwar Craton, 96
- river water, flocculent fallout from, 19
- riverine inputs, 31, 224, 227
- riverine transport, 14, 18, 21, 30, 67, 220
- Rodinian, 88
- Rodriguez Triple Junction, ferromanganese
 encrustations, 199, 200, 201–9
- Ronald Formation, 240, 243
- roplesite, 55
- rubidium (Rb)
 Calatrava Region, 256
 Deception Island, 245, 246
 Dharwar Craton, 98
 Krivoy Rog basin, 49, 51
 Pacific, 192, 193
- $\delta^{34}\text{S}$ values, 12, 64
- saline waters, 19, 85

- saline waters (*continued*)
 Baltic Sea, 216, 223
 sedimentation from, 19, 20, 22, 23, 85
 solubility in, 85, 86, 87, 88
see also seawater
- Sandur schist belt, 91–4, 95, 101
see also Dharwar Craton, Archaean greenstone belt
 formations and deposits
- Santa Cruz Formation, 17, 18
- Sat Nala Shale Formation, 107
- Sausser Group, 16, 17, 23, 87, 117, 120
- Saxagan Group, 45, 46–8, 49, 50, 52, 53, 54, 55, 57, 58,
 60, 61–3, 64, 65, 66, 67, 68, 69, 71
- scandium (Sc)
 Baltic Sea, 221
 Deception Island, 245, 246
 Dharwar Craton, 98, 99
 Krivoy Rog basin, 49, 51
 Pacific, 192, 193
- scavenging, 134, 135, 136, 186, 231, 263
- schallerite, 332
- Schleimul[']nde, 223, 225
- sea floor manganese deposits, 177
- sea floor spreading, 10
- sea-levels, 83
 changes, 12, 18, 19, 23
 highstands, 17, 22
 rise, deposition during, 84
- seamount-hosted deposits
 Pacific, 124, 126, 130, 131, 135
 northwest, 180, 183, 184, 186, 187, 190, 192, 194,
 196
 South, 140
 Peru Basin, 154, 165, 167
- seasonal variations
 Baltic Sea, 216, 217, 218
 growth rate of concretions related to, 225
- seawater
 form of elements in, 133–6
 mixing with fresh water, 23, 35
 oxygen content, Pacific, 129, 130, 135
 reactions, 7, 12, 17, 120, 134, 224
 redox potential, 75, 129, 131, 304
 as source of manganese, 15, 19, 120
see also saline waters
- sediment classification, 327
- sediment nuclei, Peru Basin, 157
- sediment pore water precipitation, 124
- sediment stiffness, Peru basin, 166
- sediment-hosted hydrothermal vein deposits, 7
- sedimentary processes, 5
- sedimentation (deposition)
 anaerobic, 21
 chemical, 71
 climate and, 88
 controls on, 11
 during inter-glacials, 84, 86
 dysaerobic, 21
 euxinic, 13, 19, 21
 glaciation and, 84
 model, 5
 in oxic waters, 13
 in reducing conditions, 22, 75
 regression and, 19, 21, 22, 83, 86
 related to redox potentials, 91, 202
 in shallow waters, 5, 15, 19, 21, 22
 tectonism and, 84–5, 86, 87, 88, 114, 119, 120
 transgression and, 33, 34, 84, 86, 87, 114
see also precipitation
- sedimentation (deposition) rates
 Baltic Sea, 215, 219–20, 221, 227
 iron, 32, 33, 34, 68
 manganese, 32, 142, 227, 297–8
 silica, 68
 South Pacific, 149
see also accretion rates; growth rates
- selective (differential) dissolution, 75, 82, 141
- selective leaching, 23, 82, 83
- SEM analysis, Kato Nevrokopi manganese oxides,
 265, 266, 269–70, 272, 344–5
- Semail Nappe deposits, 7, 10
- semi-liquid layer, Peru Basin, 153, 173
- shallow waters
 deposits, 5, 15, 19, 21, 22, 36, 70, 120
 nodules, 36, 167, 170, 173
 precipitation in, 32, 34, 35
- Shatsky rise, 181, 183, 196
- shelf-related deposits, 17, 19, 20, 82, 87, 88
 Orissa, 114, 119
 Penganga Group, 105
- Shikoku basin, 180, 181, 187
- Shimoga schist belt, 91, 92, 101
- shoreward bottom transport, 19, 20
- Si/Al ratios, Indian Ocean, 204–5, 208
- siderite, 35, 74
- silica
 coating of iron oxyhydroxide, 73
 concentrations, 33, 36, 74
 deposition, 33, 34, 63, 67, 68, 73
 dissolved, 72, 74
 hydrothermal, 29
 mobility, 57
 precipitation, 72, 73, 74
- silicate formation, in banded iron formations, 73
- siliceous microfossils, Peru Basin, 162, 164
- siliceous sedimentation, South Pacific, 149
- siliciclastic metasediments, Krivoy Rog Supergroup,
 48–50, 51, 65, 67
- silicon (Si), 131, 132
 in Archaean formations, 100
 dissolved, 68, 69, 77, 100
 Indian Ocean, 202–3, 204–5
 Kato Nevrokopi, 278
 Pacific, 139, 183, 188, 190, 191
 pathways, 43
 Krivoy Rog basin, 69–77
 precipitation, 100
 sources of, in Krivoy Rog BIF, 67–9
- silver (Ag)
 adsorption, 311
 Calatrava Region, 261
 Hokkaido, 288, 289
 Kato Nevrokopi, 271, 278
 Pacific, 139, 189, 192, 193
- size distribution of nodules, Peru Basin, 163
- Skelevat Group, 45, 46, 48, 49, 52, 57, 64, 66, 67, 69,
 70, 76
- Skelevat Magnetite deposit, 57, 58, 61

- slabs, Baltic Sea, 219
- sodium (Na)
Hokkaido, 288, 289
Indian Ocean, 202–3
Kato Nevrokopi, 274, 277, 278, 279
Krivoy Rog basin, 61
Orissa, 119
Pacific, 132, 183, 188, 190, 191
- solubility
glaciation affecting, 85
of manganese, 23, 136
in saline waters, 85
- sources
of elements, Baltic Sea, 217, 220, 227, 230
of iron, 67–9, 82–3, 133
of manganese, 13–14, 82–3, 133
- South Pacific, nodule compositional variability, 143–50
- South Thomas deposits, 6, 7, 8
- Southeast Indian Ridge, 200, 201
- Southwest Indian Ridge, 200, 201
- S.P. Lee Guyot seamount, 130
- spessartine, 118, 329
- spreading centres, 183, 196
deposits, 7, 88, 100, 124, 125
Indian Ocean, 199–209
- spring aprons, Calatrava Region, 258, 259, 260, 263
- $^{87}\text{Sr}/^{86}\text{Sr}$ values in carbonates, 12
- stabilization of manganese compounds, 331, 346
- stagnant oceans, 35, 70, 71, 85, 86
- statistical selection of nodules, 173, 174
- stoichiometry of oxides and oxyhydroxides, 301, 302, 307
- stratabound deposits, 5, 7
Calatrava Region, 263
Pacific, 124, 125, 128, 129, 130, 132, 135
- stratified basins, 13, 74
- stratified waters, 12, 19, 21, 22, 35, 71
Baltic Sea, 216, 225
- strontium (Sr)
adsorption, 311
Calatrava Region, 256, 257, 259
Deception Island, 245, 246
Dharwar Craton, 98
Krivoy Rog basin, 49, 51
Pacific, 129, 132, 189, 190, 191
Peru Basin nodules, 168, 169
- Sturtian glacial events, 12
- subaerial volcanic series, Deception Island, 240–1, 243
- subduction-related deposits, 5, 6–7, 8–9, 32
- submarine volcanic deposits, 180, 183, 195, 196, 239–50
- suboxic
diagenesis, 9, 73, 77
marine sediments, 71
waters, 33, 34, 72, 73, 75, 186–7
iron and manganese in, 72, 74–5
as source of dissolved minerals, 69
- sulphate concentrations, precipitation related to, 29, 36
- sulphides
in banded iron formations, 73
in seawater, 35, 136
- sulphur, 12, 21, 35
Hokkaido, 283
Krivoy Rog basin, 63
northwest Pacific, 192, 193
- sulphur isotopic composition, Krivoy Rog basin., 64, 65
- supercontinental breakup (rifting), 83, 84, 85, 86, 88
- supergene mineral assemblages, Kato Nevrokopi, 268, 273
- supergene processes, 17, 23–4, 92, 99, 119
- supra-subduction zones, 7, 10
- surface charge on metal oxides, 311, 312, 315
- surface nodules, Peru Basin, 162, 163, 164, 165
- swamp deposits, Calatrava Region, 263
- tabular nodules, Peru Basin, 159, 167
- takenelite, 339, 342
- tantalum (Ta), 98
- Taojiang deposit, 19, 21, 23
- Tartana mines, 266, 267
- tectonic settings, 5–7, 8–10
- tectonism, 5
atmosphere and hydrosphere composition related to, 11–12
Calatrava Region, 263
climate related to, 84–6
and heat production, 30
sedimentation related to, 84–5, 86, 87, 88
- Telefon Formation, 240, 243, 249
- temperature sensors, 331
- tephroite, 7, 328, 329, 330, 334
- terrestrial deposits, 29
- terrestrial sources of manganese, 14, 15, 22
- terrigenous inputs, 69
Baltic Sea, 227
- terrigenous sedimentation, Sandur schist belt, 98, 99, 100
- Tertiary deposits, 10, 181
- thermal subsidence, 84, 86, 87
- thorium (Th), 6, 8, 9
Baltic Sea, 221
Dharwar Craton, 98, 99, 100
northwest Pacific, 183, 192, 193
- tidal activity and sedimentation, 20
- titanium (Ti)
Krivoy Rog basin, 61, 63
Pacific, 132, 134, 139
northwest, 183, 186, 187, 188, 190, 191
- Toarcian deposits, 13, 19
- todorokite, 19
Baltic Sea., 221
Calatrava Region, 256, 258, 259, 263
Hokkaido, 283, 291, 292, 293, 294–5, 296, 297
Kato Nevrokopi, 265, 266, 267, 268, 269–72, 273, 274, 275, 276–7, 341, 345
Pacific, 128, 130, 131, 140, 182, 183, 196
Penganga, 108
Peru Basin nodules, 164, 171, 172, 174
structure, 295
- todorokite pseudomorphs, 163, 278
- Tokachidake deposit, 283, 286, 289, 290, 292, 298
- Tonga island, hydrothermal deposits, 8
- Tonga volcanic arc, 124, 132
- topographic highs
deposits, northwest Pacific, 177, 181, 183, 184, 187, 196
nodules on, Peru basin, 166, 167, 174
- total dissolved manganese, Indian Ocean, 200, 208
- transgression, 13, 17, 19, 20, 22, 23, 29, 35
and banded iron formations, 34, 35

- transgression (*continued*)
 deposition during, 21, 33, 34, 84, 86, 87, 114
 manganese and iron formations related to, 83
 transgression induced oxygen deficient water, 22
 transgression–regression cycles, 12, 18
 deposition during, 23, 66, 86, 114
- transport
 by metal-organo complexes, 87
 of iron, 17, 73, 224
 of manganese, 13–14, 17, 18, 19, 224, 279
 related to redox potentials, 91
- Transvaal basin, 68, 91, 101
 Transvaal iron formation, 35
 Transvaal Supergroup, 16, 24, 36, 84, 85, 87, 105, 114
 Triassic deposits, 6 9
 Troodos Massif, 7 10
 tungsten (W), 139, 192, 193, 245, 246
 tunnel-structured minerals
 Calatrava Region, 256, 263
 Kato Nevrokopi, 266, 270, 271, 274, 278, 279
 Turonian deposits, 13, 22
- ultra violet radiation, oxidation of iron by, 14
 United States, Exclusive Economic Zone, 124
 upward Mn-bearing fluid expulsion, 5
 upwelling
 and banded iron formation, 34, 69
 sedimentation during, 33, 34, 35, 87, 114, 119, 120
- uranium (U), 6 8, 9
 Dharwar Craton, 98, 99
 northwest Pacific, 183, 192, 193
 Úrkút, deposits, 19, 21, 23, 24, 88
- Valu Fa back arc system, 124, 132
- vanadium (V)
 Calatrava Region, 256, 257, 259
 Deception Island, 245, 246
 Dharwar Craton, 98, 99
 Krivoy Rog basin, 49, 51
 Orissa, 119
 Pacific, 129, 131, 132, 133, 134, 139
 northwest, 183, 184, 189, 190, 191
- Varangian glacial events, 12
 veil effect, 19, 20, 23
 vein infillings, 124
 vein-type hydrothermal deposits, 5 7
 veins, Calatrava Region, 258, 259
- vernadite
 Baltic Sea, 221
 Fe-poor, 182–3, 187, 221
 Fe-rich, 182, 183, 187, 221
 Fe-, Pacific, 130
 Hokkaido, 283, 291, 292, 295
 Indian Ocean, 201
 Pacific, 140, 181, 182, 184, 186, 187
- volcanic arc deposits, 124, 125, 129, 131, 199
 volcanic material nuclei, Peru Basin, 157
 volcanic structures, Deception Island, 239–50
 volcanic zones, Japan, 281–2
 volcanically active ridge and rift deposits, 140, 195
 volcanically inactive ridge deposits, 187
 volcanoclastic input, 67
 volcanoclastic sedimentation, Sandur schist belt, 98, 99
 volcanism, 5 12, 18, 30–1
- volcano-thermal inputs, 69
 volcanogenic-hydrothermal deposits, Calatrava
 Region, 261–2, 263
 vredenburchite, Orissa, 118, 119
- wad deposits
 Calatrava Region, 258, 259, 263
 Hokkaido, 284, 285, 286, 287, 293–4
- water balance, Baltic Sea, 216
- water depth
 and deposits, northwest Pacific, 180, 186, 194
 nodule composition related to, Pacific, 140, 141, 147
 nodule shape related to, Peru Basin, 161
 sedimentation and, Baltic Sea, 215
- water treatment plant
 oxides from sand filters, 313–21
 X-ray emission spectra, 349, 352, 354, 355
- weathering, 5 14, 19, 22, 23, 24, 119
 chemical, 67, 69
 Kato Nevrokopi, 268, 269, 278–9
 and oceanic silica flux, 33
- X-ray emission spectra, 349, 350–5
 XRD analysis, manganese oxide, 266, 267, 269, 277
 Yap Arc, 124, 128, 132, 133, 183, 207
 Yeswanthanagar Formation, 92–3, 94, 99
 Ytterbium (Yb), Pacific, 139, 192, 193
 yttrium (Y)
 Baltic Sea, 219
 Calatrava Region, 256
 Deception Island, 245, 246
 Dharwar Craton, 98
 Krivoy Rog basin, 49, 51
 Pacific, 132, 136
 northwest, 183, 184, 189, 190, 191
- Yukomanbetu-onsen deposits, 283, 287, 288, 289, 290,
 291, 292, 293, 294, 295, 296, 297, 298
- zero point of charge, pH_{zpc} , 310, 315
 zinc (Zn), 6 9, 31, 134
 adsorption, 310, 311, 312, 313–24
 Baltic Sea, 219, 223, 225, 230, 231
 Calatrava Region, 256, 257, 259, 261
 Deception Island, 245, 248, 249
 Dharwar Craton, 98, 100
 Hokkaido, 288, 289, 295, 297
 Indian Ocean, 201, 202–3, 205
 Kato Nevrokopi, 270, 274, 277, 278, 279, 345
 Krivoy Rog basin, 49, 51, 63, 73
 Orissa, 119, 120
 Pacific, 129, 131, 132, 133, 135, 136, 139
 northwest, 183, 186, 189, 190, 191, 196
 Peru Basin nodules, 168, 169
- zincian rancieite, 339, 340–1
 chemical composition, 342–4, 345
 formation, 345–6
 structure, 342, 344–5
- zirconium (Zr)
 Calatrava Region, 256
 Dharwar Craton, 98, 99
 Krivoy Rog basin, 49, 51
 Pacific, 139, 190, 191
 Peru Basin nodules, 168, 169
- Zn/Fe ratios, Indian Ocean, 202–3, 205–6, 208
 ZnOH^+ , 311

